MANCHESTER 1824

The University of Manchester

EXPERIMENTAL AND COMPUTATIONAL STUDY OF THE BEHAVIOUR OF FREE-CELLS IN DISCHARGING SILOS

A thesis submitted to the University of Manchester for the degree of

Doctor of Philosophy

in the Faculty of Engineering and Physical Sciences

2011

STUART ANDERSON MACK

SCHOOL OF CHEMICAL ENGINEERING AND ANALYTICAL SCIENCE

Contents

LIST OF TABLES

NOMENCLATURE

A	orifice area
A^*	area of the orifice after the removal of the empty annulus in equation 2.18
B	parameter defined in equation 2.3
b	rectangular orifice width
c	cohesion
c'	constant in equation 2.25
C_N	normal damping coefficient
C_T	tangential damping coefficient
d	particle diameter
d_{char}	characteristic dimension of particles
D_c	container diameter in equation 2.15
D_h	hydraulic mean diameter
D_h^*	hydraulic mean diameter after the removal of the empty annulus in 2.18
D_0	diameter of circular orifice
Ð	Walkers distribution factor
f	friction coefficient between grain and container wall
F_{Fags}	friction force at and after gross sliding
F_{Fbgs}	friction force before gross sliding
F_N	normal contact force
F_{ND}	normal damping force
F_{NE}	normal elastic force
F_T	tangential contact force
F_{TD}	tangential damping force
F_0	function value of hopper in equation 2.24

F_p function value of particles in equation 2.24

g acceleration due to gravity

h initial particle height on ramp

H height of silo

I moment of inertia

k parameter found to vary between 1.3 and 2.9

k_N normal spring stiffness

k_s maximum stiffness experienced in the system

k_T tangential spring stiffness

K Janssen constant

l rectangular orifice length

L_r ramp length

m particle mass

p_s horizontal pressure of grains in equation 2.1

r_0 critical radius in neighbourhood lists book keeping scheme

r_i interaction cut-off ration in neighbourhood lists book keeping scheme

$\dot{r}$ linear velocity vector

$\ddot{r}$ linear acceleration vector

R particle radius

R_n random number

S length of side of a container in equation 2.1; shape factor in equation 2.15

t time

u horizontal velocity; dimensionless coefficient of rolling friction

v vertical velocity

v_{cr} vertex radius of polygon particles

v_T tangential component of relative velocity between the particles

w container thickness

W mass flow rate

x depth of the slice from the top surface in equation 2.1

y_c distance the particle comes to rest on the flat from the bottom of the inclined ramp

z vertical distance parameter

$Z'(d_{eff})$ function in equation 2.25

Greek letters

α hopper half angle; azimuth angle of polygon particle

α^* angle between stagnant zone boundary and vertical

β elevation angle of polygon particle

γ specific weight of the material in equation 2.1

γ_{CD} coefficient of critical damping

δ_N normal displacement between two particle centres *i* and *j*

δ_R constant in equation 8.11

δ_T tangential displacement between the surfaces of the spheres since their initial contact

δ_{Tmax} maximum tangential displacement until sliding occurs

θ static angle of repose between the container sides; angle of inclination of ramp

θ_H hopper angle from the horizontal

θ_0 static angle of repose without container sides

$\dot{\theta}$ angular velocity vector

$\ddot{\theta}$ angular acceleration vector

λ parameter in equation 3.17

μ coefficient of sliding friction

$\mu_{r,pp}$ particle-particle rolling friction (mm)

$\mu_{r,pw}$ particle-wall rolling friction (mm)

$\mu_{s,pp}$ particle-particle sliding friction (mm)

$\mu_{s,pw}$ particle-wall sliding friction (mm)

μ_s kinetic angle of repose

ξ function of particle diameter in 3.17

ρ_b bulk density

ρ_p particle density

ρ_v concentration of voids

σ normal stress

τ shear stress

Φ internal angle of friction

ϕ_d angle between stagnant zone boundary and horizontal

ω angular velocity

ABSTRACT

EXPERIMENTAL AND COMPUTATIONAL STUDY OF THE BEHAVIOUR OF FREE-CELLS IN DISCHARGING SILOS

The University of Manchester

This study aims to deduce an appropriate shape and density for an electronic free-cell that could be placed into a silo so that position and other desired physical parameters could be recorded.

To determine how density and shape affects the trajectory and displacement of free cells, the trajectory and displacement of cylindrical, cuboid and triangular prism free-cells of equivalent volume was investigated in a discharging quasi 3D silo slice. The free-cells were placed at twelve different starting positions spread evenly over one half of the 3D slice. Tests were conducted using a monosized batch of spherical particles with a diameter of approximately 5 mm. Tests were also conducted in a binary mixture consisting of particles of different sizes (5 mm/4 mm) and the same density (1.28 g/cm^3) and a binary mixture consisting of particles of different size (6 mm/5 mm) and different densities (1.16 g/cm^3/1.28 g/cm^3).The rotation of the free cells was also briefly discussed.

Computer simulations were conducted using the Discrete Element Method (DEM). The simulation employed the spring-slider-dashpot contact model to represent the normal and tangential force components and the modified Euler integration scheme was applied to calculate the particle velocities and positions at each time step. One trial of each of the metal and plastic, cylindrical, cuboid and triangular prism free cells was compared with the average of three experimental trials. The trajectory and displacement of a representative particle positioned at the same starting position as the free cell was also obtained from DEM simulation and compared with the path and displacement of each of the free cells to determine which free cell followed the particle most closely and hence to determine a suitable free cell that would move with the rest of the grains.

Spherical particles are idealised particles. Therefore tests were also conducted with a small number of polyhedral particles, to deduce their flow rate and the critical orifice width at which blockages were likely to form. Simulations were also conducted to test the feasibility of the DEM in modelling the behaviour of these polyhedral particles.

Results indicate that for a free cell to move along the same trajectory and have the same displacement and velocity as an equivalent particle in the batch it should have a similar density to the majority of the other particles. A cylindrical free cell of similar density to the particles was found to follow the path of the representative particle more closely than the cuboid or triangular prism. Polyhedral particles were found to have a greater flow rate than spherical particles of equivalent volume.

Stuart Anderson Mack **PhD** **June 2011**

DECLARATION

No portion of the work referred to in this thesis has been submitted in support of an application for another degree or qualification at this or any other university or other institute of learning.

COPYRIGHT STATEMENT

ACKNOWLEDGEMENTS

I would like to very much thank my supervisor Professor Colin Webb for his support and patience throughout this project. I would also like to thank Professor Trevor York for his support and encouragement and I am also grateful to the other members of the Wireless Sensor Networks for Industrial Processes research group in the School of Electrical and Electronic Engineering for making suggestions and providing encouragement in the early stages of the project. I would also like to thank very much Dr Paul Langston at the University of Nottingham for providing his DEM code and also for his patience and understanding during the time I was learning about the DEM and analysing the program code.

Thanks also to Professor Richard Williams from the Institute of Particle Science and Engineering at the University of Leeds and Dr. Esther Ventura-Medina from the School of Chemical Engineering and Analytical Science at the University of Manchester for examining my thesis.

I would also like thank my family for their support and encouragement throughout the project and other students who have worked in the laboratories in the Satake Centre who have been friendly and helped to make the research process an enjoyable experience.

Introduction

1 Introduction

1.1 The context of the project

Granular materials are present in many forms. Granular materials can range in size from flour in bread mills, up to large granite stones in quarries. The efficient storage and transportation of granular materials is becoming increasingly important as industry has to compete in an ever tougher global marketplace.

Industrial scale food production uses large quantities of natural granular materials that may be stored in grain silos or in grain mountains (Figure 1.1). Sufficient storage of natural granular materials is paramount, as if the material spoils or becomes contaminated then it could be rendered useless. Insufficient storage conditions can cause wheat grains to become mouldy, making people or animals ill if they consume it.

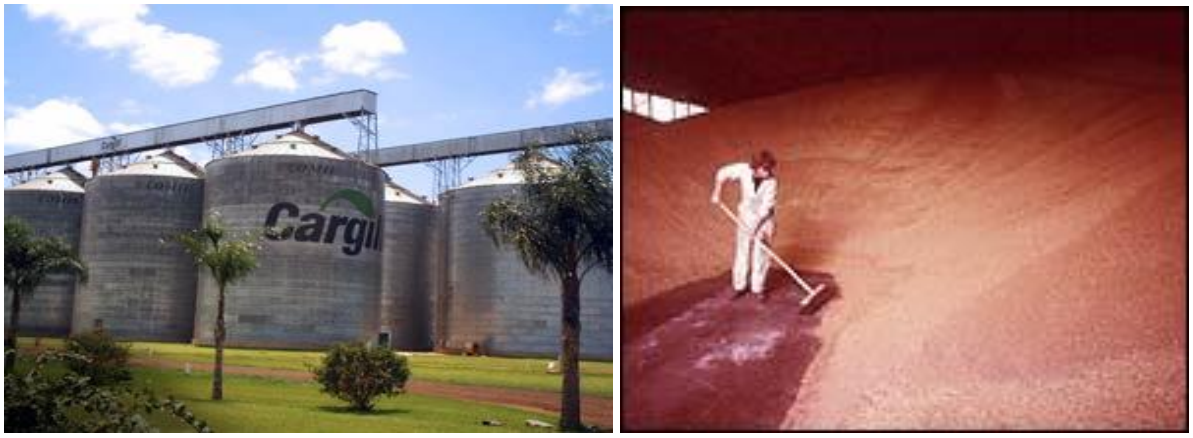

Figure 1.1: a) grain silos; b) grain mountain
http://www.wsn4ip.org.uk/documents/toxicwheat.pdf

This research work is part of a larger, EPSRC funded, project investigating Wireless Sensor Networks for Industrial Processes (WSN4IP). This larger project has the long term aim of developing a system to "scatter" large numbers of small capsules into industrial processes such that they can sense their environment and transmit data to a host computer, possibly even responding to commands so as to influence the process. These capsules or 'free-cells' would be designed with wireless communication capability and placed in the silo, or grain mountain, free to move with the surrounding grain. They will record such things as the temperature and

moisture content. Each of the ‘free-cells’ will transmit data to each other and back to a central computer (Figure 1.2).

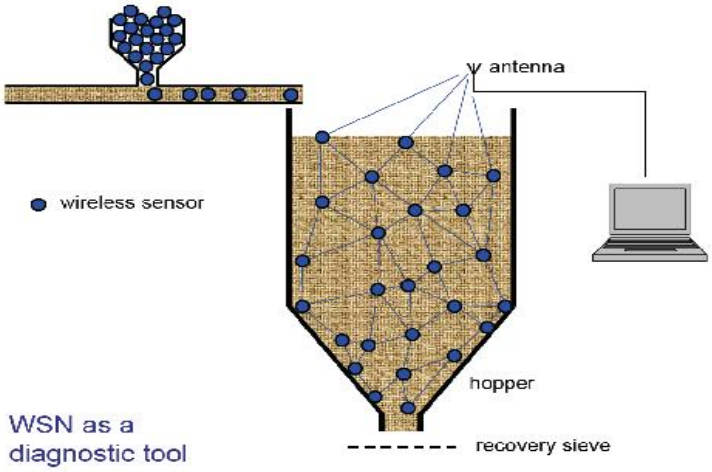

Figure 1.2: Schematic diagram of free-cell capsules in a grain silo (http://wsn4ip.org.uk/schematic.php)

1.2 Aims and Objectives

The WSN4IP research group are conducting tests in a 3D industrial scale silo. Tests are being conducted to determine how efficient the electronics are in enabling communication to take place ‘through’ the grains between each of the ‘free-cells’. Tests are being conducted using prototype free-cells that are much larger than the wheat grain particles. This is due to the limitations in reducing the size of the electronic circuit boards.

The aim of this work is to determine the physical characteristics of the larger ‘free-cells’ with the objective that they follow the same path and rotate nearly identically during discharge, to a wheat grain particle starting from an equivalent position to the free-cell in the silo after filling. It the case of ‘free-cells’ that are larger than the particles in the batch, the centre of mass of the ‘free-cells’ should follow the same path and rotate around a similar position during discharge to a wheat grain particle in the batch at an equivalent starting position as the centre of mass of the ‘free-cells’.

The research may also help to understand how other foreign bodies, such as people or dropped tools, move in discharging silos.

1.3 Definition of a free-cell

A ‘free-cell’ is defined as an object that is free to move in the silo during fill, storage and discharge. It is not fixed to the sides of the silo or hindered in any way. The ‘free-cell’ may have similar properties to the rest of the grains in the silo, or it may have completely different properties. The ‘free-cell’ is usually distinguishable by colour, or some other property, such as its internal structure e.g. electronic circuitry in the case of electronic ‘free-cells’.

1.4 Size constraints

The size of the free-cells is constrained by technology. Ideally the free-cells should be very similar in size to the rest of the grains in the batch. The miniaturisation of electronic circuitry is improving all the time. The WSN4IP research group have developed prototype electronic free-cells, which are about 10 cm in diameter, which is clearly much bigger than wheat grains. It is for this reason that this study investigates the displacement and rotation of free-cells larger than the grains in the batch.

It is proposed to use free-cells in silos storing wheat grain for use in food production. It is important that they can be easily captured upon discharge from the silo and industrial partners suggested a diameter of spherical free-cells should be about 30 cm to enable this. Constraints on the size of the free-cells, due to problems in how to retrieve them during discharge, seem less of a problem, as one can easily envisage that various techniques could be applied to capture them such as making the surface of the free-cells metallic and capturing them using magnets.

1.5 Solving the problem

Deducing an appropriate free-cell that moves and rotates similar to the bulk particles in a silo has been studied by applying experimental and computational methods developed in this work. Preliminary experiments to deduce the kinematics of free-cells, conducted with wheat grain, are presented and discussed in chapter 3, with the aim of understanding the physics of granular matter during the discharge from a silo and deducing the suitability of wheat grain

for use in determining some general conclusions about the movement and rotation of free-cells in discharging silos.
Preliminary tests reveal that the discharge of wheat grain from a silo is not reproducible.

Free-cells of three different densities (and three simple shapes: circular, triangular and square cross sections are initially investigated in a very simple idealised system of mono-sized spheres of identical density. Spherical particles were used in the experiments for two reasons. One reason was to rule out the possibility that the moisture content and surface properties of the particles were not being substantially affected on different days and to make easy comparisons with computational simulations of granular flow using the Discrete Element Method.

The investigation is then extended to the study of the behaviour of the ‘free-cells’ in the more complicated system of a binary mixture of spheres of the same density and then a binary mixture of spheres of two different sizes and densities. Bimodal samples were simulated and experimented with to increase the complexity in the batch and an attempt to simulate a particle system approaching that of a real granular system as found in real life. Spheres are an idealised granular material, so experiments and computational simulations have also been conducted with polyhedral granular materials.

The term ‘silo’ has so far been used to describe the container used to store granular materials. However, it is more precise to use the words ‘hopper’ or ‘bunker’ to describe the different parts of a silo. The word ‘bunker’ is used if the walls are parallel and form a container of constant cross-section and ‘hopper’ is used when the walls converge towards a relatively small opening at the base (Nedderman, 1992). This terminology will be applied throughout this thesis.

1.6 Granular material flow: An overview.

Charles-Augustin de Coloumb, famous for his work in electricity and magnetism, was probably the first to attempt to understand the physics of granular media (Campbell, 2006) He proposed that the maximum angle supported by a sand heap, could be understood by considering the frictional properties of two solid bodies in contact (Clement, 1999) (Figure 1.3).

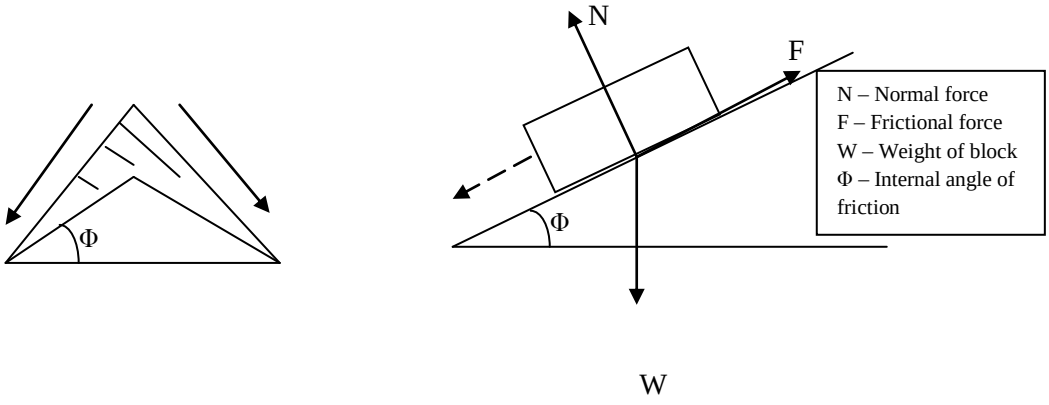

Figure 1.3: Coulomb's proposal that the maximum angle supported by a sand heap could be understood in analogy with the friction properties of two solid bodies in contact (Clement, 1999)

He proposed that the maximum angle of the slope of a sand pile Φ is such that any extra granular material will slide down similarly to the block on the slope. The angle Φ is the internal angle of friction of the granular material. In a non-cohesive material the internal angle of friction is equal to the angle of repose.

Hagen in 1852 and Janssen in 1895 conducted the first known investigations on granular materials in storage containers. Early work concerned the wall and internal stresses in silos and attempts were made to derive correlations of the mass flow rate, with the hopper dimensions and particle physical properties and dimensions (Beverloo et. al. 1961; Al-Din & Gunn, 1984), based on the results from experimental data. The theory of soil mechanics was applied to granular flow (Jenike, 1961) and equations were derived to predict the stress and velocity distributions in discharging silos (Pemberton, 1965; Morrison and Richmond, 1976).

The invention of the personal computer and the increase in computing power since the late 1980's, has enabled granular flow to be modelled computationally. The main method of modelling granular systems computationally was developed by Cundall in 1971 and was named the Distinct Element Method, but is now widely referred to as the Discrete Element

Method (DEM). Cundall and Strack (1979) later developed the DEM to model systems of 2D circular discs. The DEM has been developed to model non-spherical particles and more efficient integration schemes have been studied and applied, improving both the accuracy and speed of simulations. DEM code is also being parallelized, enabling the modelling of large numbers of particles and increasing the feasibility of modelling industrial scale granular material behaviour, involving billions of individual particles.

1.7 Scope of the thesis

A review of the literature related to granular flow in hoppers is presented in chapter 2. A simple hopper flow process is described, starting from the filling stage and the development of the wall and internal stresses in the material. Models developed to predict the stress and velocity distributions during discharge are outlined. Segregation during the discharge phase is discussed and an overview of the correlations developed to estimate the mass flow rate of material through the orifice is presented. Previous work investigating the flow of free-cells in various granular materials is also introduced. In chapter 3 the equipment and experimental methods employed in this study to determine the input parameters for the DEM simulations and the trajectories of the free-cells in the mono and binary mixtures are described.
In chapter 4 comparisons between the results obtained from practical experiments to determine the trajectories of the metal, plastic and hollow free-cells in a monosized batch of particles are presented and discussed and in chapter 5 the effect of changing the particle mix, by comparing the trajectories of the free-cells in monosized particles and to different binary mixtures are presented and discussed. In chapter 6 the time taken for the free cells to travel from twelve different starting positions in the silo is presented and discussed. In chapter 7 a short discussion on the rotation of the free-cells is discussed. Chapter 8 provides details of the background to the Discrete Element Method (DEM). An overview of past work is discussed and the background theory of the DEM applied to model the interactions between spheres and the spheres and the free-cell is presented. The methods used to model the flow of polyhedral particles, is also discussed. The results of the practical experiments conducted to deduce the input parameters for the DEM simulations and the trajectories of the different free-cells in the mono and binary mixtures of particles are presented in chapter 9. In chapter 10 the results obtained from DEM simulations and the comparison with experimental results, are presented and discussed and in chapter 11 the results obtained from experiments and DEM simulations

of polyhedral particles are presented and discussed. Chapter 12 provides a summary and conclusion of the main findings of the study and chapter 13 is a discussion of recommendations for further study.

Mechanics of silo flow, flow patterns and discharge

2 Mechanics of silo flow, flow patterns and discharge rate

2.1 Introduction

In this section a review of the literature on granular flow is introduced. The literature is introduced in the order it relates to a silo flow process, starting with the filling method and progressing to the discharge phase. The final subsection is a review of the literature related to the flow of free-cells in discharging silos. An understanding of each of the phases in a silo process is useful in understanding why the spherical particles and free-cells used in this work behave as they do. The stress distribution between the particles and the particles and the walls within a silo is affected by the filling method and may affect the velocity distribution of the particles and hence the path followed by the free-cells. The free-cells are larger than the rest of the particles in the batch and segregation of the free-cells may take place, hence a discussion of factors affecting the segregation in a granular material are mentioned. An understanding of the factors affecting the flow rate of the particles and the discharge time through the orifice is important, as the time taken and path followed by the free-cells will also be affected. Section 2.2 begins by introducing the simple theories that were developed to describe the stress distribution in a silo and then the general flow patterns observed within a discharging silo are discussed. Section 2.3 details the causes of segregation in a silo during the filling and discharging phases and section 2.4 describes the various models developed to describe the processes taking place between the particles within the silo during discharge and more sophisticated methods in determining the stress distribution. In section 2.5 the formulae developed to predict the flow rate of the particles through the orifice are presented

2.2 A basic silo flow process

A basic silo flow process starts with the filling process as shown in Fig.2.1 (a). Rotter et al. (1998) noted that the filling process is important as it determines the packing structure, internal and wall stress and the shape of the top surface, which later influences the stress and flow patterns during discharge.

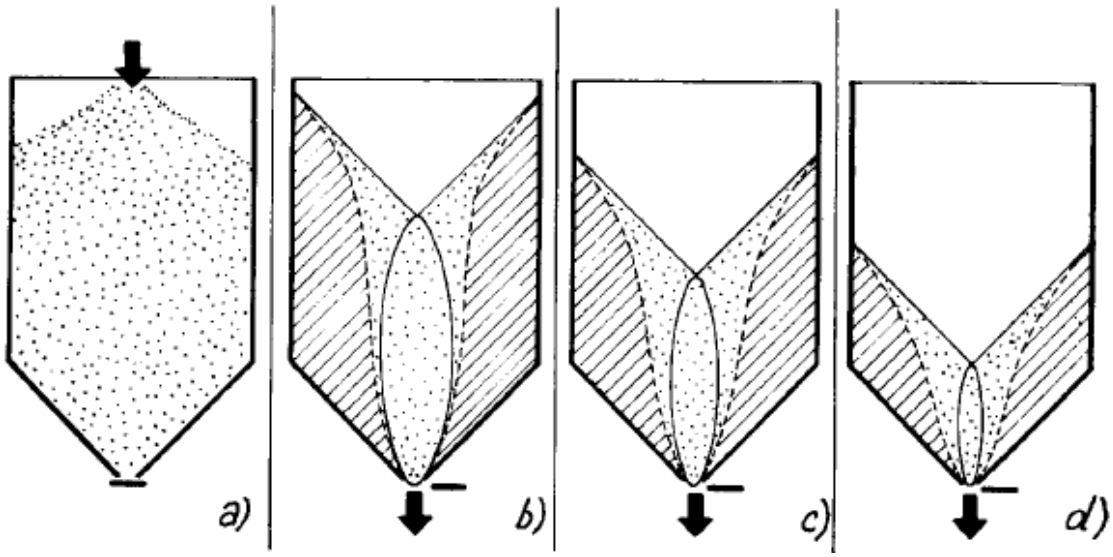

Figure 2.1: The discharge phase in a silo (Kvapil, 1965)

The granular material is allowed to settle and come to rest in the silo. In large industrial silos the material may be stored for many days or months.

During storage the granules interact mainly via contact forces. The contact forces include the normal elastic force between two individual grains and the tangential friction force between grains. The distribution of the contact forces is highly disordered with large force chains enclosing regions of relatively small load (Clement, 1999). The force chains are supported by the walls. Hagen in 1852 (Sperl, M, 2006) was the first to discover that the weight of granular material in a container is supported by the walls. He observed that the pressure exerted on a metal plate initially increased up to a maximum value and remained constant as the height of material was increased. Janssen in 1895 conducted experiments with corn and derived an equation to determine the pressure distribution throughout the silo. Janssen assumed that the pressure was uniform across any cross section of the silo and that the vertical pressure was proportional to the horizontal pressure.

The pressure at any height in the silo is given as (Sperl, 2006)

$$p = \frac{s\gamma}{4K}\left(1 - e^{-4K\frac{x}{s}}\right) \qquad 2.1$$

where *s* is the length of a side of the container which encloses a circular container, *x* is the depth of the slice from the top surface, γ is the specific weight, $K = \frac{p_s f}{p}$ where *K* is the *Janssen constant* and where p_s is the horizontal pressure of the grains and *f* is the friction coefficient between the grain and the container wall.

Figure 2.2 shows the pressure in a Janssen element where *x* is the depth below the top surface of the material and *p* is the pressure.

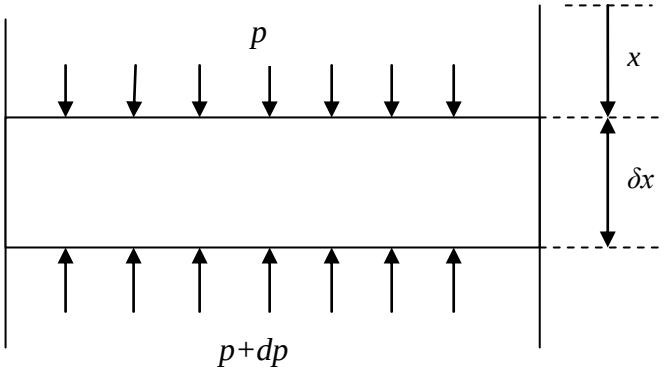

Figure 2.2: Pressure in a Janssen element

Janssen's theory assumed that the horizontal and vertical pressure in an element of the grain bed was constant across any cross section of the silo and increased with depth. This implies that there can be no shear stress on the wall. However, Janssen assumed that the vertical pressure was proportional to the horizontal pressure, which results in a contradiction.

Walker (1966) considered the stress distribution near the walls in a hopper and modified the Janssen constant, *K*, to take account of the active and passive states of failure between the grains and the wall, by application of Mohr-Coloumb failure diagram. The active and passive failure states, or *Rankine states*, can be described as follows. The active stress is the stress on a wall that is moving outward and the slip within the material is in a downward and outward direction as shown in Figure 2.3a. The passive stress is stress on a wall that is moving inwards and causing inward and upward failure within the material as shown in Figure 2.3b. The horizontal stress between these two values will be stable and cause no slip within the material (Nedderman, 1992).

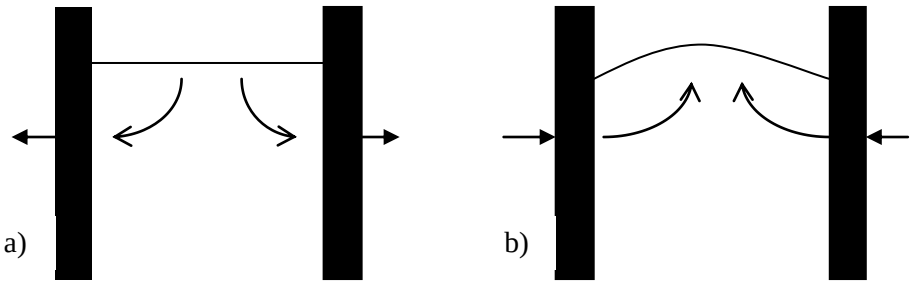

Figure 2.3: Stresses on a silo wall. On the left, a), the active state and on the right, b), the passive state.

Walker's analysis showed that the stresses in a granular material cannot be independent of radial position. Walker defined a distribution factor, Ð, to account for this.

Walters (1973) investigated the apparent presence of very large stresses developing within silos, resulting in the bunker failing to hold the material inside. Walters proposed that there existed a boundary between an active stress state and a passive stress state, within the bunker during discharge.

Enstad (1975) extended Walkers analysis by assuming that the horizontal and vertical stresses in a granular material are constant on a spherical surface spanning the hopper. During filling and storage, force chains develop within the structure of the granular material Figure 2.4. These chains support the weight of the material. In between the network of chains many particle contacts are unloaded. During discharge theses force chains develop and collapse throughout the granular material.

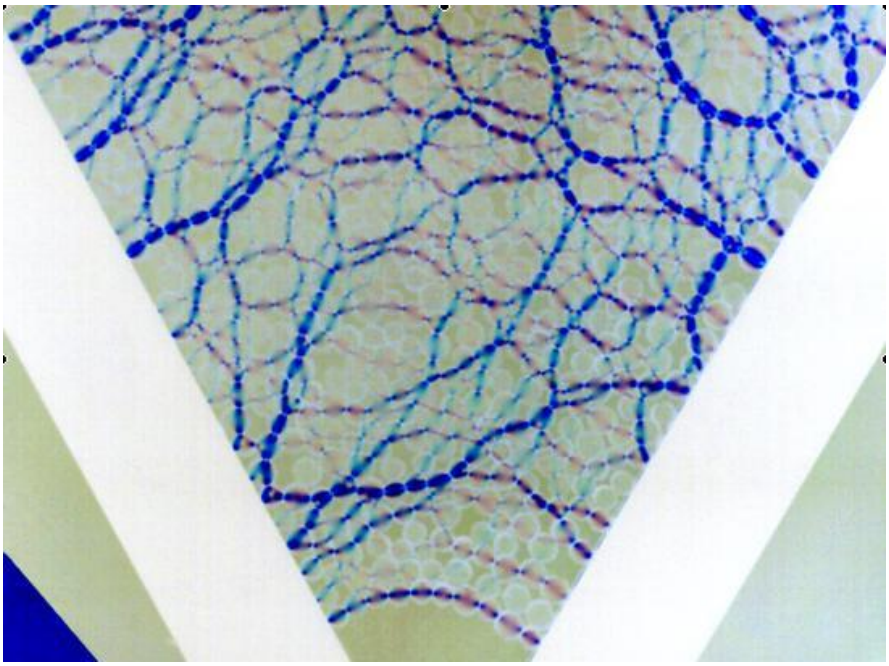

Figure 2.4: Diagram showing the force chain in a hopper
http://www.phy.duke.edu/~jt41/research.html#pictures

Discharge begins when the orifice opens and material flows out of the hopper and through the orifice (Figure 2.1b). The material moves due to the failure along narrow planes, or shear bands, of several particles thick.

The discharge rate fluctuates very slightly over time scales less than 0.01 seconds as shown in Figure 2.5. Arches form and collapse around the orifice as the material flows out of the hopper (Brown and Richards (1965), Datta et al. (2008)).

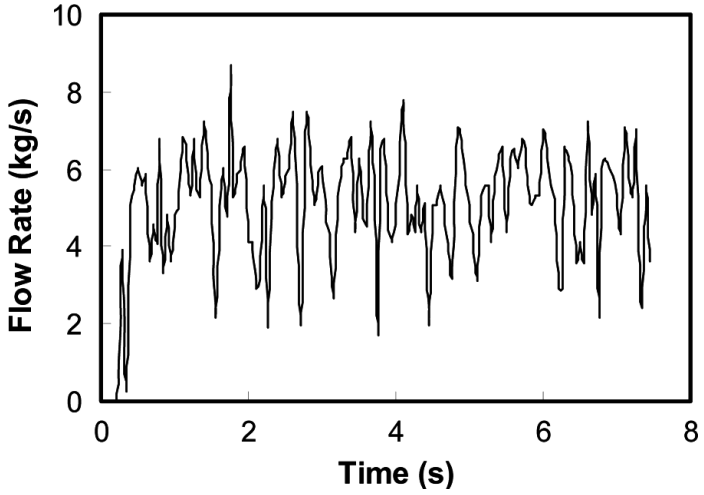

Figure 2.5: Variation in the mass flow rate at the orifice during discharge (Datta et al., 2008)

The velocity pattern inside the hopper is dependent upon the hopper dimensions. When the orifice is opened (Figure 2.1b), there is a slight delay before the initiation of flow. The voidage of the material increases from the bottom upwards. This is known as the *Reynolds'* principle of dilatancy. The granular material 'prepares' itself to flow through the orifice. If the material cannot dilate then discharge will not take place. The flowing material is observed to rarely flow through the space immediately adjacent to the edge of the aperture (Brown and Richards (1965)). Michalowski (1984, 1987) observed two mechanisms of flow, a *mass mechanism* and a *plug mechanism* (Figures 2.6 and 2.7). The *mass mechanism* is characterised as follows: After the orifice is opened two curvilinear rupture surfaces propagate upwards from the orifice, crossing at the axis of symmetry of the hopper and then reach the walls. The next pair of rupture surfaces develops at the points at which the first pair reaches the walls. More and more of the material starts to move as the rupture surfaces expand. The process is repeated until the rupture surfaces meet at the top surface of the material. Meanwhile the surfaces in the lower part move down. The flow pattern then becomes irregular until the material forms a steady flow pattern (Figure 2.6g). Upon initiation of the *plug mechanism* material starts to flow in a narrow zone separate from the stationary zones by two roughly vertical surfaces. Shortly after the orifice is opened the plug zone reaches the top surface and expands sideways, so that the stationary zones gradually reduce in size. Rupture surfaces develop within the upper and lower part of the plug zone (Figure 2.7).

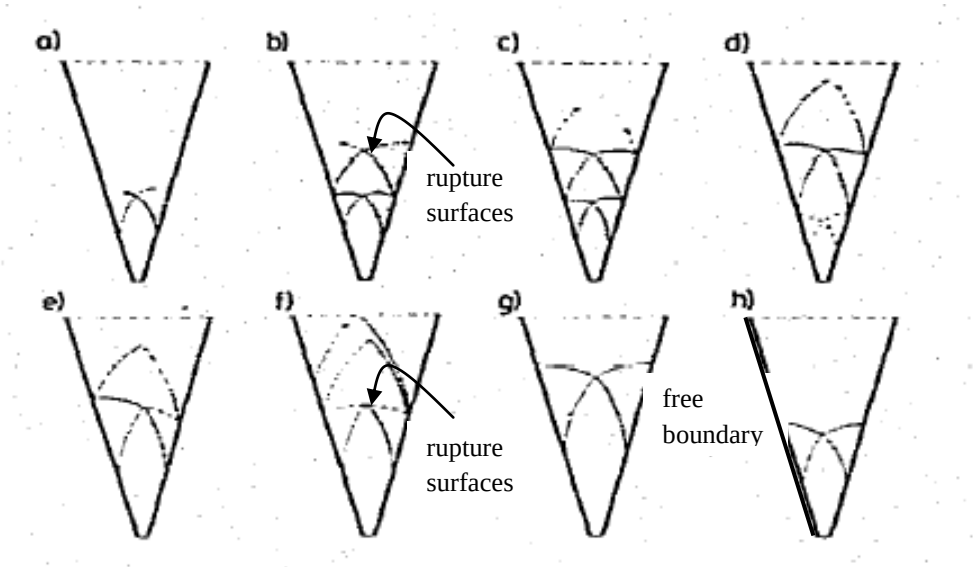

Figure 2.6: The rupture surfaces in the initial mass mechanism (a-f) and during the advanced flow (g, h) (Michalowski, 1984)

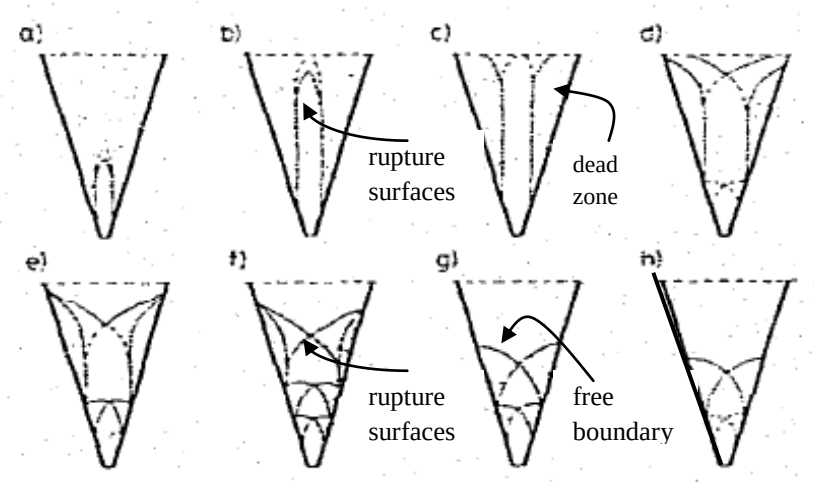

Figure 2.7: The rupture surfaces in the initial plug mechanism (a-f) and during the advanced flow (g, h) (Michalowski, 1984)

During discharge an ellipsoid of motion is formed in the hopper having an approximately constant ratio of the major and minor semi-axes. For a given material the dimensions of the ellipsoid are practically identical for hoppers of different dimensions. The finer the grains the slimmer and more elongated are the ellipsoids of motion (Kvapil, 1965). Dilatant waves pass continuously through the flowing core resulting in a fluctuating voidage (Figure 2.8) in the material Brown and Richards (1960).

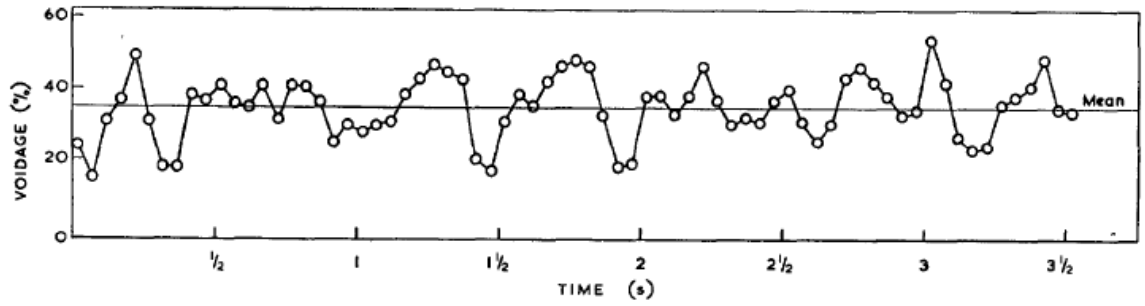

Figure 2.8: Fluctuating voidage at a distance of 11.5 cm perpendicular from a 12 cm orifice, obtained from the motion of a single layer of ball bearings (diameter 0.32 cm) on a glass plate inclined at a few degrees to the horizontal (Brown and Richards, 1960)

Balevičius et al. (2011) noted that the speed of the dilatant waves is dependent upon the inter-particle contact network and material damping and friction.

Tűzűn (1982) defines three flow patterns as shown in Figure 2.9. Type A in which all the material flows out of the hopper, type B where a stagnant region of material forms that does not extend to the top surface and type C in which the stagnant zone reaches the top surface.

The flow pattern exhibited by a granular material depends on the particle properties, the hopper half angle and the height of the top surface. In type C flow a depression is formed in the top surface and material cascades down it towards the centre line. In the middle of flow zone of type C there is a core of fast flowing dilated material.

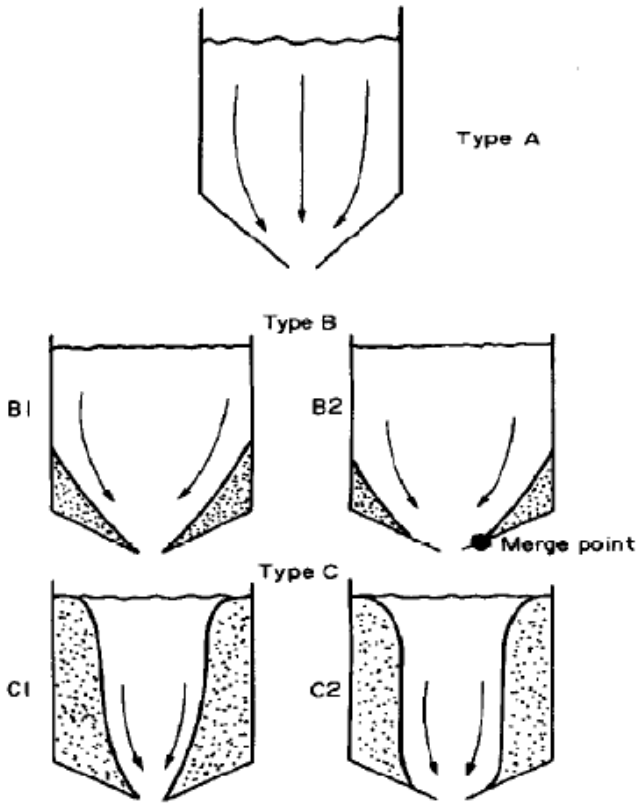

Figure 2.9: Flow patterns observed by Tüzün (1982)

Other authors studied the flow patterns of granular materials and noted similar features. Natarajan et al. (1995) conducted experiments by placing tracer particles into a small 3D chute and observed three flow regimes, a central uniform flow regime, a low-shear transition regime and an outer moderate-shear regime. Pariseau (1969) observed three flow zones, and zones of rapid velocity change between regions of gradual velocity change suggesting the presence of velocity discontinuities in the flow pattern.

In this study ‘mass-flow’ will refer to silos in which material flows out in a first in – first out pattern and ‘funnel-flow’ will refer to silos in which dead zones form and material flows out along a central core.

2.3 Segregation

Segregation in granular materials occurs when the system contains one or more different sets of particles. The particles may differ is size, density or shape. The free cells used in this study are larger than the particles in the batch, so it is possible that they may segregate through the other particles. An understanding of the mechanisms controlling segregation is therefore discussed in this section.

In the study presented in this thesis tests were conducted with binary mixtures of spherical particles. One batch consisted of particles of the same density but different size and another batch consisted of particles of different size and different density.

Segregation occurs during the filling stage (Shinohara, 2002) and during the formation of a heap on the top surface and during the discharge phase. In a binary mixture of particles of two different sizes the larger particles are referred to as *coarse* particles and the smaller particles are the *fines*. Artega (1990) observed two mechanisms by which segregation occurs. Which of the mechanisms is observed is dependent upon the size ratio of the two different particles and/or the density of the two types of particles and the fines fraction. The two regimes are the:

i) Coarse continuous phase: Velocity field is dominated by a coarse particle lattice and fines fill the void space of the coarse lattice (Figure 2.10). This phase occurs when the ratio of the fines to the coarse particles is small.

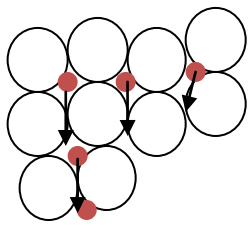

Figure 2.10: Fines filling void space in a coarse lattice

ii) Fines continuous phase: The granular structure is dominated by a fine particle lattice within which the coarse particles are retained in relatively small numbers (Figure 2.11).

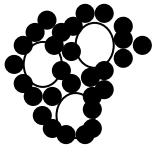

Figure 2.11: Coarse particles in a fine particle lattice

If the size ratio is large, the smaller particles percolate through the gaps created by the larger particles. If the size ratio is small, the smaller particles tend to gravitate towards to wall during filling or towards the fast moving core during discharge, resulting in fluctuations in the local bulk porosity in different sections of the material during flow. The transition from the coarse to the fines continuous phase was observed to occur over very small weight fractions of fine particles, typically 27-28%, for particle size ratio greater than 7 (Artega, 1990). When the particle size ratio is less than 4 then the coarse continuous phase extends over a much larger range. Artega (1990) observed that negligible or no segregation occurred in binary mixtures of size ratio greater than 5 at fines fractions of greater than 20%, while mixtures with size ratios of less than 3 exhibited size segregation up to fines fractions of 50-60%. The mass discharge rate was found to increase as the fines fraction increased. The packing density of a binary mixture of particles of different size is greater than the packing density of a monosized batch of particles. A maximum packing density was observed to occur when the void filling process by the fines ceases. Segregation was found to be important whenever the particles are allowed to shear, such as next to the stagnant zone boundary in funnel flow.

Shinohara (2003) investigated the segregation of a binary mixture of particles of different densities but the same size in a 2D hopper with a feeder. The denser particles were found to concentrate close to the central feeder point, similar to the ones in size segregation. Density segregation in a binary mixture was found to occur on the top surface of the heap on a layer of constant thickness. During flow down the heap the denser particles sink or penetrate through ‘dynamically formed’ voids in the descending layer. The lighter particles are pushed away by the penetrating dense particles and then they occupy the void spaces vacated by the dense particles. The bottom of the descending layer is thus predominantly composed of denser particles.

Ketterhagen (2008) investigated the effect of the particle properties, hopper geometry and wall friction on segregation patterns in a quasi-3D wedge shaped hopper with two periodic boundary conditions. Similar results to those of Artega (1990) were observed, namely that the extent of segregation decreases as the fraction of fines increases and that as the fines fraction increases, the void fraction reaches a minimum at which percolation is very limited. Ketterhagen (2008) observed that increasing the fines fraction still further resulted in the void fraction increasing, but no percolation as the system becomes 'fines continuous'. Varying particle density ratio was shown to have negligible effect on the segregation. Ketterhagen (2008) studied the effect of the particle-wall and particle-particle friction coefficient on segregation in a discharging hopper. A large wall friction was found to result in percolation of fines possibly as a result of increased velocity gradients and shearing and because the particles near the silo walls are nearly static, such that the fines near the walls tend to be retained in the hopper and are not discharged until the end. At a hopper wall angle of 55º the particle-particle sliding friction most significantly affects the initial and final portion of discharge and has a minimum effect on the middle portion. An increase in the particle-particle friction results in the initial material flowing through the orifice to contain an excess of fines. This is as a result of the increasing bed porosity with increasing particle-particle friction. A greater porosity results in an increase in the rate of percolation which is observed as an excess of fines in the initial material discharged. A small particle-particle friction results in a small depression forming on the top of the bed that lasts for some. Small particles percolate down towards the hopper walls and are the last to discharge. For a large particle-particle friction a v-shaped depression forms at the same point during discharge but lasts a shorter time because slip planes develop near the hopper walls and a large number of particles move *en masse* towards the centreline, removing the v-shape and segregation. Regions of fines depleted material which would normally roll down and slide down the v-surface and out of the hopper are left on the top surface and are the last to be discharged.

Ketterhagen (2008) also considered the effect of silo geometry on segregation. It was shown that as the hopper walls became steeper the material discharged contained an increasing excess of fines until towards the end of discharge when the material discharged consisted of a majority of coarse particles. The depletion of fines towards the end of discharged was attributed to the percolation of small particles which are not retained within the hopper as they

would be in a flat bottomed hopper. Fines are continually discharged leaving the top layer of material depleted in fines. Increasing the bed height while keeping the width constant results in the fraction of fines discharged the same, but the width of the fines depleted region decreases. Increasing the hopper width while keeping the bed height constant, results in the amount of fines decreasing earlier, and the width of the fines depleted region increases with increasing hopper width. Discharge from hoppers is shown to be relatively uniform up to the point where the fill level is equal to the hopper width. Then as the head decreases, the mass fraction of fines in the discharge initially decreases and then increases towards the end of discharge. All significant discharge effects are shown to take place towards the end of discharge.

Drahun (1983) conducted tests in a small 3D slice hopper (Figure 2.12) in which the bottom was inclined at an angle θ from the horizontal. Particles of different size but the same density were allowed to pour into the hopper. The smaller particles were found to percolate down to the bottom of the incline. Tests conducted with particles of the same size but different density resulted in the lighter particles flowing to the bottom of the incline.

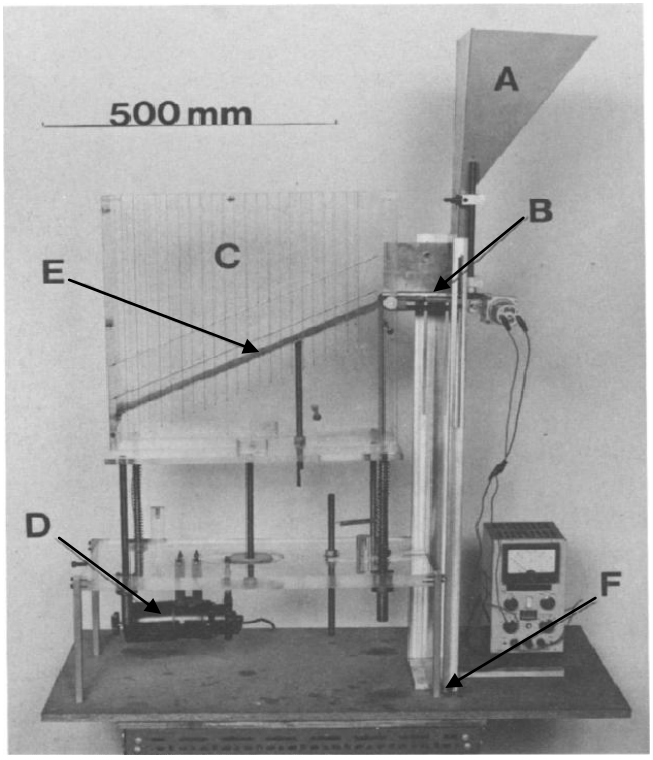

Figure 2.12: The inclined plane; A, feed hopper for bulk material, B, conveyor, C, container, D, motor for lowering box, E, inclined plane, F, hinge for setting free surface horizontal during analysis.

Balevičius et al. (2011) conducted experiments in three different hoppers (Figure 2.13), a plane wedge hopper, a space wedge hopper and a flat bottomed hopper. The gradual and *en masse* filling methods were used, but it was found that the filling method had a minimal effect on the discharge. If the walls were rough the top surface of the material during discharge transformed from a convex to a concave shape. A depression zone formed at the beginning of the discharge process, which deepens during further discharge. If the hopper sides are made steeper, when the angle of the sides coincides with the angle of repose of the material some of the particles cascade down to the central flowing core. Particle dilation takes place in the flowing core indicating a reduction in the magnitude of the particle contact forces in the discharge time period. Balevičius et al. (2011) determined that dilation takes place due to inter-particle friction, which allows for material shearing as a result of an increase in the porosity and in turn a reduction in the particles contact forces.

In this study the plane wedge hopper was used. Balevičius et al. (2011) found that an anisotropic (different in each direction) velocity distribution with domination of the vertical velocity component was clearly observed. This component resulted in particle movement towards the centre

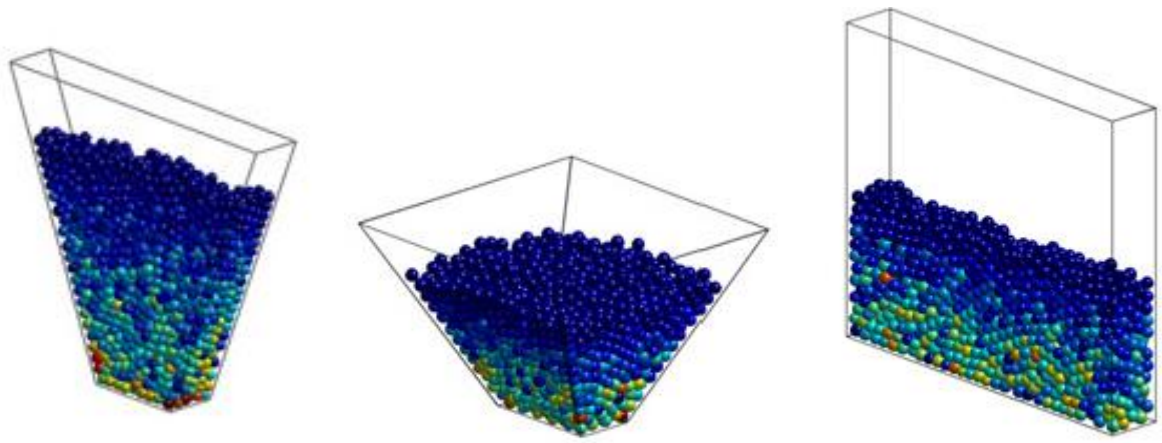

Figure 2.13: a) Plane wedge hopper, b) space wedge hopper, c) flat bottomed hopper. Balevičius et al. (2011)

2.4 Models developed to describe the flow of granular materials.

Various models have also been developed to predict the velocity and stress distributions in discharging hoppers. The displacement and velocity of the free-cells is heavily dependent on the velocity and stress distributions within the silo, hence an understanding of the basic ideas developed to understand the mechanics of the flow is important in understanding why the free-cells follow a certain path in the silo. The models can generally be divided into two different groups, continuum and discrete. The continuum models essentially ignore the particulate nature of the material flowing and treat it more like a fluid, averaging the forces between individual particles over a continuum. The most popular of the continuum approaches is the Plasticity Theory, which relates the stress and velocity of the discharging material by a flow rule. In discrete models, each individual particle is considered and all forces acting on or between particles are resolved. In this study a discrete model, the Discrete Element Method (DEM) was used to model the particle flow. The DEM is discussed in detail chapter 8 and results from simulations and experiments are compared and discussed. In this section a brief description of simple theories to predict the stress and velocity patterns in discharging granular materials is discussed and the basic outline of the plasticity theory is introduced.

2.4.1 The kinematic model

The first hypothesis involving the Kinematic model was developed by Litwiniszyn (1971). He postulated that the particles are confined to a set of hypothetical cages (Figure 2.14). When the particle leaves cage 1 there is a probability **p** that it is replaced by the particle in cage 2 and a probability 1-**p** that it is replaced from cage 3. Generally **p** = 0.5 but can be ±1 near to the wall.

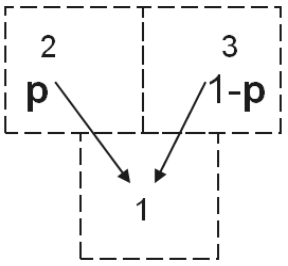

Figure 2.14: Litwiniszyn's particle cages

Mullins (1972) modelled the flow of the granules in terms of 'voids', instead of particles and developed the concept of a continuum limit. Particles move downwards to fill voids created by other particles that are also moving downwards, towards the orifice. The voids are randomly distributed upwards from the orifice.

It was assumed that the voids are spread throughout the hopper by non-interacting random walks, so that in the continuum limit, at scales larger than the grain diameter, the concentration of voids $\boldsymbol{\rho_v}$ satisfies the diffusion equation

$$\frac{\partial \rho_v}{\partial z} = B\frac{\partial^2 \rho_v}{\partial x^2} \qquad 2.2$$

Nedderman and Tüzün (1979a,b) consider the granular material to flow as shown in Figure 2.15

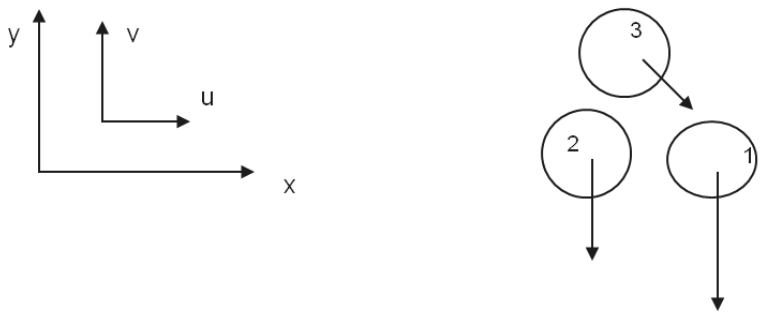

Figure 2.15: Nedderman and Tüzün model of how granules move in a discharging hopper

If the downward velocity of particle 1 is greater than that of particle 2 then it is likely that particle 3 will move to the right i.e. there is a relationship between the horizontal velocity *u* and the gradient of the vertical velocity $\partial v / \partial x$.

This results in the simple relationship

$$u = -B\frac{\partial v}{\partial x} \qquad 2.3$$

where *B* is a constant dependent on the nature of the material.

Granular materials are generally incompressible, so the equation is substituted into the 2D continuity equation

$$\frac{\partial u}{\partial x} + \frac{\partial v}{\partial y} = 0 \qquad 2.4$$

to give

$$\frac{\partial v}{\partial y} = B\frac{\partial^2 v}{\partial x^2} \qquad 2.5$$

This equation is identical in form to the result of Mullin's model and Litwiniszyn's for the case **p** = 0.5.

2.4.2 The spot model

Bazant (2006) developed the spot model to model the flow of granular materials. It was proposed that in a dense random packing of particles, a particle moves together with its nearest neighbours, in a 'cage', over short distances, before the 'cage' of particles gradually breaks over larger distances. In a discharging hopper cage breaking may occur slowly, over a time scale of the time to reach the orifice. Each cage of particles follows an independent random walk throughout discharge. Each cage of particles contributes in applying a force on a group of neighbouring particles (Figure 2.16). The cages of particles move by filling 'spot' voids which diffuse up through the hopper. A value of *B* in equation 2.5 can be determined by considering the diffusion length, which is a measurement of the rate at which the spot moves upwards.

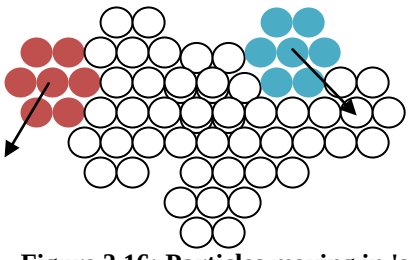

Figure 2.16: Particles moving in 'spots' consisting of groups of particles

2.4.3 Plasticity Theory

Plasticity theory is based on the idea that granular materials discharge by the process of shear along certain critical planes. The interactions between individual particles are averaged over a continuum. An ideal material obeys the *Coulomb yield criterion* which limits the magnitude of the shear stress that can occur within a granular material. The shear stress τ along the slip planes is found to depend on the normal stress σ acting on the plane and is described by (Nedderman, 1992)

$$\tau = f(\sigma) \qquad 2.6$$

In *ideal Coulomb materials* equation 2.6 takes a linear relationship

$$\tau = \mu\sigma + c \qquad 2.7$$

where μ is the coefficient of friction and *c* is the cohesion.

The Coulomb failure criterion can be used with Mohr's circle in *Mohr-Coulomb failure analysis* to deduce the combinations of normal and shear stresses that exist at various points in a material and the resulting velocity field (Drucker and Prager, 1951).

Figure 2.17 shows the stresses on a wedge.

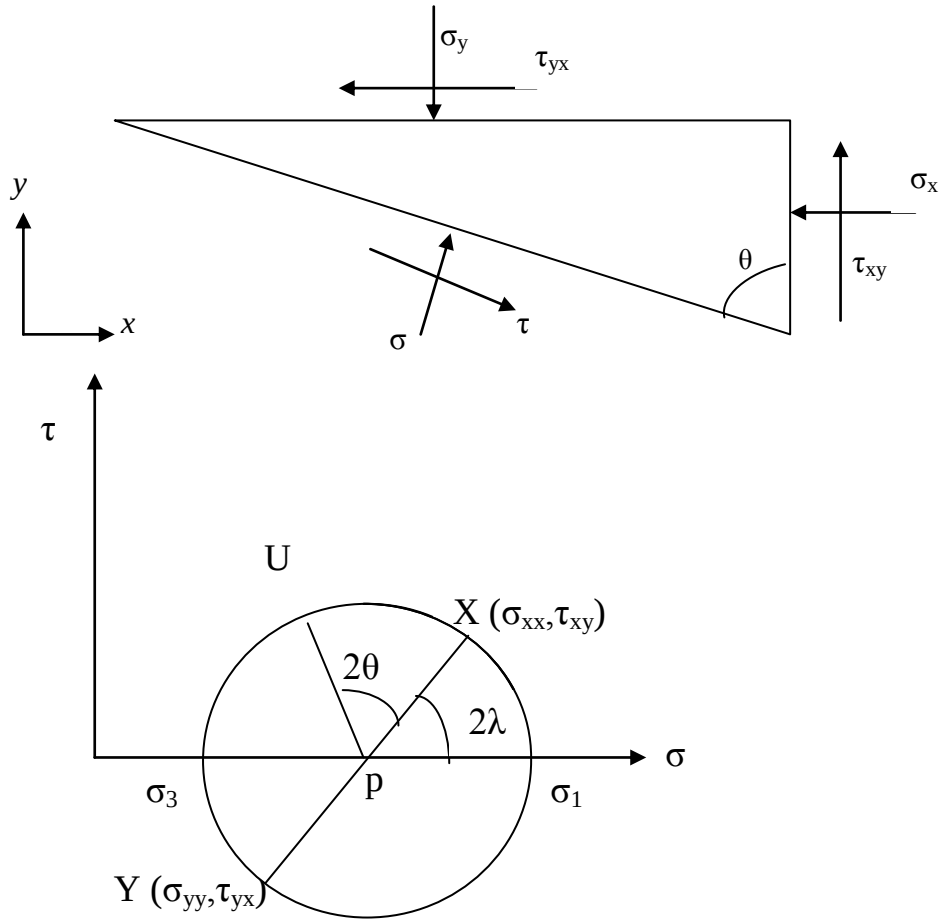

Figure 2.17: Mohr's circle for the stresses on a wedge of material

Sliding of the material will only take place if the Coulomb line, described by equation 2.7, touches Mohr's circle. The Coulomb line for an ideal Coulomb material can never cut Mohr's circle.

Spencer (1964) developed the basic Coulomb theory of plasticity by proposing that the material satisfy the criteria that the strain at any point may be considered as the resultant of simple shears on the two surface elements where Coulomb's yield condition is met.

Pemberton (1965) applied Spencer's theory to the flow of granular materials in wedge shaped channels. Morrison and Richmond (1976) extended Spencer and Pemberton's work by including gravitational and acceleration terms. The disadvantage in applying plasticity theory to the flow of granular materials is that the essential detail on the particle scale is lost and hence it cannot readily provide information on the flow of free-cells in granular materials.

2.5 Mass flow rate & stress

Obtaining an accurate value of the mass flow rate W from a hopper is important in measuring its efficiency and is the main mechanism that affects the time taken for the free cells to flow out through the orifice. Nedderman et al. (1982) provided a summary of much of the early work into the study of mass flow rate, so only a brief summary of the major findings is given below.

Janssen (1895) observed that the weight of material in a hopper is distributed along the walls and the stress state at the orifice is virtually independent of height *H*. Most early experimentalists found that there is no dependence of *W* on *H* provided that *H* exceeds a critical value of about 2.5 times the orifice diameter D_0.

Various workers found that

$$W \propto D_0^n \qquad \textbf{2.8}$$

where *n* is a positive integer and D_0 is the orifice diameter .

Franklin and Johanson (1955) suggest for a circular flat bottomed orifice

$$W = \frac{\rho_p D_0^{2.93}}{(6.288\mu_s + 23.16)(d + 1.889) - 44.90} \qquad \textbf{2.9}$$

where μ_s is the kinetic angle or repose, or angle of internal friction, *d* is particle diameter and ρ_p.They also conducted tests to determine the influence of the silo walls on the flow rates and found that when the difference between orifice and column diameter is greater than about 30 particle diameters, the influence of the wall is negligible. They also propose a multiplication factor for hoppers inclined at an angle θ_H giving

$$W_{\theta_H} = W \frac{\cos \mu_s + \cos \theta_H}{\cos \mu_s + 1} \qquad \textbf{2.10}$$

where θ_H is the hopper angle from the horizontal and μ_s is the internal kinetic angle of repose.

Beverloo (1961) conducted experiments on cylindrical bunkers with circular, square, rectangular and triangular orifices filled with sand, linseed, spinach, watercress, rapeseed, kale and swede and turnip seeds. It was deduced from dimensional analysis that

$$W \propto \rho_b g^{\frac{1}{2}} D_0^{\frac{5}{2}} \qquad 2.11$$

where g is the acceleration due to gravity and ρ_b is the bulk density of the material.

Beverloo et al. (1961) plotted $W^{2/5}$ against D_0 and obtained a straight line that intercepted the vertical axis, which was correlated with the particle diameter to give kd. The value of k was found to be a function of particle shape and the following correlation was obtained

$$W = C\rho_B \sqrt{g}(D_0 - kd)^{\frac{5}{2}} \qquad 2.12$$

for circular orifices, where d is the particle diameter and ρ_B is the bulk density prior to discharge and k was found to vary between 1.3 and 2.9 and C to be approximately 0.58. The term kd may represent the displacement thickness of the shear layer in the material approaching the orifice (Neddermann, 1992).

Equation 2.12 is only applicable for cylindrical bunkers. In mass flow conical hoppers the hopper half angle has to be considered. Rose and Tanaka (1959) reported that the mass flow rate was proportional to $(\tan\alpha^* \times \tan\phi_d)^{-0.35}$ provided that $\alpha^* < 90 - \phi_d$, where ϕ_d is the angle between the stagnant zone boundary and the horizontal, which can be assumed to be 45º and α^* is the angle between the stagnant zone boundary and the vertical giving

$$W_\alpha = W\, F(\alpha^*, \phi_d) \qquad 2.13$$

where

$$F(\alpha, \phi_d) = (\tan\alpha^* \tan\phi_d)^{-0.35} \text{ for } \alpha < 90 - \phi_d$$

$$\mathbf{F = 1} \qquad \mathbf{for\ \alpha > 90 - \phi_d} \qquad \mathbf{2.14}$$

The earliest study into the effect that the orifice shape has on the mass flow rate was conducted by Fowler and Glastonbury (1959). They reported that the mass flow rate *W* from a cylindrical bunker could be written as a function, in the form

$$\frac{W}{\rho_p A\sqrt{2gD}} = f\left[\left(\frac{D}{d}\right)\cdot\left(\frac{H}{d}\right)\cdot\left(\frac{\rho_p}{\rho_b}\right)\cdot S\cdot\left(\frac{D_C}{d}\right)\right] \qquad \mathbf{2.15}$$

where, *A*, is the area of the orifice, ρ_p, is the particle density, ρ_b, is the bulk density, *D*, is the orifice diameter, D_C, is the container diameter, *d*, is the particle diameter, *H* is the material head height above the orifice and *S* is the orifice shape factor which is defined in terms of the hydraulic mean diameter D_h where

$$D_h = 4 \times \frac{A}{\text{perimeter of orifice}} \qquad \mathbf{2.16}$$

The statistical correlation of 247 results obtained from experiments on flat bottomed hoppers with circular, elliptic, rectangular, square, pentagonal, hexagonal and triangular orifices and filled with sand, rape seed, wheat, rice and sugar resulted in equation 2.17

$$\frac{W}{\rho_B A\sqrt{2gD_h}} = 0.236\left(\frac{D_h}{d_s}\right)^{0.185} \qquad \mathbf{2.17}$$

Nedderman et al. (1982) noted that Fowler and Glastonbury's equation makes no allowance for the empty annulus. Therefore the following analysis was deduced by Nedderman (1992) to derive an equation for the mass flow rate through orifices of various shapes.

Applying the concept of the empty annulus, then

$$W \propto A^* \sqrt{D_h^*} \qquad 2.18$$

where A^* and D_H^* are the area and hydraulic mean diameter of the orifice after the removal of the empty annulus.

For a circular orifice, these quantities can be written as

$$A^* = \frac{\pi}{4}(D_0 - kd)^2 \qquad 2.19$$

and

$$D_H^* = (D_0 - kd) \qquad 2.20$$

where D_0 is the orifice diameter, k, is a dimensionless parameter and d is the particle diameter.

Equation 2.18 can then be written as

$$W = \frac{4C}{\pi}\rho_b A^* \sqrt{gD_H^*} \qquad 2.21$$

For an orifice of length l and width b

$$A^* = (b - kd)(l - kd) \qquad 2.22$$

and

$$D_H^* = 4(b - kd)(l - kd)/2(l + b - 2kd) \qquad 2.23$$

Al-Din and Gunn (1984) conducted experiments in cylindrical bunkers using glass ballotini of diameter 500µm and 100µm and fluidisable cracking catalyst of diameter 80µm. They experimented with circular, square, half square triangle, rectangular and elliptical orifices and obtained the following formula

$$\frac{Wb^2}{F_0 F_n \rho_b \sqrt{g} A (b/d)^{0.124} (b - 1.15d)^{2.5}} = 0.456 \pm 12.36\% \qquad 2.24$$

where b is the orifice width or diameter and F_0 = 1.4 for rectangular orifices and F_p = 1.0 for spheres, where F_0 is defined as the orifice coefficient and F_p is the particle flow coefficient, whose values were obtained by non-linear regression of experimental results.

Nedderman (1992) noted that the flow becomes erratic if the particle diameter d < 400μm and the orifice diameter D_0 < 6d. Humby et al. (1998) modified the Beverloo equation to calculate the mass flow rate of binary mixtures of particles of equal density in a flat bottomed hopper with a circular orifice. They proposed the formula

$$W = C' \rho_p \eta_d \sqrt{g} \left[D_o - Z' \left(d_{eff} \right) \right]^{\frac{5}{2}} \qquad 2.25$$

where C' = 0.58, Z', is a function of the effective diameter characterising the mixture and d_{eff} is dependent upon particle size distribution, ρ_p, is the particle density and η_d is the flowing packing density.

In the study presented in this thesis tests were conducted with binary mixtures of spherical particles in a 3D wedge shaped hopper slice. To assist in the analysis of this, equation 2.21 can be modified for a b x l slot orifice. It is proposed that the mass flow rate of a binary mixture will be given by

$$W = \frac{4C'}{\pi} \rho_p \eta_d A^{*'} \sqrt{g D_H^{*'}} \qquad 2.26$$

where

$$A^{*'} = (b - Z')(l - Z') \qquad 2.27$$

and

$$D_H^{*\prime} = \frac{4(b-z')(l-z')}{2\,(l+b-2z')} \qquad 2.28$$

Qais Abdullatif Buali (1999) conducted experiments to determine the effect of varying the material bed height, the hopper width, particle size and hopper half angle, orifice size and moisture content on the discharge rate, as part of an MSc project. It was found that the discharge rate was independent of the material bed height and the hopper width. Particle size was found to have a negligible effect on discharge rate. The orifice size and hopper half angle were found to have a major effect on the flow rate. The orifice size and flow rate were found to satisfy the linear relationship between $W^{2/5}$vs. D_h as proposed by Beverloo (1961). The effect of increasing the hopper half angle was a decrease in the flowrate until a critical angle was reached. A further increase in the hopper half angle resulted in no further effect on the discharge rate. An increase in the moisture content of the wheat grains resulted in a decrease in the flowrate at a critical percentage moisture content.

2.6 The flow of free-cells in discharging silos

The majority of studies involving free-cells or tracer particles have been conducted with the intention of determining the flow fields in discharging silos. The accuracy of experimental measurements is dependent upon the ability of the tracer particles or free-cells to follow the surrounding material as close as possible.

Most studies involving placing free objects in silos have been conducted with the aim of accurately deducing the velocity profile during discharge, by measuring the residence time of objects, such as radio pill transmitters (Perry et al., 1976), coke nuggets and epoxy spheres (Graham et al., 1986), steel and Perspex spheres (Nedderman, 1988), radio frequency tags (Ooi et al., 1998; Chen et al., 2004) and sugar lumps (Job et al., 2009). Free objects have been used to measure the silo wall and internal pressures (Handley and Perry, 1967) and the dispersion of particles close to the centre line using a different coloured particle (Medina, 1998).

Nedderman (1988) placed two sizes of steel sphere, one having a diameter twice as large as the other, and a Perspex sphere, into a conical hopper/bin and obtained the time taken for them to emerge through an orifice. The steel spheres had a density seven times greater than the Perspex sphere. Nedderman placed the spheres into the hopper down a guide tube. The large steel sphere had the smallest residence time and the Perspex sphere the greatest time. Cleaver (1993) attributed this slight difference in residence time to the more dense ball bearings burrowing further into the material than the less dense Perspex sphere after free-fall down the guide tube. Experiments using steel and ceramic spheres of similar size revealed that the steel sphere burrowed a few centimetres under the surface but the ceramic free-cell remained on the surface. Nedderman (1988) observed that there was a delay between the onset of discharge in the hopper, and the movement of the free-cells, which had to be taken into account when evaluating the time of travel. There was also negligible difference in the time of travel between the two sizes of ball bearing. It was concluded that the density and size of the free-cells was therefore unimportant.

Perry (1976) placed radio transmitter pills into a small mass flow bunker filled with sand. Previous observations recorded that the radio pills moved from a vertical orientation when they entered the hopper section of the bunker. It was observed that the velocity of the pills was equal to the velocity of the top surface of the sand and therefore the radio pills flowed synchronously with the surrounding sand.

Graham et al. (1987) inserted markers to measure the residence time and test the predictions of the kinematic model in an axisymmetric silo. Experiments were conducted with monosized ‘smooth’ epoxy spheres and multiple sized ‘rough’ coke particles. The tracer particles were on average about five times bigger than the average particle size of the grains. The tracer particles were epoxy and plastic spheres in the hopper filled with epoxy spheres and coke and ceramic spheres in the hopper filled with coke. It was found that the variations in size, density, shape and surface properties of the tracer particles did not affect the results.
Job et al (2009) conducted experiments in a storage silo of a sugar refinery. The silo had been designed for mass flow, but was found to be exhibiting funnel flow, due to excessive moisture. The residence time of sugar lumps, used as tracer particles in a silo filled with sugar ingots was obtained. The sugar cubes were chosen as they had the same density as the sugar

ingots. Reference is made to the fact the difference in size between the ingots and cubes may result in some segregation of the cubes, which may affect the results, but this is deemed to be negligible due to the non-spherical shape of the ingots.

Positron Emission Particle Tracking (PEPT) (Figure 2.18) is a technique developed to record the velocity and trajectory of particles in multiphase systems. Yang et al. (2007) provide a description of the technique, given below. The first reported use of PEPT to analyse multiphase systems was given by Bemrose et al. (1988) who used the technique to analyse particulate flow in a fluidized bed. It has been applied to understanding, for example, spherical particle motion in rotating drums (Paker et al. 1997), but there is no known literature that reports the use of Positron Emission Particle Tracking to determine the velocity and displacement of particles in hoppers and silos. However, the technique has the potential to be useful and so it is reported here for completeness.

The technique involves a labelled tracer particle, a positron camera and a location algorithm used for locating the tracer and calculating the speed. The tracer particle is labelled with a radionuclide which decays by β^+ decay with the emission of a positron. Each positron rapidly annihilates with an electron giving rise to a pair of γ rays which are emitted almost exactly back to back. The camera consists of two positron sensitive detectors mounted ach side of the field of view and use to detect the pairs of γ rays. The two γ rays are simultaneously detected in the two detectors and define a trajectory passing close to the surface. The location algorithm calculates the point which minimizes the sum of perpendicular distances to the various trajectories. Many of the detected events are corrupted but algorithms have been developed that discard the corrupted events and calculate the location using just uncorrupted events. The velocity of the labelled particle can be determined from successive locations as it passes through the view of the camera (Yang et al. 2007).

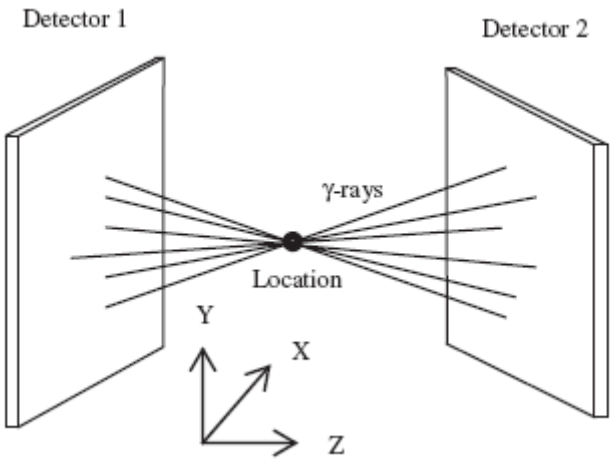

Figure 2.18: Positron Emission Particle Tracking

Yang et al. (2007) developed the Multiple Positron Emission Particle Tracking Technique such that it is capable of tracking multiple particles rather than just one.

Equipment and methods

3 Equipment and Methods

3.1 Introduction

In this section the details of the equipment used in the practical experiments is described. This includes. Initial experiments were conducted on quasi 3D silo used by previous researchers. In this work that silo is referred to as the Mark I hopper. Initial tests to determine the kinematics of wheat grains and free cells were conducted in this hopper. These tests indicated the difficulty in obtaining reliable data using wheat grains and constraints in the possible hopper and silo dimensions. A new quasi 3D silo was designed and constructed and the dimensions of each of the components are provided and the range of silo and hopper dimensions is given. The particles used to replace the wheat grains are introduced and the rational behind using them is discussed. Spherical particles are very ideally shaped particles, so tests were also conducted to determine the discharge characteristics of a batch of polyhedral dice, whose physical properties and dimensions are listed. All methods used in the practical experiments to study the flow and discharge of spherical particles, polyhedral particles and the trajectory of free-cells are presented and discussed.

3.2 Equipment

3.2.1 Free Cells

In section 2.2 previous studies using free-cells of tracer particles were discussed. A free-cell is defined as a particle that is free to move with the other particles in the batch, compared to particles that are fixed to the sides of the hopper, or held static in the granular media. Free cells can have a different size and shape to the other grains in the media or may have identical properties to the other grains, but are coloured differently or have radio transmitter equipment enclosed in them, to distinguish them from the other grains.

The free cells used in the experiments in this study (Figure 3.1) were of three different shapes and were constructed of three different materials. The different materials were chosen using what was available in the workshop and so that a range of densities of free cells could be tested. The shapes were chosen because they are simple shapes and because the cuboid and

triangular prism may be more representative of a foreign body trapped in a silo. Free cells larger than the grains were tested because in a real system the electronics restrict how small the free cells can be. The size of the free cells may affect the displacement of the surrounding particles, but the aim of this study is to deduce the kinematics of the different free cells, with the intention of deducing an appropriate shape and density of free cell such that it moves with the majority of the surrounding particles.

Figure 3.1: Free cells used in this study. From top to bottom: metal, PVC and hollow shapes

Cylindrical, cuboid and triangular prism free cells were manufactured from metal and PVC plastic. The hollow free cells were constructed from an assortment of materials. Each free cell was designed so that the cross sectional area was the same (Figure 3.2). Constant cross-sectional area and free cell volume was chosen so that experiments could be conducted to deduce how the shape of the free cells affected their trajectory during hopper discharge. The cross sectional area was initially chosen based on the appropriate size of the cylindrical sensor such that it would flow through the orifice, without getting trapped. The appropriate orifice width was chosen so that the flow pattern of the particles in the hopper could be easily observed and it was deduced by trial and error that the cylindrical and cuboid free cells would pass through the orifice unhindered. The triangular free-cell did get trapped in the orifice, but this was deemed to be a small problem, as the investigation was about deducing the displacement and path of the free cells in the silo and not what happened at the orifice. A diameter of 2 cm for the cylindrical free cell was thus chosen as an appropriate size. The cross sectional area of the cylinder was calculated and then the sides of the triangle and square were calculated using simple formulae. The length of the free cells was a constant 24 mm so that

they could easily slide between the front and back Perspex sheets. The ratio of the length to the cross sectional area of the free cells L/A ≈ 2.4/π. The centre of gravity (Figure 3.3) of the free cells was assumed to lie at the centre of the free cells and was not measured. The density and side length or diameter of the free cells is shown in figure 3.3.

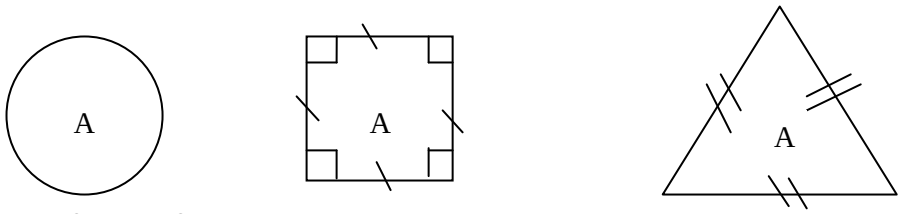

Area = πr^2 = π cm^2 Length = 24 mm

Figure 3.2: The cross sectional area of the cylindrical, cuboid and triangular prism free-cells

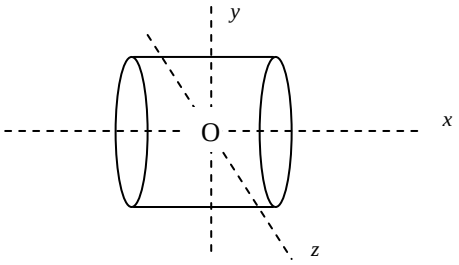

Figure 3.3: The centre of gravity O of a cylindrical free cell.

Table 3.1: Free-cell dimensions

	Metal	**PVC Plastic**
Density g cm^{-3}	8.0	1.2
Volume cm^3	7.5	7.5

Shape of cross section	Square	Triangle	Circle
Side length/diameter cm	$\sqrt{\pi}$	$\sqrt{\frac{4\pi}{\sqrt{3}}}$	2

3.2.2 Mark I 3D slice hopper

Initial experiments were conducted in a small 3D slice hopper (Figure 3.4) designed by Buali (1999) as part of an MSc project.

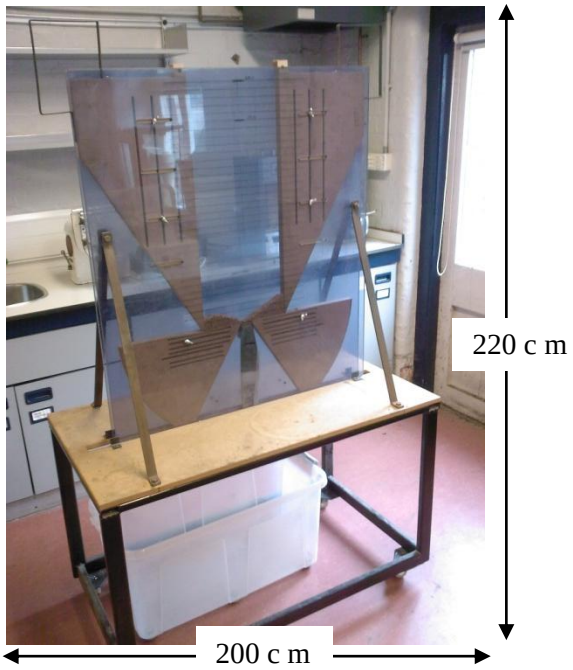

Figure 3.4: Mark I 3D slice hopper

The five main geometrical aspects in the experimental silo were the width, height, orifice size, hopper angle and the depth or thickness of the hopper.

The silo used by Buali (1999) and the subsequent new silo designed in this study are scaled down versions of the types used in industry. Iturrioz et al. (2007) tested the performance of the Discrete Element Method in representing the scale effect. They deduced that the stress and strain rates, the interparticle forces and the elastic modulus of the particles and the damping factor between the particles would be affected by changing the scale of the silo. Feng et al. (2009) established three similarity principles that would have to be scaled between silos of different sizes, the geometric, mechanical and dynamic principles. They deduced that the stress and strain rates would change with scale and the lengths, volume, area and density of the particles would all have to be scaled down for a smaller system to be representative of the particles in the industrial scale silo. The particle packing would also have to be the same on both scales for the smaller model to be representative of the industrial scale silo. Therefore the

results obtained in this study cannot be generalised to an industrial scale silo, unless all the variables used in this study are scaled up accordingly and match those observed in an industrial scale silo.

The Mark I hopper consisted of six pieces. The front and back walls were made of Poly Vinyl Chloride (PVC) to allow observation of the flow inside the hopper. The vertical bin walls and the inclined hopper sidewalls were constructed from MDF wood. Eight sets of ten holes had been drilled through the PVC sheets in addition to two holes at the bottom. The holes were later converted into long slots to increase the freedom of movement of the wooden sides. Slots were cut out of the wooden pieces so that they could be easily moved to alter the hopper angle and orifice size. Initially there were three slots cut out of the wooden pieces, but later two further slots were cut out of the bottom pieces to allow a greater freedom of movement of the hopper walls. The PVC sheets were clamped together using two metal guides attached to the wooden table and the wooden pieces were secured using screws and wing nuts. The height of material was varied by pouring more or less of it into the hopper and the orifice was secured during filling by placing folded up newspaper into the orifice. The orifice was opened by pulling out the folded newspaper.

Figure 3.5 shows a schematic diagram of the original Mark I hopper designed by Buali (1999) and figure 3.6 shows the location of the holes on the PVC sheets.

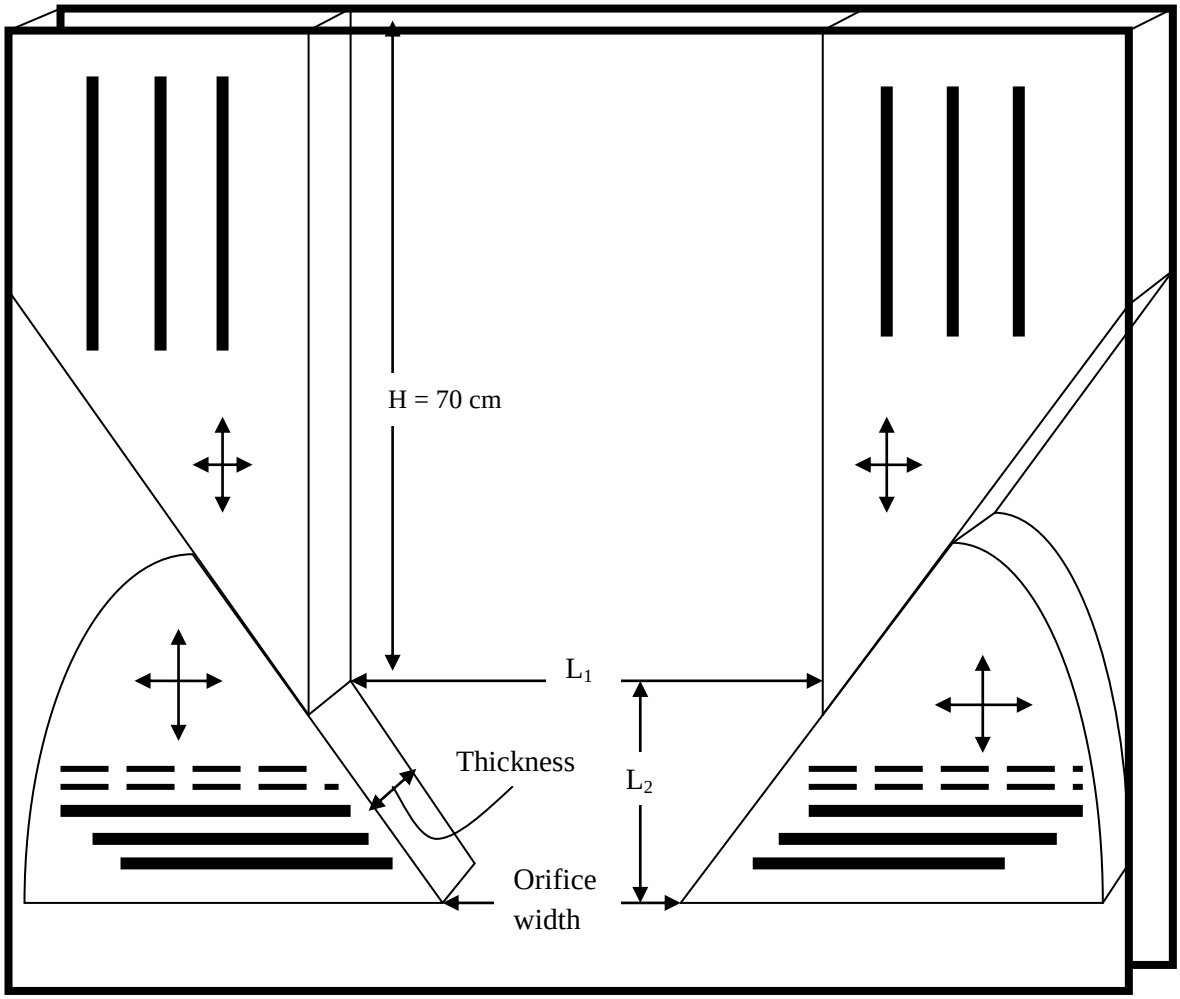

Figure 3.5: Schematic diagram of the Mark I hopper designed by Buali (1999). Arrows indicate the directions of possible adjustments of each piece. Dotted lines indicate extra slots that were cut later

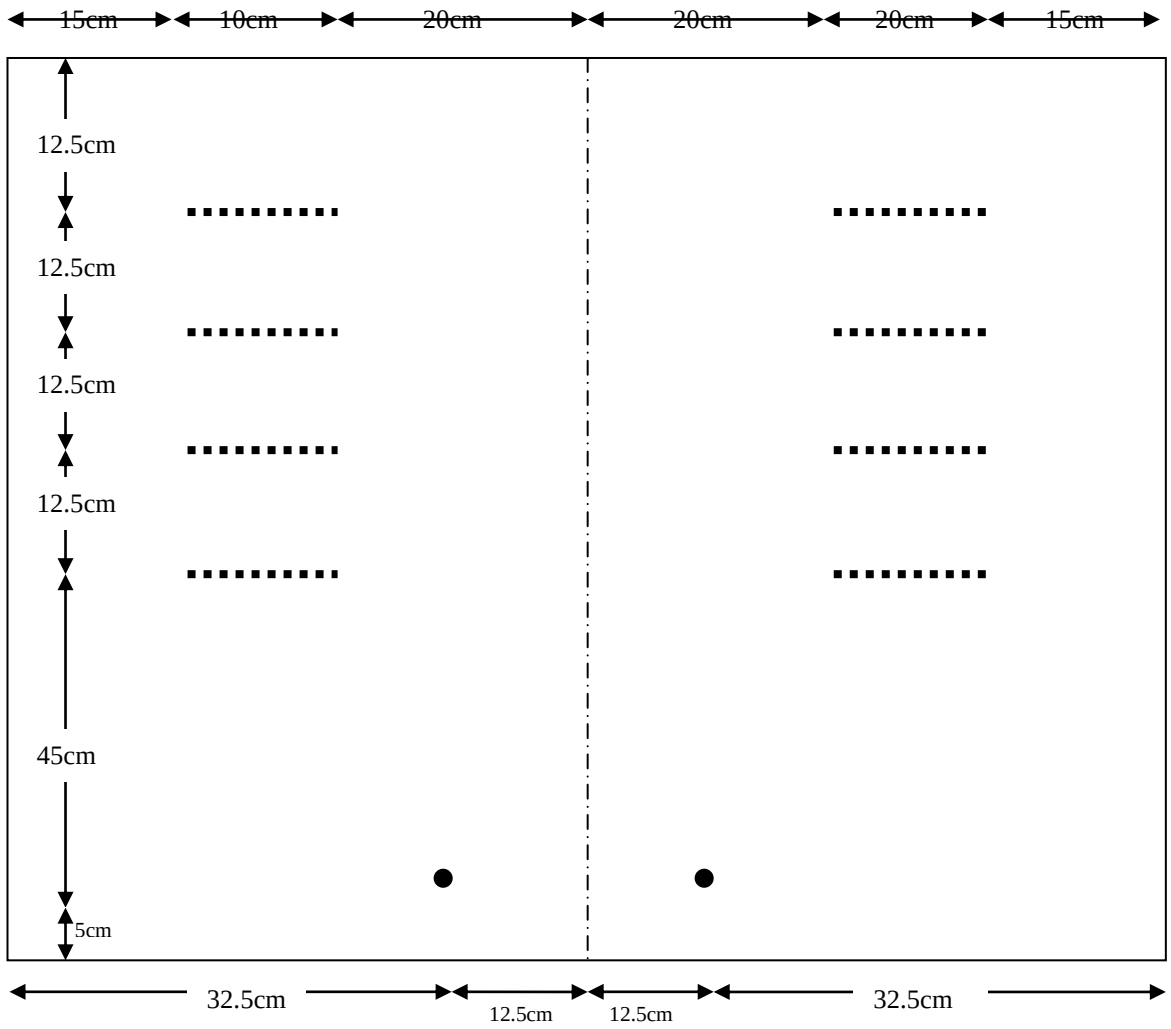

Figure 3.6: Diagram showing the location of the holes on the Perspex sheets

The hopper was designed so that the hopper half angle, α, could be varied between 30º and 90º and the orifice width could be varied between 0 - 20cm. The width of the hopper L_1 could be varied between 0 and 40cm and the maximum height of material ($H+L_2$) was 95cm. The thickness of the hopper slice was fixed at 26mm.

3.2.3 Tests conducted using the Mark I hopper

Preliminary experiments to test the suitability of wheat grains for use in the study of the kinematics of the free cells were conducted in the Mark I hopper with the hopper half angle set to be 90º (flat bottomed). Metal, PVC and wooden cylindrical, triangular and cuboid free-cells were placed on the top surface of the hopper filled with a hard wheat (variety Malacca), with dimensions shown in figure 3.7. The free cell volume is approximately 200 times larger than the volume of a wheat grain. The bed height was 70 cm. The orifice was set to a length of 3cm. This was chosen based on a simple experiment in which the orifice was set at lengths 1cm, 2cm and 3cm.

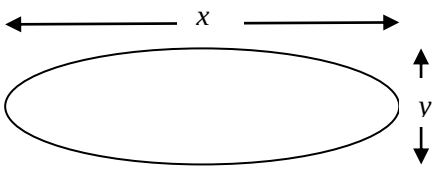

Figure 3.7: The dimensions of a Malacca wheat grain, where for different granules *x* varies between 5 mm and 7 mm and *y* varies between 3mm and 4 mm.

Grain was poured into the silo and allowed to discharge. When the orifice was set to 3cm the grain flowed unhindered through the orifice in all five trials and when it was set to 1cm it blocked in all five trials. Setting the orifice length to 2cm resulted in it blocking in 3 out of 5 trials. Davies and Desai (2008) studied the blockage in vertical slots and found that continuous flow is observed in horizontal slots greater than $3.3d_{char}$ where d_{char} is the characteristic dimension of the particles. A wheat grain with a minor dimension 3mm and major dimension 7mm will flow through a horizontal slot with width 30mm very easily. The wheat was allowed to discharge from the hopper and the time taken for the free-cells to reach the orifice was recorded using a technique developed in this project (see section 3.3). The results were analysed using VirtualDub and plotted in a graph. Each experiment was repeated three times to provide an approximate idea about the kinematics of the free cells.

3.3 Method used to record the trajectory and time of the trajectory of the free cells.

Initial tests, using a method developed in this work, were conducted to deduce the time taken for cylindrical free cells of different density to flow from the top surface of the grain, to the orifice, during discharge. A stopwatch was used to record the time. The stopwatch was stopped and started by hand, which meant that the accuracy of the time recorded depended upon the reaction time of the person stopping and starting the stopwatch. To improve the accuracy in the measurements a video camera was used. The video camera was chosen based on the resolution, the number of frames per second and the memory capability. A Hitachi DZ-HS300E/E video camera was chosen. The major specifications of the camera are given in appendix 2.

The camera was set to FINE so that the images would be of reasonable quality, but would not use too much memory. The zoom and focus were not fixed, but were adjusted according to the clarity of the image, on the particular day the camera was being used.

The video camera was calibrated by conducting a simple test. Four marks were drawn on the front Perspex sheet along the centre line (Figure 3.8). The rig was filled to the maximum height and the Perspex cylindrical free-cell was placed on the top surface along the centre line. The video camera was switched on and the orifice and the stopwatch were opened and switched on simultaneously.

When the free-cell reached the first mark the stopwatch was stopped and the free-cell and the grain discharged from the hopper. The video camera was stopped. The process was repeated. However, the second time the time taken for the free-cell to reach the second mark was recorded using the stopwatch and the video camera. The test was repeated a further two times to obtain the time taken for the free-cell to reach the third and forth markers.

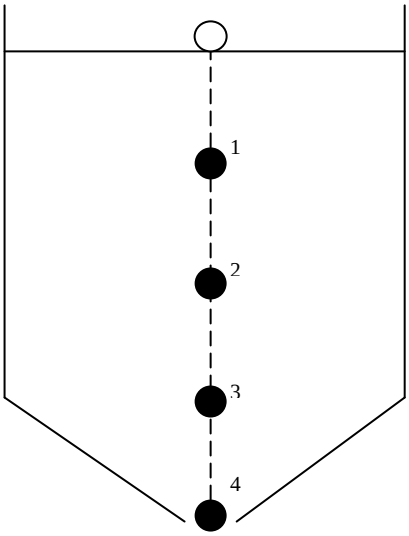

Figure 3.8: Diagram showing marks on Perspex sheet in tests to calibrate the video camera

The video camera images were viewed using VirtualDub 1.9.9 with an MPEG-2 plugin. The Virtual Dub software was chosen as the individual images recorded by the video camera could be viewed separately and the clock was accurate to $1/100^{th}$ second. The images were recorded at 1/25 s. The time t_1 on the clock in the VirtualDub software, at which the orifice was opened, was recorded and each image was quickly viewed by moving the bar on the timeline. The time at which the free cell reached the desired position t_2 was recorded and the time for the free cell to travel from the top surface to the desired position was obtained by subtracting t_1 from t_2. The results from the tests to determine the time taken to travel from the top surface to each of the points 1, 2, 3 and 4 from the video camera and the stopwatch were compared to deduce that the times recorded were in reasonable agreement.

3.4 Preliminary experiments to investigate the effect of density of free cells on their trajectories

In order to deduce an appropriate density of the free cells to use in the experiments a set of three cylindrical free cells of widely different density was tested. Figure 3.9 shows the time taken for three different densities of cylindrical free-cells to travel from the top surface of the grain to the orifice, averaged over five trials. The density of the free cells was determined by weighing them on a set of scales accurate to 1.0×10^{-8} kg and dividing the result by the

volume. As the width is gradually increased the time increases to a plateau. However, when the silo width is 28 cm there is a peak in the time. It was supposed that this peak occurred when the walls of the 3D slice were no longer impinging on the flowing core. However it may be due to experimental error. As the tests conducted in the wheat grain were preliminary experiments to deduce the suitability of the wheat grain for use in more precise tests, no errors were calculated.

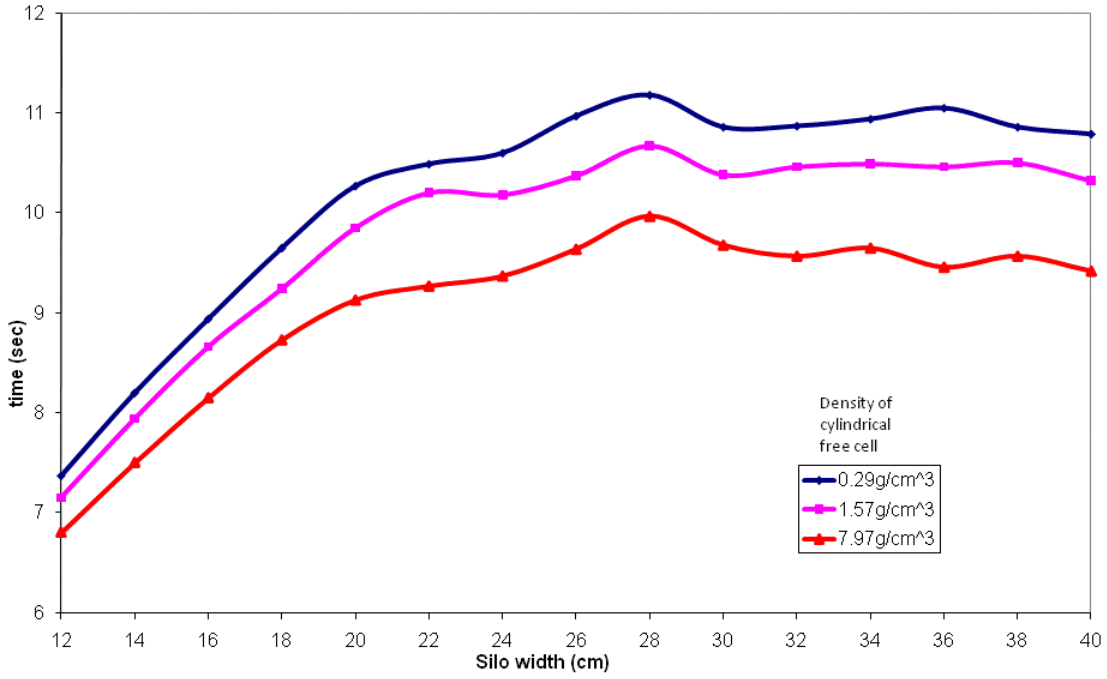

Figure 3.9: Average time taken over five trials for three cylindrical free-cells of diameter 2 cm, thickness 2.4 cm and densities 0.29 g/cm^3, 1.57 g/cm^3 and 7.97 g/cm^3 to travel from the top surface of the grain to the orifice during discharge in Malacca wheat grains with approximate ellipsoid dimensions of major axis between 3 mm and 7 mm and minor axis between 3 mm and 4 mm

3.5 Preliminary experiments to investigate the effect of size of free cells on their trajectories

The size of the free cells in relation to the rest of the particles could be important in determining an appropriate free cell that moves with the surrounding grain. Tests were therefore conducted with cylindrical free cells of diameter 4 cm, 10 cm and 14 cm and thickness 2.4 cm. Figure 3.10 shows the time taken for three different diameters of cylindrical free-cells to travel from the top surface of the grain to the orifice, averaged over five trials.

The results were inconclusive, but it was clear that the cylindrical free-cell of diameter 4cm travelled faster than the 10cm and 14cm diameter cylindrical free-cells. The effect of the size of the free cells on their displacement and velocity during silo discharge was not investigated any further in this work, but could be part of some further investigations.

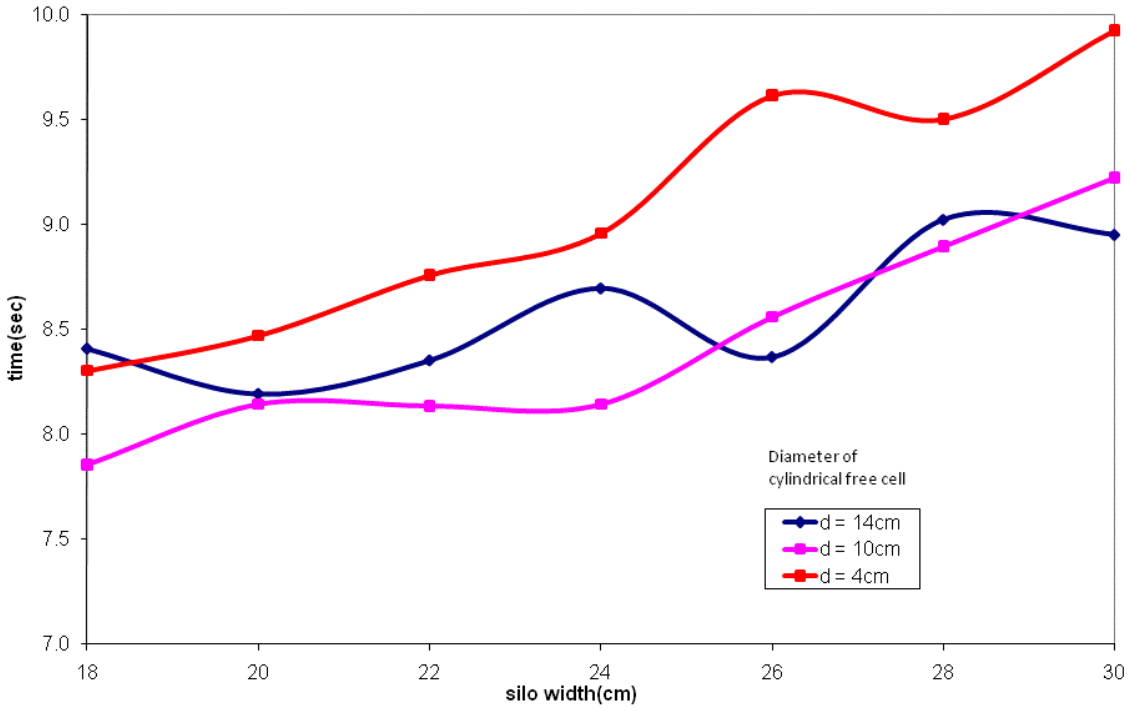

Figure 3.10: Average time taken over five trials for cylindrical Perspex free cells of density 1.6 g/cm^3 and diameter 4 cm, 10 cm and 14 cm and thickness 2.4 cm to travel from the top surface of grain to the orifice during discharge in Malacca wheat grains with approximate ellipsoid dimensions of major axis between 3 mm and 7 mm and minor axis between 3 mm and 4 mm.

3.6 Preliminary experiments to investigate the effect of shape of free cells on their trajectories

As well as density and size, the shape of the free cells was considered as a possible important factor in deducing a suitable free cell that would move with the surrounding particles. Figure 3.11 shows the time taken for three different shaped free-cells of the same volume to travel from the surface of the grain to the orifice, averaged over five trials. It appears from the graph that the shape of the free-cells has no effect on the time of travel.

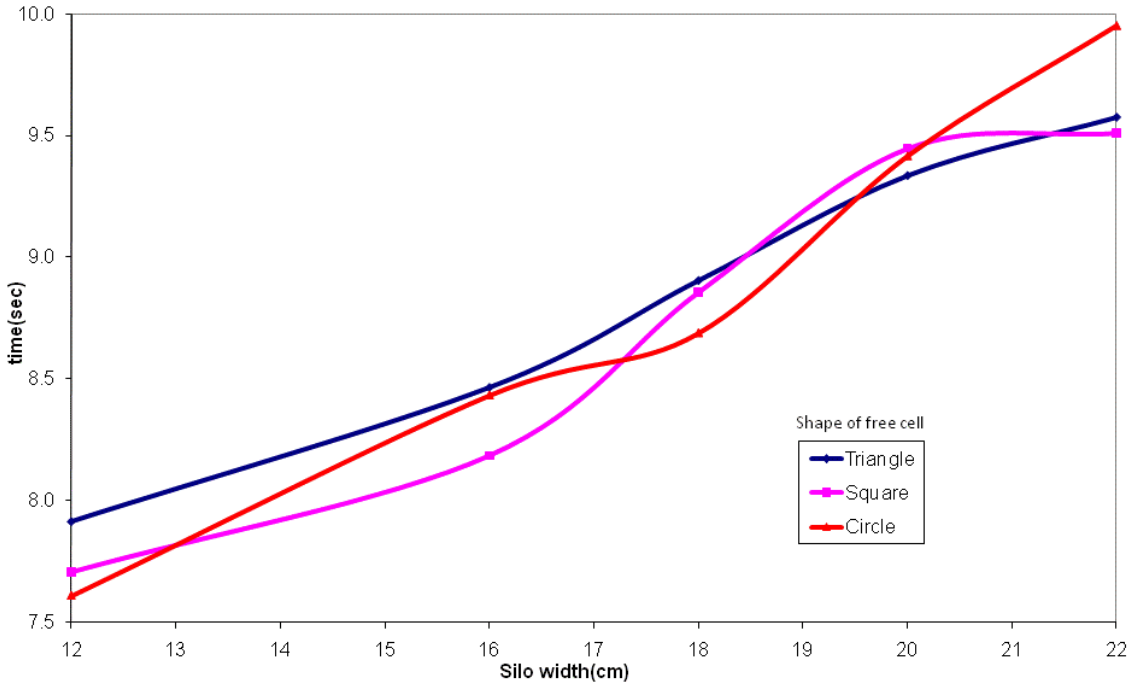

Figure 3.11: Average time taken from five trials for cylindrical, cuboid and triangular prism free-cells of density 1.6 g/cm^3, cross sectional area π cm^2 and thickness 2.4 cm to travel from the surface of the grain to the orifice during discharge in Malacca wheat grains with approximate ellipsoid dimensions of major axis between 3 mm and 7 mm and minor axis between 3 mm and 4 mm.

3.7 Discrepancies in the data

Most of the experiments conducted to deduce suitable sizes, shapes and densities of free cells were conducted on different days. It was observed that the time taken for the free cells to travel from the top surface to the orifice varied on consecutive days. It was considered that either the humidity of the air or the moisture content of the wheat grain was affecting the movement of the free cells. An experiment was conducted in which each of the 4 cm and 14 cm Perspex cylindrical free cells was placed on the top surface of the wheat along the centre line and the time taken for them to travel to the orifice was recorded. Each experiment was conducted five times. The experiments were then repeated on a second day, when the humidity was greater. Figure 3.12 shows the average time taken, over five trials, on the two separate days for cylindrical free-cells to travel from the top surface of the grain to the orifice during discharge in a hopper of width 30cm. It can clearly be observed from Figure 3.9 that the time taken for the free cells to travel to the orifice on the two days was different. Before

conducting the experiments on day 2 the hopper dimensions were measured to check none of the hopper pieces had slipped. The humidity in the laboratory was measured and found to be 42% on day 1 and 46% on day 2.

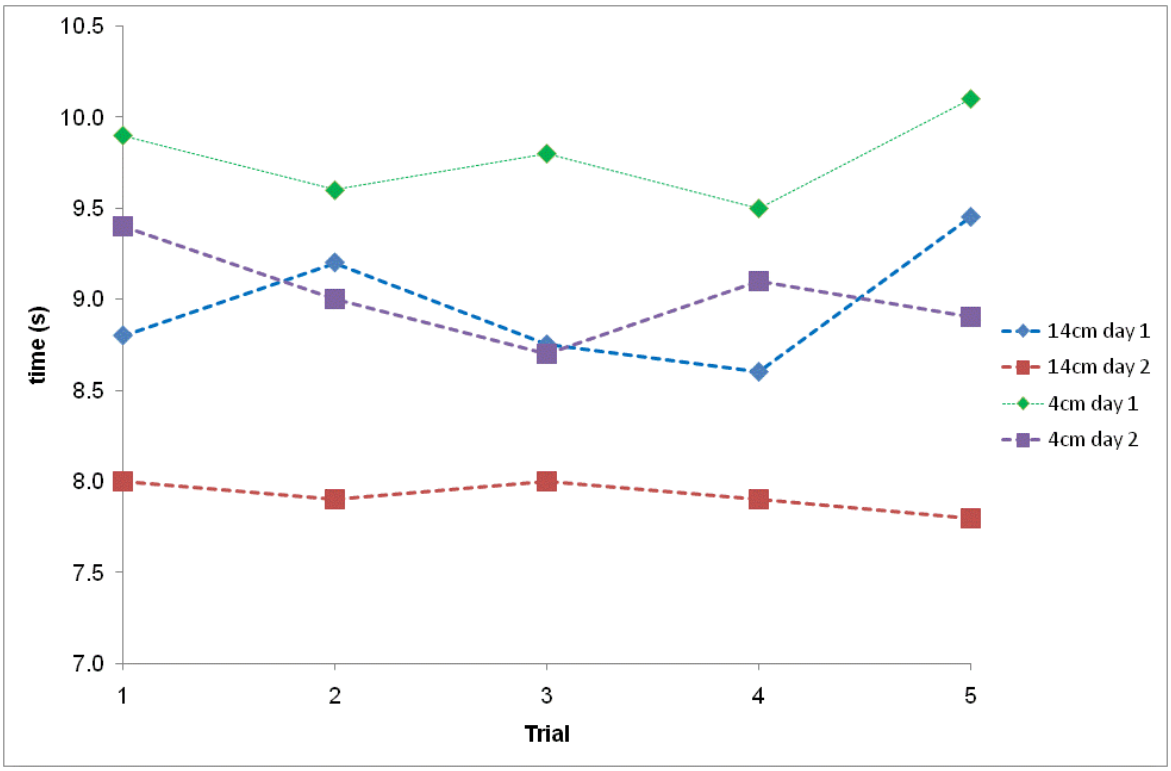

Figure 3.12: Time taken on two separate days, for Perspex cylindrical free-cells of diameter 4 cm and 14 cm and thickness 2.4 cm to travel from the top surface of the grain, to the orifice, during discharge. The results of five trials of the same experiment are shown.

The difference in the humidity on the two days was considered as a possible cause of the difference in the results. Forsyth et al. (2002) had conducted experiments with glass spheres to determine how the relative humidity of the surrounding air affects the movement of the spheres past each other. Spheres of diameter between 0.025-3 mm were tested and it was found that the transition between smooth flow of the spheres and 'stick-slip' flow occurred at a relative humidity of approximately 75%.

The experiments using the wheat were conducted during the winter months and the humidity in the lab was continually measured during the daytime. The air conditioning in the lab was switched off during the night, and air from outside could easily flow into the lab during the night, so it was unknown whether the relative humidity in the lab ever reached 75%. Unlike glass spheres wheat grains absorb the surrounding moisture and take many hours to dry out. It is likely that the cohesiveness of the wheat grains varies with moisture content. Relative

humidity and associated moisture content of the wheat could therefore have been responsible for the difference in the results on the two days.

3.8 Drawbacks in the Mark I hopper slice

There were some drawbacks in the Mark I hopper that made it difficult to use. The four pieces of MDF wood used to construct the sides of the 3D hopper slice were rather cumbersome to move. At hopper half angles, other that 90º, the maximum hopper width obtainable was only 40 cm. This decreased for decreasing hopper half angle. The hopper width could also only be varied in 2 cm intervals. The pieces of MDF had also started to bow with time and they were cumbersome to move around. A new Mark II hopper with a wider range of hopper length and hopper half angle was designed. The new Mark II hopper was designed so that it was easier to alter the dimensions than the Mark I hopper.

3.9 Mark II 3D slice hopper

All further practical experiments reported in this thesis were conducted in a Mark II 3D hopper slice as shown in Fig 3.13.

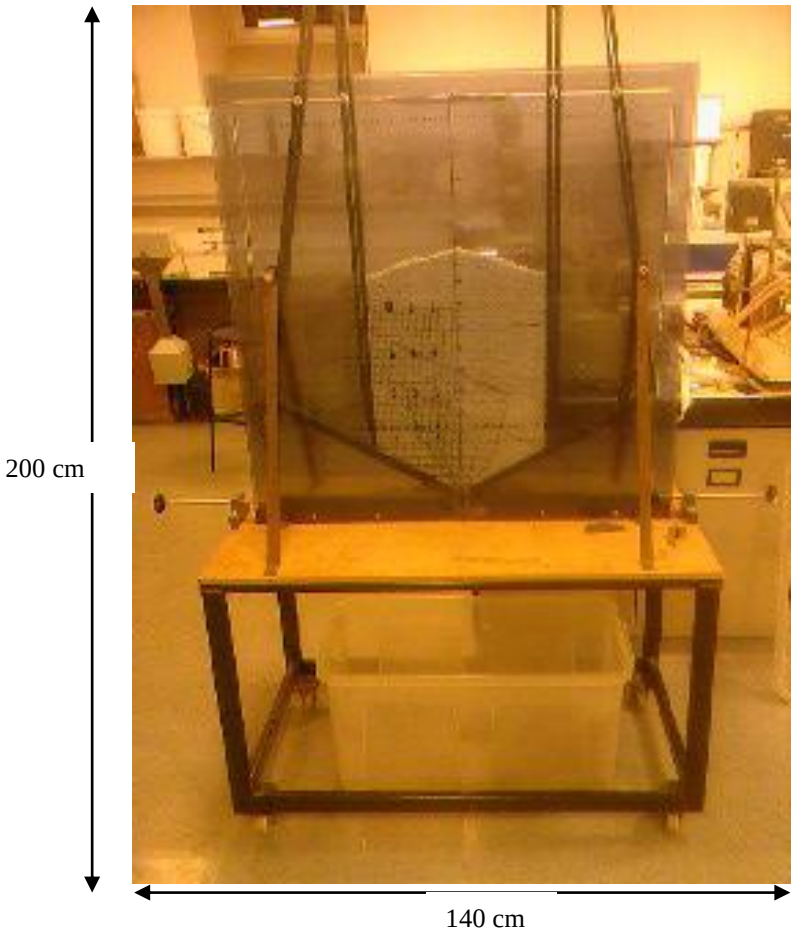

Figure 3.13: General view of 3D hopper slice filled with white cellulose acetate spheres

The new hopper was designed for ease of use. The Mark I hopper was cumbersome to use and the wooden pieces were difficult to move about. The new hopper was designed so that the pieces were easy to move and there was maximum freedom of movement, so a wide range of hopper angles (0 - 90º), orifice widths (0 – 12 cm) and bin widths (100cm) could be attained.

3.9.1 Hopper components

The hopper was constructed from each of the following pieces, as indicated in figures 3.14a, 3.14b and 3.14c.

The front and back walls were made from two clear Perspex sheets of thickness 6 mm. Slots of width 5mm were cut into the sheets so that the hopper angle and bin walls could be adjusted.

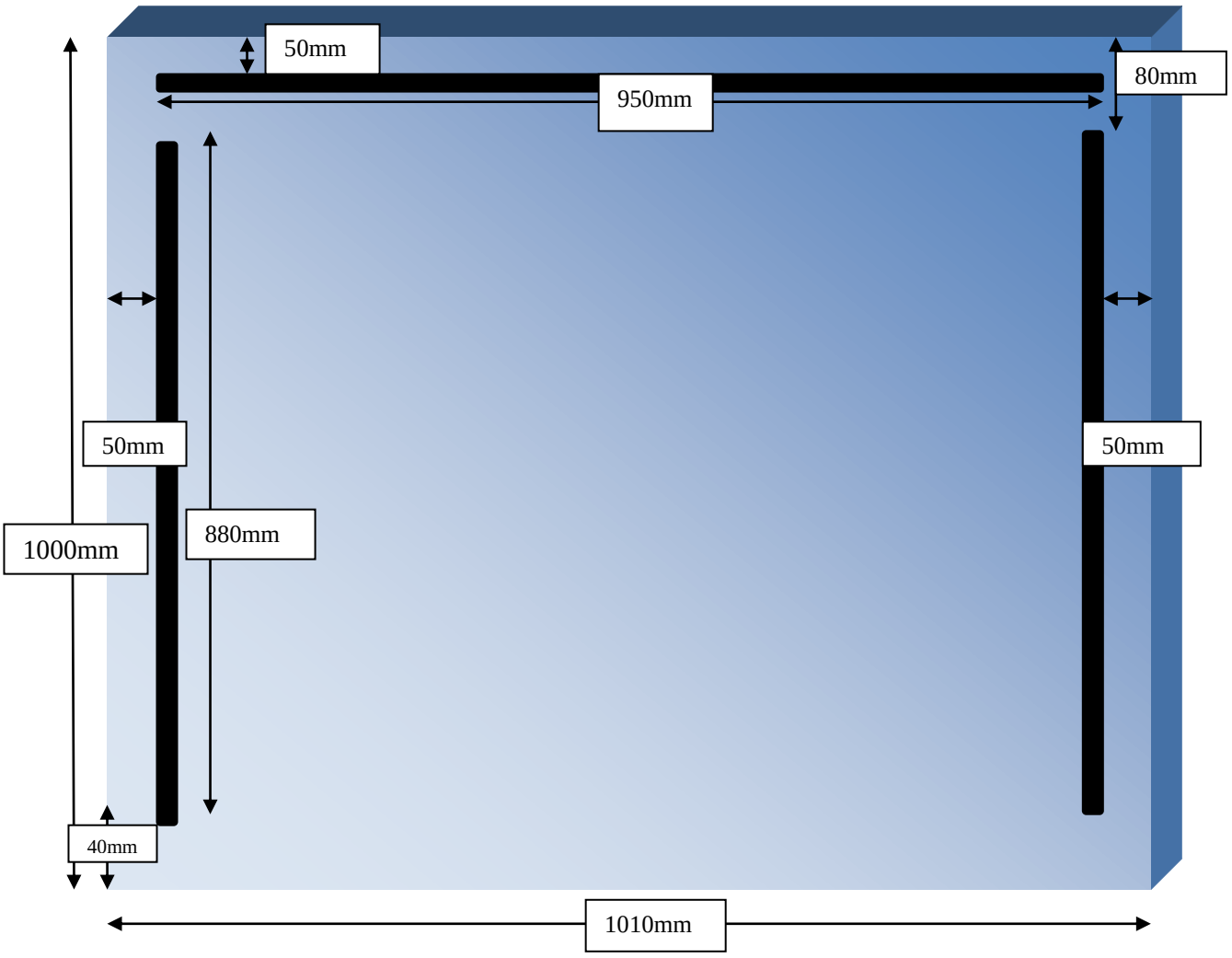

Figure 3.14a: The Perspex (x 2) sheets comprising the front and back walls of the 3D silo

The bin and hopper sides were made of Perspex strips. They had a thickness of 24mm so that they fitted between the Perspex sheets. Slots of width 5mm were cut out of the strips.

Grey Perspex strips x2
for hopper bottom

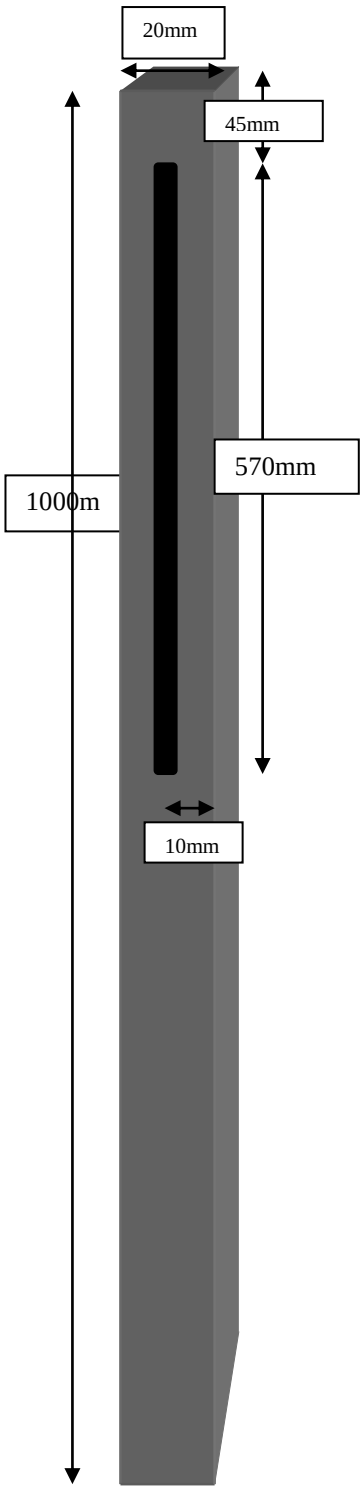

Grey Perspex strips x2
for bin sides

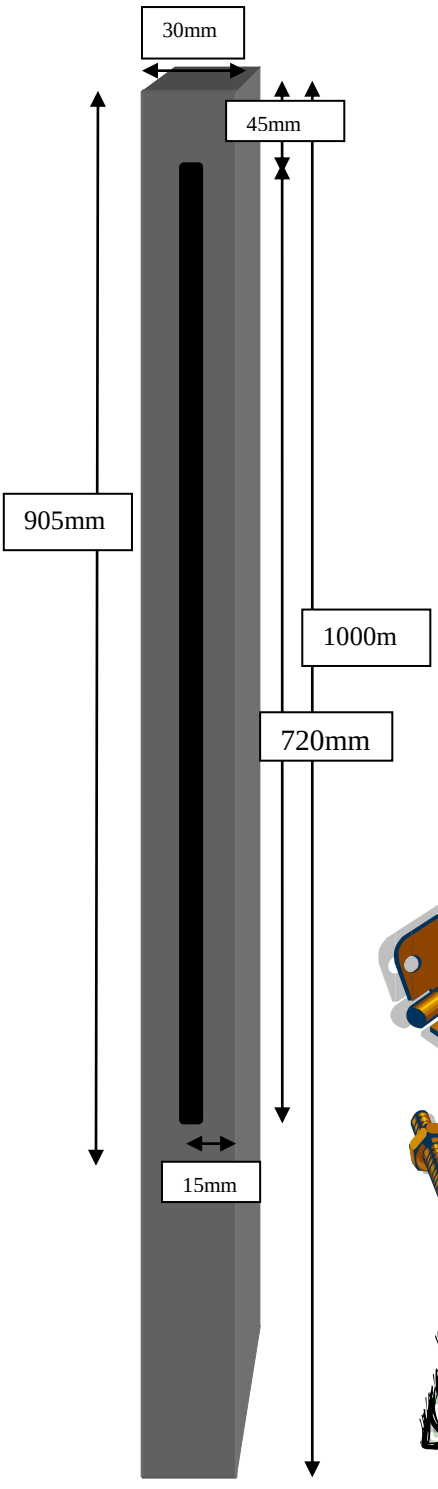

Grey Perspex strips x2
to support bottom

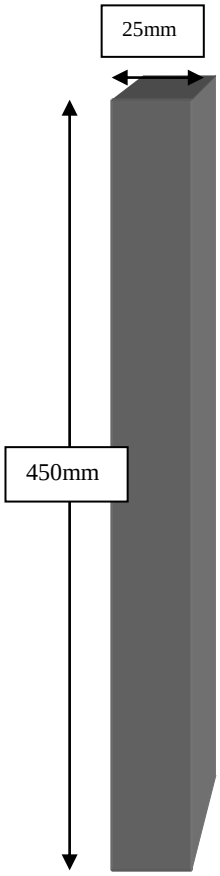

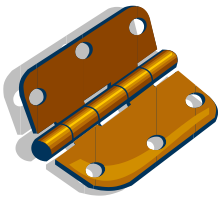

section of piano hinge x2

4 long screws with bolts to secure hopper and bin

4 large screws to secure Perspex sheets

x2 thread rod l = 300mm d = 10mm with handle

x2 Perspex strips for altering the orifice width. Hole drilled at one end for screw thread to be attached.

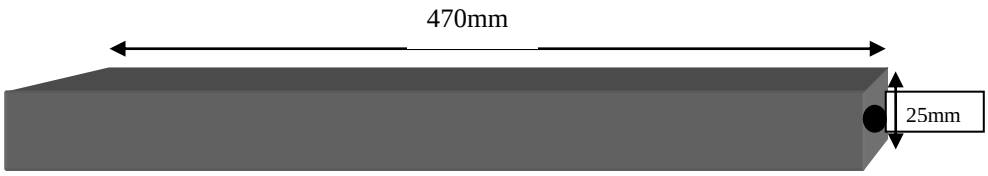

x2 Perspex strips to secure the Perspex sheets at the bottom of the rig. Holes drilled to secure Perspex sheets at bottom of rig.

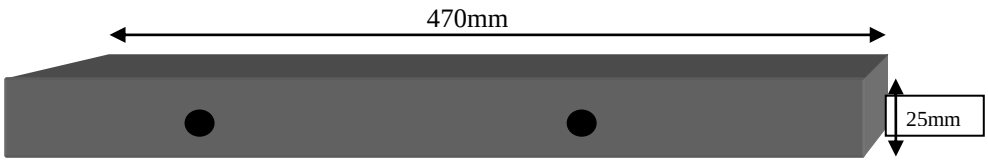

x2 to hold screw thread

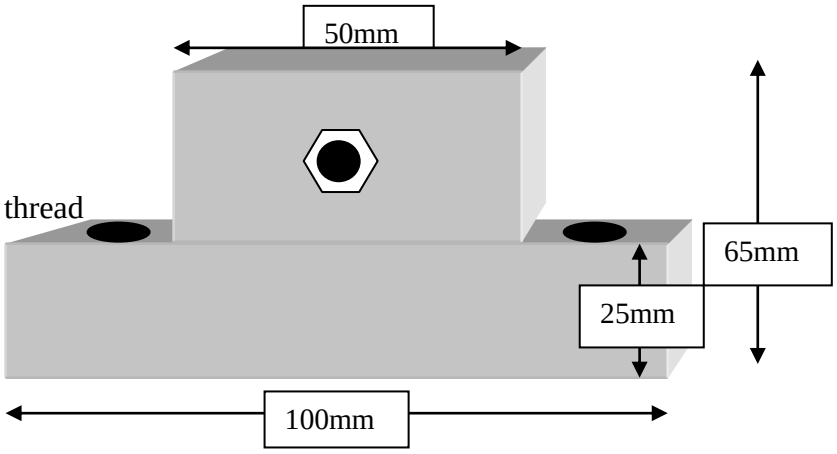

Figure 3.14b: Various pieces used to construct the bin and hopper sides

Two Perspex blocks were glued together to make an end piece to hold the screw thread. A bolt was placed in each block to turn the screw thread as a means of altering the orifice width. The block was secured to the table with two screws.

x4 strips were bent to hold the Perspex sheets in place.

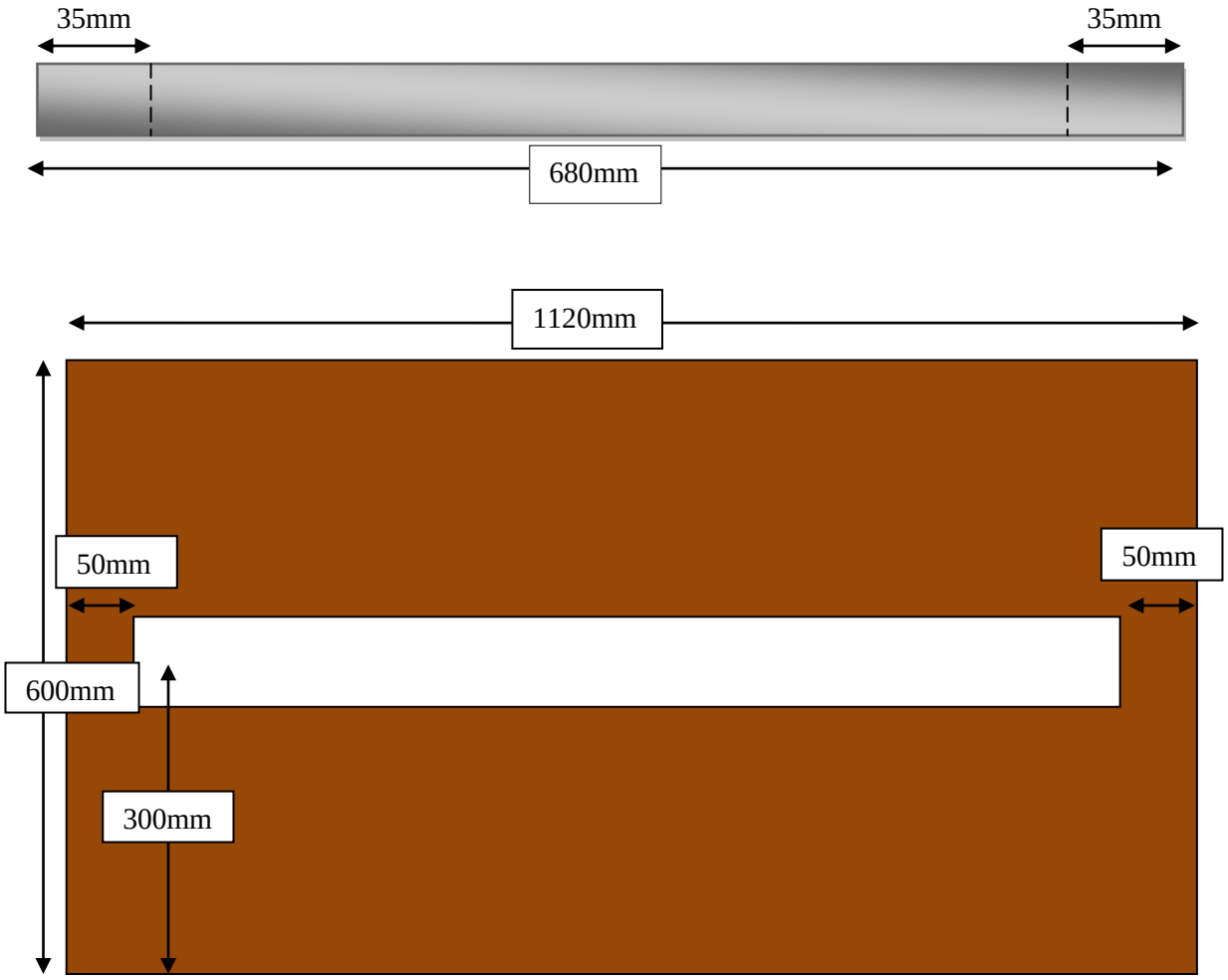

Figure 3.14c: Cross-sectional view of the table that the 3D hopper slice was placed on and the metal strips holding the Perspex sides in place

The hopper and bin constructed from the Perspex sheets was positioned on a wooden table and a slot of width 35mm was cut out along the centre. Holes were drilled for the blocks holding the screw thread and the metal strips holding the Perspex sheets. The wooden table was placed on a metal frame of height 700mm from the ground. The metal frame was fitted with wheels to enable it to be moved around.

Each piece was fitted together as shown in Figure 3.15 where the arrows indicate possible adjustments.

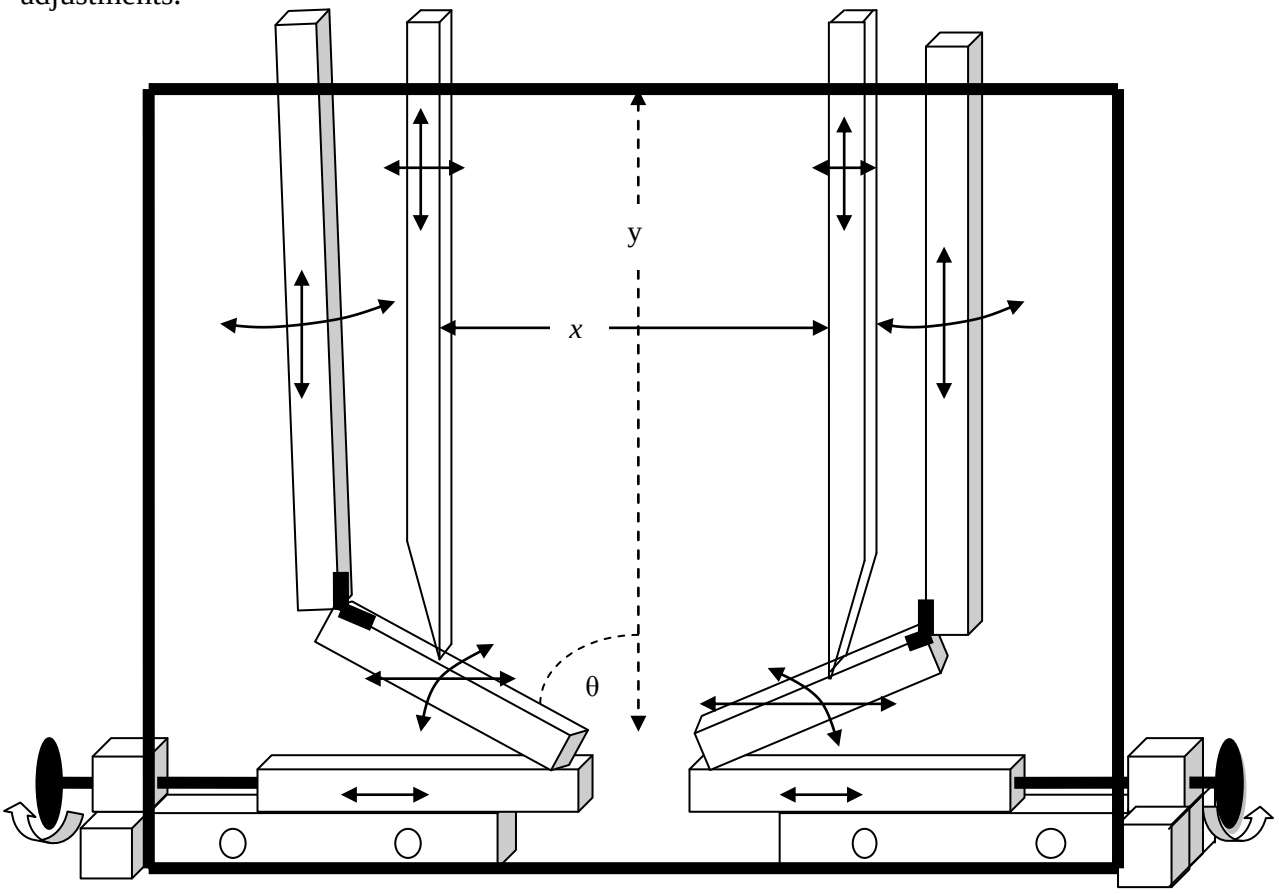

Figure 3.15: Schematic diagram of Mark II hopper. Arrows indicate possible adjustments

The distance between the Perspex sheets was set to 24mm and the hopper half angle θ can be varied between 20º - 90º. The width of the silo, *x*, could be varied between 0 – 100 cm, which was dependent on the hopper half angle. The smaller the value of θ results in a reduction in the range of potential widths. The distance from the orifice to the top of the hopper, *y*, was approximately 100 cm

3.10 Selecting appropriate particles

Initial experiments were conducted using the wheat, as discussed in section 3.2.3. The discrepancies in the data shown in figure 3.12 led to consideration of particles made from materials whose physical properties would be less affected by environmental factors i.e. temperature, humidity.

To enable comparison with DEM simulations and to reduce possible humidity effects the decision was made to experiment with spherical particles, ideally with a similar volume and density to Malacca wheat grains. The average volume of a wheat grain was calculated by measuring the volume of ten grains, this was determined to be sufficient by application of the formula

$$n = \frac{1.96^2 \sigma^2}{E^2}$$

where σ is the standard deviation and *E* is the allowable error. The average volume of ten grains was determined to be 0.054 cm^3 with a standard deviation of 0.005 cm^3. Based on the range of dimensions of the wheat grains present in the batch the allowable error is 0.004 cm^3 which gives a value of *n* of approximately 6. Hence ten grains is a sufficient sample size to obtain the average volume

The volume of each was obtained by application of the Archimedes principle. A grain was dropped into a small cylinder of water and the volume of water displaced was calculated. The average weight of a grain was obtained by weighing ten grains.

The average weight of a grain was determined to be 0.0707 g and the average diameter of a sphere of equivalent volume was calculated to be 0.47 cm. The average density of a wheat grain was calculated to be approximately 1.30±0.1 g/cm^3. Any changes in the moisture content of the wheat grain are likely to alter the value of the density.

Spherical cellulose acetate particles of density 1.28 g/cm^3 and approximate diameter 0.5 cm where therefore chosen to represent a monosized idealised batch of Malacca wheat grains. The particles were obtained from Engineering Laboratories Inc in the USA.

Real granular materials are not composed of monosized particles, so tests were also conducted with binary mixtures of particles.

Experiments were conducted using binary mixtures consisting of particles of two different sizes but identical density and two different sizes with different densities. Cellulose acetate spheres of diameter 5 mm were mixed with cellulose acetate spheres of 4 mm to make up the binary mix of particles of the same density. The 4 mm cellulose acetate spheres were also obtained from Engineering Laboratories Inc in the USA. The 5 mm cellulose acetate spheres were also mixed with 6 mm Airsoft pellets of average volume 0.112cm^3, average mass 0.1232g and average density 1.16g/cm^3. The Airsoft pellets were supplied by a small private supplier and were manufactured in an unspecified, low density plastic material. Each of the three types of spherical particles used in the experiments is shown in Figure 3.16.

3.11 Polyhedral dice and bubble gum balls

It has previously been mentioned that experiments were conducted using a batch of polyhedral particles. Three hundred and twenty two particles were used. The methods used to determine the flow rate are described in section 3.5. So as to allow comparisons with other work tests were also conducted with 322 spherical particles with nearly identical volume. Six different shapes of polyhedral dice were tested. The dice and bubble gum balls, as shown in Figure 3.17a,b and Figure 3.18. The principle particle data are shown in Table 3.2a, 3.2b and 3.2c.

Initial tests with the bubble gum balls and polyhedral dice revealed that the total discharge times were about 2 seconds. Obtaining the fractional discharge rate was impossible with the Hitachi video camera as the number of frames per second was only accurate to the nearest 1/25s and the shutter speed was automatic, varying according to the amount of light available. A Phantom V710 colour high speed video camera was obtained from the EPSRC Engineering Instrument Pool on behalf of the Rutherford Appleton Laboratory. The specifications are given in appendix 3.

Table 3.2a: Physical properties of the spherical particles.

a) Spheres	A	B	C
Colour	Yellow	white	black
Diameter cm	0.587	0.485	0.396
Density gcm^{-3}	1.16	1.28	1.28
Particle-Particle			
sliding friction	0.3249	0.3249	0.3249
rolling friction	0.0011	0.0022	0.0042
Particle-Wall			
sliding friction	0.3057	0.3057	0.3057
rolling friction	0.0210	0.0212	0.0415
Coeff of restitution	0.82	0.81	0.85
Angle of repose between rig sides	28°	27°	26°
Angle of repose in heap	19°	19°	20°

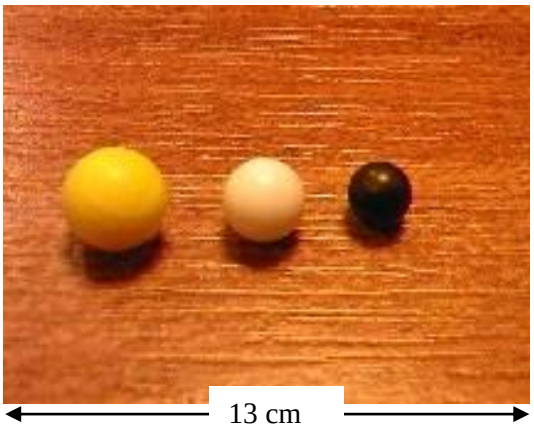

Figure 3.16: Three different sizes of spherical particles

Table 3.2b: Physical properties and dimensions of the polyhedral dice.

	No	Volume cm^3	Density gcm^{-3}	Side length cm
Pentagonal trapezohedra	90	2.73	1.65	see Fig.3.31
Octahedra	31	2.57	1.56	1.76
Tetrahedra	29	1.05	2.19	2.08
Icosahedra	81	5.02	1.27	1.32
Hexahedra type 1	55	3.83	1.17	1.56
Hexahedra type 2	36	3.55	1.17	1.56

Total number = 322

Table 3.2c Physical properties of dice and bubble gum balls.

Parameter	**Value**
Particle dimensions	a) For polyhedra see Table b b) r = 1 cm
Particle density	a) For polyhedra see Table b b) 1.34 gcm^{-3}
Coefficient of restitution	a) 0.54, b) 0.59
Friction Coefficients	
Sliding	a) and b) 0.2800
Rolling (spheres) particle-wall	0.0190
particle-particle	0.0005
Angle repose of bubble gum balls between rig sides	40º
Angle repose of bubble gum balls in heap	22º

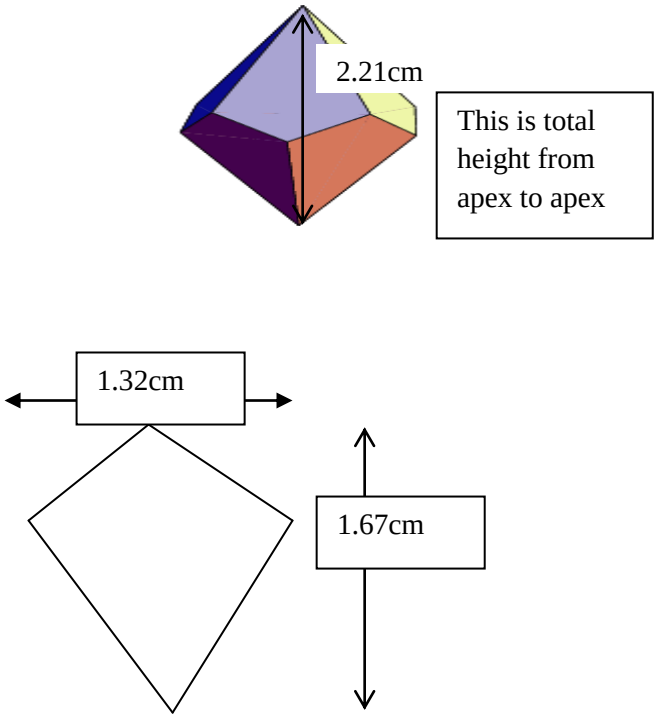

Figure 3.17a: Dimensions of the pentagonal trapezohedron

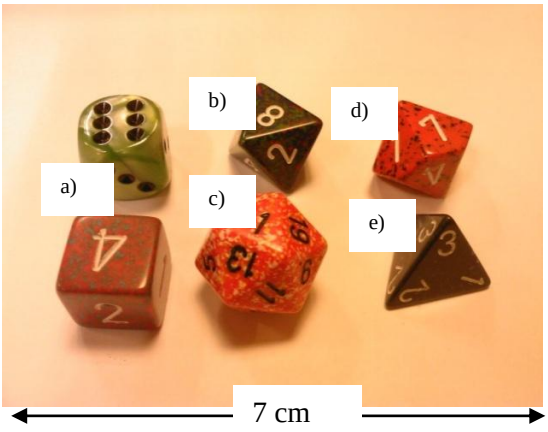

Figure 3.17b: Polyhedral dice used in practical experiments. From left to right, down each column: a) two types of hexahedron, b) octahedron, c) icosahedron, d) pentagonal trapezohedron, e) tetrahedron

Figure 3.18: Bubble gum balls

3.12 Experiments to deduce the flow of the free cells

Experiments to deduce the flow of the free cells in the monosized particles were conducted in a batch of 50000 white particles. Various numbers of particles were considered. A suitable number was chosen by testing how long it would take the DEM program to simulate a certain number of particles and so that meaningful experimental data could be obtained from the practical experiments.

The hopper half angle was fixed at 60º so that the particles discharged in the funnel flow regime. This was determined from observation as it is unknown whether the theoretical predictions are accurate enough (Nedderman, 1992). The walls were fixed a distance 40cm apart so that they did not penetrate the flowing core. The funnel flow regime was chosen because mass flow patterns are well understood (Ooi et al., 1998).

The rig was filled to the level of the positions 1 to 12 in turn, as shown in Figure 3.20 and the particles near the position were levelled flat using two sticks and the free cell particles placed carefully onto the particles using two sticks to lower them into position (Figure 3.19). The initial position of the free-cells is shown in Figure 3.19. The rest of the particles were then carefully poured into the rig so they did not disturb the free cell.

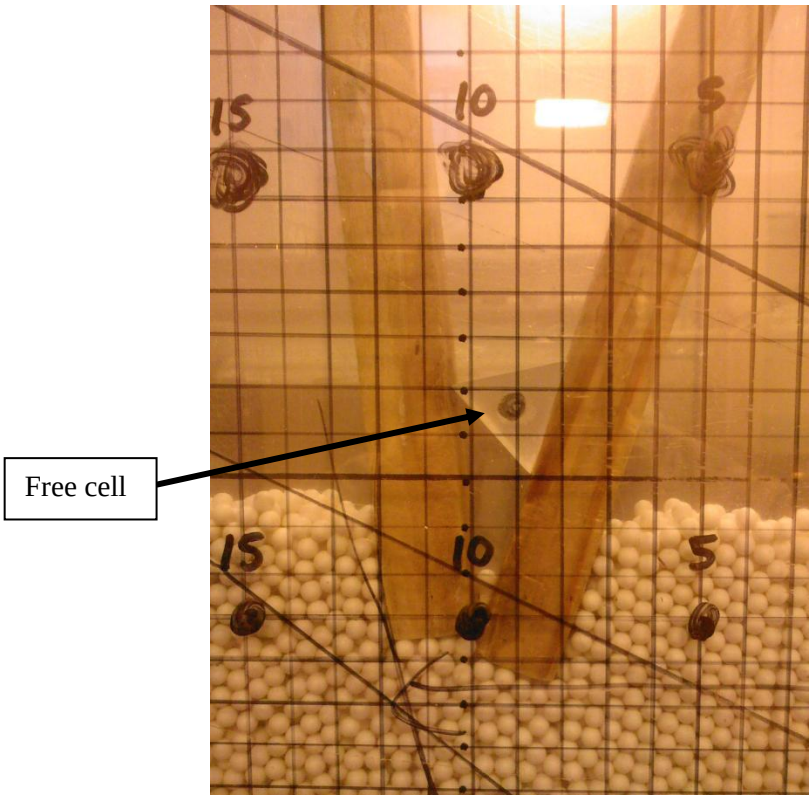

Figure 3.19: Method used to place the free-cells in the silo

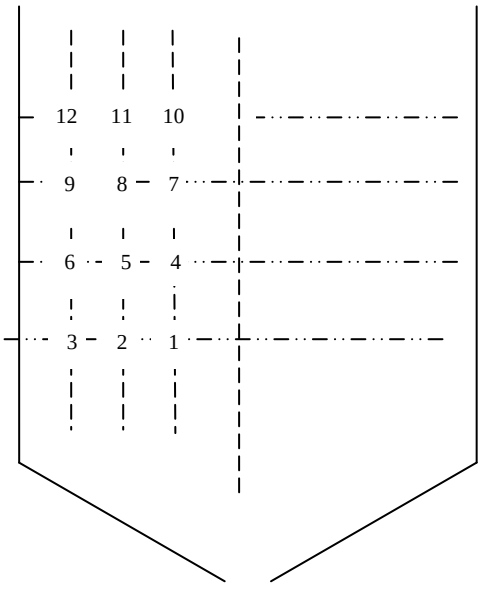

Figure 3.20: Initial position of the free-cells

The video camera was switched on and the orifice was opened. The particles and free-cell flowed out of the rig. Each of the free-cells was placed at the positions 1 to 12 with each

experiment repeated five times, so that the average time taken for the free-cell to reach the orifice could be obtained.

Experiments were also conducted with binary mixtures of particles. The number of particles was chosen so that the height of the top surface was approximately equal for the monosized and binary mixtures of particles. A set of 50,000 white particles was used in experiments to determine the displacement and velocity of the free cells in a monosized batch. To investigate the effect of adding smaller particles, or fines, to the monosized batch, on the displacement and velocity of the free cells, it was deduced that each of the batches should occupy the same volume in the silo. There didn't appear to be a way of calculating the appropriate number of particles so the binary mixtures were poured into the hopper in batches of 1000 and 500 until the equivalent height that the white (5 mm) monosized mix had reached.

A mixture of 42,500 particles composed of 34,000 (80%) white and 8500 (20%) yellow particles and a mixture of 55,000 particles composed of 44,000 (80%) white and 11,000 (20%) black was poured into the silo.

The experiments conducted using the mono-sized batch was repeated using the binary mixtures. The binary mixtures were poured randomly into the rig and the experiments were conducted five times.

3.13 Summary

In this section the equipment used in the practical experiments and the rationale for using it has been described. Tests were conducted using wheat grains in an existing quasi 3D silo slice, named as the Mark I hopper, to deduce the kinematics of the free cells and the ease in using the hopper. Discrepancies in the results and the constraints in the hopper dimensions led to the design and manufacture of a new quasi 3D hopper slice and the choice of spherical particles. The physical properties and dimensions of these particles are presented. Tests were conducted with a set of polyhedral particles and spherical particles of approximately similar volume and the physical properties and dimensions of these particles are also presented.

The experimental methods used to determine the mass flow rate and the displacement and trajectories of the free cells are described.

The experimental results and discussion of the trajectories of the metal, plastic and hollow free-cells

4 The experimental results and discussion of the trajectories of the metal, plastic and hollow free-cells

4.1 Introduction

In this section, the results obtained from practical experiments to determine the trajectories of the metal, plastic and hollow, cylindrical, cuboid and triangular free-cells in the white mono-sized (5 mm) batch and the binary mix of white (5 mm) and black (4 mm) particles are presented. As has been previously mentioned, the aim of the experiments was to deduce an appropriate shape and density of free-cell such that the position of the centre of the free-cell follows the same path as would a particle in the batch, initially positioned at the same position of the free cell in the bed. It was difficult to obtain the trajectory followed by the representative particle experimentally, as the particles that started near the front or back walls were drawn into the centre of the rig and it was impossible to observe them. However, the trajectories of the representative particle obtained from DEM simulation are included for comparison. Placing the free-cells in the exact starting position was not always possible, as they tended to move when other particles were poured on top of them. The starting position varied by about ± 5mm during each trial.

Results comparing the trajectories and displacements of the different densities of the cylindrical, cuboid and triangular prism free-cells of the same volume are compared and discussed. Each experiment was repeated three times and the results from each of the three trials are shown.

Two starting positions were chosen to investigate how the trajectories of the free-cells were affected by the velocity profile of the surrounding grain. Position 12 was near the top of the bed where the velocity profile is reasonably predictable and position 5 was at a position where the boundary between the flowing core of material and the stagnant zone was observed to form in the monosized particles and where the particle velocities are stochastic in nature. The stagnant zone was boundary was determined by observing the material discharging from the hopper by eye and drawing a curve on the Perspex sheet. Figure 4.1 shows where the stagnant zone formed in the monosized batch in relation to the two starting positions.

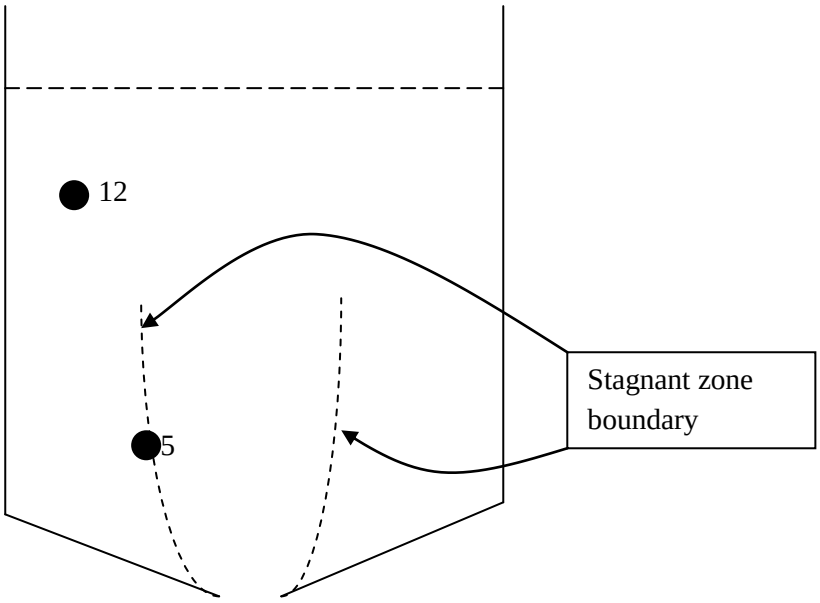

Figure 4.1: The position of the stagnant zone boundary in the discharging monosized white particles in relation to the positions 5 and 12

There is no reliable method for predicting the angle of the stagnant zone boundary and the value has to be determined from observation (Nedderman, 1995). A value of 45º is typically assumed if no other information is available (Anand, 2008).

The data used to plot the graphs was determined from the recordings of the discharging silo. The first recording of the position of the free-cells was prior to the opening of the orifice, at their starting positions and subsequent recordings of the positions of the free-cells were recorded at 1 second intervals after the opening of the orifice. Nedderman (1995) deduced an equation to determine the time τ taken for the stagnant zone boundary to reach varying heights in the silo during the dilation of the particles upon the initiation of discharge. Nedderman (1995) noted that the value of τ in a flat bottomed cylindrical silo with diameter 0.65 m and orifice diameter 0.065 m was 0.4 s to reach a height of 0.36 m and 0.9 s to reach a height of 0.52 m. The bed height in the hopper used in this study was approximately 0.50 m and observations of the recordings of the silo discharge indicate the delay in the time between the orifice opening and the particles in the silo starting to move was 0.04 s, which was the frame rate of the digital recorder. The error in the time in each of the figures is ±0.04 s and the error in the position is about ±0.0025 m.

4.2 Comparison between the results obtained from experiments with free-cells of different density

4.2.1 The trajectory and displacement of the metal, plastic and hollow free cells starting from position 12.

Figure 4.2 shows the trajectories of three trials of each of the metal, plastic and hollow cylindrical free-cells in the discharging white (5 mm) particles. The trajectory followed by the representative particle is also shown.

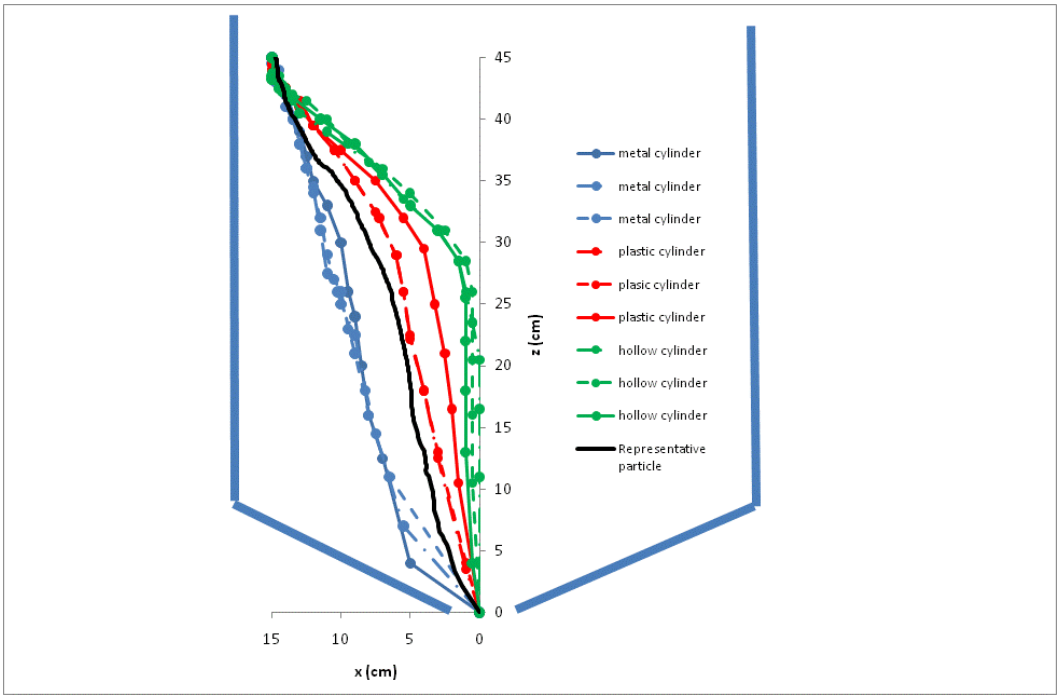

Figure 4.2: Graph showing the trajectories of three trials of each of the metal, plastic and hollow cylinder free-cells and the representative particle in the discharging white (5mm) particles

The plastic cylinder follows a trajectory very similar to the representative particle. The maximum deviation between the three trials is approximately 2 cm along the horizontal. Two trials of the plastic cylinder follow near identical paths. The metal cylinder flows through the surrounding material, rather than with it. Observations appear to show that the metal cylinders follow the outline of the fast flowing core, by moving in the transition band between the flowing particles and particles at rest in the dead zone. The path followed by the metal cylinder over three trials is very similar until it reaches a height about 12 cm from the orifice where the paths deviate by a maximum of 4 cm. The hollow cylinder tends to move just under

the surface of the bed ‘floating’ on top of the particles below it and moves towards the fast flowing central region. The paths over three trials vary by approximately 1 cm along the horizontal. The average path followed by the metal, plastic and hollow free-cells each over three trials varies from the path followed by the tracer particle by a maximum of 4 cm, 3 cm and 6 cm respectively.

Figure 4.3 shows the vertical displacement-time graph for three trials of the metal, plastic and hollow cylindrical free-cells in the discharging white (5 mm) particles. The trajectory followed by the representative particle is also shown.

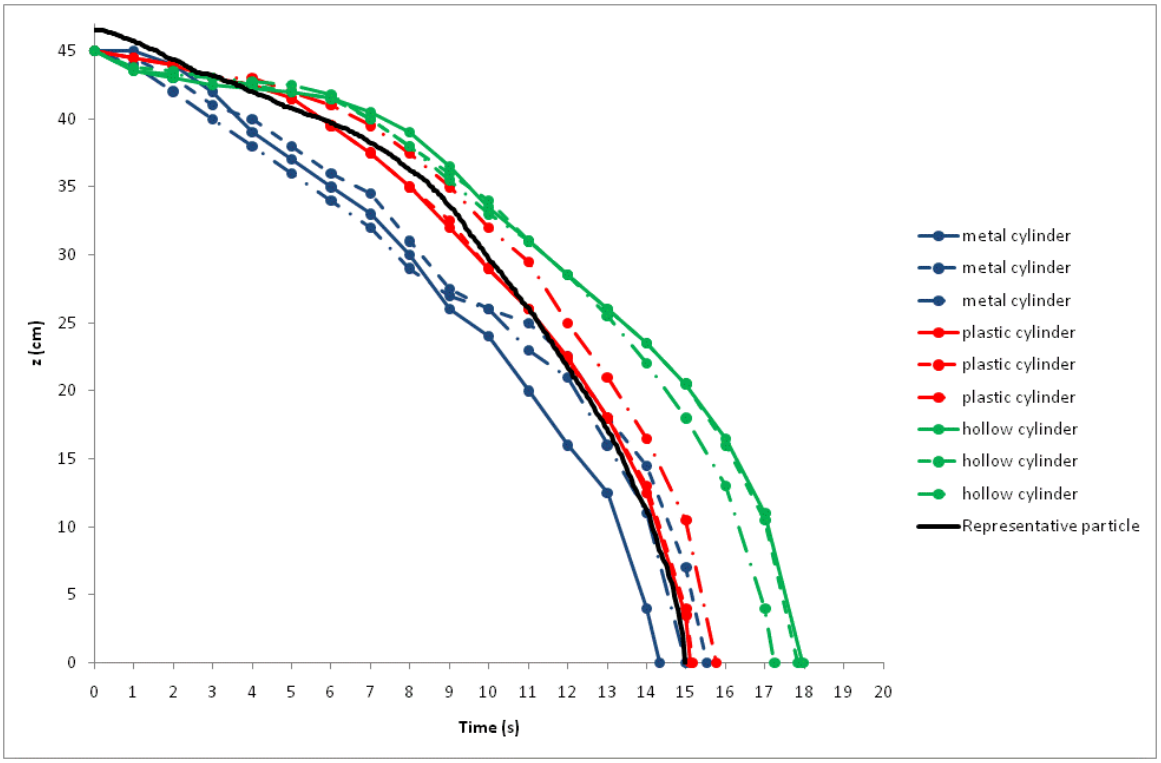

Figure 4.3: Graph showing the vertical displacement-time graph for three trials of the metal, plastic and hollow, cylindrical free-cells and the representative particle in the white (5 mm) particles

Figure 4.4 shows the horizontal displacement-time graph of three trials of the metal, plastic and hollow, cylindrical free-cells in the discharging white (5 mm) particles. The trajectory followed by the representative particle is also shown.

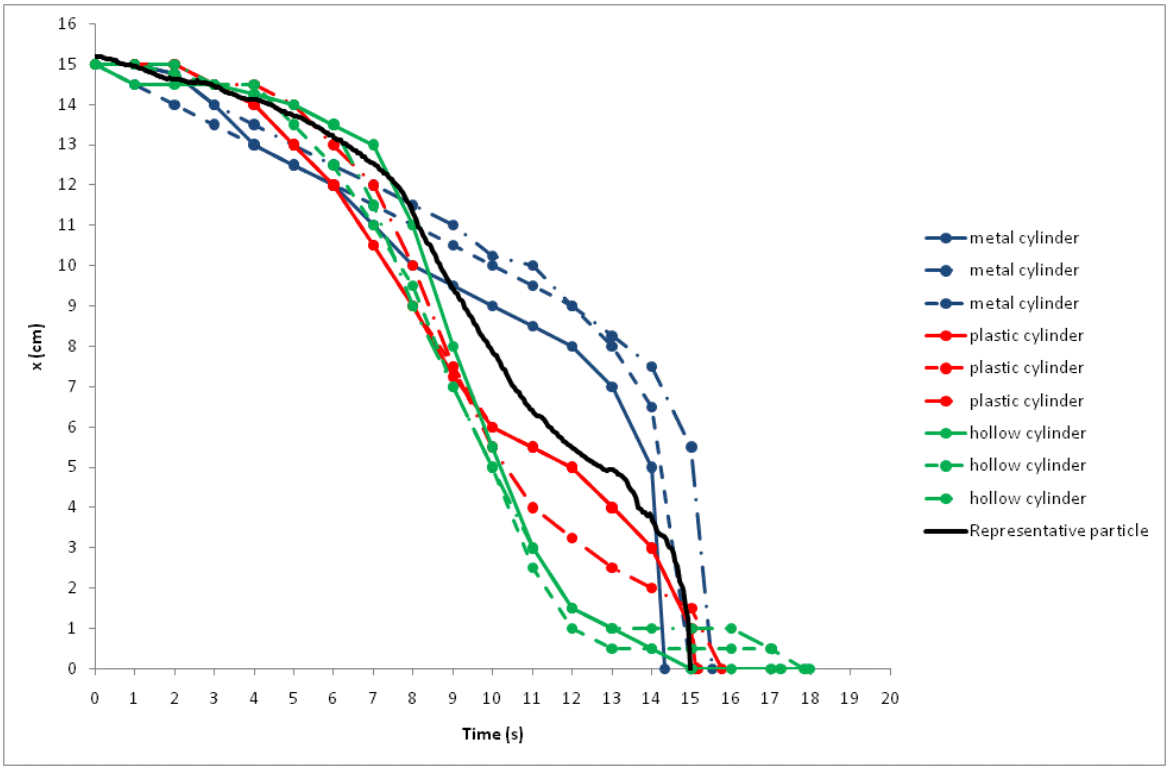

Figure 4.4: Graph showing the horizontal displacement-time graph for three trials of the metal, plastic and hollow, cylindrical free-cells and the representative particle in the white (5 mm) particles

The hollow cylinder takes approximately 13% longer than the plastic cylinder and 17% longer than the metal cylinder to reach the orifice. The plastic cylinder takes approximately 7% longer to reach the orifice than the metal cylinder. The curves showing the vertical displacement, z, against time show that the vertical velocity of the cylindrical free cells varies by about 25%. The metal cylinder has the greatest vertical velocity and the hollow cylinder the smallest.

The curves showing the horizontal displacement against time, in figure 4.5, show the metal cylinder initially has an approximately constant velocity, before very quickly accelerating towards the orifice. The horizontal displacement of the hollow cylinder shows a gradual increase in the horizontal velocity to a maximum before suddenly decelerating to rest for a few seconds and then falling through the orifice.

The horizontal displacement of the plastic cylinder has very similar profile to the representative particle. The plastic cylinder quickly accelerates to a maximum horizontal velocity and then after about 11 seconds decelerates very close to rest, before accelerating to the orifice. The deceleration at 11 seconds is at the point where the representative particle and free-cell reaches the edge of the flowing core. The particles in the flowing core move quickly. Particles on the edge of the boundary gradually move across the thin transition layer, until they are sucked into the fast flowing core and quickly accelerate to the orifice.

Figure 4.5 shows the trajectories of three trials of the metal, plastic and hollow cuboid free-cells in the discharging white (5 mm) particles. The trajectory followed by representative particle is also shown.

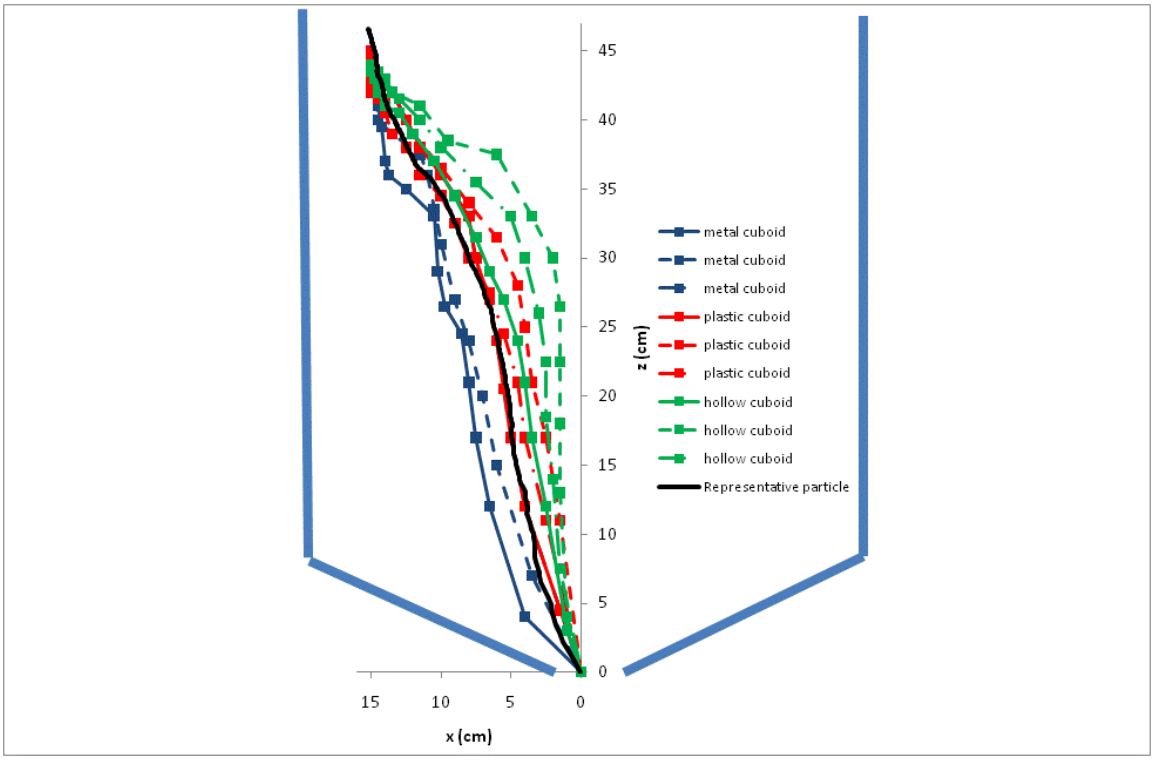

Figure 4.5: Graph showing the trajectories of three trials of each of the metal, plastic and hollow cuboid free-cells and the representative particle in the discharging white (5 mm) particles

The metal cuboid appears to flow through the discharging material, following very closely the outline of the flowing core and the paths vary by a maximum of 2 cm. The hollow cuboid, however, follows three quite different trajectories during each trial. One of the trials of the hollow cuboid follows a very similar trajectory to the plastic cuboid. The greatest difference in the paths followed by the hollow cuboid is at the top of the silo, where the paths vary by a

maximum of 6 cm along the horizontal. The path followed by the plastic cuboid varies by a maximum of 3 cm along the horizontal. The curve of one trial of the plastic cuboid and the trajectory followed by representative particle are very nearly identical. The average path followed by the metal, plastic and hollow cuboids over three trials varies from the path followed by the representative particle by a maximum of 3 cm, 1 cm and 4 cm respectively.

Figure 4.6 shows the vertical displacement-time graph for three trials of the metal, plastic and hollow, cuboid free-cells in the discharging white (5 mm) particles. The trajectory followed by the representative particle is also shown

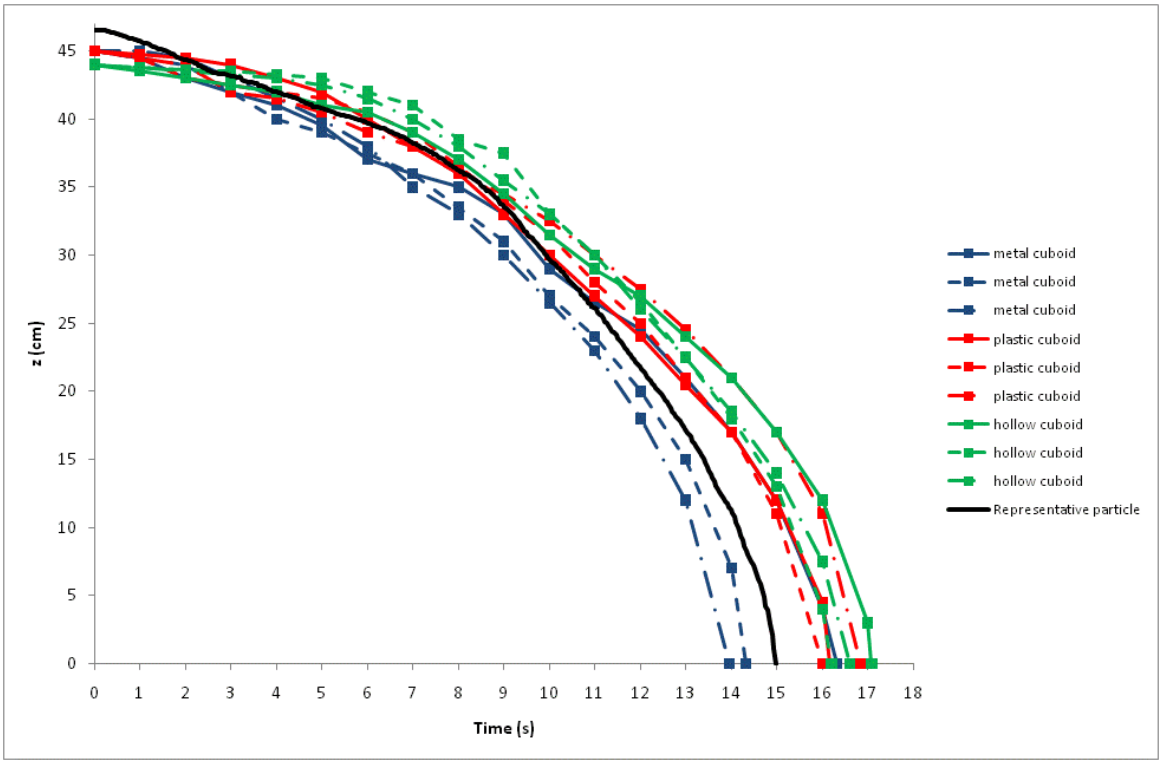

Figure 4.6: Graph showing the vertical displacement-time graph for three trials of the metal, plastic and hollow cuboid free-cells in the discharging white (5 mm) particles. The trajectory followed by the representative particle is also shown

The three trials of the plastic and hollow cuboids have nearly identical vertical displacement curves and hence travel with very similar vertical velocity. One of the trials of the metal cylinder is also shown to follow the same trajectory as two of the curves followed by the plastic cuboid, at 9 seconds after the initiation of discharge. This is because on of the trials had a larger displacement than the other two, as represented by the solid blue line in figure 4.6. The other two trials of the metal cylinder travel on average 18% faster than the plastic

and hollow cuboids. The plastic cuboid free cells travel with a similar velocity to the representative particle during the first 11 seconds after discharge, but then the plastic and cuboid free cells travel faster than the representative particle. The hollow and plastic cuboid free-cells take an average of 10% longer to reach the orifice than the representative particle and two of the trials of the metal cuboid take approximately 6% less to reach the orifice than the representative particle.

Figure 4.7 shows the horizontal displacement-time graph of three trials of the metal, plastic and hollow, cuboid free-cells in the discharging white (5 mm) particles. The trajectory followed by the representative particle is also shown.

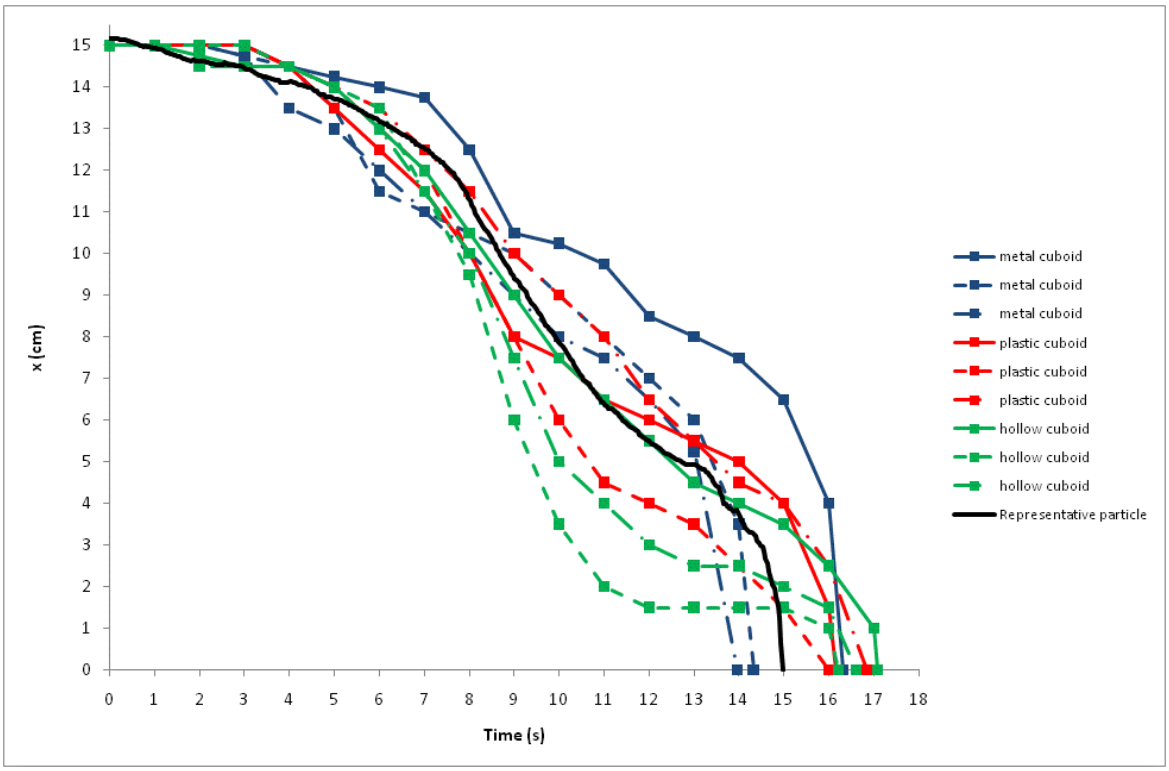

Figure 4.7: Graph showing the horizontal displacement-time graph for three trials of the metal, plastic and hollow cuboid free-cells in the discharging white (5mm) particles. The trajectory followed by the representative particle is also shown

The hollow cuboid initially accelerates uniformly to a constant velocity and then decelerates as it reaches the orifice. The plastic cuboid generally has a similar horizontal displacement profile to the tracer particle, namely, a uniform acceleration until it reaches a constant velocity (which is less than the velocity of the metal cuboid) and slows down when it reaches the edge of the fast flowing core and is dragged into the core and quickly accelerates to the orifice. The

metal cuboid has a less predictable horizontal velocity. The horizontal velocity is generally less than the plastic and hollow cuboids, but upon entering the fast flowing core it quickly accelerates, resulting in two of the trials reaching the orifice faster than the representative particle.

Figure 4.8 shows the trajectories of three trials of the metal, plastic and hollow triangular prism free-cells in the discharging white (5 mm) particles starting from position 12. The trajectory followed by the representative particle is also shown.

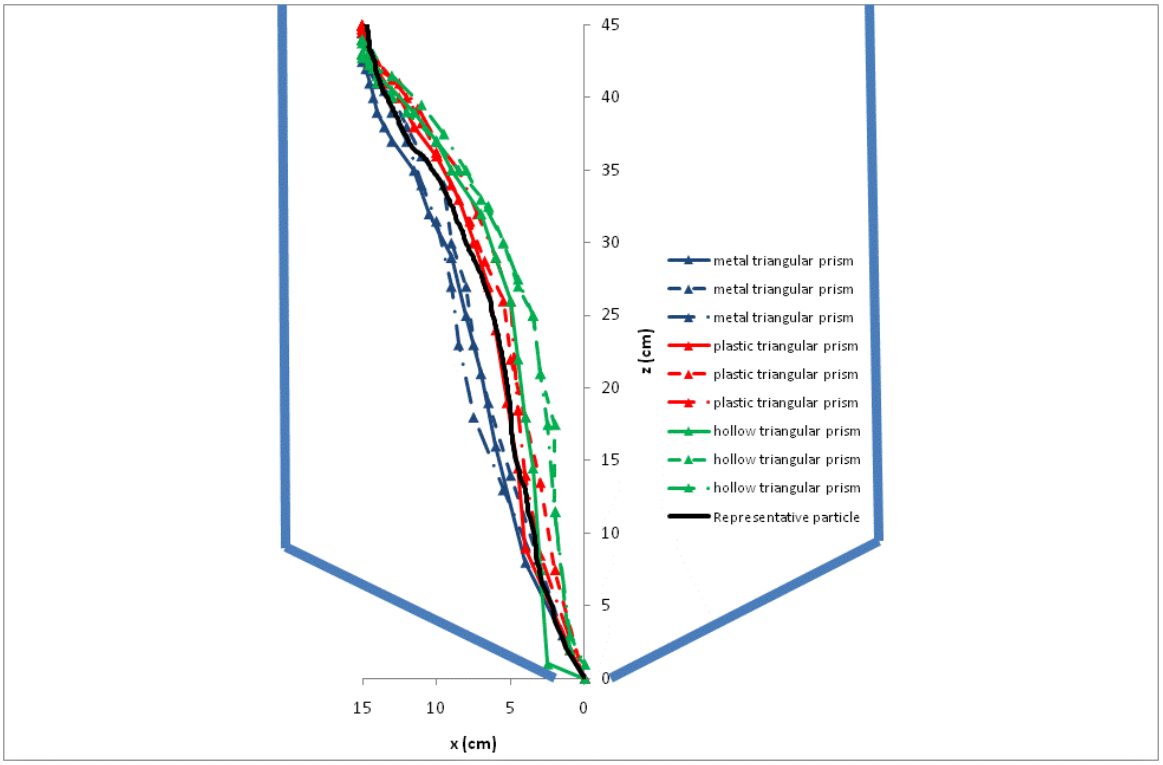

Figure 4.8: Graph showing the trajectories of three trials of each of the metal, plastic and hollow cuboid free-cells in the discharging white (5 mm) particles. The trajectory followed by the representative particle is also shown

The three trials of each of the metal, plastic and triangular prism free-cells follow very similar trajectories. The trajectory of the metal, plastic and hollow triangular prisms each vary by a maximum of 2 cm over three trials. The average of three trials of each of the metal triangular prism, plastic triangular prism and hollow triangular prism vary from the path followed by the representative particle by a maximum of 3 cm, 0.5 cm and 2 cm along the horizontal respectively. Unlike the hollow cylinder and hollow cuboid, the hollow triangular prism moves in the discharging material, rather than ‘floating’ on the particles below it.

Figure 4.9 shows the vertical displacement-time graph for three trials of the metal, plastic and hollow, triangular prism free-cells in the discharging white (5 mm) particles. The trajectory followed by the representative particle is also shown.

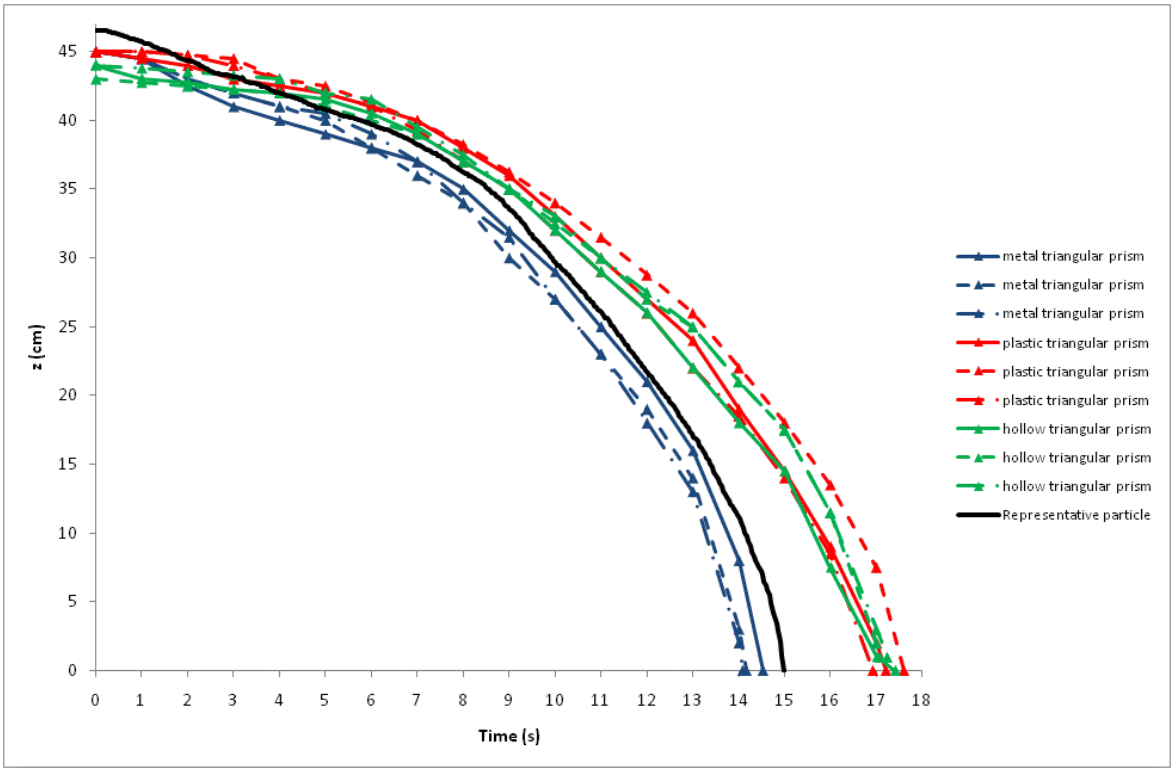

Figure 4.9: Graph showing the vertical displacement-time graph for three trials of the metal, plastic and hollow triangular prism free-cells in the discharging white (5mm) particles. The trajectory followed by representative particle is also shown

The time taken by the representative particle to reach the orifice is only approximately 5% greater than the metal cuboid, whilst the plastic and hollow triangular prisms take about 17% longer to reach the orifice than the representative particle. This is an unexpected result. The metal triangular prism may travel at a similar speed to representative particle because it is hindered by its shape. Observations of the flow show that the metal triangular prism moves only slightly faster than the surrounding particles. The triangular prism was initially position so that one of its sides was parallel to the horizontal, x, axis. Upon the initiation of discharge the triangular prism rotates clockwise by about 30º so that one of its corners points along the direction of flow. It then gradually rotates a further 30º so that the corner points vertically downwards and when it reaches the bottom surface of the hopper it then rotates clockwise a further 90º and falls through the orifice.

Figure 4.10 shows the horizontal displacement-time graph of three trials of the metal, plastic and hollow, triangular prism free-cells in the discharging white (5 mm) particles. The trajectory followed by the representative particle is also shown.

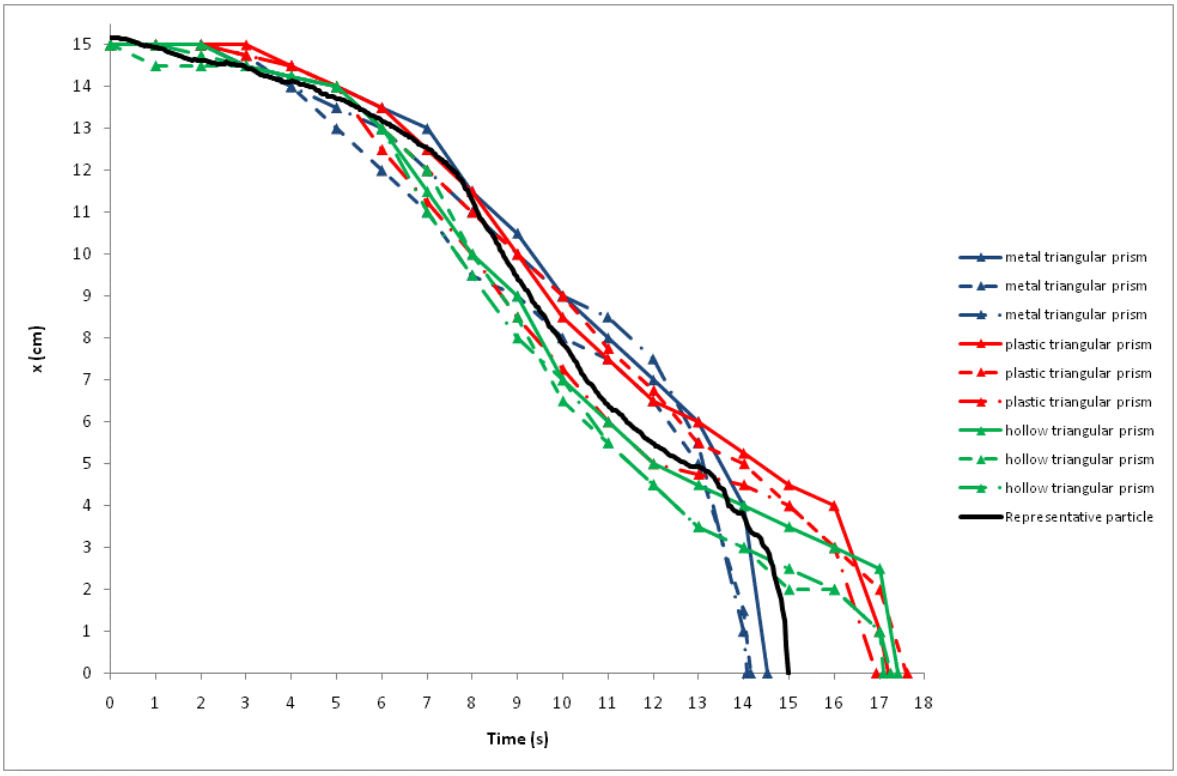

Figure 4.10: The horizontal displacement-time graph for three trials of the metal, plastic and hollow triangular prism free-cells in the discharging white (5mm) particles starting from position 12. The trajectory followed by the representative particle is also shown

The three trials of the hollow triangular prism have a horizontal velocity profile very similar to the horizontal velocity of the representative particle during the first 14 seconds, but over an average of three trials the hollow triangular prism varies from the path of the representative particle by 0.5 cm. At approximately 14 seconds after the initiation of flow the representative particle accelerates to the orifice but the triangular prism tends to gradually move horizontally, before accelerating towards the orifice. The lack of mass in the hollow triangular prism causes it to be easily buffeted at the edge of the flowing core.

Summary

It would appear from the results that the plastic cylinder, cuboid and triangular prism follow closest to the trajectory of the representative particle. However, the time taken for them to reach the orifice is 15.5, 16.5 and 17.2 seconds respectively, while the representative particle takes 15 seconds. The horizontal and vertical velocity of the plastic cylinder is closest to that of the representative particle than the plastic cuboid and plastic triangular prism.

4.2.2 The trajectory and displacement of the metal, plastic and hollow free cells starting from position 5.

Figure 4.11 shows the trajectories of three trials of the metal, plastic and hollow cylindrical free-cells in the discharging white (5 mm) particles starting from position 5. The trajectory followed by the representative particle is also shown.

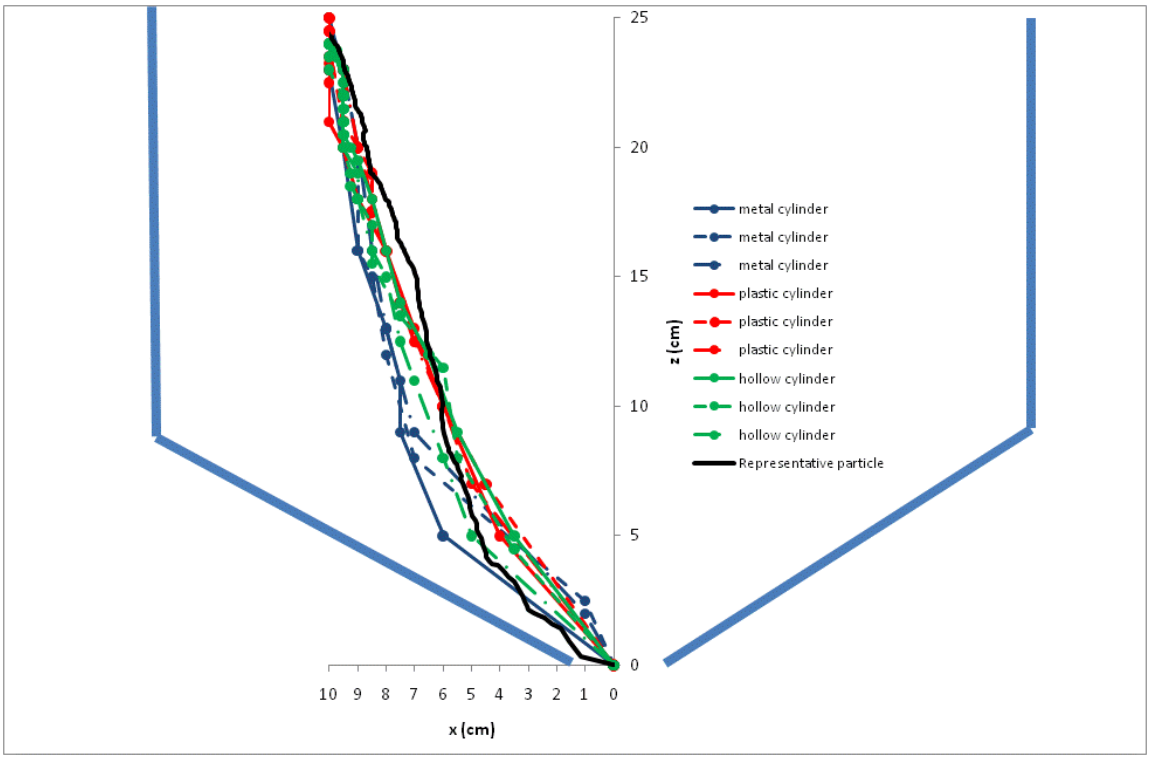

Figure 4.11: Graph showing the trajectories of three trials of each of the metal, plastic and hollow cylinder free-cells in the discharging white (5 mm) particles starting from position 5. The trajectory followed by the representative particle is also shown.

The metal cylinder is shown to clearly flow through the material rather than with it, until a point at about 10 cm above the orifice at which point the three trials of the metal cylinder

follow different trajectories. The first trial shows the metal cylinder follows along the edge of the flowing core, but the other two trials result in the metal cylinder travelling in the flowing core. The plastic and hollow cylinders follow a very similar trajectory, varying in average over three trials by 0.25 cm, which is supported by observations in videos which appear almost identical in time and displacement.

Figure 4.12 shows the vertical displacement-time graph for three trials of the metal, plastic and hollow, cylindrical free-cells in the discharging white (5 mm) particles, starting from position 5. The trajectory followed by the representative particle is also shown.

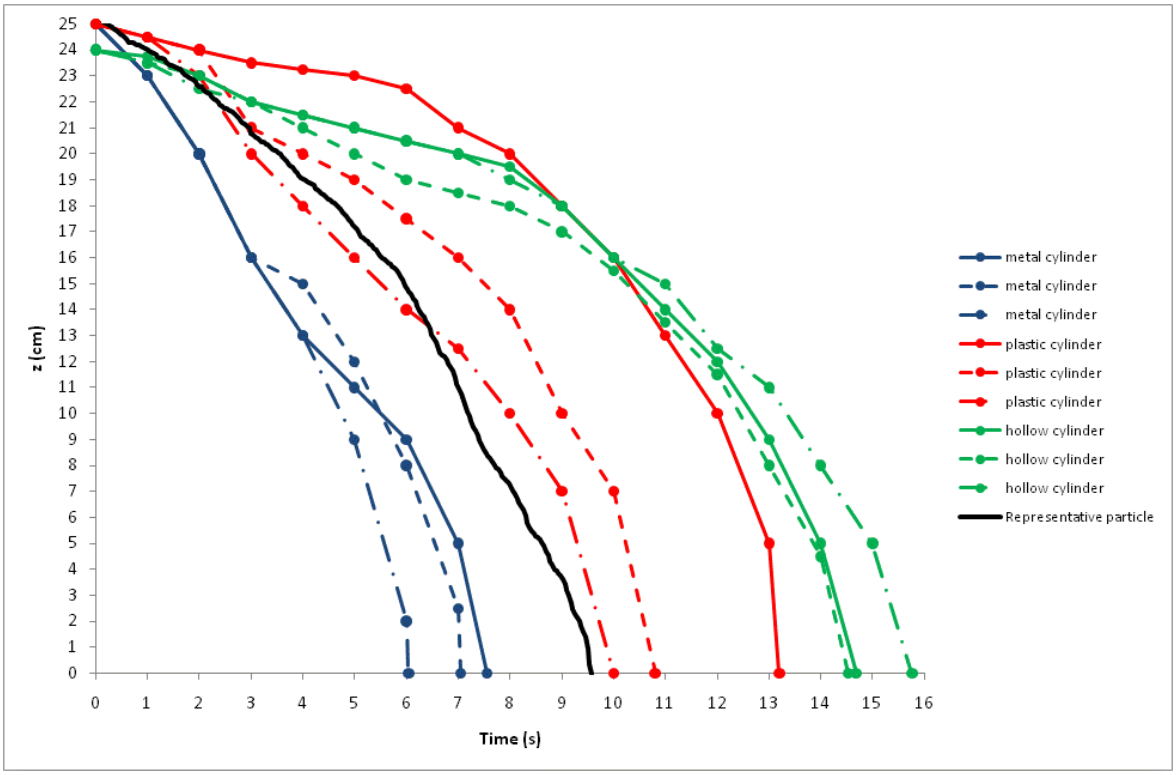

Figure 4.12: Graph showing the vertical displacement-time graph for three trials of the metal, plastic and hollow cylindrical free-cells in the discharging white (5 mm) particles, starting from position 5. The trajectory followed by the representative particle is also shown.

The hollow cylinder has the smallest vertical velocity, followed by the plastic cylinder and then the metal cylinder which travels fastest. The hollow cylinder takes on average 225% longer to reach the orifice than the metal cylinder. The metal cylinder takes on average 24% less time to reach the orifice than representative particle and the hollow cylinder takes on average 58% longer than representative particle. Over three trials the plastic cylinder has a wide range in the time taken to reach the orifice, varying between 10 and 13.2 seconds, which

may be due to the stochastic nature of the particle velocities in this region, along the stagnant zone boundary. The metal cylinder on the other hand moves through the discharging material and the hollow cylinder is gently carried by the particles moving past it.

Figure 4.13 shows the horizontal displacement-time graph of three trials of the metal, plastic and hollow, cylindrical free-cells in the discharging white (5 mm) particles, starting from position 5. The trajectory followed by the representative particle is also shown.

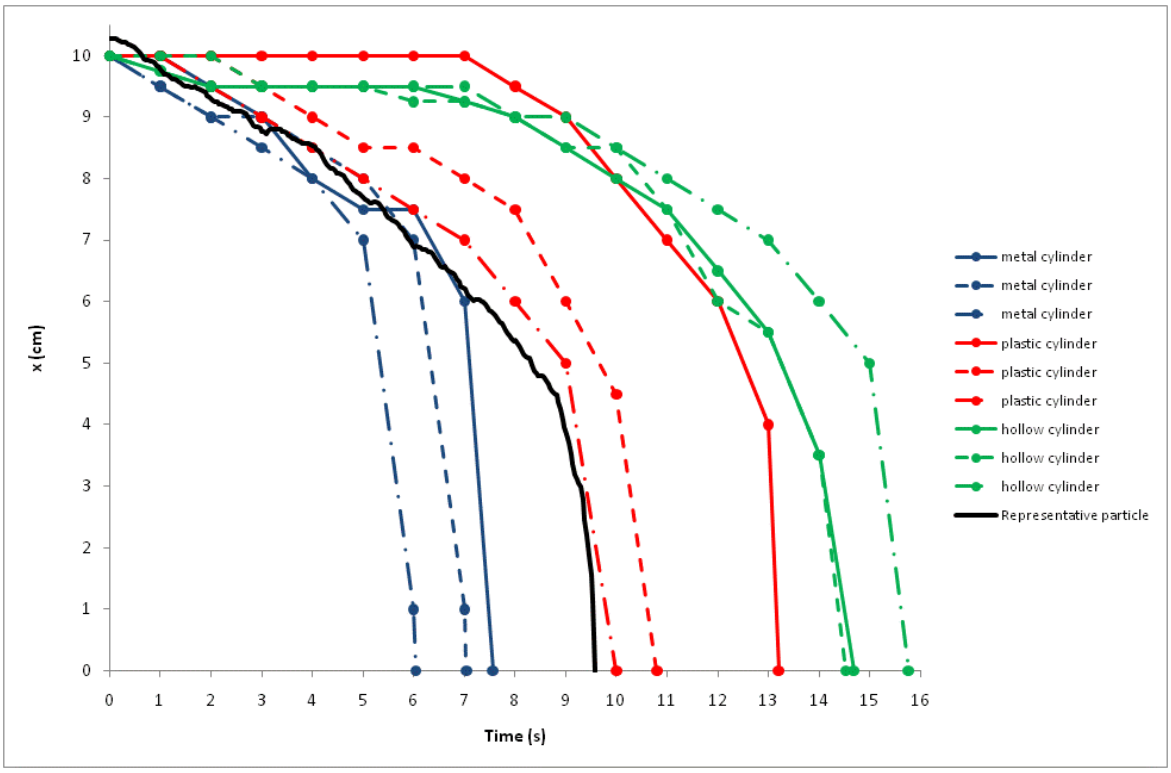

Figure 4.13: Graph showing the horizontal displacement-time graph for three trials of the metal, plastic and hollow cylindrical free-cells in the discharging white (5 mm) particles. The trajectory followed by the representative particle is also shown.

One trial of the plastic cylinder and two trials of the hollow cylinder show that during the first 7 seconds after the orifice has been opened the horizontal velocity is virtually zero. This is because the starting position 5 is along the boundary of the flowing core, in which the particles only gradually move. The flowing core is in the shape of a parabola. The point on the parabola at which the starting point 5 is positioned, is very nearly parallel to the vertical axis and the surrounding particles are only moving slowly downwards. The top bed of material moves down the silo and the focus of the parabola decreases and the horizontal and vertical velocities of the particles and the free-cell increases.

Figure 4.14 shows the trajectories of three trials of the metal, plastic and hollow cuboid free-cells in the discharging white (5 mm) particles starting from position 5. The trajectory followed by the representative particle is also shown.

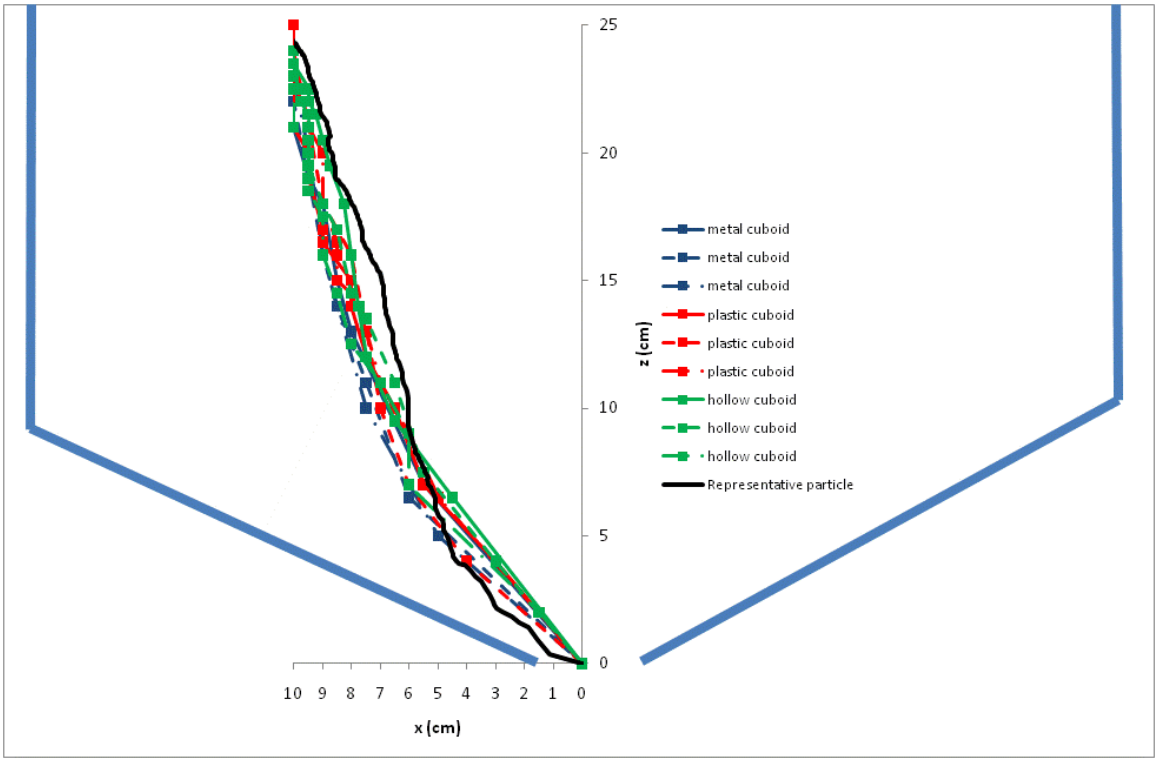

Figure 4.14: Graph showing the trajectories of three trials of each of the metal, plastic and hollow cuboid free-cells in the discharging white (5 mm) particles starting from position 5. The trajectory followed by the representative particle is also shown.

It is difficult to find any distinguishing features, as the slightly different trajectories are likely to be the result of the stochastic nature of the flow.

Figure 4.15 shows the vertical displacement-time graph for three trials of the metal, plastic and hollow, cuboid free-cells in the discharging white (5mm) particles, starting from position 5. The trajectory followed by the representative particle is also shown.

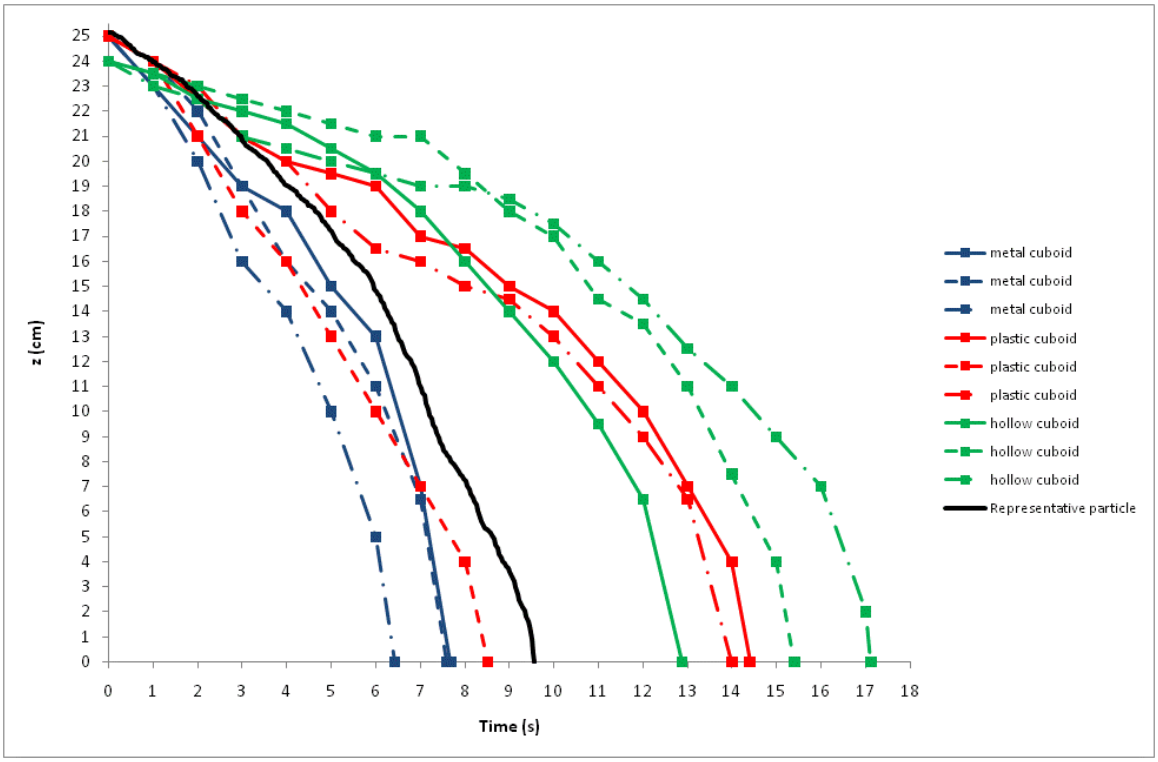

Figure 4.15: Graph showing the vertical displacement-time graph for three trials of the metal, plastic and hollow cuboid free-cells in the discharging white (5 mm) particles, starting from position 5. The trajectory followed by the representative particle is also shown

The metal cuboid follows a very similar trajectory over three trials and reaches the orifice an average of 36% faster than the representative particle. Two of the plastic cuboids are shown to follow very similar trajectories, but one of the trials shows the plastic cuboid with a very similar vertical velocity and time as the metal cuboid. However, the velocity of the plastic cuboid over the three trials is similar when the plastic cuboid is approximately 11 cm from the orifice, but the velocity of one trial of the plastic cuboid is 83% faster than the other two in travelling the first 14 cm vertically. This is because one trial of the plastic cuboid resulted in it experiencing a force that pushed it further into the edge of the dead zone, impeding its movement, unlike the other two trials when the plastic cuboid coasted along the edge of the dead zone. The hollow cuboid and plastic cuboid take an average of 58% and 29% longer than representative particle, respectively, to reach the orifice and the metal cuboid takes on average 30% less time to reach the orifice than the representative particle.

Figure 4.16 shows the horizontal displacement-time graph of three trials of the metal, plastic and hollow, cuboid free-cells in the discharging white (5 mm) particles, starting from position 5. The trajectory followed by the representative particle is also shown.

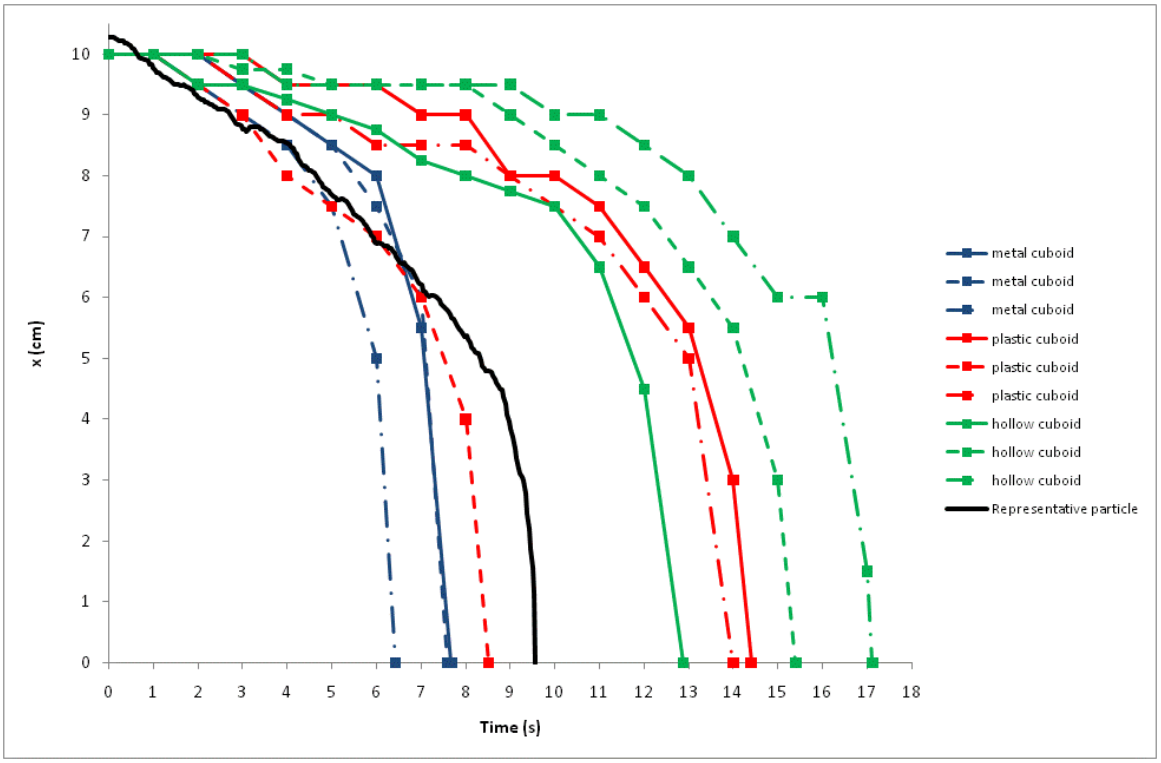

Figure 4.16: Graph showing the horizontal displacement-time graph for three trials of the metal, plastic and hollow cuboid free-cells in the discharging white (5 mm) particles, starting from position 5. The trajectory followed by the representative particle is also shown.

It was mentioned previously that two trials of the plastic cuboid had a similar velocity, but one trial resulted in the plastic cuboid exhibiting similar characteristics to the velocity and time to reach the orifice, as the metal cuboid. This is probably the result of the stochastic nature of the flow along the boundary between the flowing core of material and the stagnant region. The horizontal velocity curves in figure 4.16 show that when the free-cells and representative particle are 6 cm horizontally from the orifice, they all travel at a velocity of 6 cm/s. It is at this point that the free-cells and representative particle are in the flowing core.

Figure 4.17 shows the trajectories of three trials of the metal, plastic and hollow triangular prism free-cells in the discharging white (5 mm) particles starting from position 5. The trajectory followed by the representative particle is also shown.

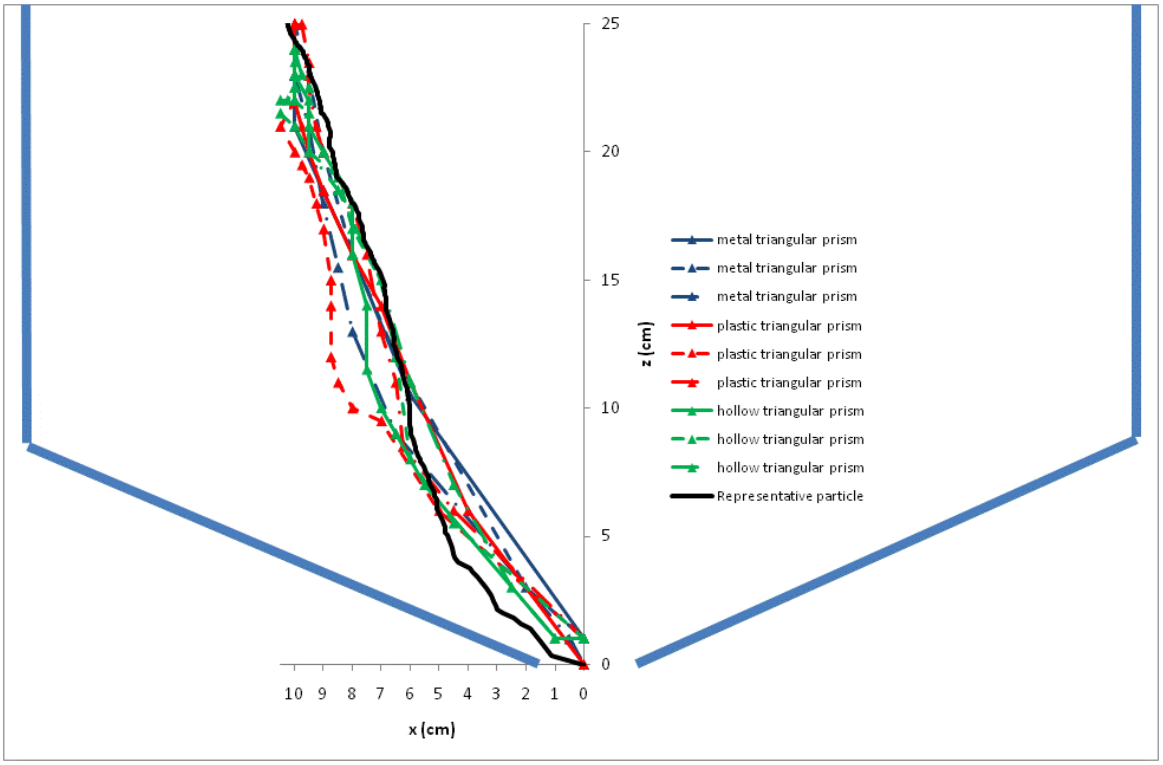

Figure 4.17: Graph showing the trajectories of three trials of each of the metal, plastic and hollow triangular prism free-cells in the discharging white (5 mm) particles starting from position 5. The trajectory followed by the representative particle is also shown.

It is difficult to distinguish any differences between the trajectories taken by the metal, plastic and hollow triangular prisms. None of the three different densities of triangular prism follows the same trajectory as the representative particle, but over an average of three trials they are all in agreement.

Figure 4.18 shows the vertical displacement-time graph for three trials of the metal, plastic and hollow, triangular prism free-cells in the discharging white (5 mm) particles, starting from position 5. The trajectory followed by the representative particle is also shown.

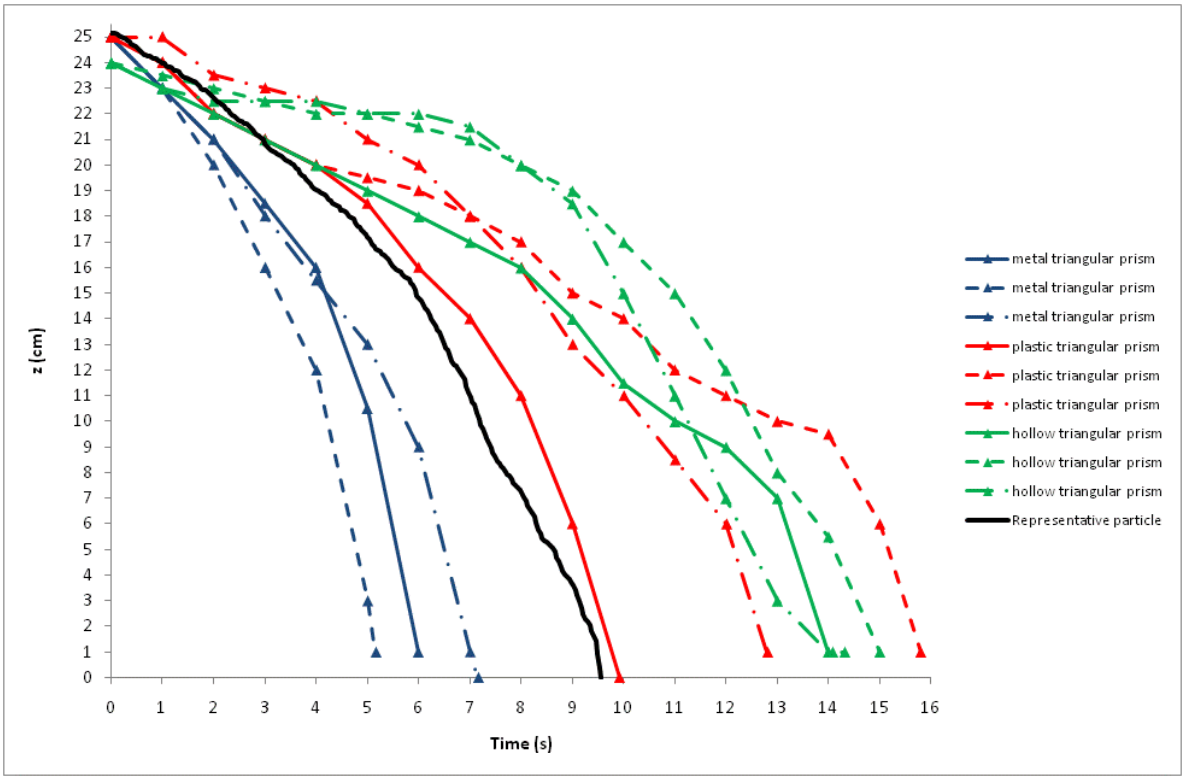

Figure 4.18: Graph showing the vertical displacement-time graph for three trials of the metal, plastic and hollow triangular prism free-cells in the discharging white (5 mm) particles, starting from position 5. The trajectory followed by the representative particle is also shown.

The metal triangular prism takes an average of 58% less time than the representative particle to reach the orifice. In similarity to the cuboid, the plastic triangular prism has the widest range in vertical velocity over the three trials, varying between 1 cm/s and 6 cm/s and it takes on average 35% longer to reach the orifice than the representative particle. Only one of the three trials of the plastic triangular prism has a similar vertical velocity to the representative particle. The hollow triangular prism takes an average 53% more time to reach the orifice than the representative particle. In some of the trials of the triangular prism, it comes to rest at 1cm above the orifice. This is because it became trapped in the orifice by surrounding particles (Figure 4.19). It was released by tapping it.

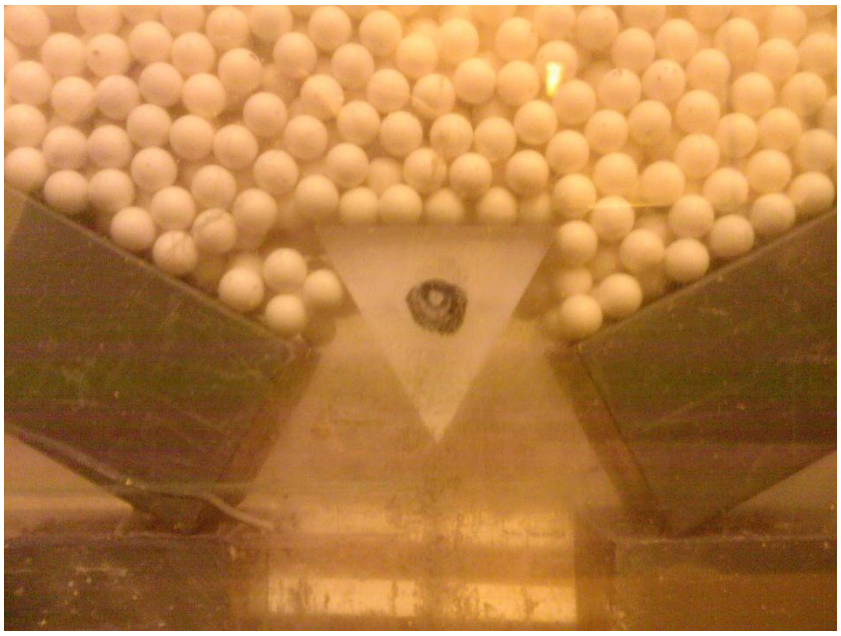

Figure 4.19: Plastic triangular prism caught in the orifice

Figure 4.20 shows the horizontal displacement-time graph of three trials of the metal, plastic and hollow, triangular prism free-cells in the discharging white (5 mm) particles, starting from position 5. The trajectory followed by the representative particle is also shown.

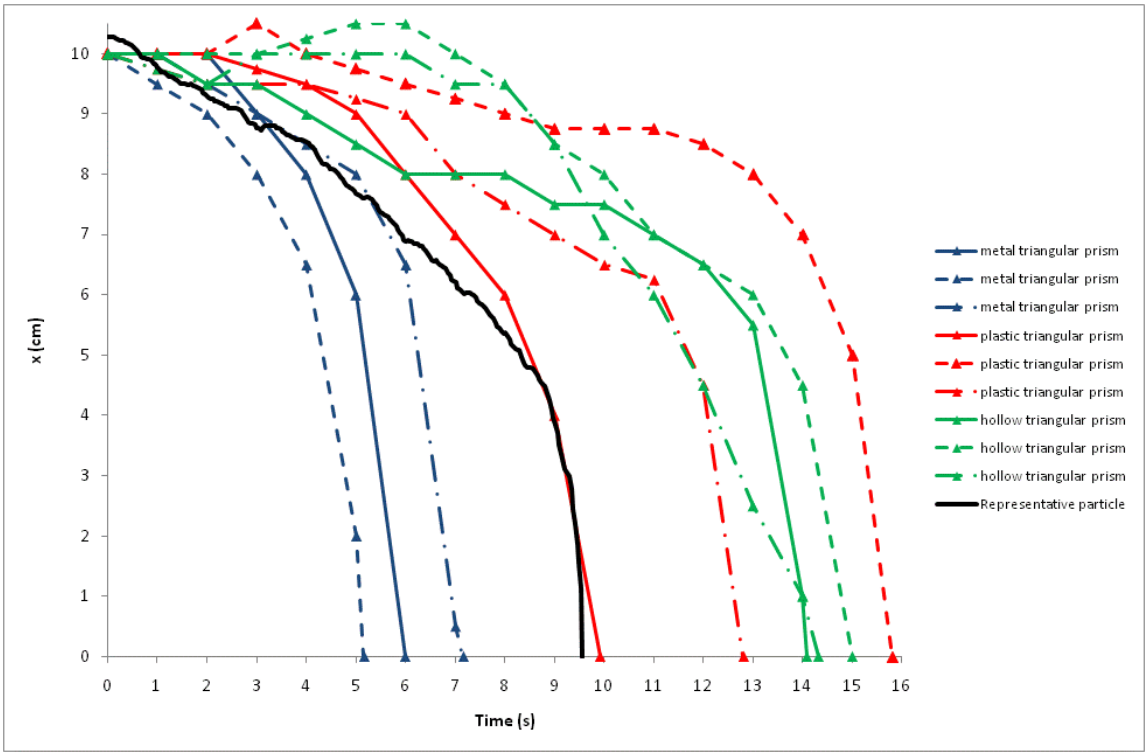

Figure 4.20: Graph showing the horizontal displacement-time graph for three trials of the metal, plastic and hollow triangular prism free-cells in the discharging white particles. The trajectory followed by the representative particle is also shown

The horizontal displacement-time graph of the triangular prisms shows one trial of the hollow triangular prism and one trial of the plastic triangular prism, in which the distance of the free-cell from the orifice increases. This was the result of the triangular prism free-cells rotating clockwise, which in turn resulted in the particles above pushing onto the side of the face *A* of the triangular prism (Figure 4.21).

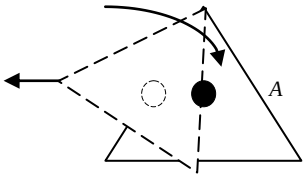

Figure 4.21: Rotation of triangular prism a short time after the opening of the orifice

The horizontal velocities of the plastic triangular prism have the greatest range in values. The horizontal velocity over the initial 5 cm from position 5 varies from between 0.56 cm/s in trial 1, 0.42 cm/s in trial 2 and 0.33 cm/s in trial 3.

4.2.3 Summary

The trajectories of the plastic, metal and hollow triangular prisms are highly stochastic and it is difficult to deduce which of them follows the representative particle the closest. At east one of the three trials of the plastic cylinder, plastic cuboid and plastic triangular prism has a similar horizontal and vertical velocity to the representative particle.

4.3 Conclusion

The results presented in the previous section indicate that for a free cell to move along a similar trajectory as a representative particle, it should have a similar density to the particles. The density of each of the metal, plastic and hollow free-cells was 7.90 g/cm^3, 1.20 g/cm^3 and 0.29 g/cm^3 respectively and the density of the particles was 1.28 g/cm^3. If the free-cell is too dense it will move through the material and if it is too light, in the case of particles starting at position 12, it will tend to float along the top of other particles. Starting from position 12 the shape of the free-cells only appear to be of significant affect if the density of the free-cells is less than the density of the particles. Figure 4.22 shows the clear differences between the trajectories followed by the metal, plastic and hollow triangular prisms.

The three different densities of triangular prisms followed more similar trajectories over three trials than the cylinders or cuboids. The cuboids have the most unpredictable horizontal and vertical velocities of the three shapes. Starting from position 5 the plastic free-cells have the most unpredictable velocity when they are placed at position 5, while the metal and hollow free-cells generally follow more predictable trajectories over three trials. The plastic and hollow free-cells appear to follow very similar trajectories from position 5. However, the time taken to reach the orifice can vary considerably. The time taken for the hollow cylinder free-cell to reach the orifice varied between 9.68 and 16.68 seconds and the time taken for the plastic cylindrical free-cell to reach the orifice varied between 9.08 and 9.60 seconds. The

free-cell in the experimental trial that took 16.68 seconds was observed to creep very slowly along the boundary, between the flowing core and the stagnant region. Particles in the flowing core travelled around and underneath the hollow cylinder (Figure 4.23). Free-cells of any shape, but similar density to the majority of the particles in the silo may be suitable at starting positions where the velocity and stress field is well defined.

Figure 4.22 shows the trajectories of the hollow cylinder, cuboid and triangular prism free cells in the white (5mm) particles, starting from position 12. The trajectory followed by the representative particle is also shown.

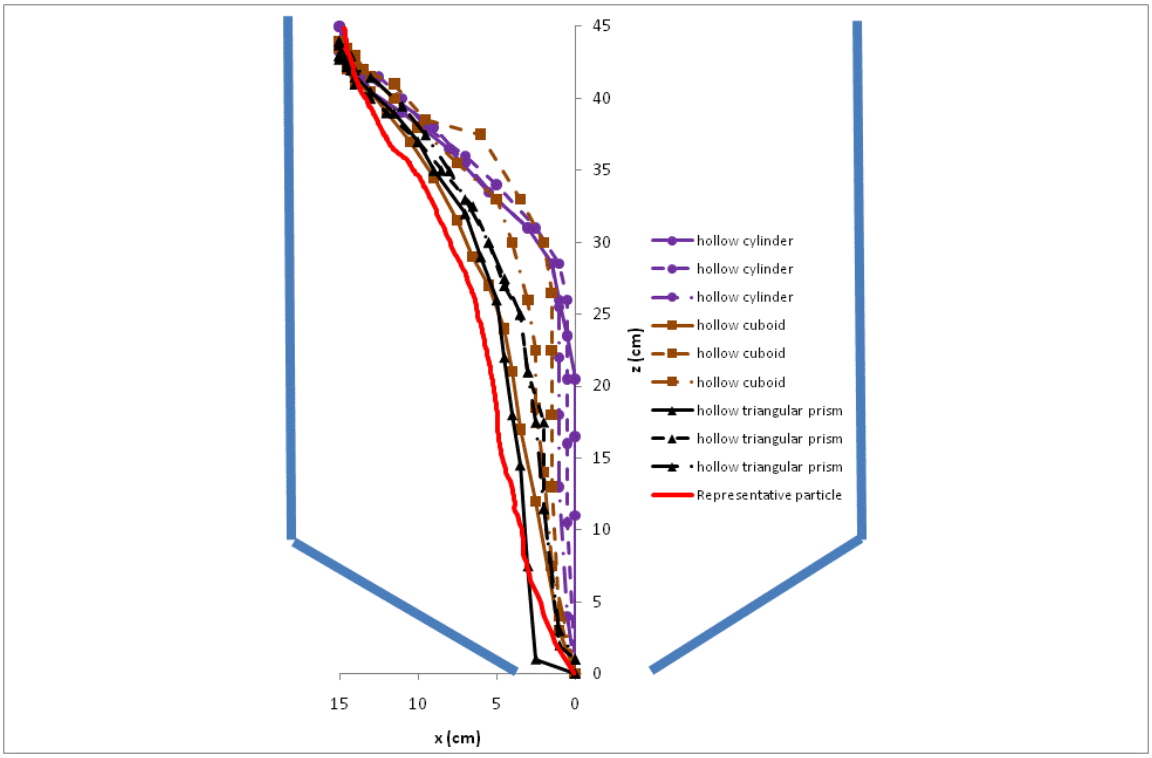

Figure 4.22: Graph showing the trajectories of the hollow cylinder, cuboid and triangular prism free-cells in the white (5mm) particles, starting from position 12. The trajectory followed by the representative particle is also shown

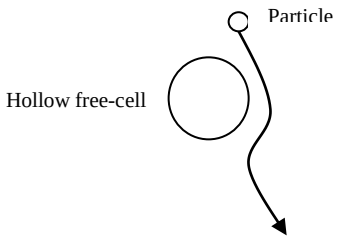

Figure 4.23: Diagram showing the trajectory taken around the hollow cylindrical free- cell, by a particle in the flowing core

The experimental results and discussion of the comparison between the trajectories of the free-cells in the monosized batch and the binary mixtures of particles in the discharging 3D slice silo

5 The experimental results and discussion of the comparison between the trajectories of the free-cells in the monosized batch and the binary mixtures of particles in the discharging 3D slice silo

5.1 Introduction

In this section the results obtained from practical experiments to compare the trajectory and displacement of three trials of the metal, plastic and hollow free-cells in different batches of particle mixtures are presented and discussed. The monosized white (5 mm) and an 80% white (5 mm)/20% black (4 mm) and an 80% white (5 mm)/20% yellow (6 mm) binary mixture were experimented with. The presence of segregation during filling and emptying was observed and this will be discussed. The positions 5 and 12 were selected as the starting positions, for the reasons given in section 4 and so that comparisons between the experiments using monosized and binary mixtures could be compared. Placing the free-cells in the exact starting position was not always possible, as they tended to move when other particles were poured on top of them. The starting position varied by about ±5 mm during each trial. The pink lines show the trajectory of the free-cells in the monosized white particles and the black and yellow lines show the path taken by the free-cells in the white/black and white/yellow binary mixtures respectively.

5.2 Segregation during filling and emptying

Segregation in the binary mixtures was observed to occur during the filling and emptying of the 3D slice silo. During the filling phase the binary mixture consisting of the white (5 mm)/Yellow (6 mm) particles was observed to segregate. A greater fraction of the less dense, but larger yellow particles collected in the dead zones and towards the edge of the silo than the white particles. There was no noticeable segregation of the white (5 mm)/black (4 mm) particles during filling.

During the discharge phase, the white (5 mm)/black (4 mm) binary mixture was observed to segregate along the central core region (Figure 5.1). The black particles discharged along one half of the slice and the white particles along the other half, with a noticeable gradient along the cross section of the bed.

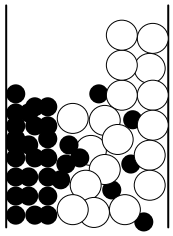

Figure 5.1: Comparing the trajectories of each of the metal, plastic and hollow cylindrical free-cells in the monosized batch of particles and the two binary mixtures of particles

5.3 Comparison between the trajectories and velocities of the metal cylinder, plastic cylinder and hollow cylinder free cells in the white monosized particles and the white/yellow and white/black binary mixtures.

Figure 5.2 shows the trajectory taken by three trials of the metal cylinder in the monosized white (5 mm) particles and the binary mixtures of 80% white (5 mm)/20% black (4 mm) and 80% white (5 mm)/20% yellow (6 mm), starting from position 12.

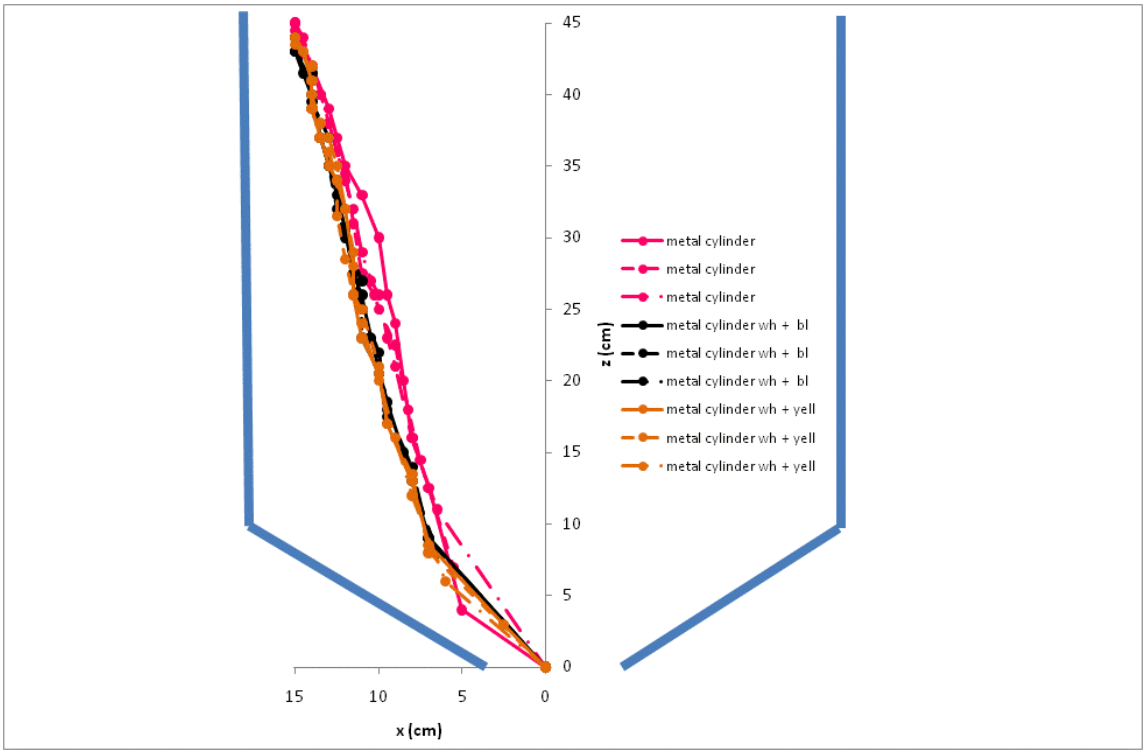

Figure 5.2: The trajectory taken by three trials of the metal cylinder in the monosized white particles (pink) and the binary mixtures of 80% white (5mm)/20% black (4mm) (black) and 80% white (5mm)/ 20% yellow (6mm) (yellow), starting from position 12

The trajectories followed by the metal cylinder in the white/black and white/yellow mixtures appear to overlap each other. There is a clear difference between the trajectories followed by the metal cylinder in the binary mixtures and in the monosized batch of particles. The path followed by the metal cylinder in the monosized particles, varies from the path followed by the metal cylinder in the binary mixtures by up to 2 cm along the horizontal.

Figure 5.3 shows the vertical displacement-time graph for the metal cylinder in the monosized white (5mm) particles and the binary mixtures of 80% white (5 mm)/20% black (4 mm) and 80% white (5 mm)/20% yellow (6 mm), starting from position 12.

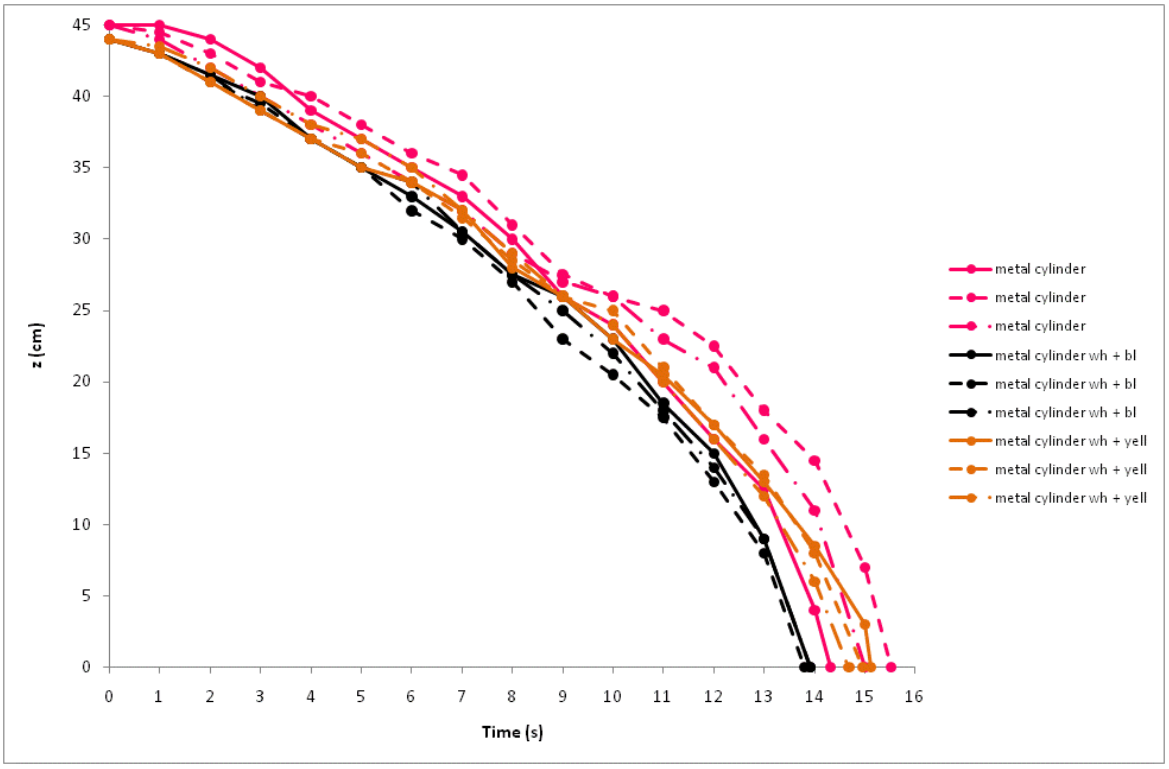

Figure 5.3: The vertical displacement-time graph for the metal cylinder in the monosized white (5 mm) particles and the binary mixtures of 80% white (5 mm)/20% black (4 mm) and 80% white (5 mm)/20% yellow (6 mm), starting from position 12

The metal free-cell takes an average 7% shorter time in the white/black mix than the white monosized batch of particles and the white/yellow mix. The metal cylinder tends to flow through the discharging particles in the mono and binary batches of particles. The slightly faster vertical velocity of the metal cylinder in the white/black binary mixtures may indicate that the particles have a greater freedom of movement in the 3D slice and hence the metal free-cell has more freedom of movement. The metal cylinder travels with a vertical uniform acceleration of 0.4 cm/s^2

Figure 5.4 shows the horizontal displacement-time graph for the metal cylinder in the monosized white (5 mm) particles and the binary mixtures of 80% white (5 mm)/20% black (4 mm) and 80% white (5 mm)/20% yellow (6 mm), starting from position 12.

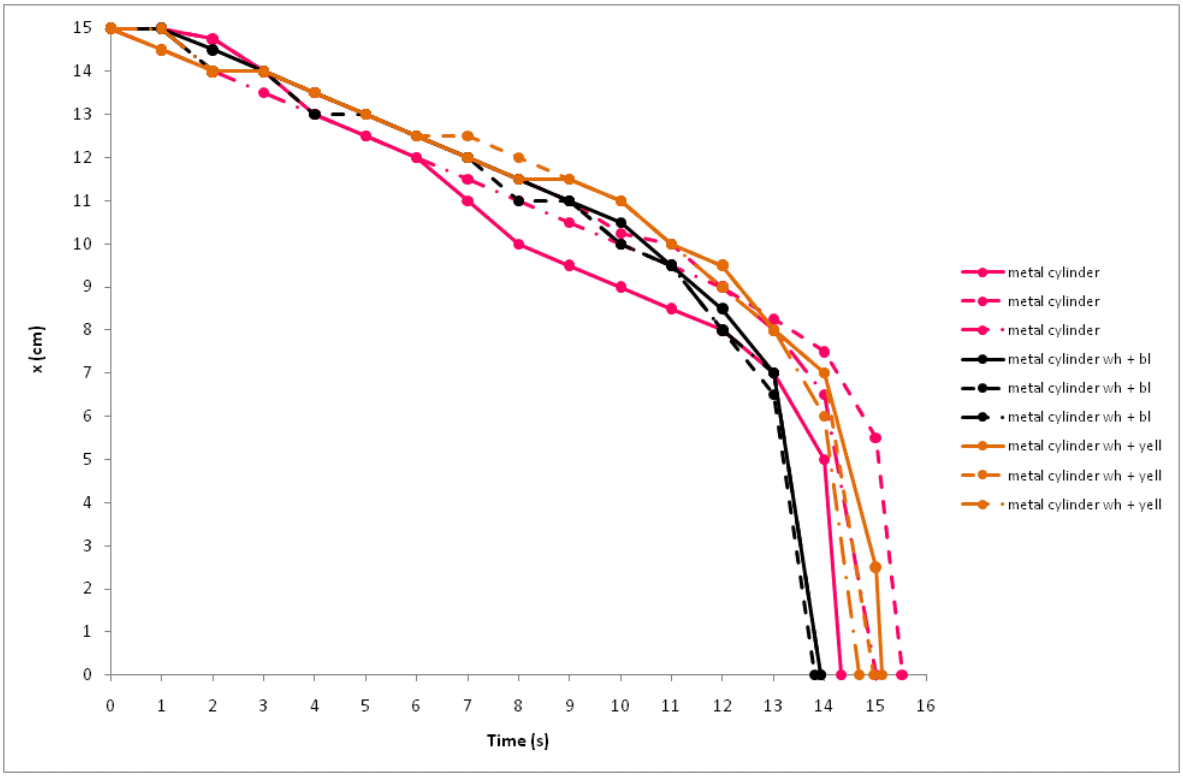

Figure 5.4: Graph showing the horizontal displacement-time graph for the metal cylinder in the monosized white (5 mm) particles and the binary mixtures of 80% white (5 mm)/20% black (4 mm) and 80% white (5 mm)/20% yellow (6 mm), starting from position 12

The time taken for the metal cylinder to reach the orifice is on average 15 seconds in each of the binary mixtures. The shape of the curves over three trials in the monosized and binary mixtures is very similar. The range in the position of the metal cylinder over three trials up until 1 second prior to reaching the orifice is a maximum of 2 cm in the monosized particles and 1 cm in the binary mixtures. On average the metal cylinder travels at a constant horizontal velocity of 0.6 cm/s in the initial 14 seconds after the opening of the orifice prior to rapidly accelerating through the orifice.

Figure 5.5 shows the trajectory taken by three trials of the plastic cylinder in the monosized white particles and the binary mixtures of 80% white (5 mm)/20% black (4 mm) and 80% white (5 mm)/20% yellow (6 mm), starting from position 12.

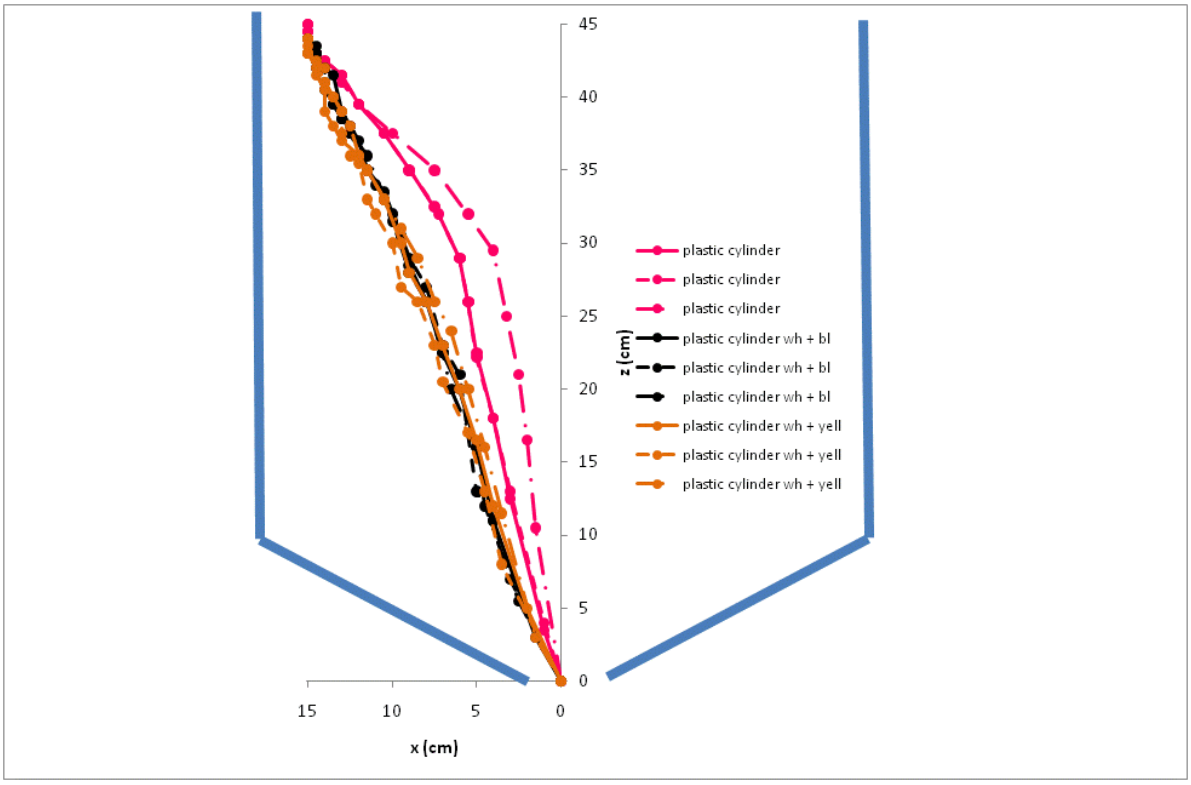

Figure 5.5: The trajectory taken by three trials of the plastic cylinder in the monosized white particles (5mm) and the binary mixtures of 80% white (5 mm)/20% black (4 mm) and 80% white (5 mm)/ 20% yellow (6 mm), starting from position 12

The trajectories followed by the plastic cylinder in the binary mixtures are shown to overlap each other quite considerably. The trajectory followed by the plastic cylinder in the monosized white particles is almost identical over two trials but one trial results in a path that deviates from that of the other two trials by a maximum of 2.5 cm along the horizontal. The particles in binary mixtures have been observed in this study to 'jostle' past each other more easily than in monosized batches, resulting in a wider core of flowing material. Binary mixtures also have greater static and flowing bulk densities than monosized batches of particles (Humby, 1998). Position 12 in binary mixtures is on the edge of the flowing core that extends to the top of the bed. In the batch of white particles position 12 is on the outside

of the flowing core and the free-cell travels down towards the centre line along a layer of material just under the top of the bed.

Figure 5.6 shows the vertical displacement-time graph for the plastic cylinder in the monosized white (5 mm) particles and the binary mixtures of 80% white (5 mm)/20% black (5 mm) and 80% white (5 mm)/20% yellow (6 mm), starting from position 12.

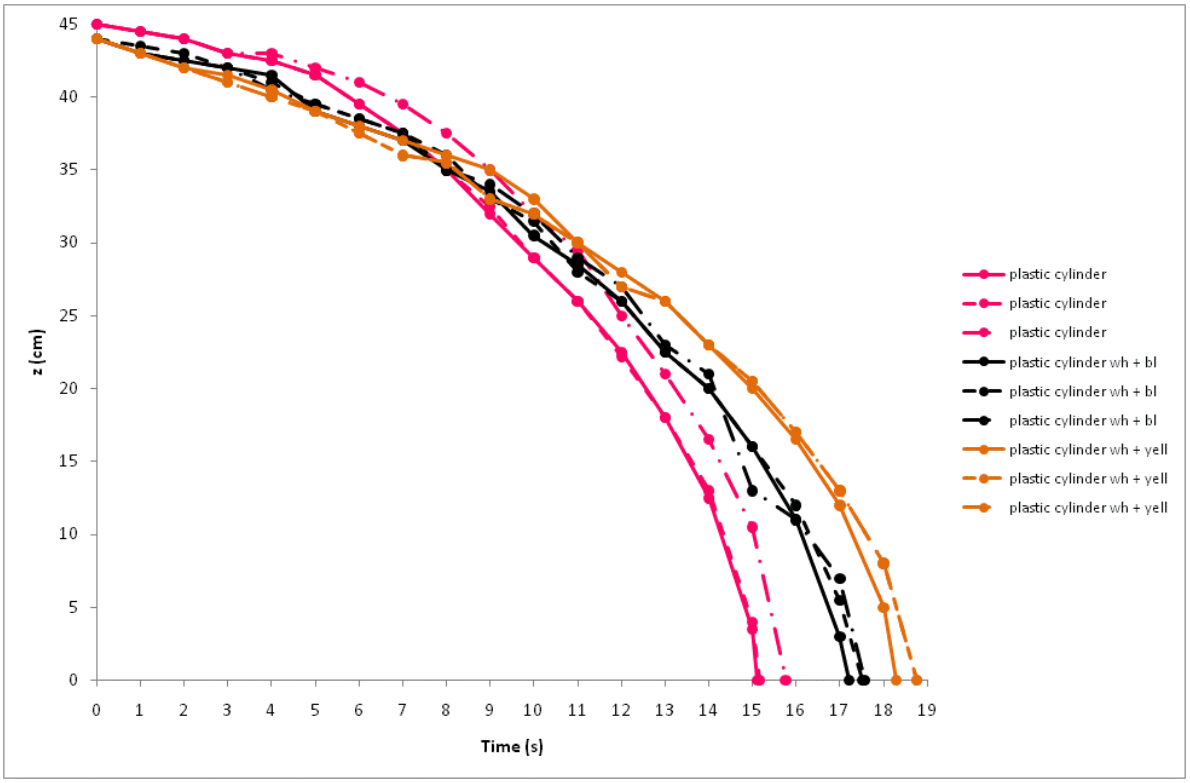

Figure 5.6: Graph showing the vertical displacement-time graph for the plastic cylinder in the monosized white (5 mm) particles and the binary mixtures of 80% white (5 mm)/20% black (4 mm) and 80% white (5 mm)/20% yellow (6 mm), starting from position 12

The vertical velocity of the plastic cylinder is 6% faster in the white/black binary mix than in the white/yellow binary mix and the vertical velocity of the plastic cylinder in the monosized batch of particles is an average 13% faster than in the white/black mix and 19% faster than in the white/yellow particles. The plastic cylinder in the monosized particles travels with a uniform vertical acceleration of 0.38 cm/s^2 in the white/black binary mixture with a uniform vertical acceleration of 0.29 cm/s^2 and in the white/yellow mixture with a uniform vertical acceleration of 0.26 cm/s^2. The free-cell in the white monosized batch of particles is likely to have travelled faster, because it was transported along a layer of material just under the bed to

the flowing core of material, where the velocity is greatest. The free-cell in the binary mixture of yellow/white particles possibly took longer to reach the orifice than in the white/black particles, because the yellow particles have a larger diameter than the black particles resulting in a restriction in their freedom of movement. The emptying time of the 3D silo slice filled with the binary mixtures is greater than when it is filled with the monosized particles.

Figure 5.7 shows the horizontal displacement-time graph for the plastic cylinder in the monosized white (5 mm) particles and the binary mixtures of 80% white (5 mm)/20% black (4 mm) and 80% white (5 mm)/20% yellow (6 mm), starting from position 12.

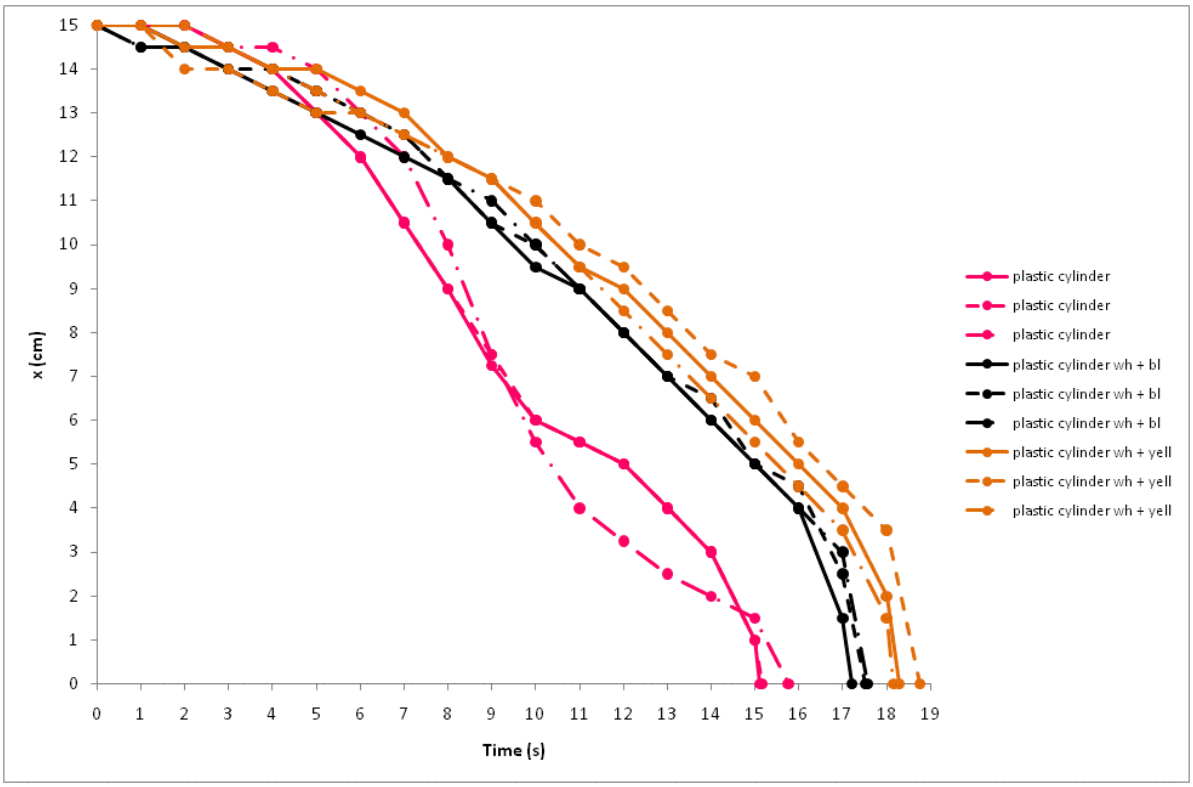

Figure 5.7: Graph showing the horizontal displacement-time graph for the plastic cylinder in the monosized white (5 mm) particles and the binary mixtures of 80% white (5 mm)/20% black (4 mm) and 80% white (5 mm)/20% yellow (6 mm), starting from position 12

The horizontal displacement-time graph shows that the plastic cylinder in the binary mixtures has a very similar horizontal velocity, which is quite different from the horizontal velocity in the monosized white particles. The horizontal velocity of the plastic cylinder in the monosized particles is about twice as fast (200%) as the plastic cylinder in the binary mixtures between 7 and 11 seconds after the opening of the orifice. The horizontal velocity of the plastic cylinder in the binary mixtures is on average constant at 0.63 cm/s between 2 cm from the starting

position and 2 cm from the orifice. The difference between the horizontal displacement of the plastic cylinder in the monosized particles and the binary mixtures may be due to the wider flowing core in the binary mixtures, as discussed in chapter 4.

Figure 5.8 shows the trajectory taken by three trials of the hollow cylinder in the monosized white (5 mm) particles and the binary mixtures of 80% white (5 mm)/20% black (4 mm) and 80% white (5 mm)/20% yellow (6 mm), starting from position 12.

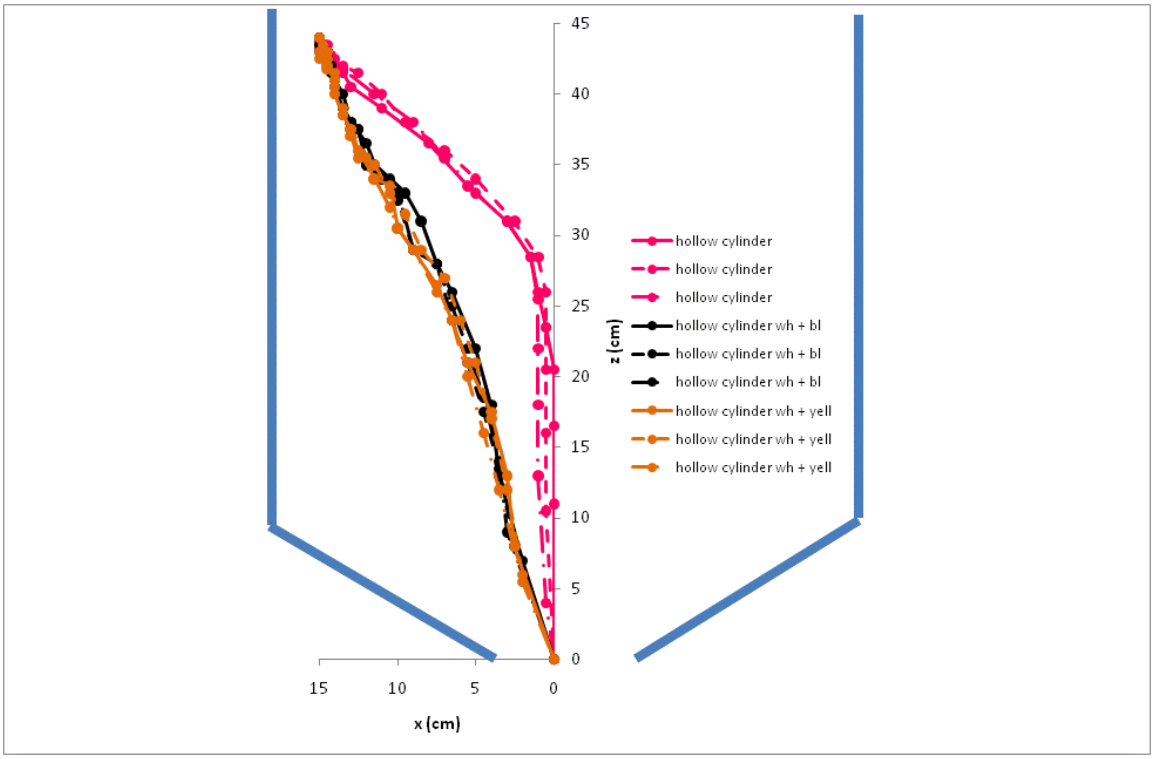

Figure 5.8: The trajectories followed by three trials of the hollow cylinder in the monosized white (5 mm) particles and the binary mixtures of 80% white (5 mm)/20% black (4 mm) and 80% white (5 mm)/ 20% yellow (6 mm), starting from position 12

The trajectories followed by the hollow cylinder are nearly identical in the binary mixtures but the trajectory in the monosized particles is considerably different. This is most probably because of the wider flowing core in the binary mixtures compared to the monosized particles.

It is interesting to note how the hollow cylinder is dragged with the other particles during discharge, but in the white monosized particles, it moves towards the top of the bed and then flows down the centre of the fast flowing core.

Figure 5.9 shows the vertical displacement-time graph for the hollow cylinder in the monosized white (5 mm) particles and the binary mixtures of 80% white (5 mm)/20% black (4 mm) and 80% white (5 mm)/20% yellow (6 mm), starting from position 12.

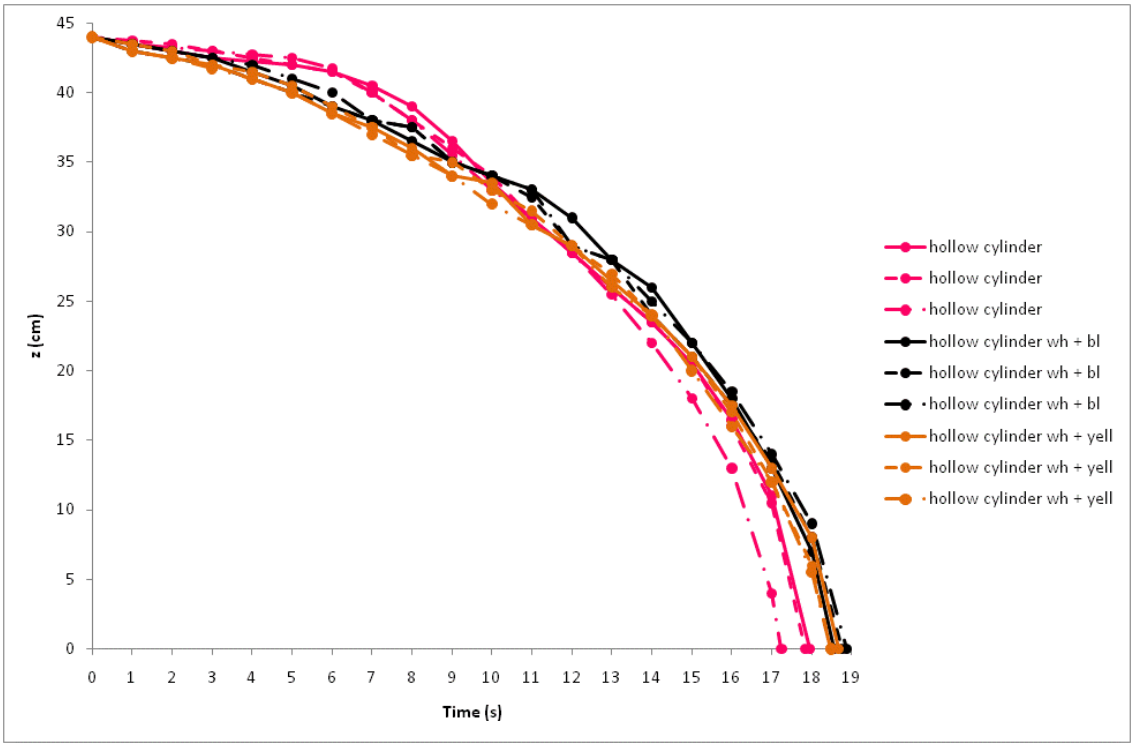

Figure 5.9: The vertical displacement-time graph for the hollow cylinder in the monosized white (5 mm) particles and the binary mixtures of 80% white (5 mm)/20% black (4 mm) and 80% white (5 mm)/20% yellow (6 mm), starting from position 12

The hollow cylinder shows a general vertical uniform acceleration of approximately 0.3 cm/s in the monosized white particles and binary mixtures.

Figure 5.10 shows the horizontal displacement-time graph for the hollow cylinder in the monosized white (5 mm) particles and the binary mixtures of 80% white (5 mm)/20% black (4 mm) and 80% white (5 mm)/20% yellow (6 mm), starting from position 12.

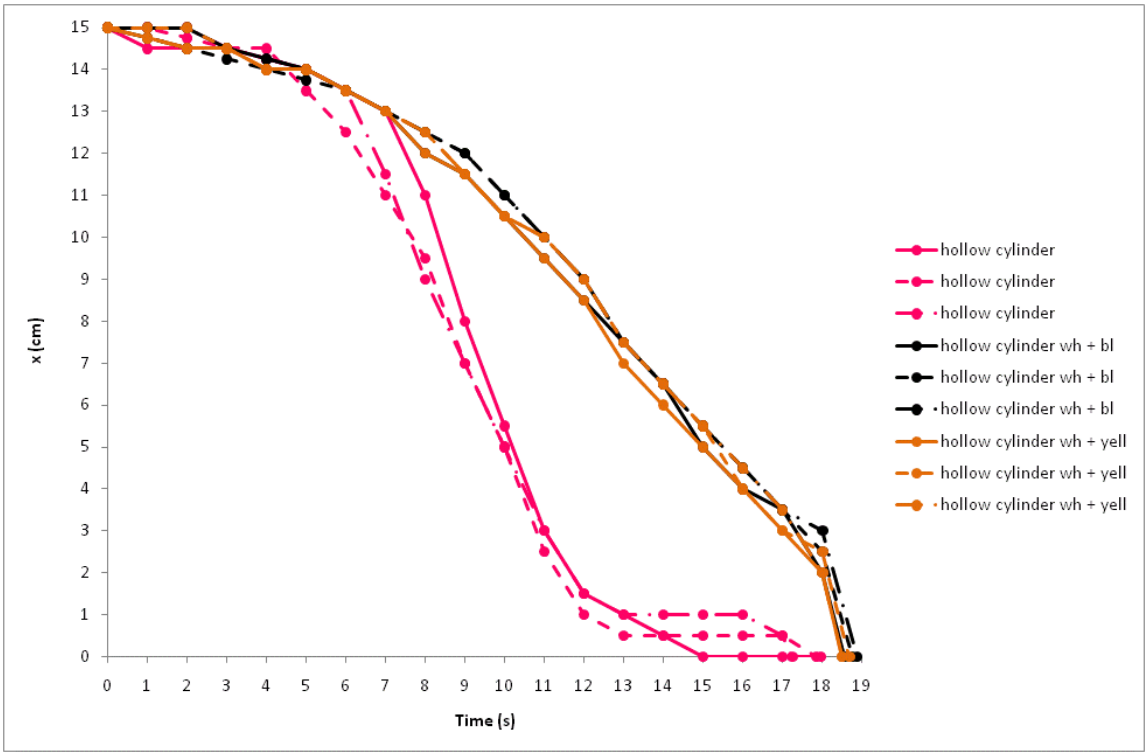

Figure 5.10: The horizontal displacement-time graph for the hollow cylinder in the monosized white (5 mm) particles and the binary mixtures of 80% white (5 mm)/20% black (4 mm) and 80% white (5 mm)/20% yellow (6 mm), starting from position 12

The hollow cylinder in the monosized particles is shown to gradually accelerate horizontally to a uniform velocity of 12 cm/s prior to having zero horizontal velocity for about 3 seconds before it is ragged through the orifice. This is because the particles near the orifice are travelling rapidly and flowing past the cylinder. The hollow cylinder in the binary mixtures accelerates uniformly in the horizontal direction at 0.07 cm/s^2 in the initial 9 seconds to an average constant velocity of 1 cm/s prior to travelling through the orifice.

5.4 Summary

The metal cylinder is shown to follow a very similar trajectory in the monosized particles and binary mixtures. It travels with an average vertical acceleration of 0.4 cm/s^2 and average vertical velocity of 0.6 cm/s. This is most likely due to its density, which enables it to segregate through the other particles in the bed. The trajectory and displacement of the plastic

cylinder in the binary mixtures is very similar, but there is a difference of 2.5 cm between the trajectories of the three experimental trials in the monosized particles. The average uniform vertical acceleration of the plastic cylinder is 0.38 cm/s^2, 0.29 cm/s^2 and 0.26 cm/s^2 in monosized, white/black and white/yellow mixtures respectively and the average horizontal velocity of the plastic cylinder is 0.63 cm/s in the monosized and binary mixtures. The displacement of the plastic cylinder in the binary mixtures is also shown to be similar and the hollow cylinder travels towards the top of the bed and gets carried down the central core in the monosized particles, buts travels with the surrounding particles in the binary mixtures. The hollow cylinder was found to accelerate uniformly at 0.3 cm/s^2 vertically in both the monosized and binary mixtures and it travelled by up to 12 cm/s horizontally in the monosized particles and 1 cm/s horizontally in the binary mixtures.

5.5 Comparison between the trajectories and velocities of the metal cuboid, plastic cuboid and hollow cuboid free cells, in the white monosized particles and the white/yellow and white/black binary mixtures

Figure 5.11 shows the trajectories followed by three trials of the metal cuboid in the monosized white (5 mm) particles and the binary mixtures of 80% white (5 mm)/20% black (4 mm) and 80% white (5 mm)/20% yellow (6 mm), starting from position 12.

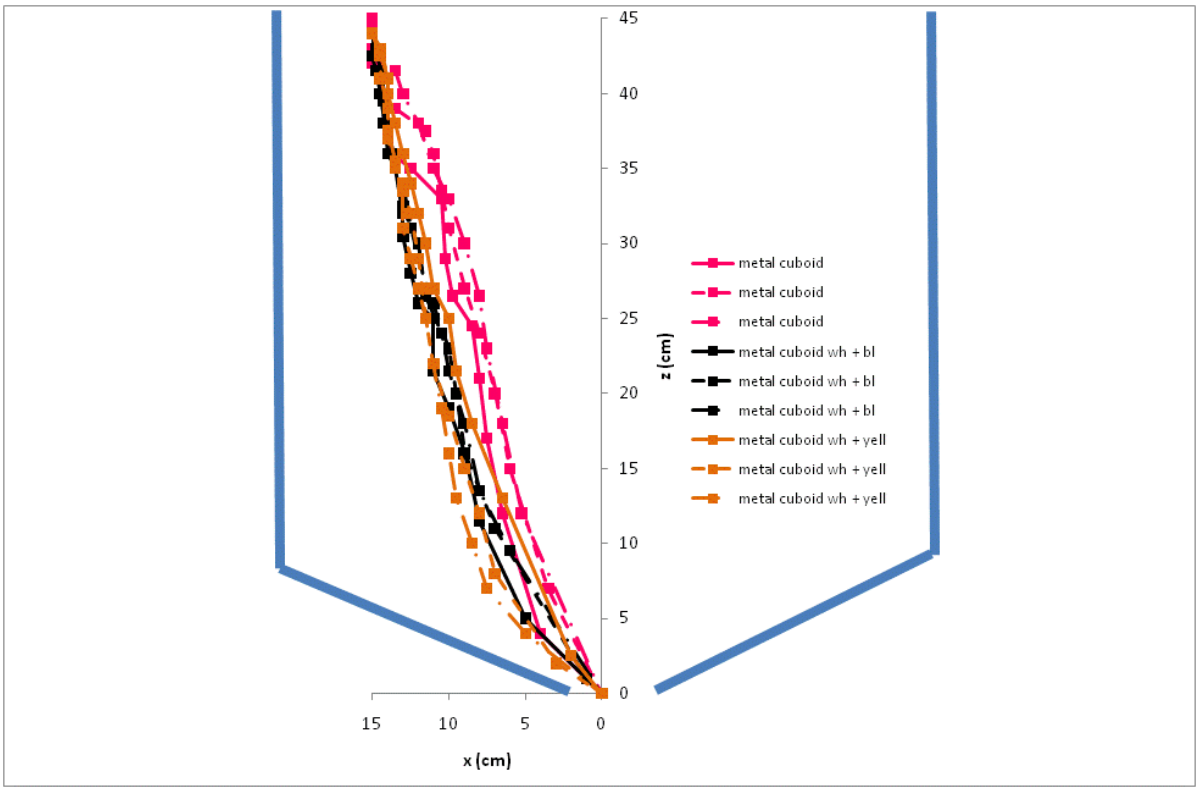

Figure 5.11: The trajectory followed by three trials of the metal cuboid in the monosized white (5 mm) particles and the binary mixtures of 80% white (5 mm)/20% black (4 mm) and 80% white (5 mm)/ 20% yellow (6 mm), starting from position 12

The difference in the paths followed by the metal cuboid in each of the three batches is wider than the differences in the paths followed by the metal cylinder. The path followed by the metal cuboid varies by up to 2 cm, 1 cm and 4 cm along the horizontal in the white, white/black and white/yellow batches respectively. This suggests that the shape of the cuboid may be affecting its movement, whilst the cylinder travels easily through the particles.

Figure 5.12 shows the vertical displacement-time graph for the metal cuboid in the monosized white (5 mm) particles and the binary mixtures of 80% white (5 mm)/20% black (4 mm) and 80% white (5 mm)/20% yellow (6 mm), starting from position 12.

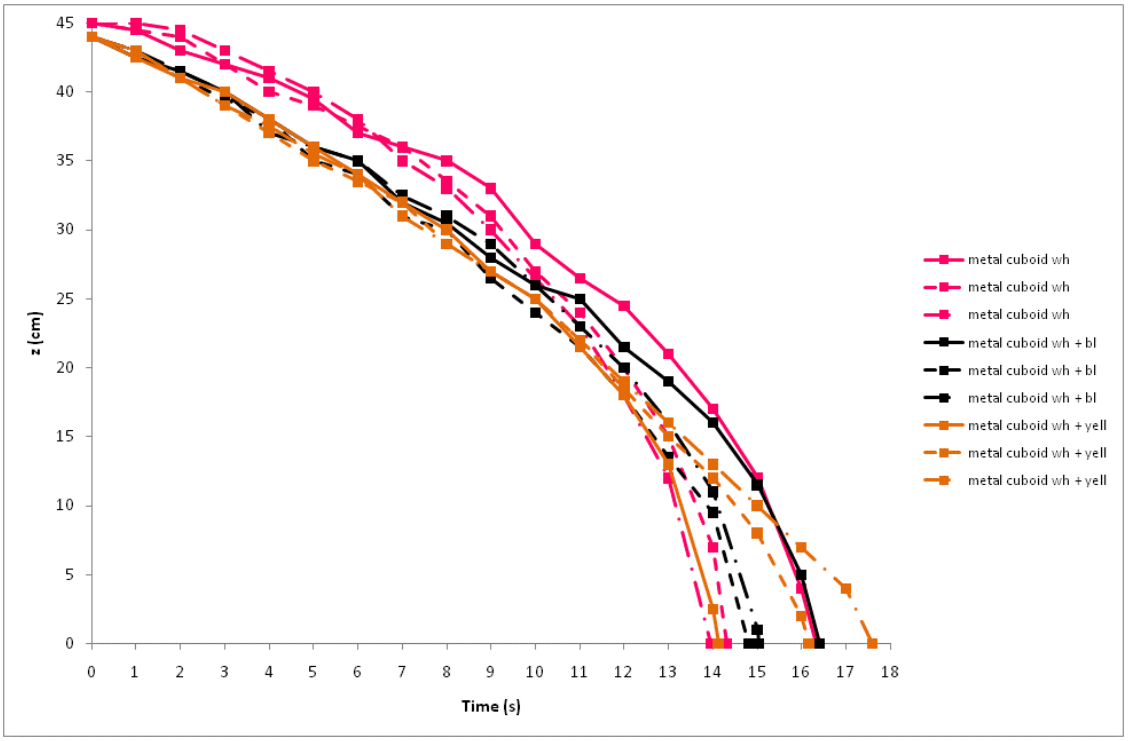

Figure 5.12: Graph showing the vertical displacement-time graph for the metal cuboid in the monosized white (5 mm) particles and the binary mixtures of 80% white (5 mm)/20% black (4 mm) and 80% white (5 mm)/20% yellow (6 mm), starting from position 12

The vertical velocity of the metal cuboid in the monosized and binary mixtures is nearly identical during the first 10 seconds after the initiation of discharge having a value of approximately 2 cm/s. The slight difference in the positions of the curves is due to the slightly different starting positions. The paths over the three trials diverge after about 10 seconds and the time taken to reach the orifice varies between 14-17.5 s in the white/yellow mixture, 15-16.5 s in the white/black mixture and 14-16.5 s in the monosized particles.

Figure 5.13 shows the horizontal displacement-time graph for the metal cuboid in the monosized white (5 mm) particles and the binary mixtures of 80% white (5 mm)/20% black (4 mm) and 80% white (5 mm)/20% yellow (6 mm), starting from position 12.

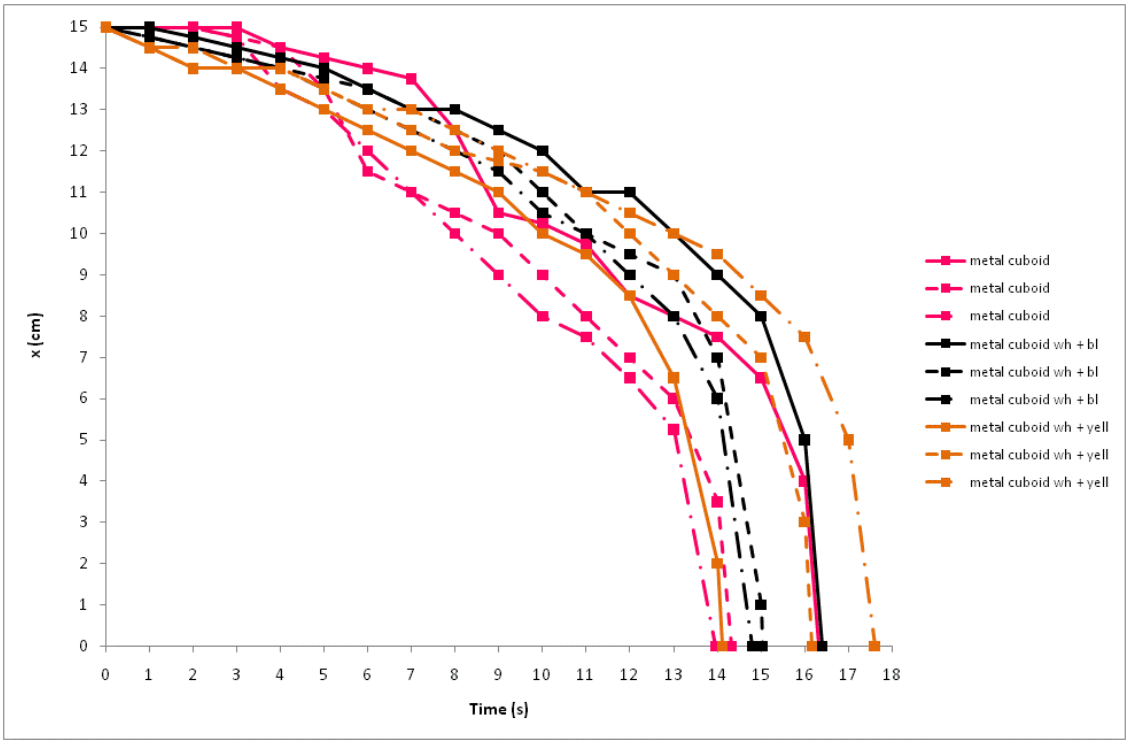

Figure 5.13: Graph showing the horizontal displacement-time graph for the metal cuboid in the monosized white (5 mm) particles and the binary mixtures of 80% white (5 mm)/20% black (4 mm) and 80% white (5 mm)/20% yellow (6 mm), starting from position 12

There is some variation in the horizontal velocity of the metal cuboid in the monosized particles and binary mixtures over three trials. The horizontal velocity of the metal cuboid in the monosized particles varies by between 1 cm/s and 2 cm/s and in the white/black particles between 0.33 cm/s and 0.5 cm/s and in the white/yellow between 0.33cm/s and 0.58 cm/s. The time taken for the metal cuboid to reach the orifice ranges from between 14 and 17.7 seconds.

Figure 5.14 shows the trajectory followed by three trials of the plastic cuboid in the monosized white (5 mm) particles and the binary mixtures of 80% white (5 mm)/20% black (4 mm) and 80% white (5 mm)/20% yellow(6 mm), starting from position 12.

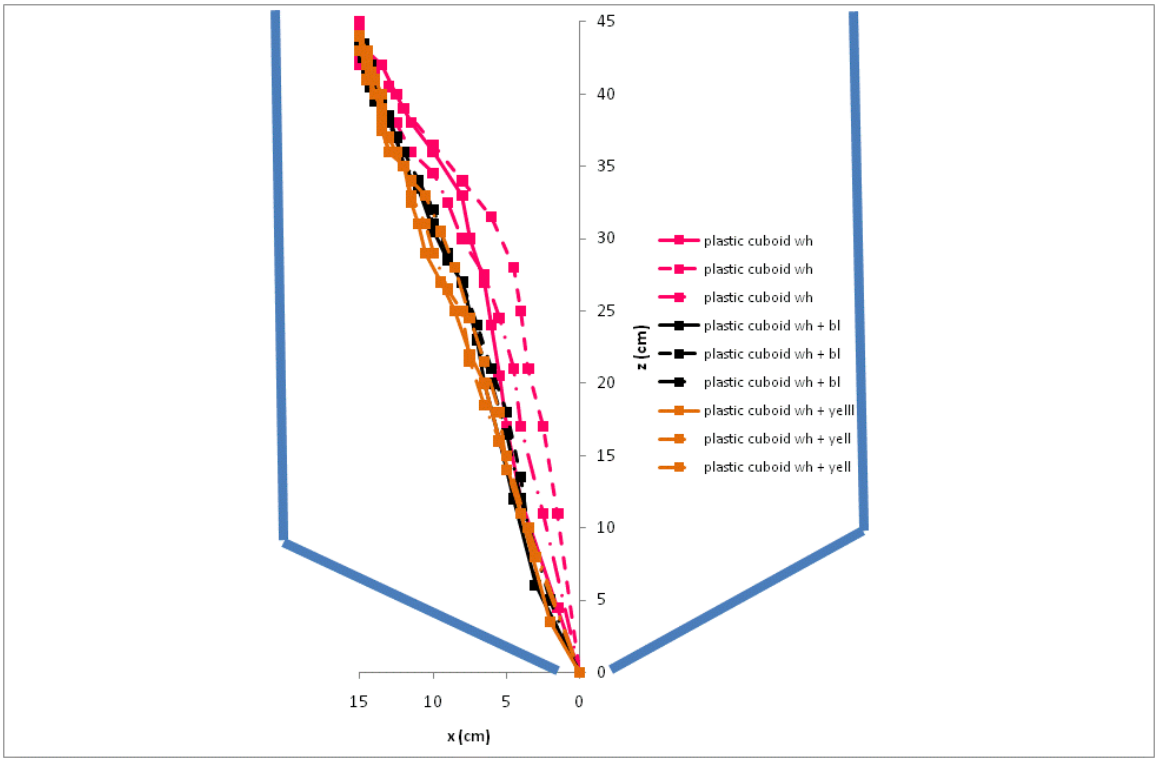

Figure 5.14: The trajectory followed by three trials of the plastic cuboid in the monosized white (5 mm) particles and the binary mixtures of 80% white (5 mm)/20% black (4 mm) and 80% white (5 mm)/ 20% yellow (6 mm), starting from position 12

Over three trials the plastic cuboid follows a very similar path in the binary mixtures. The paths vary by up to 1 cm along the horizontal in the white/yellow mixture and up to 0.5 cm in the white/black mixture. In the monosized white particles the paths vary by up to 3 cm along the horizontal over three trials.

Figure 5.15 shows the vertical displacement-time graph for the plastic cuboid in the monosized white (5 mm) particles and the binary mixtures of 80% white (5 mm)/20% black (4 mm) and 80% white (5 mm)/20% yellow (6 mm), starting from position 12.

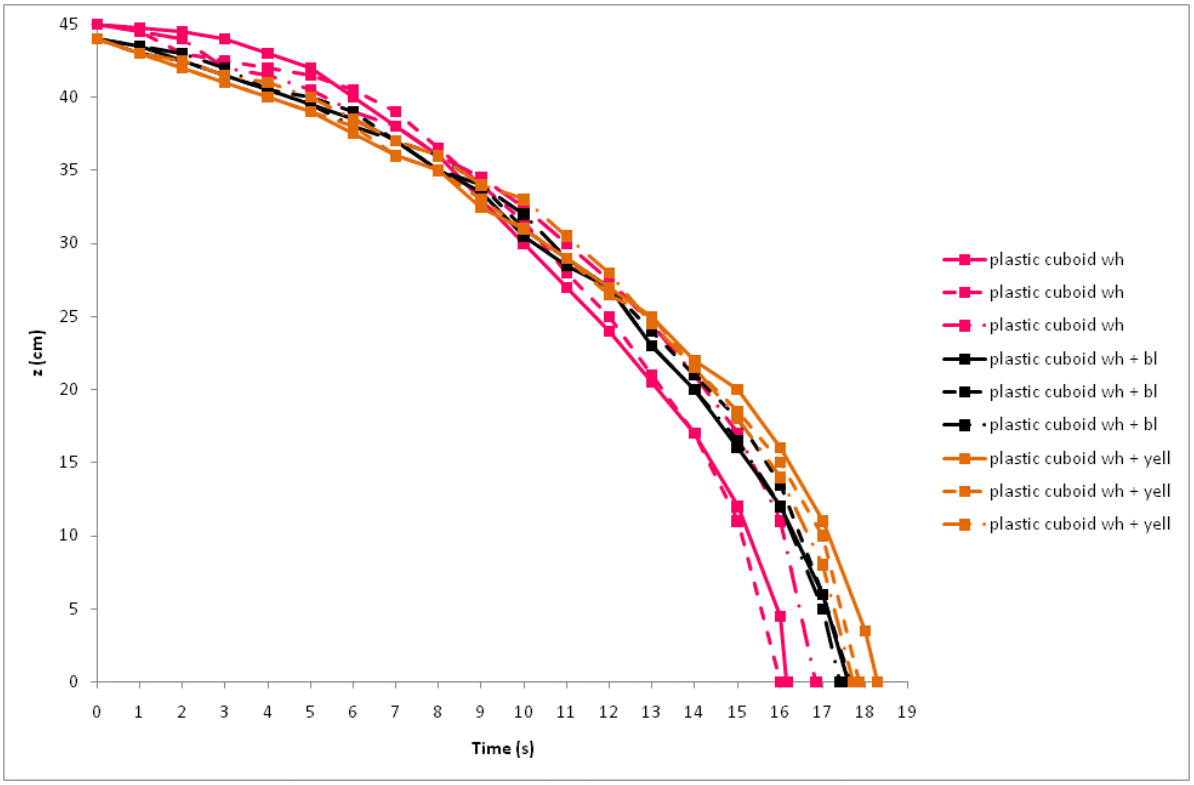

Figure 5.15: The vertical displacement-time graph for the plastic cuboid in the monosized white (5 mm) particles and the binary mixtures of 80% white (5 mm)/20% black (4 mm) and 80% white (5 mm)/20% yellow (6 mm), starting from position 12

The plastic cuboid in the monosized particles travels with an approximately uniform acceleration of 0.32 cm/s^2 compared to approximately 0.27 cm/s^2 in the binary mixtures.

Figure 5.16 shows the horizontal displacement-time graph for the plastic cuboid in the monosized white (5 mm) particles and the binary mixtures of 80% white (5 mm)/20% black (4 mm) and 80% white (5 mm)/20% yellow (6 mm), starting from position 12.

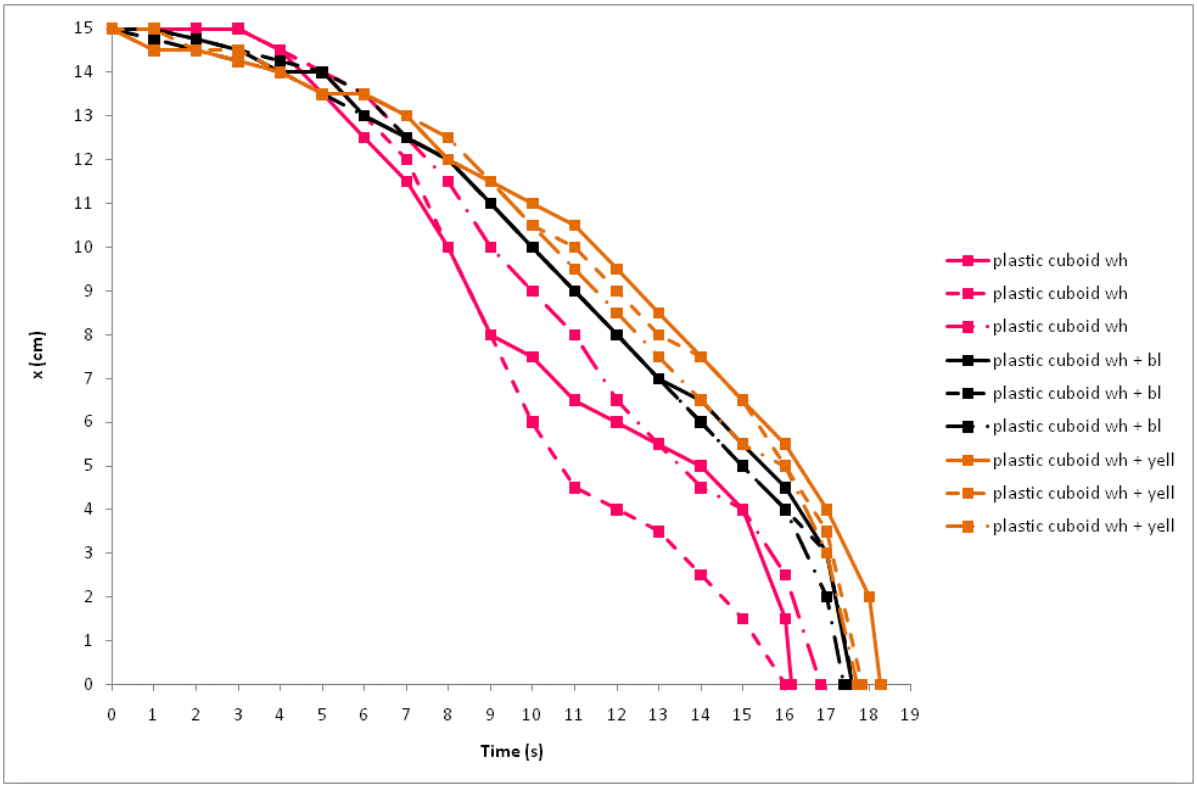

Figure 5.16: The horizontal displacement-time graph for the plastic cuboid in the monosized white (5 mm) particles and the binary mixtures of 80% white (5 mm)/20% black (4 mm) and 80% white (5 mm)/20% yellow (6 mm), starting from position 12

In the binary mixtures, the plastic cuboid gradually uniformly accelerates horizontally at 0.07 cm/s^2 to a constant velocity of 1 cm/s, prior to rapidly accelerating through the orifice. In the monosized particles the plastic cuboid accelerates to a less predictable velocity of between 1.4 cm/s and 2.7 cm/s.

Figure 5.17 shows the trajectory followed by three trials of the hollow cuboid in the monosized white (5 mm) particles and the binary mixtures of 80% white (5 mm)/20% black (4 mm) and 80% white (5 mm)/20% yellow (6 mm), starting from position 12.

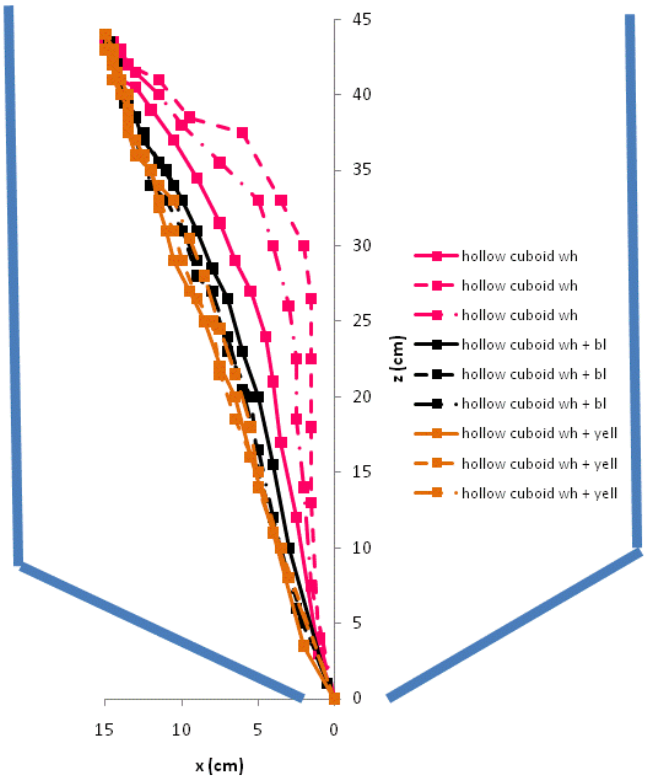

Figure 5.17: The trajectories followed by three trials of the hollow cuboid in the monosized white (5mm) particles and the binary mixtures of 80% white (5mm)/20% black (4mm) and 80% white (5mm)/ 20% yellow (6mm), starting from position 12

The trajectory of the hollow cuboid in the binary mixtures is very similar over three trials. The trajectories in the white/black binary mixture vary by a maximum of 1 cm along the horizontal and the trajectories in the white/yellow mix vary by a maximum of 1.5 cm over three trials. The trajectories in the monosized particles vary by up to 5 cm along the horizontal. The vertical and horizontal velocity of the hollow cuboid in the binary mixtures is very similar to the vertical and horizontal velocity of the plastic cylinder.

Figure 5.18 shows the vertical displacement-time graph for the hollow cuboid in the monosized white (5 mm) particles and the binary mixtures of 80% white (5 mm)/20% black (4 mm) and 80% white (5 mm)/20% yellow (6 mm), starting from position 12.

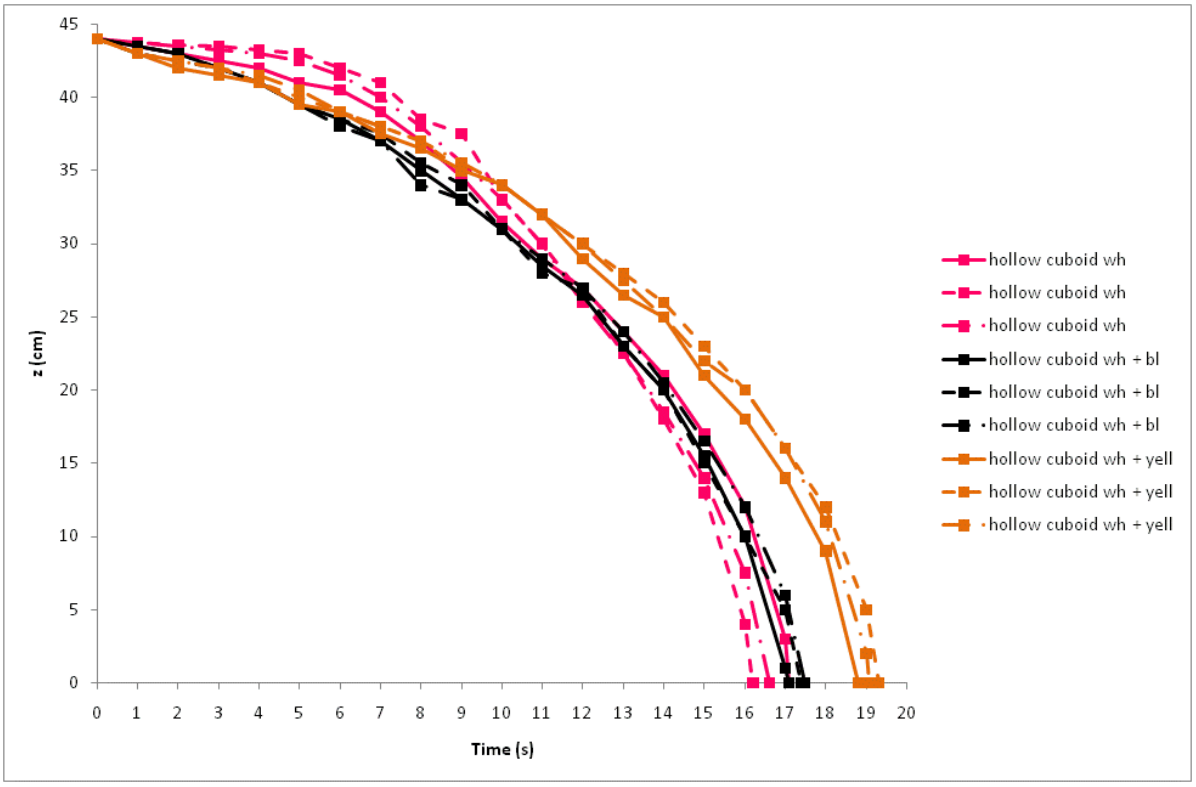

Figure 5.18: The vertical displacement-time graph for the hollow cuboid in the monosized white (5 mm) particles and the binary mixtures of 80% white (5 mm)/20% black (4 mm) and 80% white (5 mm)/20% yellow (6 mm), starting from position 12

There is significant difference between the vertical velocities of the hollow cuboid in the two binary mixtures. The hollow cuboid takes an average of 19 seconds to reach the orifice in the white/yellow mixture and an average 17.5 seconds in the white/black mixture. In the final 6 seconds prior to travelling through the orifice the hollow cuboid accelerates uniformly at a similar rate of 1.52 cm/s^2 in the monosized and white/black binary mixture. The hollow cuboid accelerates uniformly at approximately 0.12 cm/s^2 from position 12 to the orifice.

Figure 5.19 shows the horizontal displacement-time graph for the hollow cuboid in the monosized white (5 mm) particles and the binary mixtures of 80% white (5 mm)/20% black (4 mm) and 80% white (5 mm)/20% yellow (6 mm), starting from position 12.

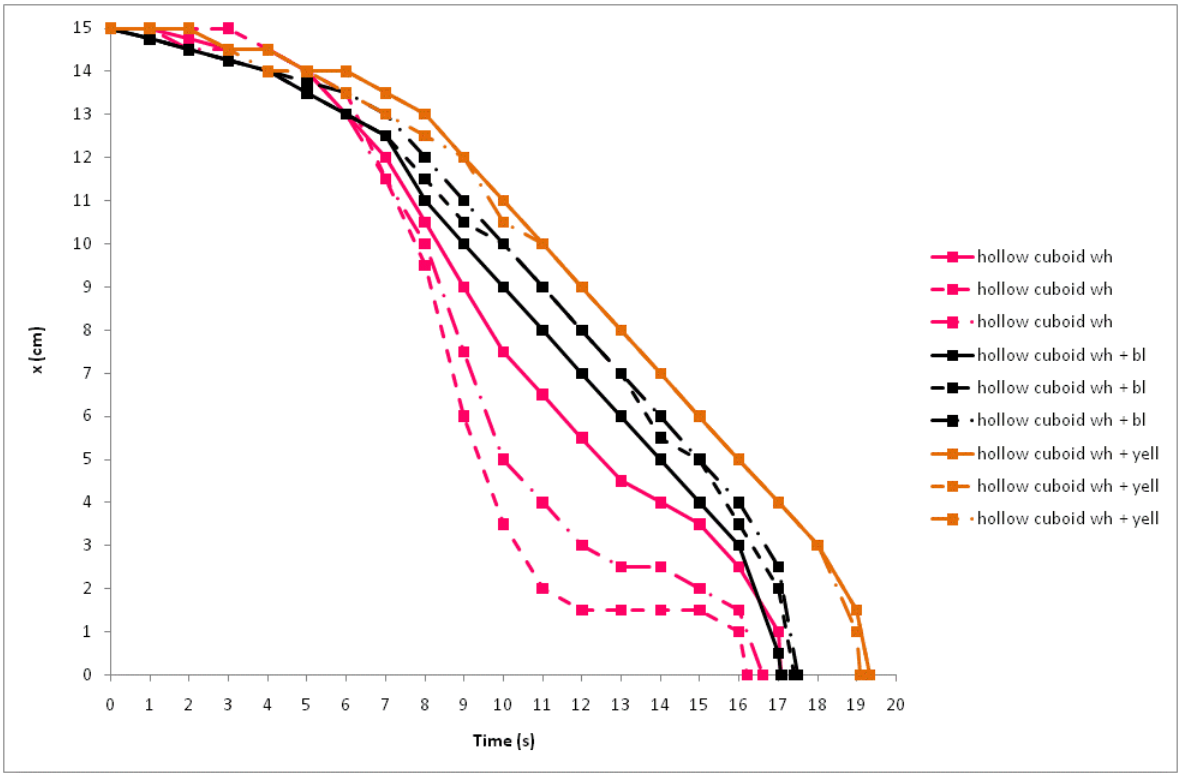

Figure 5.19: The horizontal displacement-time graph for the plastic cuboid in the monosized white (5 mm) particles and the binary mixtures of 80% white (5 mm)/20% black (4 mm) and 80% white (5 mm)/20% yellow (6 mm), starting from position 12

In the binary mixtures the hollow cuboid free cell slowly accelerates to a constant horizontal velocity of approximately 0.95 cm/s, prior to rapidly accelerating through the orifice. In the monosized particles the velocity of the hollow cuboid varies between 1.33 cm/s and 2.5 cm/s. In one trial in the monosized particles the hollow cuboid has zero horizontal velocity for approximately 3 seconds prior to passing through the orifice. This is as a result of the particles travelling rapidly towards the orifice and along the edge of the hollow cuboid, before it is eventually dragged into the flow.

5.6 Summary

In this section the trajectories of the metal, plastic and hollow cuboids in the white monosized particles and the white/yellow and white/black binary mixtures have been presented and discussed. The trajectory of the cuboids in the binary mixtures is very much the same. The paths vary by only up to 2 cm. However, in the monosized particles the trajectories vary by up to 5 cm. The horizontal and vertical displacements of the cuboids in the binary mixtures vary by only about 1 cm/s. The vertical displacement of the monosized particles and binary mixtures varies by up to approximately 11% and the horizontal displacement is considerably different in the monosized particles compared to the binary mixtures.

5.7 Comparison between the trajectories and velocities of the metal triangular prism, plastic triangular prism and hollow triangular prism free cells in the white monosized particles and the white/yellow and white/black binary mixtures

Figure 5.20 shows the trajectories of three trials of the metal triangular prism in the monosized white (5 mm) particles and the binary mixtures of 80% white (5 mm)/20% black (4 mm) and 80% white (5 mm)/20% yellow (6 mm), starting from position 12.

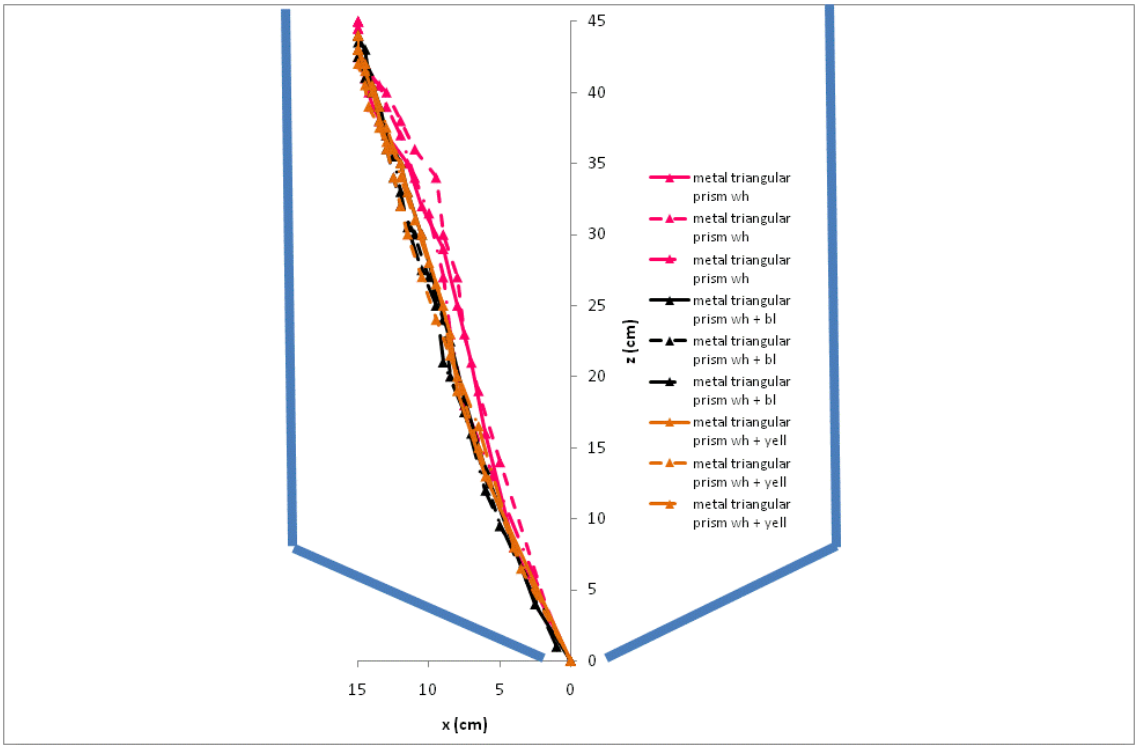

Figure 5.20: The trajectories of three trials of the metal triangular prism in the monosized white (5 mm) particles and the binary mixtures of 80% white (5 mm)/20% black (4 mm) and 80% white (5 mm)/ 20% yellow (6 mm), starting from position 12

The paths followed by the metal triangular prism, over three trials, in each of the binary mixtures and the monosized particles is very similar. The path of the triangular prism in the white/black mixture varies by about 0.3cm and in the white/yellow mixture by about 0.5 cm. In the monosized particles the path over three trials varies by up to 1.5 cm. The horizontal and vertical velocity of the metal triangular prism is very similar in the binary mixtures and the monosized particles. The general features are similar to observations of the metal cylinder.

The only significant difference is that the velocity of the metal triangular prism is on average 7% faster than the metal cylinder.

Figure 5.21 shows the vertical displacement-time graph for the metal triangular prism in the monosized white (5 mm) particles and the binary mixtures of 80% white (5 mm)/20% black (4 mm) and 80% white (5 mm)/20% yellow (6 mm), starting from position 12.

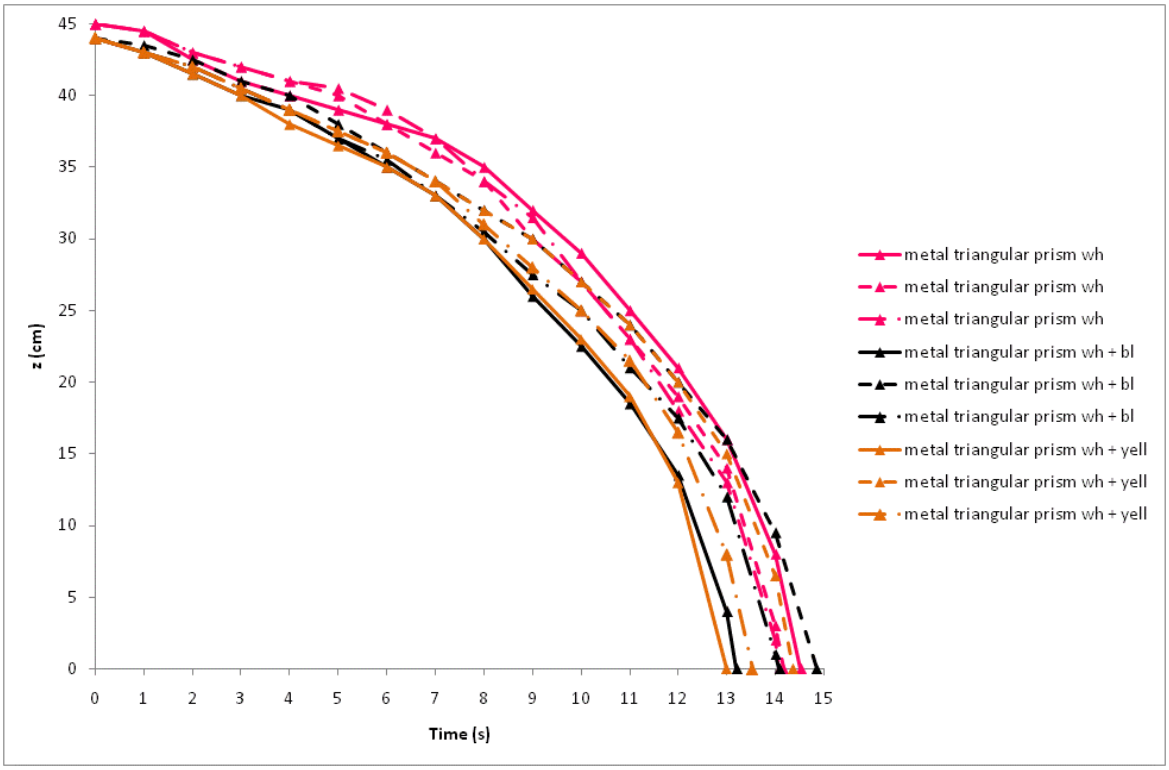

Figure 5.21: The vertical displacement-time graph for the metal triangular prism in the monosized white (5 mm) particles and the binary mixtures of 80% white (5 mm)/20% black (4 mm) and 80% white (5 mm)/20% yellow (6 mm), starting from position 12

The metal triangular prism has a very similar vertical displacement in the monosized white particles and the binary mixtures. The average time taken for the metal triangular prism to reach the orifice is 14 seconds and it travels from rest to the orifice with an average uniform vertical acceleration of 0.46 cm/s^2.

Figure 5.22 shows the horizontal displacement-time graph for the metal triangular prism in the monosized white (5 mm) particles and the binary mixtures of 80% white (5 mm)/20% black (4 mm) and 80% white (5 mm)/20% yellow (6 mm), starting from position 12.

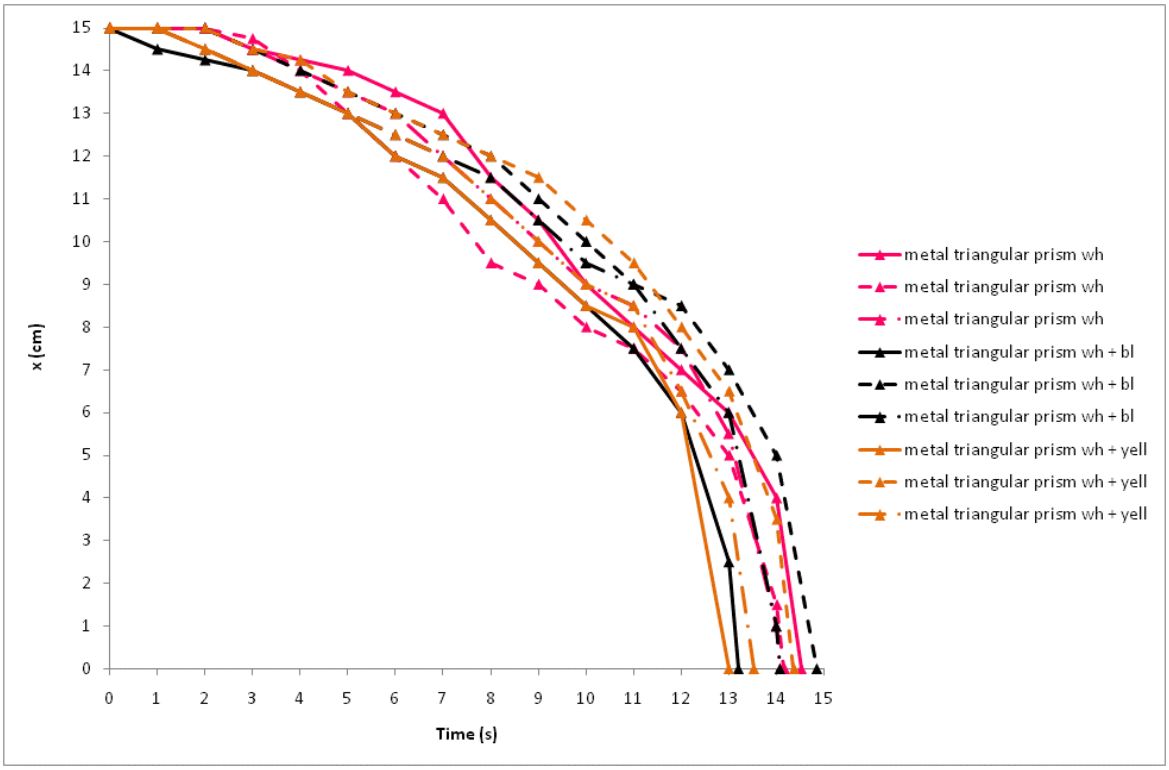

Figure 5.22: The horizontal displacement-time graph for the metal triangular prism in the monosized white (5 mm) particles and the binary mixtures of 80% white (5 mm)/20% black (4 mm) and 80% white (5 mm)/20% yellow (6 mm), starting from position 12

In similarity to the vertical displacement of the metal triangular prism the horizontal displacement of the metal triangular prism is very similar in the monosized particles and the binary mixtures. The metal triangular prism accelerates horizontally from rest at an average of 0.1 cm/s^2 prior to rapidly accelerating through the orifice.

Figure 5.23 shows the trajectories of three trials of the plastic triangular prism in the monosized white (5 mm) particles and the binary mixtures of 80% white (5 mm)/20% black (4 mm) and 80% white (5 mm)/20% yellow (6 mm), starting from position 12.

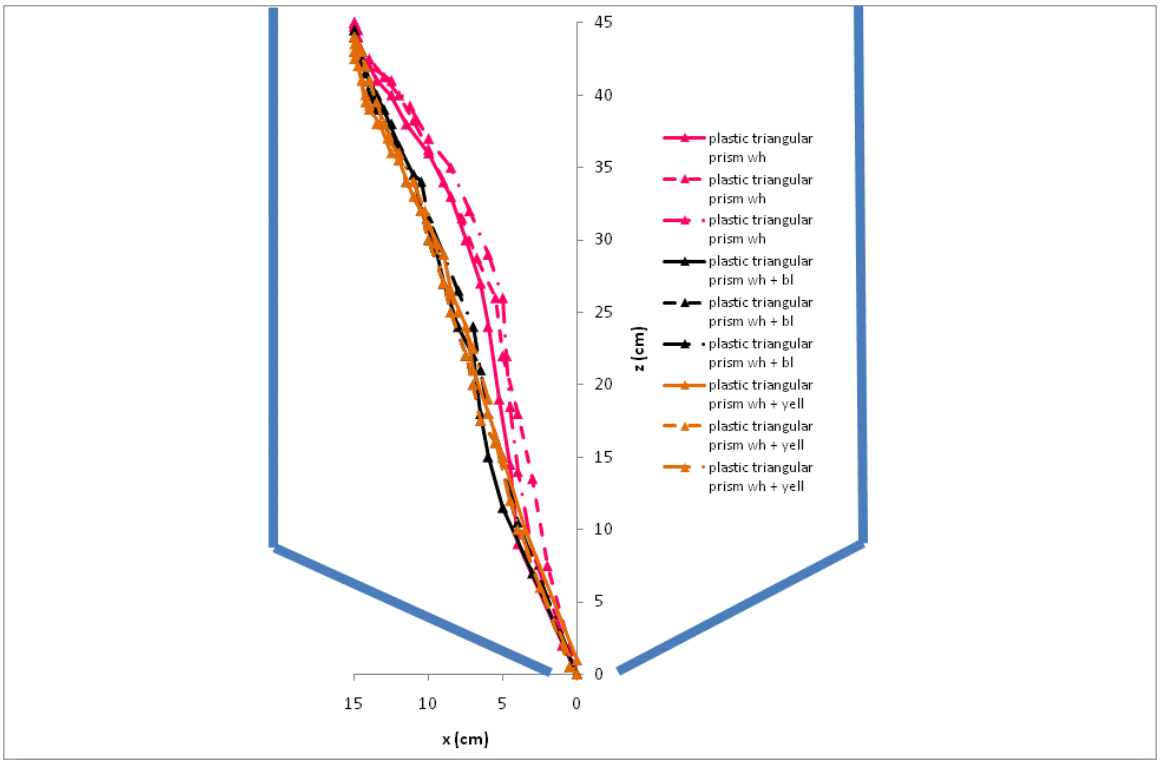

Figure 5.23: The trajectories of three trials of the plastic triangular prism in the monosized white (5 mm) particles and the binary mixtures of 80% white (5 mm)/20% black (4 mm) and 80% white (5 mm)/ 20% yellow (6 mm), starting from position 12

The path followed by the plastic triangular prism over three trials in the monosized particles and binary mixtures shows similar characteristics to the path followed by the metal triangular prism. The path followed by the plastic triangular prism varies by up to 1 cm in the white/black mixture, 0.5 cm in the white/yellow mixture and 1.5 cm in the monosized particles.

Figure 5.24 shows the vertical displacement-time graph for the plastic triangular prism in the monosized white (5 mm) particles and the binary mixtures of 80% white (5 mm)/20% black (4 mm) and 80% white (5 mm)/20% yellow (6 mm), starting from position 12.

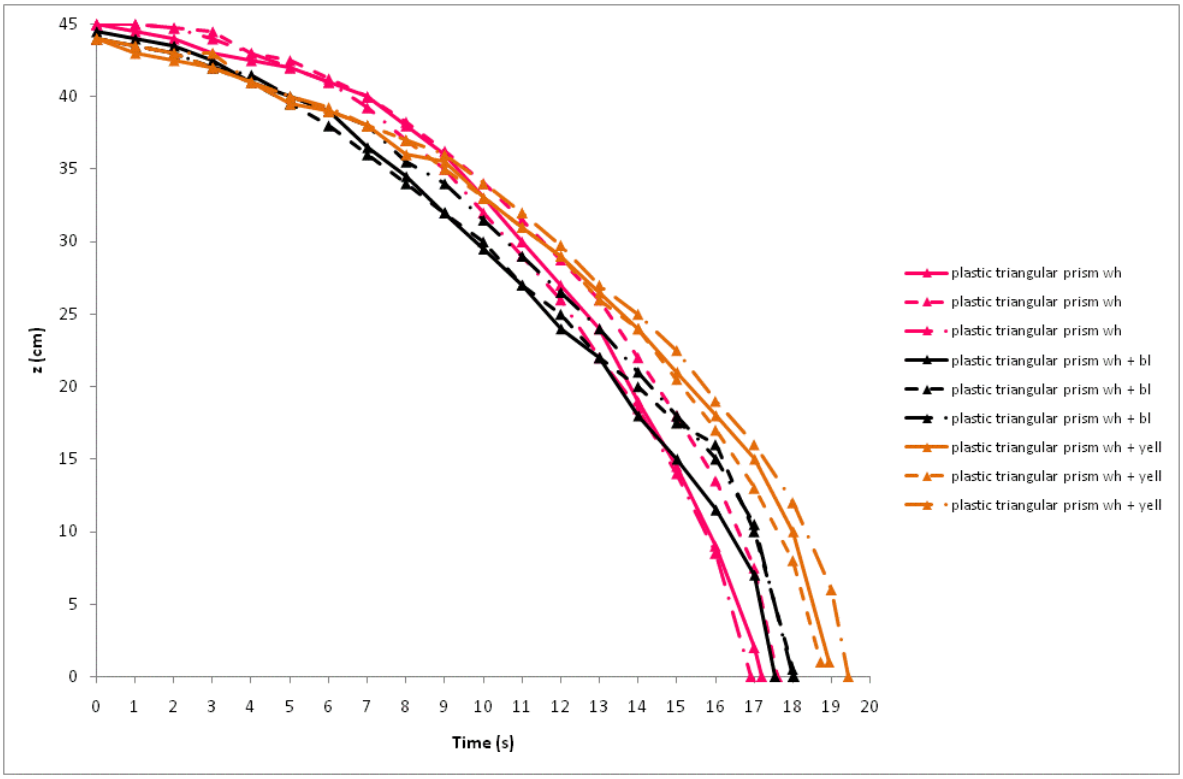

Figure 5.24: Graph showing the vertical displacement-time graph for the plastic triangular prism in the monosized white (5 mm) particles and the binary mixtures of 80% white (5 mm)/20% black (4 mm) and 80% white (5 mm)/20% yellow (6 mm), starting from position 12

The time taken for the plastic triangular prism in the monosized white particles to reach the orifice is on average 4% greater than in the white/black binary mix and 10% greater than in the white/yellow binary mix. The plastic triangular prism takes 7% longer to reach the orifice in the white/yellow mixture than in the white/black mixture. The gradient of the vertical displacement curves for the plastic triangular prism is very similar. The plastic triangular prism travels with an average vertical uniform acceleration of 0.27 cm/s^2.

Figure 5.25 shows the horizontal displacement-time graph for the plastic triangular prism in the monosized white (5 mm) particles and the binary mixtures of 80% white (5 mm)/20% black (4 mm) and 80% white (5 mm)/20% yellow (6 mm), starting from position 12.

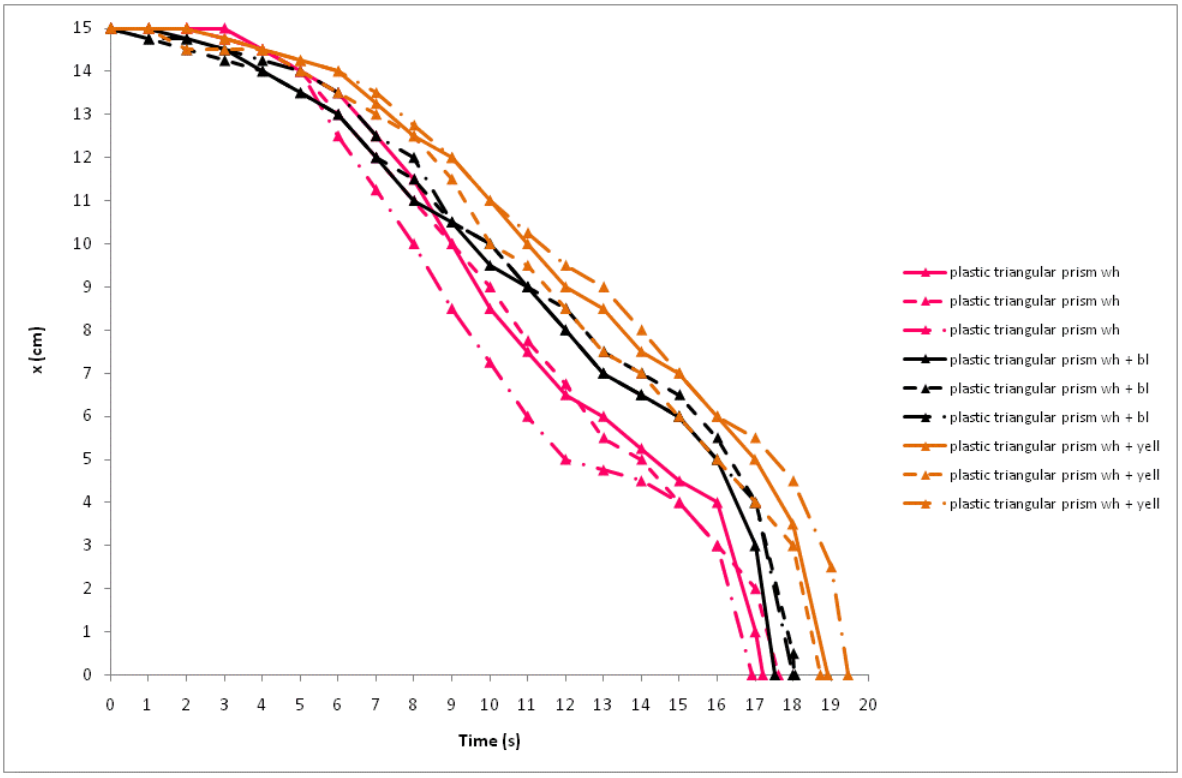

Figure 5.25: Graph showing the horizontal displacement-time graph for the plastic triangular prism in the monosized white (5 mm) particles and the binary mixtures of 80% white (5 mm)/20% black (4 mm) and 80% white (5 mm)/20% yellow (6 mm), starting from position 12

The horizontal velocity of the plastic triangular prism in the monosized white particles is 1 cm/s and in the binary mixtures is on average 0.83 cm/s, between 7 and 12 seconds after the opening of the orifice. The plastic triangular prism in the monosized particles gradually increases to a maximum and then at 5cm horizontally from the orifice the free-cell decelerates prior to rapidly accelerating towards the orifice. As has been mentioned in section the deceleration is caused by the free-cell reaching the edge of the flowing core, where the particles have a greater vertical velocity than horizontal velocity. The flowing core in the binary mixtures is wider than in the monosized white particles, hence the more gradual reduction in horizontal velocity at 2 cm horizontally from the orifice.

Figure 5.26 shows the trajectories of three trials of the hollow triangular prism in the monosized white (5 mm) particles and the binary mixtures of 80% white (5 mm)/20% black (4 mm) and 80% white (5 mm)/20% yellow (6 mm), starting from position 12.

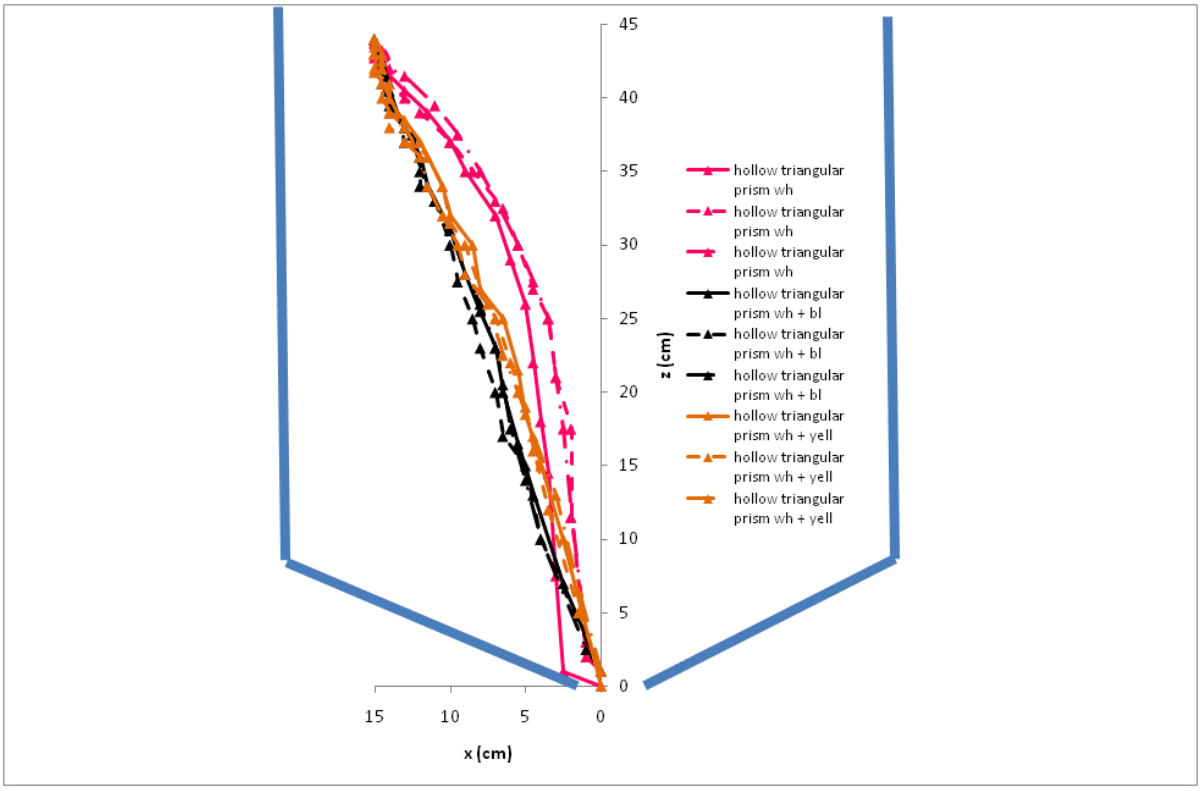

Figure 5.26: The trajectories of three trials of the hollow triangular prism in the monosized white (5 mm) particles and the binary mixtures of 80% white (5 mm)/20% black (4 mm) and 80% white (5 mm)/20% yellow (6 mm), starting from position 12

The hollow triangular prism follows a very similar path over three trials in the binary mixtures. The paths only differ by up to 0.5 cm in the white/yellow and white/black mixtures. The path taken over three trials in the white monosized particles varies by up to 2 cm.

Figure 5.27 shows the vertical displacement-time graph for the hollow triangular prism in the monosized white (5 mm) particles and the binary mixtures of 80% white (5 mm)/20% black (4 mm) and 80% white (5 mm)/20% yellow (6 mm), starting from position 12.

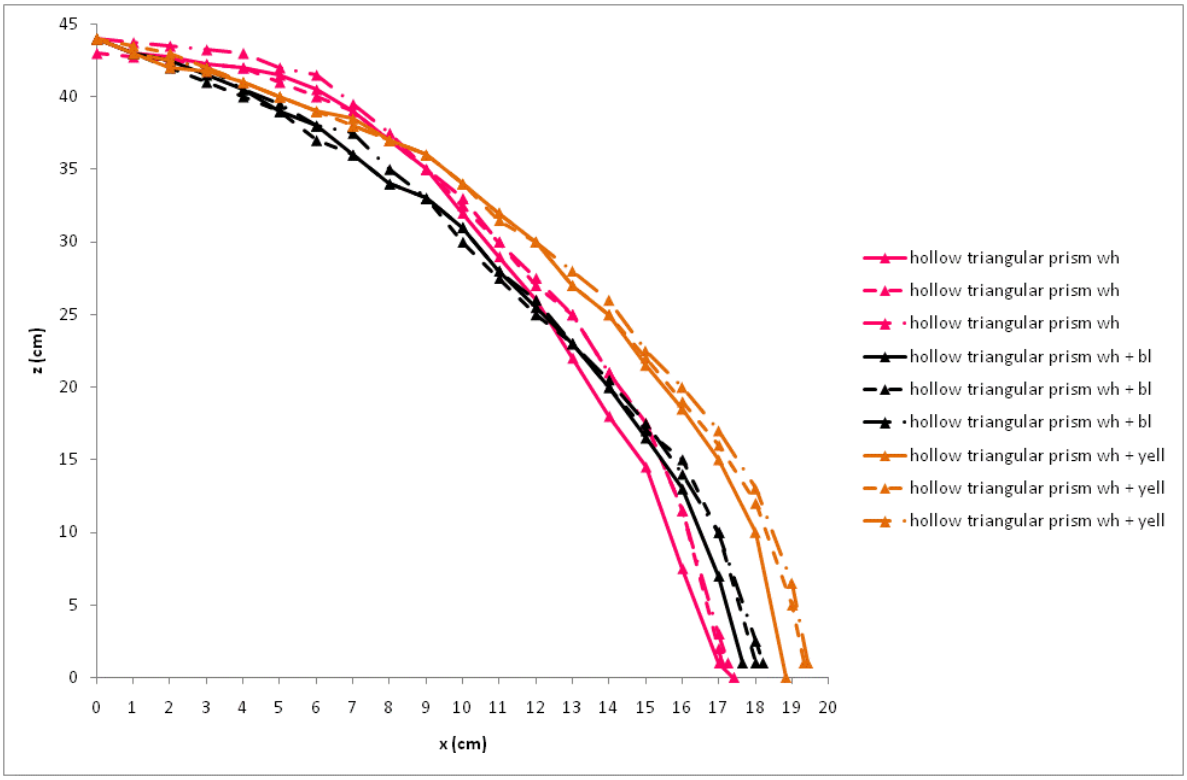

Figure 5.27: Graph showing the vertical displacement-time graph for the hollow triangular prism in the monosized white (5mm) particles and the binary mixtures of 80% white (5mm)/20% black (4mm) and 80% white (5mm)/20% yellow (6mm), starting from position 12

The time taken for the hollow triangular prism to travel to the orifice is an average of 17.5 seconds, 18 seconds and 19.2 seconds in the white monosized, white/black binary mixture and white/yellow binary mixture respectively. The hollow triangular prism travels with an average vertical uniform acceleration of 0.29 cm/s^2, 0.27 cm/s^2 and 0.24 cm/s^2 in the monosized, white/black binary mixture and white/yellow binary mixture respectively.

Figure 5.28 shows the horizontal displacement-time graph for the plastic triangular prism in the monosized white (5 mm) particles and the binary mixtures of 80% white (5 mm)/20% black (4 mm) and 80% white (5 mm)/20% yellow (6 mm), starting from position 12.

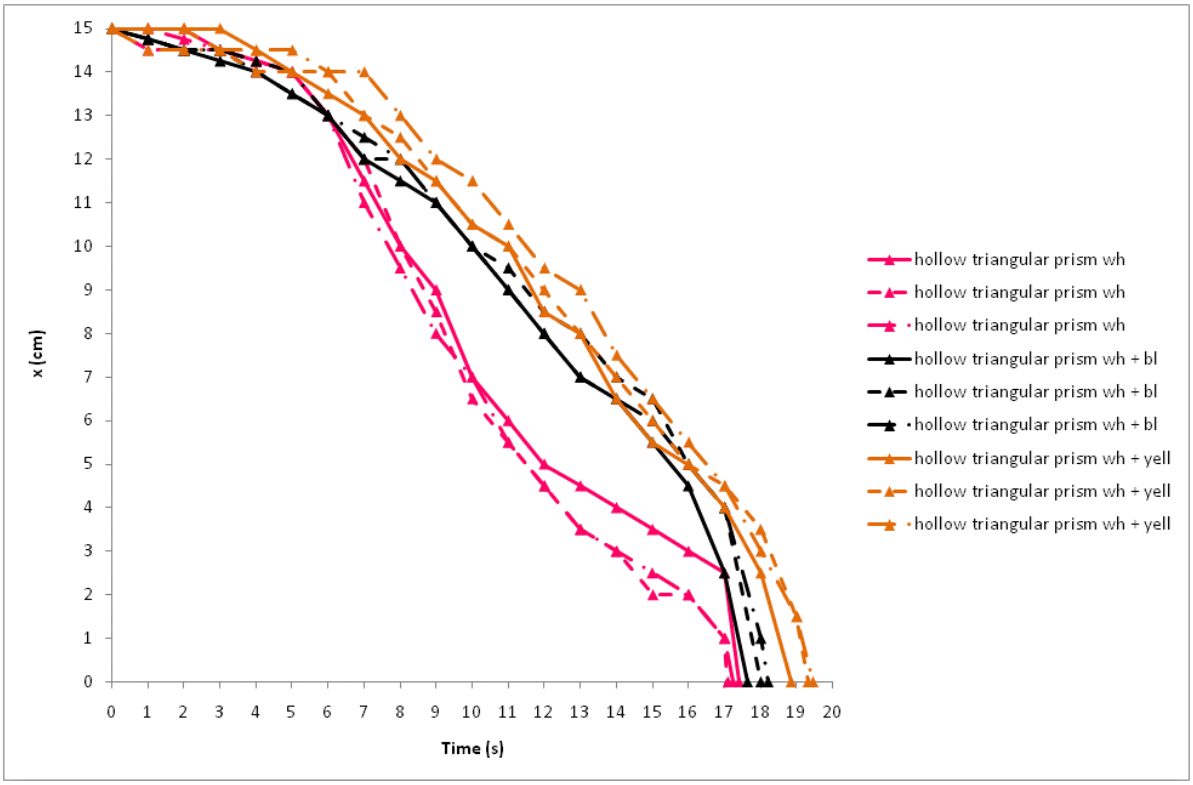

Figure 5.28: Graph showing the horizontal displacement-time graph for the hollow triangular prism in the monosized white (5 mm) particles and the binary mixtures of 80% white (5 mm)/20% black (4 mm) and 80% white (5 mm)/20% yellow (6 mm), starting from position 12

The hollow triangular prism gradually accelerates to an average velocity of 0.9 cm/s in the binary mixtures prior to rapidly accelerating through the orifice. In the monosized particles the hollow triangular prism accelerates to a maximum horizontal velocity of 2 cm/s, prior to decelerating and then rapidly accelerating through the orifice.

5.8 Summary

The metal triangular prism travels with an average vertical acceleration of 0.46 cm/s^2 in the monosized and binary mixtures and the plastic triangular prism travels with an average vertical acceleration of 0.27 cm/s^2 in the monosized and binary mixtures. The average vertical velocity of the hollow triangular prism is 0.29 cm/s, 0.27 cm/s and 0.24 cm/s in the monosized particles and the white/black and white/yellow binary mixtures. The average horizontal acceleration of the metal triangular prism is 0.1 cm/s^2 and the greatest average horizontal velocity is 1 cm/s and 2 cm/s in the plastic triangular prism and hollow triangular prism respectively, while the greatest velocity in the binary mixtures is 0.83 cm/s and 0.9 cm/s for the plastic triangular prism and hollow triangular prisms respectively.

5.9 Comparison between the trajectories and velocities of the metal cylinder, plastic cylinder and hollow cylinder free cells, in the white monosized particles and the white/yellow and white/black binary mixtures starting from position 5

Figure 5.29 shows the trajectory of three trials of the metal cylinder in the monosized white (5 mm) particles and the binary mixtures of 80% white (5 mm)/20% black (4 mm) and 80% white (5 mm)/20% yellow (6 mm), starting from position 5.

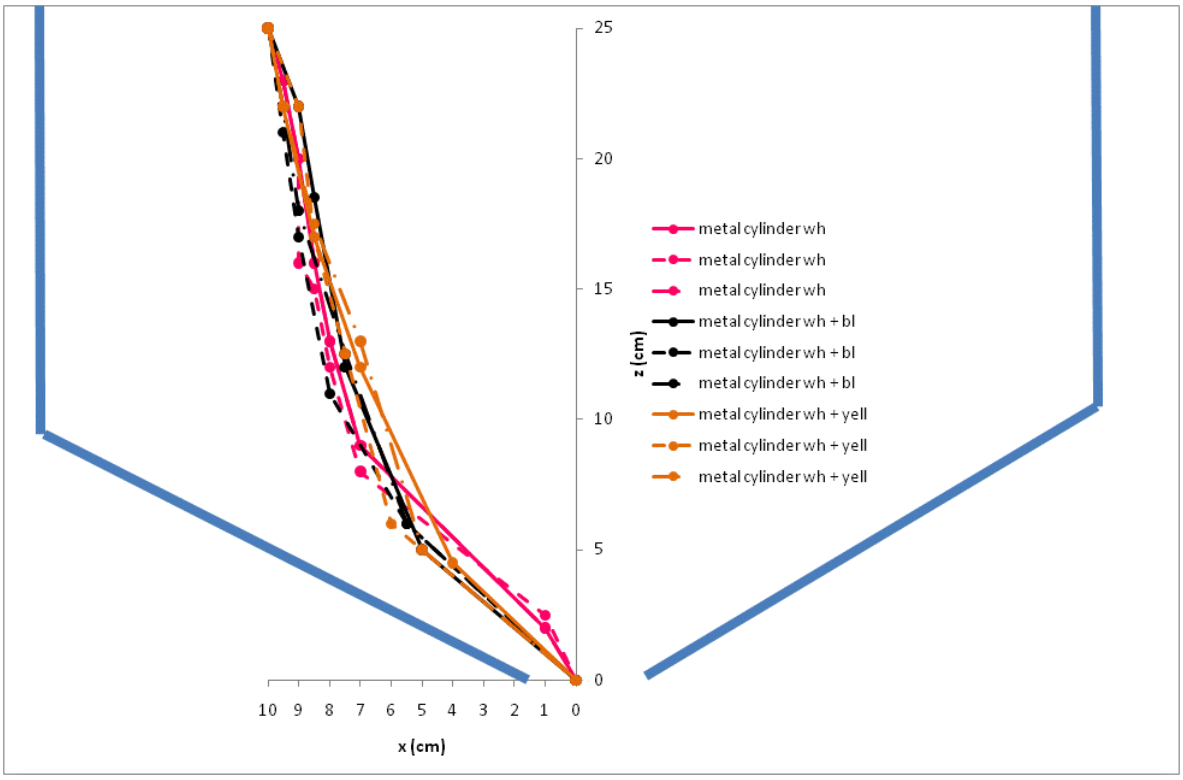

Figure 5.29: The trajectory of three trials of the metal cylinder in the monosized white (5 mm) particles and the binary mixtures of 80% white (5 mm)/20% black (4 mm) and 80% white (5 mm)/ 20% yellow (6 mm), starting from position 5

The trajectories of the metal cylinder in the monosized white particles and the white/yellow, white/black binary mixtures are very similar. The paths over three trials diverge greatest at a height approximately 6 cm from the orifice. The difference in the paths followed by the metal cylinder in the monosized particles is approximately 1 cm, in the white/yellow binary mixture 1.5 cm and in the white/black binary mixture 1 cm.

Figure 5.30 shows the vertical displacement-time graph for the metal cylinder in the monosized white (5 mm) particles and the binary mixtures of 80% white (5 mm)/20% black (4 mm) and 80% white (5 mm)/20% yellow (6 mm), starting from position 5.

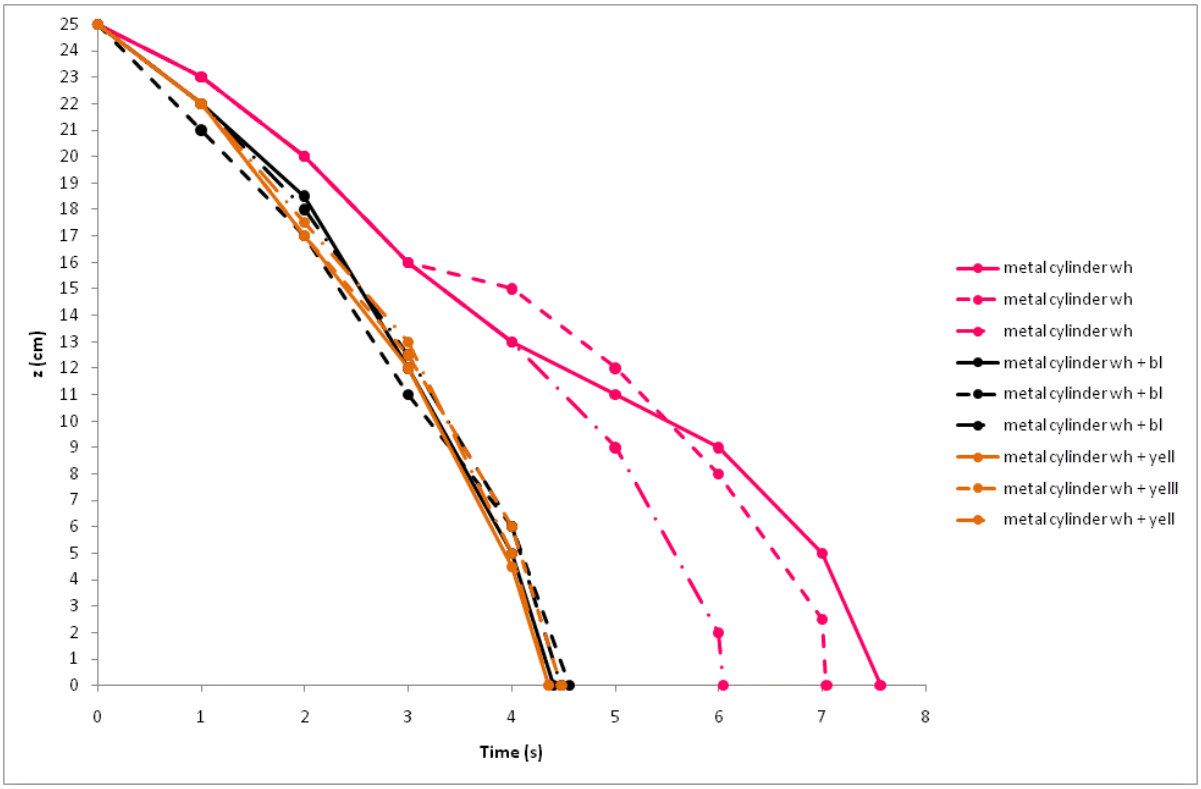

Figure 5.30: Graph showing the vertical displacement-time graph for the metal cylinder in the monosized white (5 mm) particles and the binary mixtures of 80% white (5 mm)/20% black (4 mm) and 80% white (5 mm)/20% yellow (6 mm), starting from position 12

The displacement of the metal cylinder in the white/yellow and white/black binary mixtures is very similar. The velocity of the metal cylinder in the binary mixtures travels at an initial velocity of 3.5 cm/s and accelerates to 8 cm/s as it approaches the orifice. However, the displacement of the metal cylinder in the monosized particles is nearly identical during the first three seconds after the initiation of discharge and then the paths diverge. The time taken for the metal cylinder to reach the orifice in the binary mixtures is approximately 4.5 s and in the monosized particles the time taken to reach the orifice varies between 6 s and 7.5 s.

Figure 5.31 shows the horizontal displacement-time graph for the metal cylinder in the monosized white (5 mm) particles and the binary mixtures of 80% white (5 mm)/20% black (4 mm) and 80% white (5 mm)/20% yellow (6 mm), starting from position 12.

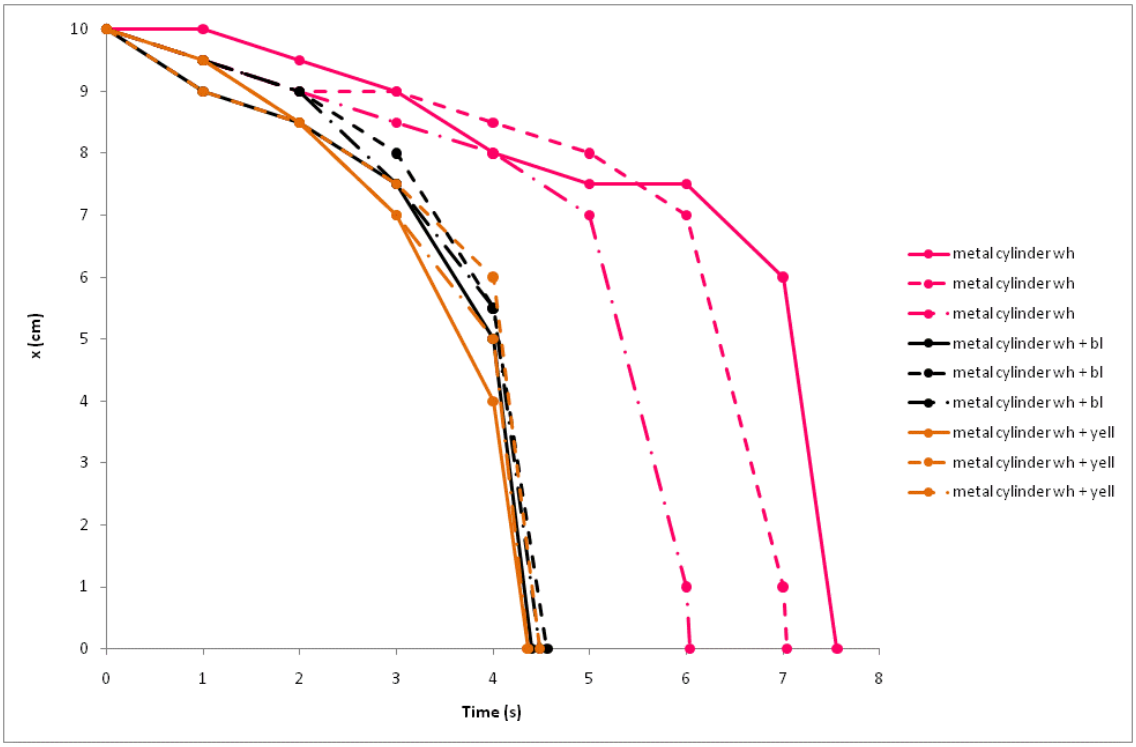

Figure 5.31: Graph showing the horizontal displacement-time graph for the metal cylinder in the monosized white (5 mm) particles and the binary mixtures of 80% white (5 mm)/20% black (4 mm) and 80% white (5 mm)/20% yellow (6 mm), starting from position 5

In slight contrast to the vertical displacement-time graph the horizontal displacement of the metal cylinder in the binary mixtures is similar but the velocity fluctuates over the three trials between 0.7 cm/s and 3 cm/s. The velocity of the metal cylinder is an average of 0.5 cm/s during approximately the first 6 s after the opening of the orifice and then rapidly accelerates to approximately 14 cm/s down to the orifice. The metal cylinder takes on average 52% longer to reach the orifice in the monosized particles than in the binary mixtures.

Figure 5.32 shows the trajectories of three trials of the plastic cylinder in the monosized white (5 mm) particles and the binary mixtures of 80% white (5 mm)/20% black (4 mm) and 80% white (5 mm)/20% yellow (6 mm), starting from position 5.

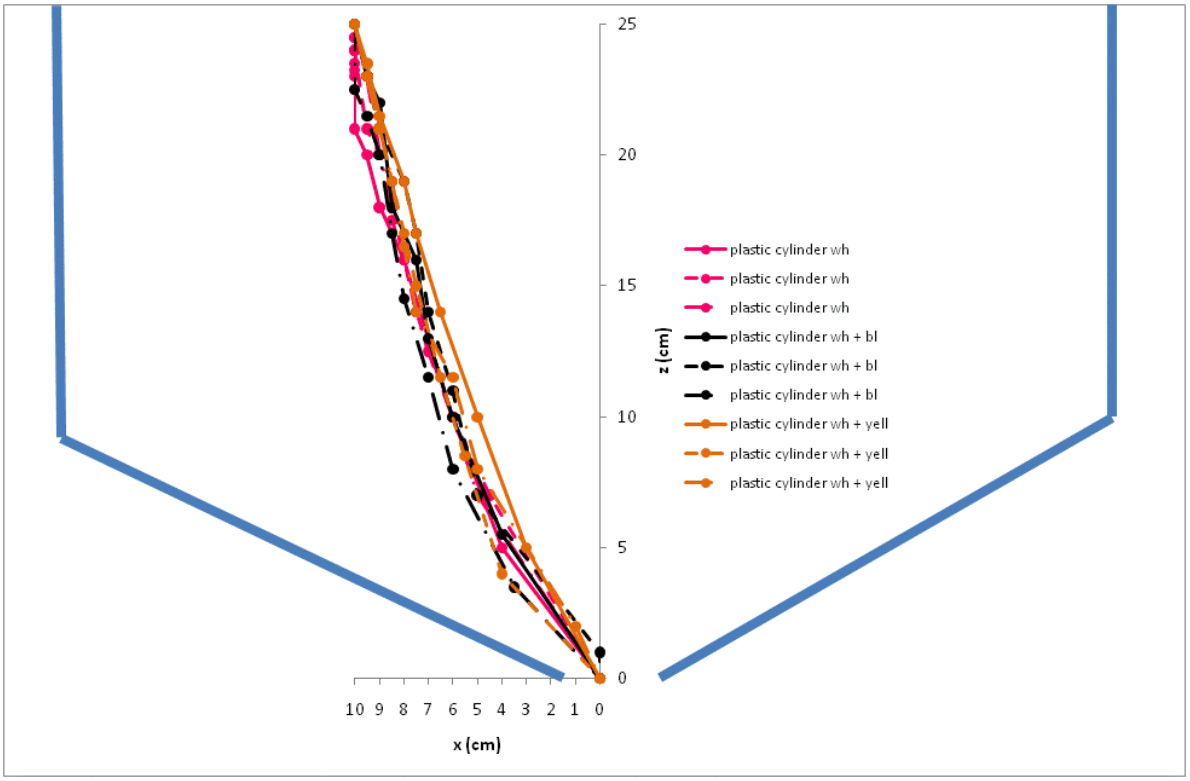

Figure 5.32: The trajectories of three trials of the plastic cylinder in the monosized white (5 mm) particles and the binary mixtures of 80% white (5 mm)/20% black (4 mm) and 80% white (5 mm)/ 20% yellow (6 mm), starting from position 5

The path followed by the plastic cylinder in the white monosized particles and the binary mixtures is very similar. The paths differ by up 1.5 cm over three trials in each of the particle batches.

Figure 5.33 shows the vertical displacement-time graph for the plastic cylinder in the monosized white (5 mm) particles and the binary mixtures of 80% white (5 mm)/20% black (4 mm) and 80% white (5 mm)/20% yellow (6 mm), starting from position 5.

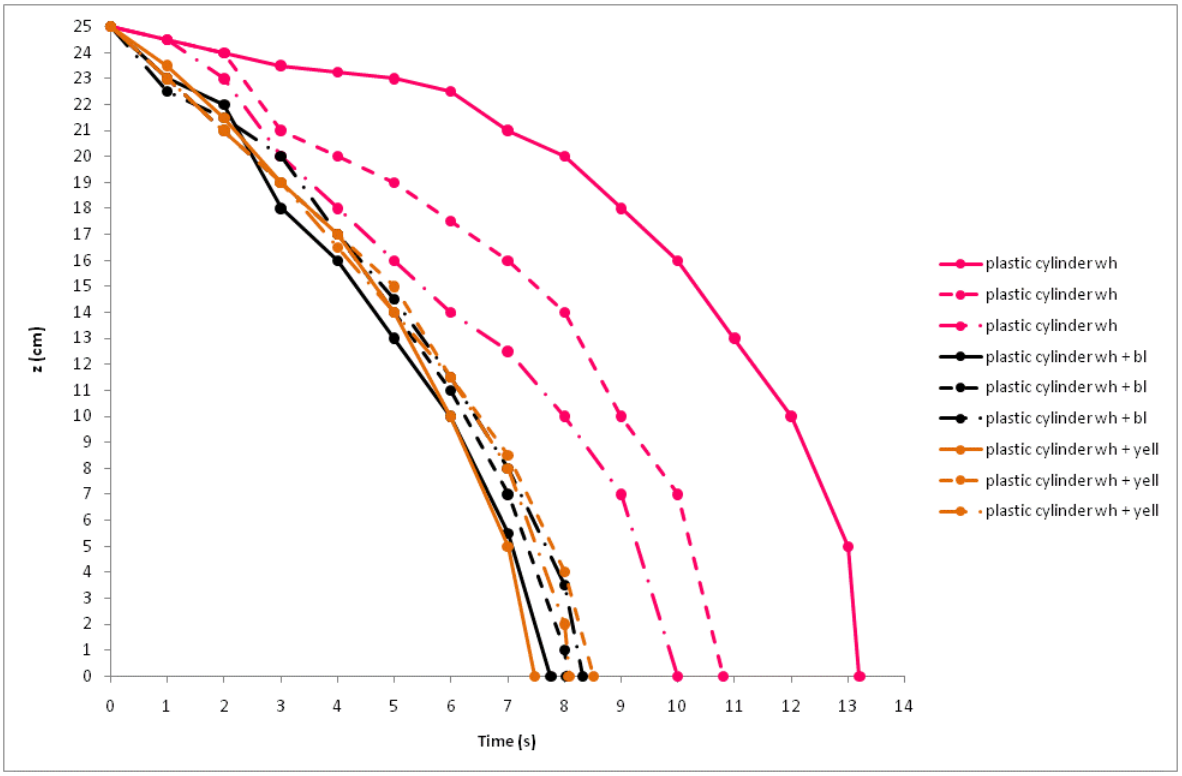

Figure 5.33: Graph showing the vertical displacement-time graph for the plastic cylinder in the monosized white (5 mm) particles and the binary mixtures of 80% white (5 mm)/20% black (4 mm) and 80% white (5 mm)/20% yellow (6 mm), starting from position 5

In similarity to the metal cylinder, the plastic cylinder also travels vertically with approximately the same velocity in the white/yellow and white/black binary mixtures, initially travelling at about 2.5 cm/s and then accelerating to about 5 cm/s as it approaches the orifice. The vertical velocity in the monosized particles, however, varies considerably in the initial 7 seconds after the orifice has been opened, from between 0.6 cm/s to 1.7 cm/s. The time taken for the plastic cylinder to reach the orifice in the monosized particles takes 10, 10.9 and 13 cm/s in each of three trials respectively compared to in the binary mixtures where the plastic cylinder takes on average 8 s to reach the orifice.

Figure 5.34 shows the horizontal displacement-time graph for the plastic cylinder in the monosized white (5 mm) particles and the binary mixtures of 80% white (5 mm)/20% black (4 mm) and 80% white (5 mm)/20% yellow (6 mm), starting from position 5.

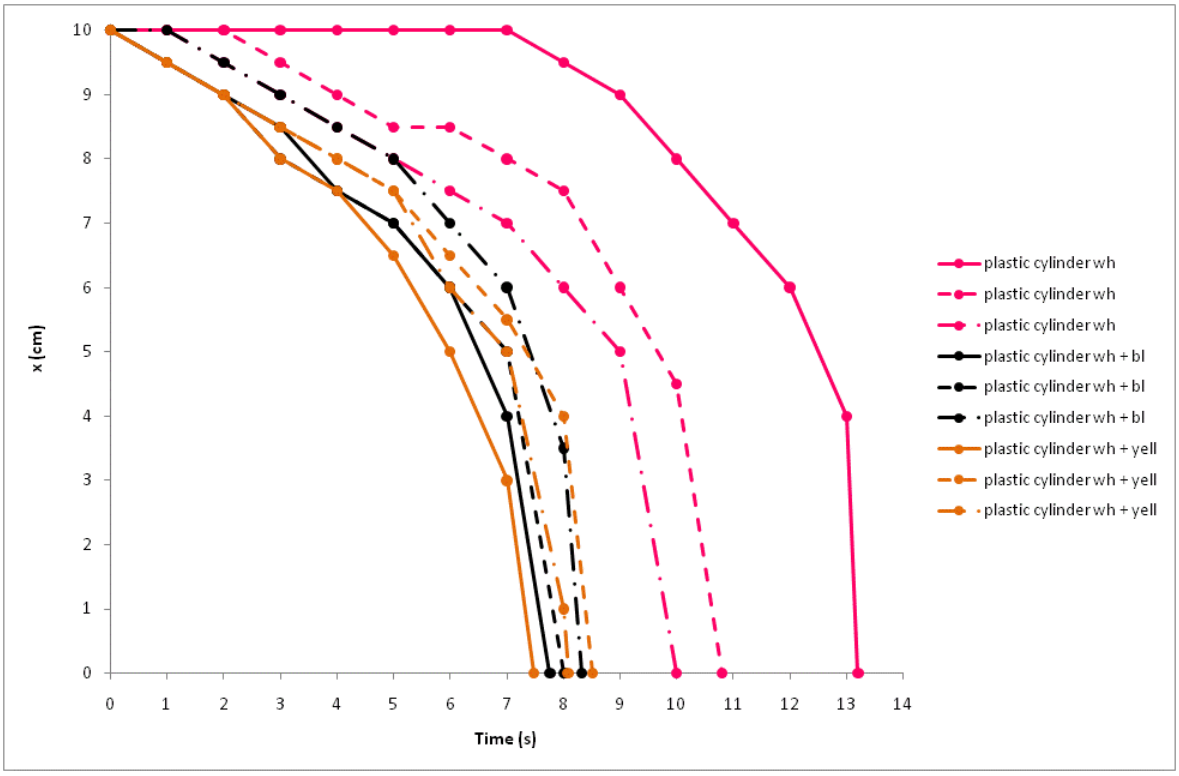

Figure 5.34: Graph showing the horizontal displacement-time graph for the plastic cylinder in the monosized white (5 mm) particles and the binary mixtures of 80% white (5 mm)/20% black (4 mm) and 80% white (5 mm)/20% yellow (6 mm), starting from position 5

The horizontal velocity of the plastic cylinder in the binary mixtures is nearly identical at 0.5 cm/s during the initial 5 s after the opening of the orifice but then varies slightly to between 1 cm/s and 4cm/s before accelerating to the orifice at about 10 cm/s. The plastic cylinder appears to have zero horizontal velocity for about 1 s in one trial in the white/black particles and 2 and 7 seconds in two trials in the monosized particles. This is because the plastic cylinder is initially placed at position 5 which is along the stagnant zone/flowing core boundary. The flowing core is wider in the binary mixtures, but position 5 in the monosized batch is along the boundary. It was observed that the plastic cylinder only gradually moved vertically for the first 7 seconds after the orifice had been opened.

Figure 5.35 shows the trajectories of three trials of the hollow cylinder in the monosized white (5 mm) particles and the binary mixtures of 80% white (5 mm)/20% black (4 mm) and 80% white (5 mm)/20% yellow (6 mm), starting from position 5.

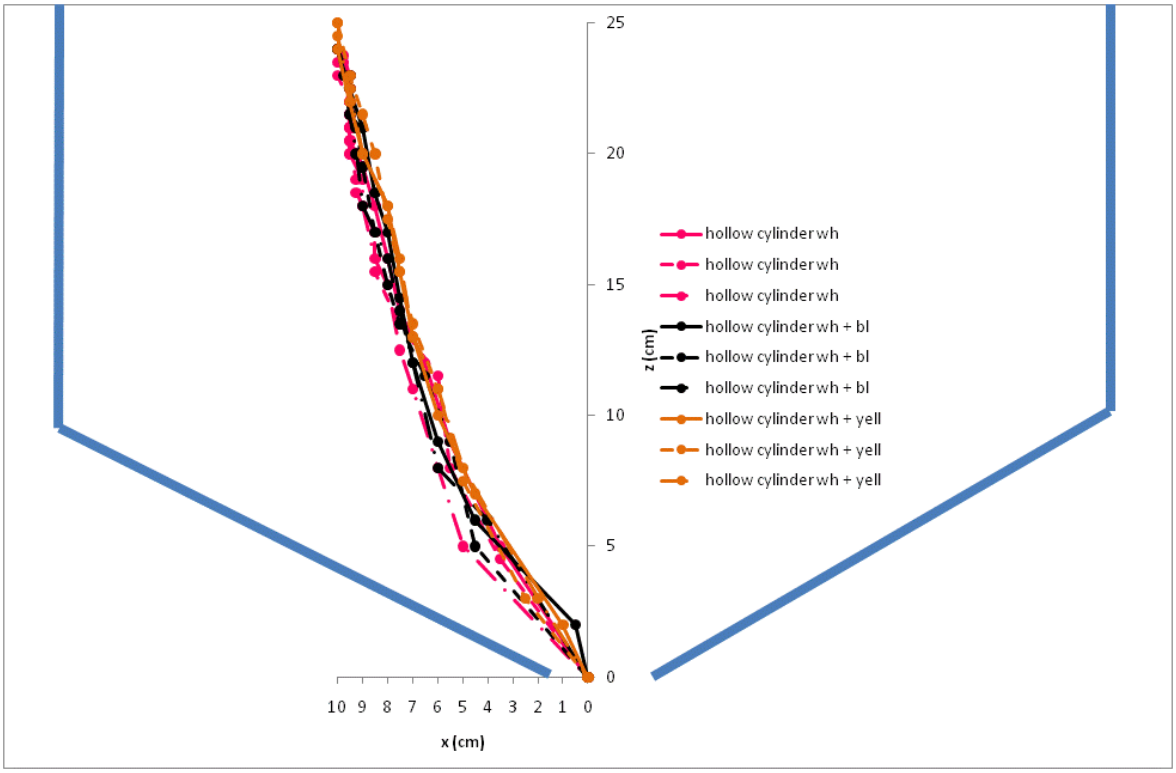

Figure 5.35: The trajectories of three trials of the hollow cylinder in the monosized white (5 mm) particles and the binary mixtures of 80% white (5 mm)/20% black (4 mm) and 80% white (5 mm)/ 20% yellow (6 mm), starting from position 5

The path followed by the hollow cylinder is very similar in the monosized white particles and the two binary mixtures. The paths deviate the greatest by approximately 2 cm at the position 5cm vertically and 4cm horizontally from the orifice.

Figure 5.36 shows the vertical displacement-time graph for the hollow cylinder in the monosized white (5 mm) particles and the binary mixtures of 80% white (5 mm)/20% black (4 mm) and 80% white (5 mm)/20% yellow (6 mm), starting from position 5.

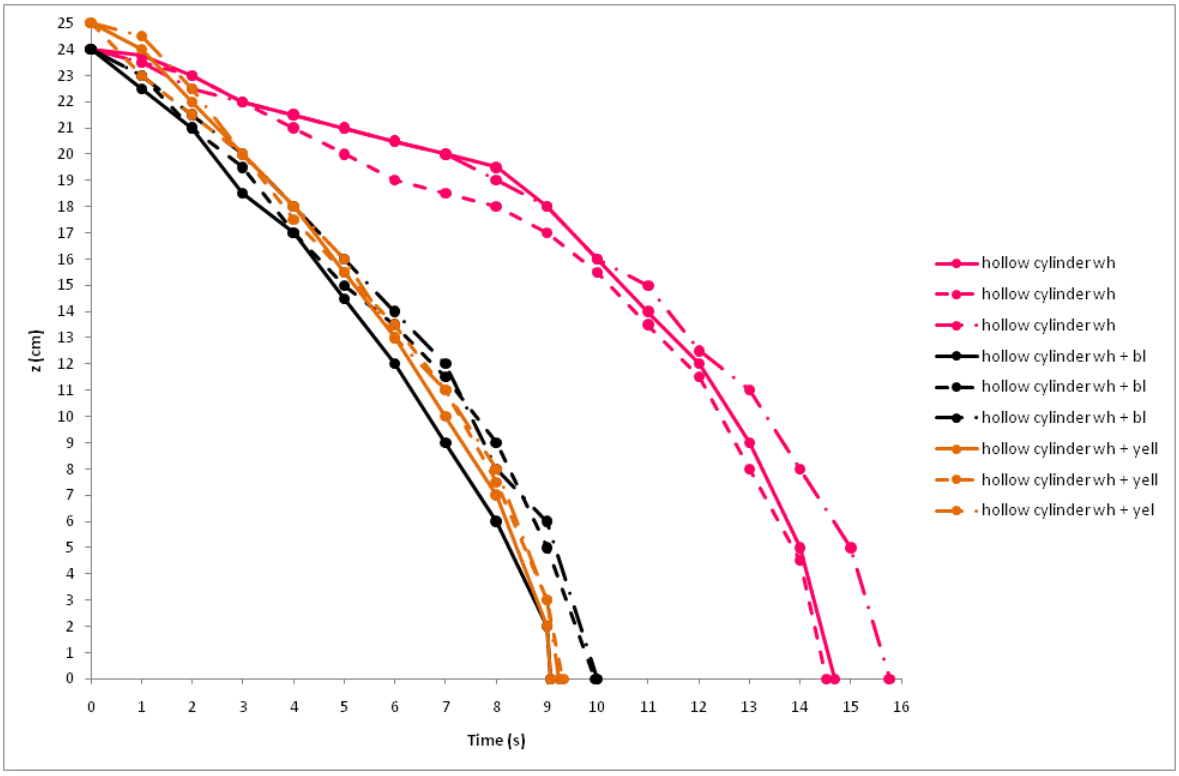

Figure 5.36: Graph showing the vertical displacement-time graph for the hollow cylinder in the monosized white (5 mm) particles and the binary mixtures of 80% white (5 mm)/20% black (4 mm) and 80% white (5 mm)/20% yellow (6 mm), starting from position 5

The vertical velocity of the hollow cylinder in the binary mixtures is approximately 2.2 cm/s in all three trials for the majority of the displacements, only increasing in the final 0.5 s before passing through the orifice. Unlike the metal and plastic cylinders the vertical velocity of the hollow cylinder is similar over the three trials, varying by only about 0.1 cm/s over tree trials. The time taken for the hollow cylinder in the binary mixtures to reach the orifice is approximately 9.5 s and in the monosized particles it is 60% greater taking 15.2 s.

Figure 5.37 shows the horizontal displacement-time graph for the hollow cylinder in the monosized white (5 mm) particles and the binary mixtures of 80% white (5 mm)/20% black (4 mm) and 80% white (5 mm)/20% yellow (6 mm), starting from position 5.

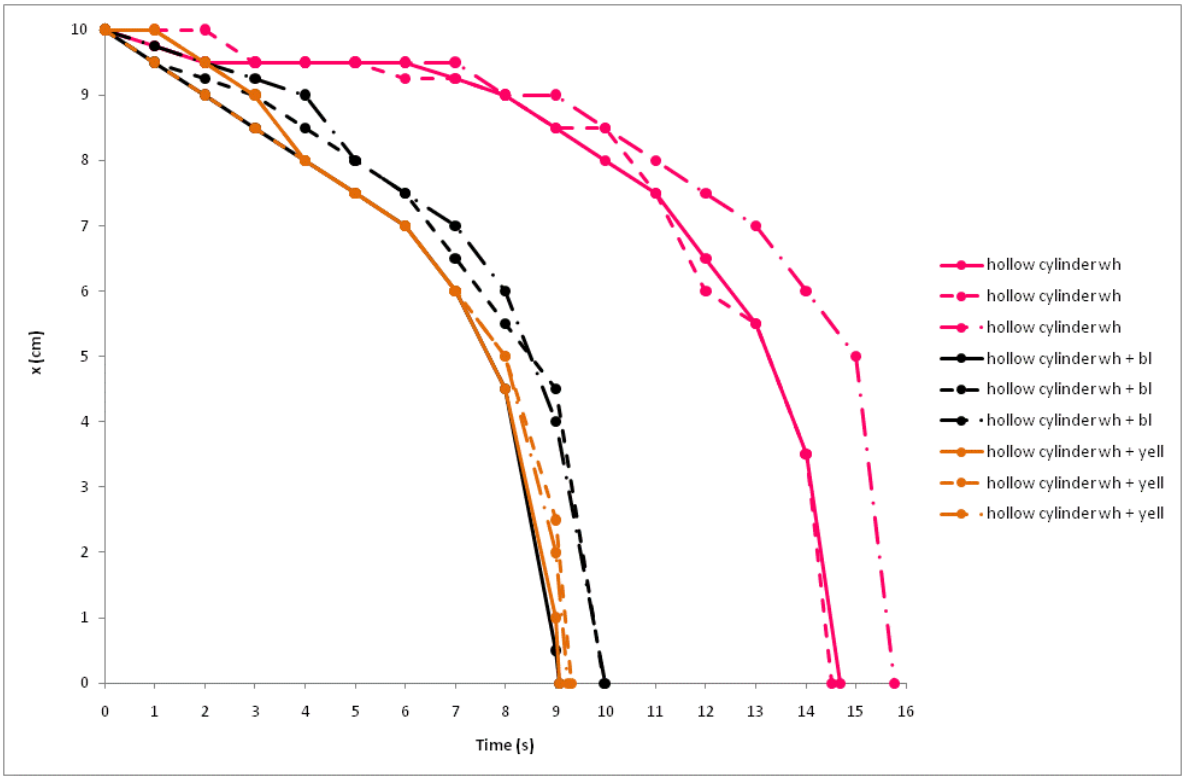

Figure 5.37: Graph showing the horizontal displacement-time graph for the hollow cylinder in the monosized white (5 mm) particles and the binary mixtures of 80% white (5 mm)/20% black (4 mm) and 80% white (5 mm)/20% yellow (6 mm), starting from position 5

In similarity to the plastic cylinder the hollow cylinder creeps along the edge of the dead zone, resulting in approximately zero horizontal velocity during the first 8 seconds after the opening of the orifice. The velocity of the hollow cylinder in the binary mixtures is very similar at 1 cm/s during the first 7 seconds after the orifice has been opened before accelerating to 3 cm/s in the final 2 seconds prior to passing through the orifice. The hollow cylinder takes on average 9.5 s to reach the orifice in the binary mixtures and 60% longer at 15.2 s to reach the orifice in the monosized white particles.

5.10 Summary

The metal, plastic and hollow cylinders each exhibit similar characteristics in the binary mixtures. The horizontal and vertical velocity of the cylindrical free cells in the monosized and binary mixtures is the same, but in the monosized particles there tends to be an initial 7 to 8 seconds where the cylindrical free cells move very slowly prior to accelerating. This was observed to be due to the cylinders travelling in the boundary between the flowing core and the stagnant region in the monosized particles. In the binary mixtures the flowing core is wider and the cylinders flow with the particles in the core unhindered by those in the stagnant region. The vertical velocity of the metal cylinder in the binary mixtures varies between 3.5 and 8 cm/s and the maximum vertical velocity of the plastic cylinder and hollow cylinder is 5 cm/s and 2.2 cm/s respectively. The time taken for the metal cylinder, plastic cylinder and hollow cylinder to reach the orifice in the binary mixtures is an average of 4.5 seconds, 8 seconds and 9.5 seconds respectively and in the monosized particles 6.8 seconds, 11.4 seconds and 15.2 seconds respectively.

5.11 Comparison between the trajectories and velocities of the metal cuboid, plastic cuboid and hollow cuboid free cells, in the white monosized particles and the white/yellow and white/black binary mixtures starting from position 5

Figure 5.38 shows the trajectories of three trials of the metal cuboid in the monosized white (5 mm) particles and the binary mixtures of 80% white (5 mm)/20% black (4 mm) and 80% white (5 mm)/20% yellow (6 mm), starting from position 5.

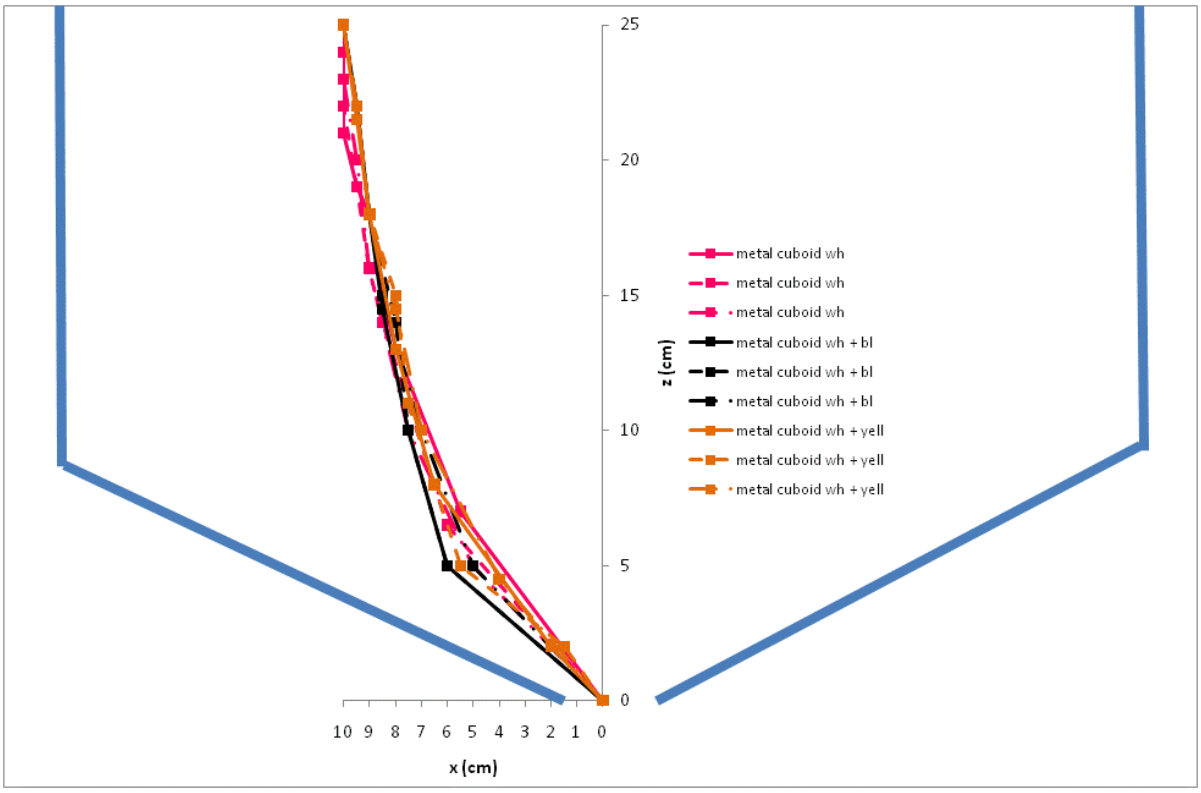

Figure 5.38: The trajectories of three trials of the metal cuboid in the monosized white (5 mm) particles and the binary mixtures of 80% white (5 mm)/20% black (4 mm) and 80% white (5 mm)/ 20% yellow (6 mm), starting from position 5

The path followed by the metal cuboid in the monosized particles and binary mixtures is very similar. The paths differ the greatest at the point 5 cm horizontally and 5 cm vertically above the orifice by about 2 cm.

Figure 5.39 shows the vertical displacement-time graph for the metal cuboid in the monosized white (5 mm) particles and the binary mixtures of 80% white (5 mm)/20% black (4 mm) and 80% white (5 mm)/20% yellow (6 mm), starting from position 5.

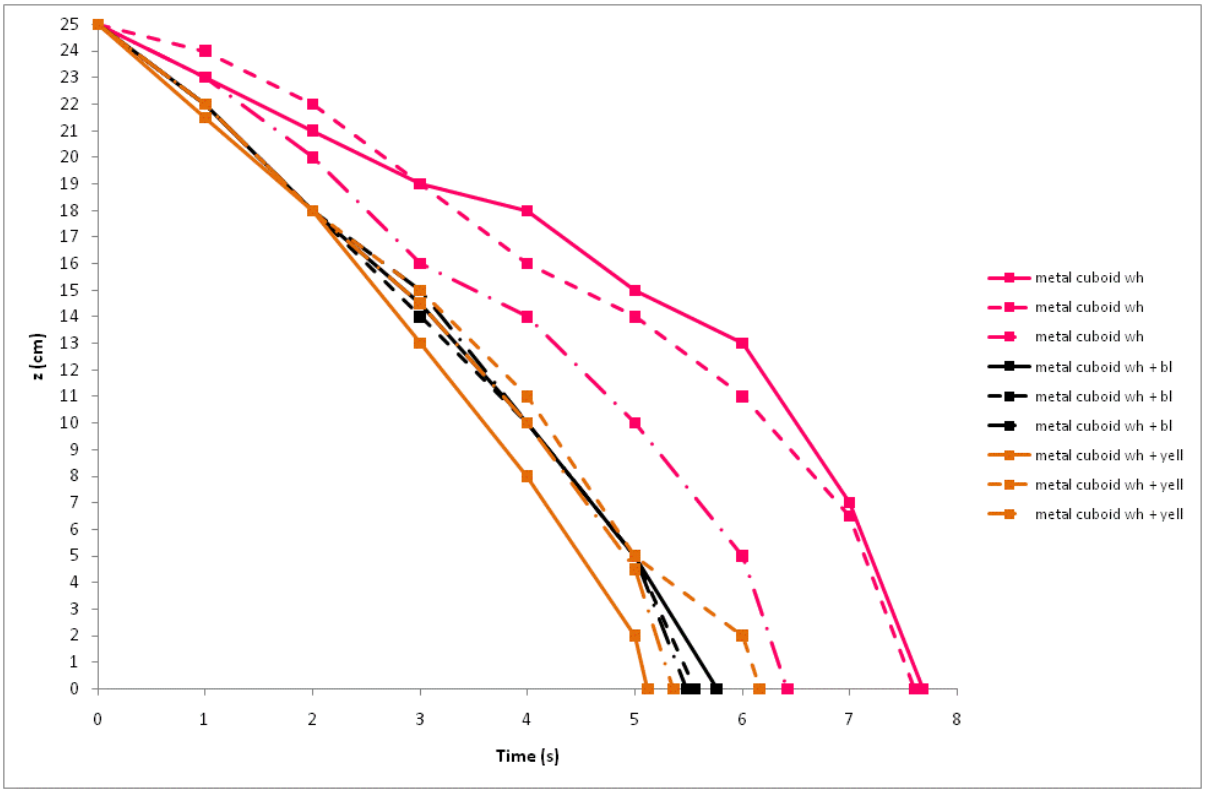

Figure 5.39: Graph showing the vertical displacement-time graph for the metal cuboid in the monosized white (5 mm) particles and the binary mixtures of 80% white (5 mm)/20% black (4 mm) and 80% white (5 mm)/20% yellow (6 mm), starting from position 5

In similarity to the metal, plastic and hollow cylinders the velocity of the metal cuboid is similar in the binary mixtures, varying between 4 cm/s and 6 cm/s in each of the three trials. The velocity of the metal cuboid in the monosized particles varies from between 1.7 cm/s and 3.3 cm/s in the initial 4 seconds after the initiation of discharge and 11 cm/s in the final second before travelling through the orifice. The time taken for the metal cuboid in the binary mixtures to reach the orifice is about 5.5 s but the time taken for the metal cuboid in the monosized particles to reach the orifice is 6.5 s in one trial and approximately 7.7 s in two trials.

Figure 5.40 shows the horizontal displacement-time graph for the metal cuboid in the monosized white (5 mm) particles and the binary mixtures of 80% white (5 mm)/20% black (4 mm) and 80% white (5 mm)/20% yellow (6 mm), starting from position 5.

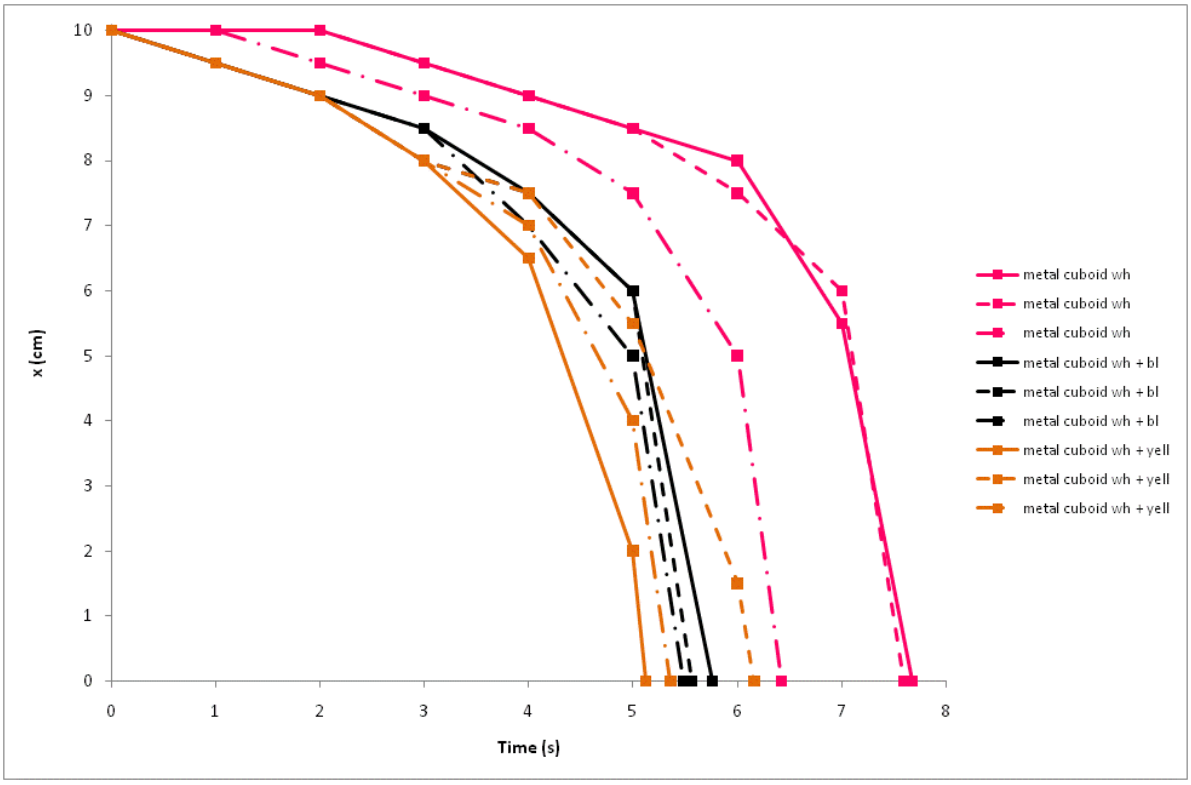

Figure 5.40: Graph showing the horizontal displacement-time graph for the metal cuboid in the monosized white (5mm) particles and the binary mixtures of 80% white (5 mm)/20% black (4 mm) and 80% white (5 mm)/20% yellow (6 mm), starting from position 5

Over three trials the trajectories of the metal cuboid in the binary mixtures has a horizontal velocity varying between 0.25 cm/s and 2 cm/s during the first 5 seconds after the opening of the orifice and then in the final second before travelling through the orifice it reaches a velocity of about 12 cm/s. The metal cuboid moves horizontally in the binary mixtures, immediately after the orifice has been opened. In the monosized white particles, it only moves vertically during the first 1-2 seconds. The metal cuboid takes on average 29% longer to reach the orifice in the monosized particles than in the binary mixtures.

Figure 5.41 shows the trajectories of three trials of the plastic cuboid in the monosized white (5 mm) particles and the binary mixtures of 80% white (5 mm)/20% black (4 mm) and 80% white (5 mm)/20% yellow (6 mm), starting from position 5.

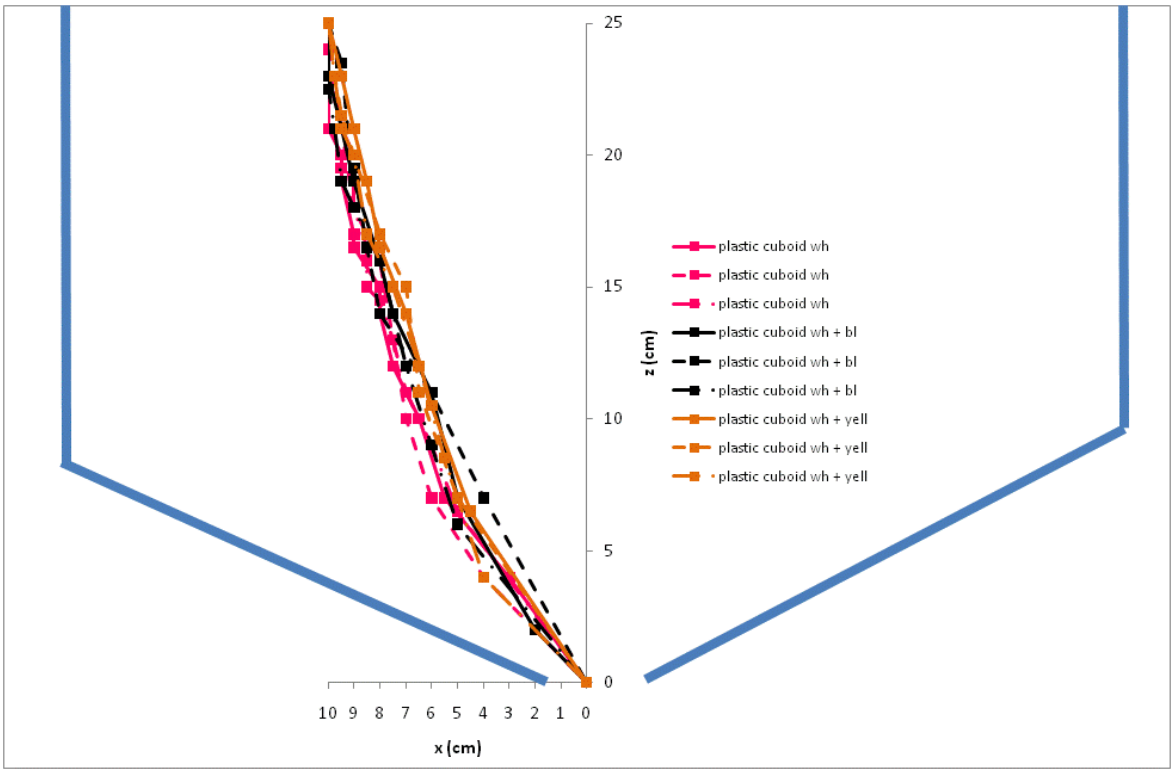

Figure 5.41: The trajectories of three trials of the plastic cuboid in the monosized white (5 mm) particles and the binary mixtures of 80% white (5 mm)/20% black (4 mm) and 80% white (5 mm)/ 20% yellow (6 mm), starting from position 5

The trajectories of the plastic cuboid in the monosized white particles and the binary mixtures differ by up to 2 cm along the horizontal axis.

Figure 5.42 shows the vertical displacement-time graph for the plastic cuboid in the monosized white (5 mm) particles and the binary mixtures of 80% white (5 mm)/20% black (4 mm) and 80% white (5 mm)/20% yellow (6 mm), starting from position 5.

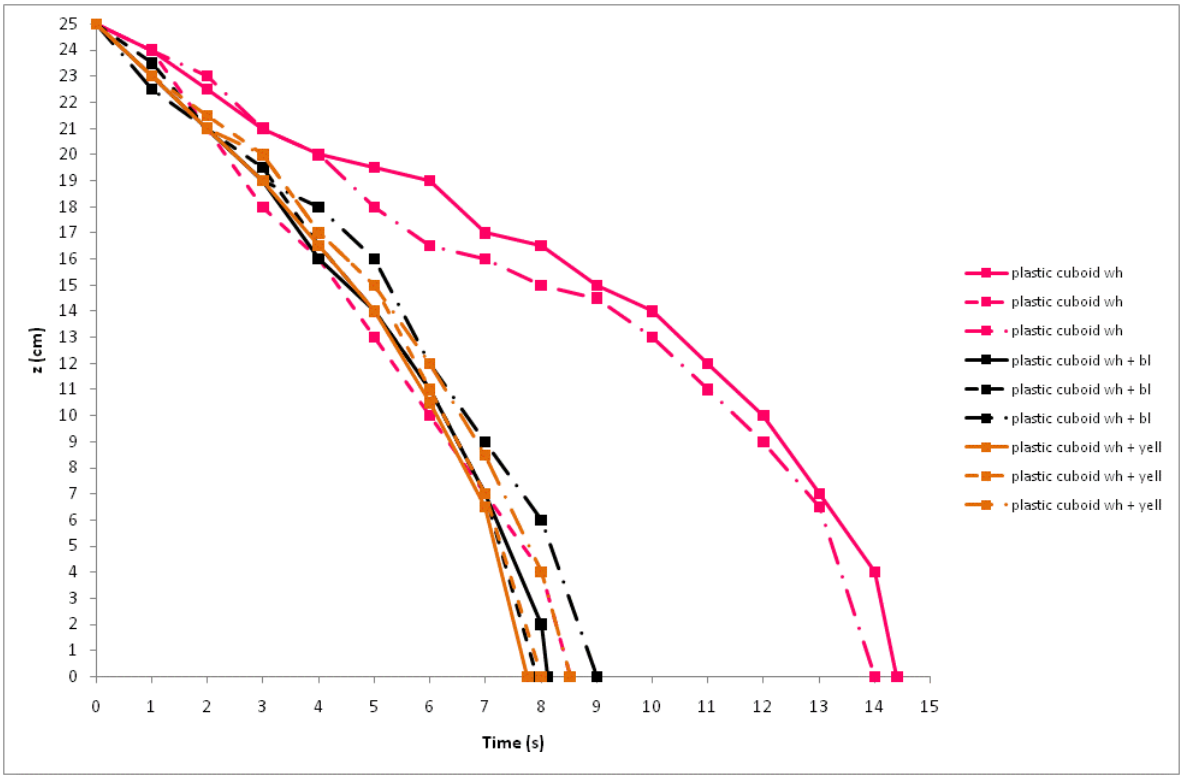

Figure 5.42: Graph showing the vertical displacement-time graph for the plastic cuboid in the monosized white (5 mm) particles and the binary mixtures of 80% white (5 mm)/20% black (4 mm) and 80% white (5 mm)/20% yellow (6 mm), starting from position 5

The vertical velocity of the plastic cuboid in the binary mixtures is very similar and varies from 2 cm/s in the first 6 seconds after the initiation of discharge to 6 cm/s in the final 2 seconds before passing through the orifice. One trial of the plastic cuboid in the monosized white particles is also shown to have the same velocity as when it is placed in the binary mixtures. This indicates that the plastic cuboid must be pushed into the flowing core where it can easily move, while in the other two cases the plastic cuboid moves slowly along the boundary of the flowing core, travelling with a velocity of 1 cm/s in the first 12 seconds after the opening of the orifice and 5 cm/s in the final 2 seconds before it travels down to the orifice.

Figure 5.43 shows the horizontal displacement-time graph for the plastic cuboid in the monosized white (5 mm) particles and the binary mixtures of 80% white (5 mm)/20% black (4 mm) and 80% white (5 mm)/20% yellow (6 mm), starting from position 5.

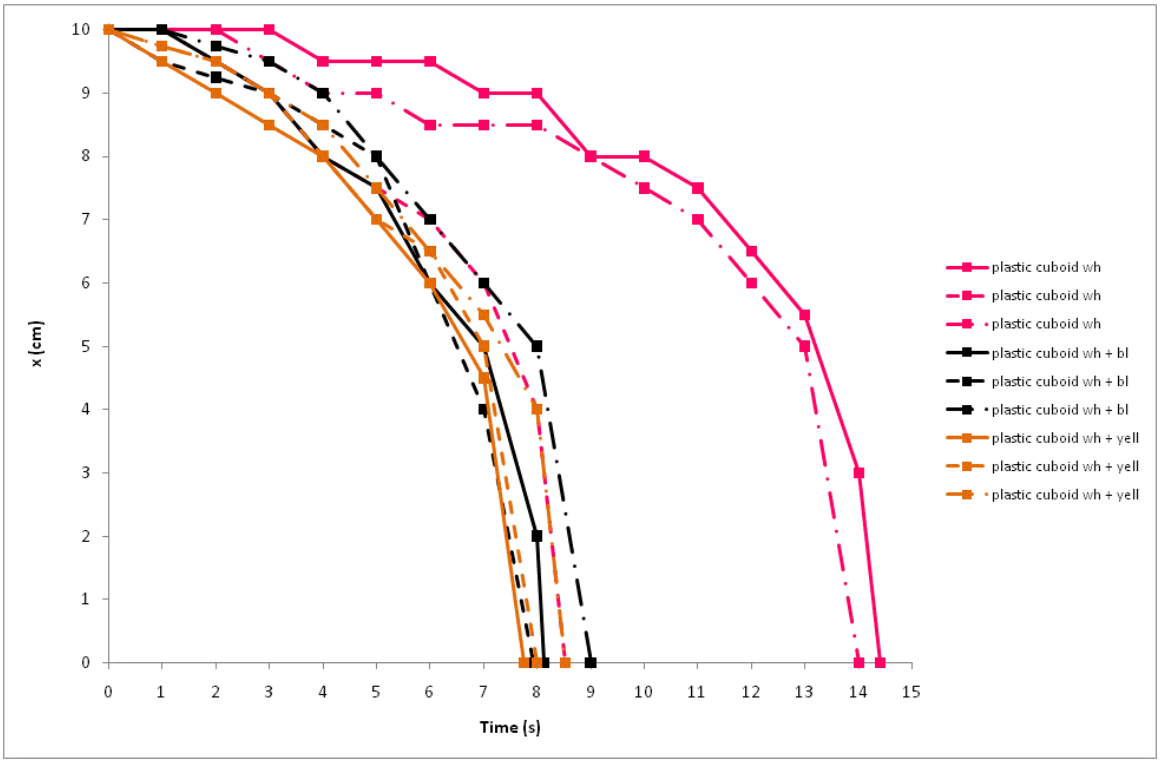

Figure 5.43: Graph showing the horizontal displacement-time graph for the plastic cuboid in the monosized white (5 mm) particles and the binary mixtures of 80% white (5 mm)/20% black (4 mm) and 80% white (5 mm)/20% yellow (6 mm), starting from position 5

The velocity of the plastic cuboid in the binary mixtures is very similar over each of three trials, varying between 0.5 cm/s and 5 cm/s. As has been mentioned one trial in the monosized particles results in the plastic cuboid following a similar path to that in the binary mixtures, this is shown to be due to the slow horizontal velocity of approximately 0.5 cm/s. In the final second prior to passing through the orifice the plastic cuboid travels at the same velocity in both the monosized particles and binary mixtures.

Figure 5.44 shows the trajectories of three trials of the hollow cuboid in the monosized white (5 mm) particles and the binary mixtures of 80% white (5 mm)/20% black (4 mm) and 80% white (5 mm)/20% yellow (6 mm), starting from position 5.

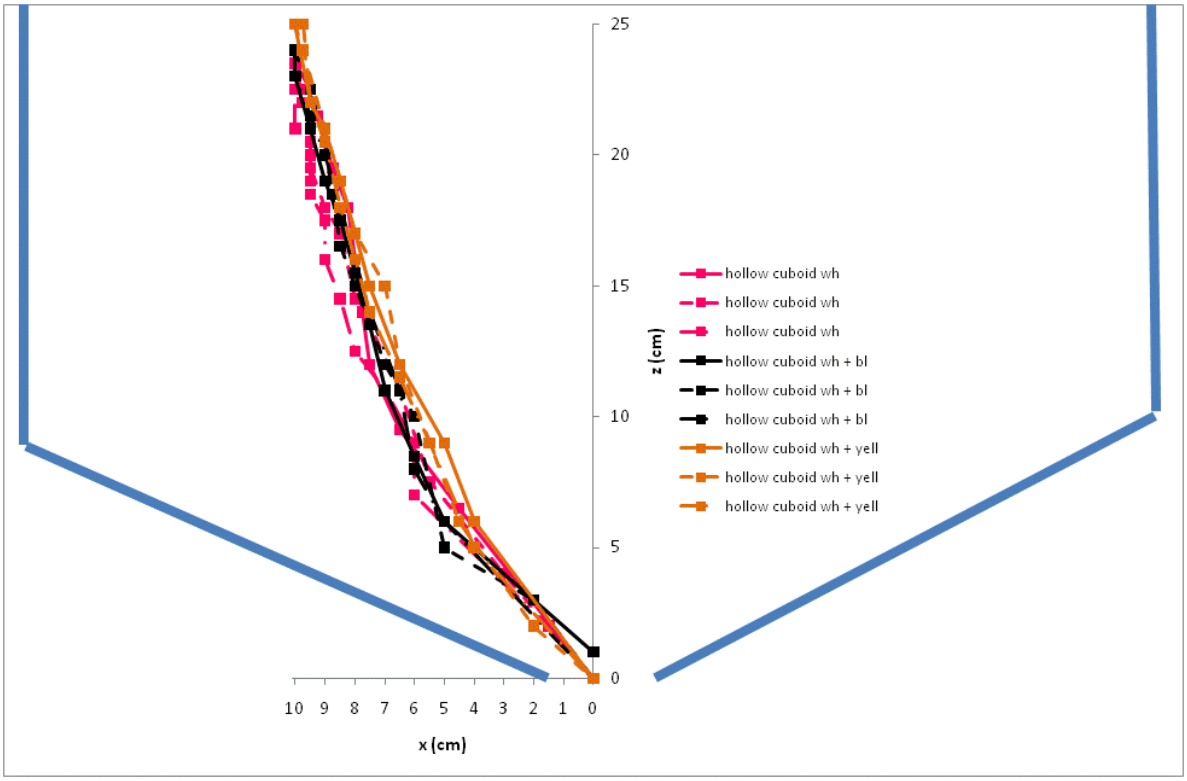

Figure 5.44: The trajectories of three trials of the hollow cuboid in the monosized white (5 mm) particles and the binary mixtures of 80% white (5 mm)/20% black (4 mm) and 80% white (5 mm)/ 20% yellow (6 mm), starting from position 5

The paths followed by the hollow cuboid are very similar in the monosized particles and the binary mixtures, although the paths appear very stochastic in nature. The paths differ by up to 2 cm along the horizontal. One trial of the hollow cuboid in the white/black binary mixture is shown to stop just above the orifice. This was because the hollow cuboid became trapped in the orifice, similar to the triangles in the monosized particles and as will be shown later, the triangles in the binary mixtures.

Figure 5.45 shows the vertical displacement-time graph for the hollow cuboid in the monosized white particles and the binary mixtures of 80% white (5 mm)/20% black (4 mm) and 80% white (5 mm)/20% yellow (6 mm), starting from position 5.

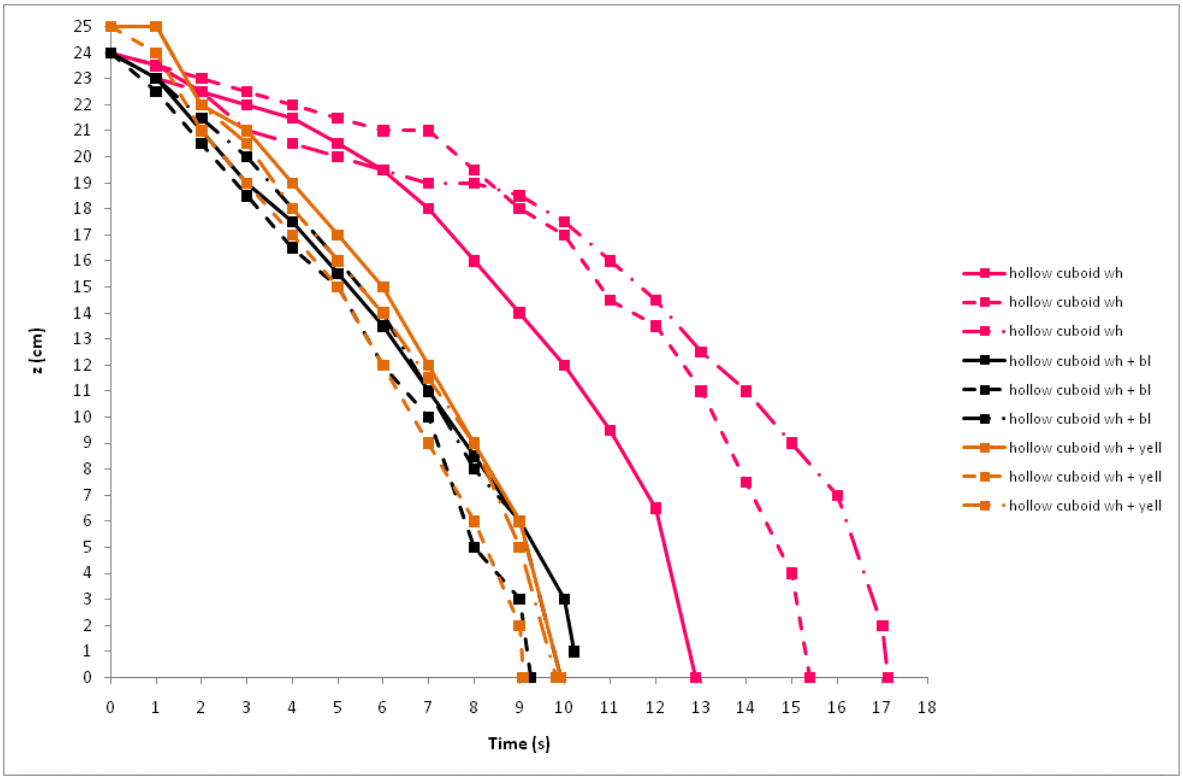

Figure 5.45: Graph showing the vertical displacement-time graph for the hollow cuboid in the monosized white (5 mm) particles and the binary mixtures of 80% white (5 mm)/20% black (4 mm) and 80% white (5 mm)/20% yellow (6 mm), starting from position 5

The velocity of the hollow cuboid in the binary mixtures is very similar at 2.4 s throughout the majority of its path to the orifice. The hollow cuboid in the monosized particles, on the other hand, varies throughout its path, travelling at approximately 0.6 cm/s in the first 6 seconds after the orifice has been opened and then varying between 1.2 cm/s and 2 cm/s until about 1 second before it travels through the orifice. The time taken for the hollow cuboid to reach the orifice in the binary mixtures is on average 9.5 s, but in the monosized particles it varies between 13 s and 17.1 s.

Figure 5.46 shows the horizontal displacement-time graph for the hollow cuboid in the monosized white (5 mm) particles and the binary mixtures of 80% white (5 mm)/20% black (4 mm) and 80% white (5 mm)/20% yellow (6 mm), starting from position 5.

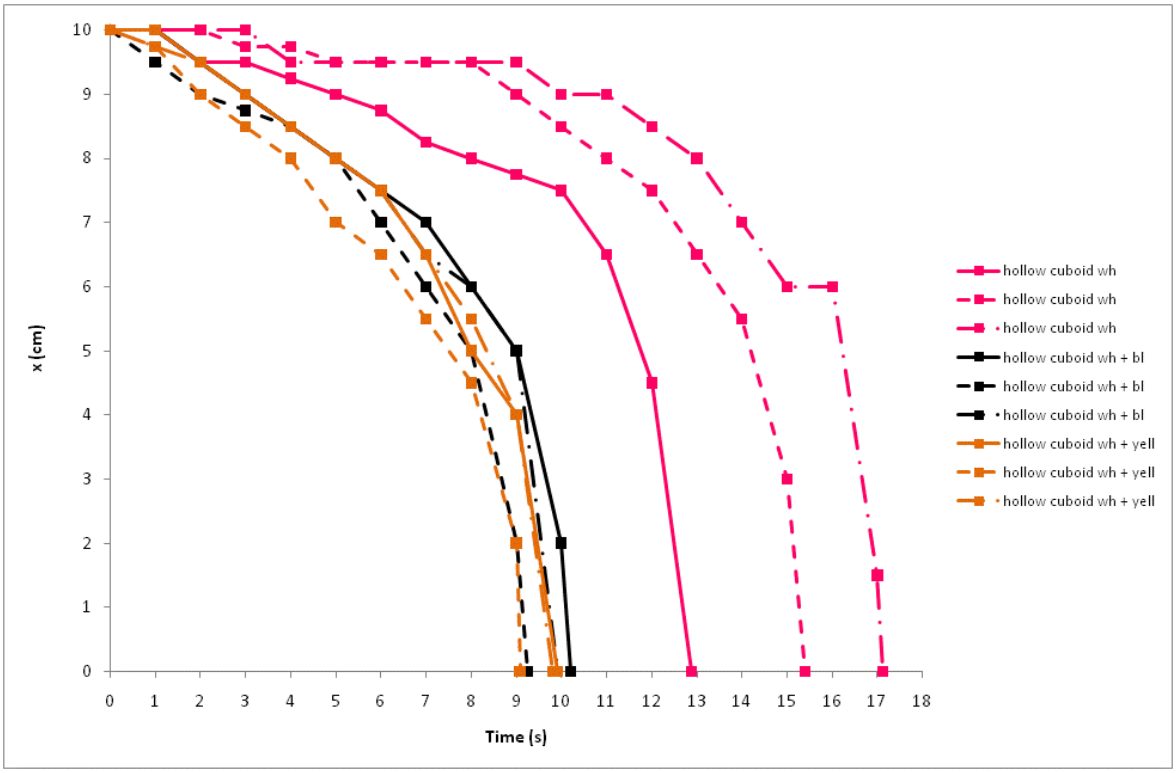

Figure 5.46: Graph showing the vertical displacement-time graph for the hollow cuboid in the monosized white (5 mm) particles and the binary mixtures of 80% white (5 mm)/20% black (4 mm) and 80% white (5 mm)/20% yellow (6 mm), starting from position 5

In similarity to the hollow cylinder the hollow cuboid travels with a horizontal velocity that is nearly the same over each of the three trials at 0.63 cm/s during the first 8 seconds after the initiation of discharge. The range of the velocity in the monosized particles is greater than in the binary mixtures and in two of the trials the hollow cuboid has zero horizontal velocity for about 5 seconds as it creeps along the edge of the flowing core.

5.12 Summary

In similarity to the cylinders the cuboids follow near identical paths in the silo from position 5 to the orifice. The horizontal and vertical velocities of the cuboids are similar in the binary mixtures, but due to the particles in the flowing core flowing along the sides of the cuboids, the cuboids in the monosized particles take longer to reach the orifice than in the binary mixtures. The paths between the three trials of each of the cuboids vary by up to 2cm. The time taken for the metal cuboid, plastic cuboid and hollow cuboids to reach the orifice in the monosized particles is 7.3 seconds, 14.2 seconds and 15.1 seconds respectively and in the binary mixtures is 5.5 seconds, 8.4 seconds and 9.5 seconds.

5.13 Comparison between the trajectories and velocities of the metal triangular prism, plastic triangular prism and hollow triangular prism free cells, in the white monosized particles and the white/yellow and white/black binary mixtures

Figure 5.47 shows the trajectories of three trials of the metal triangular prism in the monosized white (5 mm) particles and the binary mixtures of 80% white (5 mm)/20% black (4 mm) and 80% white (5 mm)/20% yellow (6 mm), starting from position 5.

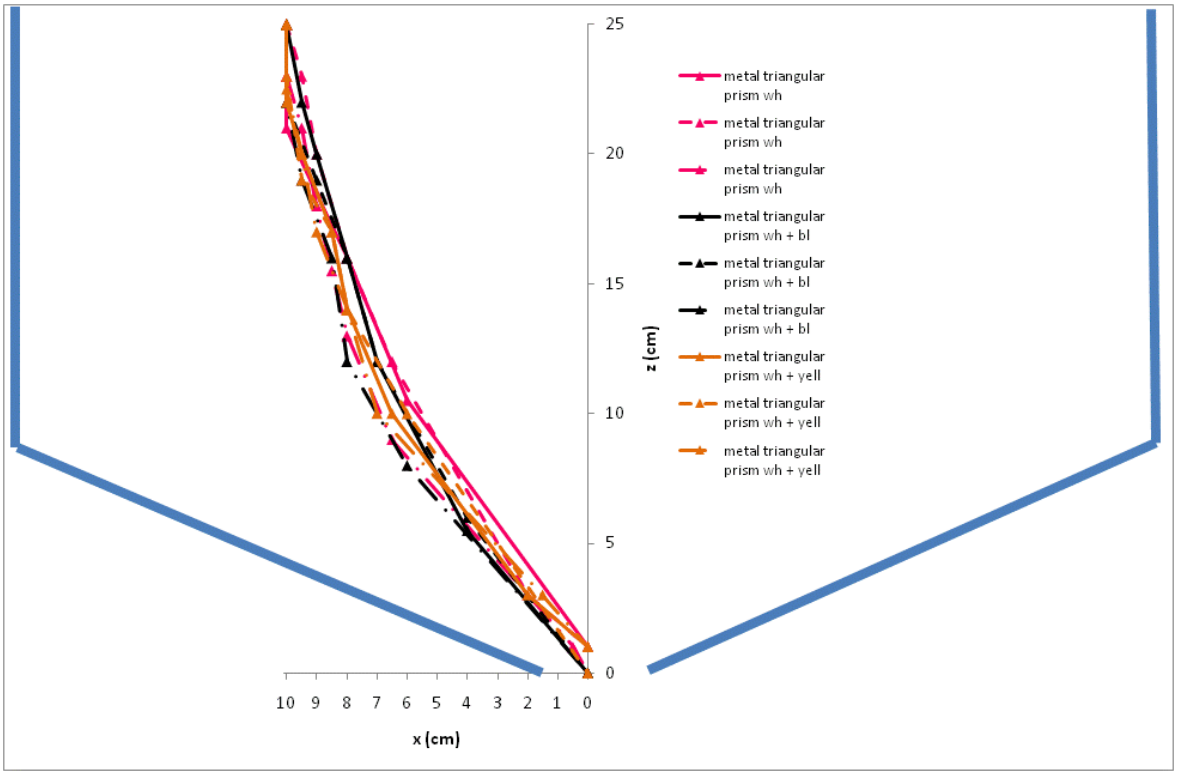

Figure 5.47: The trajectories of three trials of the metal triangular prism in the monosized white (5 mm) particles and the binary mixtures of 80% white (5 mm)/20% black (4 mm) and 80% white (5 mm)/ 20% yellow (6 mm), starting from position 5

The trajectories of the metal triangular prism in the monosized particles and the binary mixtures vary by up to 1.5 cm along the horizontal. The metal triangular prism flowed through the orifice in all three trials in the white/black binary mixture, two trials in the monosized particles and one trial in the white/yellow binary mixture. The orientation and the angle that the triangular prism approaches the orifice are crucial in determining whether it will flow through the orifice or become trapped.

Figure 5.48 shows the vertical displacement-time graph for the metal triangular prism in the monosized white (5 mm) particles and the binary mixtures of 80% white (5 mm)/20% black (4 mm) and 80% white (5 mm)/20% yellow (6 mm), starting from position 5.

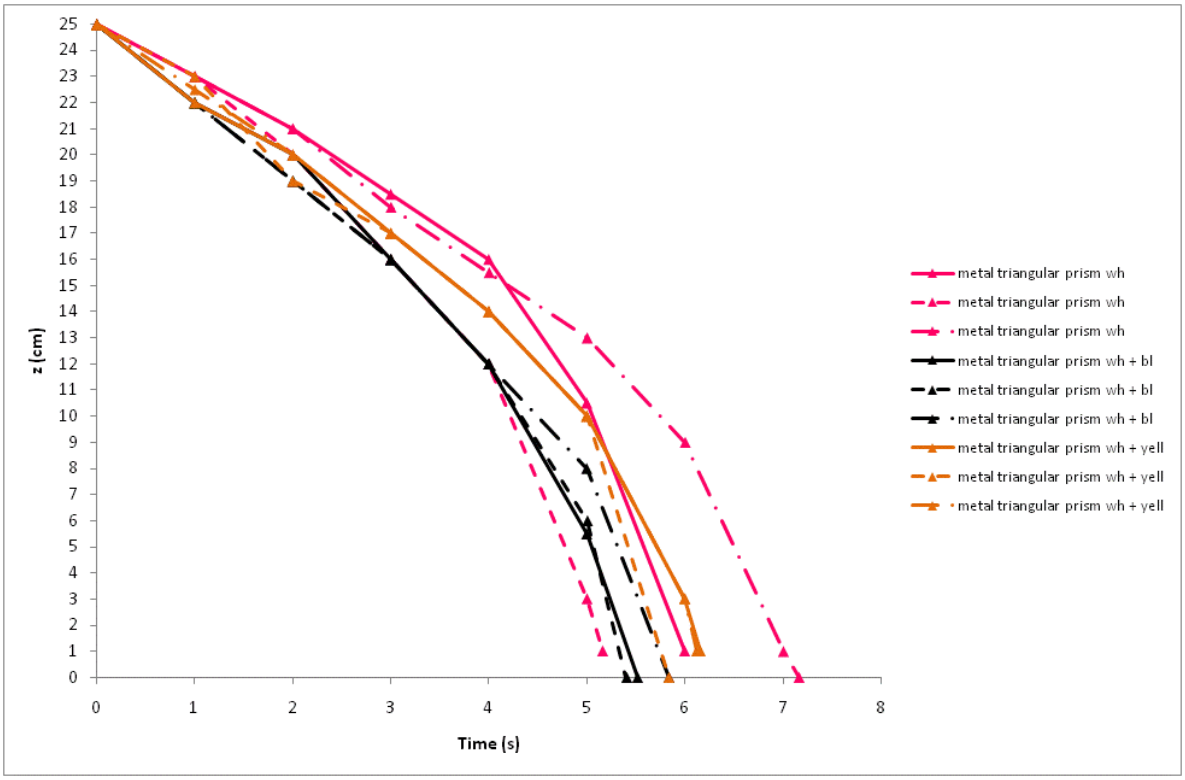

Figure 5.48: Graph showing the vertical displacement-time graph for the metal triangular prism in the monosized white (5 mm) particles and the binary mixtures of 80% white (5 mm)/20% black (4 mm) and 80% white (5 mm)/20% yellow (6 mm), starting from position 5

There exist some considerable overlap between the trajectories followed by the metal triangular prism in the monosized particles and binary mixtures. During the first 5 seconds the velocity over three trials in each of the three particle batches varies by between 2.4 cm/s and 3 cm/s. In the 1 second prior to travelling through the orifice, the velocity of the metal triangular prism in all cases is approximately 12 cm/s.

Figure 5.49 shows the horizontal displacement-time graph for the metal triangular prism in the monosized white (5 mm) particles and the binary mixtures of 80% white (5 mm)/20% black (4 mm) and 80% white (5 mm)/20% yellow (6 mm), starting from position 5.

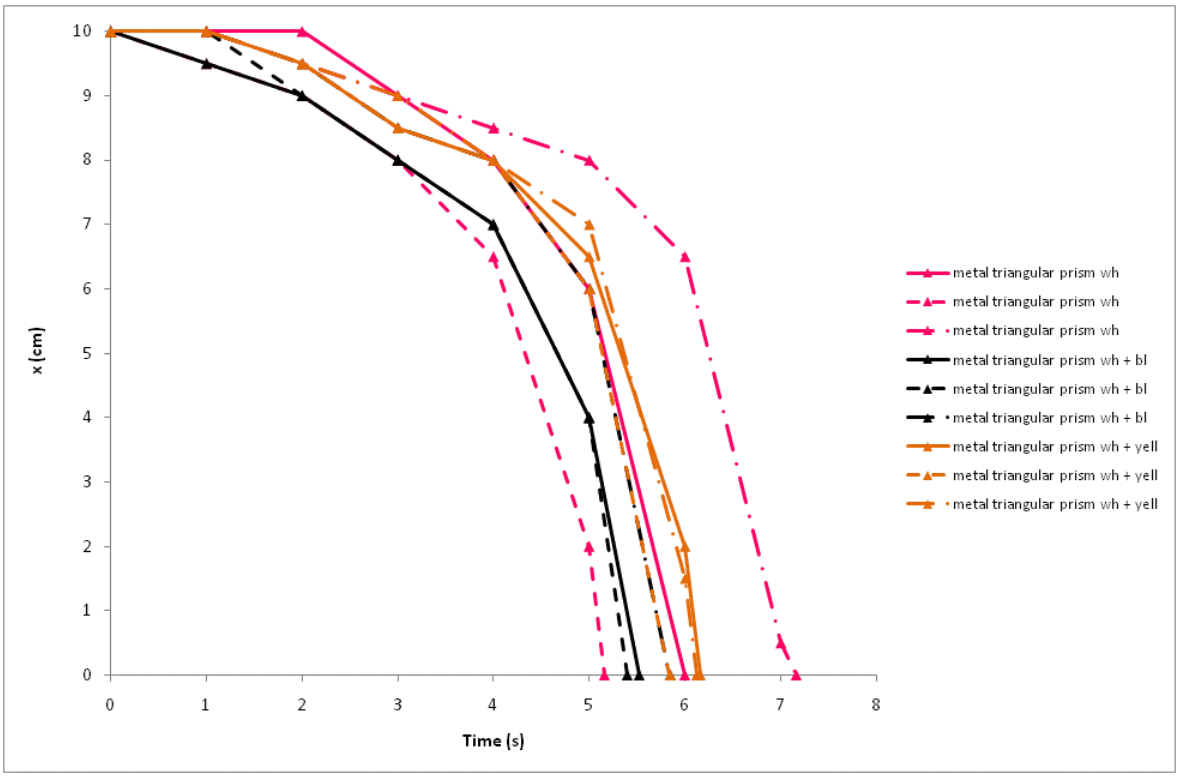

Figure 5.49: Graph showing the horizontal displacement-time graph for the metal triangular prism in the monosized white (5 mm) particles and the binary mixtures of 80% white (5 mm)/20% black (4 mm) and 80% white (5 mm)/20% yellow (6 mm) starting from position 5

The horizontal velocity of the metal triangular prism, over three trials in the monosized and binary mixtures, varies between 0.4 cm/s and 0.75 cm/s and the velocity in the final second before passing through the orifice is approximately 9 cm/s. The time taken for the metal triangular prism to reach the orifice in all three different batches is on average about 5.8 seconds. The similar trajectories indicate that the metal triangular prism has the ability to move through the discharging particles rather than with them. The shape of the triangular prism is such that it has pointed corners which enable it to cut through the gap between the other particles.

Figure 5.50 shows the trajectory taken by three trials of the plastic triangular prism in the monosized white (5 mm) particles and the binary mixtures of 80% white (5 mm)/20% black (4 mm) and 80% white (5 mm)/20% yellow (6 mm), starting from position 5.

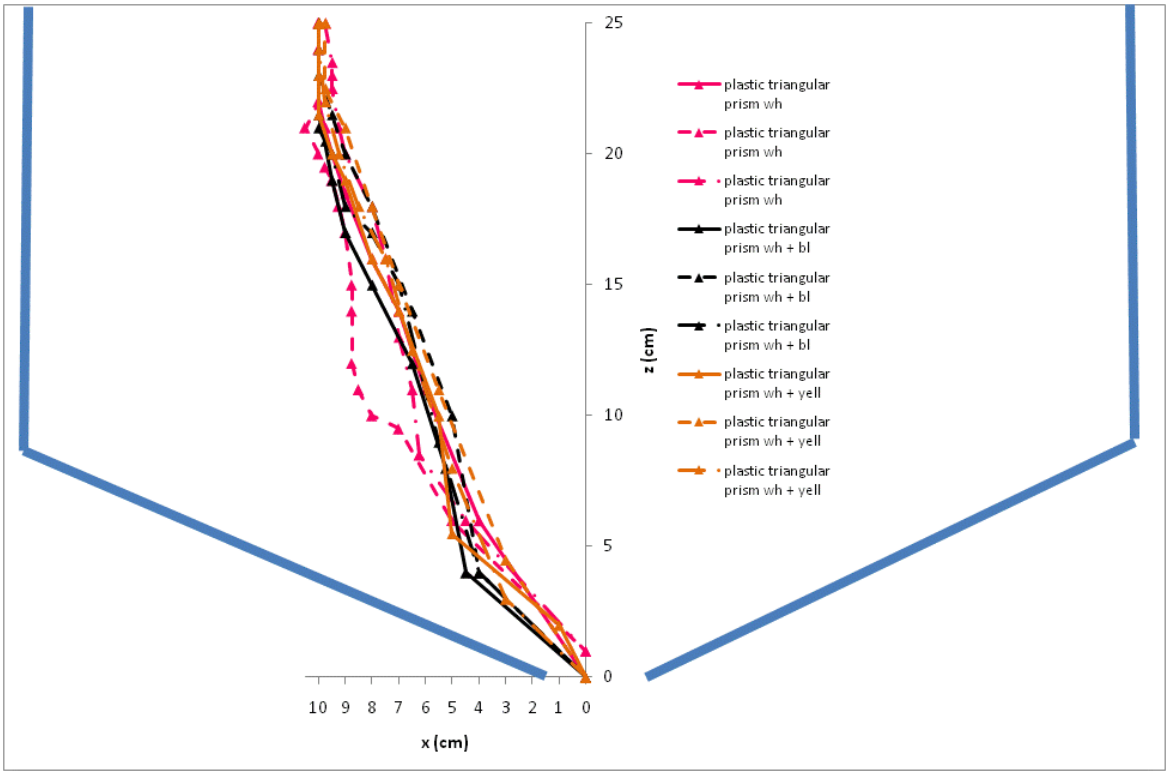

Figure 5.50: The trajectories of three trials of the plastic triangular prism in the monosized white (5 mm) particles and the binary mixtures of 80% white (5 mm)/20% black (4 mm) and 80% white (5 mm)/ 20% yellow (6 mm), starting from position 5

Compared to the haphazard trajectory followed by the plastic triangular prism in the monosized white particles, the plastic triangular prism in the binary mixtures follows a more predictable trajectory, varying by up to 2 cm along the horizontal. The plastic triangular prism became caught in the orifice during only one trial of the monosized white particles and flowed through the orifice during all trials in the binary mixtures.

Figure 5.51 shows the vertical displacement-time graph for the plastic triangular prism in the monosized white (5 mm) particles and the binary mixtures of 80% white (5 mm)/20% black (4 mm) and 80% white (5 mm)/20% yellow (6 mm), starting from position 5.

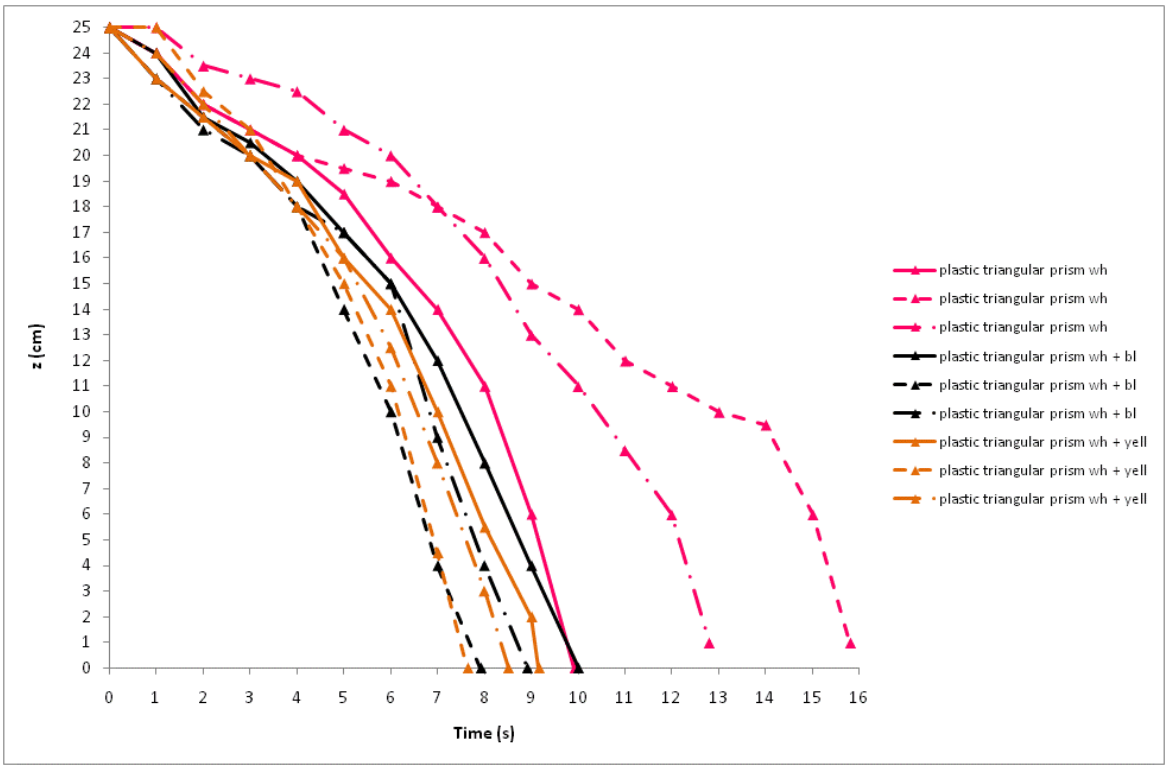

Figure 5.51: Graph showing the vertical displacement-time graph for the plastic triangular prism in the monosized white (5 mm) particles and the binary mixtures of 80% white (5 mm)/20% black (4 mm) and 80% white (5 mm)/20% yellow (6 mm), starting from position 5

The vertical velocity of the plastic triangular prism in the binary mixtures is about 1.3 cm/s in the first 6 seconds after the initiation of discharge and 5.3 cm/s in the final 3 seconds before it travels through the orifice. The time taken for the plastic triangular prism to travel to the orifice in the binary mixtures is on average 9 seconds white in the binary mixtures it varies between 10 and 16 seconds.

Figure 5.52 shows the horizontal displacement-time graph for the plastic triangular prism in the monosized white (5 mm) particles and the binary mixtures of 80% white (5 mm)/20% black (4 mm) and 80% white (5 mm)/20% yellow (6 mm), starting from position 5.

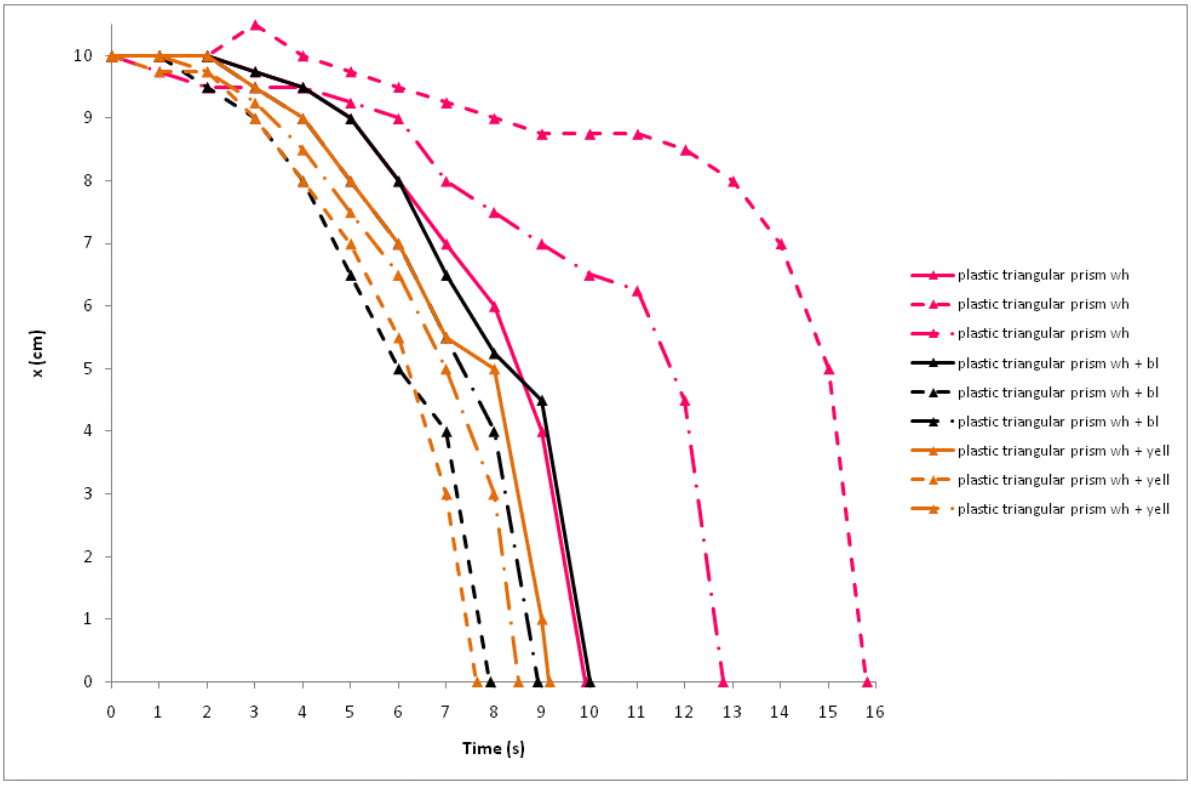

Figure 5.52: Graph showing the horizontal displacement-time graph for the plastic triangular prism in the monosized white (5 mm) particles and the binary mixtures of 80% white (5 mm)/20% black (4 mm) and 80% white (5 mm)/20% yellow (6 mm), starting from position 5

The horizontal velocity of the plastic triangular is very similar in both of the binary mixtures over three trials. It gradually accelerates fro rest at an average of 0.25 cm/s^2 in both binary mixtures until it reaches the orifice.

Figure 5.53 shows the trajectories of three trials of the hollow triangular prism in the monosized white (5 mm) particles and the binary mixtures of 80% white (5 mm)/20% black (4 mm) and 80% white (5 mm)/20% yellow (6 mm), starting from position 5.

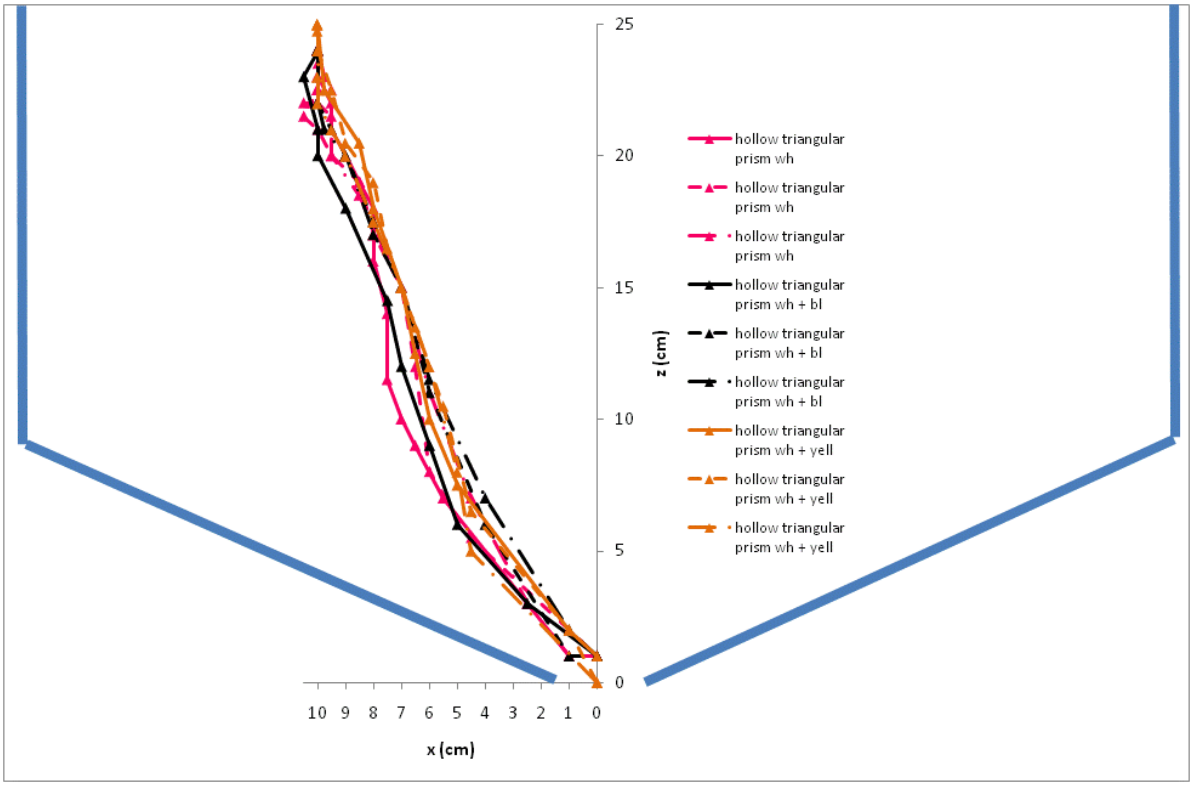

Figure 5.53: The trajectories of three trials of the hollow triangular prism in the monosized white (5 mm) particles and the binary mixtures of 80% white (5 mm)/20% black (4 mm) and 80% white (5 mm)/ 20% yellow (6 mm), starting from position 5

The trajectories of the hollow triangular prism in the monosized particles and binary mixtures are very similar, varying by up to 2 cm along the horizontal. The hollow triangular prism became trapped in the orifice in all three trials in the monosized white particles and white/black binary mixture and during only one trial in the white/yellow binary mixture.

Figure 5.54 shows the vertical displacement-time graph for the hollow triangular prism in the monosized white (5 mm) particles and the binary mixtures of 80% white (5 mm)/20% black (4 mm) and 80% white (5 mm)/20% yellow (6 mm), starting from position 5.

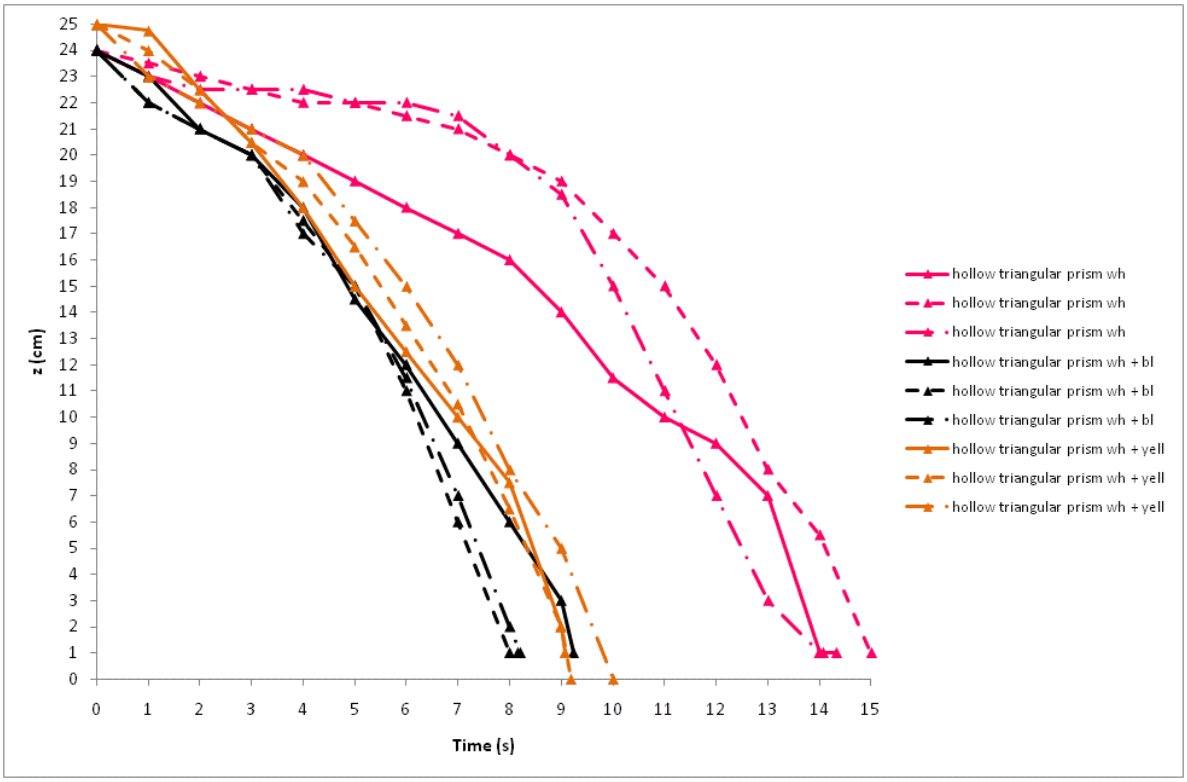

Figure 5.54: Graph showing the vertical displacement-time graph for the hollow triangular prism in the monosized white (5 mm) particles and the binary mixtures of 80% white (5 mm)/20% black (4 mm) and 80% white (5 mm)/20% yellow (6 mm), starting from position 5

In similarity to the metal and plastic triangular prisms the vertical velocity of the hollow triangular prism is very similar in both binary mixtures, averaging approximately 1.2 cm/s in the first 5 seconds and 4 cm/s in the 5 seconds prior to passing through the orifice. The velocity of the hollow triangular prism in the first 8 seconds after the initiation of discharge varies between 0.5 cm/s and 1 cm/s and in the final 6 seconds of its trajectory between 2.7 cm/s and 4.5 cm/s.

Figure 5.55 shows the horizontal displacement-time graph for the hollow triangular prism in the monosized white (5 mm) particles and the binary mixtures of 80% white (5 mm)/20% black (4 mm) and 80% white (5 mm)/20% yellow (4 mm), starting from position 5.

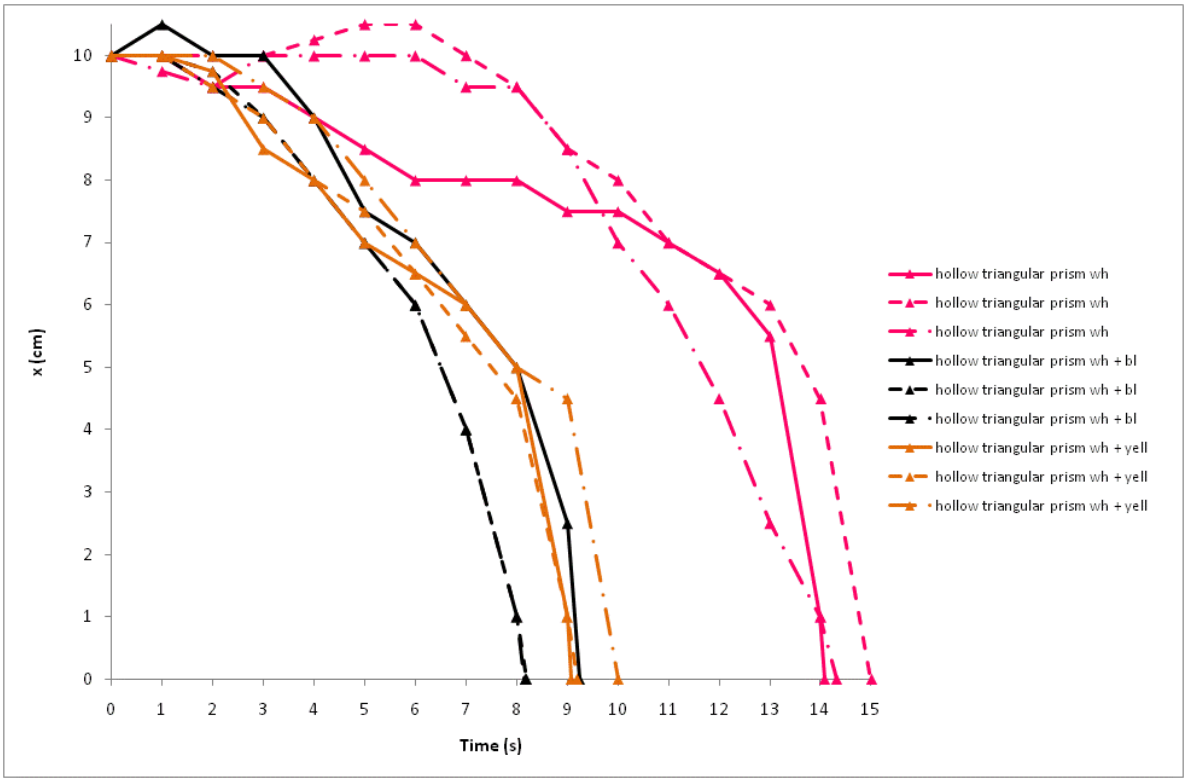

Figure 5.55: Graph showing the horizontal displacement-time graph for the hollow triangular prism in the monosized white (5 mm) particles and the binary mixtures of 80% white (5 mm)/20% black (4 mm) and 80% white (5 mm)/20% yellow (6 mm), starting from position 5

The horizontal velocity of the hollow triangular prism is very similar in the binary mixtures, varying between about 0.6 cm/s in the first 6 seconds and 2 cm/s in the final 3 seconds of the trajectories. The hollow triangular prism experiences a slight horizontal velocity away from the orifice, in similarity to the plastic triangular prism, during one trial in the white/black binary mixtures. The time taken for the hollow triangular prism to reach the orifice is on average 9 seconds in the binary mixtures and 14.5 seconds in the monosized particles.

5.14 Summary

The triangular prisms in the monosized particles flow a very stochastic trajectory and appear to be easily buffeted around by the other particles. The metal triangular prism has a similar horizontal and vertical displacement in the monosized and binary mixtures, but the plastic and hollow triangular prisms experience are affected by the velocity of the other particles near the stagnant zone boundary as discussed in chapter 4. The average time taken for the metal, plastic and hollow triangular prisms to reach the orifice in the monosized particles is 5.8 seconds, 13 seconds and 14.5 seconds and in the binary mixtures is 5.8 seconds, 9 seconds and 9 seconds respectively. The maximum vertical velocity of the metal, plastic and hollow triangular prisms is 12 cm/s, 5.3 cm/s and 4.5 cm/s respectively.

5.15 Conclusion

It is interesting to note that the different free-cells behave very similarly in each of the binary mixtures. This is despite the fact that the white (5 mm)/black (4 mm) binary mixture and the white (5 mm)/Yellow (6 mm) binary mixtures consist of 20% of particles that have a 50% difference in size and 8% difference in density. The free cells are found to take 50% less time to reach the orifice in the binary mixtures than in the monosized particles. The differences between the trajectories in the monosized and binary mixtures can partly be attributed to the greater value of ϕ_d, the angle between the stagnant zone boundary and the horizontal, which was discussed in chapter 4. This in turn results in the time taken for the free-cells in the binary mixtures to be less than in the monosized particles. The trajectories and velocities of the free-cells in the monosized particles, starting from position 5, tended to vary quite considerably over three trials, especially during the initial few seconds after the opening of the orifice. However, the trajectories of the free-cells in the binary mixtures over three trials, tended to follow very similar trajectories at very similar velocities. As well as the binary mixtures exhibiting a greater value of ϕ_d, the free-cells also appear to move more easily in the binary mixtures. The plastic and hollow triangular prisms followed very haphazard trajectories from position 5, in the monosized white particles, but very similar trajectories over three trials in the binary mixtures. This is mostly likely because the particles in a binary mixture have grater freedom of movement. The packing density of binary mixtures of particles may be greater

than monosized particles, but the variation in the packing structure is greater in binary mixtures than in monosized particles.

The time taken for the free-cells to reach the orifice from initial starting positions 1 to 12

6 The time taken for the free-cells to reach the orifice from initial starting positions 1 to 12

6.1 Introduction

Experiments were conducted to determine the time taken for each of the free-cells to flow to the orifice from each of the 12 starting positions, after the orifice had been opened. In the previous section it was concluded that the trajectories followed by the plastic free-cells were in closer agreement to the trajectory of the representative particle. Therefore, only the results comparing the plastic free-cells will be discussed. The reader is referred to the CD enclosed with this thesis, which contains equivalent results obtained from experiments using the metal, plastic and hollow free-cells.

6.2 Time taken for plastic free-cells to travel to the orifice from each of the twelve starting positions.

Figure 6.1a shows the time taken after the orifice has been opened, for the plastic free-cells to reach the orifice, from each of the initial positions 1-12 in the white (5mm) particles.

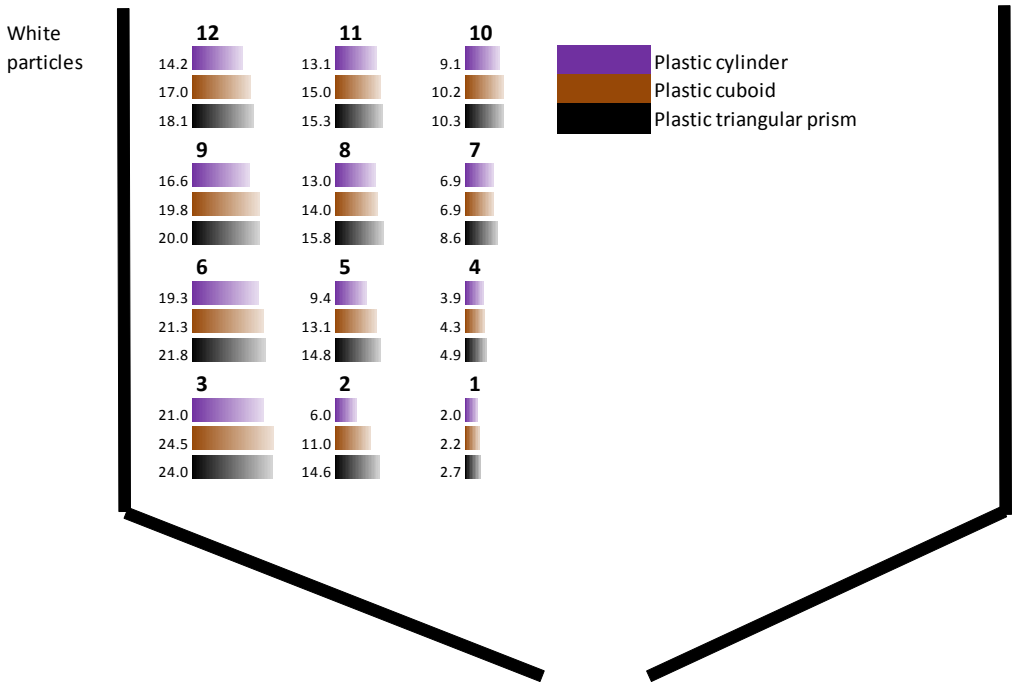

Figure 6.1a: Time taken after the orifice has been opened for the plastic-free cells in the white (5mm) monosized particles to reach the orifice

The plastic cylinder takes the least time to reach the orifice from all the positions and the plastic triangular prism takes longer to reach the orifice than the plastic cuboid, except at position 12 where the plastic cuboid takes 0.5 s longer. The free-cells placed at position 12 take the longest time to reach the orifice.

Figure 6.1b shows the time taken after the orifice has been opened for the plastic free-cells to reach the orifice from each of the initial positions 1-12 in the white particles.

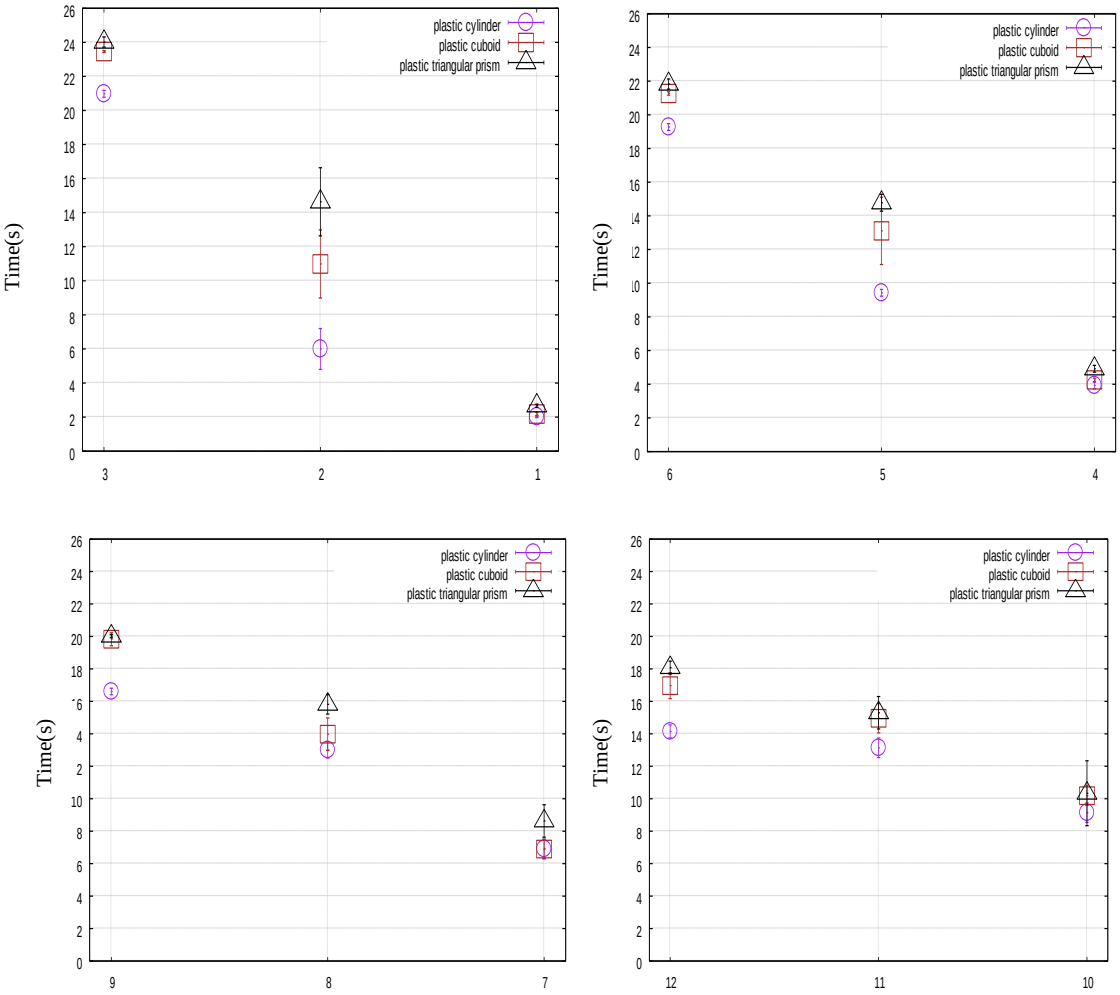

Figure 6.1b: Time taken after the orifice has been opened, for the plastic free-cells in the white (5mm) monosized particles to reach the orifice, from each of the initial positions 1-12. Each point represents the average over five trials and the range of the results from the five trials is shown

The time taken for the plastic free-cells is shown to increase with height in the flowing core and to increase with increasing horizontal distance from the orifice along each row. The plastic free-cells at position 3 take the longest time to reach the orifice upon the initiation of

discharge. Free-cells starting from position 2 showed the greatest variability over the five trials. The plastic cylinder takes the shortest time to reach the orifice followed by the plastic cuboid and the plastic triangular prism respectively. At positions 1,3,4,6 and 9 the time taken for the plastic cuboid and plastic triangular prism is very similar.

Figure 6.2a shows the time taken after the orifice has been opened, for the plastic free-cells to reach the orifice, from each of the initial positions 1-12 in the white (5 mm)/Yellow (6 mm) binary mixture.

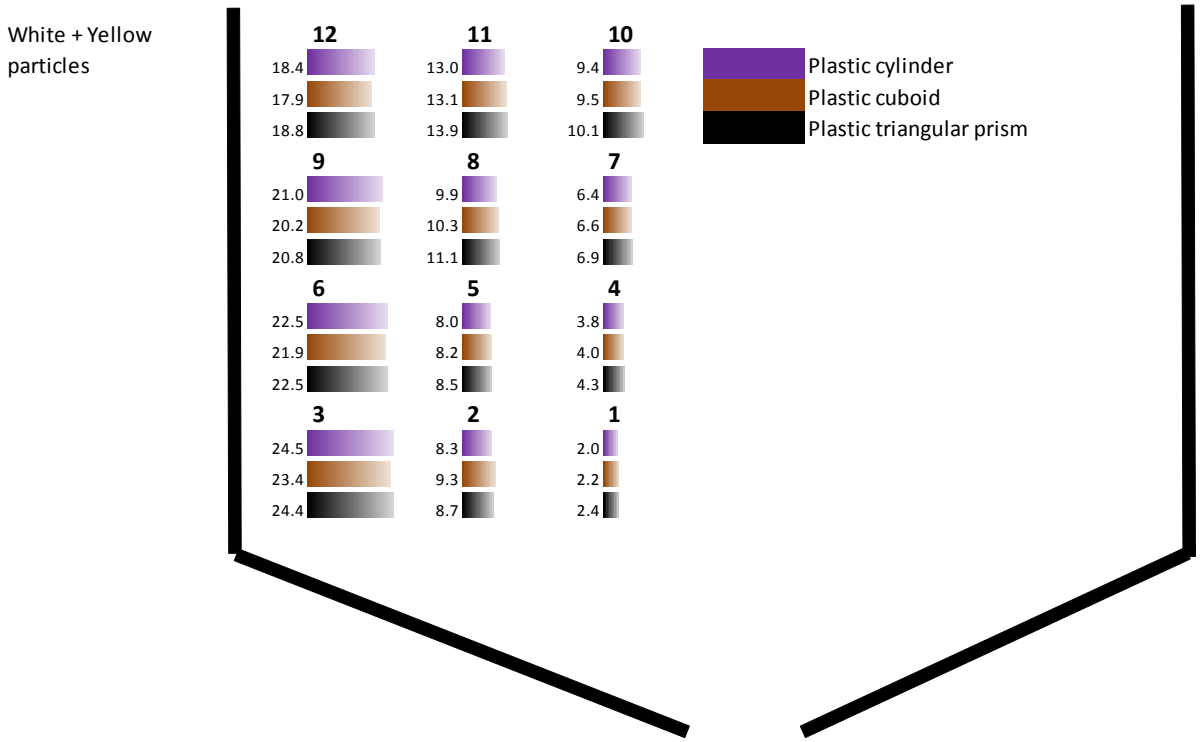

Figure 6.2a: Time taken after the orifice has been opened for the plastic-free cells in the 80% white (5 mm)/ 20% yellow (6 mm) particles to reach the orifice

The plastic cylinder takes the shortest time to reach the orifice in the positions within the flowing core i.e. 1, 2, 4, 5, 7, 8, 10 and 11 and the plastic triangular prism takes the longest time, except at position 2, where the plastic cuboid takes longer. Outside the flowing core the time taken by the plastic shapes to travel to the orifice appears to be approximately similar.

Figure 6.2b shows the time taken after the orifice has been opened, for the plastic free-cells to reach the orifice, from each of the initial positions 1-12 in the white (5 mm)/Yellow (6 mm) particles.

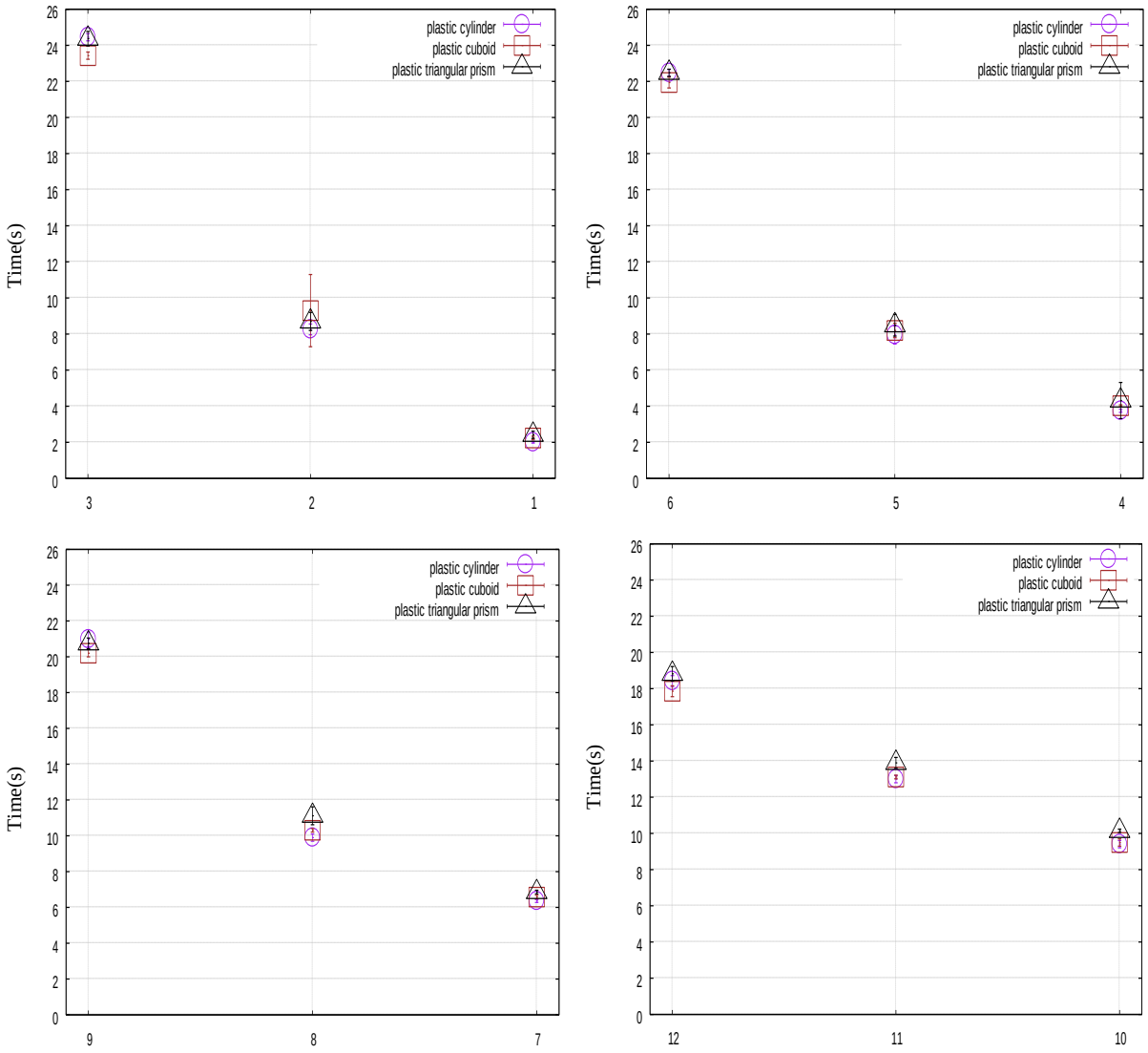

Figure 6.2b: Time taken after the orifice has been opened, for the plastic free-cells in the 80% white (5 mm)/ 20% yellow (6 mm) binary mixture, to reach the orifice from each of the initial positions 1-12. Each point represents the average over five trials and the range of the results from the five trials is shown

In similarity to the results for the white particles, the time taken for the plastic free-cells to reach the orifice increases with height in the flowing core. The free-cells starting in position 3 take the longest time to reach the orifice. However, the difference between the average time taken for the plastic cylinder, cuboid and triangular prism is very small and the variation over five trials is very small, suggesting that the plastic free-cells follow a similar trajectory during

each trial. Again, the greatest variation between the results of the time taken for the plastic cuboid, to reach the orifice, is when it starts from position 2. This is most likely because the particles in the flowing core will initially flow along the side of the cuboid, until it is eventually pulled into the core and out through the orifice. This process, however, is highly stochastic resulting in the large time variation. The difference in the time taken between free-cells of different shape to reach the orifice is not that large, suggesting that shape of free-cell may not be important in terms of the time of travel to reach the orifice.

Figure 6.3a shows the time taken after the orifice has been opened, for the plastic free-cells to reach the orifice, from each of the initial positions 1-12 in the white (5mm)/black (4mm) binary mixture.

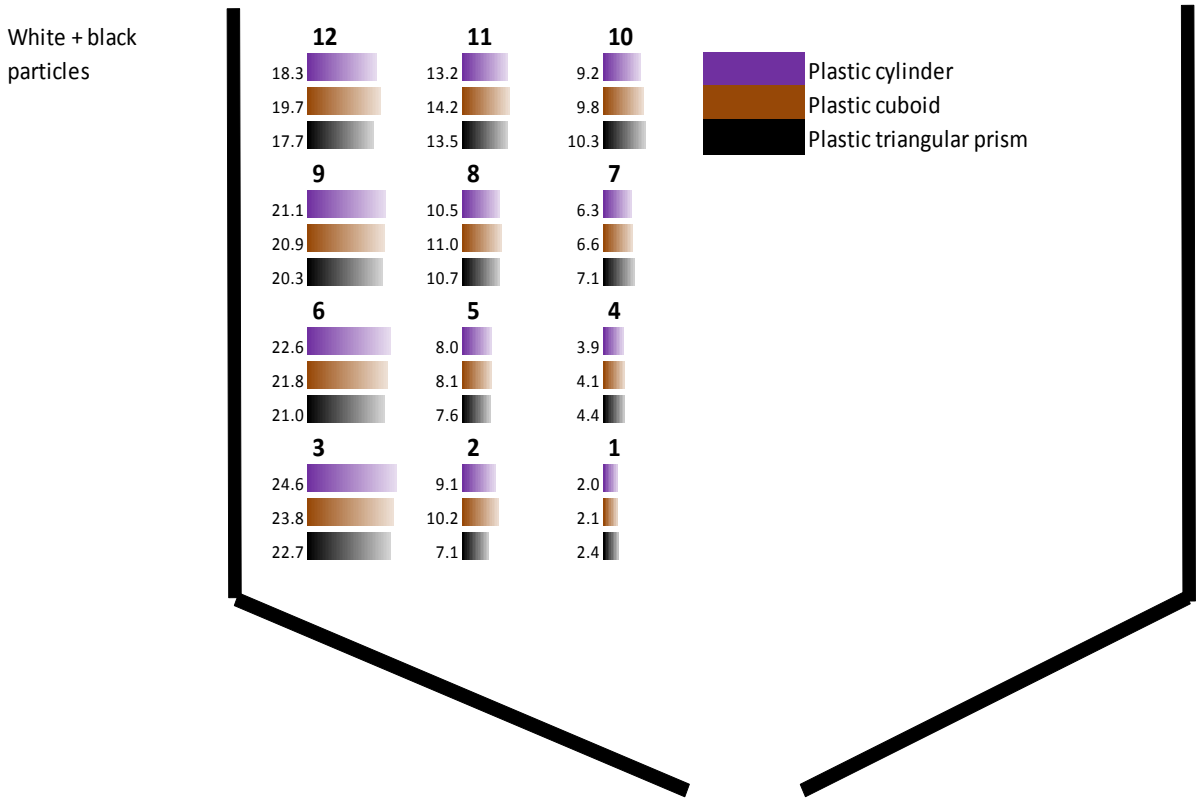

Figure 6.3a: Time taken after the orifice has been opened for the plastic-free cells in the 80% white (5mm)/ 20% black (4mm) particles to reach the orifice

The plastic triangular prism takes the longest time to reach the orifice than the plastic cylinder and cuboid at positions 1, 4, 7 and 10, but the plastic cuboid takes the longest time to reach the orifice than the other two shapes at positions 2, 5, 8 and 11. Apart from position 2 the

times vary by up to 1 second, which may be due to stochastic effects rather than an important phenomenan.

Figure 6.3b shows the time taken after the orifice has been opened, for the plastic free-cells to reach the orifice, from each of the initial positions 1-12 in the white particles.

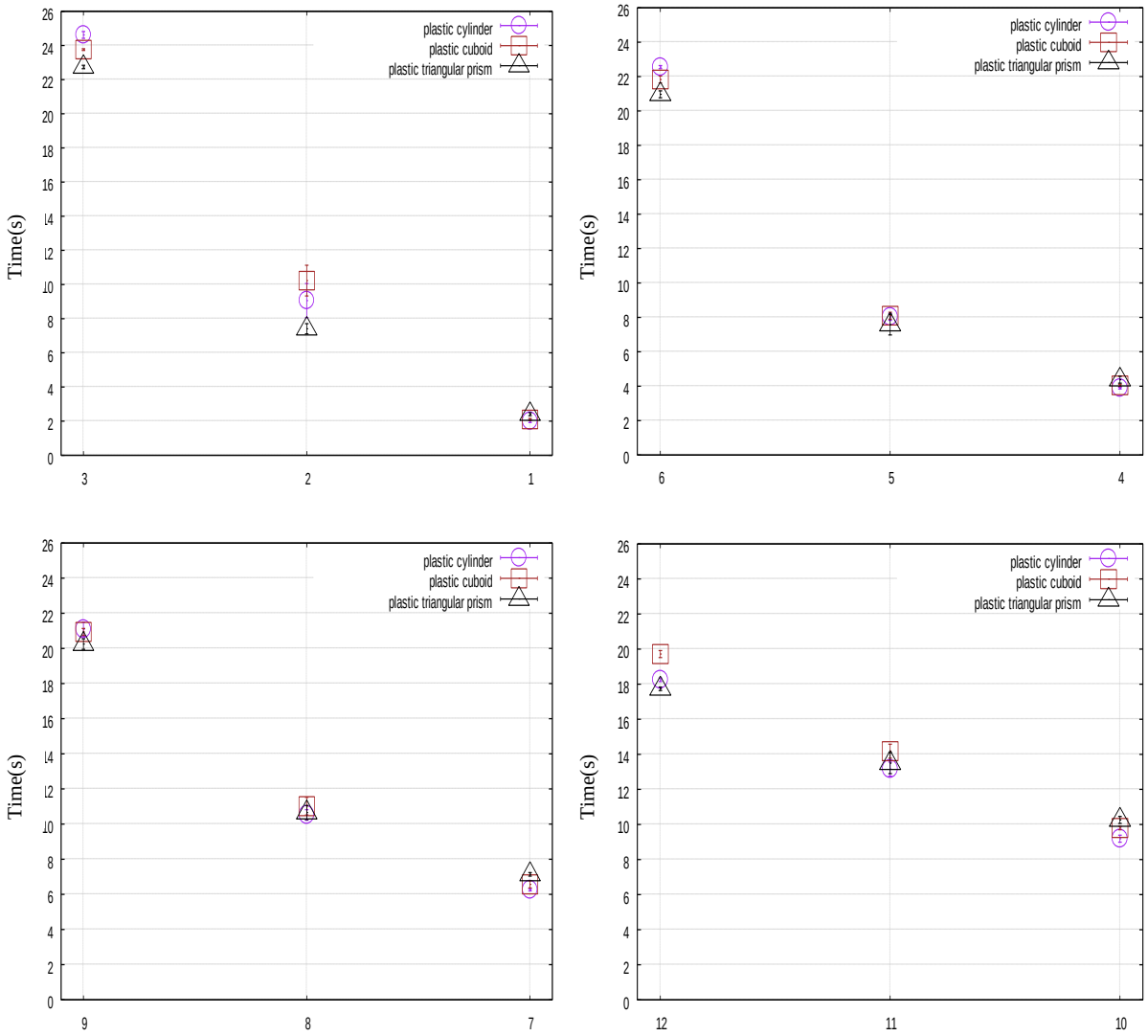

Figure 6.3b: Time taken after the orifice has been opened, for the plastic free-cells in the 80% white (5 mm)/ 20% black (4 mm) binary mixture, to reach the orifice from each of the initial positions 1-12. Each point represents the average over five trials and the range of the results from the five trials is shown

The time taken for each of the plastic free-cells to flow through the orifice from each of the position 1 – 12 is very similar. The greatest difference between the results occurs when the free-cells start from position 2. However, the range of the results over five trials is small,

indicating that the free-cells follow a similar trajectory during each trial. The time taken for the free-cells to reach the orifice in the flowing core increases with height and the free-cells placed at starting position 3, take the longest time to reach the orifice upon the initiation of discharge.

Figure 6.4a shows the time taken after the orifice has been opened, for the plastic cylinder to reach the orifice, from each of the initial positions 1-12 in the white (5 mm) monosized particles, white (5 mm)/black (6 mm) binary mixture and white (5 mm)/black (4 mm) binary mixture.

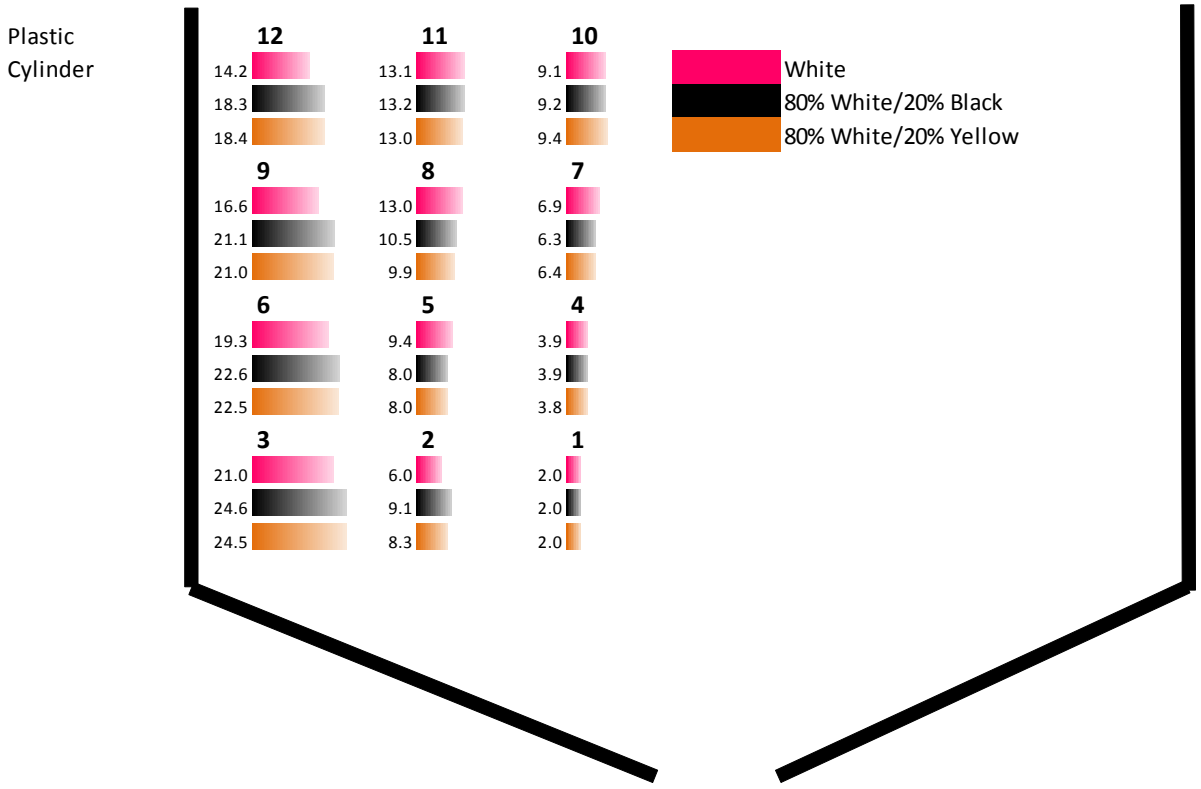

Figure 6.4a: Time taken after the orifice has been opened for the plastic cylinder in the white (5 mm) monosized particles and the 80% white (5 mm)/ 20% yellow (6 mm) and 80% white (5 mm)/ 20% black (4mm) binary mixtures to reach the orifice

The time taken for the plastic cylinder to reach the orifice in the monosized particles and each of the binary mixtures is very similar from starting positions 1, 4, 7 and 10, which are nearly along the centre line. Outside the central core, near the wall of the silo at positions 3, 6, 9 and 12 the plastic cylinder takes the shortest time to reach the orifice in the monosized white particles. The time taken for the plastic cylinder to reach the orifice appears to be most variable at position 2 and 5, which are near the stagnant zone boundary.

Figure 6.4b shows the time taken after the orifice has been opened, for the plastic cylinder to reach the orifice, from each of the initial positions 1-12 in the white (5 mm), white (5mm)/Yellow (6 mm) binary mixture and the white (5 mm)/ black (4 mm).

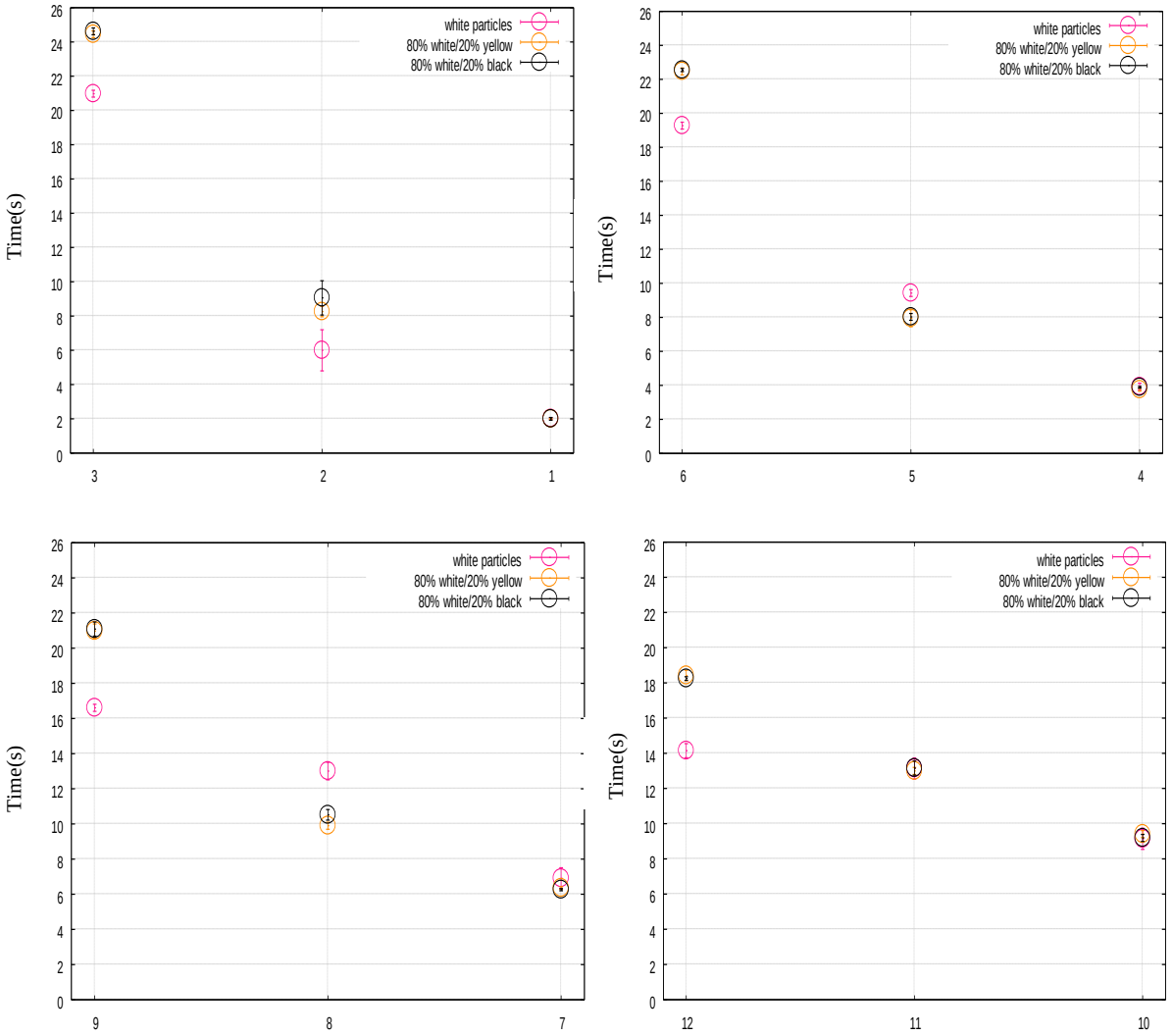

Figure 6.4b: Time taken after the orifice has been opened, for the plastic cylinder in the white (5 mm) monosized particles and the 80% white (5 mm)/ 20% black (4 mm) and 80% white (5 mm)/ 20% yellow (6mm) binary mixture, to reach the orifice from each of the initial positions 1-12

At positions 3, 6, 9 and 12 near the wall of the silo, the cylindrical free-cells take longer to reach the orifice in the binary mixtures than in the monosized white particles. This is because of the wider flowing core in the binary mixtures. In the monosized particles the horizontal velocity is greater than in the binary mixtures, so the cylinder is dragged towards the centre line faster in the monosized particles than in the binary mixtures and as a result the vertical

velocity of the cylinder is greater, resulting in the reduced time for the cylindrical free-cell reaching the orifice.

Figure 6.5a shows the time taken after the orifice has been opened, for the plastic cuboid to reach the orifice, from each of the initial positions 1-12 in the white (5 mm) monosized particles, white (5 mm)/black (6 mm) binary mixture and white (5 mm)/black (4 mm) binary mixture.

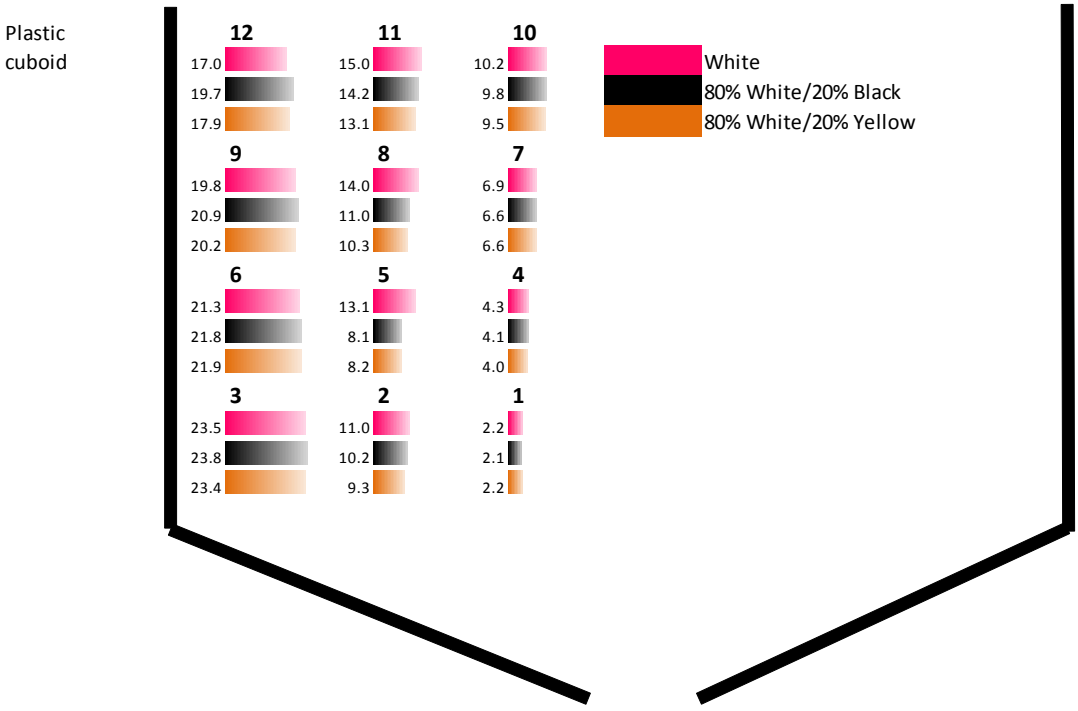

Figure 6.5a: Time taken after the orifice has been opened for the plastic cuboid in the white (5 mm) monosized particles and the 80% white (5 mm)/ 20% yellow (6 mm) and 80% white (5 mm)/ 20% black (4mm) binary mixtures to reach the orifice

The time taken for the plastic cuboid to reach the orifice looks very similar in the monosized particles and binary mixtures at positions 1, 4, 7 and 10 near the centre line and at positions 3, 6, 9 and 12 along the wall.

Figure 6.5b shows the time taken after the orifice has been opened, for the plastic cuboid to reach the orifice, from each of the initial positions 1-12 in the white (5 mm), white (5mm)/Yellow (6 mm) binary mixture and the white (5 mm)/ black (4 mm).

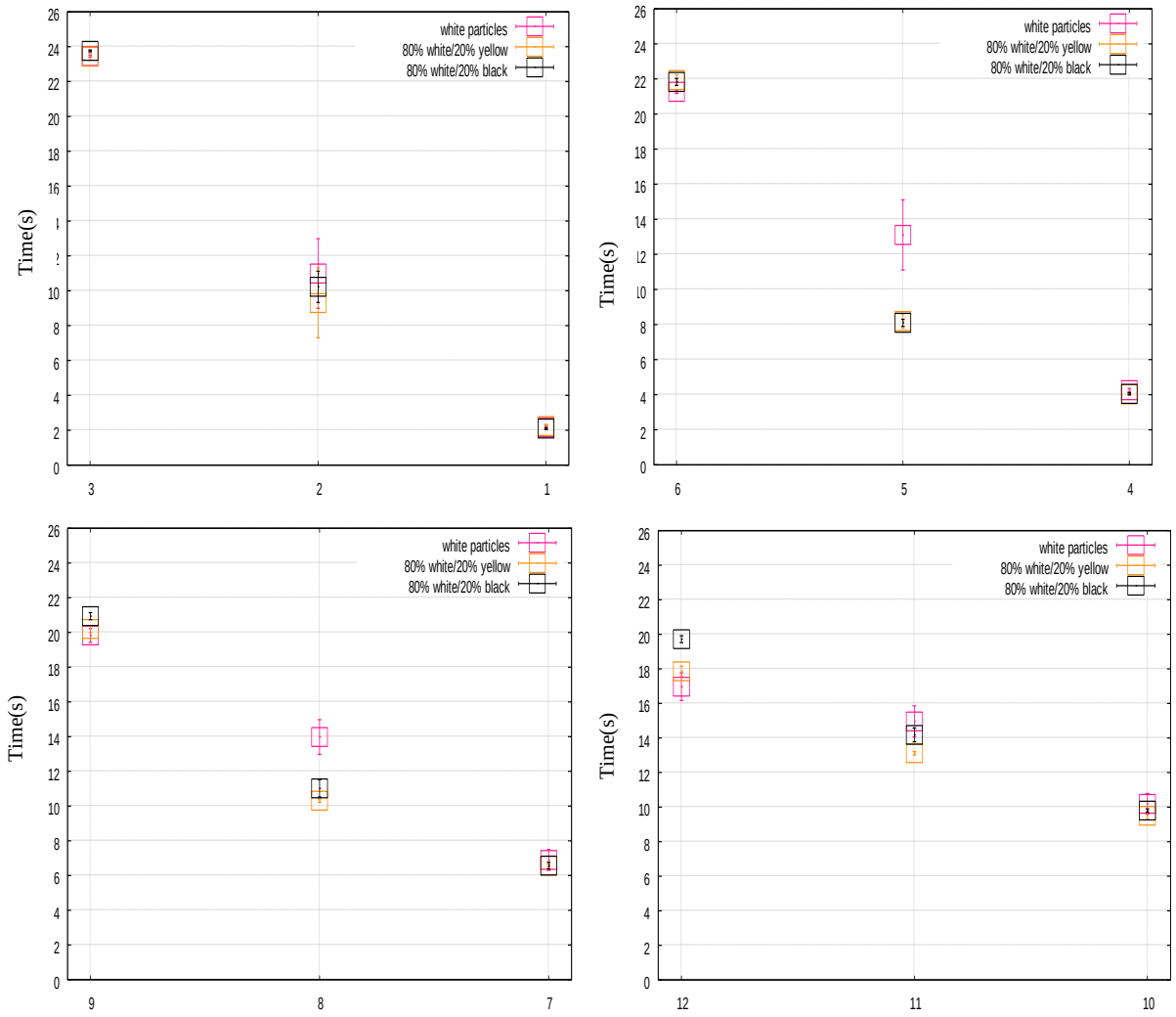

Figure 6.5b: Time taken after the orifice has been opened, for the plastic cuboid in the white (5 mm) monosized particles and the 80% white (5 mm)/ 20% black (4 mm) and 80% white (5 mm)/ 20% yellow (6 mm) binary mixture, to reach the orifice from each of the initial positions 1-12.

The time taken for the plastic cuboid to reache the orifice from position 5 and 8 is greater in the monosized white particles than in the binary mixtures. This is due to the narrower flowing core in the monosized particles which results in the cuboid getting trapped in the boundary region and hence only moving slowly. The wider flowing core in the binary mixtures enables the plastic cuboid at positions 5 and 8 to flow freely to the orifice.

Figure 6.6a shows the time taken after the orifice has been opened, for the plastic triangular prism to reach the orifice, from each of the initial positions 1-12 in the white (5 mm) monosized particles, white (5 mm)/black (6 mm) binary mixture and white (5 mm)/black (4 mm) binary mixture.

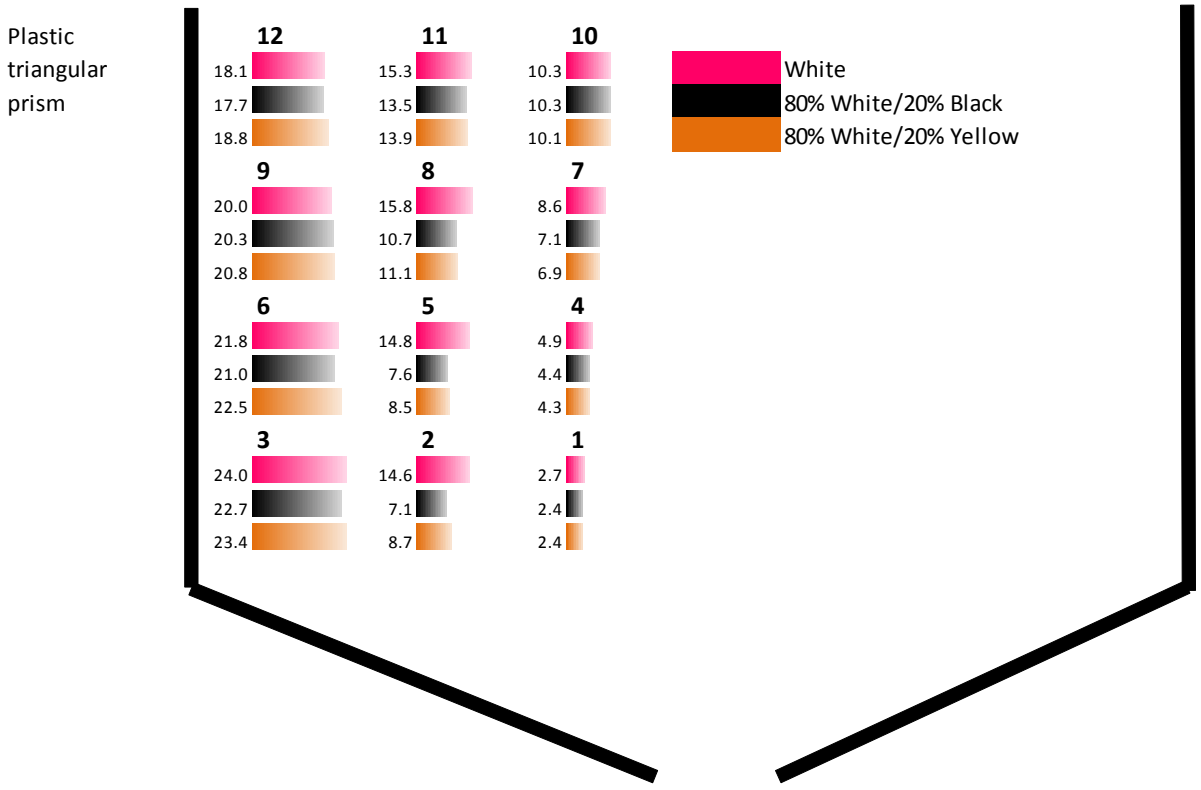

Figure 6.6a: Time taken after the orifice has been opened for the plastic triangular prism in the white (5 mm) monosized particles and the 80% white (5 mm)/ 20% yellow (6 mm) and 80% white (5 mm)/ 20% black (4 mm) binary mixtures to reach the orifice

In similarity to the plastic cuboid the plastic triangular prism takes approximately the same time in the monosized particles and binary mixtures to reach the orifice starting at positions 1, 4, 7 and 10 along the centre line and at positions 3, 6, 9, 12 along the walls.

Figure 6.6b shows the time taken after the orifice has been opened, for the plastic triangular prism to reach the orifice, from each of the initial positions 1-12 in the white (5 mm), white (5 mm)/Yellow (6 mm) binary mixture and the white (5 mm)/ black (4 mm).

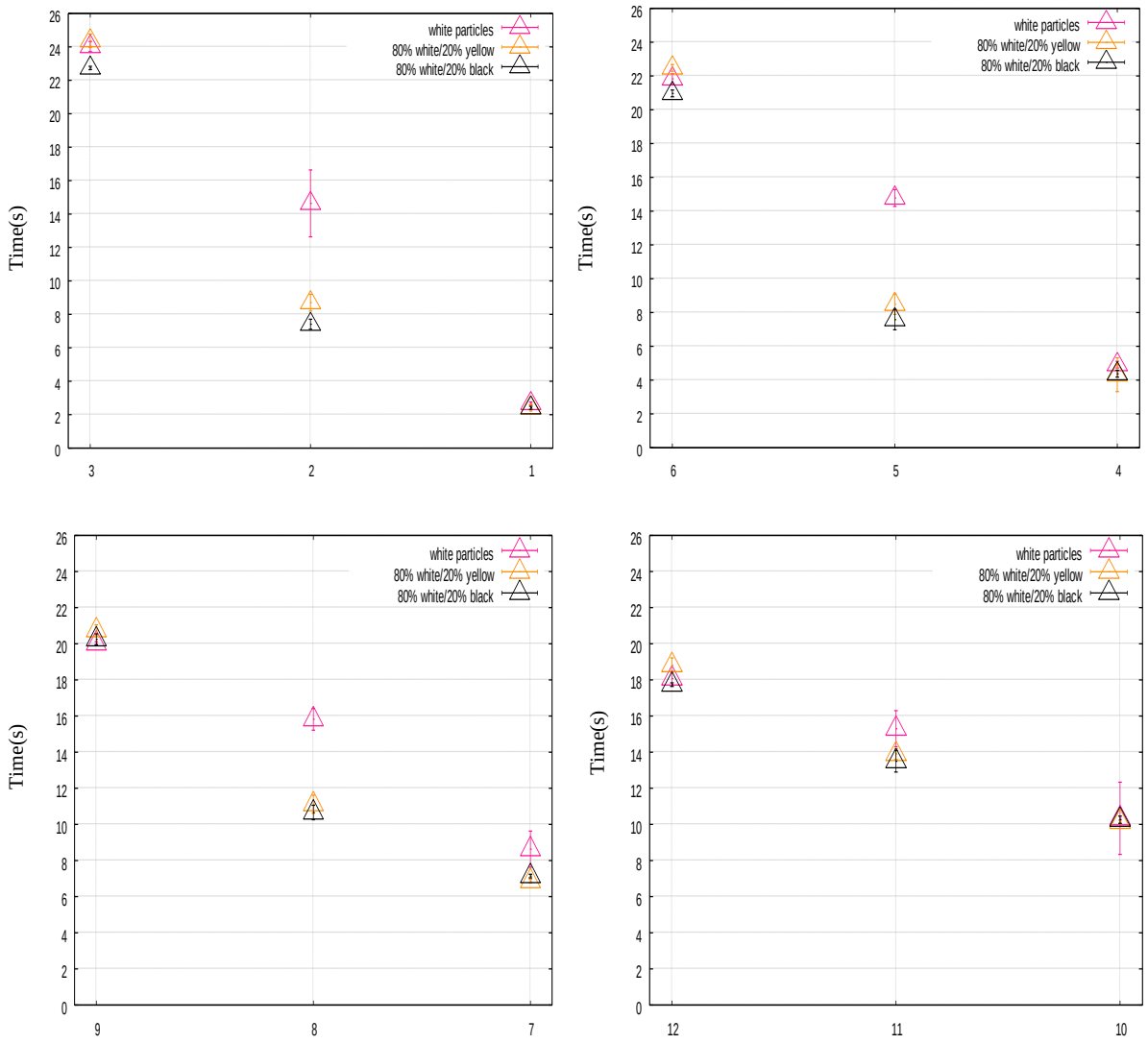

Figure 6.6b: Time taken after the orifice has been opened, for the plastic triangular prism in the white (5 mm) monosized particles and the 80% white (5 mm)/ 20% black (4 mm) and 80% white (5 mm)/ 20% yellow (6 mm) binary mixture, to reach the orifice from each of the initial positions 1-12.

The plastic triangular prism takes nearly twice as long to reach the orifice in the monosized particles than the binary mixtures, when starting from positions 2, 5 and 8. However, the range in the time taken for the plastic triangular prism to reach the orifice is very small when starting from positions 5 and 8. The range in the time taken is larger when starting from position 2. This is because the particles in the flowing core flow past the side of the triangular prism, significantly hindering its movement towards the orifice.

6.3 Conclusion

The results indicate that the shape of the free-cells has a negligible effect on the time taken for them to reach the orifice when placed in the monosized particles and the binary mixtures. Placing the plastic free-cells at position 2 appears to result in a larger range in the results over five trials, but this is to be expected as position 2 is on the edge of the stagnant zone boundary.

The time taken for the plastic-free cells to reach the orifice in the binary mixtures is nearly identical. It is only when the free-cells are positioned in the flowing core and along the stagnant zone boundary at positions 2, 5, 8 and 11 that any differences arise. There is a noticeable difference between the time taken for the plastic free-cells in the binary mixtures to reach the orifice and the time taken for the plastic free-cells in the monosized (5mm) white particles to reach the orifice. The cylinders take less time to reach the orifice in the monosized white particles when starting at positions 3, 6, 9 and 12. The time taken for the free-cells starting at position 5, 8 and 11 are in general the same in the binary mixtures, but the plastic triangular prism and plastic cuboid take longer to reach the orifice in the monosized white (5mm) particles, while the plastic cylinder appears to behave in a less obvious manner.

Further results for the metal and hollow free cells are included on a CD included at the back of this thesis. However they are not discussed and are included for reference.

Rotation of the free-cells during discharge from the silo

7 Rotation of the free-cells during discharge from the silo

The main body of results in this thesis have considered the trajectories of the free-cells as they travel from initial starting positions to the orifice during discharge. Little has been discussed about the rotation, if any, of the free-cells during transit. Electrical engineers designing equipment to be placed in electronic free-cells have requested that an ideal free-cell for use in wireless sensor network applications should not rotate at all. From the large body of data gathered during the current study it is possible to extract information on the rotation of free-cells during their transit from their original positions to the orifice in the discharging silo.

Some preliminary observations concerning the rotation experienced by the free-cells used in this study in the monosized white (5 mm) particles are considered below. The results shown below were obtained from the third of five trials, which were conducted to determine the time taken for each free-cell to reach the orifice from the positions 1 to 12. Observations of the free-cells in each of the five trials showed that the total amount of rotation experienced by each of the plastic free-cells was very much the same in each trial, varying by only about 5º.

It must be stressed that the results in this chapter are by no means an exhaustive discussion of the rotation of the free-cells, but are included for completeness and as a foundation for further study, hence the reason why only the third trial of five was examined.

Figure 7.1 shows how the plastic triangular prism rotates during its transition from position 12 to the orifice in the white (5 mm) monosized particles. In the initial 4 seconds after the opening of the orifice the triangular prism barely rotates, but as it travels through the silo some gradual rotation is observed. The angular velocity of the plastic triangular prism is greatest is the last 2 seconds prior to travelling through the orifice, having an average value of 0.7 rad/s.

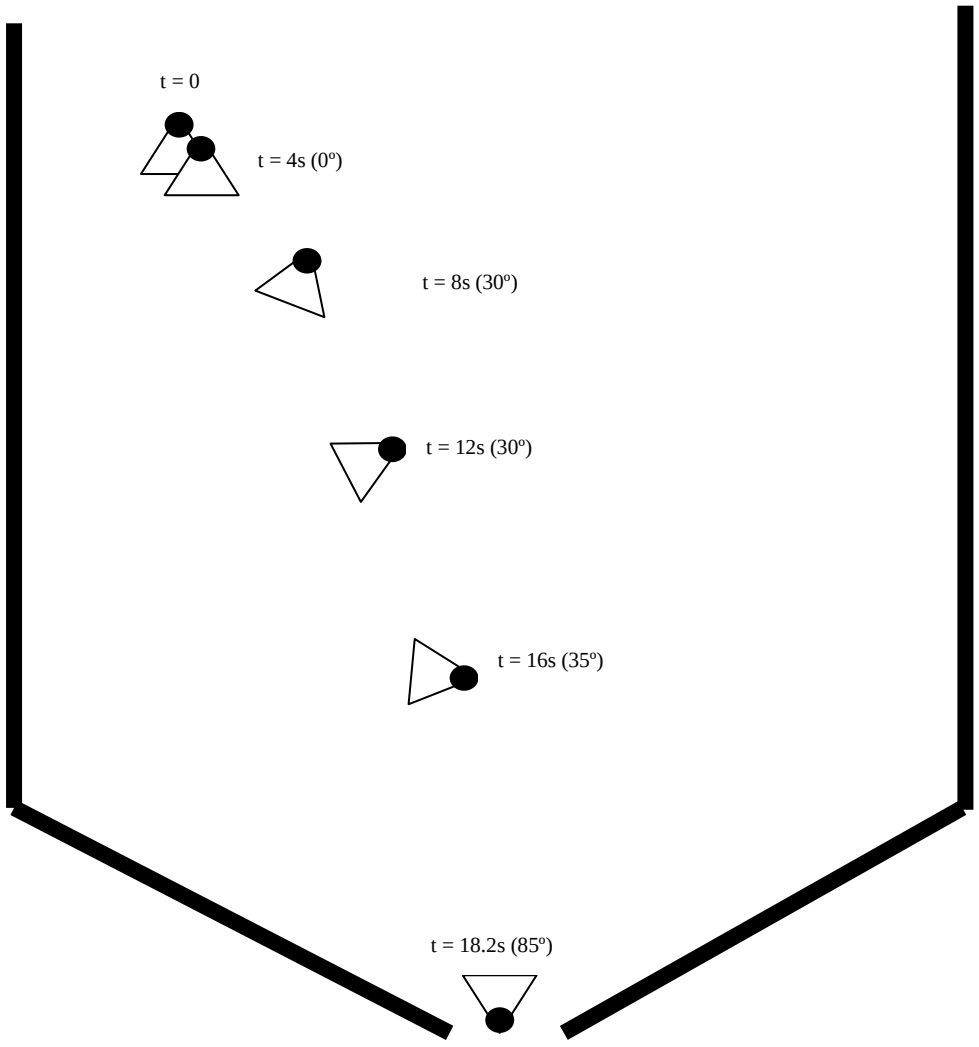

Figure 7.1: The rotation of the plastic triangular prism during its transition from position 12 to the orifice in the white (5mm) monosized particles. The position of the plastic triangular prism is shown at 4 second intervals after the opening of the orifice. The black dot is included as a reference to the position of the plastic triangular prism as it rotates and the angle is the angle the plastic triangular prism rotates each 4 second interval, where a positive angle is clockwise and a negative angle anticlockwise.

Figure 7.2 shows how the plastic cuboid rotates during its transition from position 12 to the orifice in the white (5mm) monosized particles. In contrast to the plastic triangular prism the plastic cuboid does rotate in the first 4 seconds after the initiation of discharge. During the first 12 seconds the plastic cuboid rotates 110º and the plastic triangular prism rotates 60º. However, in the next 5 seconds the triangular prism rotates nearly 120º compared to the plastic cuboid that rotates 70º. The plastic triangular prism appears to experience greater rotation forces in the flowing core than the plastic cuboid.

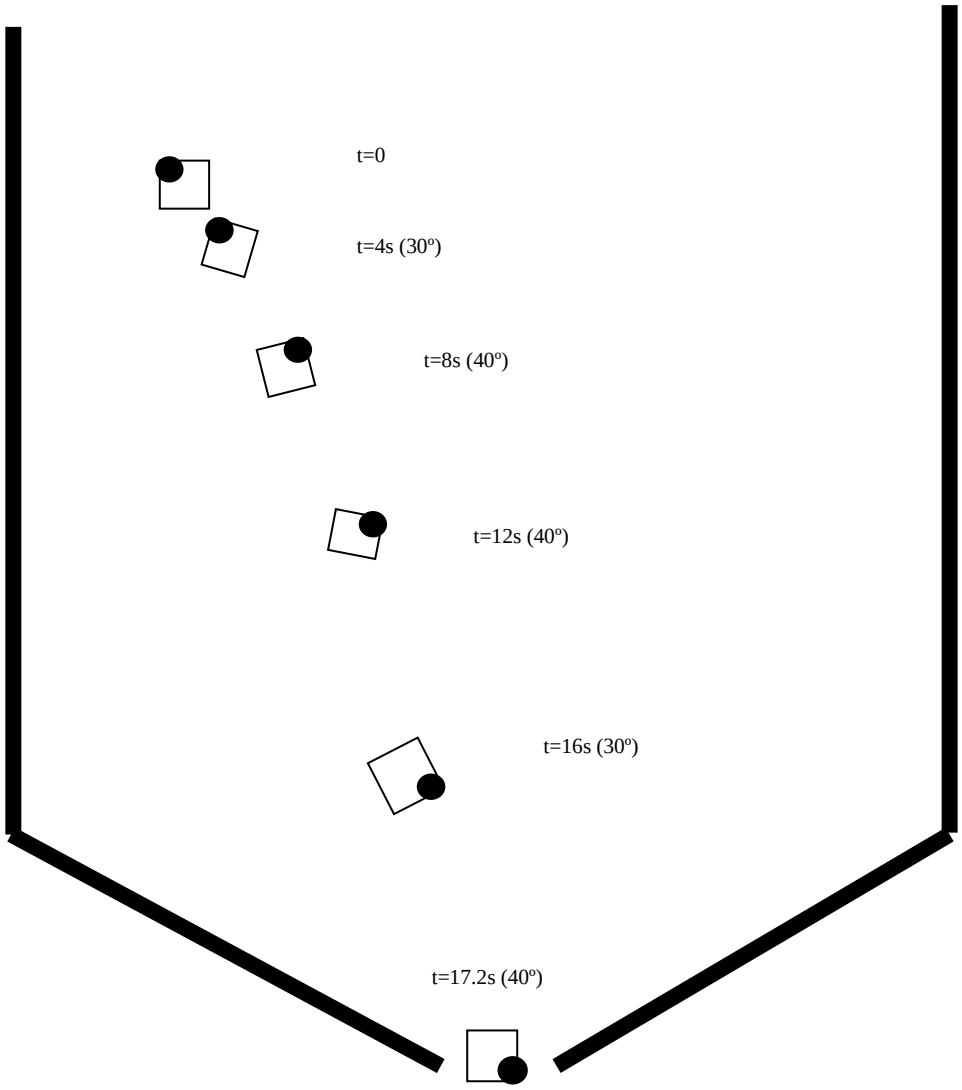

Figure 7.2: The rotation of the plastic cuboid during its transition from position 12 to the orifice in the white (5mm) monosized particles. The position of the plastic cuboid is shown at 4 second intervals after the opening of the orifice. The black dot is included as a reference to the position of the plastic triangular prism as it rotates and the angle is the angle the plastic triangular prism rotates each 4 second interval, where a positive angle is clockwise and a negative angle anticlockwise

Figure 7.3 shows how the plastic cylinder rotates during its transition from position 12 to the orifice in the white (5 mm) monosized particles. The plastic cylinder rotates at a similar rate as the plastic cuboid in the first 4 seconds, but then rotates slower than the plastic cuboid and plastic triangular prism in the next 4 seconds averaging 0.3 rad/s compared to the plastic cuboid at 0.7 rad/s and the plastic triangular prism at 0.5 rad/s. The plastic cylinder reaches the orifice quicker than the plastic cuboid and plastic triangular prism and in 2 seconds travels from a height of approximately 25 cm and rotates at $\pi/2$ rad/s. It is interesting to note that even though the angular velocity of the plastic shapes is different at the same point in time during their trajectories, they all rotate a total of 180º by the time they travel through the orifice.

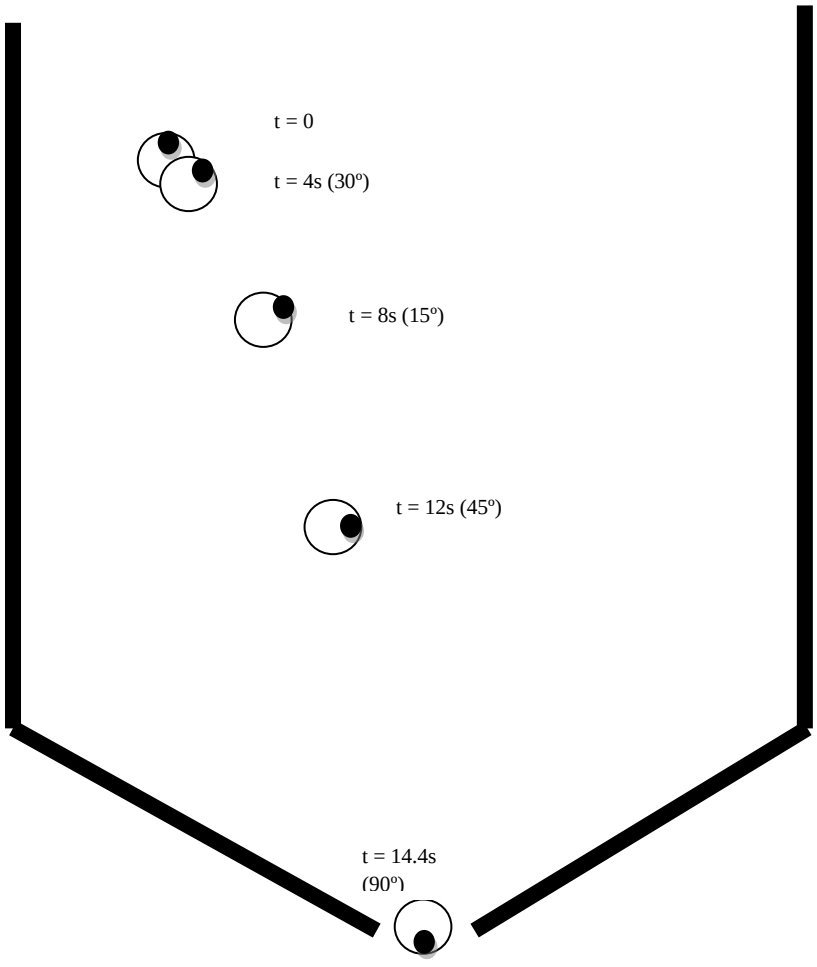

Figure 7.3: The rotation of the plastic cylinder during its transition from position 12 to the orifice in the white (5mm) monosized particles. The position of the plastic cylinder is shown at 4 second intervals after the opening of the orifice. The black dot is included as a reference to the position of the plastic triangular prism as it rotates and the angle is the angle the plastic triangular prism rotates each 4 second interval, where a positive angle is clockwise and a negative angle anticlockwise

Figure 7.4 shows how the metal triangular prism rotates during its transition from position 12 to the orifice in the white (5mm) monosized particles. In contrast to the plastic triangular prism, the metal triangular prism takes 13.3 seconds to reach the orifice compared to 18.2 seconds. The metal triangular prism does not rotate during the first 4 seconds, but then rotates by 40º between 4 and 8 seconds after the initiation of discharge and stops rotating until it reaches the side of the orifice where it slides down the wall and rotates by 20º. The metal triangular prism is observed to orientate itself such that it cuts through the discharging material and slides along the stagnant zone boundary.

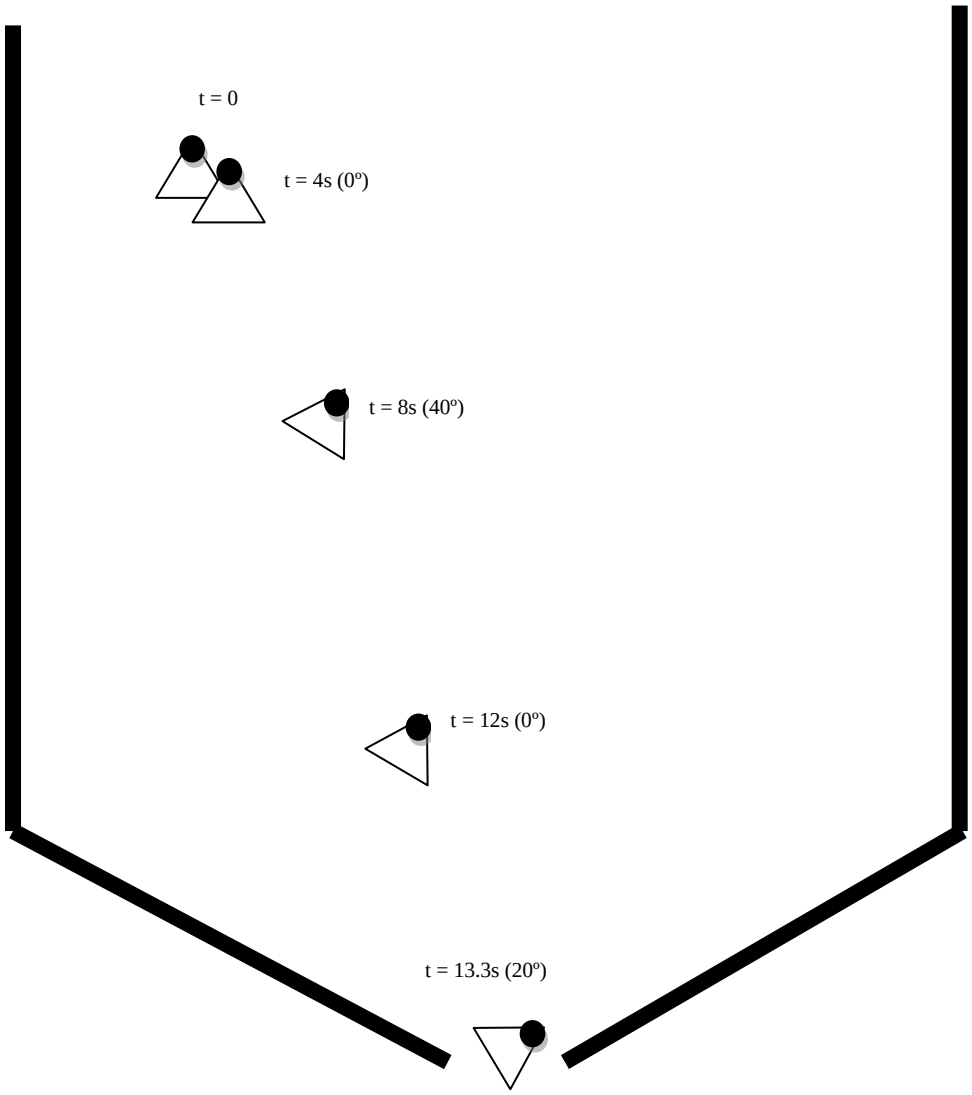

Figure 7.4: The rotation of the metal triangular prism during its transition from position 12 to the orifice in the white (5mm) monosized particles. The position of the metal triangular prism is shown at 4 second intervals after the opening of the orifice. The black dot is included as a reference to the position of the plastic triangular prism as it rotates and the angle is the angle the plastic triangular prism rotates each 4 second interval, where a positive angle is clockwise and a negative angle anticlockwise

Figure 7.5 shows how the metal cuboid rotates during its transition from position 12 to the orifice in the white (5mm) monosized particles. The metal cuboid travels faster than the plastic cuboid taking 13.4 seconds to reach the orifice compared to 17.2 seconds for the plastic cuboid. During the first 4 seconds the metal cuboid is observed to rotate 45º and then a further 30º in the next 4 seconds. The cuboid is observed to orientate itself so that one of its sides is parallel to the tangent of the edge of the flowing core, prior to passing through the orifice the metal cuboid rotates 35º anticlockwise so that the side that lid along the edge of the core slides along the bottom of the hopper.

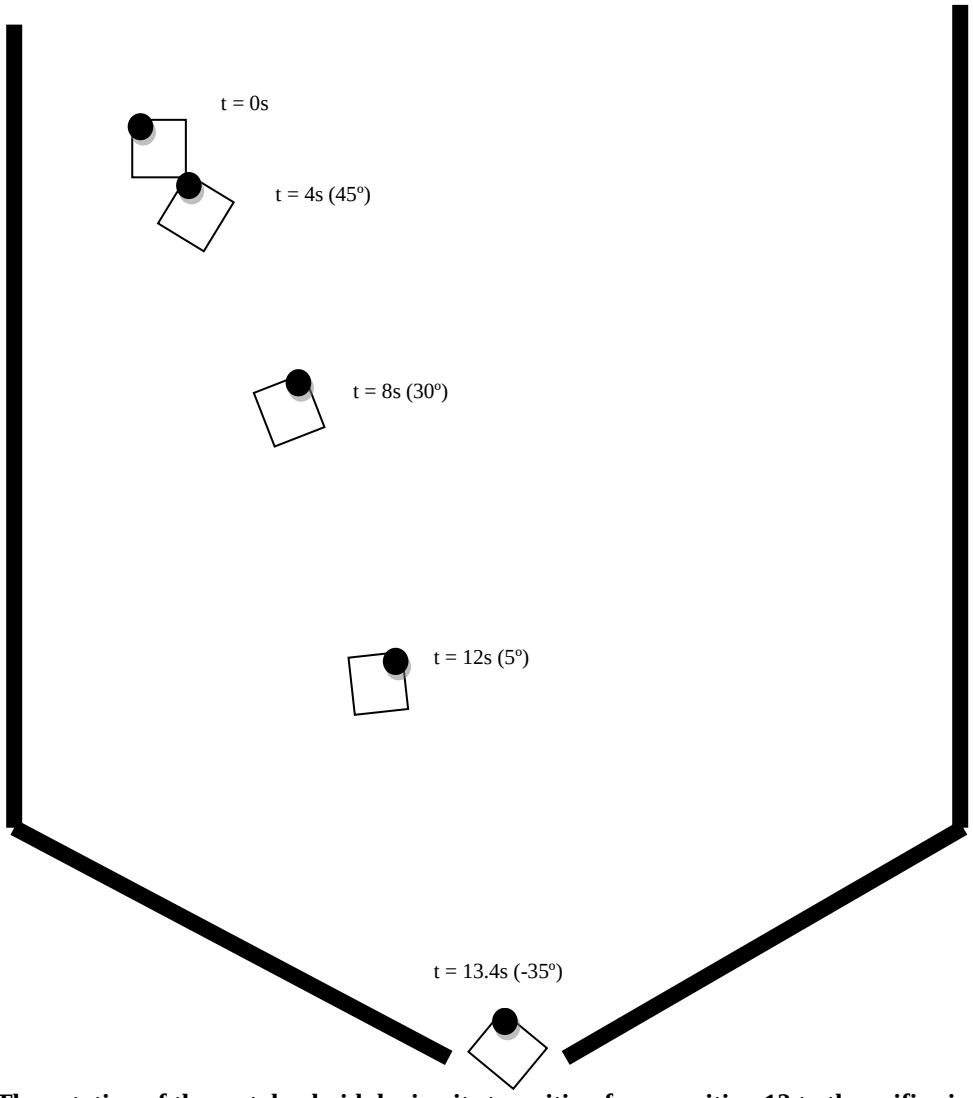

Figure 7.5: The rotation of the metal cuboid during its transition from position 12 to the orifice in the white (5mm) monosized particles. The position of the metal cuboid is shown at 4 second intervals after the opening of the orifice. The black dot is included as a reference to the position of the plastic triangular prism as it rotates and the angle is the angle the plastic triangular prism rotates each 4 second interval, where a positive angle is clockwise and a negative angle anticlockwise

Figure 7.6 shows how the metal cylinder rotates during its transition from position 12 to the orifice in the white (5mm) monosized particles. Interestingly the metal cylinder and the plastic cylinder take nearly the same time to reach the orifice. The metal cylinder takes 1.8 seconds and the plastic cylinder takes 14.4 seconds, a difference of only 0.6 seconds. In some similarity to the metal triangular prism, the metal cylinder rotates by 15º in the first 4 seconds after the initiation of discharge, but then dose not exhibit any more rotation until it reaches the walls of he hopper where it rolls towards the orifice and rotates by 75º.

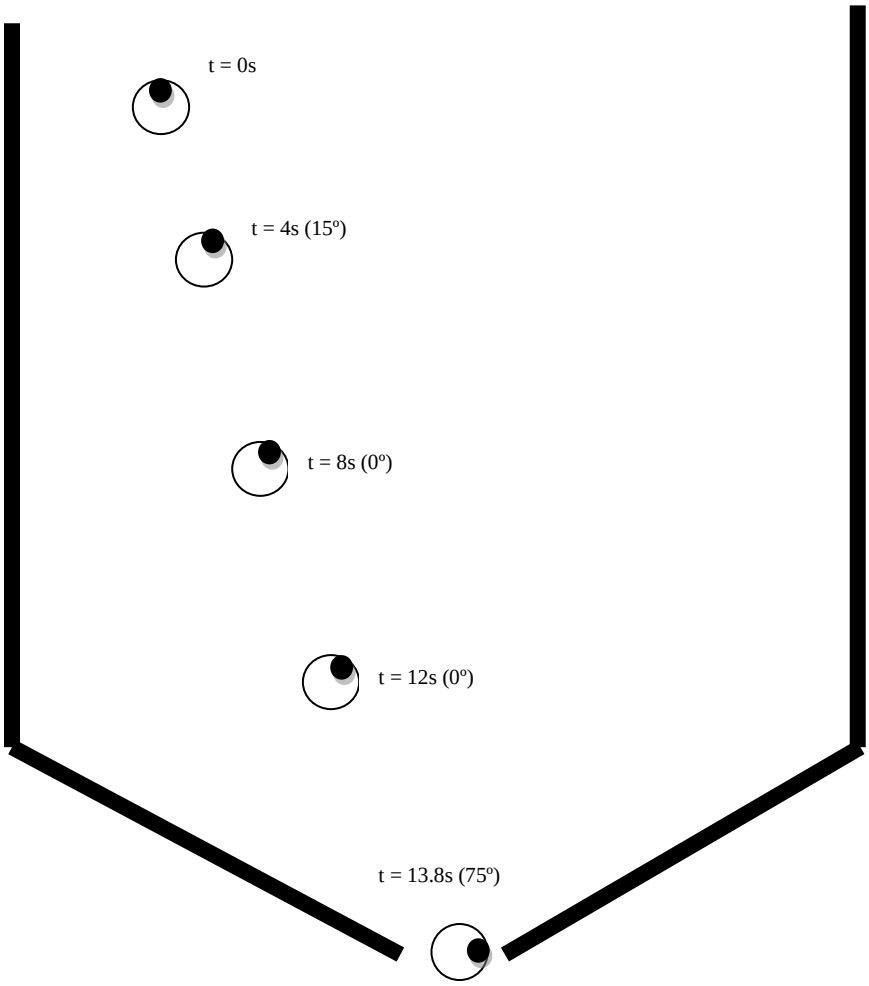

Figure 7.6: The rotation of the metal cylinder during its transition from position 12 to the orifice in the white (5mm) monosized particles. The position of the metal cylinder is shown at 4 second intervals after the opening of the orifice. The black dot is included as a reference to the position of the plastic triangular prism as it rotates and the angle is the angle the plastic triangular prism rotates each 4 second interval, where a positive angle is clockwise and a negative angle anticlockwise.

Figure 7.7 shows how the hollow triangular prism rotates during its transition from position 12 to the orifice in the white (5 mm) monosized particles. In similarity to the plastic triangular prism, the hollow triangular prism does not rotate in the first 4 seconds after the initiation of discharge. Over the next 8 seconds the hollow triangular prism rotates by 90º which is in contrast to the plastic triangular prism that rotates 60º in the next 8 seconds after the orifice has been opened. The hollow triangular prism then rotates a further 90º until it reaches the orifice, compared to the plastic triangular prism that rotates a further 120º until it reaches the orifice.

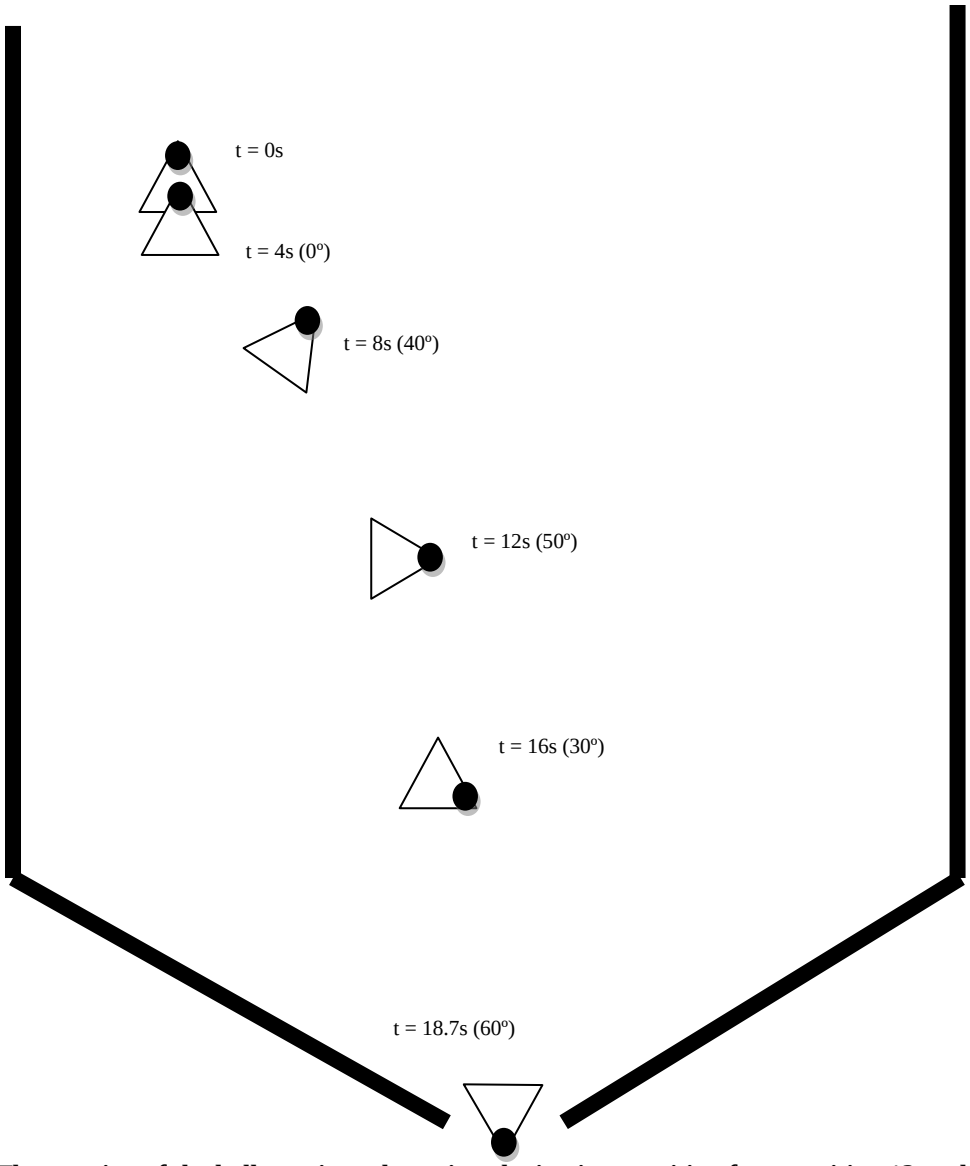

Figure 7.7: The rotation of the hollow triangular prism during its transition from position 12 to the orifice in the white (5mm) monosized particles. The position of the hollow triangular prism is shown at 4 second intervals after the opening of the orifice. The black dot is included as a reference to the position of the plastic triangular prism as it rotates and the angle is the angle the plastic triangular prism rotates each 4 second interval, where a positive angle is clockwise and a negative angle anticlockwise.

Figure 7.8 shows how the hollow cuboid rotates during its transition from position 12 to the orifice in the white (5mm) monosized particles. The hollow cuboid behaved quite differently to the plastic and metal cuboids. The hollow cuboid rotated by 5º in the first 4 seconds after the initiation of discharge compared to the plastic cuboid that rotated by 30º and the metal cuboid that rotated by 45º. Between 4 seconds and 12 seconds after the opening of the orifice the plastic cuboid experienced 115º of rotation compared to the plastic cuboid and metal cuboids that rotated 80º and 35º respectively. The hollow cuboid rotates a further 130º over the next 6.5 seconds until it reaches the orifice, compared to the plastic cuboid that rotates a further 70º. The hollow cuboid is clearly affected by the fluctuating stress field in discharging silo.

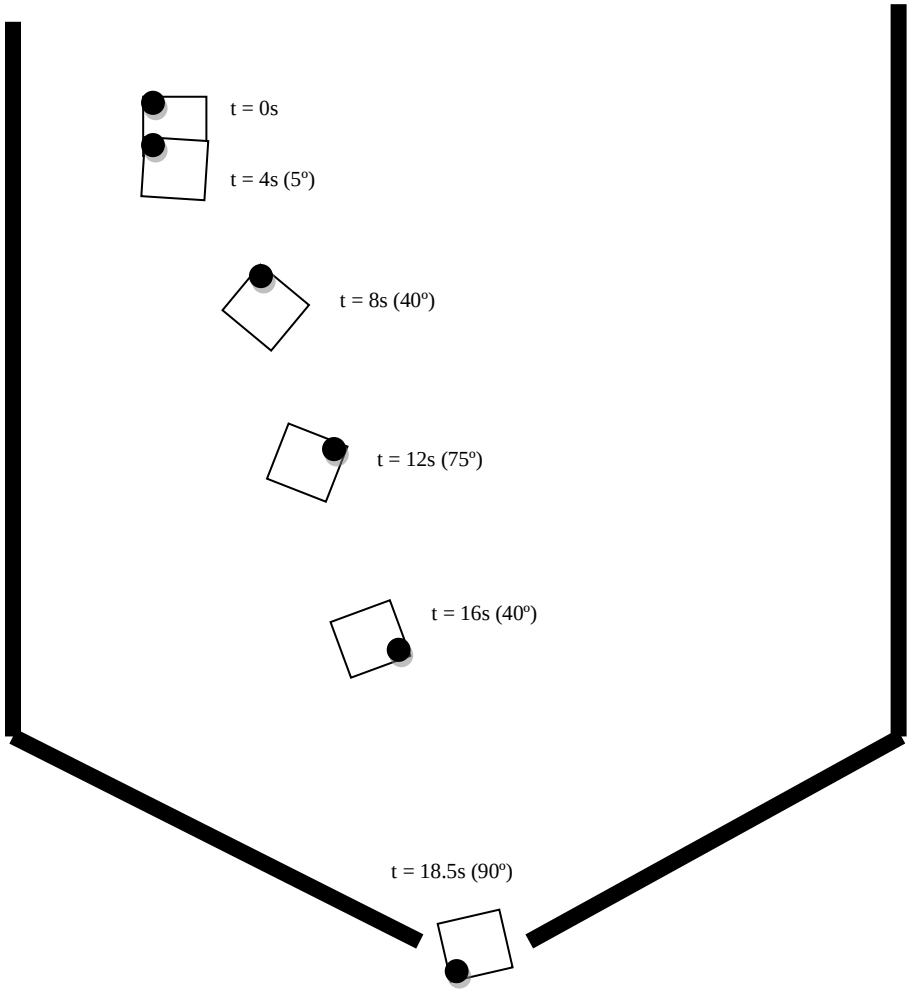

Figure 7.8: The rotation of the hollow cuboid during its transition from position 12 to the orifice in the white (5 mm) monosized particles. The position of the hollow cuboid is shown at 4 second intervals after the opening of the orifice. The black dot is included as a reference to the position of the plastic triangular prism as it rotates and the angle is the angle the plastic triangular prism rotates each 4 second interval, where a positive angle is clockwise and a negative angle anticlockwise

Figure 7.9 shows how the hollow cylinder rotates during its transition from position 12 to the orifice in the white (5mm) monosized particles. Unlike the metal and plastic cylinders and the other free-cells the hollow cylinder rotates anticlockwise by 40º during the first 4 seconds after the initiation of discharge, it is unknown what is causing this effect. The hollow cylinder then rotates by 60º clockwise in the next 4 seconds and then continues to rotate at a steady average angular velocity of 0.17 rad/s until it reaches the orifice. The hollow cylinder in total rotates as much as the metal cylinder prior to passing through the orifice.

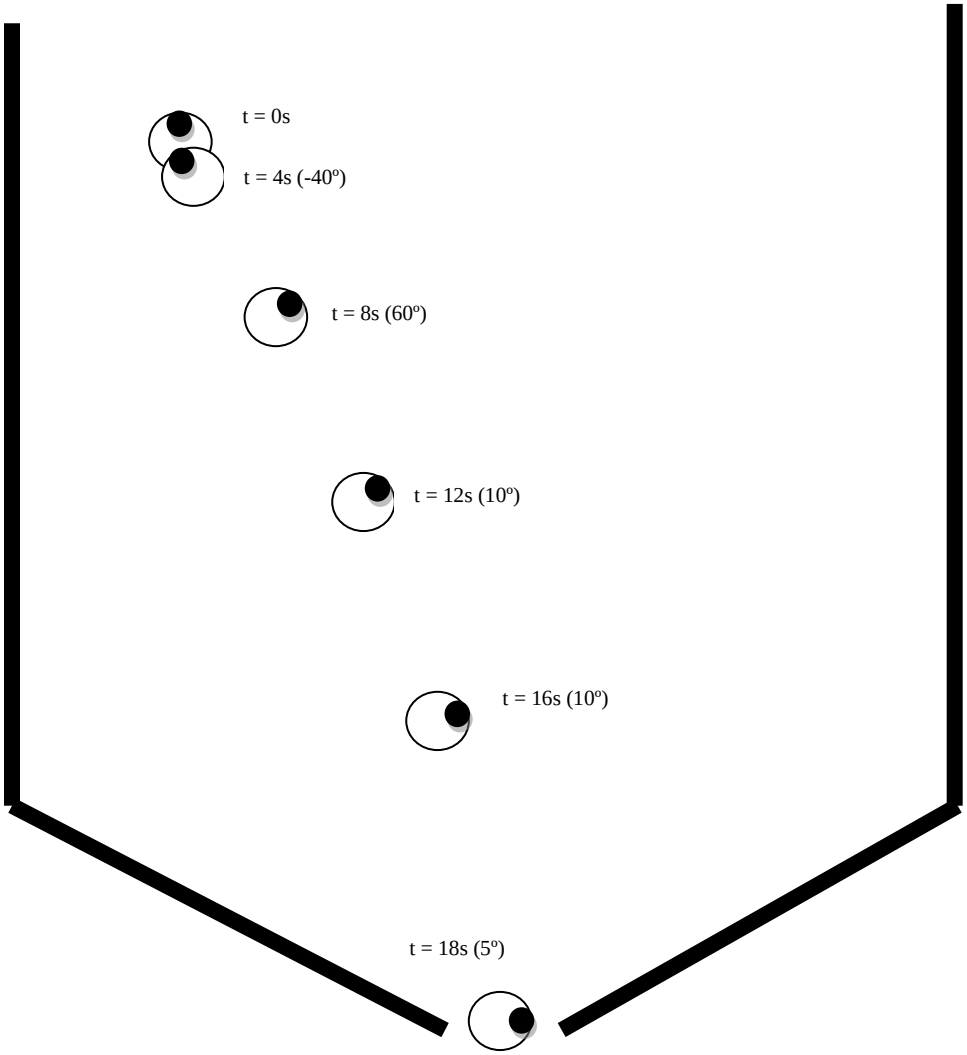

Figure 7.9: The rotation of the hollow cylinder during its transition from position 12 to the orifice in the white (5mm) monosized particles. The position of the hollow cylinder is shown at 4 second intervals after the opening of the orifice. The black dot is included as a reference to the position of the plastic triangular prism as it rotates and the angle is the angle the plastic triangular prism rotates each 4 second interval, where a positive angle is clockwise and a negative angle anticlockwise.

7.1 Conclusion

The plastic and hollow triangular prism, cuboid and cylindrical free-cells were all found to rotate by a total of 180º from their initial starting position, at position 12, to the point where they flowed through the orifice. However, the rate of rotation was different throughout their trajectories. The metal free-cells tend to rotate in the first several seconds of their trajectories, but then do not rotate throughout most of their time in the silo, until they reach the bottom of the hopper and roll towards the orifice. The metal free-cells tend to flow through the other particles, rather than with them, in a similar style to denser particles segregating through lighter particles. The velocity of the particles throughout the silo tends to vary at different positions in the hopper. The free cells are larger, so it is easy to imagine that some torque is bound to be experienced by the free cells due to this velocity gradient and hence some rotation.

The rotation experienced by the free-cells may be caused also be caused by fluctuating local stresses as discussed in section 2.2 between the particles, or brought about from the sliding friction between the particles and the free-cells.

The free cells in this study can only rotate around the axis perpendicular to the front and back walls. This limits their freedom of movement. In a 3D silo a velocity gradient is also present, so the results in this section may be a good representation of the rotation likely to be experienced in an industrial scale silo.

The Discrete Element Method

8 The Discrete Element Method

8.1 Introduction

The discrete element method (DEM) is the name given to a numerical method first applied to granular systems by Cundall and Strack in 1979. The basic idea of the DEM is that particle systems can be modelled by considering the interactions between the individual particles that constitute the whole system. The interactions between the particles consist of various forces and can include the elastic force, frictional forces, cohesion forces, van der Waals force and electrostatic forces. The particle acceleration and velocity are calculated by application of Newton's second law.

The DEM been extensively applied to simple 2D systems of spheres but applications have recently been extended considerably to model sphero-discs (Li et al., 2004), sphero-cylinders (Langston, 2004), corn-shaped particles (Tao, 2010), rectangular particles (Kohring et al., 1995) and cubes (Fraige, 2008). DEM methods have also been applied to binary mixtures of spheres (Anand et al., 2008) but as yet systems involving free-cells have not been modelled using the DEM. The DEM code to model the free-cells used in this study was developed by Dr Paul Langston at the University of Nottingham using Microsoft Visual Basic 6.

There was no significant contribution to the code in this work. The code was rewritten in FORTRAN by Paul Langston to enable any future developments, such as parallelization, to be undertaken easily. It was considered, in this work, that the simulation time of the FORTRAN program may less than the simulation time of the Visual Basic program, but there is no evidence that this is the case.

The code was treated as a 'black box' in which the values of the input parameters were determined by experiment and substituted into an input subroutine.

A basic DEM simulation involves recording the initial positions of all the particles. In a silo/hopper this process can begin by determining seeding positions at which the particles start. From these initial positions particle interactions are determined and new positions are

calculated. Particle positions and velocities are determined each time step and contact force calculations are recorded only during the event of a contact with the wall or another particle. The main feature of the DEM is that the time step should be small enough so that disturbances cannot propagate from any one particle further than its immediate neighbours. The forces and accelerations can be assumed to be constant over one single time step and the velocity varies linearly.

The application of the DEM involves four basic steps (Asmar, 2002):

1. Searching the system and referencing all particles (initial accelerations, velocities and positions).
2. Applying interaction laws (calculating forces and moments) at all particle-particle and particle-wall contacts.
3. Applying Newton's second law to determine particle motion (new accelerations, velocities and positions).
4. Updating and repeating from step 1.

In this study the DEM method was applied to the modelling of a batch of monosized spheres, a binary mixture of spheres of the same density and a set of polyhedral particles.

The determination of the new velocities and displacements of the particles requires integrating the force. Much work has been undertaken by various researches to determine accurate force models and integration schemes.

8.2 Force Models

Kruggel-Emden (2006) et al. studied various force models to accurately model normal contacts between spherical particles and compared them to results obtained from experiments. They divided force models into four groups: Continuous potential models, linear viscoelastic models, non-linear viscoelastic models and hysteric models. In continuous potential models the normal contacts can be modelled as linear spring stiffness's and it is assumed that the force potential energy is in equilibrium with the gravitational force on the surface of the

spheres. In linear viscoelastic models the normal force includes an elastic repulsion, modelled as an elastic spring and a viscous dissipation part modelled as a displacement rate dependent damper. Non-linear viscoelastic models apply Hertz theory in which the normal force is proportional to the elastic modulus of the two spheres in contact. Hysteric models include the effect of plasticity and avoid the usage of a velocity dependent damping. Hysteric models may be linear or non-linear.

Di Renzo and Di Maio (2004) compared three contact force models. A linear Hooke's spring model and a non-linear model based on Hertz theory in the normal direction and the no-slip solution of the theory developed by Mindlin and Deresiewicz (1953) for the tangential direction and a non-linear model with hysteresis, based on the theory of Hertz and Mindlin and Deresiewicz for elastic frictional collisions. Simulations of an elastic collision of a sphere with the flat surface of a wall on the macroscopic scale were compared with experimental results of Kharaz et al. (2001) and on the microscopic scale with an approximated analytical solution derived by Maw et al. (1976). It was found that the linear Hooke's spring model gives better results than the non-linear Hertz model and gives near equivalent results to the complete Mindlin and Deresiewicz model. On the microscopic scale the evolution of the tangential forces, velocities and displacements predicted by the linear model, show better agreement with the Mindlin and Deresiewicz theoretical solution. Linear model parameters precisely evaluated.

Thornton et al. (2011) compared the results obtained using different contact force models to the problem of an elastic sphere impacting with a wall. It was shown that excellent results can be obtained using the simple linear-spring model, when an appropriate spring stiffness is applied, and an appropriate ratio of tangential stiffness to normal stiffness is used. They found that the simplification of the Hertz Mindlin and Deresiewicz model by Di Renzo and Di Maio significantly alters the collisional behaviour and occasionally gives unphysical results.

8.3 Time integration schemes

The acceleration, velocity and displacement of the individual particles are obtained by integration of the force term. If an accurate simulation of the particles is to be obtained it is paramount that the integration scheme applied is both accurate and efficient.

Kruggel-Emden et al. (2008) tested various time integration schemes for the simulation of a particle impacting a fixed wall. They noted that time integration schemes can be divided into three main categories: one-step, multi-step and predictor-corrector methods. One-step methods include, amongst others, the Taylor series (Shampine, 1994) and central difference schemes (Cundall and Strack, 1979). Multi-step methods include the Verlet (1967) scheme and the predictor-corrector methods include the Adams-Bashforth-Moulton (Engeln-Mullges and Uhlig, 1996). The integration of the equations of motion accounts for a fraction of the total computational cost in each time step, however appropriate integration schemes enable the use of larger time steps and can speed up DEM simulations (Kruggel-Emden, 2008).

Kruggel-Emden et al. (2008) found that the most efficient time integration scheme in terms of computational costs was the Taylor expansion of order two and three and in systems in which most of the computing time is spent on other tasks than the time integration the position Verlet or the improved Verlet schemes are appropriate.

Fraige and Langston (2003) compared time integration schemes with application to a particle impacting a wall. These schemes were the Euler scheme, the Half-step leapfrog Verlet scheme and the Velocity modified Euler scheme. They found that the Half-step leapfrog Verlet scheme was the most accurate integration scheme overall.

8.4 Modelling 3D spheres

Spherical particles are modelled as ‘soft’ slightly poly-disperse spheres with linear interactions. The term ‘soft’ is to indicate that a certain amount of overlap, typically up to 1% of the diameter of the spheres is allowed during collisions. The method is described in detail

in Langston (1995), Asmar (2002). A brief summary of the main theoretical principles applied to the simulation is given below.

8.5 Searching and referencing (Langston, 1995)

At each time step in the simulation the model must first determine which particles are in contact. In a system containing N particles the search can involve $O(N^2)$ steps. To reduce the number of steps involved in the search for contacts to a problem of size $O(N)$, two methods are applied that were developed by Asmar (2002).

8.5.1 Neighbourhood lists (Asmar, 2002)

In Neighbourhood list book keeping schemes the program records those particle pairs with a separation distance (r between the particle centres) less than a critical value r_0, which is larger than the interaction cut-off r_i (a separation distance beyond which no interaction is assumed detectable) (Figure 8.1).

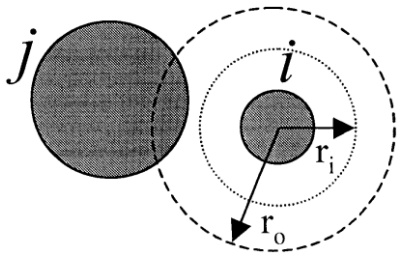

Figure 8.1: Schematic diagram of particle cut-offs

For each particle a list of neighbouring particles is stored. In subsequent time steps only particle pairs in these lists are checked for possible contact. All the neighbourhood lists are updated when there is a possibility of a particle transverse from beyond r_0 to within r_i, that is when the maximum distance travelled by any particle is equal or greater than $0.5(r_0 - r_i)$ or when new particles enter the system.

When simulating polydisperse particles, the neighbourhood lists are set up based on the largest possible value of r_i. In this study a value of $r_0 = 1.1r_i$ is used. A larger ratio would mean that the neighbourhood lists would not have to be recompiled so often, but at the expense of a longer list which would take longer to process and require more memory.

Particle pairs in contact are sorted according to a numerical index with respect to $i < j$. The contact (i, j) is the same as contact (j, i) therefore to avoid analysing the same contact twice the contact (i, j) is taken by particle i analysis, but the contact (j, i) is ignored when the search around particle j is conducted.

8.5.2 Zoning or boxing (Asmar, 2002)

To avoid having to test each particle pair for potential overlap a zoning or boxing algorithm is implemented (Langston 1995), where the system is divided into cubic cells (Figure 8.2). The cell size must be equal to the cubic outer radius of the neighbourhood list search region, r_0. All the particles whose centres are within a cell are referenced to that cell.

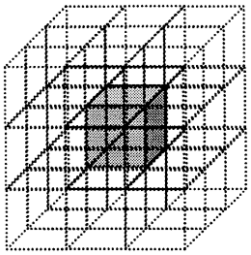

Figure 8.2: Schematic diagram of zones

Applying he zoning algorithm means that when the program sets up the neighbourhood list, it uses the referenced particles to allocate a specific particle and limits the search for 'closeness' against other particles in that one and adjacent zones only. An upper limit on the number of particles in each cell is imposed due to array size limitations. The efficiency of the algorithm is influenced by the particle size distribution which affects the number of particles that can fit in one cell. The maximum number of cells is limited due to the limits of the computer memory, which influences the cell size.

The Neighbourhood lists and boxing algorithm takes the form:

The particles in contact are determined by the following process.

Outside the loop for each particle i

i) Consider a particle i

ii) Go around loop $i = 1$ to $n - 1$

iii) For each particle *i* specify the index that corresponds to the particle in the neighbourhood list *ListFirst*

iv) Get the *x,y,z* co-ordinates of particle *i* and then determine the zone it is located in and the neighbouring zones.

Within the neighbouring zones

i) Find the number of particles in each zone and check for possible contacts with particle *i* only if the number of particles in the zone is greater than zero.

For each particle *j* in each zone

i) If the distance between particle *i* and particle *j* is below a critical threshold r_0, which is somewhat larger than the interaction cut-off r_i, then add an index corresponding to particle *j* in the neighbourhood list of particle *i*.

If no particles are left the last particle added to the list specifies the index that corresponds to the last neighbour of particle *i* in the neighbourhood list *ListLast*.

8.6 Modelling of the contact forces (Asmar, 2002)

The contact forces modelled in the DEM code are elastic, friction and damping forces (Figure 8.3). These forces are resolved in the normal and tangential directions. The linear spring-dashpot-slider model is used to model the interactions in the code.

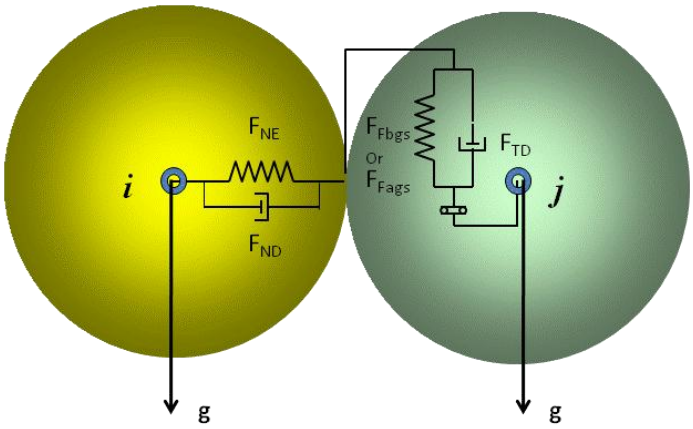

Figure 8.3: Schematic diagram of contact forces, where F_{NE} is the normal elastic force, F_{ND} is the normal damping force, F_{TD} is the tangential damping force, F_{bgs} is the friction force before gross sliding, F_{ags} is the friction force at and after gross sliding and *g* is the acceleration due to gravity.

The normal contact force F_N is given by,

$$F_N = F_{NE} + F_{ND} \qquad \textbf{8.1}$$

where F_{NE} is the normal elastic force and F_{ND} is the normal damping force.

The tangential contact force F_T is limited by the Coulomb frictional limit at which point the surface contact shears and the particles begin to slide over each other. F_T is given by

$$F_T = F_{Fbgs} + F_{TD} \qquad \textbf{8.2}$$

below the coulomb frictional limit, and

$$F_T = F_{Fags} \qquad \textbf{8.3}$$

above the Coulomb frictional limit, where F_{Fbgs} is the elastic component of the friction force prior to gross sliding, F_{TD} is the tangential damping force and F_{Fags} is the friction force at and after gross sliding.

8.6.1 The normal elastic force

The normal elastic force F_{NE} represents the repulsive force between any two particles. It is calculated using a Hooke's linear spring relationship,

$$F_{NE} = K_N \delta_N \quad \textbf{8.4}$$

where K_N is the stiffness of the spring in the normal direction and δ_N is the displacement between particles *i* and *j*.
The maximum overlap is dependent on the stiffness K_N

8.6.2 The normal damping force

The normal damping force F_{ND} is modelled as a dashpot that dissipates a proportion of the relative kinetic energy. It is given by

$$F_{ND} = C_N v_N \quad \textbf{8.5}$$

where v_N is the normal component of the relative velocity, C_N is the normal damping coefficient, which is chosen to give a required coefficient of restitution ε defined as the ratio of the normal component of the relative velocities before and after collision. C_N is given by

$$C_N = 2\gamma\sqrt{(m_{ij} K_N)} \quad \textbf{8.6}$$

where γ is the coefficient of critical damping and is calculated as,

$$\gamma = -\frac{\ln(\varepsilon)}{\sqrt{\pi^2+\ln^2(\varepsilon)}} \quad \textbf{8.7}$$

and

$$m_{ij} = \frac{m_i m_j}{m_i+m_j} \quad \textbf{8.8}$$

where m_{ij} is the mass of particles i and j with masses m_i and m_j respectively.

The coefficient of restitution is assumed to be the same for both types of particles in the binary mixture.

8.6.3 Friction force

The friction force is modelled to represent elastic and plastic deformation components. The variation of the friction force prior to gross sliding F_{Fbgs} is calculated using a simple Hooke's linear spring relationship, given by

$$F_{Fbgs} = K_T \delta_T \quad \textbf{8.9}$$

where K_T is the tangential stiffness coefficient and δ_T is the total tangential displacement between the surfaces since their initial contact. The total tangential force is limited by the Coulomb frictional limit. If δ_T exceeds δ_{Tmax} then sliding occurs and δ_T does not increase. In this case the friction force after gross sliding F_{Fags} is calculated as

$$F_{Fags} = \mu F_{NE} \quad \textbf{8.10}$$

where μ is the coefficient of friction and F_{NE} is the normal elastic force defined in equation 8.4.

δ_{Tmax} is calculated by the following relationship

$$\delta_{Tmax} = \delta_R \delta_N \quad \textbf{8.11}$$

where δ_R is a constant.

8.6.4 Tangential damping force

The tangential damping force F_{TD} is modelled as a dashpot that dissipates energy from the tangential motion. It is given by,

$$F_{TD} = C_T v_T \quad \textbf{8.12}$$

where v_T is the tangential component of the relative velocity between the particles, C_T is the tangential damping coefficient, which can be chosen to give a specified coefficient of restitution ε defined as the ratio of the post to pre-collisional tangential component of the relative velocity and given by

$$C_T = 2\gamma\sqrt{m_{ij}K_T} \quad \textbf{8.13}$$

where γ and m_{ij} are the same as in equations 8.7 and 8.8.

The calculation of the tangential force is omitted if gross sliding occurs because K_T is is zero in this region. During gross sliding F_{Fags} is the total force that dissipates energy from the tangential motion.

8.6.5 Rolling Friction

The rolling friction is modelled as an angular torque arising from the elastic hysteresis loss or viscous dissipation. The value of the particle-particle $\mu_{pp,r}$ and particle-wall $\mu_{pw,r}$ rolling friction coefficients are usually different values. It has been shown that rolling friction is necessary in achieving a simulation that accurately models the kinematics of spherical particles. Ai et al. (2011) defined two major functions of rolling resistance in a particulate system i) to dissipate energy during relative motion, which is important for dynamic flow conditions and ii) providing "packing support" so that the stability of a particulate system with an inherently stable geometry is preserved, which is important in the static phase.

8.7 Particle-wall contacts

The interaction of a particle with the hopper walls is modelled in a similar fashion to the particle-particle contact. A particle at the wall can have more than one contact with the walls if it is located in a corner. Different interaction constants can be used for particle-wall interactions.

8.8 Modelling of external forces

8.8.1 Gravitational force

The gravitational force is included in the model as a constant linear force vector acting at the centre of each particle.

8.8.2 Application of Newton's second law

Particle *i* motion is calculated by Newton's equation of motion as follows.

8.8.3 Translational motion

Translational motion can be described by the equation

$$m\frac{dv}{dt} = m\boldsymbol{g} + \sum F_n + \sum F_t \qquad \textbf{8.14}$$

where *m* is the particle mass, $\sum F_n$ is the sum of the normal forces from surrounding particles and the normal force from the wall, acting on the particle and $\sum F_t$ is the sum of all the tangential forces from surrounding particles and the wall acting on the particle, v is the linear velocity of the particle. The acceleration of the particle $\frac{dv}{dt}$ is computed from the net force, which is then integrated for velocity and displacement.

8.8.4 Rotational motion

Rotational motion can be described by the equation

$$I\frac{d\omega}{dt} = \sum(\mathrm{R}\times F_t - \mu_r R|F_n|\hat{\omega}) \qquad \textbf{8.15}$$

where ω_i and I_i are the angular velocity and moment of inertia of the particle respectively and $\boldsymbol{R}$ is a vector from the centre of the particle to the contact point with magnitude equal to the particle radius R.

The trajectories of all the particles can be traced by integrating equations 8.14 and 8.15.

Assuming that acceleration is constant over the time step Δt, the velocity vector of each particle is then determined from,

$$\dot{\boldsymbol{r}}_{t+\Delta t} = \dot{\boldsymbol{r}}_t + \ddot{\boldsymbol{r}}_t \Delta t \qquad \textbf{8.16}$$

where $\boldsymbol{r}$ is the position vector, $\dot{\boldsymbol{r}}$ is the linear velocity vector and $\ddot{\boldsymbol{r}}$ is the linear acceleration vector, and the angular velocity vector from

$$\dot{\boldsymbol{\theta}}_{t+\Delta t} = \dot{\boldsymbol{\theta}}_t + \ddot{\boldsymbol{\theta}}_t \Delta t \qquad \textbf{8.17}$$

where $\boldsymbol{\theta}$ is the angle vector, $\dot{\boldsymbol{\theta}}$ is the angular velocity vector and $\ddot{\boldsymbol{\theta}}$ is the angular acceleration vector.

The position and orientations at the end of the next time step are then determined using an explicit numerical integration, where the positions at $t + \Delta t$ are obtained directly from the acceleration at t. Applying the Euler integration scheme, the position is determined, thus

$$\boldsymbol{r}_{t+\Delta t} = \boldsymbol{r}_t + 0.5(\dot{\boldsymbol{r}}_t + \dot{\boldsymbol{r}}_{t+\Delta t})\Delta t \qquad \textbf{8.18}$$

$$\theta_{t+\Delta t} = \theta_t + 0.5(\dot{\theta}_t + \dot{\theta}_{t-\Delta t})\Delta t \quad \textbf{8.19}$$

The time step Δt is a constant value that is chosen to ensure the stability and accuracy of the numerical simulation. It is determined on the basis of the maximum stiffness and the particle with smallest mass and is given by

$$\Delta t = C\sqrt{\frac{m}{k}} \quad \textbf{8.20}$$

where *m* is the mass of the smallest particle in the system and *k* is the maximum stiffness experienced in the system. The value of *C* was set to 0.1 based on the work of Malone et al. (2008), giving a spring stiffness between 1.0 x 10^{-5} and 1.0 x 10^{-6} seconds depending on whether the plastic or metal free-cells or just the particles were being simulated.

Polydispersity is incorporated into the model by using random numbers to calculate each particle diameter sampling from a uniform distribution, where

$$d_i = d_{max} - \Delta d R_n \quad \textbf{8.21}$$

where, d_i, is the diameter of *i*, Δd is the diameter range for the particle type and R_n is a random number.

8.9 Polyhedral free-cell and spherical particles

The free-cells in the DEM simulations were considered as rounded polygons as shown below in figure 8.4.

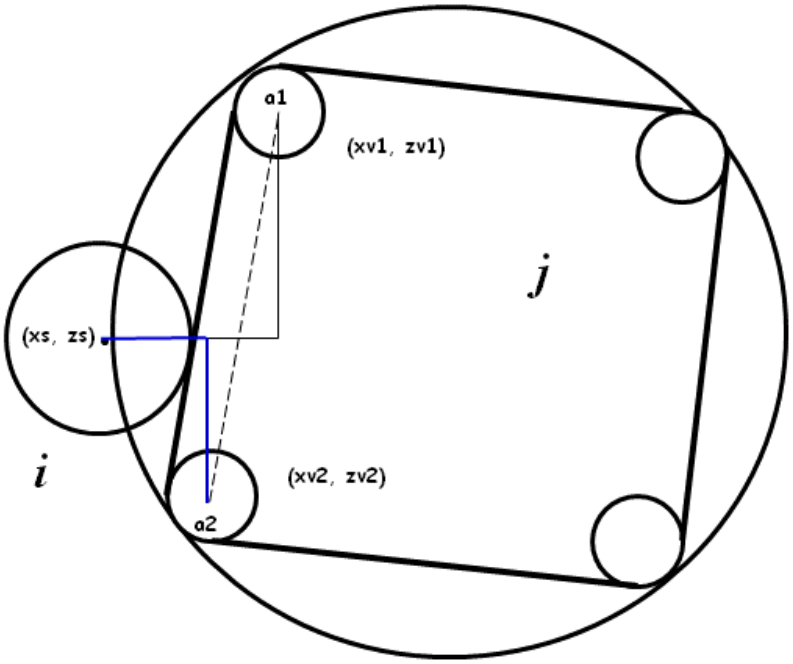

Figure 8.4: Free cell (*j*) and sphere (*i*) where (xs, zs) is the position of the centre of the circle and (xv1, xv1) and (xv2, zv2) are the positions of the vertices of the free cell

The position of the vertices of the free cell are automatically set by the program by inputting the radius of the outer large circle and the desired number of vertices i.e. three for the triangle and four for the square. The radius of curvature of the vertices and hence edges of the simulated free cell are input into the program to match the curvature on the corners of the experimental free cells. The amount of overlap between the spheres and the free cell is calculated as follows:

Let

$$ax = xv2 - xv1 \quad \textbf{8.22}$$

$$az = zv2 - zv1 \quad \textbf{8.23}$$

and

$$bx = xs - xv1 \quad \textbf{8.24}$$

$$bz = zs - zv1 \quad \textbf{8.25}$$

where $(xv1, zv1)$ and $(xv2, zv2)$ are the positions of the corners $a1$ and $a2$ respectively, of the free cell.

Then let

$$P = \frac{bx \times ax + bz \times az}{ax^2 + az^2} \quad \textbf{8.26}$$

The nearest point that the sphere is positioned at between the vertices *a1* and *a2* is obtained by letting

$$px = xs - (xv1 + P \times ax) \quad \textbf{8.27}$$

$$pz = zs - (zv1 + P \times az) \quad \textbf{8.28}$$

where *xs* and *zs* are the centre of the spherical particle.

Then,

$$dist = \sqrt{px^2 + pz^2} \quad \textbf{8.29}$$

and the amount of overlap is

$$Overlapi = radsi - dist \quad \textbf{8.30}$$

where $radsi$ is the radius of the sphere.

8.10 Polyhedral 3D model (Wang et al. 2010)

In this section a review of the theory developed by Fraige et al.(2008b) to describe the details of a DEM model for polygons is presented. This was further developed to model convex polyhedron shaped particles in 3D by Wang et al (2010). The definition of the polyhedron particles modelled here is shown in Figure 8.5. It should be noted that the vertices are "rounded", and hence the edges are correspondingly rounded. This is to facilitate the model and to acknowledge that real granular particles do not contain perfect vertices. The radius of

the "vertex-spheres" can be selected by the user. This may also have an effect on the time step required for the simulations.

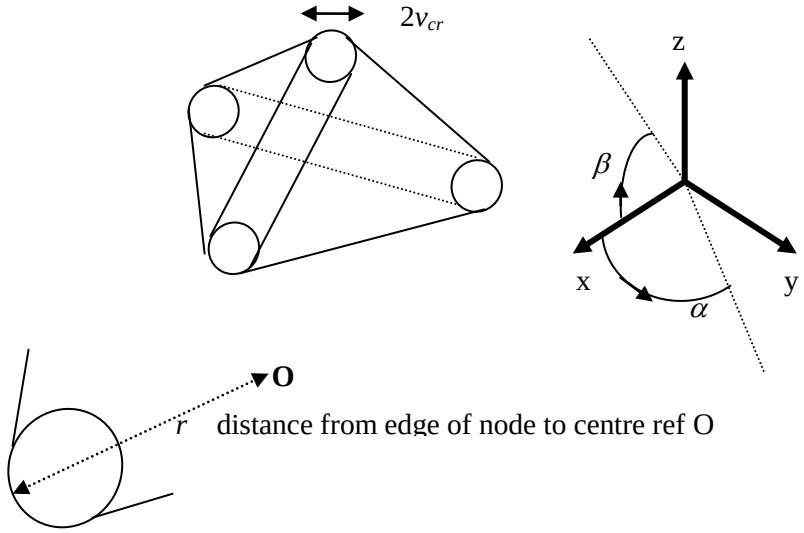

Figure 8.5: Polyhedron Particle Definition

For each type of polyhedron the user specifies the number of vertex nodes in the particle (e.g. 4 for a tetrahedron) and vertex radius v_{cr}. For each node the user specifies a radius r, azimuth angle α and elevation angle β from the particle reference centre at O. The angles are defined in a local axis system. The program calculates the vertex node centre local co-ordinates: starting at (r - v_{cr}, 0, 0) rotate about y by -β then about z by +α. The user specifies the number of triangles which define the particle surface (e.g. 4 for a tetrahedron) and identifies which 3 vertex nodes define each triangle. (The particle can be imagined as a series of triangles with cylindrical edges and spherical nodes.) The particle must be convex, that is the outer angle at each edge is always greater than 180^o. A cohesion distance is defined surrounding the outer surface (not shown). The material density is specified and the program calculates numerically the mass, centre of gravity (not necessarily at O) and moment of inertia tensor. For numerical efficiency in the particle-particle interaction model, the radius of a sphere centred on O which just encloses the particle and its cohesive region is calculated. In the current model the polyhedron does not have to be regular but the local axes must be principal axes of rotation (off diagonal elements of the moment of inertia tensor are zero).

A significant difference here with spherical particles is that: (a) there can be “multiple contact points” detected in a particle-particle interaction; (b) the combined length and area of contact could be significantly greater. This is illustrated in Figure 8.6. For each contact point the model calculates the forces using the same equations as for the spherical particles in Section 8.6. Friction force is calculated at the contact point which has the largest solid overlap i.e. there is one friction force modelled per particle-particle interaction. The tangential deformation is accumulated over several time-steps. Rolling friction is not included; there may be some rolling on the vertices, but this is not considered significant. There is no cohesion force in this study.

Figure 8.6 illustrates the scenario where two polyhedra (blue and green) contact over a region which cannot be described as a point contact. First figure is from side in plane of contact, second figure shows plane of contact. The area of contact is estimated by calculating the average co-ordinates of the four contact points.

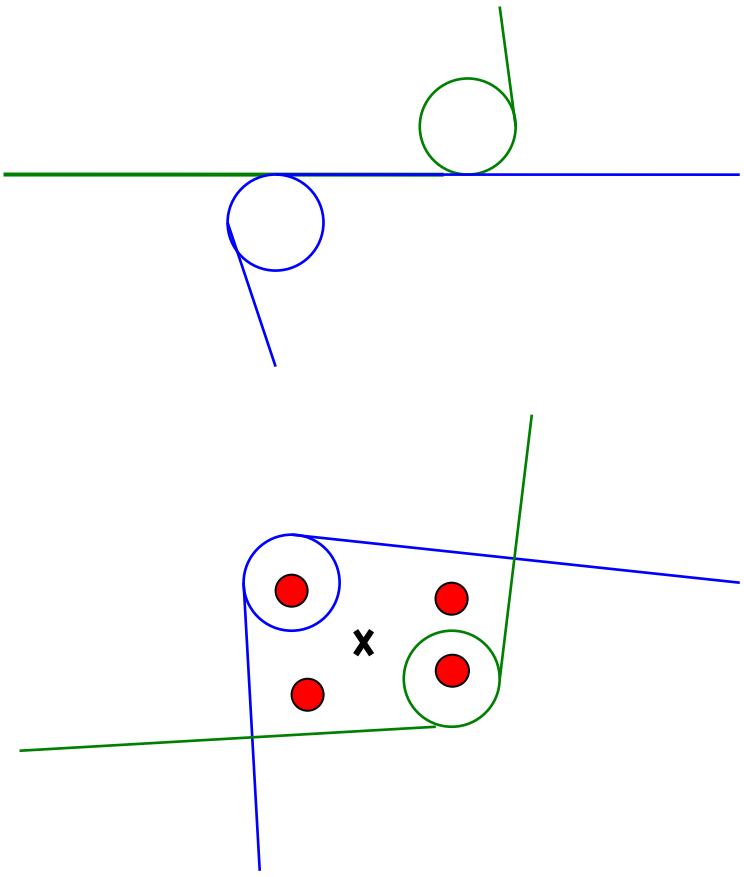

Figure 8.6: Multiple contact points

With the small particles modelled here the moment of inertia is low which can result in high angular velocities (limited to 100π radians/s here). In practice this would be limited by air drag and cohesion effects.

8.11 Choice of the initial positions of the free-cell, for comparison between experiment and simulation

Two initial positions of the free-cells to use in DEM simulations were determined from observations of the behaviour of the free-cells in the white (5 mm) monosized particles. Position 12 was furthest from the orifice and was not near any region in the silo where the stagnant zone boundary formed. Position 5 was chosen as it was at a position in the silo where the stagnant zone boundary had been observed to have formed.

8.12 Defining the position of the free-cell in the DEM

The trajectory of the free-cells in the monosized white (5 mm) particles and the white (5 mm) /black (4 mm) binary mixture was investigated by applying the DEM sphere model with the inclusion of one polygon particle. The total number of particles, including the free-cell, was input into the program. The particle number allocated to the free-cell was determined by overriding the subroutine in the program that defined the initial positions of all the particles.

The program was capable of simulating either the *gradual fill* method (Figure 8.7a) in which particles entered the silo at determined seeding points at the top of the silo and were then allowed to fall under gravity, or *en masse* (Figure 8.7b) in which the particles were initially positioned at points throughout the silo and then allowed to collapse under gravity.

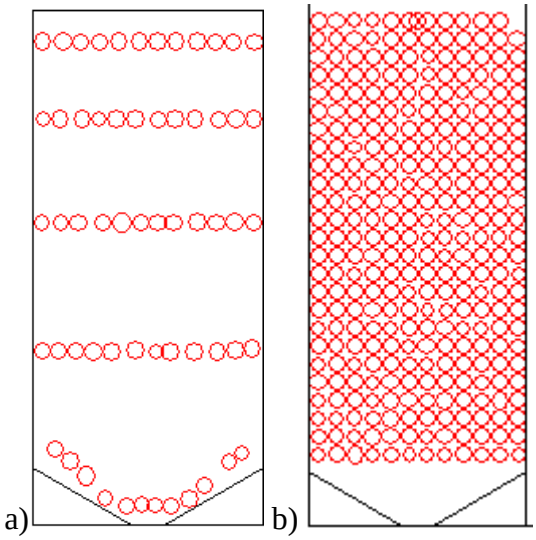

Figure 8.7: a) The gradual filling method and b) The *en masse* filling method

The filling time using the *en masse* fill method is much shorter (up to 20 times) than the filling time using the *gradual fill* method. This results in a significantly reduced total simulation time. However, using the *en masse* fill method can result in unrealistic fill stresses (Langston, 1994) in the silo, which could influence the behaviour of the free-cell.

To ensure that the position of the free-cells in the simulations was the same as in the experiments, it was necessary to determine which particle number, in the total number of particles, should be allocated to the free-cell. The particle number in the monosized white particles was determined by filling the hopper up to the level of the desired initial position (5 or 12) and then allowing the silo to empty. The number of particles was then counted by hand and weighed (as a check). The free-cell at position 12 was determined to be the 39,650th particle and at position 5 the 19,190th particle. The program was modified so that the spherical particles were positioned in rows and the free-cell was positioned on its own row. The horizontal position was determined by estimating the number of particle diameters to the initial position. The code to simulate the *en masse* filling method was written so that the particle positions were determined starting from the bottom left hand corner and then left to right, row by row. Position 12 was approximately 10 particle diameters from the left hand wall and position 5 was 20 particle diameters from the left hand side wall.

The particle number of the free-cells in the white (5 mm)/black (4 mm) binary mixtures was determined by calculating the equivalent ratio of white/black particles to white particles that filled the silo to position 5 or 12. The monosized batch consisted of 50,000 white particles, so

the ratio of particles required to fill the silo to position 12 is 39,650/50,000 = 0.793. The white/black batch consisted of 55,000 particles, so the ratio of particles required to fill the silo to position 12 can be estimated to be the 55,000 × 0.793 = 43,615th particle. The value was checked by mixing 34,892 white particles and 8,723 black particles and filling the hopper. The particles filled the hopper to the position of level 12 very well. The free-cell at position 12 in the white/black binary mixture was determined to be the 43,615th particle and at position 5 the 21,109th particle. The position of the free-cell in the DEM simulations of the binary mixture will vary slightly during each fill, as the particle type is determined randomly, hence the number of white and black particles below position 5 or 12 will vary. The initial positions of the particles and free-cell in the simulation of the binary mixture, using the *en masse* fill method is shown in Figure 8.8a and the positions of the particles just before the opening of the orifice are shown in Figure 8.8b

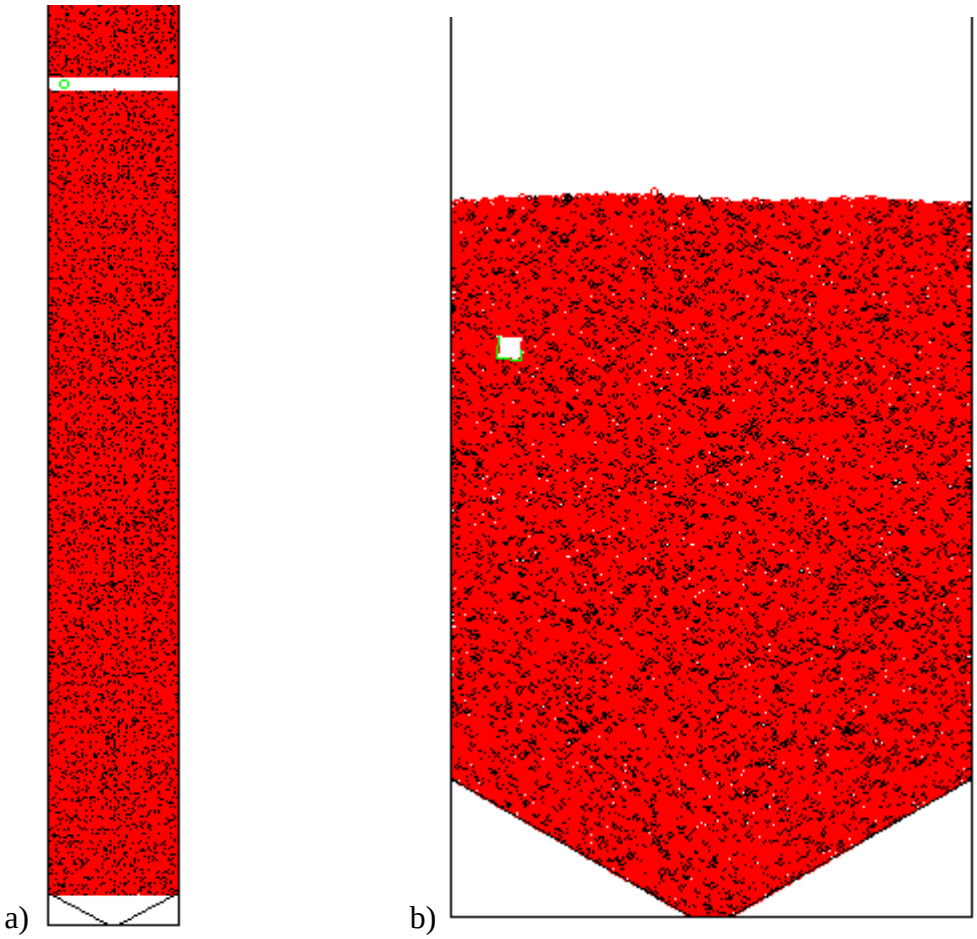

Figure 8.8: a) The particles and free-cell at their initial starting positions using the *en masse* fill method and b) just before the orifice opens and the initiation of discharge

The appropriate number of particles was also checked by considering the volume of the rig filled by the particles. The volume of the rig up to point 12 was calculated. Using the theoretical predictions developed by Song et al. (2008) for an irregular packing of spheres and the regular packing density developed by Kepler (1611), an upper and lower limit on the number of spheres required to fill the silo to position 12 can be determined.

The volume of the silo up to position 12 is 3875cm^{3}and the volume of one white (5mm) spherical particle is $\left(\frac{1}{48}\right)\pi$ cm^3.

Song et al. (2008) deduced that irregular packed spheres have a packing density of 63.4%. The volume of the silo up to position 12 occupied by the volume of the spheres is therefore 2456.75cm^3. The number of spheres in the silo is thus 37,536.

Kepler (1611) calculated that a regular packing of spheres had a packing density of $\frac{\pi}{\sqrt{18}} \approx 0.74048$. The volume of the silo up to position 12 occupied by the spheres is now calculated to be 2869.36cm^3. The number of spheres in the silo is calculated to be 43,841.

The appropriate number of spheres required should therefore be in the range

$$37{,}536 \leq N \leq 43{,}841$$

where N is the number of spheres required to fill the silo up to position 12.

The number of spheres counted out by hand and weighed was determined to be 39,650. This is between the upper and lower limit confirming that the number of particles used was reasonably accurate.

Similarly the volume of the silo up to position 5 is 525cm^3 and number of particles required to fill the silo up to position 5 is found to be in the range

$$19{,}131 \leq N \leq 22{,}344$$

The number of spheres counted out by hand and weighed was determined to be 19,190. This suggests that the spheres in the hopper section predominantly pack in an irregular packing arrangement.

8.13 Summary

This chapter provides information about the Discrete Element Method to model spherical particles and polyhedral particles. The theoretical background of the DEM is described. The filling method and the methods used to position the free-cells in the simulations were presented.

Determination of the input parameters for the DEM simulations

9 Determining the input parameters for the DEM simulations

9.1 Introduction

In this section the values of the input parameters required for the Discrete Element Simulations are presented. The results of simple tests to determine the accuracy of some of the input parameters are also discussed. The particle-particle and particle-wall sliding and rolling frictions and the coefficient of restitution were measured experimentally. The methods used to measure the values are provided in section 9.6.

9.2 Methods used to measure the particle properties

The DEM program requires the inputting of the particle properties to accurately simulate their behaviour. The methods used to obtain the particle properties are described below.

9.2.1 Particle mass

The average mass of a particle was obtained by weighing ten particles on a set of weighing scales to give a standard error of $\pm 1.0 \times 10^{-4}$g in the result.

$$\text{Average mass} = \bar{m} \pm \frac{\sigma_{n-1}}{\sqrt{n}} \quad 9.1$$

9.2.2 Particle diameter

The diameter of the spherical particles was obtained by measuring the diameter of ten of each of the particles using a digital micrometer to an accuracy of $\pm 1.0 \times 10^{-4}$ m. The mean value and error was obtained using the formula

$$\text{Average diameter} = \bar{d} \pm \frac{\sigma_{n-1}}{\sqrt{n}} \quad 9.2$$

9.2.3 Particle volume

The particle volume of the spheres was measured by displacement as described in section 3.3 for the wheat. It was also obtained using the equation

$$V = \frac{1}{6}\pi \bar{d}^3 \qquad \textbf{9.3}$$

The volumes of the polyhedra were obtained by measuring one of the sides and applying known formulae. The volume was also estimated by experiment. A small cylinder was filled with water and the diameter of the cylinder and the height of water in the cylinder were measured using a micrometer screw gauge and the volume of the water V_1 was calculated. A polyhedral particle was placed into the cylinder of water and the height of the water was measured and the volume of the water and the polyhedral were calculated V_2. The volume of the polyhedral particle was obtained by subtracting V_1 from V_2.

9.2.4 Particle density

The particle density was obtained by the use of the equation

$$\rho = \frac{\text{mass}}{\text{volume}} \qquad \textbf{9.4}$$

The accuracy of the particle density was recorded to the nearest ±0.01 gcm^{-3}.

9.2.5 Particle-wall sliding friction

Two values of the sliding friction can be defined. These are the kinetic sliding friction and the static sliding friction. Their value is found to be nearly identical between very clean polished surfaces. Hancock et al. (2010) investigated the kinetic friction of some tablets and capsules using a pin-on-disk tribometer. The tests used in this study applied a simpler method. Two tests were conducted to determine the value of the sliding friction. The particle-wall static sliding friction coefficient of the spheres was obtained by sticking four spheres together with cellotape or blu-tac and placing them on the surface of a piece of Perspex similar to those that are used in the 3D hopper slice. The angle of the surface was gradually increased, by lifting one end of it slowly by hand, until the particles started to slide (Figure 9.1a,b). Care was taken

to ensure that the cellotape or blu-tac did not come into contact with the Perspex during the measurement. The test was completed ten times using different particles and a digital angle measurer and protractor were used to record the angle of the slope. A different piece of Perspex was also used to check that the particle-wall static sliding friction value obtained was accurate. The particle-wall static sliding friction of the polyhedral was similarly obtained by placing them on a piece of Perspex and inclining the surface until the particles started to slide (Figure 9.2). The experiment was repeated several times by placing the polyhedral particle on a couple of different sides and testing with other polyhedral dice. An average value of ten trials was obtained and it was assumed that the particle-wall sliding friction coefficient between the polyhedra and the wall was the same regardless of the orientation of the polyhedra i.e. whatever edge or side was in contact with the wall.

a)  b) 

Figure 9.1: Measuring particle-wall static sliding friction of spheres for a) the cellulose acetate spheres and b) the bubble gum balls.

Figure 9.2: Measuring particle-wall static sliding friction of polyhedra.

The particle-wall kinetic sliding friction was obtained only for the yellow, white and black spheres. Practical tests and identical simulations using the DEM program were conducted to both validate the values obtained and to validate the accuracy of the DEM program. The

particle-wall kinetic sliding friction was obtained by placing the four cellotaped spheres onto an inclined Perspex surface. The surface was inclined at angles 25º, 30º, 35º and 40º, by placing a small block of metal under one end. The angles chosen were greater than the angle at which the particles had started to slide, in the previous test to determine the particle-wall static sliding friction. The spheres were released at a fixed distance of 50 cm along the horizontal.

Consider the four spheres as a block as shown in figure 9.3.

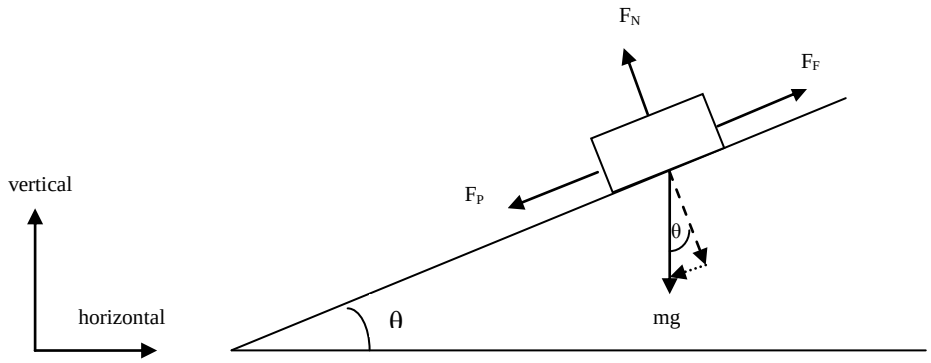

Figure 9.3: Block on an inclined plain representing the four spheres

F_P is the force parallel to the inclined surface towards the bottom of the incline. F_F is the particle-wall sliding friction force. F_N is the normal force and mg is the force of gravity.

The net force down the slope that causes the block to accelerate is given by

$$F_{NET} = F_P - F_F \qquad 9.5$$

where

$$F_P = mg \sin\theta \qquad 9.6$$

and

$$F_N = mg \cos\theta \qquad 9.7$$

and

$$F_F = \mu_k F_N \qquad 9.8$$

where μ_s is the coefficient of particle-wall kinetic sliding friction.

The block is placed on the inclined surface and accelerates from rest. The acceleration of the block is given by

$$a = \frac{F_{NET}}{m} = \frac{F_P - F_F}{m} \qquad 9.9$$

where substituting in equations 9.6 and 9.8 and simplifying gives

$$a = g(\sin\theta - \mu_k \cos\theta) \qquad 9.10$$

Rearranging to make μ_k the subject gives

$$\mu_k = \tan\theta - \frac{a}{g\cos\theta} \qquad 9.11$$

The distance *s* travelled by the block down the slope is given by

$$s = \frac{1}{2}at^2 \qquad 9.12$$

Rearranging and substituting 9.12 into equation 9.11 gives

$$\mu_k = \tan\theta - \frac{2s}{gt^2\cos\theta} \qquad 9.13$$

The value of *s* varies depending upon the angle θ where $s = \frac{0.50}{\cos\theta}$

The particle-wall coefficient of kinetic sliding friction is less than the coefficient of static sliding friction.

The values obtained for each of the three types of spheres were tested using the DEM program and compared to similar practical experiments and theoretical calculations. The program was modified to model a single particle sliding down an incline. The angular velocity was set to zero, so the particle could not rotate and only moved by sliding. Experiments were conducted with a yellow (6 mm) particle, a white (5 mm) particle and a black (4 mm) particle. The results are shown in figures 9.4, 9.5 and 9.6.

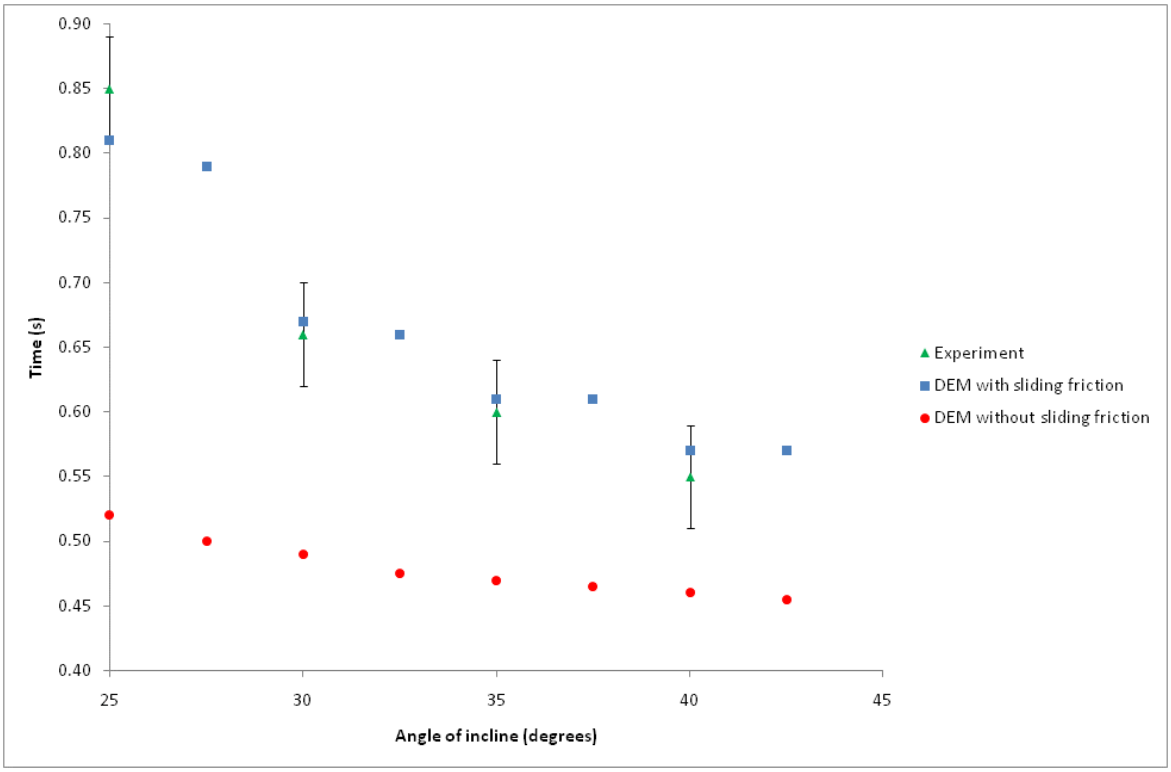

Figure 9.4: Comparison between DEM simulation and practical experiment of the time taken for a single yellow (6mm) particle to roll down an incline with and without the inclusion of sliding friction

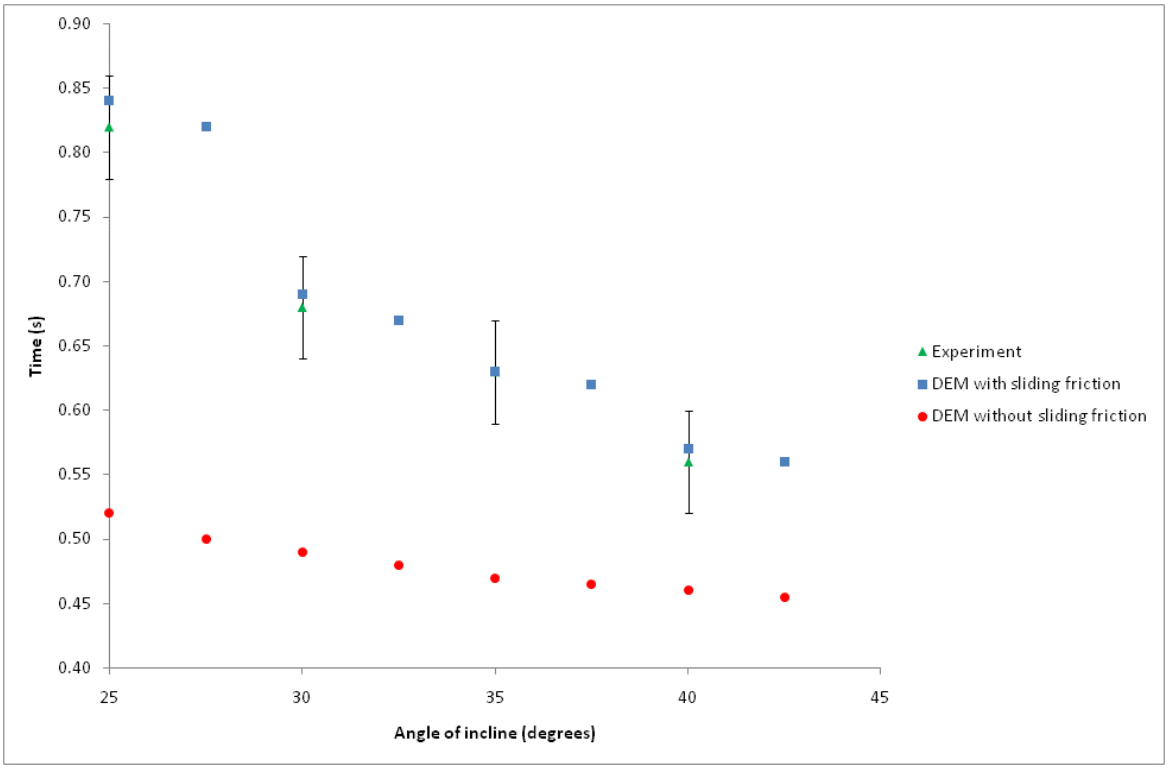

Figure 9.5: Comparison between DEM simulation and practical experiment of the time taken for a single white (5 mm) particle to roll down an incline with and without the inclusion of sliding friction

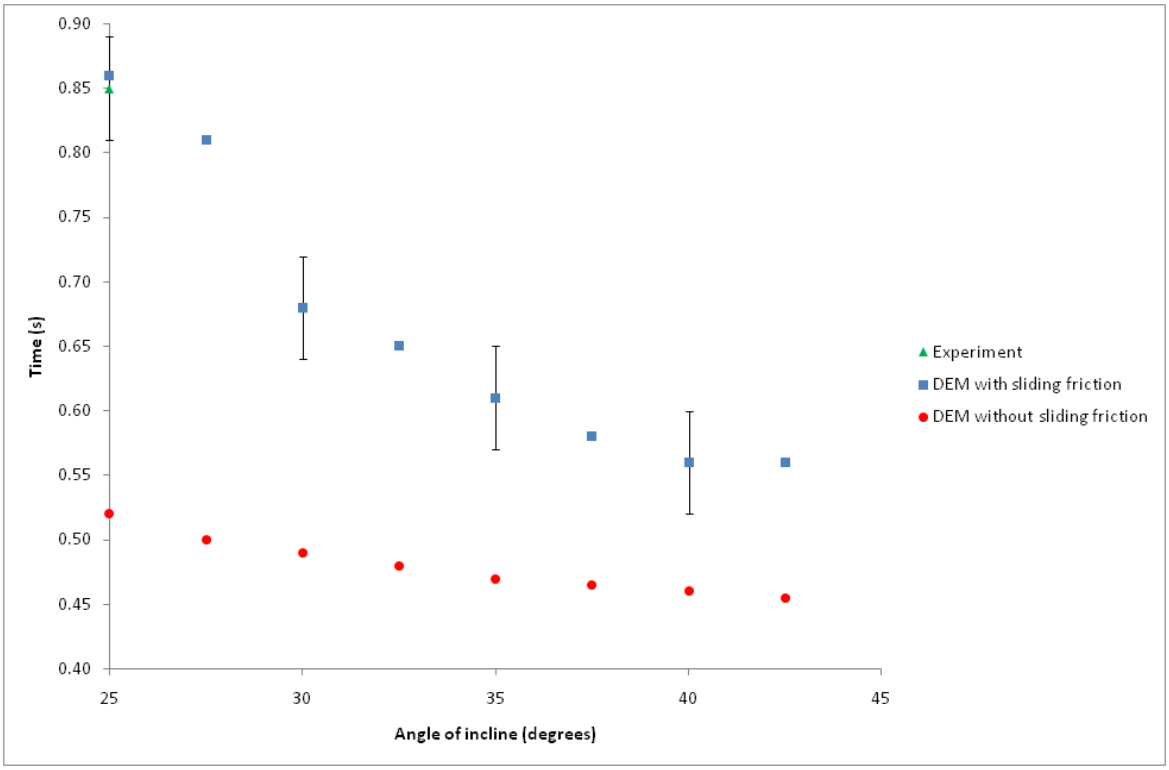

Figure 9.6: Comparison between DEM simulation and practical experiment of the time taken for a single black (4 mm) particle to roll down an incline with and without the inclusion of sliding friction

The results from DEM simulations with the inclusion of sliding friction lie within the bounds of the error bars associated with the experimental results, suggesting that the program is accurately modelling the sliding of the particles along the walls. The error in the experimental results was ±0.04 s which is as a result of the frame rate of the video recorder used to obtain the experimental data. There is some scatter in the results from the DEM simulation with sliding friction, which may be caused through noise in the DEM program caused by the error associated with the value of the sliding friction coefficient, which can only be adequately defined to an accuracy of 4 decimal places in this study.

9.2.6 Particle-particle sliding friction

In the previous section both the particle-wall kinetic and static sliding frictions were obtained. However it is difficult to obtain the particle-particle kinetic sliding coefficient of friction. Therefore only the particle-particle static sliding coefficient of friction has been obtained. The particle-particle static sliding friction of the spheres was obtained by sticking four of the spheres to a surface, and then balancing four spheres stuck together with blu-tac on top of

them (Figure 9.7). The surface was inclined, by slowly lifting one end by hand and the angle of the slope at which the particles stared to slide was recorded with a digital angle measurer and protractor. The experiment was repeated ten times with different particles for each of the types of sphere. As is the previous section, care was taken not to allow the cellotape to touch the Perspex surface. The particle-particle friction between the polyhedral was obtained by sticking one polyhedral particle to the surface and resting one of the other polyhedral on top of it (Figure 9.8). The experiment was repeated using ten different combinations of polyhedral particles.

a)  b) 

Figure 9.7: Measuring particle-particle static sliding friction of the spheres for a) cellulose acetate balls and b) bubble gum balls

Figure 9.8: Measuring particle-particle static sliding friction of the polyhedra

The coefficient of static sliding friction is given by

$$\mu_s = \tan\theta \qquad \textbf{9.14}$$

9.2.7 Particle-wall rolling friction

The particle-wall rolling friction for the spherical particles A, B and C was obtained by a method developed (Lastufka, 2004) to measure the rolling friction of car tyres.

The particle rolls down the ramp of length L_r and height, h, inclined at an angle θ and travels along the flat, coming to rest at a distance yc (Figure 9.9).

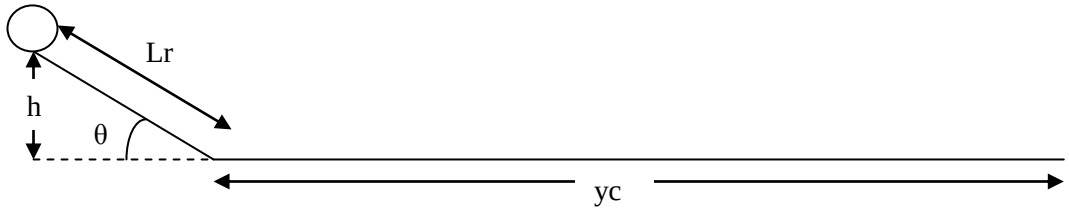

Figure 9.9: Schematic diagram showing the parameters required to calculate the particle-wall rolling friction coefficient using equation 9.15

The dimensionless rolling friction coefficient *u* calculated using the formula

$$u = \frac{-\mathrm{Lr}\sin\theta}{\mathrm{Lr}\cos\theta + \mathrm{yc}} \qquad \textbf{9.15}$$

The derivation is given in appendix A.

The ramp in this study was constructed using the Perspex strips that made up the thin sides of the 3D slice hopper, between the front and back large clear Perspex sheets.

The particle-wall rolling friction of the bubble gum balls was obtained by experiment, using the same method described in Ketterhagen (2010). There was no noticeable cohesion between the bubble gum balls or the bubble gum balls and the ramp. And they were not sticky to touch.

The particle rolls down the ramp of height *h* and travels along a Perspex strip, coming to rest at a distance yc (Figure 9.10).

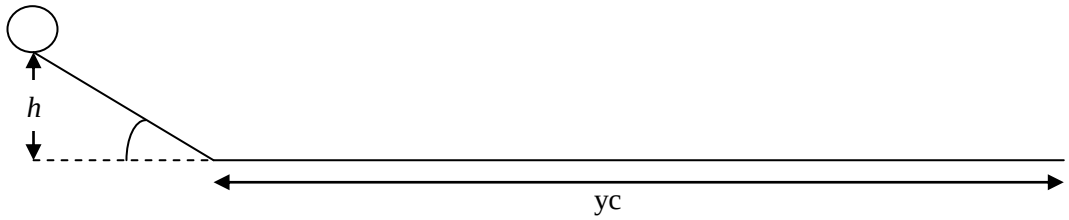

Figure 9.10: Schematic diagram showing the parameters required to calculate the particle-wall coefficient of rolling friction using equation 9.16

Figure 9.11: Measuring the particle-wall rolling friction

The dimensionless rolling friction coefficient *u* is then calculated using the formula

$$u = \frac{h}{yc} \qquad \textbf{9.16}$$

A test was conducted to evaluate the validity of the particle-wall coefficient of friction for each of three types of particle. A ramp was constructed using a length of Perspex from the sides of the quasi-3D rig. The ramp was inclined at an angle θ to the horizontal using a digital angle measurer and protractor. The vertical distance from the bottom of the ramp to the starting position was set to a constant value of 50cm (Figure 9.12).

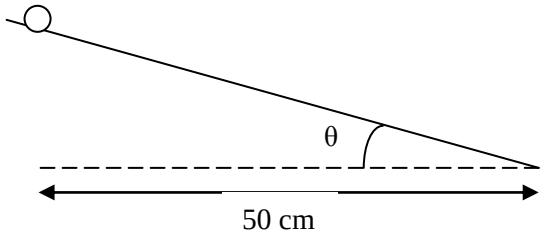

Figure 9.12: Test to deduce validity of particle-wall coefficient of rolling friction

The time taken for the particles to roll down to ramp was obtained using a video camera and each experiment was completed ten times and the average value obtained.

The particle-wall rolling friction was determined by placing each of the spheres on an incline and allowing them to roll down the slope under the force of gravity. The values of the coefficients of rolling friction determined from experiment were compared with computer simulations. The value of the particle-wall sliding friction determined in the previous section,

along with the particle-wall rolling friction coefficient, were input into the DEM program and compared with experimental results to validate the accuracy of the particle-wall friction coefficient. The results are shown in Figures 9.13, 9.14 and 9.15.

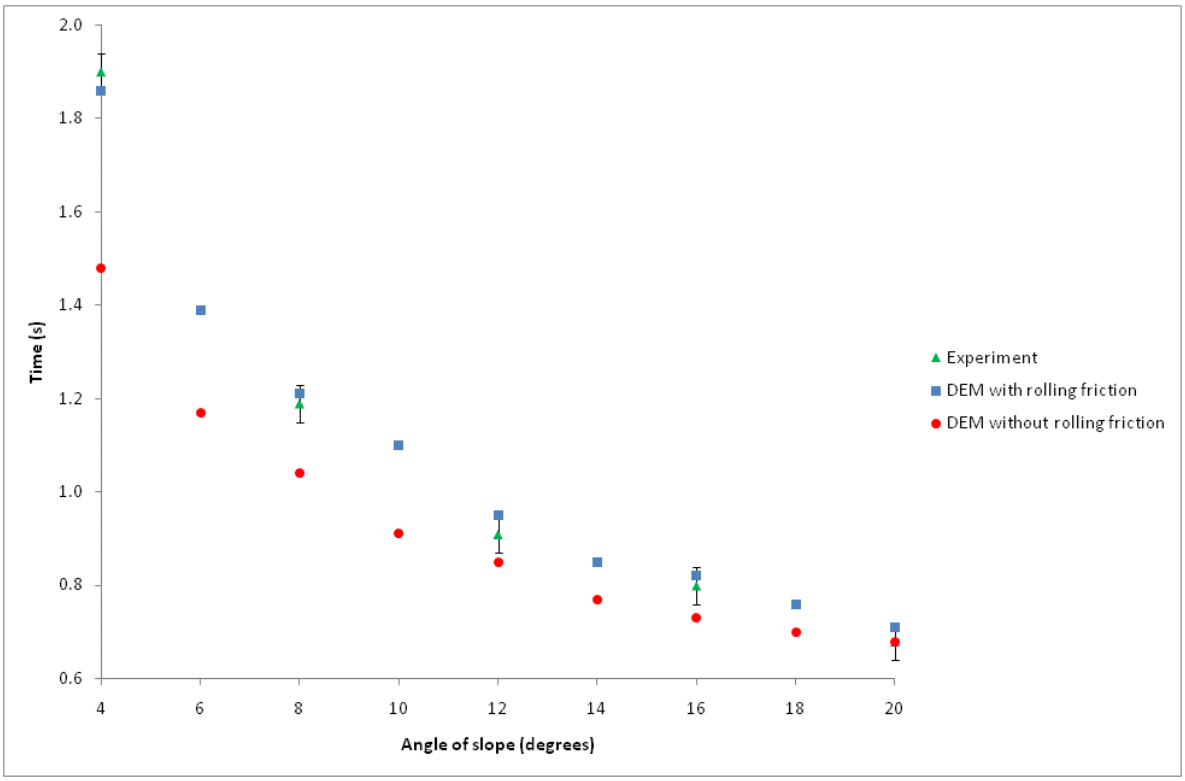

Figure 9.13: Comparison between DEM simulation and practical experiment of the time taken for a single yellow (6 mm) particle to roll down an incline with and without the inclusion of rolling friction

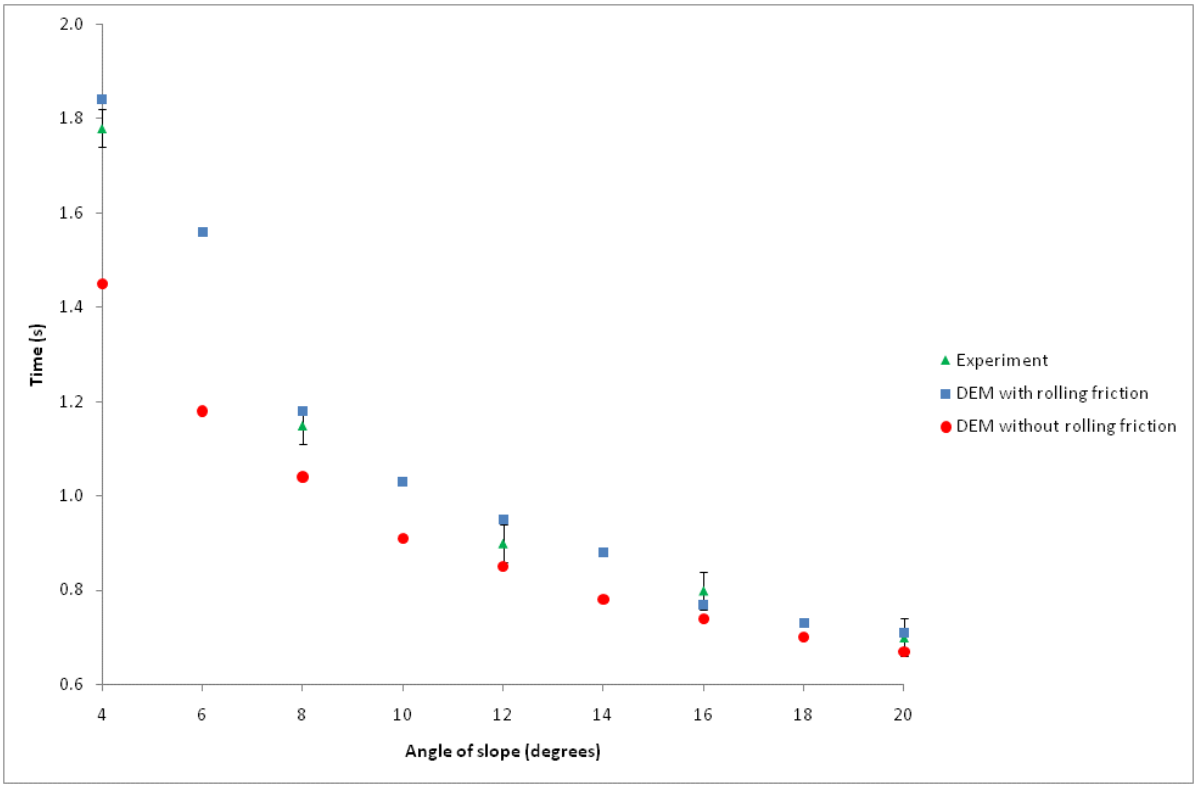

Figure 9.14: Comparison between DEM simulation and practical experiment of the time taken for a single white (5 mm) particle to roll down an incline with and without the inclusion of rolling friction

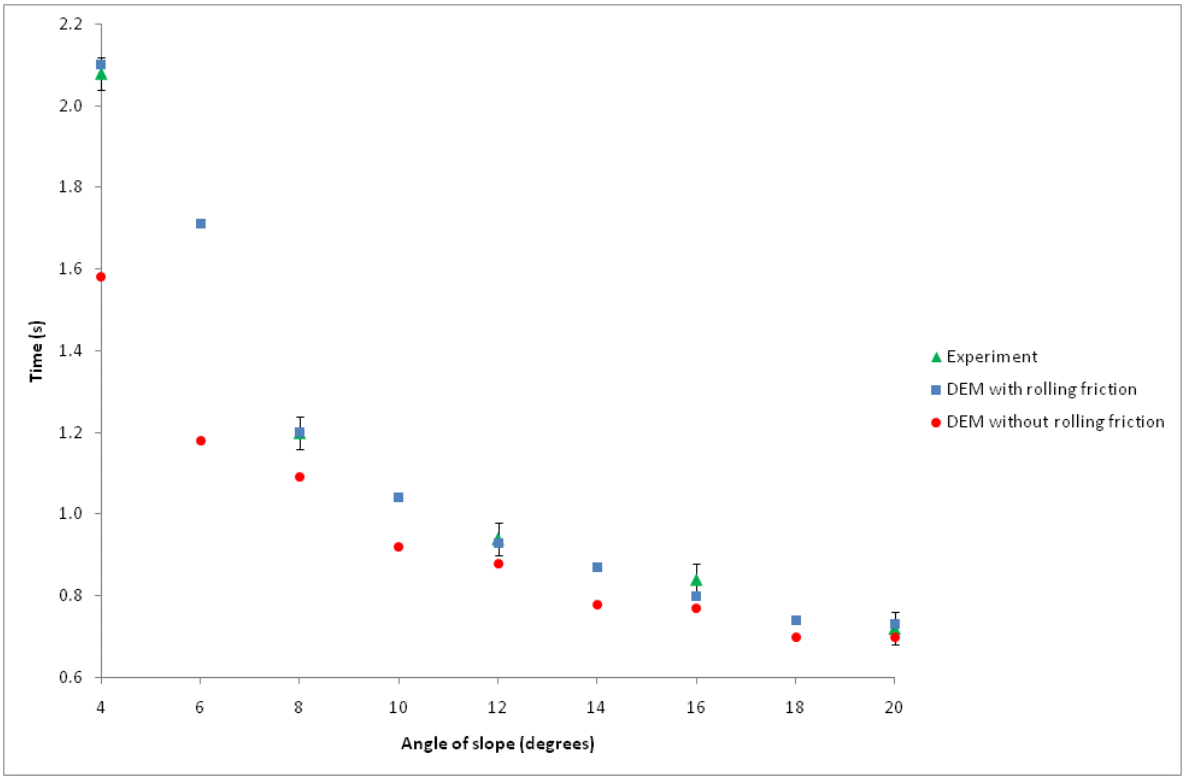

Figure 9.15: Comparison between DEM simulation and practical experiment of the time taken for a single black (4mm) particle to roll down an incline with and without the inclusion of rolling friction

The results from DEM simulations with the inclusion of rolling friction lie within the bounds of the error bars associated with the experimental results, suggesting that the DEM program is adequately modelling rolling friction. The error in the experimental results was ±0.04 s which is as a result of the frame rate of the video recorder. In similarity to the results showing the effect of including the sliding friction, there is some scatter in the results obtain from the DEM simulations with the inclusion of rolling friction, but similarly this may be due to noise in the program.

9.2.8 Particle-particle rolling friction

The particle-particle rolling friction was calculated using equation 9.17 developed by Zhou et al. (2002) that relates the angle of repose, the particle diameter and the particle-particle and particle-wall rolling and sliding frictions.

$$\theta_0 = 68.61 \times \mu_{s,pp}{}^{0.27} \times \mu_{s,pw}{}^{0.22} \times \mu_{r,pp}{}^{0.06} \times \mu_{r,pw}{}^{0.12} \times d^{-0.2} \qquad \textbf{9.17}$$

where $\mu_{r,pp}$ and $\mu_{r,pw}$ are the particle-particle and particle-wall rolling coefficients and $\mu_{s,pp}$ and $\mu_{s,pw}$ are the particle-particle and particle-wall sliding friction coefficients with dimensions of millimetres, θ_0 is the static angle of repose without the container sides and *d* is the particle diameter. The equation was obtained by a numerical fit to experimental data.

The angle of repose θ of the particles placed in the quasi-3D rig (Figure 9.16) was obtained by setting up the hopper to model a flat bottomed hopper. The hopper was allowed to drain and the angle from the horizontal to the incline of the particles left in the corners of the hopper was measured.

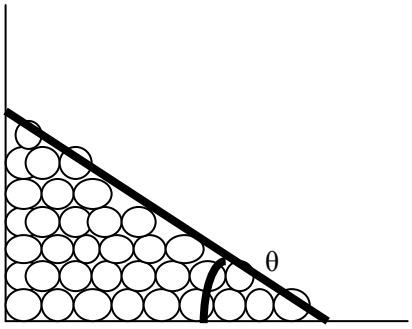

Figure 9.16: Measuring the angle of repose of the particles in the rig

The relationship between the angle of repose and the container thickness was found to be described by the formula (Zhou et al (2002))

$$\theta = \theta_0\left(1 + \lambda e^{-\xi w}\right) \qquad \textbf{9.18}$$

where w is the container thickness, θ is the static angle of repose between the container sides. It was found that $\lambda = 1$ and $\xi = 0.18/d$.

Zhou et al. (2002) discussed the prospect that the rolling friction coefficient may be proportional to particle diameter, so that the power of d becomes -0.02. A simple test was conducted using ball bearings of different diameters. A value of the particle-wall rolling friction was determined for ball bearings of diameters 4.76 mm, 6.35 mm, 7.14 mm and 8 mm using the same method described in section 9.2.7. Each point is an average of five trials. The results are shown in figure 9.17.

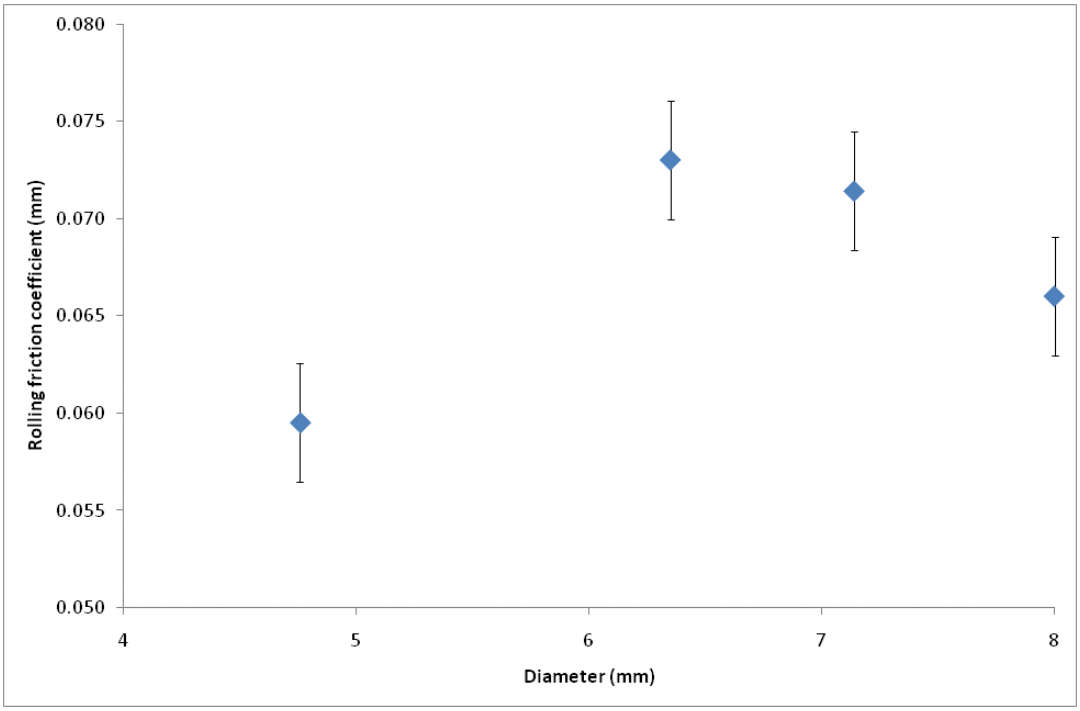

Figure 9.17: Graph showing the particle-wall rolling friction coefficient with units of length against particle diameter (mm) where each point is the average of five trials.

The test revealed inconclusive results, however setting d to -0.2 results in a value of particle-particle rolling friction coefficient with magnitude 10^{-5} while setting it to -0.02 gives a particle-particle rolling friction coefficient with a magnitude of 10^{-3} which is in agreement

with published work. This suggests a value of 0.001-0.01 (Yang et al. 2006). Hence the power of *d* was set to -0.02 in this study. Initial Discrete Element Method simulations to determine the mass flow rate of the particles result in a mass flow rate nearly half that obtained in the experiments. Including the rolling friction coefficient with magnitude 10^{-5} resulted in a negligible change in the time taken for the particles to roll to the bottom of the ramp, but setting the value of the rolling friction coefficient to 10^{-3} resulted in a time taken to roll down the ramp closer to the experimental value.

The particle-particle rolling friction was obtained by equating equations 9.17 and 9.18 and substituting in the appropriate value of the particle diameter *d* to give

$$\mu_{r,pp} = \left(\frac{\theta}{\left(1+e^{\frac{-0.18W}{d}}\right) 68.61 \times \mu_{s,pp}^{0.27} \times \mu_{s,pw}^{0.22} \times \mu_{r,pw}^{0.12} \times d^{-0.2}} \right)^{-0.06} \qquad \textbf{9.19}$$

where the power of *d* was instead set to be -0.02.

9.2.9 Angle of repose of a heap of particles

The angle of repose of the particles without the hopper sides was obtained by pouring a steady stream of particles onto a round tray. When a steady heap was obtained the angle of the heap was measured by placing a ruler along the slope and measuring the slope with a protractor. The value of the angle obtained was compared with the calculated angle from Zhou et al. (2002).

9.2.10 Particle-wall and particle-particle Coefficient of Restitution

The particle-wall coefficient of restitution was obtained by dropping particles from an initial height and recording the rebound height (Figure 9.18).

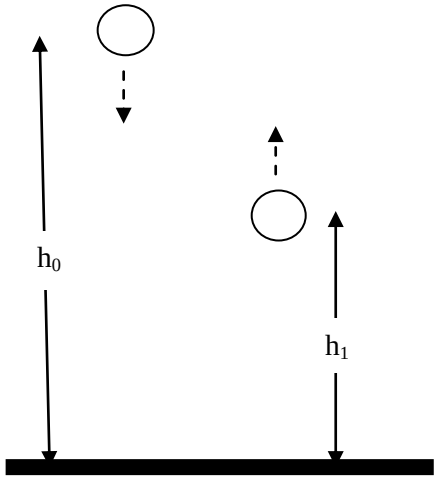

Figure 9.18: Measuring the particle-wall coefficient of restitution

The coefficient of restitution was obtained using the following formula (Malone, 2008)

$$e = \sqrt{\frac{h_1}{h_0}} \qquad \textbf{9.20}$$

The variation of the coefficient of restitution with drop height is shown in the graph below, each experiment was conducted ten times and the average value obtained.

The coefficient of restitution was obtained by dropping particles from an initial drop height, measuring the rebound height and applying equation 9.20. The coefficient of restitution is known to vary with drop height, so tests were conducted in which the drop height was varied in increments of 10 cm from 10 cm up to 100 cm. The result for each particle is shown in Figure 9.19.

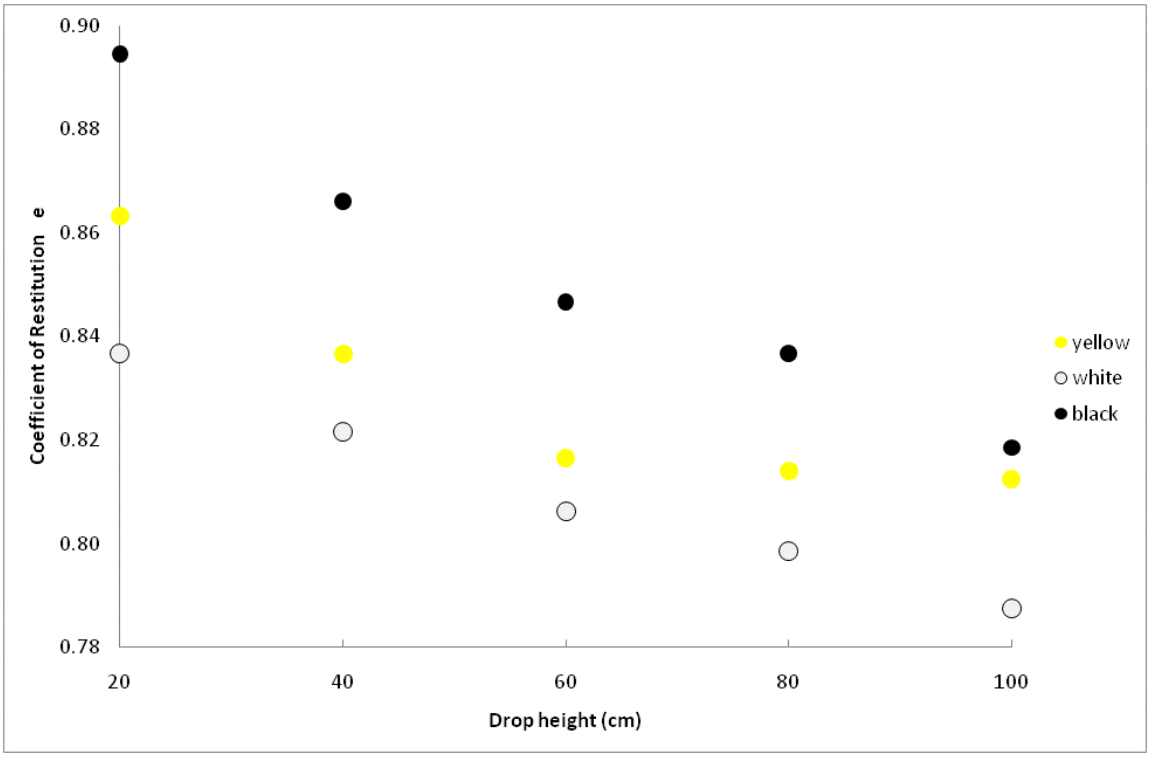

Figure 9.19: The coefficient of restitution of the yellow (6mm), white (5mm) and black (4mm) against drop height

The coefficient of restitution of a particle as shown in figure 9.19 to decrease with increasing drop height which is in agreement with the findings of Sondergaard et al. (1990) who observed that the coefficient of restitution did not vary significantly at low impact velocities (< 200 cms^{-1}) but varied as $v_i^{-1/4}$ for high impact velocities. The impact velocity v is calculated using the formula

$$v = \sqrt{2gh} \qquad \textbf{9.21}$$

where g is the acceleration due to gravity and h is the drop height. Therefore the impact velocity of the particles from drop heights 20, 40, 60, 80 and 100 cm is approximately 198, 280, 343, 396 and 443 cm s^{-1}.

The particle-particle coefficient of restitution was obtained by constructing a simple Newton's pendulum, based on the method suggested by Ollagnier et al. (2007) (Figure 9.20).

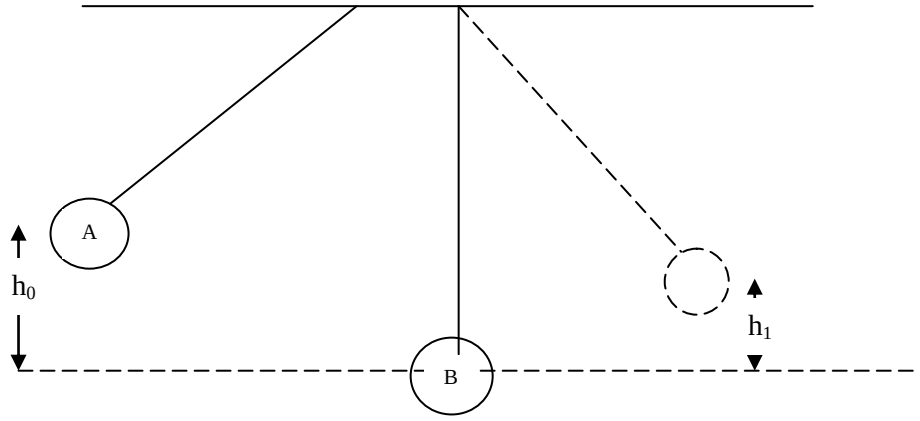

Figure 9.20: Measuring the particle-particle coefficient of restitution

A length of cotton was glued to two particles and they were positioned so that the hung vertically downwards from a strip of wood. The particles were arranged so that they were just touching each other. Two rulers were attached to the strip of wood so the heights could be measured and a video camera was used to capture the particle collision and initial height of particle A and rebound height of particle B.

Particle A was slowly lifted to a height h_0 while keeping the cotton taught. The particle was then released and collided with particle B. The height h_1 that particle B attained was recorded and the coefficient of restitution was calculated using equation 9.21.

Experiments were only conducted using the white (5 mm) and yellow (6 mm) particles as the black particles were too light and were affected by air resistance.

9.3 Experiments to deduce the average mass flow rate of the particles

To determine how accurate the DEM program was at simulating the flow of the particles and to further test the suitability of the values of the coefficients of friction, determined from experiment, the mass flow rate of the white monosized particles (5 mm) and a binary mix of black and white particles was measured. Tests were conducted by varying the hopper half angle in increments of 10º between 20º and 70º. The mass flow rate of the monosized white particles was compared with the correlations developed by Fowler and Glastonbury and Al-Din and Gunn. The mass flow rate of the binary mixture was compared with formula derived by Humby et al. (1998).

A batch of 26450 white particles was used determine the mass flow rate of the white particles. This number of particles was chosen because it enabled comparisons with DEM simulations of the mass flow rate to be quickly determined and it was a sufficient number of particles to fill the silo, to a reasonable height. More or less particles could have been used. The simulation time was only approximately 24 hours. The main aim was to determine the mass flow rate quickly and accurately. The requisite number of white particles was obtained by counting out five batches of 1000 particles, weighing them and obtaining the average weight of one particle. The average weight of one particle was then multiplied by 26450. The binary mixes were counted by hand.

A mix of 30000 white and black particles consisting of 24000 (80%) white and 6000 (20%) black was used in the experiments. This ratio was chosen with the intention that further work could consider other ratios of particles. Humby (1998) observed that the static packing density of a batch of binary particles increased as the ratio of smaller particles, or fines, to larger particles increased to 50%. It was decided therefore to test whether this affected both the mass flow rate and the displacement and velocity of the free cells. Other ratios could have equally been chosen

The rig sides were adjusted so that they were a distance 20 cm apart so that they would not affect the flow and the orifice width was set to 3 cm in experiments using the white and binary mixes. The appropriate distance to place the rig sides, so that they would impinge on the flowing core was determined using the criteria that

$$D > 2.5D_0 \text{ and } (D - D_0) > 30d \quad \textbf{9.22}$$

where, *D*, is the diameter or width of the silo, D_0, is the orifice width or diameter and, *d*, is the particle diameter (Datta, 2008). Davies and Desai (2008) found that the minimum size opening for reliable flow of non-cohesive grains from horizontal slots was 3.3*d*. Observations of the particles as they discharged from the hopper showed that the hopper walls did not impinge on the flowing core. Hence this shows the reliability in using the criteria given by Datta (2008).

A set of scales accurate to the nearest 0.1 g was used to weigh the particles. To check the scales were accurate, a small lump of metal was weighed on the scales and on a similar set of scales and the weight recorded. Each time the scales were used the metal was placed on the scales to check they were still accurate.

The orifice was closed by placing a rolled up strip of plastic in between the Perspex sheets and the strips making the hopper bottom.

The particles were poured from the top of the rig one scoop at a time, between the Perspex sheets, by placing a plastic scoop so that it was symmetrical either side of the centre line.

The particles then fell under the force of gravity, bouncing between the Perspex sheets until they impacted with the hopper bottom and other particles before coming to rest.

When the rig was filled the volume of the hopper occupied by the particles was recorded. The video camera was turned on and the orifice was opened by pulling out the rolled up strip of plastic. The particles were then allowed to free fall out of the orifice into a container below. The experiment was repeated five times.

Each experiment was repeated ten times to deduce an average discharge time and hence, to be able to calculate the mass flow rate of the particles through the orifice.

Figure 9.21 show the mass flow rate of the white (5 mm) monosized particles against hopper half angle θ

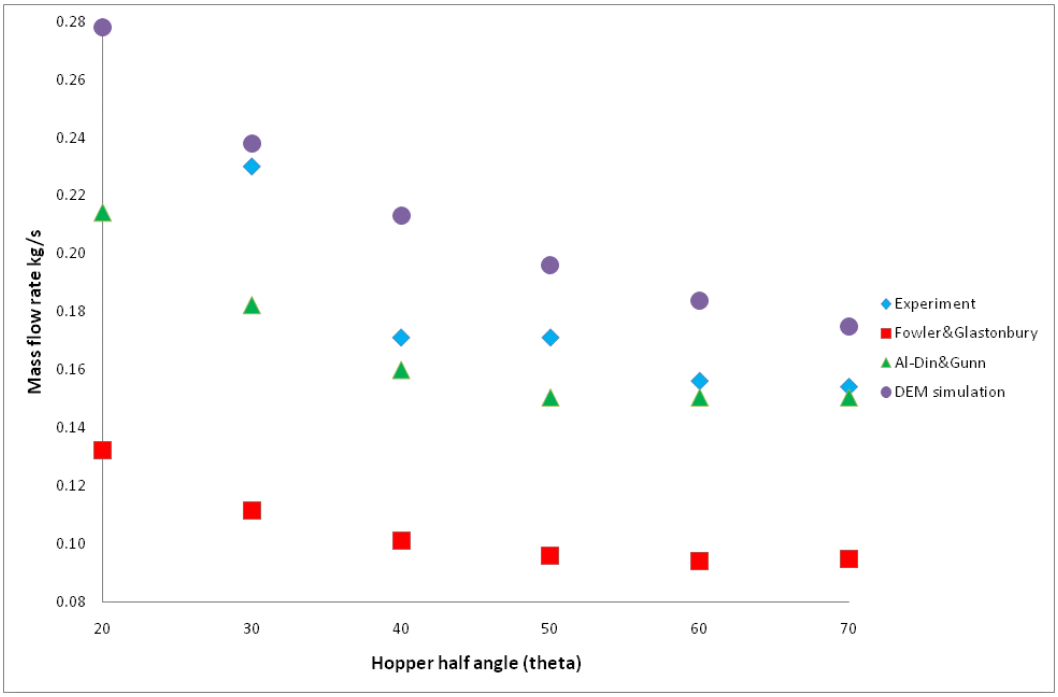

Figure 9.21: Plot of the mass flow rate against hopper half angle obtained from experiment and DEM simulation of the monosized white (5 mm) particles. The theoretical predictions of Fowler and Glastonbury and Al-Din and Gunn are also included for comparison

The mass flow rate obtained from the DEM simulation is on average 17% greater than the experimental flow rate. The DEM and experimental results are in excellent agreement in the mass flow region when the hopper half angle is between 20º and 30º. The correlation of Al-Din and Gunn is an average 26% less than the experimental results and the correlation of Fowler and Glastonbury predicts a mass flow rate of approximately 100% less than the experimental results. Steingart et al. (2005) proposed that the correlation derived by Fowler and Glastonbury (1959) fails to match experimental results, because in a hopper in which the length of the orifice is much greater than the width, at small orifice widths the particles bridge over the slot but at large widths these bridges are less of an impediment to flow. The extent of bridging would be expected to be dependent on the inter-particle forces and hence on surface roughness. Steingart et al. (2005) hypothesize that the power 3/2 should diminish to unity as the slot becomes larger and bridging switches from infrequent to non-existent.

Figure 9.22 shows the mass flow rate against time for the 80% white (5 mm)/ 20 % black (4 mm) binary mixture of particles.

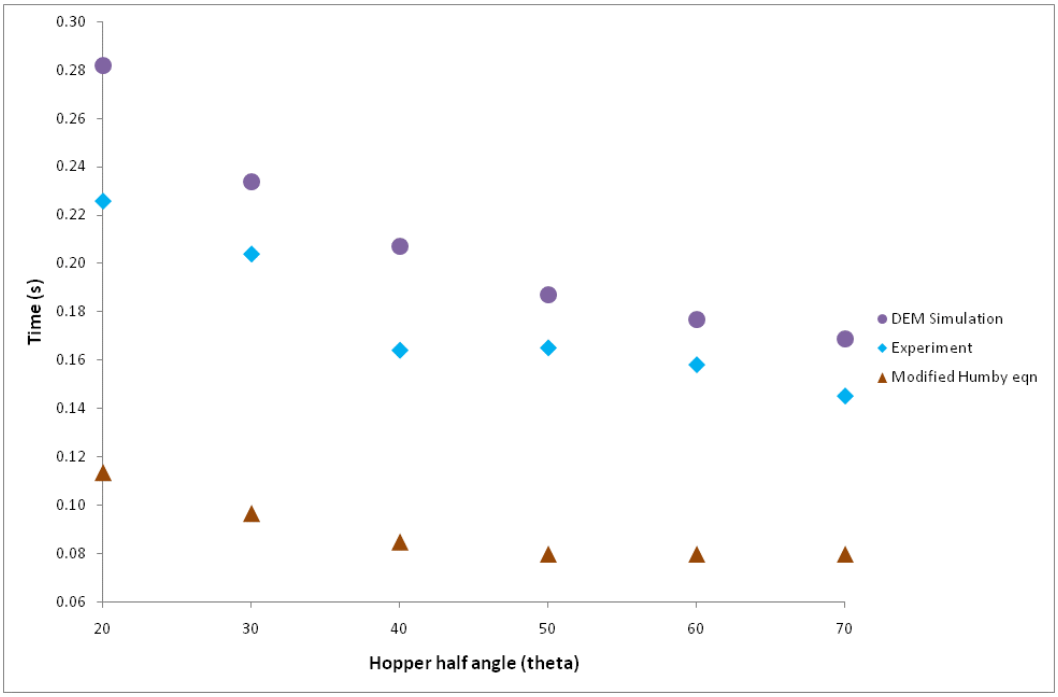

Figure 9.22: Plot of the mass flow rate against hopper half angle obtained from experiment and DEM simulation of the binary mixture of 80% white (5 mm)/20% black (4 mm) particles. The theoretical prediction of Humby is also included for comparison

The DEM simulation of the mass flow rate of the black and white binary mixture is an average of 15% greater than the experimental results and the modified Humby equation results in a mass flow rate that is 100% less than the experimental results.

In both sets of experiments the mass flow rate obtained from the DEM simulations is slightly greater than the experimental results. This possibly indicates that one of the input parameters, such as the particle-particle sliding friction, may not be large enough.

Results and discussion comparing the trajectory of the free-cells in the experiments and in the DEM simulations

10 Results and discussion comparing the trajectory of the free-cells from experiments and DEM simulations

10.1 Introduction

In this section the results obtained from DEM simulations of the trajectory of the free-cells starting from the two positions 5 and 12 are compared with the average trajectory obtained from three experimental trials. One trial of each of the metal and plastic, cylindrical, cuboid and triangular prism free cells was simulated using the DEM in monosized particles and binary mixtures. The trajectory of the representative particle obtained from DEM simulation, also starting at positions 5 and 12, is included so that the trajectory of each of the free-cells can be compared with a typical particle trajectory. One trial of each of the representative particles was conducted. In this way the most suitable free-cell could be identified for the WSN4IP project. The three experimental trials in this experiment were the same three used in the experiments in chapters 4 and 5.

10.2 The representative particle trajectory

The trajectory of a representative particle obtained from DEM simulation during discharge in the white (5 mm) monosized particles is shown in Figure 10.1.

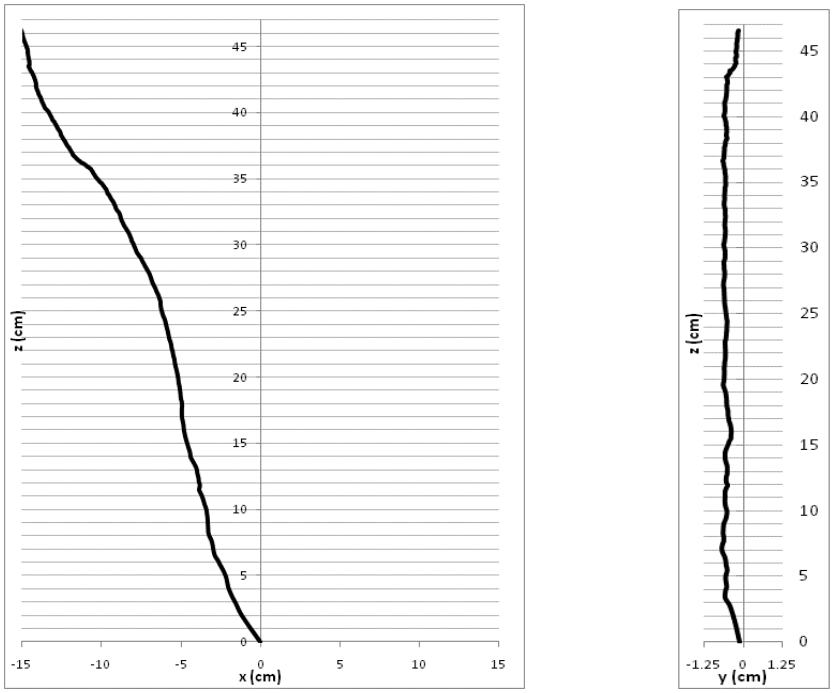

Figure 10.1: The trajectory of one white (5 mm) representative particle obtained from DEM simulation during the discharge from the silo.

The trajectory followed by the representative particle is shown to fluctuate slightly, along a generally constant vertical path. The initial position of the particle was very close to the centre line. Experimental observations of particles with initial starting positions near to the front and back walls, however, were in some instances found to migrate away from the walls, possibly towards the faster flowing central region.

The trajectory followed by a single particle in the binary mix of the white (5 mm) and black (4 mm) particles, of the same density from DEM simulation is given in Figure 10.2

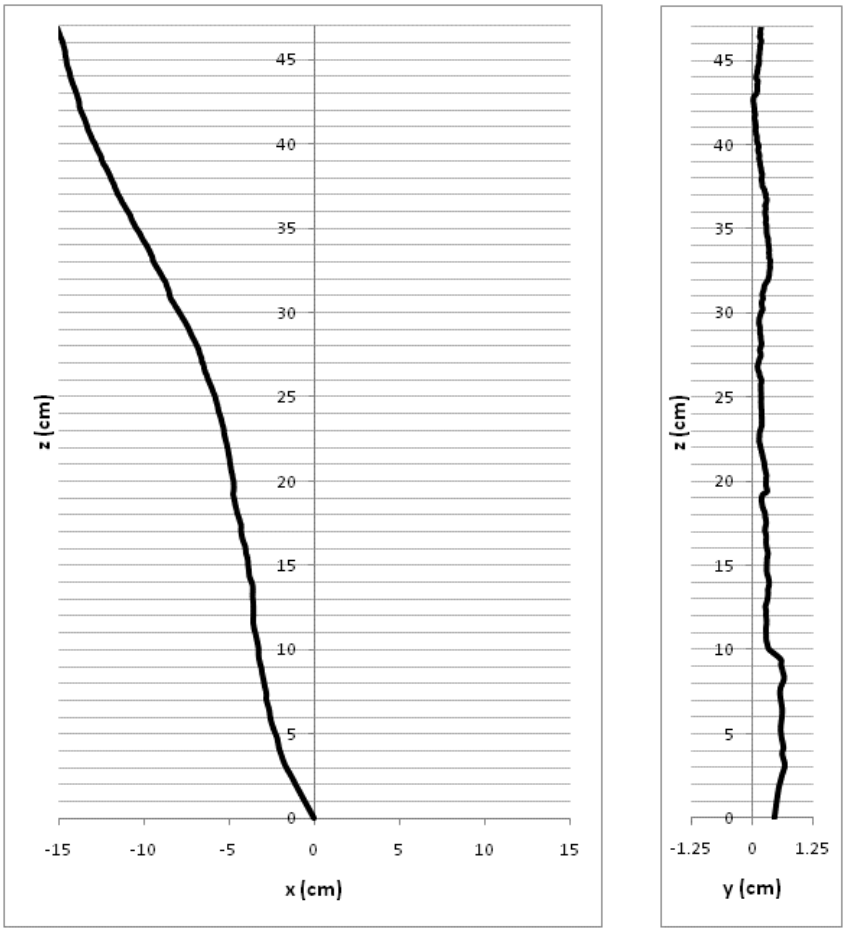

Figure 10.2: The trajectory of one representative particle in the white (5mm)/black (4mm) binary mixture obtained from DEM simulation.

The trajectory of a representative particle from DEM simulation in the binary mixture starts from an initial position very near the centre line (0, 0, *z*) between the front and back walls. This is in the faster flowing region where the particles are less affected by the frictional forces between the particles and the wall.

10.3 Comparisons between the DEM simulations and experiments of the metal and plastic cylinders and cuboids starting from position 12 in the white monosized particles.

Figure 10.3 shows the DEM simulated trajectories of the metal and plastic cylinders in a monosized batch of the white (5 mm) particles starting from position 12 and the average trajectory of three experimental trials. The trajectory of the representative particle from DEM simulation is also shown.

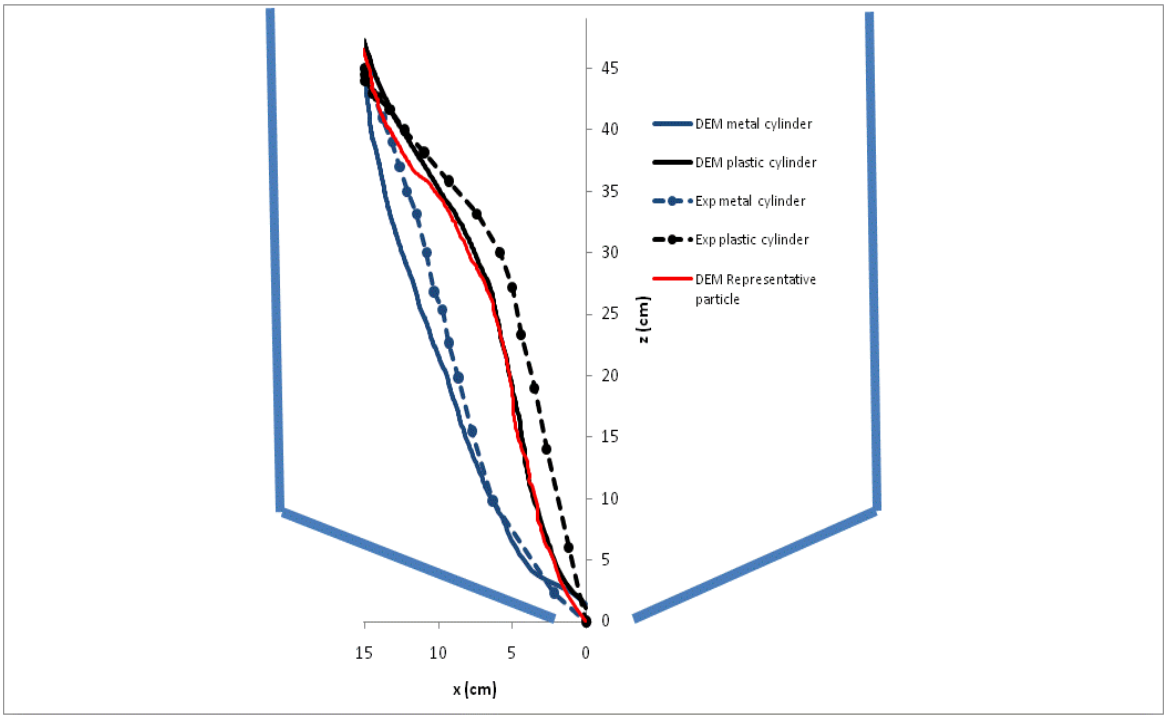

Figure 10.3: Plot of z against x showing the trajectory of metal and plastic cylindrical free-cells from position 12 in the white (5mm) monosized particles. The DEM simulation results and the average of three experimental trials and the trajectory of the representative particle are shown.

The average path of the plastic cylinder in the experiments differs from the DEM simulation of the plastic cylinder and the DEM simulation of the representative particle by up to 1.5 cm along the horizontal. The curves showing the DEM simulation of the representative particle and plastic cylinder are nearly identical. The curves showing the DEM simulated and experimental trajectories of the metal cylinder are in good agreement in the lower part of the silo but differ by up to 2 cm at z = 35 cm.

Figure 10.4 shows *z* against time for the metal and plastic, cylindrical free-cells in the white (5 mm) particles starting from position 12. The trajectory of the representative particle and the average of three experimental trials and the DEM simulation are shown. The vertical velocity of the DEM simulation of the plastic cylinder and representative particle differ by approximately 0.05 cm/s and the time taken for each of them to reach the orifice is 14.3 seconds and 15 seconds. The vertical velocity of the plastic cylinder obtained from DEM simulation and experiment also differs by only approximately 0.06 cm/s and the time taken to reach the orifice are 15.2 seconds and 14.3 seconds respectively. The vertical velocity of the metal cylinder obtained from DEM simulation and experiment is similar at approximately 2 cm/s in the first 12 seconds after the initiation of discharge, but the experimental result shows the metal cylinder travelling with a velocity of 1.7 cm/s in the 3.5 s prior to it passing through the orifice and approximately 3 cm/s in the DEM simulation.

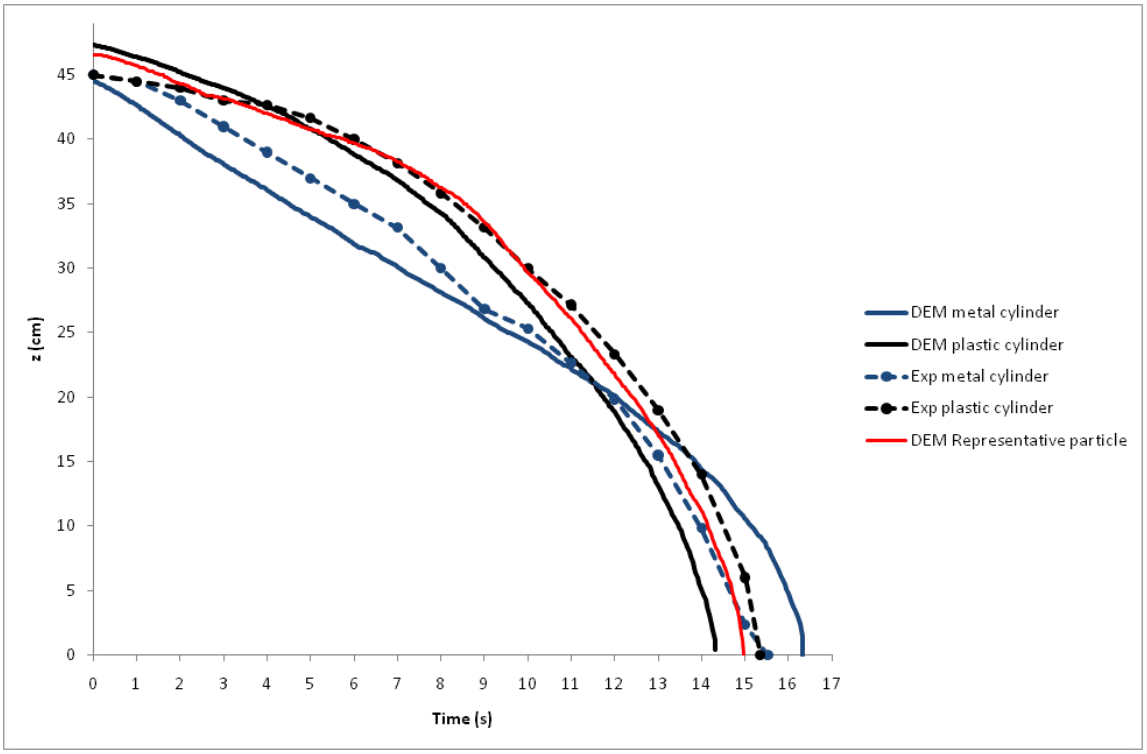

Figure 10.4: Plot of z against time for metal and plastic cylindrical fee-cells in white (5 mm) particles starting from position 12. The average of three experimental trials and the DEM simulation of the metal cylinder and the DEM simulation of the representative particle are shown.

Figure 10.5 shows *x* against time for the metal and plastic, cylindrical free-cells in the white (5 mm) particles starting from position 12. The trajectory of the representative particle and the average of three experimental trials and the DEM simulation are shown. The profile of the horizontal displacement-time curves of the DEM simulation of the plastic cylinder and the representative particle and the average experimental trial of the plastic cylinder are very similar. The velocity is shown to increase to approximately 2 cm/s during the middle portion of the trajectory and then decelerating in the final two seconds prior to accelerating through the orifice. The difference in the horizontal velocity throughout the trajectory of the plastic cylinder in DEM simulations and experiments and the DEM simulation of the representative particle is only 0.1 cm/s. The horizontal velocity of the metal cylinder in experiments and DEM simulations is also in very good agreement, varying by only 0.05 cm/s throughout the entire path. The time taken for the metal cylinder in DEM simulation and experiment to reach the orifice is 16.3 seconds and 15.5 seconds respectively.

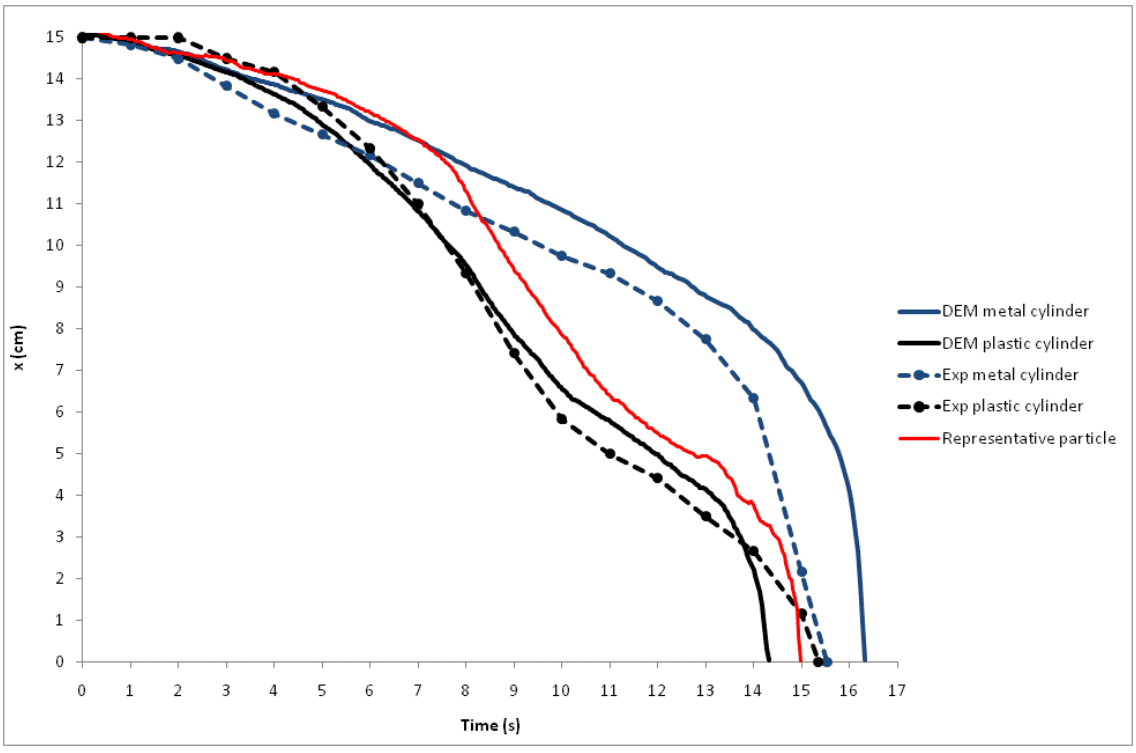

Figure 10.5: Plot of x against time for cylindrical metal and plastic free-cells in white (5 mm) particles starting from position 12. The average result of three experimental trials and a DEM simulation of the trajectory of the plastic cylinder and the DEM simulation of the representative particle are shown.

Figures 10.6 shows the vertical velocity of the plastic cylindrical free cell in the discharging white (5 mm) particles starting from position 12 obtained from DEM simulation and the average of three experimental trials respectively. The velocity of the representative particle from DEM simulation is also shown. The general trend of the three curves is similar, despite the fluctuating velocity of the plastic cylinder and representative particle obtained from DEM simulation. The value of the vertical velocity between the three curves only varies by approximately 1 cm/s in the initial 12 seconds after the opening of the orifice, but there is then a difference of up to 5 cm/s in the final few seconds prior to the plastic cylinder travelling through the orifice.

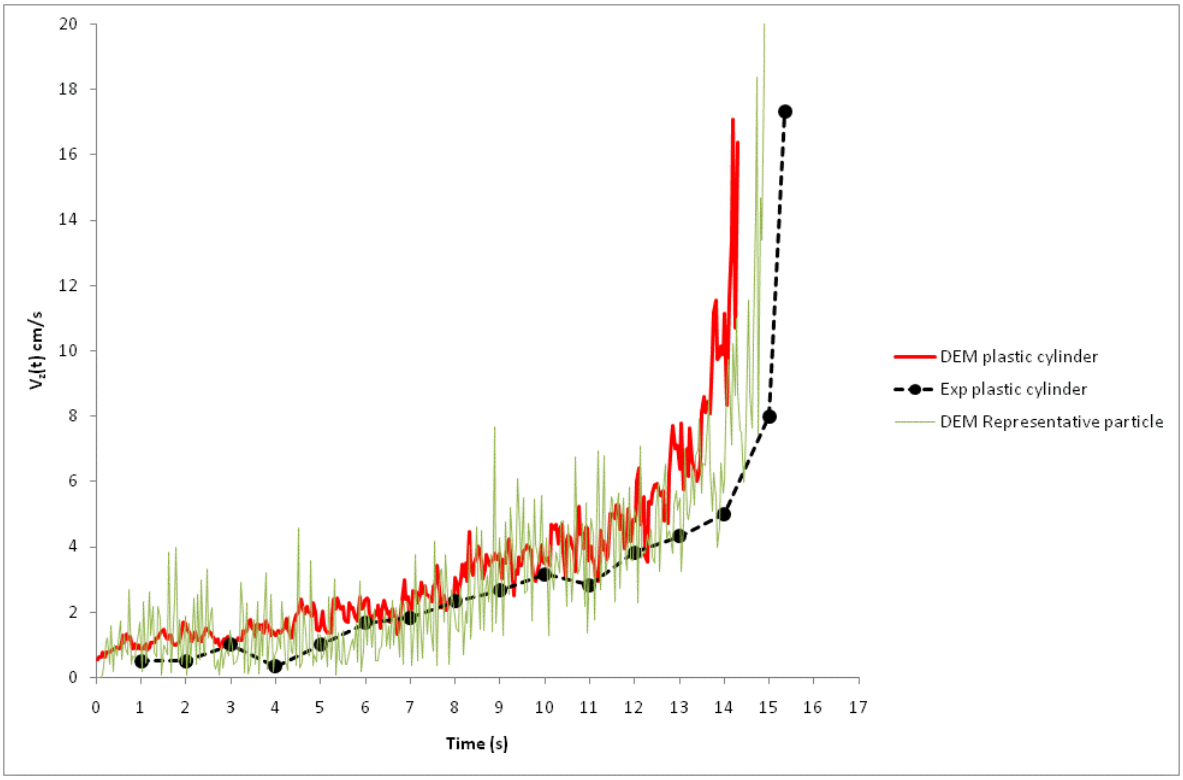

Figure 10.6: Plot of the velocity $V_z(t)$ against time for the plastic cylindrical free cell in the white (5 mm) monosized particles starting from position 12 obtained from DEM simulation and the average of three experimental trials. The velocity of the representative particle from DEM simulation is also shown.

Figures 10.7 shows the horizontal velocity of the plastic cylindrical free cell in the discharging white (5 mm) particles starting from position 12 obtained from DEM simulation and the average of three experimental trials respectively. The velocity of the representative particle from DEM simulation is also shown. The general trend of the three curves is similar. The maximum difference in the velocity of the three curves is 0.7 cm/s at 9.5 seconds after the initiation of discharge, at other times the velocity varies by approximately 0.2 seconds. After approximately 13 seconds the three curves diverge and the plastic cylinder in the DEM simulation is shown to accelerate earlier than the DEM simulated representative particle and the plastic cylinder from experiment.

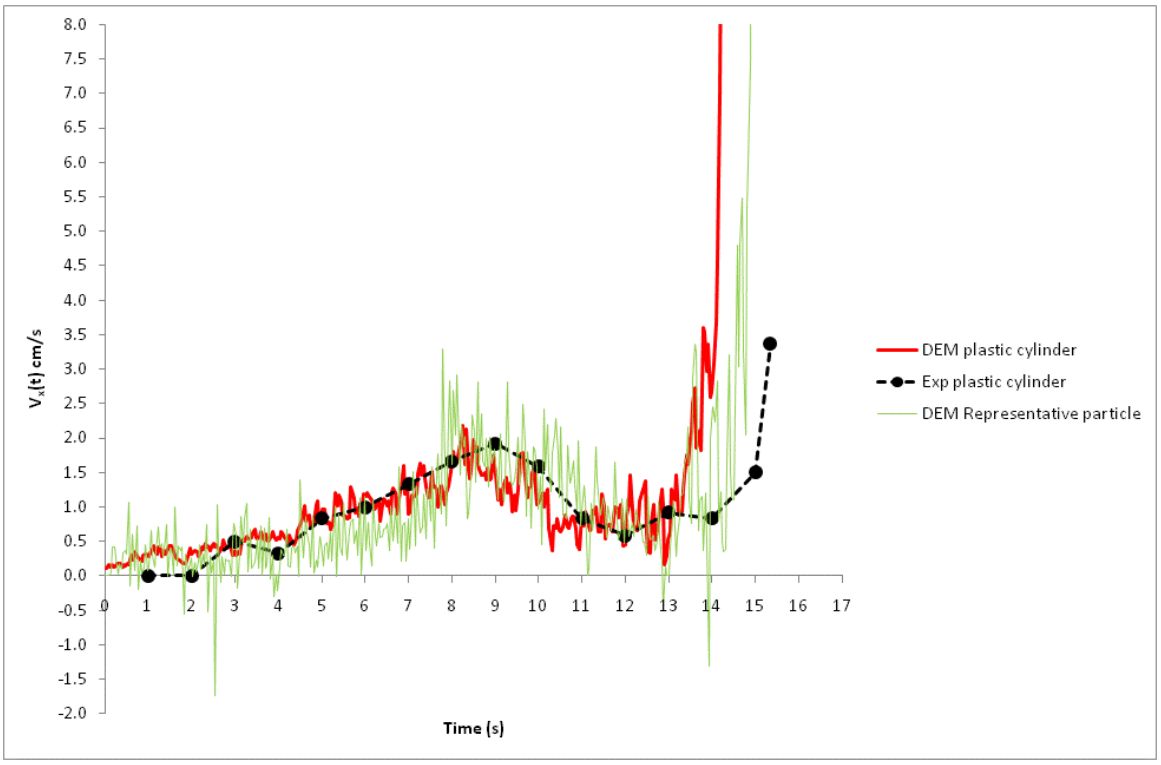

Figure 10.7: **Plot of the velocity $V_x(t)$ against time for the plastic cylindrical free cell in the white (5 mm) monosized particles starting from position 12 obtained from DEM simulation and the average from three experimental trials. The velocity of the representative particle from DEM simulation is also shown.**

Figure 10.8 shows z against x for the metal and plastic cuboids in the white (5 mm) monosized particles starting from position 12. The DEM simulations of the plastic and metal cuboids and the representative particle and the average of three experimental trials are shown. There is good agreement between the paths followed by the DEM simulation of the representative particle and the plastic cuboid. The paths differ by up to 1 cm between z = 35 cm and z = 45 cm and z = 0 and z =10 cm. The path followed by the plastic cuboid from experiment differs from the DEM simulation of the plastic cuboid by up to1cm along the horizontal. The DEM simulation of the metal cuboid differs from the DEM simulation of the representative particle and the experimental path of the metal cuboid by up to 4 cm and 2 cm respectively.

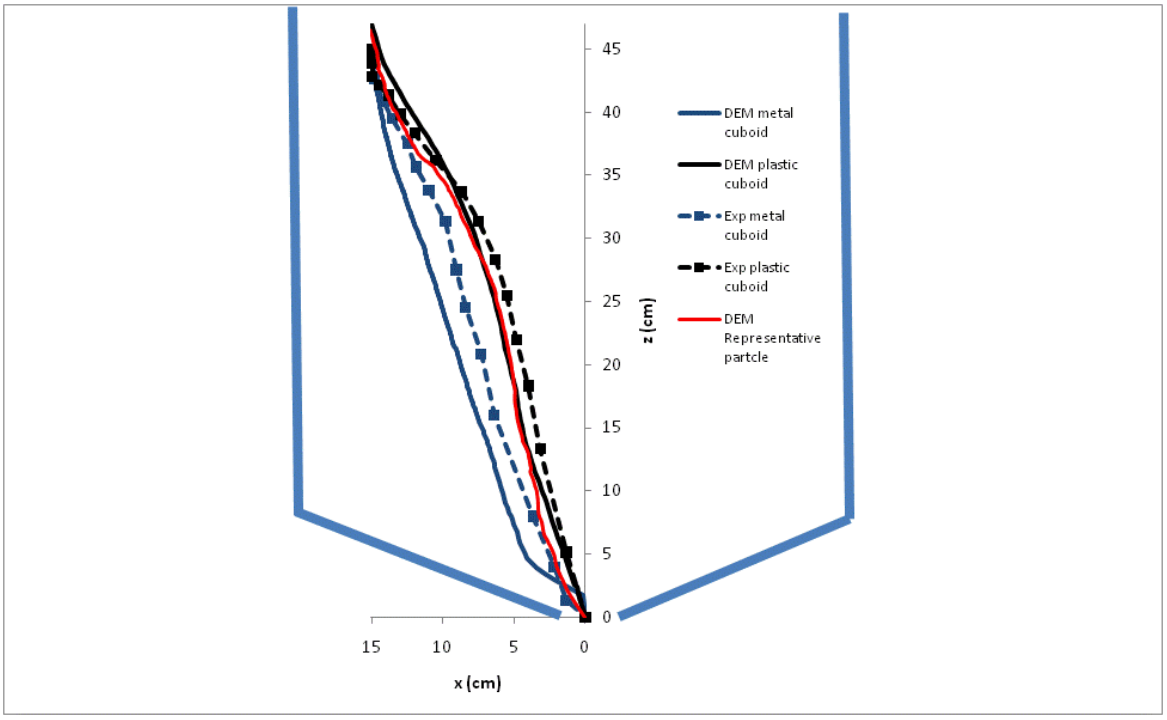

Figure 10.8: Plot of z against x showing the trajectory of metal and plastic cuboid free-cells from position 12 in the white (5 mm) monosized particles. The average of three experimental trials, the DEM simulation of the metal and plastic cuboids and the DEM simulation of a representative particle are shown.

Figure 10.9 shows *z* against time for the metal and plastic cuboid free-cells in the white monosized particles starting from position 12. The DEM simulation of the representative particle is shown and the average result from three experimental trials and the DEM simulation are shown. The curves showing the DEM simulation of the displacement of the plastic cuboid and the representative particle are very similar. The velocity differs by approximately 0.1 cm/s. The velocity of the plastic cuboid in the experiments is approximately 14 % slower. The velocity of the metal cuboid in the DEM simulations is approximately 2 cm/s in the initial 13 seconds after the opening of the orifice, compared to the metal cuboid in experiments in which the velocity varies between 0.75 cm/s and 5 cm/s. The metal cuboid in DEM simulations is shown to accelerate towards the orifice. However, the metal cuboid in experiment is shown to decelerate approximately 2 seconds prior to passing through the orifice and then travel at a constant velocity to the orifice.

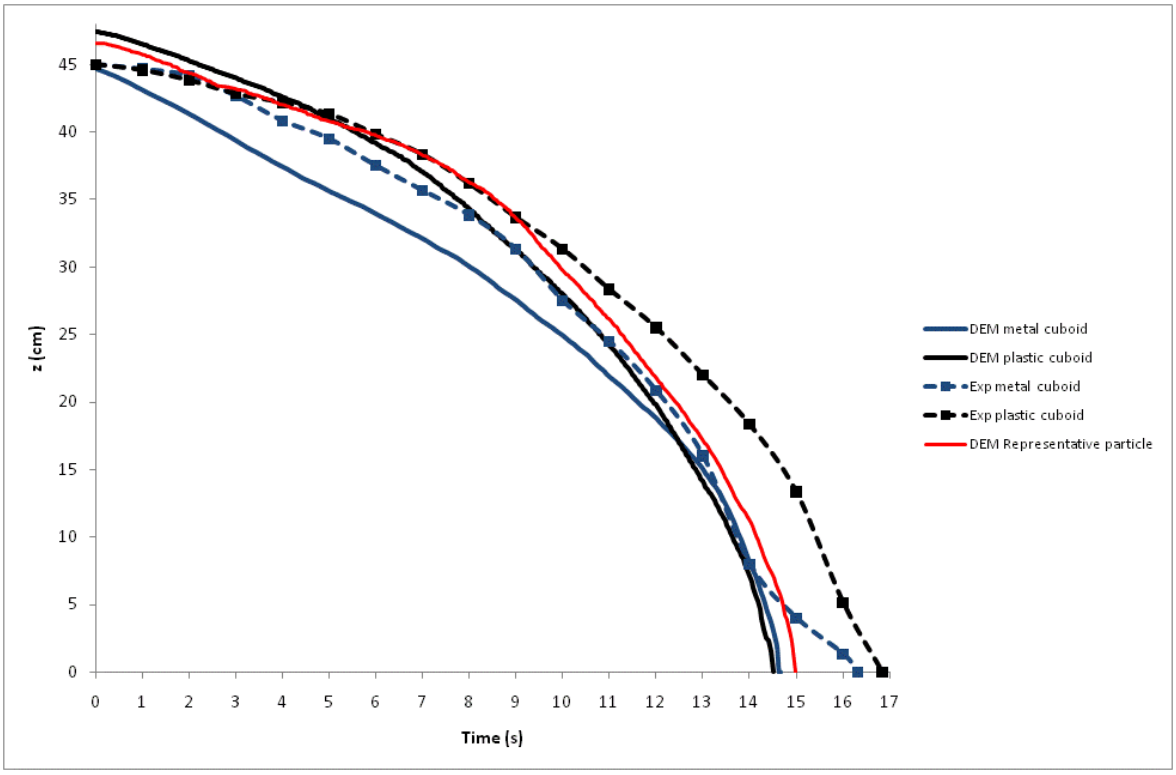

Figure 10.9: Plot showing z against time for metal and plastic cuboid free-cells in white (5 mm) particles starting from position 12. The average of three experimental trials and the DEM simulation of the metal and plastic cuboids and the DEM simulation of the representative particle are shown.

Figure 10.10 shows *x* against time for the metal and plastic, cuboid free-cells in the white (5 mm) monosized particles starting from position 12. The trajectory of the DEM simulation of the representative particle is shown and the average result from three experimental trials and the DEM simulation of the metal and plastic cuboid are shown. The profile of the curves showing the DEM simulations of the plastic cuboid and the representative particle and the plastic cuboid in experiments is similar. The plastic cuboid in experiment is shown to have a zero horizontal velocity during the first 3 seconds after the initiation of discharge. The plastic cuboid in DEM simulation quickly accelerates to 1.2 cm/s in the initial 4 seconds after the opening of the orifice compared to the representative particle and plastic cuboid in experiment that takes 8 seconds to accelerate to 1.2 cm/s. The representative particle also travels with a greater velocity at 1.75 cm/s between 8 and 11 seconds after the initiation of discharge compared to the DEM simulation of the plastic cuboid and the experimental result where it travels at 1 cm/s. The metal cuboid in experiment has an average velocity of 1.5 cm/s during the initial 13 seconds after the opening of the orifice, compared to the DEM simulation of the metal cuboid in which the velocity varies between 0.5 cm/s and 1.5 cm/s during the initial 13 seconds.

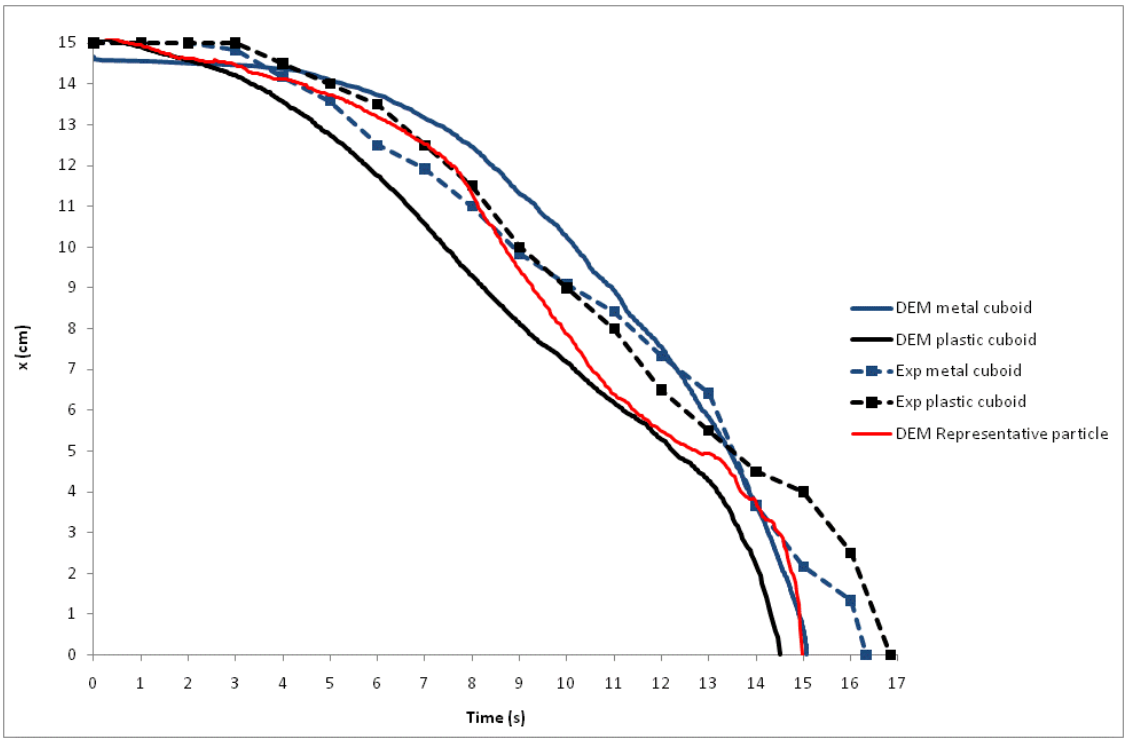

Figure 10.10: Plot showing x against time for metal and plastic cuboid free-cells in white (5 mm) monosized particles starting from position 12. The average of three experimental trials, the DEM simulation of the metal and plastic cuboids and the trajectory of the representative particle obtained from DEM simulation are shown

Figure 10.11 shows the vertical component of the velocity of the plastic cuboid free cell starting from position 12 in the discharging white (5 mm) monosized particles obtained from DEM simulation and the average of three experimental trials. The DEM simulated trajectory of the representative particle is also shown. The profile of the curves showing the DEM simulation of the plastic cuboid and the DEM simulation of the representative particle are very similar. The velocity differs by up to 2 cm/s at approximately 8 and 12 seconds after the initiation of discharge. The plastic cuboid in experiments has a velocity approximately 0.5 cm/s slower that the two curves from simulations, resulting in the velocity in the experiment rapidly increasing after 15 seconds compared to after 13 seconds in the simulations.

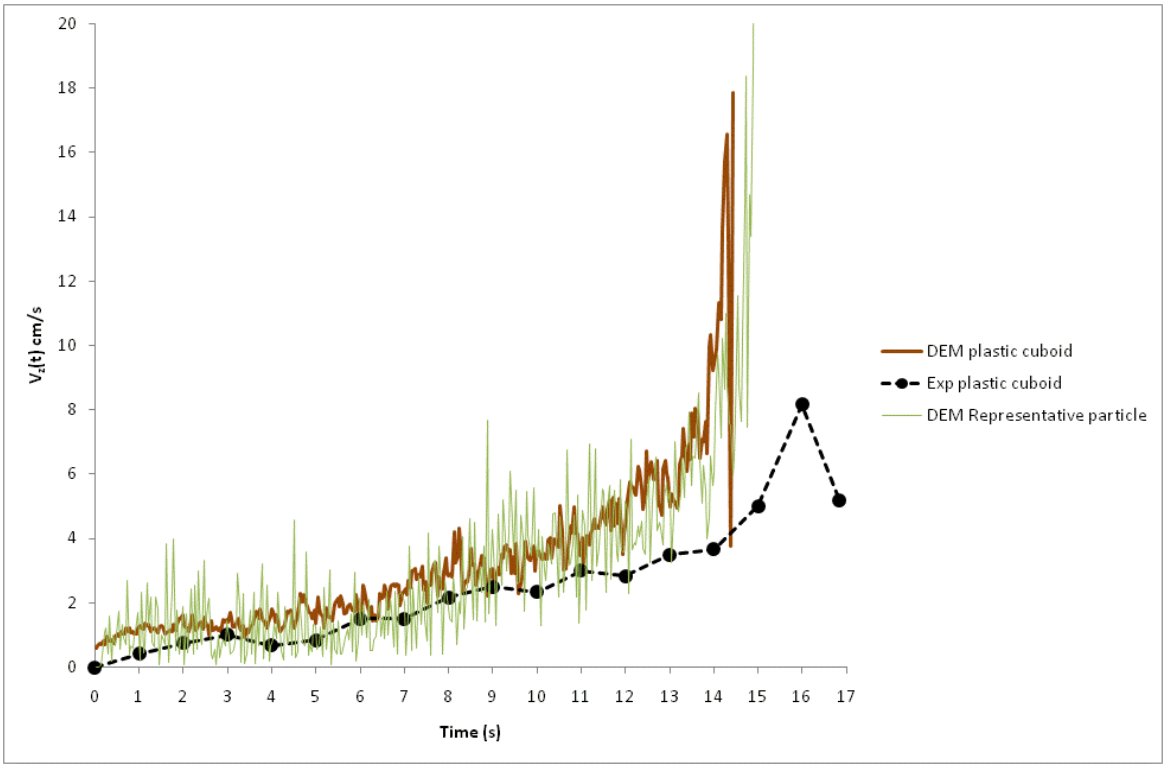

Figure 10.11: Plot of $v_z(t)$ against time for the plastic cuboid in the white (5mm) monosized particles starting from position 12. The average of three experimental trials, the DEM simulation of the plastic cuboid and the DEM simulation of the representative particle are shown.

Figure 10.12 shows the horizontal component of the velocity of the plastic cuboid free cell starting from position 12 in the discharging white (5 mm) monosized particles obtained from DEM simulation and the average of three experimental trials. The DEM simulation of the representative particle is also shown. The profile of the curves showing the DEM simulation of the representative particle and the experimental result of the path of the plastic cuboid are similar during the initial 12 seconds, varying by up to 0.5 cm/s. The DEM simulation of the plastic cuboid has a different velocity profile from the other two curves. The increase in the horizontal velocity between 8 and 10 seconds after the initiation of discharge is not visible on the curve representing the DEM simulation of the plastic cuboid. Unlike the curves showing the DEM simulation of the horizontal velocity of the plastic cuboid and representative particle the plastic cuboid in experiment does not show a rapid increase in velocity as it nears the orifice. This suggests that the simulation may not be adequately modelling the small stress fluctuations during discharge. This may be because the friction force between the particles and the cuboid was assumed to be identical on all four faces, when it may in fact vary slightly.

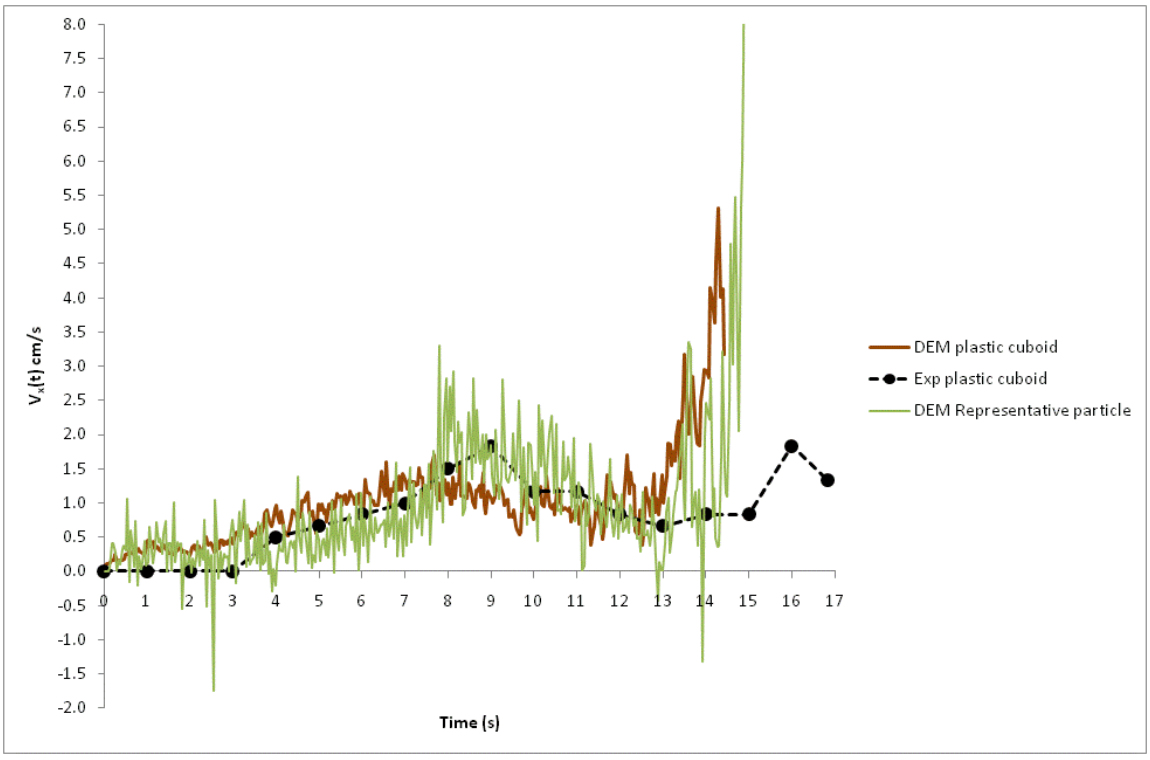

Figure 10.12: Plot of $v_x(t)$ against time for the plastic cuboid in the white (5 mm) monosized particles starting from position 12. The average of three experimental trials and the DEM simulation of the plastic cuboid and the DEM simulation of the representative particle are shown.

Figure 10.13 shows *z* against *x* for the metal and plastic triangular prisms starting from position 12 in the white (5 mm) monosized particles. The DEM simulation of the metal and plastic triangular prisms and the DEM simulation of the representative particle and the average of three experimental trials are shown. There is good agreement between the path followed by the DEM simulation of the representative particle and the average of three experimental trials of the plastic triangular prism. The paths differ by up to 1 cm along the horizontal. The DEM simulation of the plastic triangular prism results in a different path. The path followed by the plastic triangular prism in the DEM simulation differs from the DEM simulation of the representative particle and the experimental result of the plastic triangular prism by up to 3 cm along the horizontal. This may possible indicate the stochastic nature of the path followed by the plastic triangular prism, or could indicate that the DEM simulation is failing to model an important effect. There is a difference of up to 3 cm along the horizontal between the paths followed by the metal triangular prism in DEM simulation and experiment, which again could just be a result of the stochastic nature of the triangular prism. There is a difference of up to 4 cm between the DEM simulation of the representative particle and the DEM simulation of the metal triangular prism.

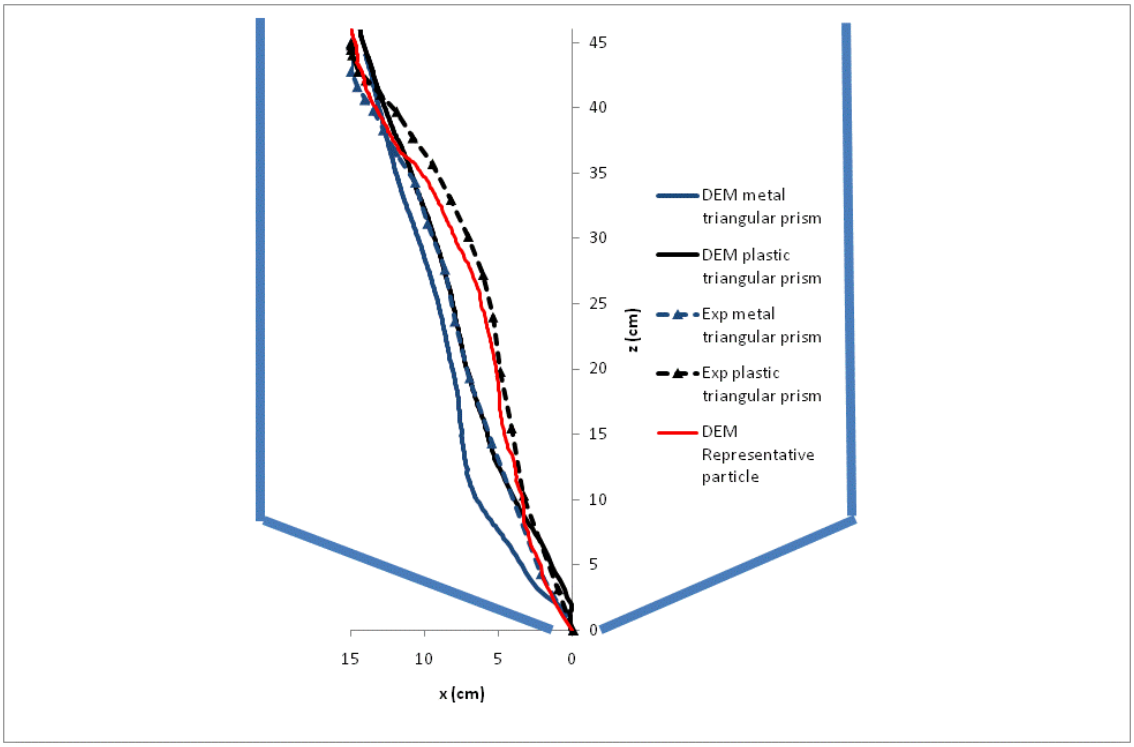

Figure 10.13: Plot showing z against x for metal and plastic triangular prism free-cells in white (5mm) particles starting from position 12. The average of three experimental trials and the DEM simulation of the metal and plastic triangular prisms and the DEM simulation of the representative particle are shown

Figure 10.14 shows z against time for the metal and plastic triangular prism free-cells in the white (5 mm) monosized particles starting from position 12. The results from the DEM simulations of the metal and plastic triangular prisms and the DEM simulation of representative particle and the results from three experimental trials are also shown. The difference between the vertical velocity of the metal triangular prism in the DEM simulation and the vertical velocity of the metal triangular prism in experiment is approximately 0.3 cm/s. The plastic triangular prism starts at z = 46 cm in the DEM simulation compared to z = 45 cm in the experiment, as a result of the difficulty in accurate positioning in the simulation. The DEM simulation of the representative particle has a very similar displacement curve the metal triangular prism in experiment. The velocity only differs by approximately 0.05 cm/s. The DEM simulation of the plastic triangular prism has a similar velocity as the DEM simulation of the representative particle in the initial 3 seconds, but then the representative particle is shown to slow down for the next 6 seconds before gradually accelerating towards the orifice at approximately 3.3 cm/s^2, compared to the plastic triangular prism in the DEM simulation that accelerates at 1.6 cm/s^2. The DEM simulation of the metal triangular prism and the experimental result showing the path of the metal triangular prism both result in the same time to reach the orifice. However, the metal triangular prism in the experiment has a velocity varying between 1 cm/s and 15 cm/s and the metal triangular prism in the DEM simulation has an average velocity of 2.5 cm/s during the initial 13.5 seconds and then accelerates to 15 cm/s in the final 0.5 seconds prior to passing through the orifice.

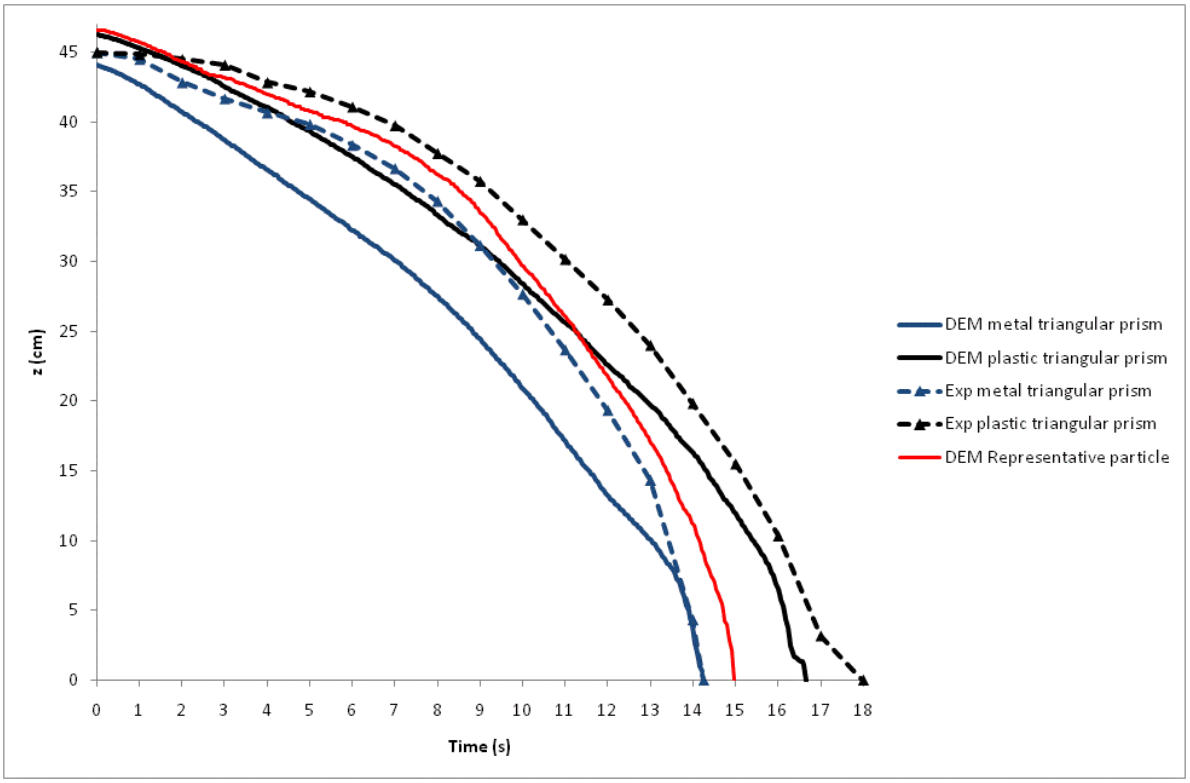

Figure 10.14: Plot showing z against time for metal and plastic triangular prism free-cells in the white (5mm) particles starting from position 12. The average of three experimental trials and the DEM simulation of the metal and plastic triangular prisms and the DEM simulation of the representative particle are shown.

Figure 10.15 shows *x* against time for the metal and plastic triangular prism free-cells in the white (5 mm) monosized particles starting from position 12. There is very little similarity between the results from experiments and simulations of either the metal triangular prism or the plastic triangular prism. However, the profile of the curves showing the displacement of the plastic triangular prism in experiment and simulation and the DEM simulation of the representative particle are similar. The initial position of the metal and plastic triangular prisms in the DEM simulations are at x = 14 cm and x = 14.5 cm respectively, compared to the initial position at x = 15 cm in the experiments. The plastic and metal triangular prisms in the experiments accelerate to a maximum velocity of 1.3 cm/s compared to the metal and plastic triangular prisms in the DEM simulations which accelerate to a maximum velocity of 0.6 cm/s in the initial 7 seconds after the opening of the orifice. The metal triangular prism in the DEM simulation and experiment then increases in velocity towards the orifice, but the plastic triangular prism is observed to slow down, prior to increasing in velocity towards the orifice.

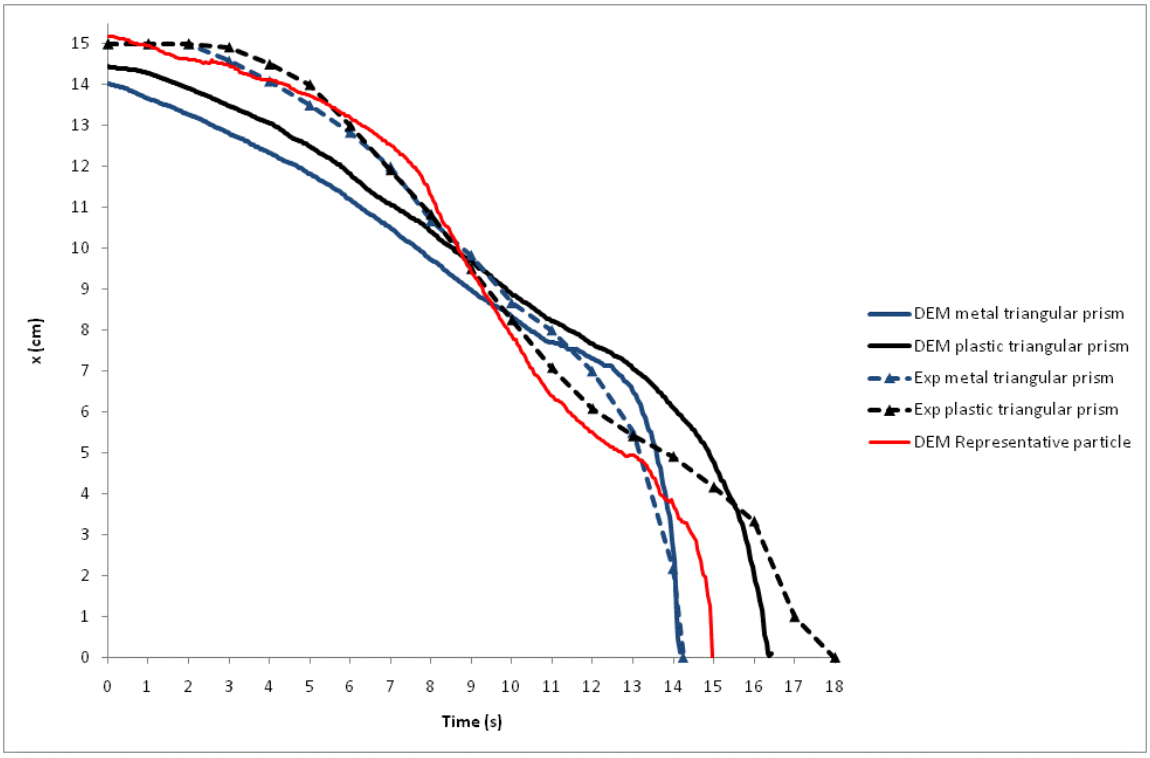

Figure 10.15: Plot showing x against time for the metal and plastic triangular prism free-cells in the white (5mm) particles starting from position 12. The average of three experimental trials and the DEM simulation of the metal and plastic triangular prisms and the DEM simulation of the representative particle are shown.

10.4 Summary

The results clearly show that the plastic cylinder is modelled more accurately by the DEM than the plastic cuboid or plastic triangular prism. The main features of the velocity of the plastic cylinder are also observed on the lines showing the velocity of the DEM simulation of the plastic cylnder and the representative particle. However, the horizontal velocity curve from the DEM simulation of the plastic cuboid fails to show the peak in velocity at 9 seconds experienced by the represenative particle and the plastic cuboid in the experiments.

10.5 Comparisons between the DEM simulations and experiments of the metal and plastic cylinders and cuboids starting from position 5 in the white monosized particles.

Figure 10.16 shows *z* against *x* for the metal and plastic cylinder free cells and the representative particle starting from position 5. The paths followed by the metal and plastic cylinders in the DEM simulations and the experimental results differ by approximately 1 cm. Neither the plastic cylinder nor the metal cylinder in experiments or simulations follow a similar path to the representative particle.

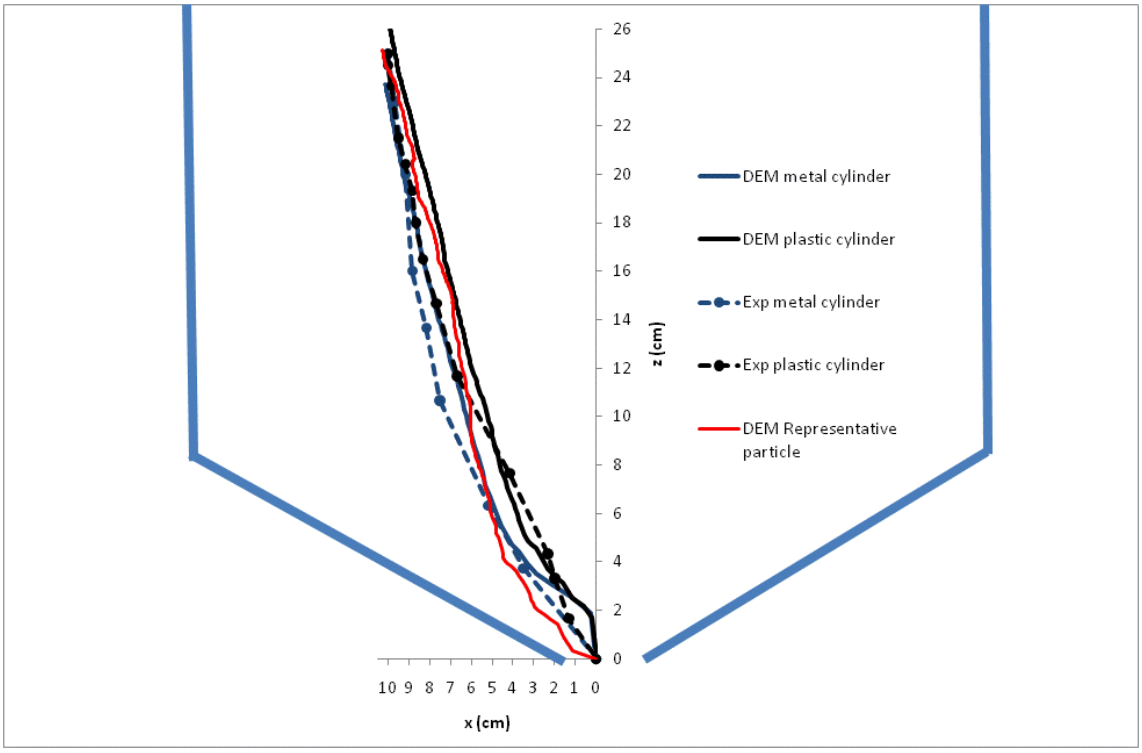

Figure 10.16: Plot showing z against x for the metal and plastic cylinders in the white (5 mm) particles starting from position 5. The average of three experimental trials, the DEM simulation of the metal and plastic cylinder and the DEM simulation of the representative particle are shown.

Figure 10.17 shows z against time for the metal and plastic cylindrical free-cells in the white (5mm) monosized particles starting from position 5. The plastic cylinder and metal cylinder in the DEM simulations started at z = 26 cm and z = 24 cm respectively compared to z = 25 cm in the experiments. This is a result of the difficulty in accurately positioning the free-cells in the simulations. The metal cylinder has a similar horizontal velocity of 2.3 cm/s in the experiments and simulations during the first 3 seconds, but the metal cylinder in the experiments then accelerates to approximately 3.6 cm/s and the metal cylinder in the DEM

simulation accelerates to 16 cm/s. The DEM simulation of the plastic cylinder is observed to be very different to that observed in experiment. The time taken for the plastic cylinder in the experiment takes 13.2 seconds to reach the orifice compared to the DEM simulation which takes 7.2 seconds. The reasons for this big discrepancy are unknown.

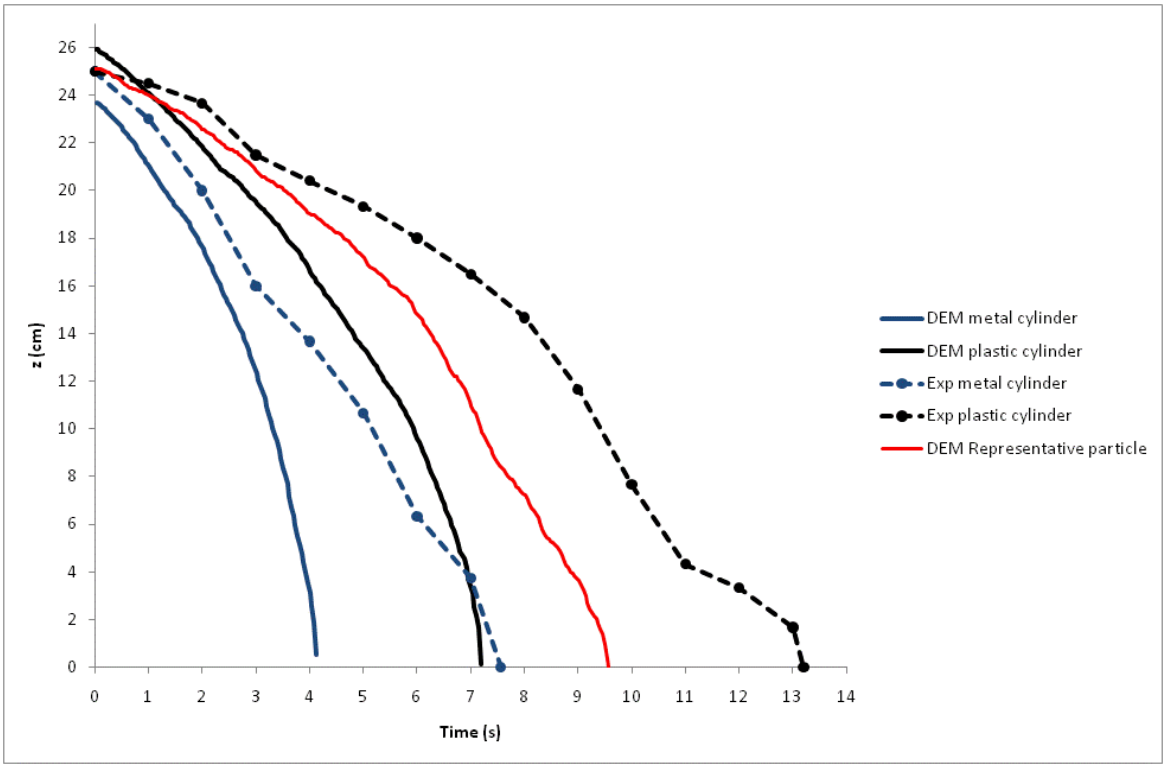

Figure 10.17: Plot showing z against time for the metal and plastic cylindrical free-cells in the white (5mm) particles starting from position 5. The average of three experimental trials, the DEM simulation of the plastic and metal cylinders and the DEM simulation of the representative particle are shown.

In similarity to figure 10.18 showing the vertical displacement against time curves of the metal and plastic cylinders in simulations and experiments the horizontal displacement against time curves are also in poor agreement. Figure 10.19 shows *x* against time for the metal and plastic cylindrical free-cells in the white (5mm) monosized particles starting from position 5. In this instance the free cells all started very close to x = 10cm, but the velocity of the metal and plastic free-cells in the simulations were observed to travel faster than the DEM simulation of the representative particle as well as the experimental results. In the initial 5 seconds the plastic cylinder in the experiments travelled with an average velocity of 0.2 cm/s compared to the plastic cylinder in the simulations that travelled with a velocity of 0.7 cm/s. The plastic cylinder in the DEM simulation then accelerated to 15 cm/s down to the orifice,

while the plastic cylinder in the experiments gradually accelerated to 2.5 cm/s and slowed down before passing through the orifice. The metal cylinder in the simulations accelerated very quickly from the initial position passing through the orifice after approximately 4.1 seconds, while metal cylinder in the experiments travelled at a steady velocity of 0.5 cm/s before accelerating to an average velocity of 3 cm/s down to the orifice.

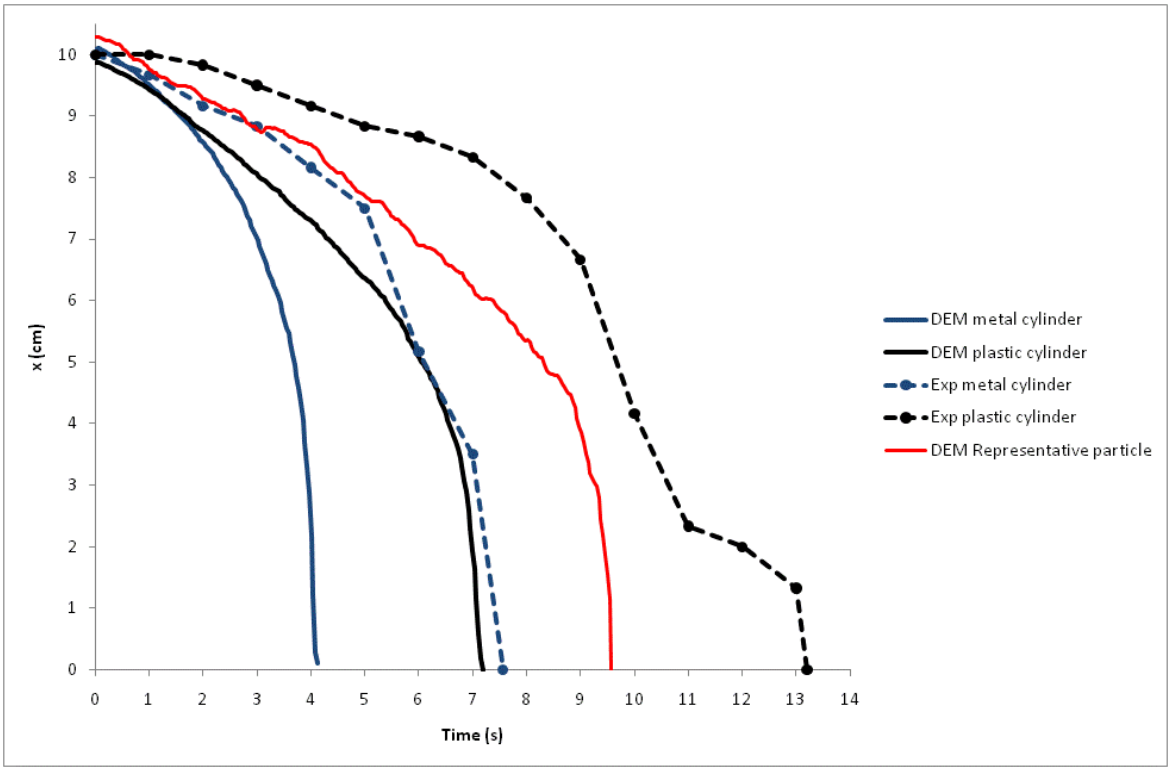

Figure 10.18: Plot showing z against time for the metal and plastic cylindrical free-cells in the white (5mm) particles starting from position 5. The average of three experimental trials and the DEM simulation of the metal and plastic cylinders and the DEM simulation of the representative particle are shown.

Figure 10.19 shows *z* against *x* for the plastic cuboid free cells starting from position 5 in the white (5mm) monosized particles. The average of three experimental trials and the DEM simulation and the trajectory of the representative particle are shown. The paths followed by the metal cuboid in the experiment and simulation differ by only 0.25 cm until z = 6 cm and x = 5 cm at which point the paths diverge. The plastic cuboid in the DEM simulation ad experiments however differ by up to 2 cm along the horizontal. Neither the metal nor the plastic cuboid in DEM simulation or experiment follows a similar path to the DEM simulation of the representative particle. The DEM simulation of the metal and plastic cuboids differ from the path followed by the DEM simulation of the representative particle by up to 1.5 cm

and 2 cm respectively and the experimental paths followed by the metal and plastic cuboids differ from the DEM simulation of the representative particle by up to 2 cm and 1.5 cm respectively. This is most likely due to the stochastic nature of granular flow.

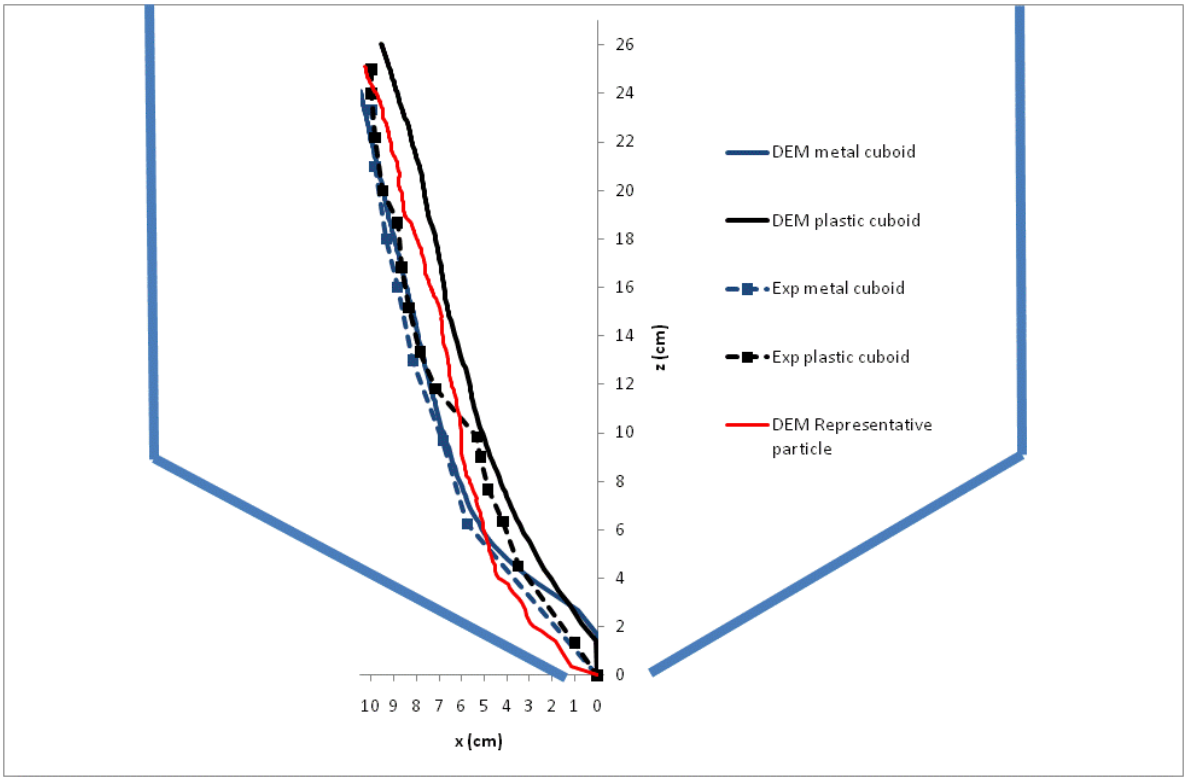

Figure 10.19: Plot of z against x for the metal and plastic cuboid free cells in the white (5 mm) particles starting from position 5. The average of three experimental trials and the DEM simulation of the metal and plastic cuboids and the DEM simulation of the representative particle are shown.

Figure 10.20 shows *z* against time for the metal and plastic, cuboid free-cells in the white (5 mm) monosized particles starting from position 5. Apart from the difference in the starting positions of the metal and plastic cuboids i.e. z = 24 cm and z = 25 cm respectively, the vertical displacement against time curves from the DEM simulations are virtually identical. The plastic cuboid in the DEM simulation is observed to have a constant acceleration of approximately 1 cm/s^2 while the plastic cuboid in the experiments travels down to the orifice with an average constant velocity of approximately 1.7 cm/s. Similarly the metal cuboid in the DEM simulation travels with a constant acceleration of 1 cm/s^2, while the metal cuboid in experiment travels with a constant velocity of 2.6 cm/s in the initial 7 seconds, prior to travelling through the orifice. Neither of the vertical displacement time curves obtained from DEM simulation or experiment resembles that of the DEM simulation of the representative particle.

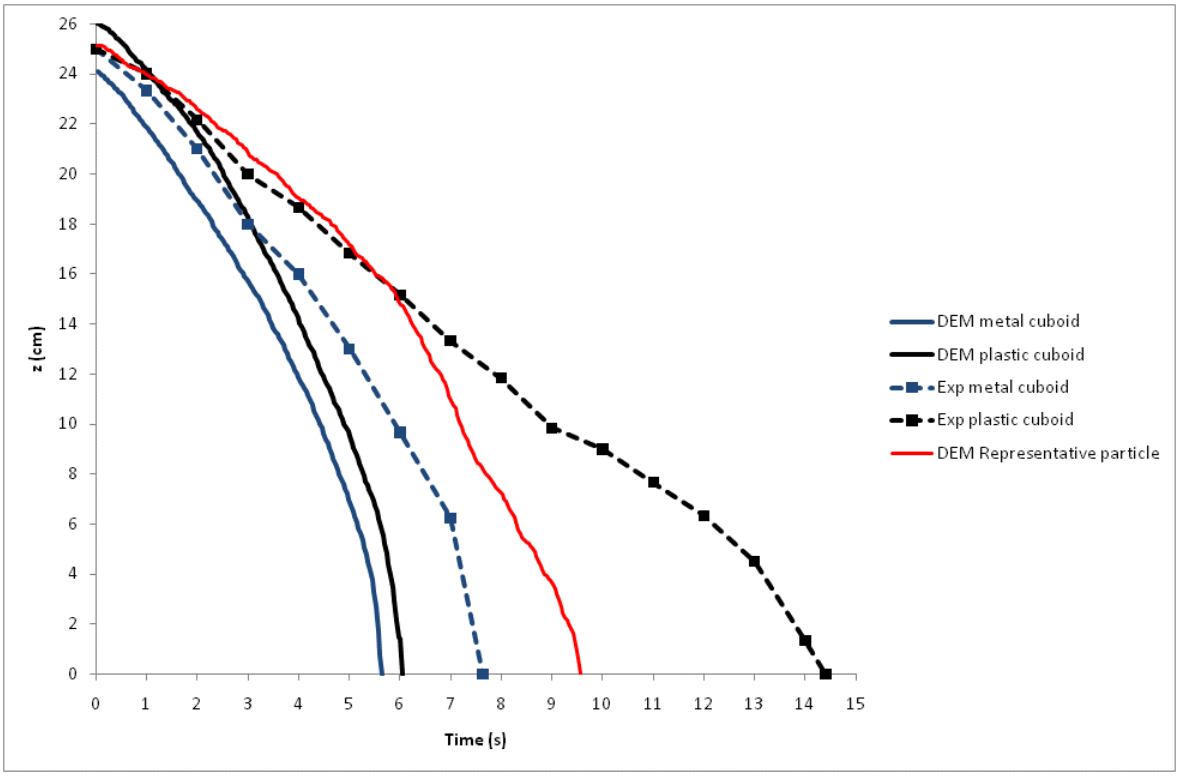

Figure 10.20: Plot showing z against time for metal and plastic cuboid free-cells in the white (5mm) monosized particles starting from position 5. The average of three experimental trials and the DEM simulation of the metal and plastic cuboids and the DEM simulation of the representative particle are shown.

Figure 10.21 shows *x* against time for the metal and plastic, cuboid free-cells in the white (5 mm) monosized particles starting from position 5. The results from DEM simulations and the trajectory of the representative particle and the average of three experimental trials are shown. In similarity to the vertical displacement against time graph for the meal and plastic cuboids there is no agreement between the results from the DEM simulations and experiments. The DEM simulations of the metal and plastic cuboid have virtually identical horizontal velocities, despite the metal cuboid starting at x = 10.5 cm and the plastic cuboid starting at x = 9.5 cm. They both have a steady horizontal velocity of 0.7 cm/s during the first 4 seconds prior to quickly accelerating towards the orifice. The metal cuboid in the experiment however travels with a variable velocity of between 0.2 cm/s and 1 cm/s until quickly accelerating to the orifice and the plastic cuboid has a variable velocity of between 0.2 cm/s and 2 cm/s prior to passing through the orifice. None of the curves are similar to the horizontal displacement of the DEM simulated representative particle.

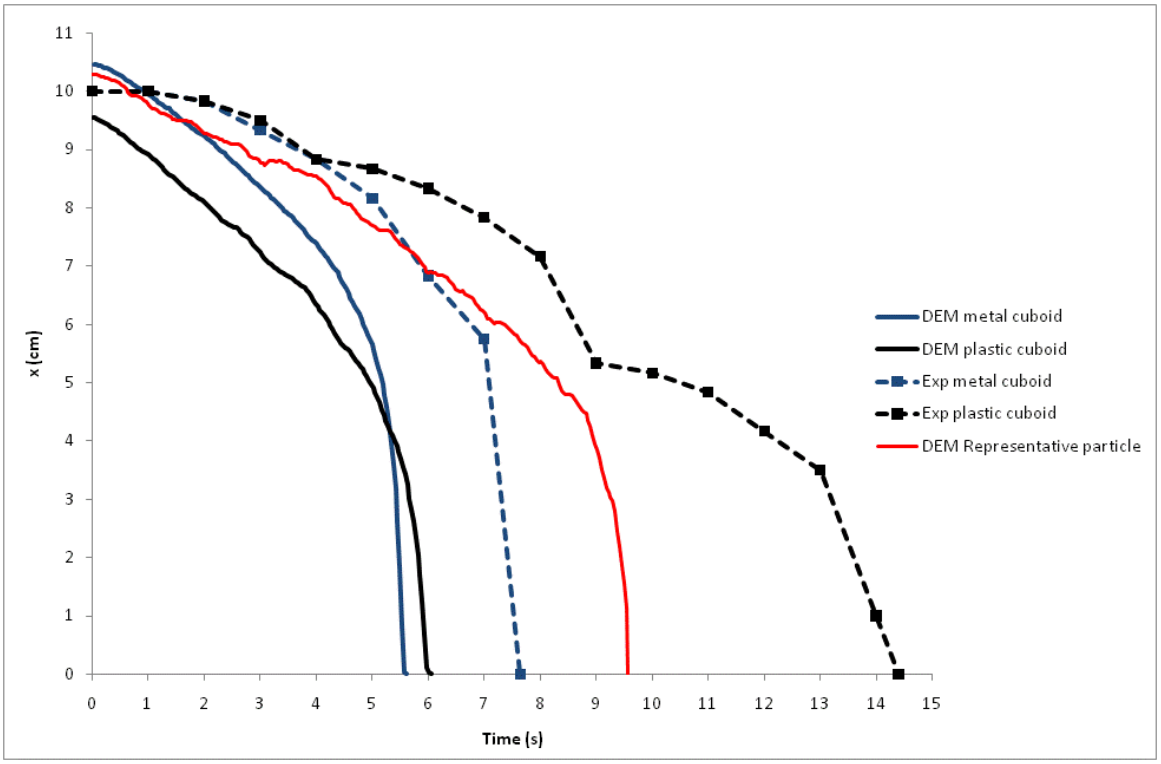

Figure 10.21: Plot showing x against time for metal and plastic cuboid free-cells in the white (5mm) monosized particles starting from position 5. The average of three experimental trials and the DEM simulation of the metal and plastic cuboids and the DEM simulation of the representative particle are shown.

Figure 10.22 shows *z* against *x* for the metal and plastic triangular prism free cells in the white (5mm) particles starting from position 5. The paths followed by the metal and plastic triangular prism in the DEM simulations and experiments cannot be compared. This is as a result of the difficulty in positioning the triangular prisms accurately in the DEM simulations. The paths followed by the metal and plastic triangular prisms in the DEM simulations look almost identical varying by only approximately 0.2 cm along the horizontal. This is as a result of them starting at a position away from the stagnant zone boundary. The paths followed by the metal and plastic triangular prisms in the experiments vary by up to 1 cm along the horizontal. The DEM simulation of the representative particle varies from the path followed by the plastic triangular prism by up to 1.5 cm along the horizontal and the metal triangular prism by up to 2 cm, suggesting that if the triangular prisms in the simulations had been positioned accurately the DEM simulations and experimental results may have been in better agreement.

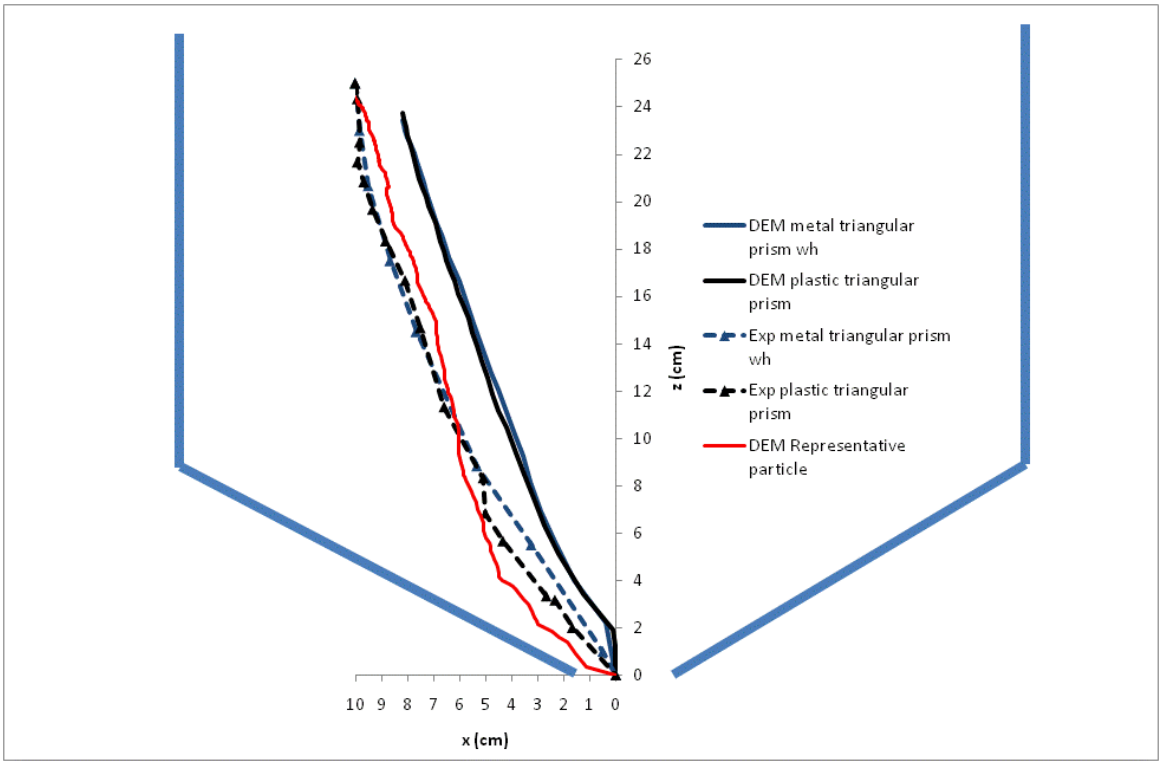

Figure 10.22: Plot of z against x for the metal and plastic triangular prism free-cells in the white (5mm) monosized particles starting from position 5. The average of three experimental trials and the DEM simulation of the metal and plastic triangular prism and the DEM simulation of the representative particle are shown.

Figure 10.23 shows *z* against time for the metal and plastic triangular prism free-cells in the white (5 mm) monosized particles starting from position 5. The initial positions of the metal and plastic triangular prisms were virtually identical (x = 8.2cm, z = 22.9 cm) and the resultant vertical and horizontal displacement curves (Figures 10.24 and 10.25) are very similar. The starting position is within the stagnant zone boundary, resulting in the unhindered movement. The time taken by the metal triangular prism in the DEM simulations to reach the orifice is 2.8 seconds and the plastic triangular prism 3 seconds. This is as previously mentioned as a result of the difficulty in accurately positioning the free-cells in the DEM simulations. In the experiments the plastic and metal triangular prisms started at x = 10 cm, z = 25 cm. The metal triangular prism travels with an average vertical velocity of 3.5 cm/s and the plastic triangular prism travels with an average vertical velocity of 1.5 cm/s throughout its trajectory through the silo. The DEM simulation of the representative particle travels with an average velocity of 1.5 cm/s in the initial 6 seconds after the opening of the orifice and 4.5 cm/s in the final 3.5 seconds prior to travelling through the orifice.

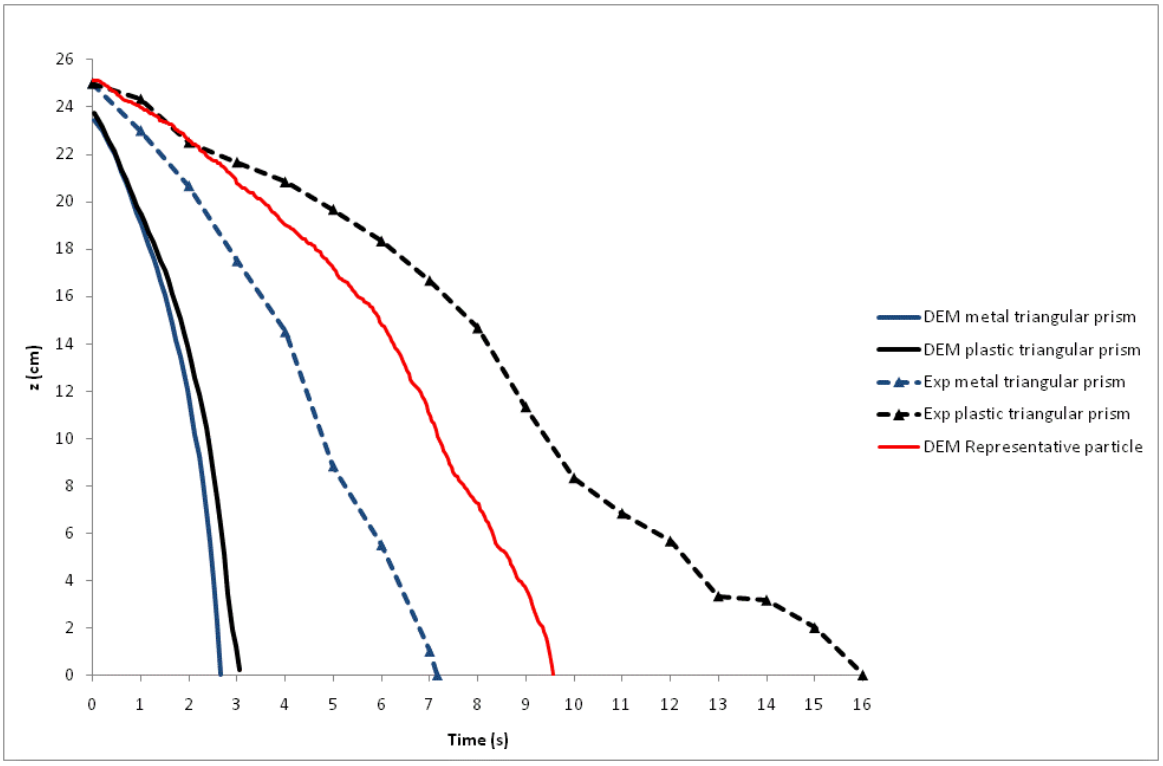

Figure 10.23: Plot of z against time for the metal triangular prism free-cells in the white (5 mm) monosized particles starting from position 5. The average of three experimental trials and the DEM simulation of the plastic and metal triangular prisms and the DEM simulation of the representative particle are shown.

Figure 10.24 shows *x* against time for the metal and plastic triangular prism free-cells in the white (5 mm) monosized particles starting from position 5. The plastic triangular prism in the experiments is slightly buffeted around by the surrounding particles in the initial 3 seconds after the opening the orifice and then it gradually accelerates at an average of 0.4 cm/s^2 for the following 7 seconds. The plastic triangular prism is then at rest for about 1 second prior to accelerating again over the next 3 seconds, slowing down again and then travelling through the orifice. The metal triangular prism accelerates to a velocity of 0.9 cm/s during the initial 2 seconds and then accelerates to a constant velocity of 2.4 cm/s. The DEM simulation of the representative particle shows that it has an average horizontal velocity of 0.5 cm/s during the initial 9 seconds after the opening of the orifice and rapidly travels 4 cm to the orifice in the next 0.6 seconds.

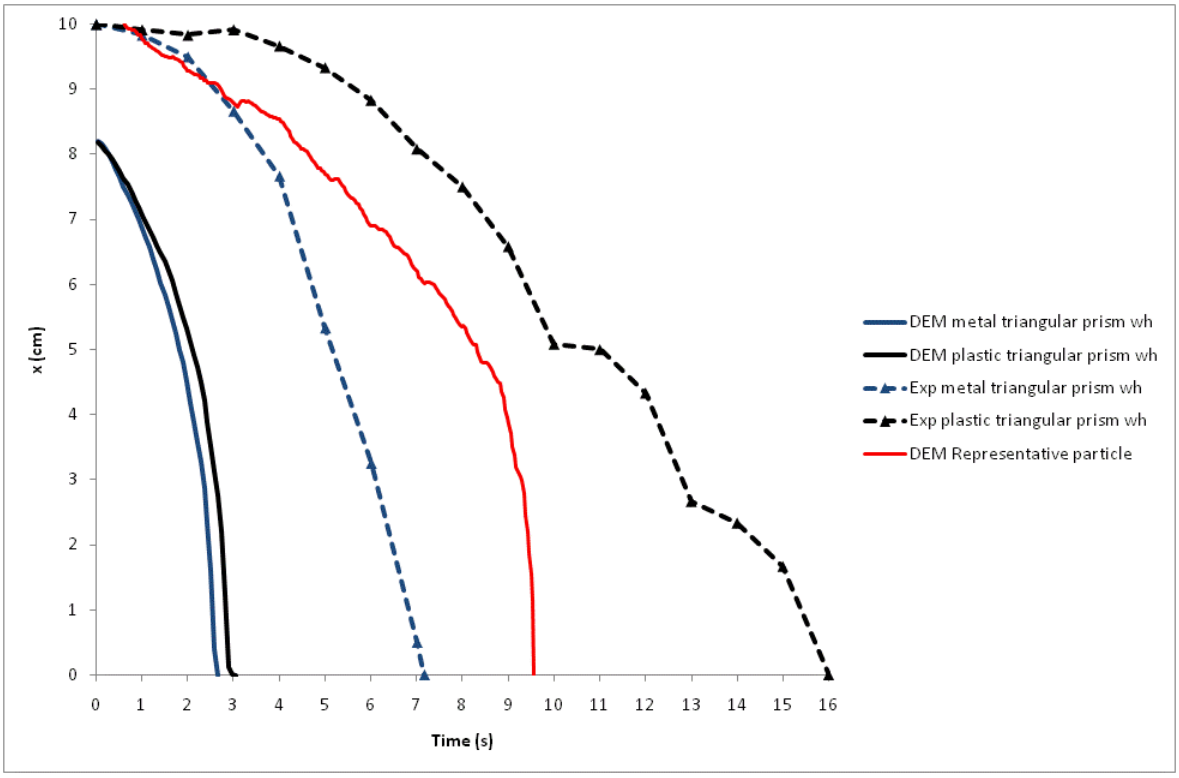

Figure 10.24: Plot of x against t for the metal and plastic triangular prism free-cells in the white (5 mm) monosized particles starting from position 5. The average of three experimental trials and the DEM simulations of the metal and plastic triangular prisms and the DEM simulation of the representative particle are shown.

10.6 Summary

The path followed by the representative particle does not agree with the paths taken by the plastic cylinder, square or triangular prism or the metal cylinder, cuboid or triangular prism. The DEM simulations and experiments of each of the free cells are in poor agreement. This is most likely due to the difficulty in accurately positioning the free cells in the simulations.

10.7 Comparisons between the DEM simulations and experiments of the metal and plastic cylinders and cuboids starting from position 12 in the white/black binary mixture.

Figure 10.25 shows *z* against *x* for the metal and plastic cylindrical free-cells starting from position 12 in the 80% white (5 mm)/ 20% black (4 mm) binary mixture. The paths followed by the metal cylinder and plastic cylinder in the experiments and DEM simulations differ by up to 1 cm and 1.5 cm respectively. The paths followed by the DEM simulation of the representative particle and the DEM simulation of the plastic cylinder are in excellent agreement differing by up to 0.5 cm. The path followed by the plastic cylinder in the experiment differs from the path followed by the DEM simulation of the representative particle by up to 2 cm.

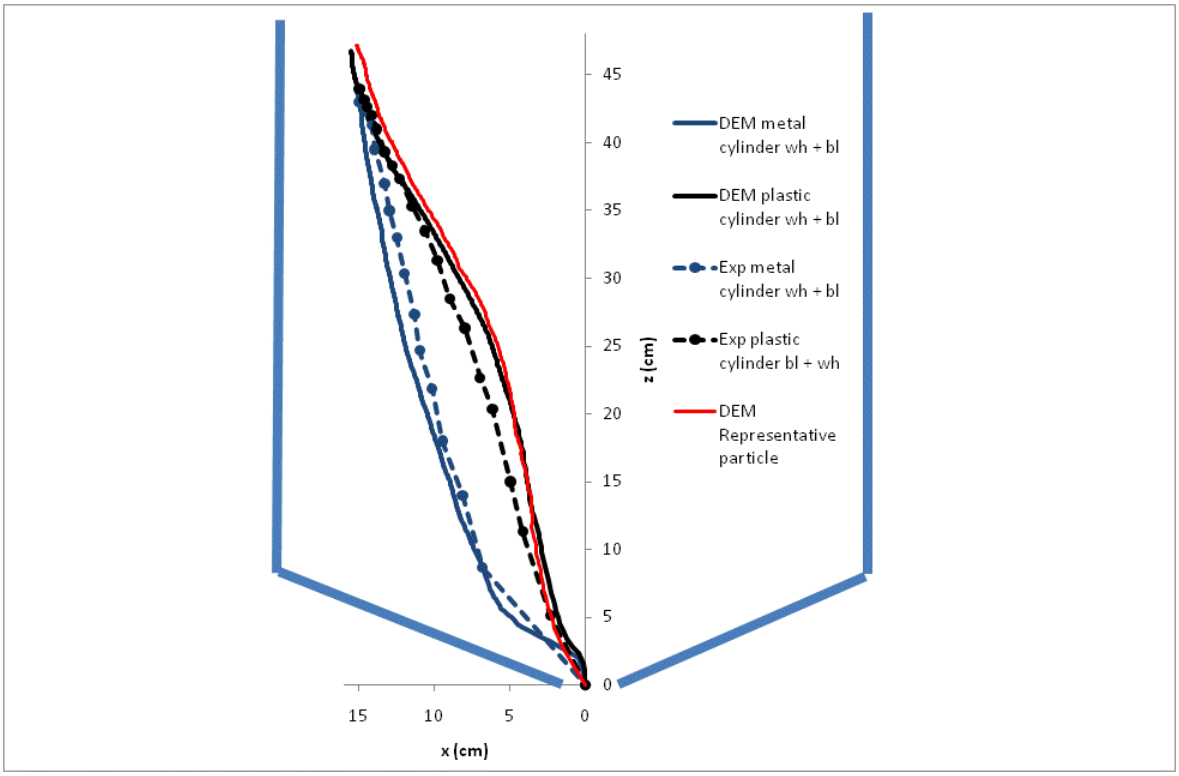

Figure 10.25: Plot of z against x showing trajectory of the metal and plastic cylindrical free-cells in the white (5 mm)/black (4 mm) binary mixture starting from position 12. The average of three experimental trials and the DEM simulation of the metal and plastic cylinders and the DEM simulation of the representative particle are shown.

Figure 10.26 shows *z* against time for the metal and plastic, cylindrical free-cells in the 80% white (5 mm)/20% black (4 mm) binary mixture starting from position 12. The vertical velocity of the metal cylinder is approximately 2.3 cm/s^2 during the first 10.5 seconds after the opening of the orifice, in both the DEM simulation and experiment. The metal cylinder in the experiments then accelerates at 5 cm/s^2 towards the orifice and the metal cylinder in the DEM simulation continues at a steady velocity of approximately 2.5 cm/s towards the orifice. With reference to Figure 10.28, apart from the fact that the plastic cylinder in the DEM simulation starts at the initial position x = 18 cm, z = 46 cm and the plastic cylinder in the experiment starts at x = 15 cm, z = 44 cm, the plastic cylinder accelerates uniformly vertically at an average of 0.5 cm/s^2 in both DEM simulation and experiment. The DEM simulation of the representative particle results in the representative particle accelerating vertically at 0.5 cm/s^2 in the initial 10 seconds after the opening of the orifice and then at 2.5 cm/s^2 in the final 4.5 seconds prior to travelling through the orifice.

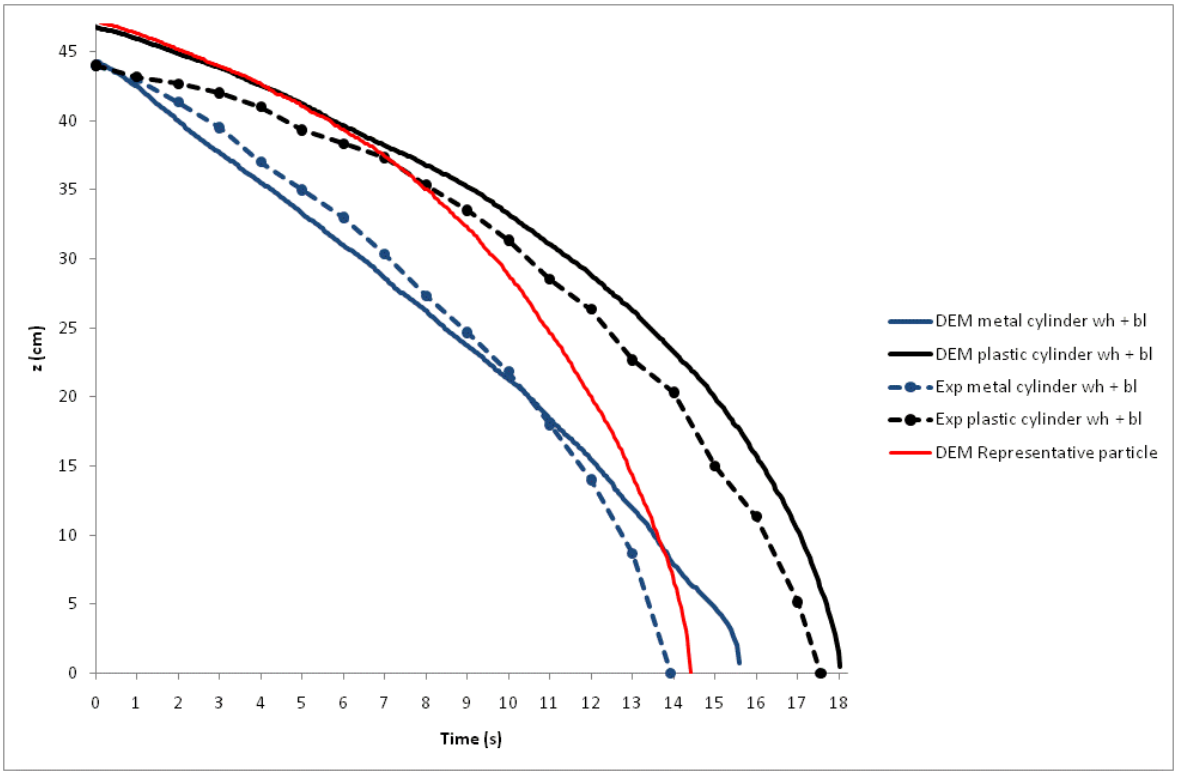

Figure 10.26: Plot of z against time showing the trajectory of the metal and plastic cylindrical free-cells from position 12 in the 80% white (5 mm)/20% black (4 mm) binary mix of particles. The average of three experimental trials and the DEM simulation of the metal and plastic cylinders and the DEM simulation of the representative particle are shown.

Figure 10.27 shows *x* against time for the metal and plastic cylindrical free-cells in the 80% white (5 mm)/20% black (4 mm) binary mixture starting from position 12. The curves showing the horizontal displacement against time for the metal and plastic cylinders, obtained from experiment, show that they both travel with an average velocity of approximately 0.3 cm/s in the initial 7 seconds and then at 0.8 cm/s in the next 6 seconds, after which the metal cylinder rapidly accelerates towards the orifice and the plastic cylinder accelerates at approximately 1 cm/s^2 towards the orifice. The plastic cylinder and the metal cylinder take 17.6 seconds and 14 seconds respectively to reach the orifice.

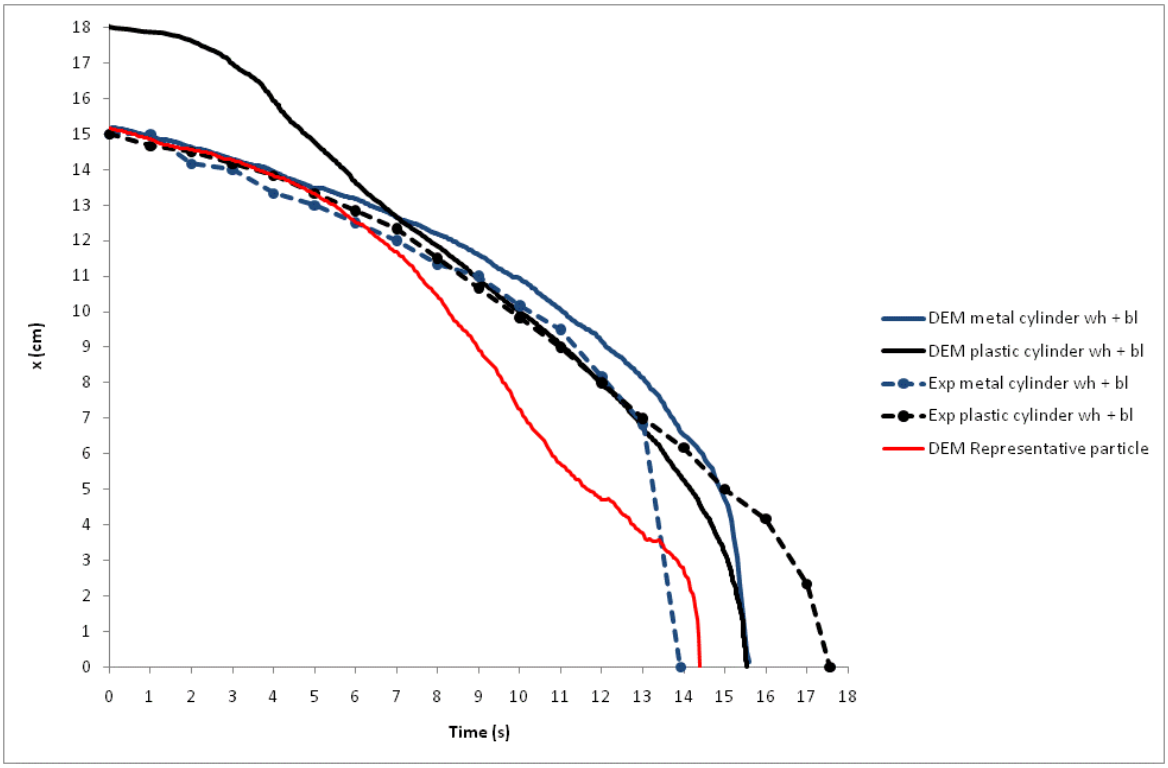

Figure 10.27: Plot of x against time showing the trajectory of the metal and plastic cylindrical free-cells from position 12 in the 80% white (5mm)/20% black (4mm) binary mix of particles. The average of three experimental trials and the DEM simulation of the metal and plastic cylinders and the DEM simulation of the representative particle are shown.

Figure 10.28 shows *z* against *x* for the metal and plastic cuboid free-cells starting from position 12 in the 80% white (5 mm)/ 20% black (4 mm) binary mixture. In similarity to the plastic cylinder, the DEM simulation of the plastic cuboid follows a similar path to the DEM simulation of the representative particle. The paths differ by only 0.5 cm along the horizontal. The path followed by the plastic cuboid in experiment differs from the DEM simulation of the plastic cuboid and the DEM simulation of the representative particle by up to 2 cm. The paths followed by the metal cuboid in DEM simulation are virtually identical until approximately *z*

= 12 cm and then the paths diverge by up to 2 cm prior to he metal cuboid passing through the orifice.

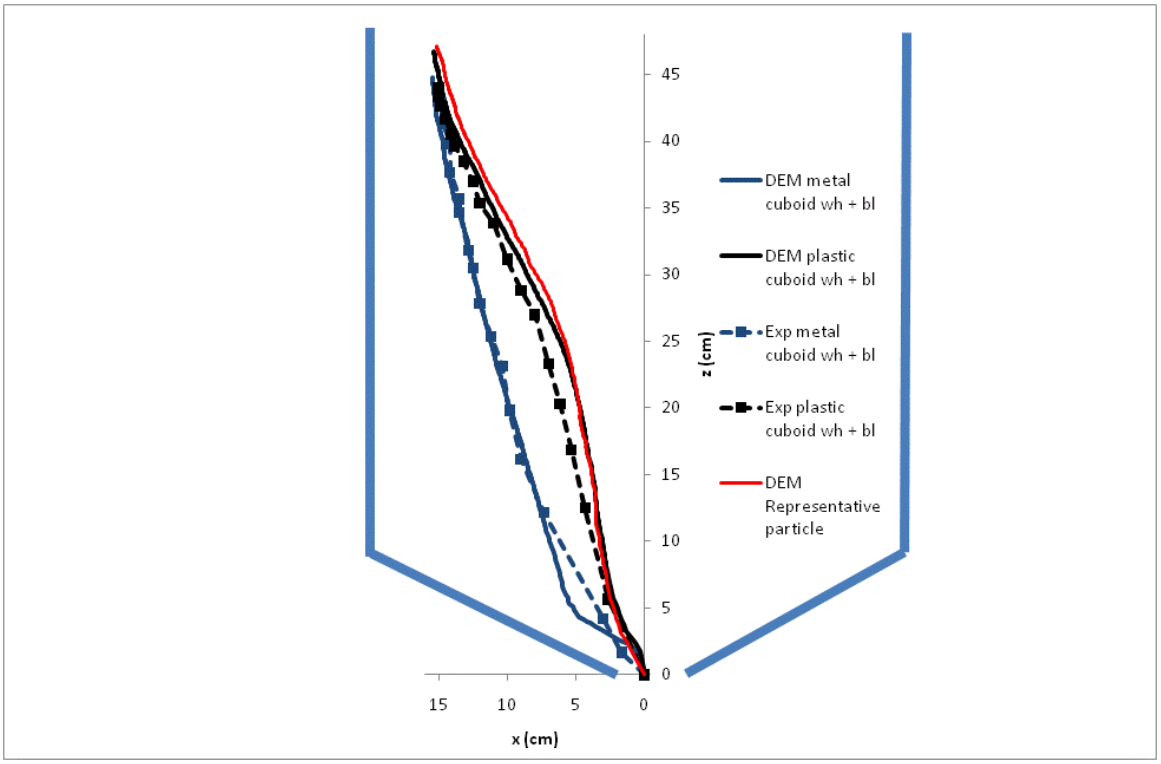

Figure 10.28: Plot of z against x showing the trajectory of metal and plastic cuboid free-cells from position 12 in the 80% white (5 mm)/ 20% black (4 mm) binary mixture of particles. The average of three experimental trials and the DEM simulation of the metal and plastic cuboid and the DEM simulation of the representative particle are shown.

Figures 10.29 shows *z* against time for the metal and plastic cuboid free-cells in the 80% white (5 mm)/20% black (4 mm) binary mixture starting from position 12. Despite the plastic cuboid in the DEM simulation starting at *z* = 47 cm and the plastic cuboid in the experiment starting at *z* = 44 cm, the vertical displacement against time curves for the plastic cuboid have a similar profile. The plastic cuboid has a steady velocity of approximately 1 cm/s during the initial 9 seconds after the opening of the orifice and then accelerates uniformly at an average of 2 cm/s^2 down to the orifice. The vertical displacement against time curves for the plastic cylinder in experiment and DEM simulation are also similar. The metal cuboid travels with an average velocity of 4 cm/s during the initial 11 seconds, prior to accelerating to 5 cm/s in the next 2 seconds and then decelerating, before travelling through the orifice. The representative particle in the DEM simulation travels at a velocity of 1 cm/s during the initial 7 seconds and

then accelerates uniformly at approximately 1.3 cm/s^2 towards the office in the following 7.5 seconds.

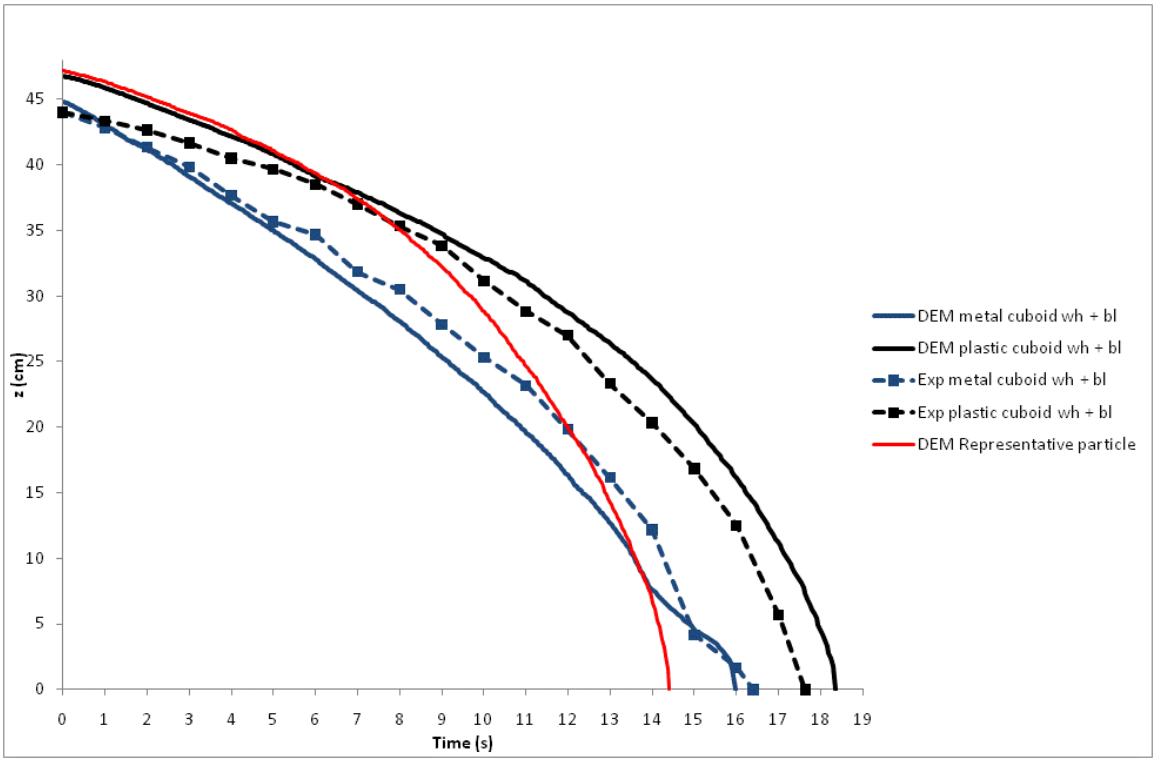

Figure 10.29: Plot of z against time showing the trajectory of the metal and plastic cuboid free-cells from position 12 in the 80% white (5 mm)/20% black (4 mm) binary mix of particles. The average of three experimental trials and the DEM simulation of the metal and plastic cuboids and the DEM simulation of the representative particle are shown.

Figure 10.30 shows *x* against time for the metal and plastic cuboid free-cells in the 80% white (5 mm)/20% black (4 mm) binary mixture starting from position 12. The horizontal displacement against time curves for the plastic cuboids in DEM simulation and experiment are very similar during the initial 13 seconds after the opening of the orifice. The plastic cuboid slowly accelerates at 0.25 cm/s until it reaches a constant velocity of approximately 1 cm/s and then the plastic cuboid in the experiment rapidly accelerates to the orifice, while the plastic cuboid in the simulation gradually decelerates prior to accelerating through the orifice. The metal cuboid in the DEM simulation and experiment has a similar velocity to the plastic cuboid during the initial 7seconds, but then the metal cuboid in the simulation travels with a velocity of approximately 0.9 cm/s, prior to slightly decelerating and then rapidly travelling through the orifice. The metal cuboid in the experiment travels with an average velocity 0.5

cm/s over the next 8 seconds, prior to rapidly accelerating towards the orifice. The representative particle in the DEM simulation gradually accelerates to 1.2 cm/s^2 and then decelerates prior to accelerating through the orifice. The plastic cuboid, metal cuboid and representative particle take an average of 18 seconds, 16.1 seconds and 14.3 seconds respectively to reach the orifice after the initiation of discharge.

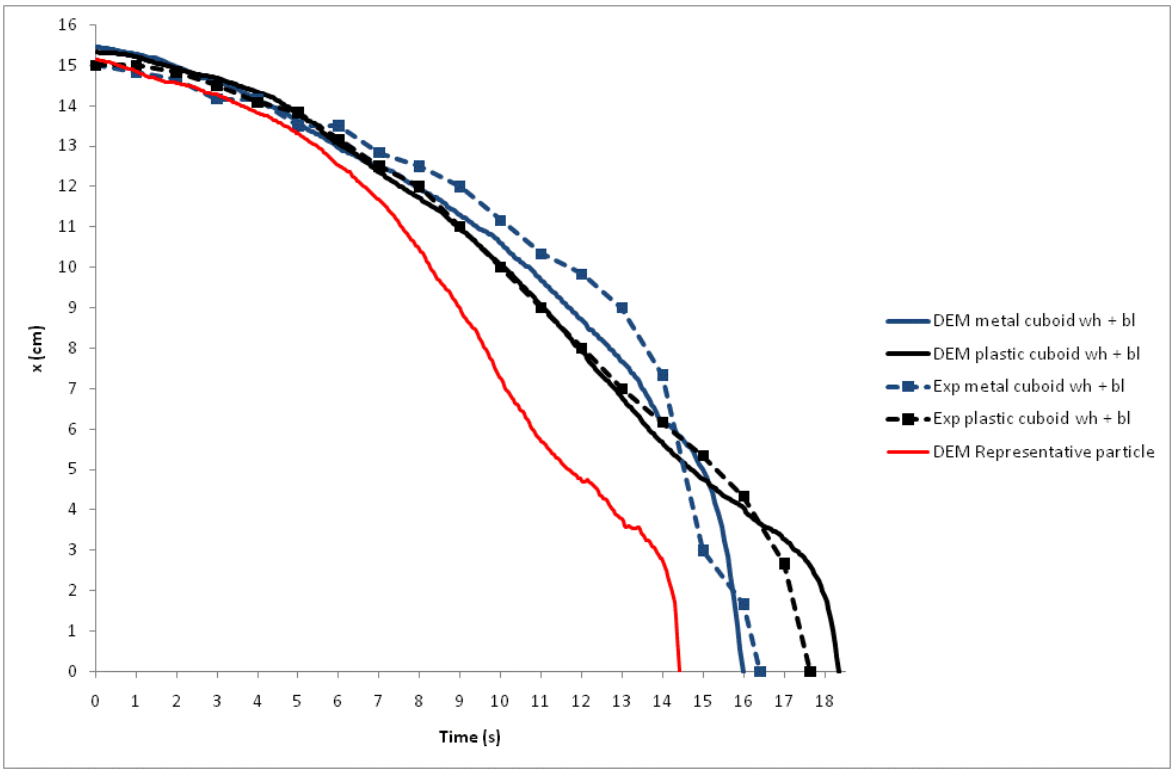

Figure 10.30: Plot of x against time showing the trajectory of the metal and plastic cuboid free-cells from position 12 in the 80% white (5 mm)/20% black (4 mm) binary mix of particles. The average of three experimental trials and the DEM simulation of the metal and plastic cuboids and the DEM simulation of the representative particle are shown.

Figure 10.31 shows *z* against *x* for the metal and plastic triangular prism free-cells in the 80% white (5mm)/ 20% black (4mm) binary mixture. The paths followed by the metal triangular prism in the DEM simulations and experiment differ by 0.5 cm along the horizontal up until the point *x* = 5cm, *z* = 10 cm at which the paths diverge by up to 1.5 cm. The paths followed by the plastic triangular prism vary by up to 1 cm along the horizontal. Neither the paths followed by the metal or plastic triangular prism in experiment nor simulation, are similar to the DEM simulation of the representative particle. The paths followed by the metal triangular prism and plastic triangular prism, in experiment and DEM simulation, vary from the path

followed by the representative particle in DEM simulation by up to 4cm and 3 cm respectively.

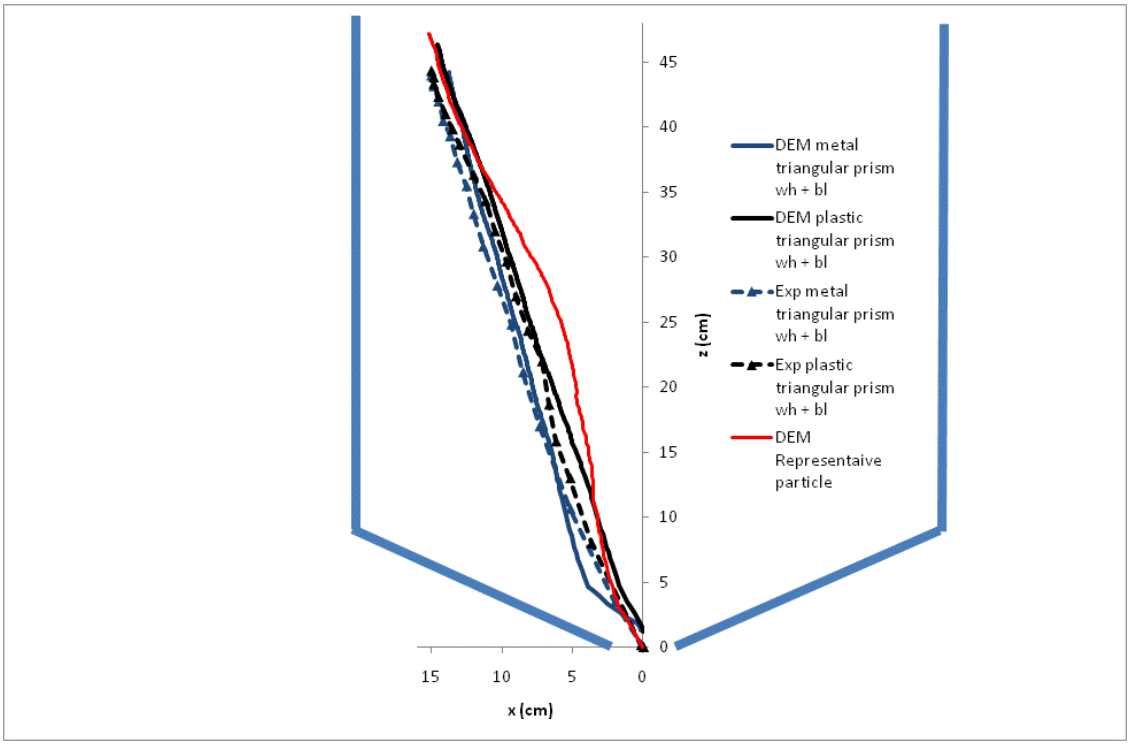

Figure 10.31: Plot of z against x showing the trajectory of metal and plastic triangular prism free-cells from position 12 in the 80% white (5 mm)/ 20% black (4 mm) binary mixture of particles. The average of three experimental trials and the DEM simulation of the metal and plastic triangular prisms and the DEM simulation of the representative particle are shown.

Figure 10.32 shows z against time for the metal and plastic triangular prisms starting from position 12 in the 80% white (5 mm)/20% black (4 mm) binary mixture. The triangular prism in the DEM simulation starts at z = 46 cm and travels with an average velocity of 1.6 cm/s in the initial 16 seconds prior to rapidly accelerating towards the orifice and the plastic triangular prism in the experiment accelerates uniformly at 0.2 cm/s^2 during the first 6 seconds and then travels with a constant velocity of 2.2 cm/s, prior to travelling through the orifice. The metal triangular prism in the DEM simulation is shown to travel with an average constant velocity of 2.8 cm/s in the initial 6 seconds and then accelerates uniformly at 3.3 cm/s towards the orifice, while the plastic triangular prism in the experiment accelerates uniformly on average, from rest, at 0.4 cm/s^2 towards the orifice. The representative particle in the DEM simulation starts at z = 47 cm and is shown to accelerate, from rest, with an average uniform acceleration of 0.5 cm/s^2. The triangular prisms became trapped in the orifice in most simulations and experiments, which is why the curves from the DEM simulations stop at approximately z =

0.5 cm. The curves showing the experimental results extend to the z = 0 line for ease of plotting.

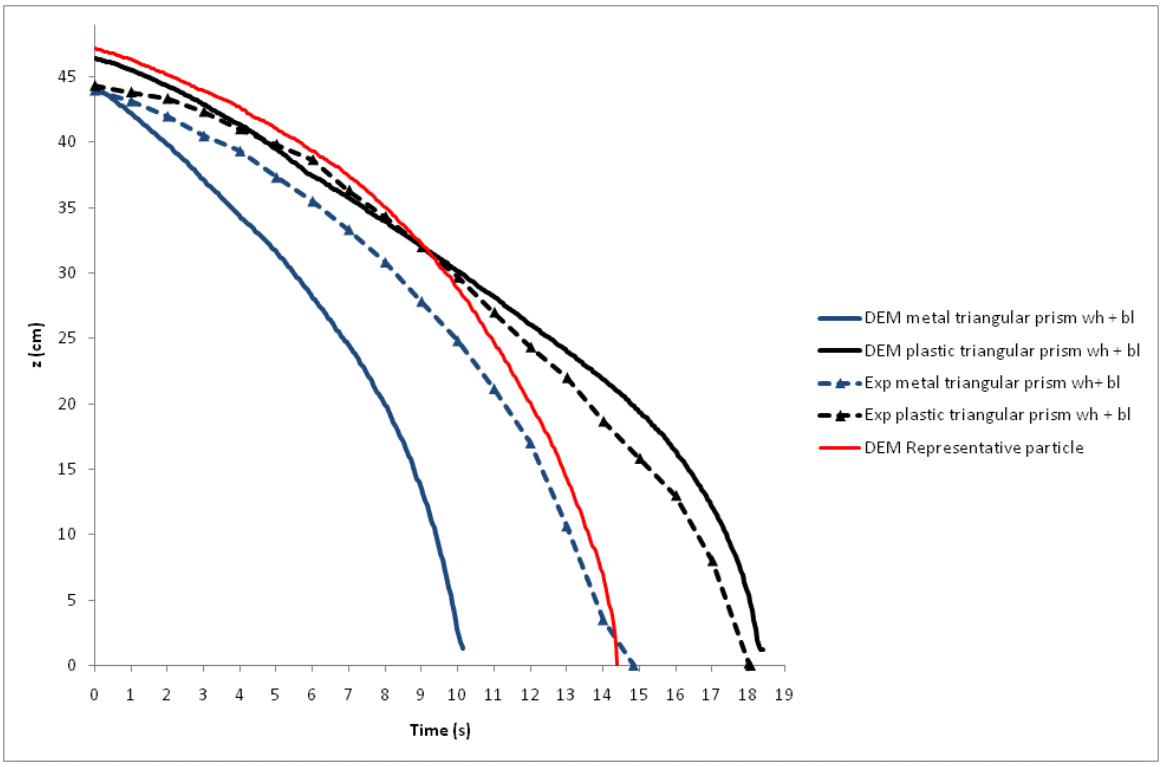

Figure 10.32: Plot of z against time showing the trajectory of metal and plastic triangular prism free-cells from position 12 in the 80% white (5 mm)/ 20% black (4 mm) binary mixture of particles. The average of three experimental trials and the DEM simulation of the metal and plastic triangular prisms and the DEM simulation of the representative particle are shown.

Figure 10.33 shows *x* against time for the metal and plastic triangular prisms starting from position 12 in the 80% white (5 mm)/20% black (4 mm) binary mixture. The horizontal velocity of the plastic triangular prism in the DEM simulation is an average of 0.6 cm/s during the initial 15 seconds and then it accelerates uniformly towards the orifice in the following 3.5 seconds at 1.1 cm/s^2. The plastic triangular prism in the experiment gradually accelerates from rest to an average velocity of 0.8 cm/s and then gradually decelerates prior to rapidly accelerating towards the orifice in the final 3 seconds. The metal triangular prism in the experiments starts at x = 15 cm and the metal triangular prism in the DEM simulations starts at x = 13.8 cm, which is most probably a reason for the different horizontal displacement curves. The metal triangular prism accelerates uniformly from rest at 0.15 cm/s^2 in the initial 10 seconds after the opening of the orifice prior to rapidly accelerating towards the orifice in the final 0.1 seconds and the metal triangular prism in the experiment uniformly

accelerates at 0.14 cm/s in the initial 6 seconds and then travels at an average velocity of 0.9 cm/s prior to accelerating to a velocity of 2.8 cm/s towards the orifice in the final 2.5 seconds. The DEM simulation of the representative particle shows that it accelerates to a uniform velocity of 1.2 cm/s, prior decelerating slightly before rapidly accelerating towards the orifice.

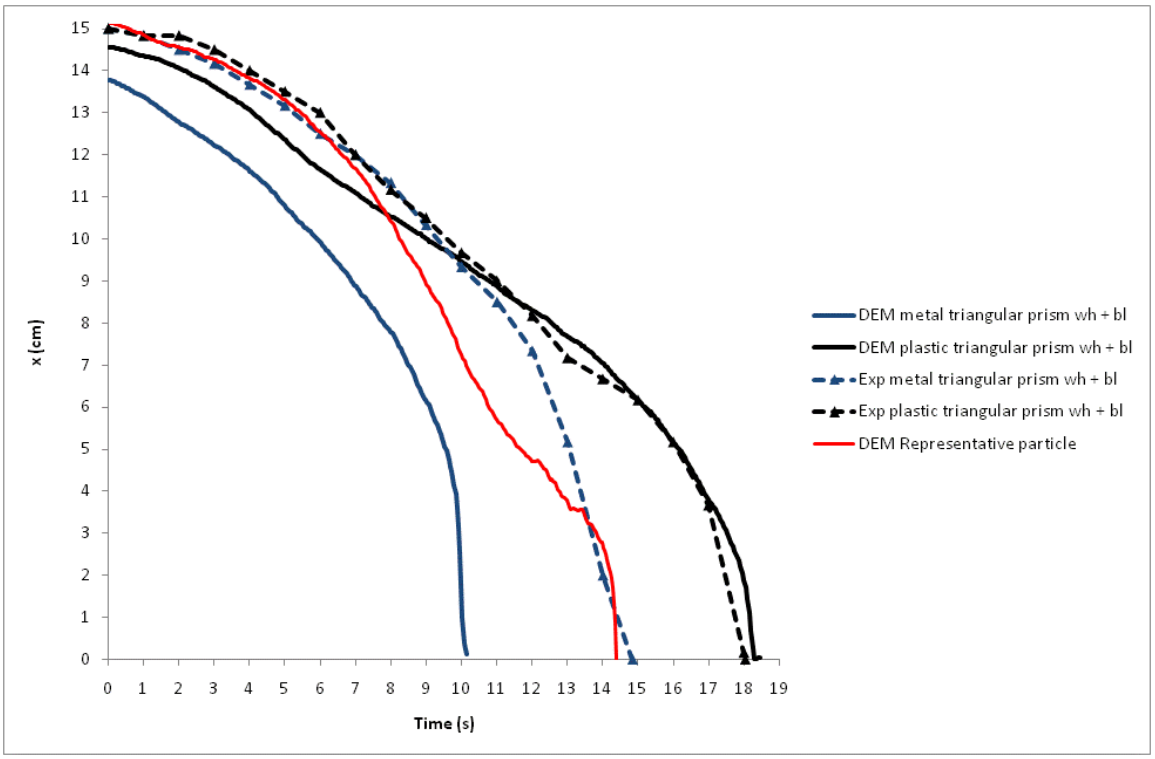

Figure 10.33: Plot of x against time showing the trajectory of metal and plastic triangular prism free-cells from position 12 in the 80% white (5mm)/ 20% black (4mm) binary mixture of particles. The average of three experimental trials and the DEM simulation of the metal and plastic triangular prisms and the DEM simulation of the representative particle are shown.

10.8 Summary

The path followed by the representative particle is closer to the paths followed by the plastic cylinder and plastic cuboid stating from position 5 than the curves for the metal cylinder and cuboid. There curves showing the DEM simulation and experiments of the vertical velocity of the plastic and metal cylinder and cuboid differ by about 0.5 seconds.

10.9 Comparisons between the DEM simulations and experiments of the metal and plastic cylinders and cuboids starting from position 5 in the white/black binary mixture.

Figure 10.34 shows *z* against *x* for the metal and plastic cylindrical prism free-cells in the 80% white (5mm)/ 20% black (4mm) binary mixture starting from position 5. The paths followed by the metal cylinder and the plastic cylinder in the DEM simulations and experiments differ by up to 1 cm along the horizontal. The DEM simulation of the representative particle differs from the path followed by the DEM simulation of the metal cylinder by 0.25 cm along the horizontal above the point x = 5 cm, z = 6cm and 2 cm below it, while the path followed by DEM simulation of the plastic cylinder varies from the DEM simulation of the representative particle by up to 1.5 cm along the horizontal.

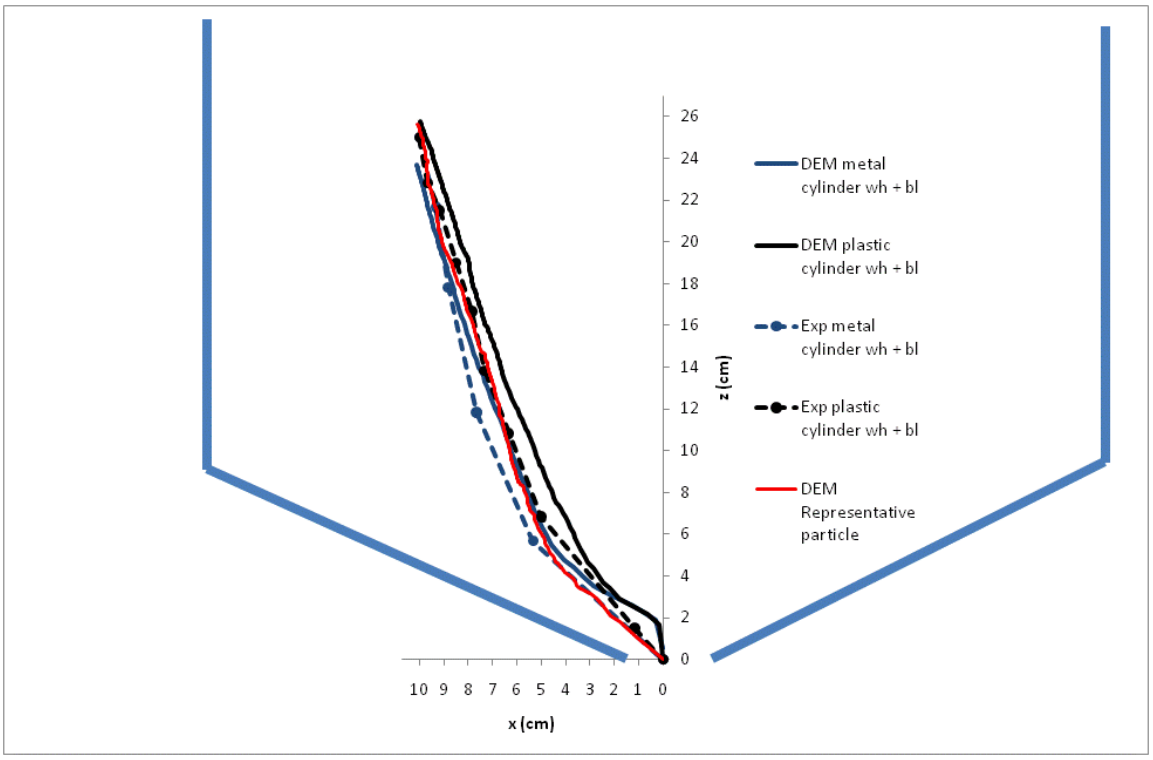

Figure 10.34: Plot of z against x showing the trajectory of metal and plastic cylindrical free-cells from position 5 in the 80% white (5 mm)/ 20% black (4 mm) binary mixture of particles. The average of three experimental trials and the DEM simulation of the metal cylinder and the DEM simulation of the representative particle are shown.

Figure 10.35 shows *z* against time for the metal and plastic cylindrical prism free-cells in the 80% white (5 mm)/ 20% black (4 mm) binary mixture starting from position 5. The metal cylinder in the DEM simulation starts at z = 23.8 cm and the metal cylinder in the experiments starts at z = 25 cm. The metal cylinder in the DEM simulation accelerates uniformly to the orifice at approximately 2.3 cm/s^2 and the metal cylinder accelerates uniformly at approximately 2.5 cm/s^2. Apart from a slight difference in velocity of approximately 0.1 cm/s during the initial 2 seconds after the opening of the orifice, the plastic cylinder in the DEM simulation and experiment accelerates uniformly to the orifice at approximately 0.8 cm/s^2. The representative particle in the DEM simulation has a velocity of 2 cm/s in the initial 2 seconds and then decelerates slightly, prior to accelerating to a constant velocity of 2.7 cm/s and then rapidly accelerating through the orifice.

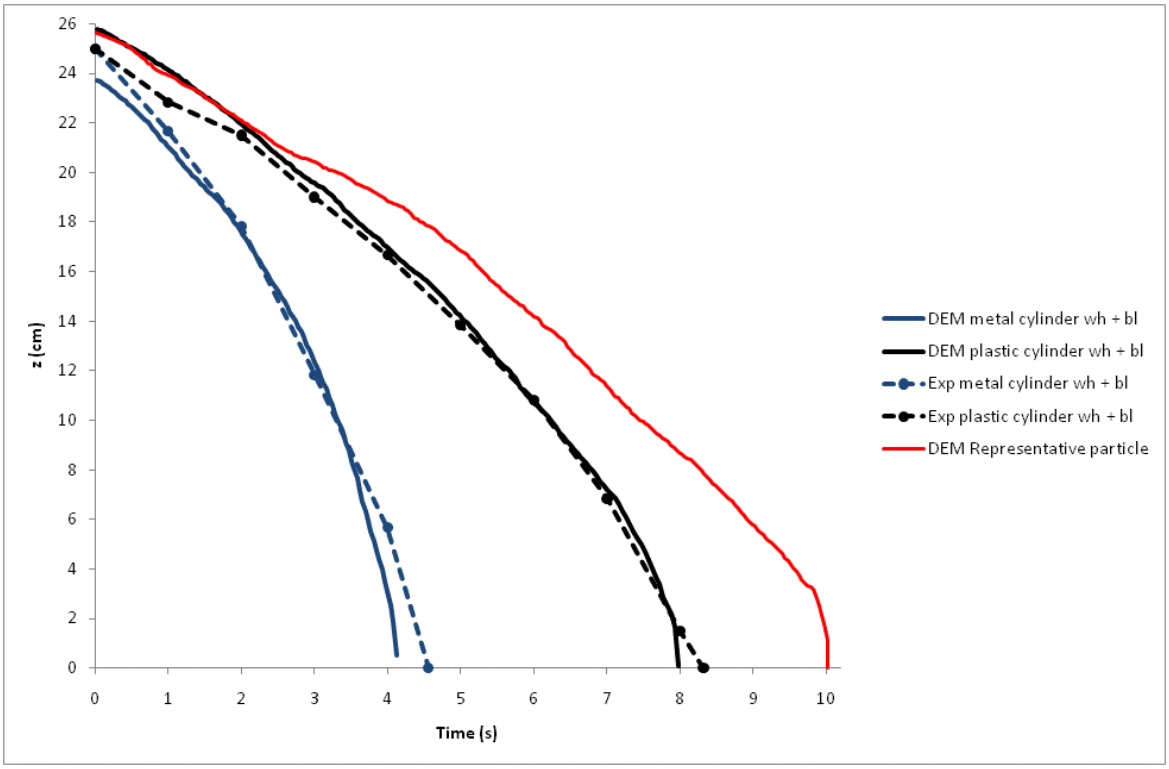

Figure 10.35: Plot of z against time showing the trajectory of metal and plastic cylindrical free-cells from position 5 in the 80% white (5 mm)/ 20% black (4 mm) binary mixture of particles. The average of three experimental trials and the DEM simulation of the plastic and metal cylinders and the DEM simulation of the representative particle are shown.

Figure 10.36 shows *x* against time for the metal and plastic cylindrical free-cells starting from position 5 in the 80% white (5 mm)/20% black (4 mm) binary mixture. The metal cylinder in the DEM simulation accelerates uniformly at 0.6 cm/s in 3.8 seconds and then rapidly accelerates towards the orifice and the metal cylinder in the experiment accelerates at 0.56 cm/s in 4 seconds prior to rapidly accelerating towards the orifice. The plastic cylinder in the DEM simulation and experiment travels at an average velocity of 0.5 cm/s in the initial 4 seconds, but then the plastic cylinder accelerates at an average of 0.6 cm/s^2 prior to rapidly accelerating through the orifice. The representative particle in the DEM simulation travels with an average velocity of 0.4 cm/s in the initial 8 seconds and then rapidly accelerates towards the orifice in the next to seconds. The metal cylinder, plastic cylinder and representative particle take an average of 4.3, 8.1 and 10 seconds to reach the orifice.

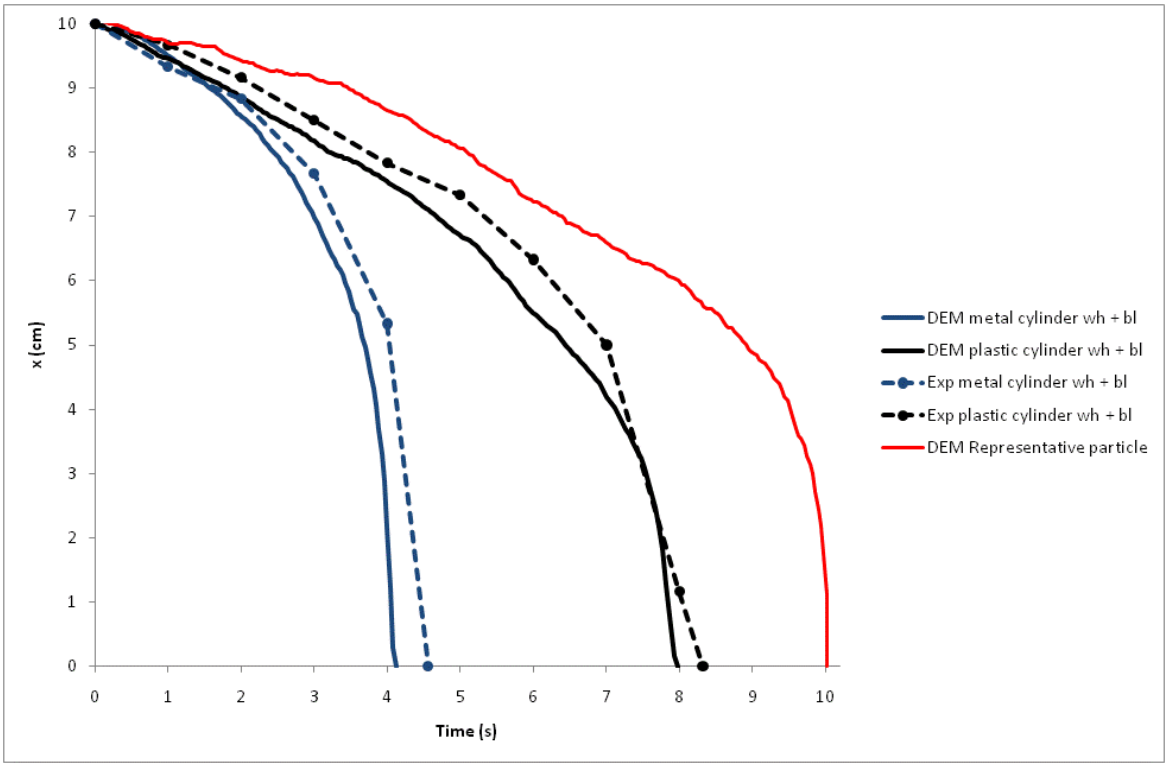

Figure 10.36: Plot of x against t showing the trajectory of metal and plastic cylindrical prism free-cells from position 5 in the 80% white (5 mm)/ 20% black (4 mm) binary mixture of particles. The average of three experimental trials and the DEM simulation of the metal and plastic cylinders and the DEM simulation of the representative particle are shown.

Figure 10.37 shows *z* against *x* for the metal and plastic cuboid free-cells starting from position 5 in the 80% white (5 mm)/ 20% black (4 mm) binary mixture of particles. The paths followed by the metal cuboid in the DEM simulation and experiment vary buy up to 1.5 cm and the paths followed by the plastic cuboid in the DEM simulation and experiment vary by up to 1.7 cm. The representative particle in the DEM simulation follows a path in between the DEM simulations and experimental results of the metal and plastic cuboids.

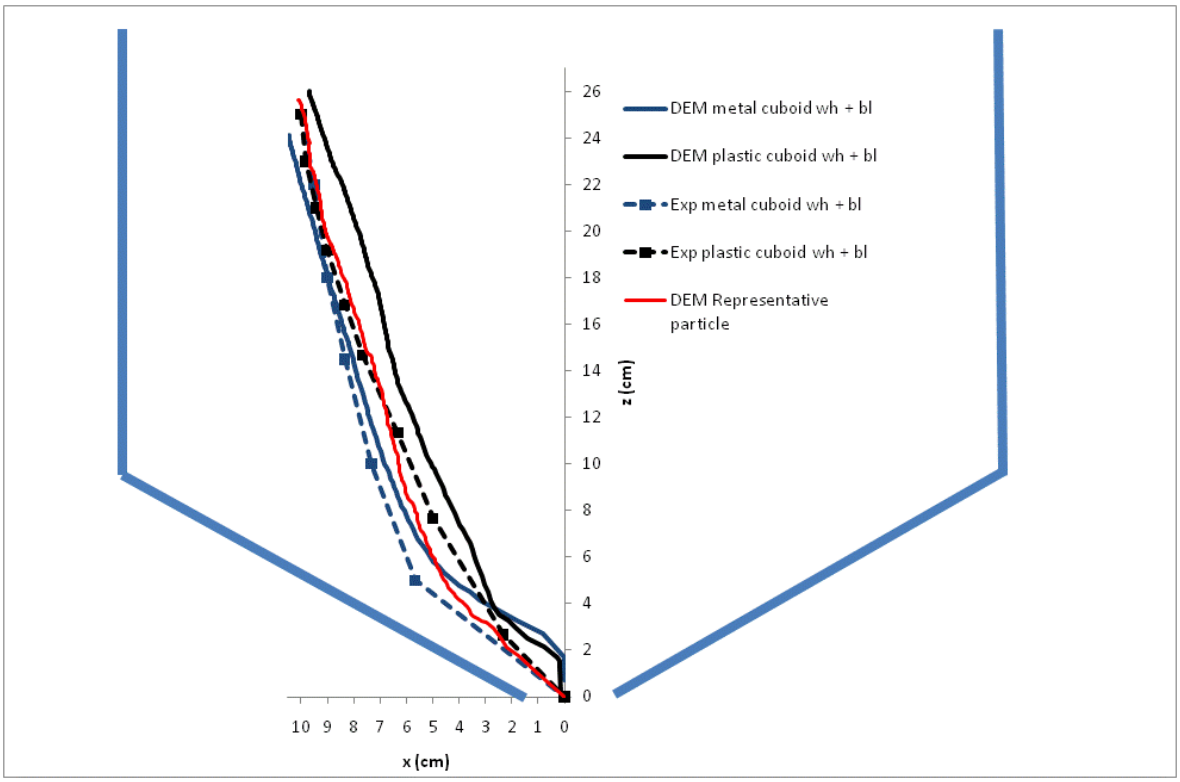

Figure 10.37: Plot of z against x showing the trajectory of metal and plastic cuboid free-cells from position 5 in the 80% white (5 mm)/ 20% black (4 mm) binary mixture of particles. The average of three experimental trials and the DEM simulation of the metal and plastic cuboids and the DEM simulation of the representative particle are shown.

Figure 10.38 shows *z* against time for the metal and plastic cuboids starting from position 5 in the 80% white (5mm)/ 20% black (4mm) binary mixture. The metal cuboid in the DEM simulation accelerates uniformly to the orifice at approximately 1.3 cm/s^2 and the metal cuboid in the experiment travels with a constant average velocity of 3.7 cm/s in the initial 3 seconds and then at 5.6 cm/s in the next 2.8 seconds. The plastic cuboid in the DEM simulation accelerates uniformly at 0.8 cm/s^2 from rest towards the orifice and the plastic cuboid in the experiment travels with an average constant velocity of 2 cm/s in the initial 5 seconds and then accelerates uniformly at 2.3 cm/s^2 prior to travelling through the orifice. The

metal cuboid and plastic cuboid take an average of 5.8 and 8 seconds to ravel through the orifice. The representative particle in the DEM simulation takes 10 seconds to travel to the orifice.

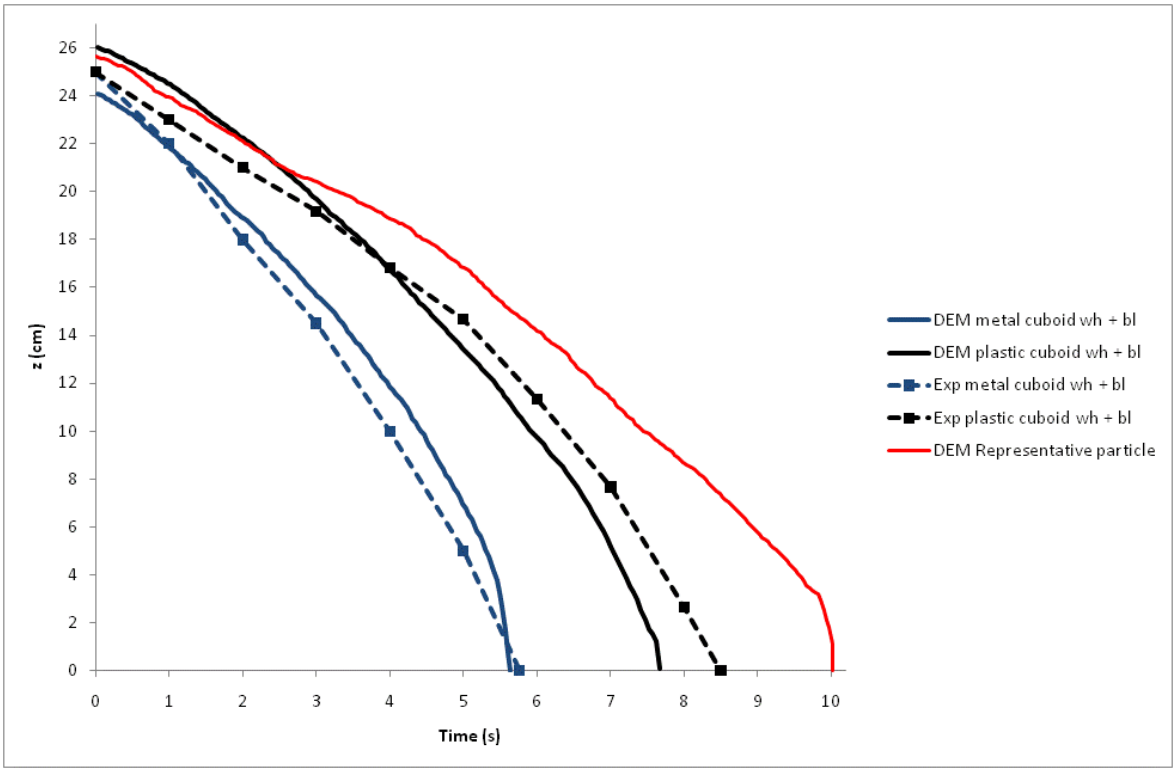

Figure 10.38: Plot of z against time showing the trajectory of metal and plastic cuboid free-cells from position 5 in the 80% white (5 mm)/ 20% black (4 mm) binary mixture of particles. The average of three experimental trials and the DEM simulation of the metal cuboid and the DEM simulation of the representative particle are shown.

Figure 10.39 shows *x* against time for the metal and plastic cuboids starting from position 5 in the 80% white (5 mm)/ 20% black (4 mm) binary mixture. The metal cuboid in the DEM simulation started at the position x = 10.5 cm, while the metal cuboid in the experiment started at x = 10 cm. Despite this the curves have a very similar profile. The metal cuboid in the experiments and simulations accelerates uniformly horizontally on average at 0.4 cm/s^2 prior to rapidly accelerating through the orifice. The metal cuboid in the DEM simulation travels with an average velocity of 0.6 cm/s prior to accelerating towards the orifice and the metal cuboid in the experiment accelerates uniformly towards the orifice from rest at an average of 0.2 cm/s^2.

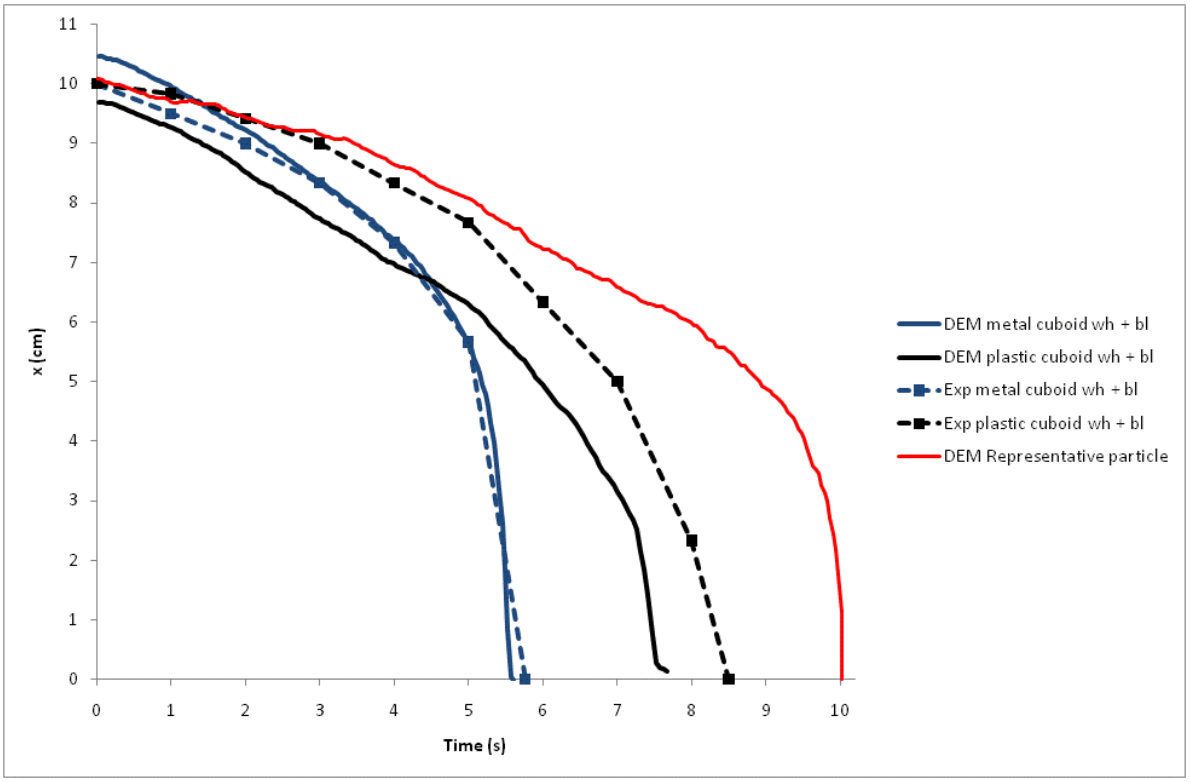

Figure 10.39: Plot of x against time showing the trajectory of metal and plastic cuboid free-cells from position 5 in the 80% white (5 mm)/ 20% black (4 mm) binary mixture of particles. The average of three experimental trials and the DEM simulation of the metal and plastic cuboids and the DEM simulation of the representative particle are shown.

Figure 10.40 shows z against *x* for the metal and plastic triangular prism free-cells in the 80% white (5mm)/ 20% black (4mm) binary mixture starting from position 5. The metal triangular prism in the DEM simulation started at x = 7.5 cm, z = 24 cm, while the metal triangular prism in the experiment started at x = 8.5 cm, z = 25 cm. Despite this their paths are virtually identical until the point x = 4 cm, z = 11cm where there paths diverge and differ by up to 2 cm along the horizontal. The metal triangular prism is observed to penetrate further into the bed of particles. The paths followed by the metal and plastic triangular prisms in the experiments differ by up to 1 cm along the horizontal. The results form the DEM simulation and experiments are very different, the paths differ by up to 3 cm along the horizontal. The representative particle in the DEM simulation follows the paths taken by the metal and plastic triangular prism in the experiments reasonably well. The paths differ by up to 1 cm, suggesting that the large difference between the DEM simulations of the metal and plastic triangular prisms and experimental results may be due to the difficulty in positioning the free-cells at the initial starting position in the DEM simulations.

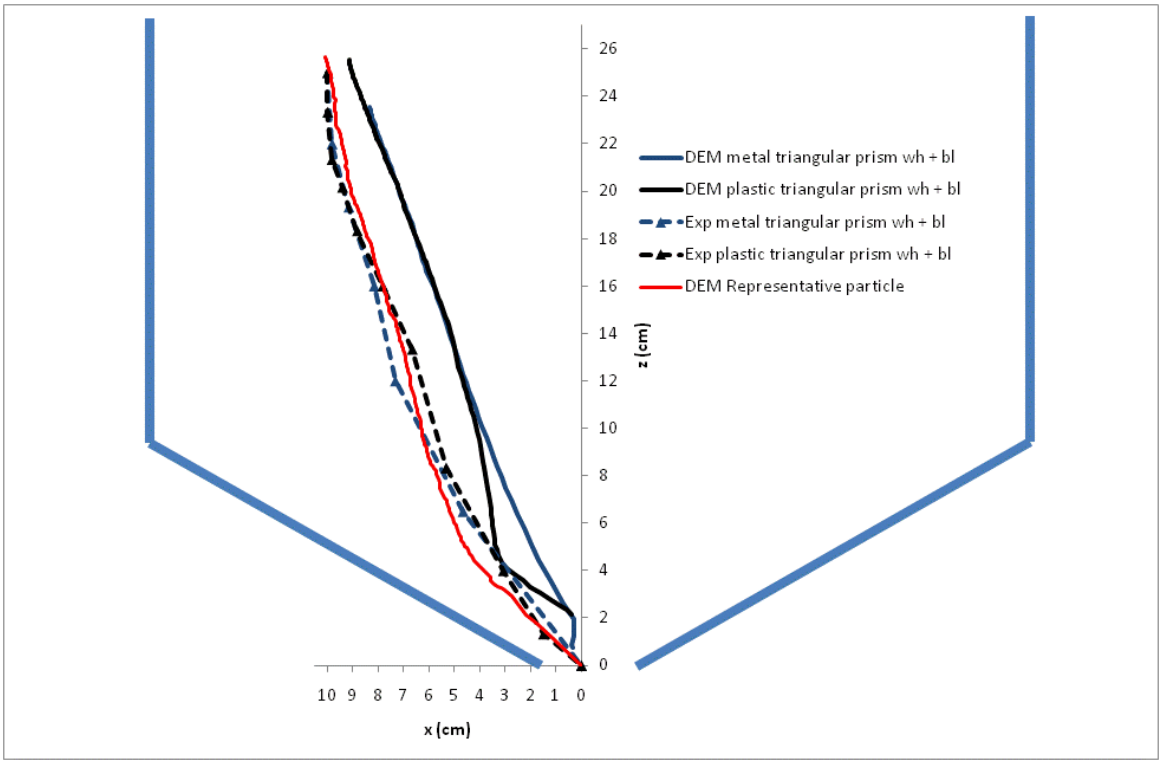

Figure 10.40: Plot of z against x showing the trajectory of metal and plastic triangular prism free-cells from position 5 in the 80% white (5 mm)/ 20% black (4 mm) binary mixture of particles. The average of three experimental trials and the DEM simulation of the metal and plastic triangular prism and the DEM simulation of the representative particle are shown.

Figure 10.41 shows *z* against time for the metal and plastic triangular prism free-cells in the 80% white (5 mm)/ 20% black (4 mm) binary mixture starting from position 5. The vertical displacement against time curves for the metal triangular prism obtained from DEM simulation and experiment are somewhat different. The metal triangular prism in the DEM simulation accelerates uniformly to the orifice at an average of 5.2 cm/s^2, while the metal triangular prism in the experiment accelerates to the orifice uniformly at 1.4 cm/s^2. The plastic triangular prism in the DEM simulation is observed to accelerate at 1 cm/s^2 in the initial 5 seconds prior to travelling at a velocity of 12 cm/s in the following 1 second towards the orifice. The plastic triangular prism in the experiment is shown to travel with a constant velocity of approximately 2 cm/s during the initial 2 seconds and then accelerate uniformly at approximately 1 cm/s^2. The representative particle in the DEM simulation is observed to have a similar profile as the plastic triangular prism in the experiment but it follows a constant velocity of 2.6 cm/s after the initial 2 seconds, rather than accelerating.

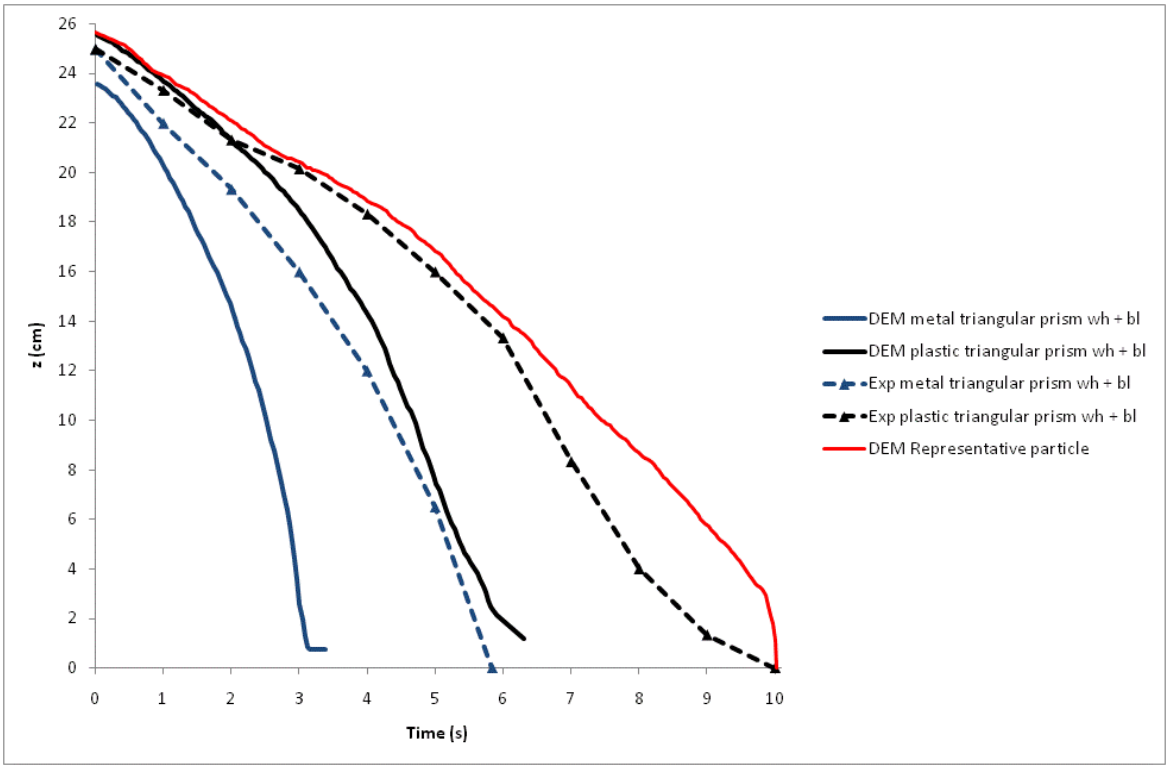

Figure 10.41: Plot of z against time showing the trajectory of metal and plastic triangular prism free-cells starting from position 5 in the 80% white (5 mm)/ 20% black (4 mm) binary mixture of particles. The average of three experimental trials and the DEM simulation of the metal and plastic triangular prisms and the DEM simulation of the representative particle are shown.

Figure 10.42 shows *x* against time for the metal and plastic triangular prism free-cells in the 80% white (5 mm)/ 20% black (4 mm) binary mixture starting from position 5. The DEM simulations of the metal and plastic triangular prisms start at the initial horizontal positions *x* = 8.4 cm and *x* = 9.1 cm respectively, compared to the initial position *x* = 10 cm in the experiments. This is most likely the cause of the different paths between the simulations and experiments. The metal triangular prism in the DEM simulation is observed to accelerate uniformly at approximately 1.9 cm/s^2, while the metal triangular prism in the experiment is observed to accelerate uniformly to the orifice at 0.6 cm/s^2. The plastic triangular prism in the DEM simulation is observed to gradually accelerate at 0.4 cm/s^2, prior to rapidly accelerating to the orifice, while the plastic triangular prism in the experiment accelerates uniformly at 0.2 cm/s^2, prior to slightly slowing down in the 2 seconds prior to reaching the orifice. The triangular prism either became trapped in the orifice or flowed through, hence the reason for the graphs from the DEM simulations stopping at the point *x* = 0.25 cm.

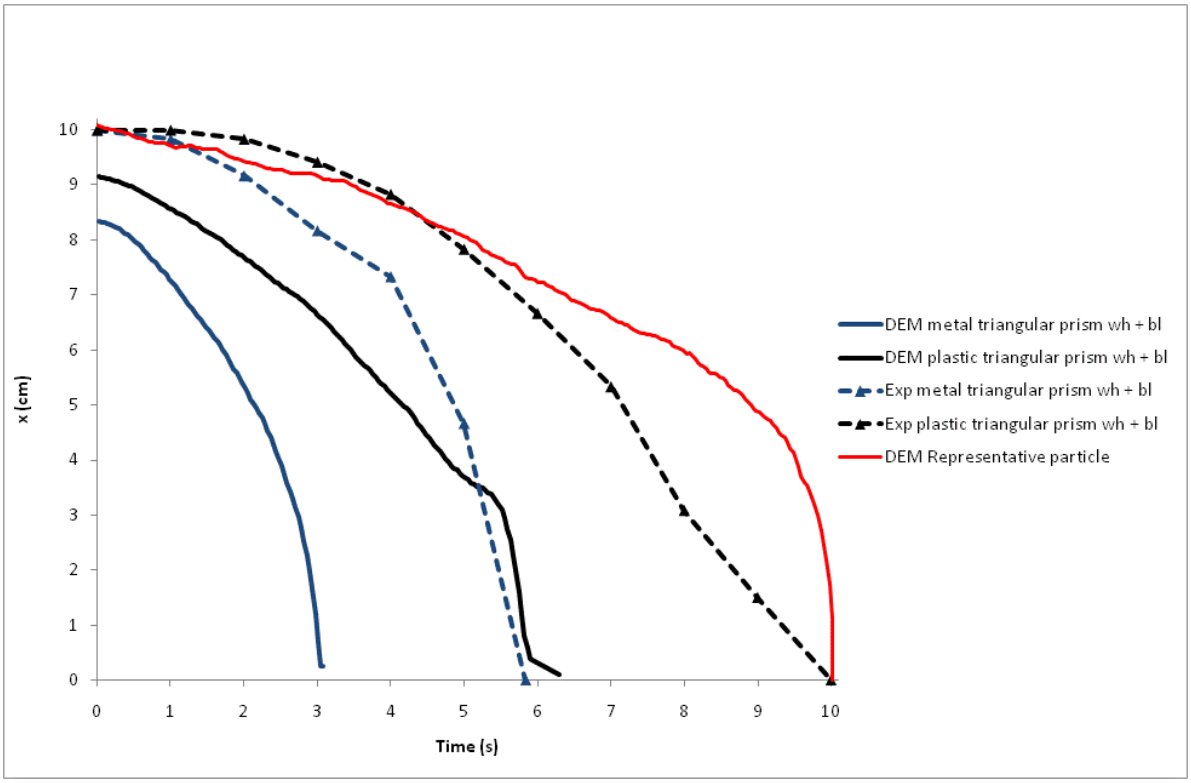

Figure 10.42: Plot of x against time showing the trajectory of metal and plastic triangular prism free-cells from position 5 in the 80% white (5mm)/ 20% black (4mm) binary mixture of particles. The average of three experimental trials and the DEM simulation of the metal and plastic triangular prisms and the DEM simulation of the representative particle are shown.

10.10 Summary

The path of the representative particle obtained from DEM simulation shows no agreement with the DEM simulations of the metal and plastic cylinders, cuboids or triangular prisms. The DEM simulations and experimental results of the metal and plastic cylinders vary in time to reach the orifice by only varies by 0.5 seconds. The DEM simulation and experiment of the metal cuboid is also in agreement on the vertical and horizontal displacement, but due to the different starting positions of the plastic cuboid the displacement is somewhat different although the shape of the curves is the same. Similarly, the difficulty in positioning the triangular prisms resulted in a different displacement time curves obtained from experiment and simulation.

10.11 Conclusion

Results indicate that there is generally better agreement between the trajectories of representative particles and of the free-cells starting from position 12, compared to position 5. There is also better agreement between experiments and simulations of the trajectories in the mono-sized particles than in the binary mix of different sized particles. This is most likely because of the more complex stress and velocity profiles in the binary mixture, compared to the more orderly crystalline structure in the monosized particles. The simulated and experimental trajectories of the plastic cylinder and the representative particles have the greatest agreement between their trajectories and velocities from starting position 5 and 12 in the monosized and binary mixture. The plastic cuboid follows a very similar trajectory to the representative particle starting from position 12 in the monosized particles and binary mixture, but its horizontal and vertical velocities are different in the binary mixture. This is because it was unknown whether the representative particle in the DEM simulations of the binary mixture was a white (5 mm) or a black particle (4 mm).

In general the results are very good despite the fact that the corners of the simulated free-cells were slightly rounded, so there could be some rolling friction on the corners. The *en masse* filling method used in the simulations is known to result in unrealistic static wall stresses (Langston, 2004). It may be the case that the static internal stresses are also affected by the filling method in this study.

The results indicate that the DEM has the potential to model the flow of free-cells in discharging hoppers despite the discrepancies between the experimental and simulated results when the free-cells are initially positioned where the stagnant zone boundary forms. The behaviour of the granular particles is difficult to predict along the stagnant zone boundary and more experimental work needs to be done to investigate the stress and velocity fields in this region.

Polyhedral particles

11 Polyhedral particles

11.1 Introduction

In this section the results of experiments to deduce the behaviour of polyhedral particles are discussed. The work in this section is part of a paper submitted to Powder Technology.

11.2 Comparison of DEM and experimental static packing

Fig. 11.1 shows a visual comparison between the DEM simulations and experiments for the static packing of the polyhedral particles in the hopper at hopper half angles $\alpha = 30^{o}$, 60^{o} and 90^{o}. There is good agreement between packing heights. A range of particle orientations is observed in the DEM and experimental packing's, which qualitatively appear similar. Fig. 11.2 shows a comparison for the spheres. The spheres are shown to pack in a uniform crystalline structure. This crystalline structure is shown to break down at the sides of the hopper in both the DEM and experiment as shown in Fig.11.1c. It is well known that a small polydispersity can disorder the structure, but since the primary objective here is experimental comparison, the mono-sized particles were used.

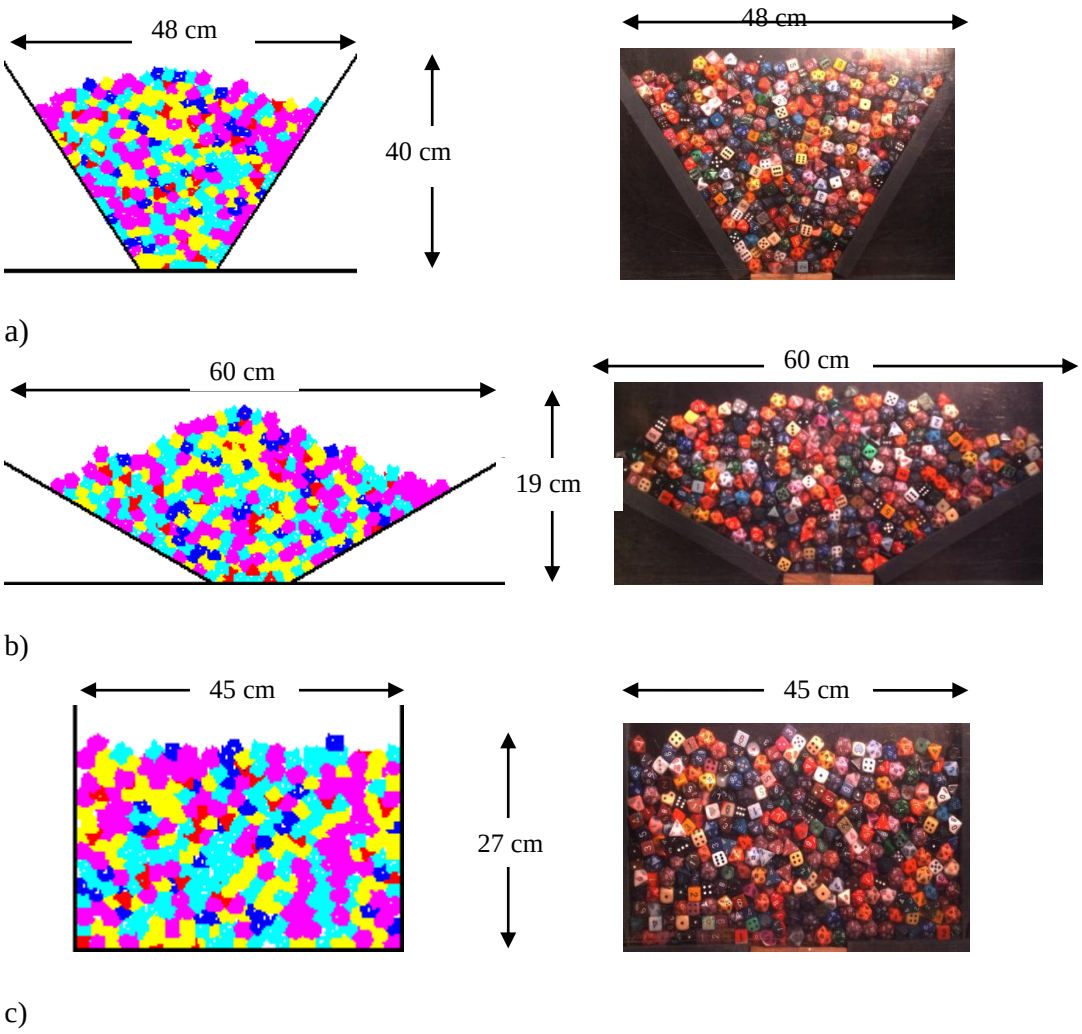

Figure 11.1: Hopper filled with polyhedral particles, on the left DEM simulation and on the right practical experiment, for hopper half angle a) 30º, b) 60º, c) 90º and orifice length 10 cm.

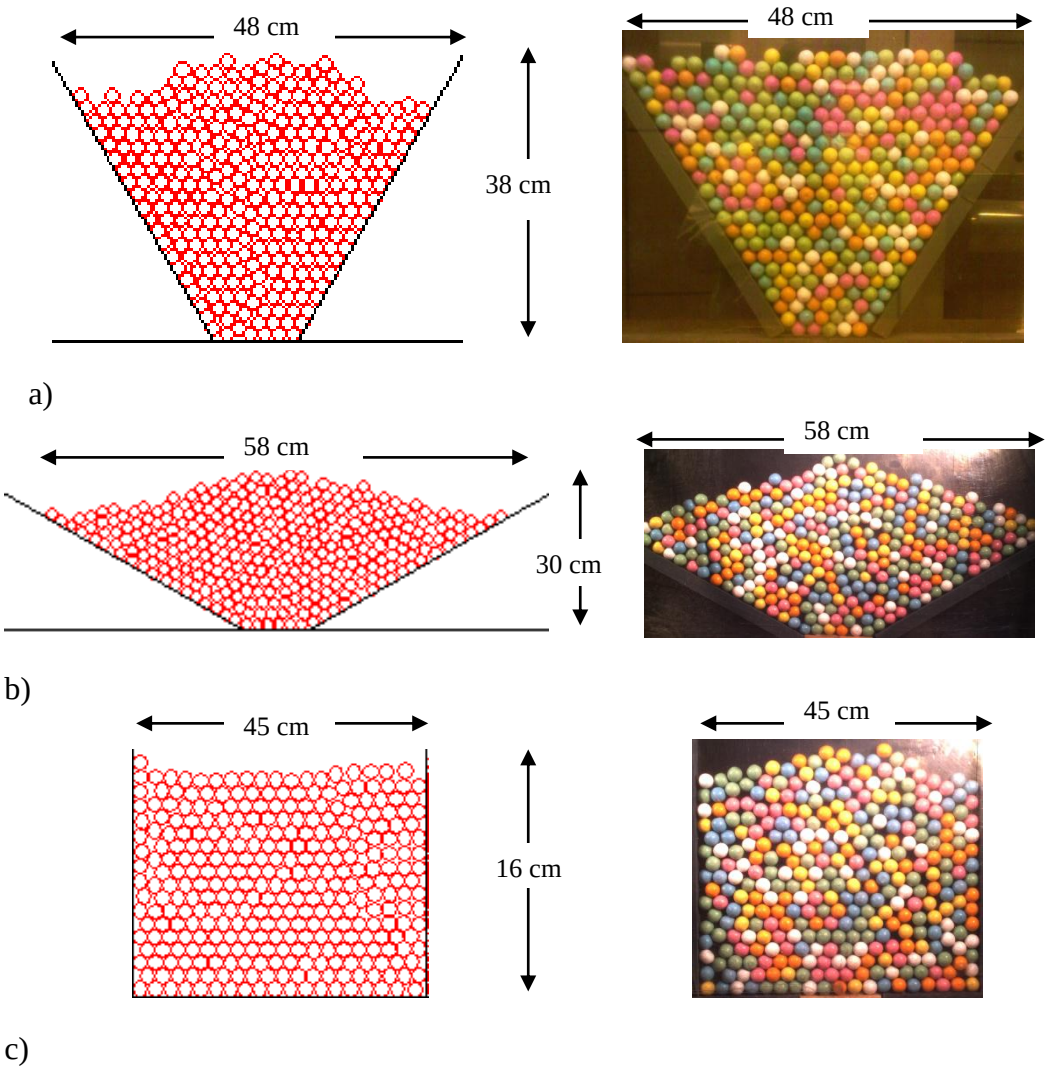

Figure 11.2: Hopper filled with slightly polydisperse spheres, on the left DEM simulation and on the right experiment, for hopper half angle a) 30º, b) 60º, c) 90º.

11.3 Experimental flowrate

Particle flowrate at the orifice is analysed by examining the recorded images of the particles discharging from the three angles α = 30º, 60º and 90º for both the polyhedra and the spheres. Experimental tests of the polyhedra and spheres were conducted three times at each of the hopper half angles. Figure 11.3 shows the fraction of polyhedral particles discharged from the hopper against time *t*. Apart from the case at angle α = 30º, where arching and flow blockage of the polyhedra occurred, particles discharge smoothly. The particles are shown to accelerate to a steady rate within the first 0.1 s when the orifice is opened. The dice in the 30 degree hopper take on average 1.3 seconds to completely discharge, while the 60 degree hopper takes

1.7 seconds to completely discharge. The dice in the 90 degree hopper only partially discharge as some of them remain in the corners. Out of three trials the average fraction of dice discharged through the orifice in the 90 degree hopper is 75%, which takes approximately 2.2 seconds.

Figure 11.4 shows the fraction of spheres discharged from the hopper against *t*. The spheres are shown to flow out of the hopper with a uniform velocity in the 30º and 60º hopper angle cases. In the 60º hopper angle case the flow rate slightly decreases in the last 0.2 s before the hopper is empty. In the 90º hopper angle case the flow rate is uniform for the first 1.5 s and then decreases as the particles in the corners start to flow out. The video shows them "jostling for position" in the hopper as they flow out. In the 60º and 90º hoppers the polyhedra and spheres are observed to exhibit "core flow" in which a central funnel of polyhedra are initially shown to flow out of the hopper. The spheres in the 30 degree hopper take 1.3 seconds to completely discharge, while the spheres in the 60 degree hopper take an average of 1.9 seconds to completely discharge. In similarity to the dice, the spheres in the 90 degree hopper become caught in the corners and the average fraction of dice discharged through the orifice in the 90 degree hopper is 88%, which takes approximately 2.5 seconds.

Polyhedra and spheres both side of the funnel, collapse and join the flow in the central core. In the 30º case the polyhedra and spheres exhibit "mass flow". There is a greater variation in the results from the three trials of the polyhedral flow than the flow of the spheres.

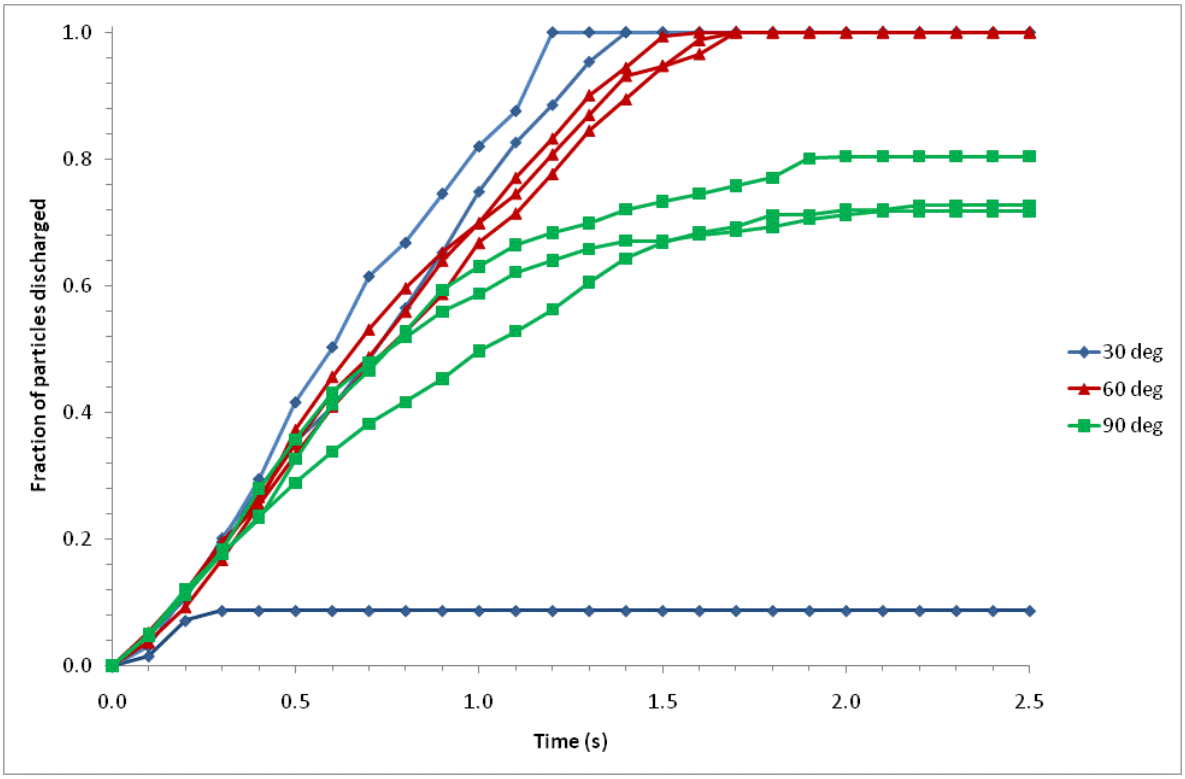

Figure 11.3: Experimental discharge dynamics of the polyhedra

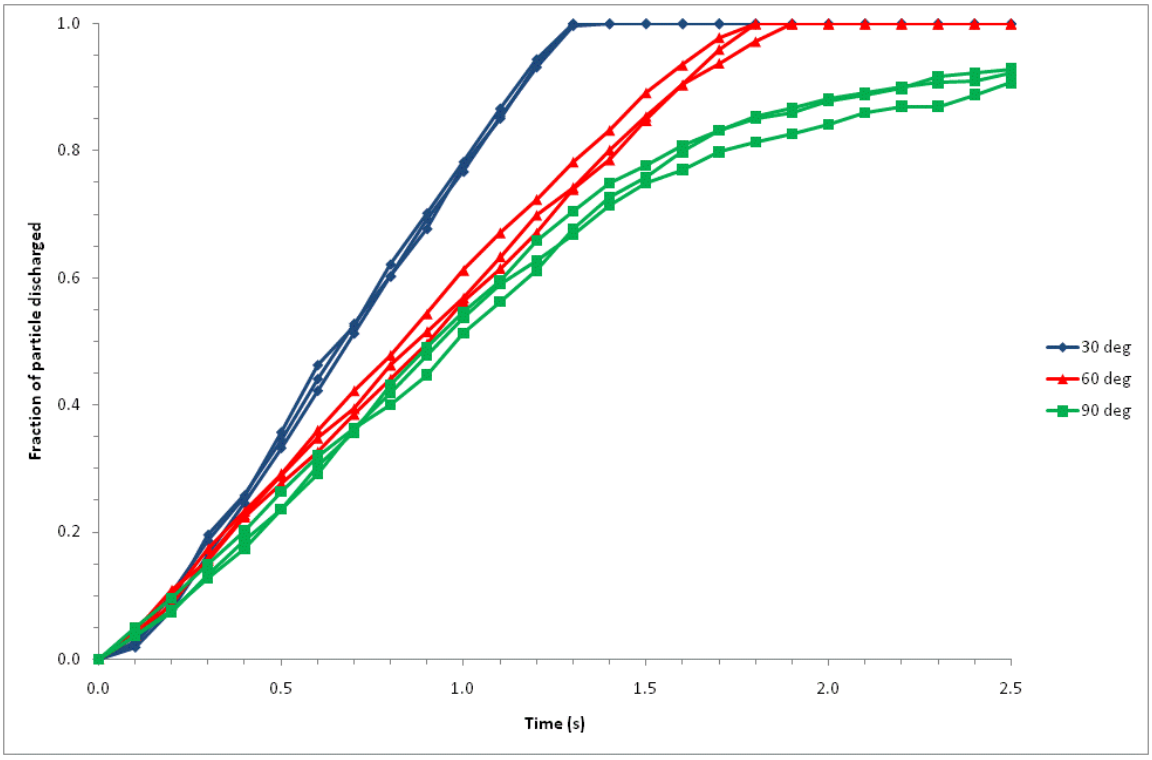

Figure 11.4: Experimental discharge dynamics of three experimental trials for the spheres

Averaged flow rates of the three trials of the polyhedra and spheres are shown in Figure 11.5. In the 90º hopper the polyhedra discharge at a very similar rate to the spheres and more of the particles accumulate in the corners. An average of 75% of the polyhedra completely discharges from the 90 degree hopper, compared to 88% of the spheres. In the 60º hopper the polyhedra flow 20% faster than the spheres and take an average of 1.7 seconds to completely discharge compared to 1.9 seconds for the spheres. The 30º hopper case is more complex; the flow rates are similar, however a blockage occurs during one of the polyhedral particle flow cases.

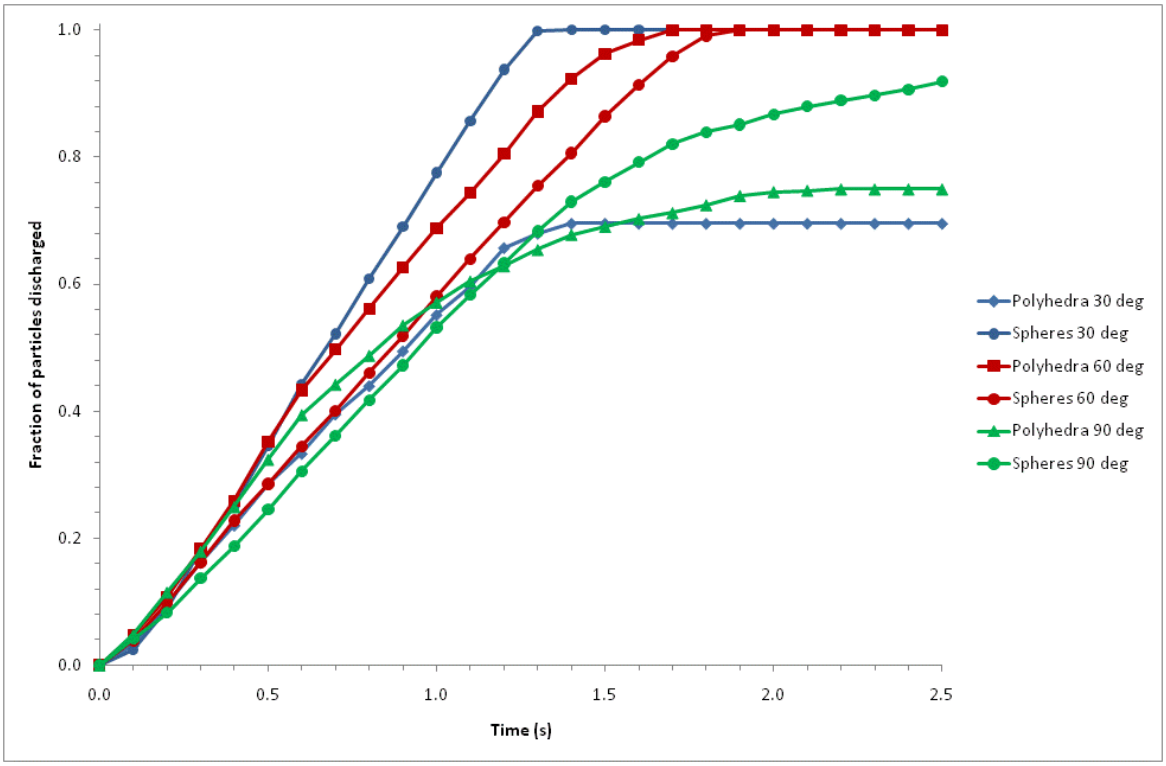

Figure 11.5: Comparison of average experimental discharge dynamics between the polyhedra and the spheres

11.4 Comparison of DEM and experimental flow behaviour

Figure 11.6 shows a comparison of the DEM and experimental flow rate for the polyhedra averaged over 3 cases for each. Very good agreement is shown for the 90º and 60º cases. The 30º cases are different due to the blockage that occurred in one of the experiments. Blockages are considered later. There are some slight differences between the DEM and experimental results. This is most likely due to the non-linear and stochastic nature of the contacts and discharge patterns, resulting from the numerous combinations of particle packing's that are available with the five different types of 322 dice. The polyhedra in the DEM simulation of the 30º hopper take 1.8 seconds to completely discharge compared to 1.7 seconds in the experiments and 78% of the polyhedra in the DEM simulation discharge from the 90º hopper compared to 75% in the experiment.

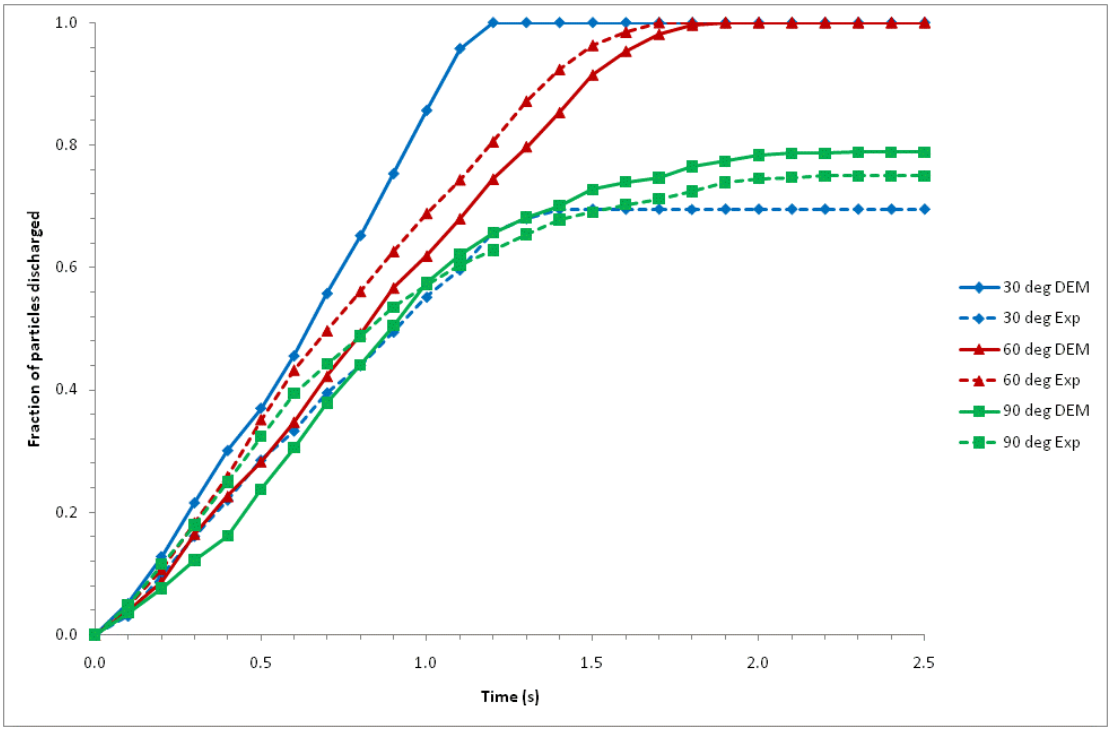

Figure 11.6: Comparison of DEM and average experimental discharge for the polyhedra

Simulation and video images of the particle flow patterns are shown in Figs 11.7, 11.8 and 11.9 for the 30º, 60º and 90º cases respectively. In the case of angle $\alpha = 30º$ the packing top profile is different after 0.5s, as it was prior to discharge, but after 0.8 and 1.0s there is a close similarity between the experiment and simulation. Similarly the 60º hopper shows differing top profiles at start and after 0.5 s and 0.8 s but a similar profile after 1.0s. The 90º hopper case shows a slightly faster flow in the experiment compared to the simulation and a greater number of particles in the experiment piling up at the corners. After 1.0 s experiment and simulation look similar.

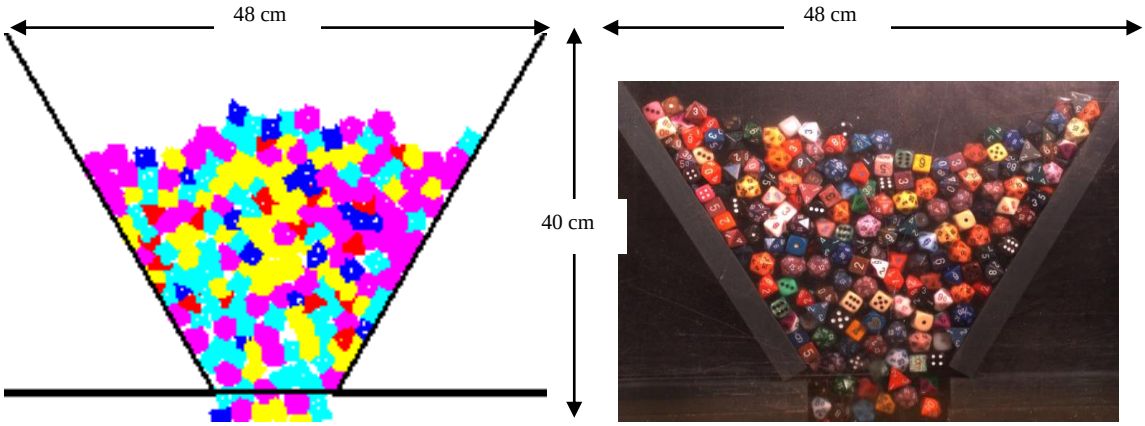

a) t = 0.5s

b) t=0.8s

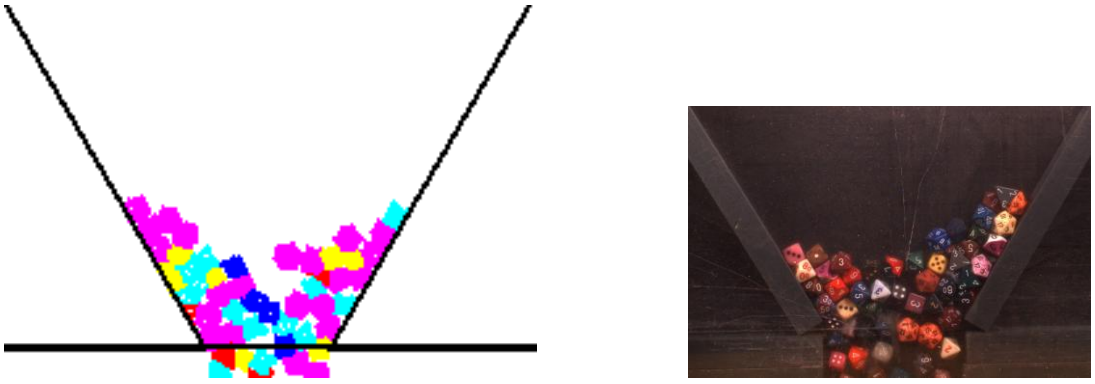

c) t = 1.0s

Figure 11.7: Polyhedra discharging at hopper half angle 30° a) t = 0.5 s, b) t = 0.8 s, c) t = 1.0 s and orifice length 12 cm

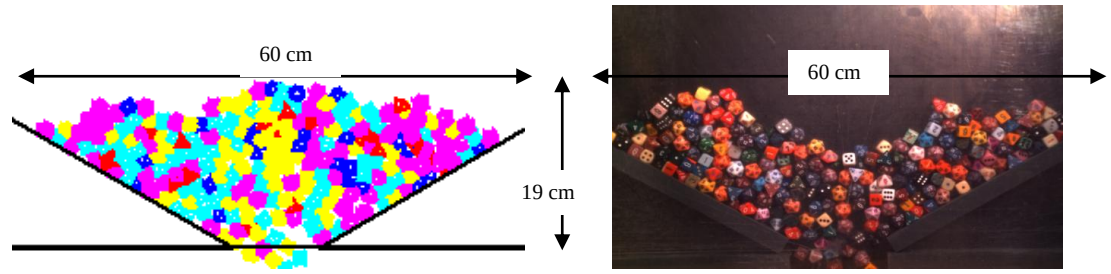

t = 0.5 s

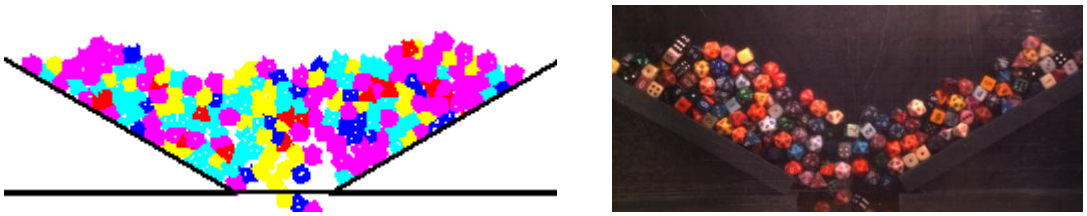

t = 0.8 s

t = 1.0s s

Figure 11.8: Polyhedra discharging at hopper half angle 60º and orifice length 12 cm

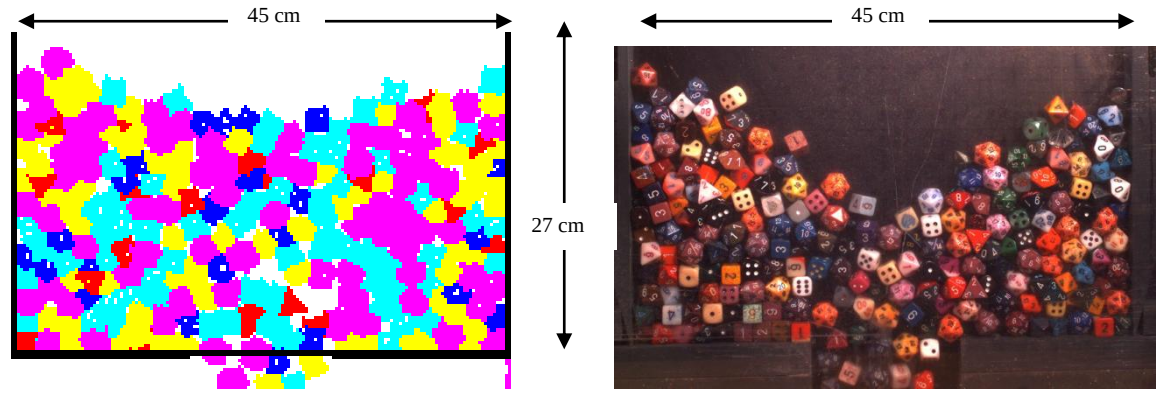

a) t = 0.5s

b) t = 0.8 s

c) t = 1.0s

Figure 11.9: Polyhedra discharging at hopper half angle 90º and orifice length 12 cm

A comparison of the DEM and experimental flow rate for the spheres is shown in Figure 11.10. The spheres in the 30º hopper take an average of 1.4 seconds to discharge in the DEM simulation and 1.3 seconds in the experiment and the spheres in the 60º hopper take 2.1 seconds to discharge in the DEM simulation and 1.9 seconds in the experiment. The fraction of spheres discharged from the 90º hopper is approximately 95% in both the DEM simulation and the experiment.

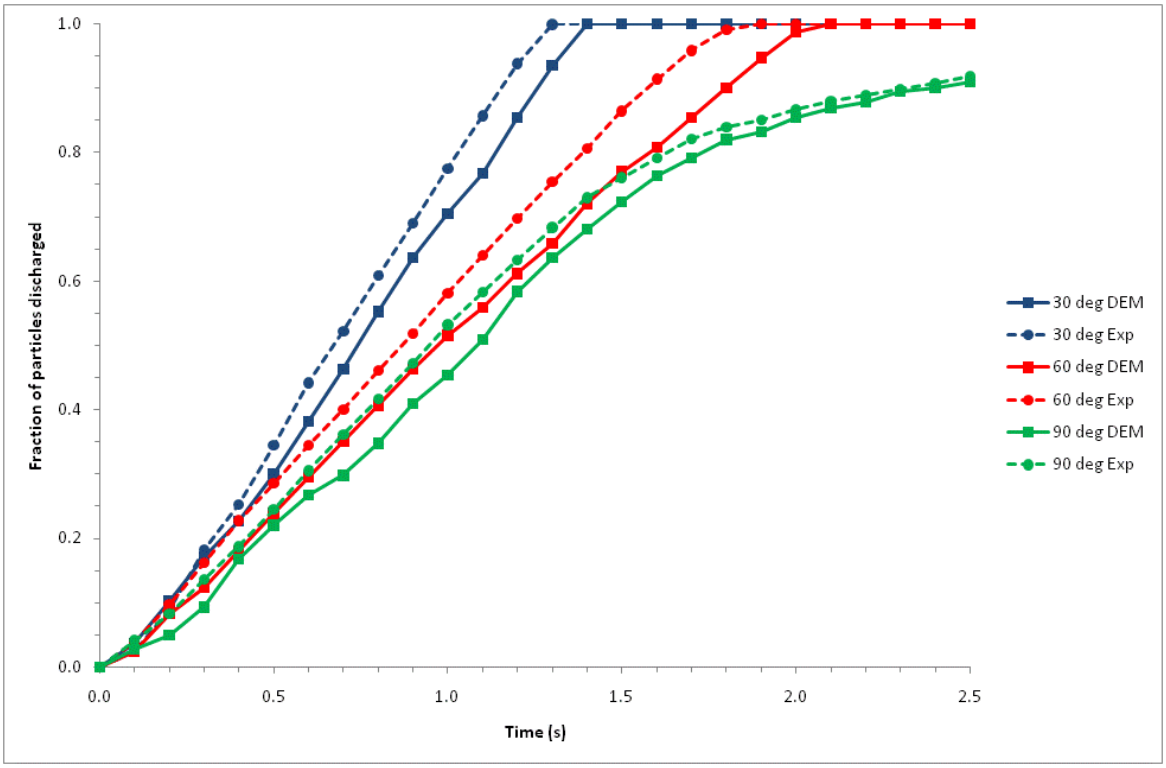

Figure 11.10: Comparison of DEM and average experimental discharge for the spheres

11.5 Comparison of sphere and polyhedra flow from DEM data

Figure 11.11 shows a comparison of the results from the DEM simulations of the flow of the polyhedra and volume equivalent spheres with identical friction and damping and rolling friction. A comparison of polyhedra and equivalent sphere flow is complex here. Generally the polyhedra flow slightly faster than the equivalent spheres. This is probably due to inter-planar surface sliding. However, for the 90^{o} hopper the flow is slower towards the end and more particles are retained in the corners as expected. Polyhedra also have a much greater tendency to blockage as discussed later. In the 30º hopper the spheres take 1.4 seconds to discharge compared to the polyhedra which take 1.2 seconds. In the 60º hopper the spheres take 2.1 seconds compared to the polyhedra which take 1.9 seconds. In the 90º hopper 90% of the spheres discharge compared to 78% of the polyhedra.

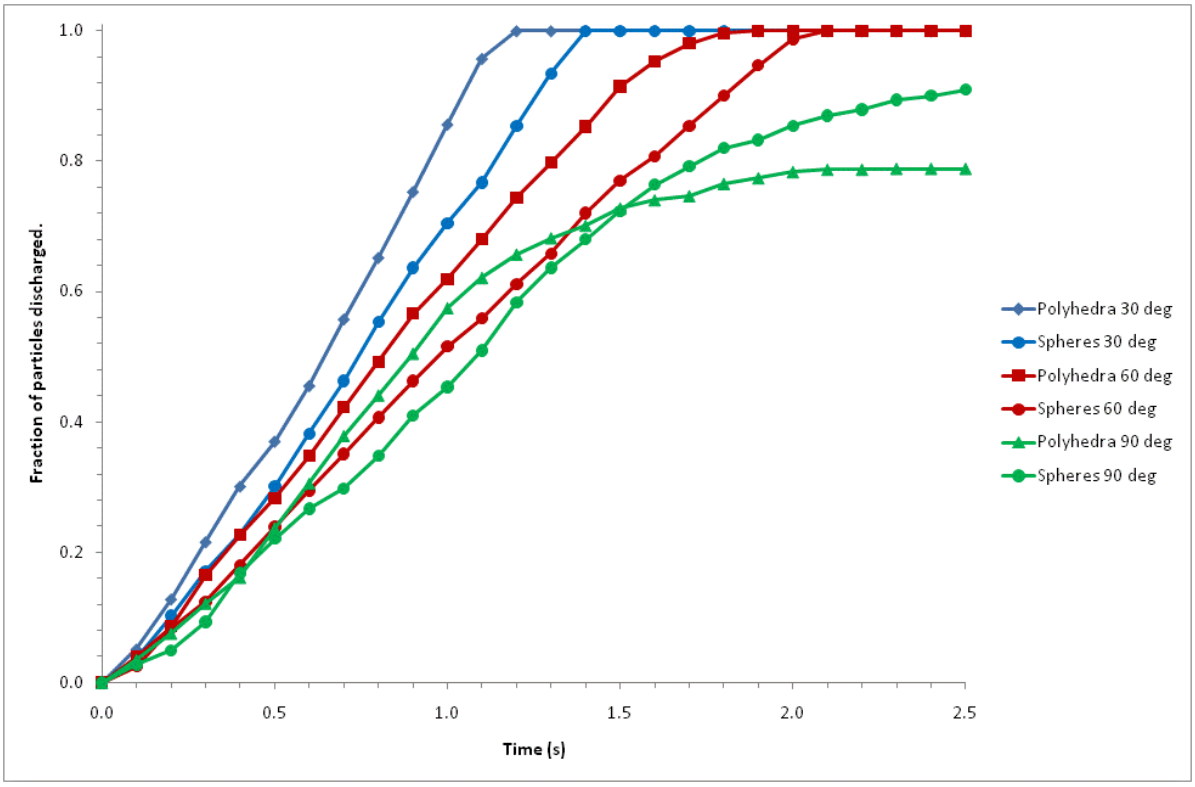

Figure 11.11: Comparison of DEM polyhedra and DEM sphere discharging. Total volume and mass of spheres is the same as for the polyhedra

11.6 Sensitivity of polyhedra flow to friction

The coefficient of friction between the polyhedra was assumed to be identical in the DEM simulations for all combinations of particle contacts. In reality this is not the case, each contact will have a slightly different coefficient of friction, so some simulations were undertaken to test the sensitivity of the results to friction. Figure 11.12 shows the variation in the flow rate of the polyhedra at three different coefficients of friction. Setting the coefficient of friction at the smaller value of 0.28 resulted in slightly faster (20%) flow, but setting it to 0.306 and 0.364 gave very similar results. (The higher friction gives a very small increase in discharge at some points – this is probably stochastic.) It is considered that differences in friction could account for some of the small differences observed between experiment and simulation. If DEM is to be used in a predictive capacity sensitivity to friction should be considered.

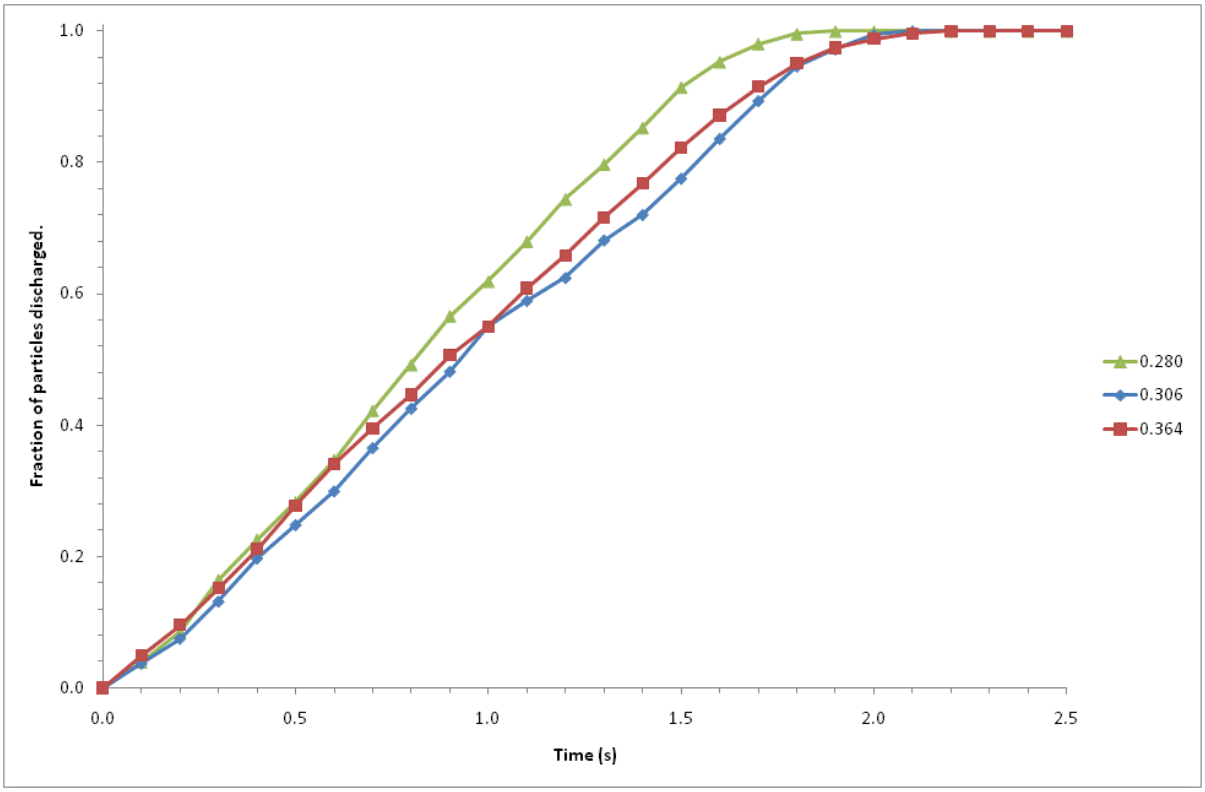

Figure 11.12: Comparison of DEM polyhedra simulations at hopper angle 60° for three values of the friction coefficient

11.7 Critical Orifice diameter

Blockages occurred in the polyhedra experiments in the hopper angle α = 30º. The orifice length was set to 12cm in the DEM and experimental comparisons so that a relatively unimpeded flow could be established in the hopper. Experimental tests were conducted at angles α = 30º, 60º and 90º to deduce a critical orifice length at which hopper discharge was unlikely. DEM simulations were also conducted at different values of the orifice length. Figure 11.13 shows the blockage that occurred in a hopper with angle α = 30º and orifice length 10cm for experiment and DEM. The arching structure is similar in these cases. Figure 11.14 shows the probability of a blockage occurring. The experimental results were obtained from ten trials at angles α = 30º, 60º and 90º and orifices lengths 6, 7, 8, 9, 10, 11 and 12cm. The critical orifice width generally increases as the hopper half-angle decreases. Surprisingly the probability of discharge dips at orifice length 10cm the 60º and 90º hoppers. It is considered that these must be statistical aberrations. The results from DEM simulations to

estimate the orifice length at which there is a 0.5 chance of a blockage occurring are also shown in Figure 11.14. There is generally good agreement between the DEM simulations and experiment.

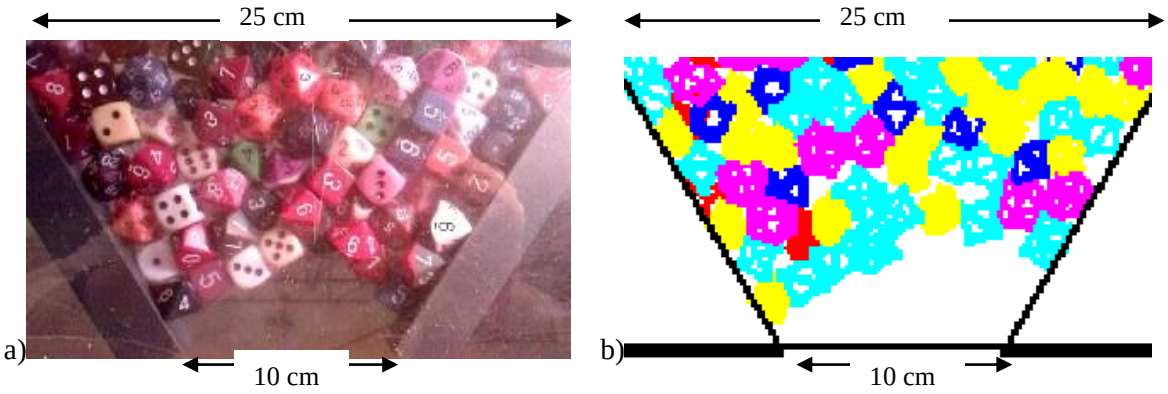

Figure 11.13: Polyhedral dice blocked in hopper with half angle 30° and orifice length 10cm. a) Experiment, b) DEM

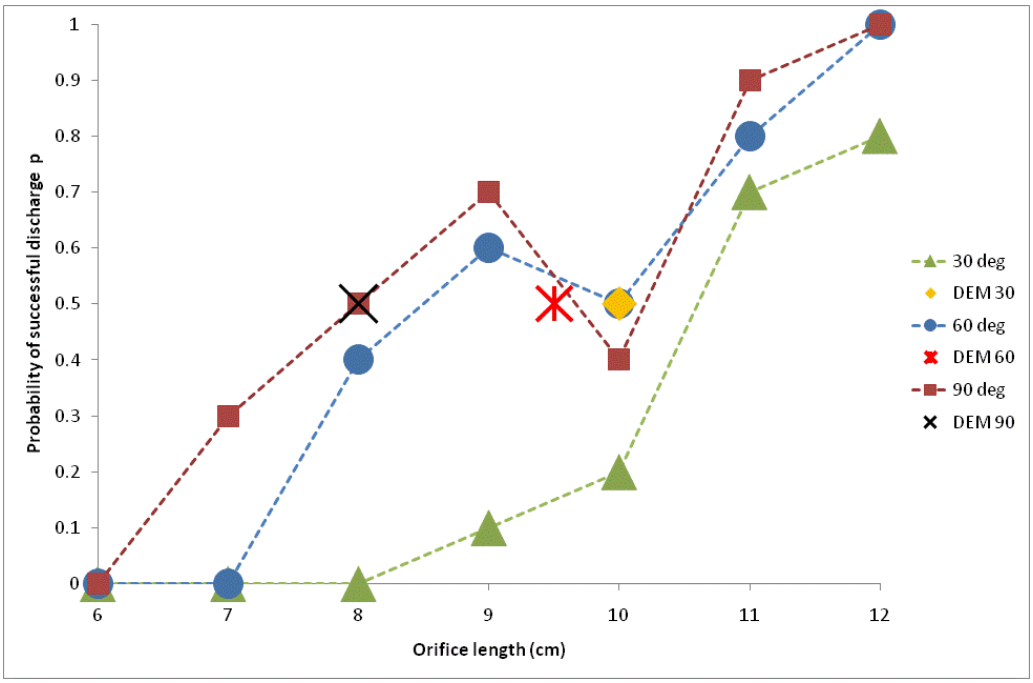

Figure 11.14: Probability of successful polyhedral discharge at hopper half angles 30°, 60° and 90° for different experimental orifice lengths and estimate of DEM orifice length for 50% successful discharge

11.8 Conclusion

Comparisons have been made between DEM simulations and practical experiments of 322 non-cohesive large particles in a small 3D hopper at angles $\alpha = 30^{\circ}$, 60° and 90°. Polyhedral particles and spheres have been examined. The static packing height, flow rate and critical orifice length for the spheres and polyhedra were compared and visual inspections were made of the packing structure, flow patterns and blocked arch structure. DEM simulations of both the polyhedra and the spheres showed good general agreement with experiment. The discharge rate of the polyhedra is moderately sensitive to the particle-particle friction coefficient. Polyhedra flow is generally slightly faster than the spheres. This may be because the polyhedra have many flat surfaces which enable them to slide past each other more easily. Slow motion videos of the flowing polyhedral particles show their ability to pack more tightly and slide past each other more easily than the spheres. However, polyhedra have a greater tendency for blockage. There are some differences between the top surface profiles in the DEM simulations and experiments. This is mostly likely due to the inability to exactly replicate the filling method between the experiments and the simulations. However this has not greatly affected the flow rate. The likelihood of a blockage occurring is greater for the hopper with angle $\alpha = 30^{\circ}$ and more polyhedral particles, than spheres, pile up in the corners in the 90° hopper half angle case. The use of the "soft" linear spring to model the particle contacts has shown to be accurate in predicting the flowrate and flow patterns of polyhedral particles.

Overall summary and conclusions

12 Overall summary and conclusions

Practical experiments and computer simulations have been conducted with the aim of deducing a suitable shape and density of free-cell that moves along as close as possible, with the other particles, during the discharge phase from a silo. This is to enable electronic free cells that will record their position and physical properties such as humidity, to be placed in the silo and help to pinpoint any problems with the movement of the grain during discharge.

Experiments were conducted in a quasi 3D slice silo rig, with Perspex sides, to enable a clear view of the behaviour of the particles and the free-cell. The experimental results obtained in this work can be used as a basis to understand the mechanics of free cells in industrial scale silos. The stress, strain, elastic modulus, particle size, particle density and gravity experienced in an industrial scale silo would all have to be scaled down accordingly, resulting in smaller particles and increasing the runtime in Discrete Element Method simulations. The quasi 3D slice rig was designed to enable easy adjustment of the various pieces and a wide range of possible dimensions. Circular, cuboid and triangular free-cells were chosen as they were considered to be so very different in shape, that any important phenomena could hopefully clearly be observed and compared. The shapes all had an identical volume of 7.50 cm^3.The materials were chosen so that free-cells with densities greater and less than the particles could be studied. Free-cells were constructed using a metal of density 8.0 g/cm^3 and a plastic of density 1.2 g/cm^3. Hollow free-cells, consisting of a thin shell open at both ends, were also used in the practical experiments. Spherical particles were used in the experiments to reduce the complexity in the system and to enable easy comparisons between experiments.

The trajectory of the free-cells was examined in a batch of monosized white (5 mm) particles of density 1.28 g/cm^3 and two binary mixtures. The binary mixtures consisted of 80% white (5 mm)/ 20% black (4 mm) of density 1.28 g/cm^3 and 80% white (5 mm)/20% yellow (6 mm) of density 1.28 $g/cm^3$and 1.16 g/cm^3 respectively.

A DEM simulation of each of the metal and plastic, cylindrical, cuboid and triangular prism free cells was conducted to model the trajectories of the free-cells from two different positions in the silo using a program written in Microsoft Visual Basic by Dr Paul Langston at the University of Nottingham. The code was re-written in FORTRAN for this study, to enable it to be easily adapted to model other hopper systems or for parallelization programming.

One of the starting positions in the DEM simulations was at the top of the silo, in a region away from the stagnant zone boundary and the other starting position was at a position at which the stagnant zone boundary was observed to form. The DEM simulations were compared with the results from practical experiments to evaluate the suitability of the DEM, with the intention in the future of relying solely on results obtained from simulations and hence doing away with the need for costly practical experiments.

The path followed by the particle in each of the monosized and binary mixtures that was positioned at the same starting position as each of the free cells was also obtained. This enabled comparisons between the trajectories and displacements of each of the free cells to be compared with the particle and hence determine the appropriate free cell that would move with the surrounding grains.

Practical experiments were conducted to deduce the input parameters required by the program. Tests were conducted to deduce the particle-particle and particle-wall sliding friction coefficients, the particle-particle and particle-wall rolling friction coefficients and the particle stiffness. The program modelled the particle-particle and particle-wall interactions as linear interactions and employed the simple spring-slider-dashpot model. The modified Euler integration scheme was used to integrate the force and obtain the velocities and positions of the particles after each time step. The program was tested by comparing the results obtained from simple experiments to deduce the time taken for one particle to roll down an incline and slide down an incline (this was conducted by setting the angular velocity to be zero), thus evaluating the accuracy of the particle-wall rolling and sliding friction coefficients obtained from experiment. The DEM program was further tested by conducting experiments and simulations to obtain the discharge rate of the white (5 mm) monosized particles and the white (5 mm)/ black (4 mm) binary mixture by varying the hopper half angle in increments of 10º.

The plastic cylinder was found to have the same trajectory, displacement and velocity curves as the representative particle and the DEM simulation. At least one of the three trials of the plastic cylinder, plastic cuboid and plastic triangular prism in the monosized particles was found to be the same as the path followed by the representative particle. There was some difficulty in positioning the triangular free cells accurately in the simulations as they tended to slide along the top of the particles below them, which affected the results. The time taken for the free cells in the binary mixtures to reach the orifice was approximately 50% greater than

the time taken in the monosized particles. The trajectories and displacements of the plastic cuboid and plastic cylinder showed the time taken to reach the orifice differing by 2% between the DEM simulation and experiment. The trajectory and displacement of the free cells obtained from DEM simulation and experiment when they were initially position where the stagnant zone boundary was observed to form varied considerably and the time taken for them to reach the orifice could vary by up to 100%. The metal free cells were found to segregate through the other particles and the rotated by between 60º and 90º. The plastic and hollow free cells were both found to rotate by 180º. The slightly rounded corners of the triangular and cuboid free-cells may have influence the results and therefore a rolling friction component between the particles and the free-cells may have to be incorporated into the DEM computer program. The fact that the *en masse* filling method was used may have slightly affected the results.

Spherical particles are idealised particles, so tests were also conducted with a small number of polyhedral particles. In a previous study, Wang et al. (2011) modelled regular polyhedra with rounded vertices. Combinations on spheres, tetrahedra and octahedral were modelled using the DEM. This work builds on this previous work by comparing experimental and DEM simulations in order to test the accuracy of the DEM in the modelling of polyhedral particles. Three hundred and twenty two polyhedral particles consisting of 91 hexahedra (55 of type 1, 36 of type 2 that had more rounded corners than type 1), 81 icosahedra, 29 tetrahedra, 31 octahedra and 90 trapezohedra were poured into the 3D hopper slice and allowed to discharge through the orifice. . The discharge rate of the polyhedral particles was compared with spheres of very similar average volume and average density to the 322 polyhedral particles. The flow rate of the polyhedra and spheres was found to be similar in the 90º hopper. The polyhedra flowed 20% faster than the spheres in the 60º hopper. The flow rate of the polyhedra and spheres was also similar in the 30º hopper but polyhedra particles were found to block more frequently than spheres. The critical orifice length at which blockages occurred was deduced and it was found that the critical orifice length decreased as the hopper half angle increased. The results show that the DEM polygon method is accurate in modelling polyhedral particles.

Recommendations for further studies

13 Recommendations for further studies

Experiments and computer simulations in this study have many limitations. The use of a 3D silo slice has enabled the behaviour of free-cells of different densities and shapes to be examined, but practical applications require understanding the behaviour of free cells in large 3D industrial scale silos. Work needs to be conducted in an industrial scale 3D silo and identical computer simulations should be conducted to further test the feasibility of using the Discrete Element Method to model the flow of free-cells in discharging silos. The DEM program could be parallelized to enable the modelling of billions of particles. Granules found in industrial applications are not spherical and therefore further research could consider modelling the displacement of free-cells in non-spherical particles such as long elongated particles or polyhedra. Natural grains can sometimes develop moisture on their surfaces due to the weather or the climate. Further work could consider how inter-particle cohesion affects the flow of free-cells.

The method used to position the free-cells in the silo in the DEM simulations needs to be improved. Presently the free-cells drop down into the hopper with the other particles, and the triangular prism and cuboid free-cells slide along the particles below them. The triangular prism and cuboid were initially orientated so that one of their sides was parallel to the horizontal. Further work could consider different initial orientations of the triangular prism and cuboid. The behaviour of other shapes such as rectangles and rhombi and other shapes with several sides could also be studied. The change in the orientation of the free-cells during discharge from the hopper has only been given a brief mention in this study. Further work needs to consider the rotation of various different shaped free-cells with the aim of deducing general patterns. This may go towards obtaining an ideal shape of free-cell that does not rotate when placed at any initial position in the silo.

Experimental results indicate that the behaviour of the free-cells in the two different boundary mixtures is very similar. Further studies could investigate the trajectory of the free-cells in binary mixtures with different ratios of each type of particle.

Plasticity theory has been applied to the modelling of granular materials. Morrison and Richmond (1976) developed a model to represent the streamlines of the flow of a granular

material from a hopper. Further work could extend this model to incorporate free-cells by applying appropriate boundary conditions.

References

REFERENCES

Able, R. M. G., Othen, S. M. & Nedderman, R. M. 1996. The exit time distribution during the batch discharge of a cylindrical bunker. Chemical Engineering Science, 51, 4605-4610.

Ai, J., Chen, J. F., Rotter, J. M., Oo, J. Y. 2011. Assessment of rolling resistance in discrete element simulations. 206 269-282

Al-Din, N. & Gunn, D. J. 1984. The flow of non-cohesive solids through orifices. Chemical Engineering Science, 39, 121-127.

Artega, P. & Tüzün, U. 1990. Flow of binary mixtures of equal-density granules in hoppers--size segregation, flowing density and discharge rates. Chemical Engineering Science, 45, 205-223.

Asmar, B. N., Langston, P. A., Matchett, A. J. & Walters, J. K. 2002. Validation tests on a distinct element model of vibrating cohesive particle systems. Computers & Chemical Engineering, 26, 785-802.

Balevičius, R., Kačianaukas, R., Mróz, Z., Sielamowicz, I. 2008. Discrete particle investigation of friction effect in filling and unsteady/steady discharge in three-dimensional wedge-shaped hopper. Powder Technology, 187, 159-174.

Bazant, M. Z. 2006. The Spot Model for random-packing dynamics. Mechanics of Materials, 38, 717-731.

Bemrose, C. R., Fowles, P., Hawkesworth, M. R., O' Dwyer, M. A. 1988. Application of Particle Emission Tomography to particulate flow measurements in chemical engineering process. Nuclear Instruments and Methods in Physical Research A273 874-880

Beverloo, W. A., Leniger, H. A. & Van De Velde, J. 1961. The flow of granular solids through orifices. Chemical Engineering Science, 15, 260-269.

Bharadwaj, R., Smith, C. & Hancock, B. C. 2010. The coefficient of restitution of some pharmaceutical tablets/compacts. International Journal of Pharmaceutics, 402, 50-56.

Brown, R. L., Richards, J. C. 1959. Exploratory study of the flow of granules through apertures. Trans. Instn. Chem. Engrs., 37, 108-119.

Buali, Q. A. MSc Dissertation: Studies of wheat flow in an experimental hopper. 1999. Satake Centre for Grain Process Engineering, Department of Chemical Engineering, University of Manchester. 660.2 BUA

Campbell, C. S. 2006. Granular material flows - An overview. Powder Technology, 162, 208-229.

Chen, J. F., Rotter, J. M., Ooi, J. Y. & Zhong, Z. 2005. Flow pattern measurement in a full scale silo containing iron ore. Chemical Engineering Science, 60, 3029-3041.

Cleaver, J. A. S. & Nedderman, R. M. 1993. Measurement of velocity profiles in conical hoppers. Chemical Engineering Science, 48, 3703-3712.

Clement, E. 1999. Rheology of granular media. Current Opinion in Colloid & Interface Science, 4, 294-299.

Cundall, P. A. and Strack, O. D. L. 1979. A discrete numerical model for granular assemblies. Geotechnique, 29, 19.

Datta, A., Mishra, B. K., Das, S. P. & Sahu, A. 2008. A DEM Analysis of Flow Characteristics of Noncohesive Particles in Hopper. Materials and Manufacturing Processes, 23, 195 - 202.

Davies, C. E. and Desai, M. 2008. Blockage in vertical slots: Experimental measurement of minimum slot width for a variety of granular materials. Powder Technology, 183, 436-440.

Di Renzo, A. and Di Maio, F. P. 2004. Comparison of contact force models for the simulation of collisions in DEM based granular flow codes. Chemical Engineering Science, 59 525-541

Drahun, J. A. and Bridgewater, J. 1983. The mechanisms of surface segregation. Powder Technology, 36, 39-53

Drucker, D. C. and Prager, W. 1952. Soil mechanics and plastic analysis or limit design. Quarterly of Applied Mathematics, 10, 157-165

Engeln-Mullges, G. and Uhlig, F. 1996. Numerical algorithms with FORTRAN. Springer

Enstad, G. 1975. On the theory of arching in mass flow hoppers. Chemical Engineering Science, 30, 1273-1283.

Feng, Y. T., Han, K., Owen, D. J. R., Loughran, J. 2009 On upscaling of Discrete Element Models: Similarity principles. Engineering Computations, 26 (6) 599-609

Forsyth, A. J., Hutton, S., Rhodes, M. J. 2002. Effect of cohesive interparticle force on the flow characteristics of granular material. Powder Technology, 126, 150-154

Fowler, R. T. & Glastonbury, J. R. 1959. The flow of granular solids through orifices. Chemical Engineering Science, 10, 150-156.

Fraige, F. Y., Langston, P. A. & Chen, G. Z. 2008. Distinct element modelling of cubic particle packing and flow. Powder Technology, 186, 224-240.

Franklin, F. C. & Johanson, L. N. 1955. Flow of granular material through a circular orifice. Chemical Engineering Science, 4, 119-129.

Graham, D. P., Tait, A. R. & Wadmore, R. S. 1987. Measurement and prediction of flow patterns of granular solids in cylindrical vessels. Powder Technology, 50, 65-76.

Hancock, B. C., Mojica, N., St.John-Green, K., Elliott, J. A. & Bharadwaj, R. 2010. An investigation into the kinetic (sliding) friction of some tablets and capsules. International Journal of Pharmaceutics, 384, 39-45.

Handley, M. F. & Perry, M. G. 1968. Stresses in granular materials flowing in converging hopper sections. Powder Technology, 1, 245-251.

Humby, S., Tüzün, U. and Yu, A. B. 1998. Prediction of hopper discharge rates of binary granular mixtures. Chemical Engineering Science, 53, 483-494.

Iturrioz, I. and Morquio, A. 2007 Performance of the Discrete Element Method to represent the scale effect. Mechanics of Solids in Brazil

Jenike, A. W. 1967. Flow and storage of solids. Bulletin 123, Utah Engineering Station.

Job, N., Dardenne, A. and Pirard, J.-P. 2009. Silo flow-pattern diagnosis using the tracer method. Journal of Food Engineering, 91, 118-125.

Ketterhagen, W. R., Curtis, J. S., Wassgren, C. R., Hancock, B. C. 2008. Powder Technology, 179, 126-143.

Ketterhagen, W. R., Bharadwaj, R. and Hancock, B. C. 2010. The coefficient of rolling resistance (CoRR) of some pharmaceutical tablets. International Journal of Pharmaceutics, 392, 107-110.

Kepler, Johannes (1611), Strena seu de nive sexangula (The six-cornered snowflake), ISBN 978-1589880535

Kharaz, A. H., Gorman, D. A., Salaman, A. D. 2001. An experimental study of the elastic rebound of spheres. Powder Technology, 120, 281-291.

Kohring, G. A., Melin, S., Puhl, H., Tillemans, H. J. & Vermöhlen, W. 1995. Computer simulations of critical, non-stationary granular flow through a hopper. Computer Methods in Applied Mechanics and Engineering, 124, 273-281.

Kruggel-Emden, H., Sturm, M., Wirtz, S., Scherer, V. 2008. Selection of an appropriate time integration scheme for the discrete element method (DEM). Computers and chemical engineering, 32, 2263-2279.

Kvapil, R. K. 1965. Gravity flow of granular materials in hoppers and bins. International Journal of Rock Mechanics and Mining Sciences & Geomechanics Abstracts, 2, 25-34, IN3-IN8, 35-41.

Langston, P. A., Al-Awamleh, M. A., Fraige, F. Y. & Asmar, B. N. 2004. Distinct element modelling of non-spherical frictionless particle flow. Chemical Engineering Science, 59, 425-435.

Langston, P. A., Tüzün, U. & Heyes, D. M. 1994. Continuous potential discrete particle simulations of stress and velocity fields in hoppers: transition from fluid to granular flow. Chemical Engineering Science, 49, 1259-1275.

Langston, P. A., Tüzün, U. & Heyes, D. M. 1995. Discrete element simulation of granular flow in 2D and 3D hoppers: Dependence of discharge rate and wall stress on particle interactions. Chemical Engineering Science, 50, 967-987.

Lastufka, M. 2004. Grand Prix Racing – The science of fine pinewood cars. http://www.lastufka.net/lab/cars/why/mrollf.htm

Li, J., Langston, P. A., Webb, C. & Dyakowski, T. 2004. Flow of sphero-disc particles in rectangular hoppers--a DEM and experimental comparison in 3D. Chemical Engineering Science, 59, 5917-5929.

Litwiniszyn, J. 1971. Symposium Franco-Polonais, Warsaw

Malone, K. F. & Xu, B. H. 2008. Determination of contact parameters for discrete element method simulations of granular systems. Particuology, 6, 521-528.

Maw, N., Barker, J. R., Fawcett, J. N. 1976. The oblique impact of elastic spheres. Wear 38, 101-114

Medina, A., Andrade, J. & Treviño, C. 1998. Experimental study of the tracer in the granular flow in a 2D silo. Physics Letters A, 249, 63-68.

Michalowski, R. L. 1984. Flow of granular material through a plane hopper. Powder Technology, 39, 29-40.

Michalowski, R. L. 1987. Flow of granular media through a plane parallel/converging bunker. Chemical Engineering Science, 42, 2587-2596.

Morrison, H. L. and Richmond, O. 1976. Application of Spencer's ideal soil model to granular materials flow. Journal of Applied Mechanics, 5.

Mullins, W. W. 1972. Stochastic Theory of Particle Flow under Gravity. Journal of Applied Physics, 43, 665-678.

Mullins, W. W. 1974. Experimental evidence for the stochastic theory of particle flow under gravity. Powder Technology, 9, 29-37.

Natarajan, V. V. R., Hunt, M. L. & Taylor, E. D. 1995. Local measurements of velocity fluctuations and diffusion coefficients for a granular material flow. Journal of Fluid Mechanics, 304, 1-25.

Nedderman, R. M. 1988. The measurement of the velocity profile in a granular material discharging from a conical hopper. Chemical Engineering Science, 43, 1507-1516.

Nedderman, R. M., Tüzün, U., Savage, S. B. & Houlsby, G. T. 1982. The flow of granular materials--I: Discharge rates from hoppers. Chemical Engineering Science, 37, 1597-1609.

Nedderman, R. M., Tüzün, U., Savage, S. B. & Houlsby, G. T. 1982. The flow of granular materials--I: Discharge rates from hoppers. Chemical Engineering Science, 37, 1597-1609.

Nedderman, R. M. Statics and Kinematics of granular materials, Cambridge University Press 1992. ISBN 0 521 40435 5

Nedderman, R. M. 1995. The use of the kinematic model to predict the development of the stagnant zone boundary in the batch discharge of a bunker. Chemical Engineering Science 50 (6) 959-965

Ollangier, A., Doremus, P., Imbault, D. 2007 Contact particles calibration in a discrete element code. Laboratoire Sols, Solides, Structures, risque, Grenoble, France http://geo.hmg.inpg.fr/frederic/articles/GED_2007/Article-C.pdf

Ooi, J. Y., Chen, J. F. & Rotter, J. M. 1998. Measurement of solids flow patterns in a gypsum silo. Powder Technology, 99, 272-284.

Pariseau, W. G. 1969. Discontinuous velocity, fields in gravity flows of granular materials through slots. Powder Technology, 3, 218-226.

Pemberton, C. S. 1965. Flow of imponderable granular materials in wedge-shaped channels. Journal of the Mechanics and Physics of Solids, 13, 351-360.

Perry, M. G., Rothwell, E. & Woodfin, W. T. 1975. Model studies of mass-flow bunkers: I. Development of the radio pill technique for dynamic pressure and velocity measurements. Powder Technology, 12, 51-56.

Perry, M. G., Rothwell, E. & Woodfin, W. T. 1976. Model studies of mass-flow bunkers II. Velocity distributions in the discharge of solids from mass-flow bunkers. Powder Technology, 14, 81-92.

Rose, H. F. and Tanaka, T., (1959). Rate of discharge of granular materials from bins and hoppers. The Engineer 208, 465 (1959).

Rotter, J. M., Holst, J. M. F. G., Ooi, J. Y., Sanad, A. M. 1998. Silo pressure predictions using discrete–element and finite–element analyses. Philosophical Transactions of the Royal Society of London. Series A: Mathematical, Physical and Engineering Sciences, 356, 2685-2712.

Shampine, L. F. 1994. Numerical solution of ordinary differential equations. New York: Chapman and Hall.

Shinohara, K. & Golman, B. 2003. Density segregation of a binary solids mixture during batch operation in a two-dimensional hopper. Advanced Powder Technology, 14, 333-347.

Shinohara, K., Golman, B. & Nakata, T. 2001. Size segregation of multicomponent particles during the filling of a hopper. Advanced Powder Technology, 12, 33-43.

Sondergaard, R., Chaney, K. & Brennen, C. E. 1990. Measurements of Solid Spheres Bouncing Off Flat Plates. Journal of Applied Mechanics, 57, 694-699.

Song, C., Wang, P. & Makse, H. A. 2008. A phase diagram for jammed matter. Nature, 453, 629-632.

Spencer, A. J. M. 1964. A theory of the kinematics of ideal soils under plane strain conditions. Journal of the Mechanics and Physics of Solids, 12, 337-351.

Sperl, M. 2006. Experiments on corn pressure in silo cells – translation and comment of Janssen's paper from 1895. Granular Matter, 8, 59-65.

Steingart, D. A. and Evans, J. W. Measurements of granular flows in two-dimensional hoppers by particle image velocimetry. 2005. Chemical Engineering Science, 60, 1043-1051.

Thonton, C., Cummins, S. J., Cleary, P. W. 2011. An investigation of the comparative behaviour of alternative contact force models during elastic collisions. Powder Technology doi: 10.1016/j.powtec.2011.01.013

Tüzün, U., Houlsby, G. T., Nedderman, R. M. & Savage, S. B. 1982. The flow of granular materials--II Velocity distributions in slow flow. Chemical Engineering Science, 37, 1691-1709.

Vertlet, L. 1967. Computer experiments on classical fluids. I: Thermodynamical properties of Lennard-Jones molecules. Physical Review, 159 (1), 98-103.

Walker, D. M. 1966. An approximate theory for pressures and arching in hoppers. Chemical Engineering Science, 21, 975-997.

Walters, J. K. 1973. A theoretical analysis of stresses in axially-symmetric hoppers and bunkers. Chemical Engineering Science, 28, 779-789.

Walters, J. K. 1973. A theoretical analysis of stresses in silos with vertical walls. Chemical Engineering Science, 28, 13-21.

Wang, J., Yu, H.S., Langston, P., Fraige, F. 2011. Particle shape effects in discrete element modelling of cohesive angular particles, 13(1), 1-12

Yang, Z., Fryer, P. J., Bakalis, S., Fan, X., Parker, D. J., Seville, J. P. K. 2007 An improved algorithm for tracking multiple freely moving particles in a Positron Emission Particle Tacking system. Nuclear Instruments and Methods in Physics Research A, 577 585-594

Zhou, Y. C., Xu, B. H., Yu, A. B. & Zulli, P. 2002. An experimental and numerical study of the angle of repose of coarse spheres. Powder Technology, 125, 45-54.

Appendix 1

Rolling friction equation

The equation for the rolling friction was derived based on calculation on a website about the science of grand prix cars. http://www.lastufka.net/lab/cars/why/mrollf.htm

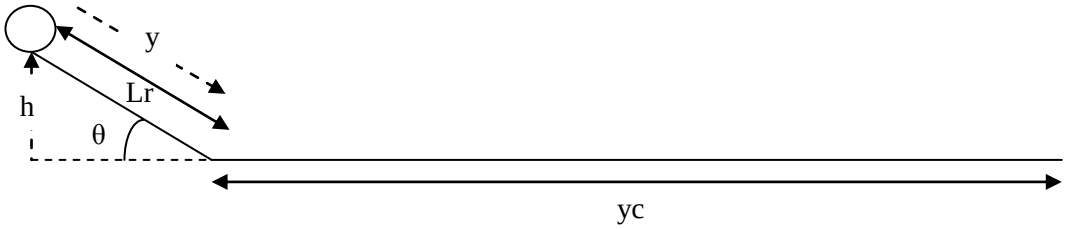

Consider a spherical particle of radius R rolling a distance L_r down a ramp inclined at an angle θ with an angular velocity ω given by

$$\omega = \frac{v}{R} \qquad \textbf{A1}$$

The particle reaches the bottom of the ramp and then rolls along a flat strip, coming to rest at a distance yc from the bottom of the ramp.

The position of the particle is raised to the centre of the wheel instead of along the track for simplicity.

$$h\,(y) = -\,(L_r - y)\sin\theta \qquad \textbf{A2}$$

where y is the distance measured from the top of the ramp surface.

The energy expended on the ramp in overcoming friction is

$$u\int_0^y N dy \qquad \textbf{A3}$$

where N is the force normal to the ramp, given by $mg\cos\theta$ and u is the non-dimensional rolling friction coefficient.

Therefore

$$u\int_0^y N dy = u\int_0^y mg\cos\theta dy = umgy\cos\theta \qquad \textbf{A4}$$

Let

$$D_f = umg \qquad \textbf{A5}$$

where D_f is the force of friction on the flat and let

$$D_r = umg\cos\theta = D_f\cos\theta \qquad \textbf{A6}$$

be the force of friction on the ramp.

The velocity of the particle at the bottom of the ramp can be obtained by considering the conservation of energy.

potential energy at bottom of ramp	=	gravitational potential energy	+	linear kinetic energy	+	rotational kinetic energy	+	work done by friction
$-mgL_r\sin\theta$	=	mgh	+	$\frac{mv^2}{2}$	+	$\frac{I\omega^2}{2}$	+	$D_r y$

A7

letting h = h (y) and substituting A1 and A2 into A7 gives

$$-mgL_r\sin\theta = -mg(L_r - y)\sin\theta + \frac{mv^2}{2} + \frac{Iv^2}{2R^2} + D_r y \qquad \textbf{A8}$$

let

$$M = m + \frac{I}{R^2} \quad \textbf{A9}$$

the inertial mass (the effective mass of a spinning object).

Then

$$-mgL_r \sin\theta = -mg\,(L_r - y)\sin\theta + \frac{Mv^2}{2} + D_r y \quad \textbf{A10}$$

simplifying gives

$$y\,(-mg\sin\theta - D_r) = \frac{Mv^2}{2} \quad \textbf{A11}$$

rearranging to make v the subject gives

$$v = \sqrt{\frac{2y\,(-mg\sin\theta - D_r)}{M}} \quad \textbf{A12}$$

The velocity of the sphere at the bottom of the ramp v_0 is obtained by setting $y = L_r$ to give

$$v_0 = \sqrt{\frac{2L_r\,(-mg\sin\theta - D_r)}{M}} \quad \textbf{A13}$$

Now consider the conservation of energy along the flat, some of which is lost due to the rolling friction between the particle and the surface of the flat.

Initial kinetic energy of particle at bottom of ramp	=	Kinetic energy of particle as it travels long the flat	+	Work done by rolling friction

$$\frac{Mv_0^2}{2} = \frac{Mv^2}{2} + D_f y \qquad \textbf{A14}$$

The work due to the rolling friction is the difference between the initial and final energy. With no external acceleration the expression can be solved for v (y).Rearranging A14 gives

$$v^2 = v_0^2 - \frac{2D_f y}{M} \qquad \textbf{A15}$$

$$\therefore v\,(y) = \sqrt{v_0^2 - \frac{2D_f y}{M}} \qquad \textbf{A16}$$

$$\therefore \int_0^{y_c} \frac{dy}{\sqrt{v_0^2 - \frac{2D_f y}{M}}} = \int_0^t dt \qquad \textbf{A17}$$

Integrating and simplifying gives

$$t\,(y_c) = \frac{v_0 M}{D_f} - \sqrt{\frac{v_0^2 M^2}{D_f^2} - \frac{2y_c M}{D_f}} \qquad \textbf{A18}$$

solving for y_c gives

$$y_c = v_0 t\,(y_c) - \frac{D_f t\,(y_c)^2}{2M} \qquad \textbf{A19}$$

substituting y_c into v (y) and simplifying to get v (t) gives

$$v(t) = v_0 - \frac{D_f t}{M} \quad \textbf{A20}$$

When the particle comes to rest the velocity is zero

$$v(t_c) = 0 \quad \textbf{A21}$$

and the time taken for the particle to travel from the bottom of the ramp to rest is given by

$$t_c = \frac{v_0 M}{D_f} \quad \textbf{A22}$$

The coasting distance is how far the particle travels in the coasting time. Therefore

$$y_c = y_c(t_c) = v_0 t_c - \frac{t_c^2 D_f}{2M} \quad \textbf{A23}$$

substituting A22 into A23 and simplifying gives

$$y_c = \frac{v_0^2 M}{2D_f} \quad \textbf{A24}$$

substituting equations A13 and A24 into A6 gives

$$u = \frac{-L_r \sin\theta}{L_r \cos\theta + y_c} \quad \textbf{A25}$$

where u is the non-dimensional coefficient of rolling friction.

Appendix 2

Table 3.3: Hitachi DZ-HS300E/E Major specifications

Charge-coupled device CCD	1/16th inch interlaced
Total No. Pixels	800,000
Total No. Effective Pixels	410,000
Lens	F1.8-3.2 f=2.2-55mm Filter diameter: 34mm Thread pitch: 0.5mm
Zoom	Optical 25x 100x-1200x with digital zoom added
Required minimum illumination	0.3 lx in low light mode
Viewfinder	0.2-inch colour TFT/~200,000 pixels
LCD monitor	2.7-inch colour TFT/~120,000 pixels
Electronic image stabiliser	Electronic type
Shutter speed	1/4 - 1/4000 seconds (movie)
Self-timer recording	Still recording only
Capacity of built in HDD	~8GB
Maximum recordable time	HDD ~110 mins (XTRA) ~180 mins (FINE) ~360 mins (STD)
Power consumption	3.2W (in FINE mode)
PC connection terminal x1	
Recording mode	Movie with sound
Recordable card	SD memory card
Dimensions (W x H x D)	61 X 90 x 135
Weight	435 g
Operating temperature (humidity)	0-40ºC (less than 80%) 0-30ºC when connected to PC
Various DVD's and SD memory cards can also be used with the video camera	

Appendix 3

Table 3.4: Phantom V710 colour high speed video camera specifications

Maximum fps	7500 full resolution, 1,400,000 max
Shutter speed	1μs
High resolution timing system	>20ns resolution
Internal shutter	Hands free/remote current session
Memory segmentation	Up to 63 segments
Built in memory RAM	8Gb
ISO (ISO-12232 SAT)	7000 Mono, 2100 colour
Pixel bit depth	8 and 12 bit
Dimensions (L,W,H) without lens	31.1, 14, 12.7
Weight	5.4kg
Power	90watts@24VDC
Operating temperature (humidity)	0ºC-40ºC (8%-80%)
10Gb Ethernet cable View recordings immediately via video-out port	